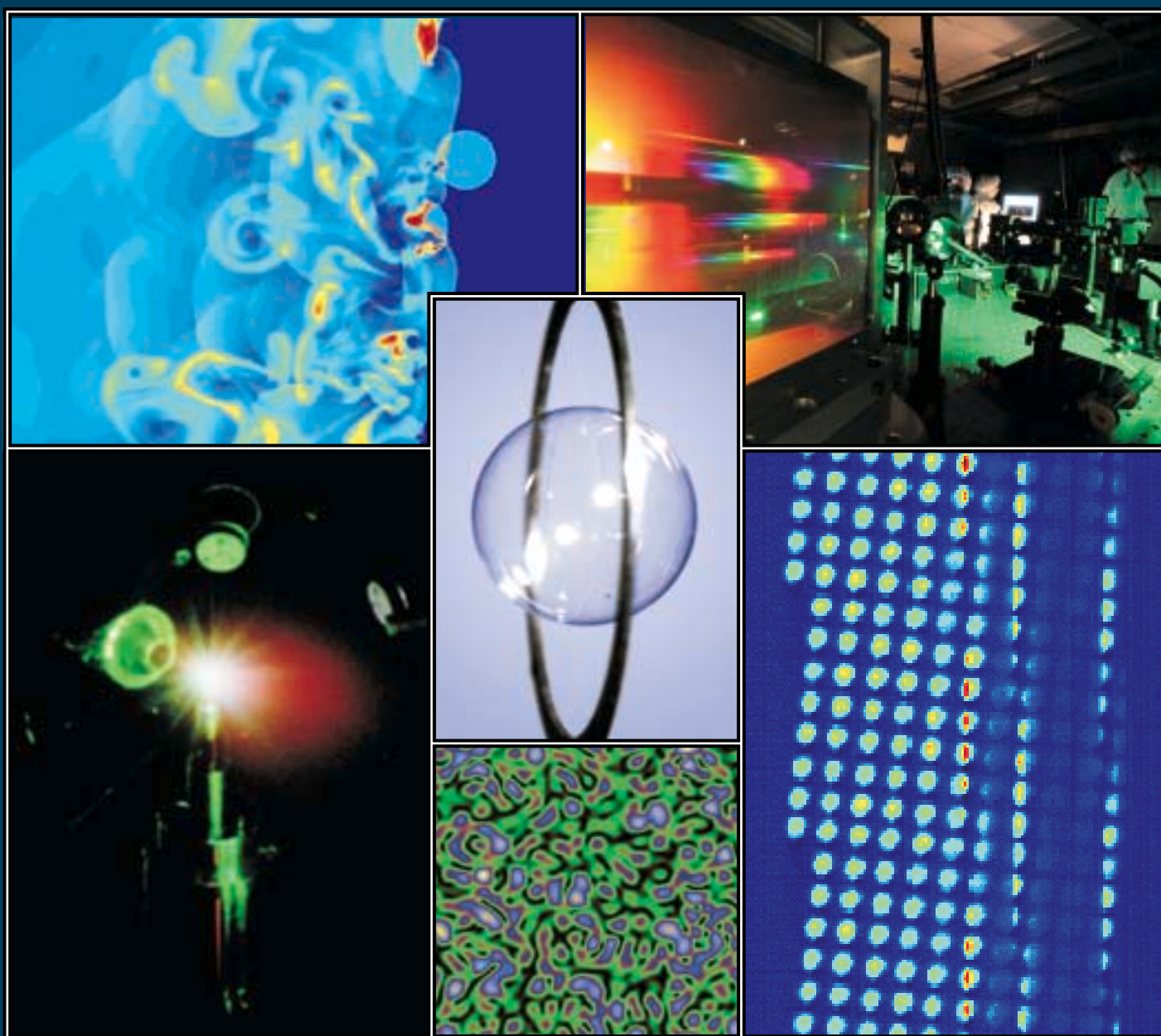# LLE 2002 Annual Report

October 2001 – September 2002

UR
LLE

Cover Photos

Upper Left: Foam layers have been the subject of much interest in inertial confinement fusion (ICF) target design. Target designs utilizing foam layers have been proposed for use at LLE on OMEGA, at the National Ignition Facility (NIF), and in reactor-scale ICF fusion facilities. All of these designs make use of laser pulses that launch multiple shocks, which must be well timed. Because a portion of the shock energy is used to homogenize the foam material, the porosity of the foam layer has the potential to change the shock speed and timing. This figure shows a plot of density for a shock propagating through a foam, simulated by the adaptive-mesh refinement code AMRCLAW, in collaboration with Adam Frank and Alexei Poludnenko of the UR's Department of Physics and Astronomy. AMRCLAW is being used to study the effects of porosity on shock timing for wetted-foam layers relevant to OMEGA and NIF target designs.

Lower Left: Thirty-three planar cryogenic target shots were taken on OMEGA in 2002. This photograph was taken on a target shot on which the equation of state (EOS) of liquid deuterium was investigated. These experiments use cryogenic target handling, advanced diagnostics, and the large, uniform laser spots available on OMEGA to provide important data to help clarify previous disagreements between theoretical models and laboratory experiments in this area.

Center: LLE scientists made significant progress in 2002 in developing experimental designs for direct-drive ignition experiments on the NIF. Recent work indicates that it may be possible to carry out high-performance direct-drive implosions on the NIF using the x-ray drive beam configuration. In preparation for future direct-drive experiments on the NIF, a NIF-scale prototype target assembly was demonstrated at LLE and is shown in this photograph. A 3.175-mm-diam spherical target was mounted onto a 125-mm-thick, 7.34-mm-outside-diam Ti ring using four spider silk strands. The target assembly had a resonant frequency of 125 Hz and was compatible with the NIF target chamber geometry.

Lower Center: This image of the on-target laser electric-field intensity was simulated by the parallel, three-dimensional, laser–plasma interaction (LPI) code pF3D. Lawrence Livermore National Laboratory (LLNL) developed the pF3D code primarily for modeling LPI in hohlraum plasmas. LLE scientists are adapting pF3D to simulate direct-drive conditions. The electric-field intensity shown in this figure displays the characteristic speckle pattern produced by distributed phase plates (DPP's). The individual maxima (or "hot spots") can exceed the average incident intensity by several times. Laser-driven parametric scattering instabilities such as stimulated Brillouin scattering (SBS) or decay instabilities like the two-plasmon decay (TPD) are preferentially driven in these hot spots due to the elevated light intensities.

Upper Right: A key element of future ultrahigh-intensity lasers is a stable, high-efficiency laser source capable of generating broad-bandwidth pulses that can be amplified by a high-power amplifier system. Optical parametric chirped-pulse amplification (OPCPA) is a novel laser concept that is well suited for this application. LLE's OPCPA system recently demonstrated one of the highest efficiencies for such systems currently available. The OPCPA concept is based in part on an LLE-invented concept: chirped-pulse amplification (CPA). The CPA idea created a revolution in laser technology by enabling the development of ultrahigh-intensity [i.e., $>10^{15}$ W (petawatt)] lasers. LLE and LLNL are currently collaborating on the development of large diffraction gratings required for petawatt lasers.

Lower Right: This photograph shows an array of capsule core images recorded on an NLUF experiment to study temperature and density gradients in implosion cores of indirect-drive targets. The experiment, carried out by a collaborative team headed by the University of Nevada, Reno, makes use of a new multispectral x-ray imaging diagnostic (MMI-2), which is based on an LLE-developed diagnostic. MMI-2 uses an array of pinholes coupled to a Bragg mirror to record numerous narrowband x-ray images spanning the 3- to 5-keV photon energy range. Each image of the core spans ~75 eV along the spectral axis. Groups of images are combined to produce line-based images. Continuum-based images can also be extracted from the data.

University of Rochester
Laboratory for Laser Energetics

DOE/SF/19460-468
January 2003

LLE 2002 Annual Report

October 2001 – September 2002

UR
LLE

Inertial Fusion Program and
National Laser Users' Facility Program

Contents

Executive Summary

The fiscal year ending September 2002 (FY02) concluded the fifth year of the first renewal of cooperative agreement DE-FC03-92SF19460 with the U.S. Department of Energy (DOE). The cooperative agreement was renewed for an additional five-year period in January 2003. This report—the final one for the first five-year cooperative agreement renewal—summarizes progress and research at the Laboratory for Laser Energetics (LLE), operation of the National Laser Users' Facility (NLUF), and programs concerning the education of high school, undergraduate, and graduate students during the year.

Inertial Confinement Fusion Research

LLE is the lead laboratory for research on direct-drive laser fusion for application and a gain demonstration on the National Ignition Facility (NIF). The NIF is currently under construction at the Lawrence Livermore National Laboratory (LLNL). We have emphasized a number of important areas this past year that should bear directly on the potential success of a direct-drive ignition and burn experiment on the NIF. "First Results from Cryogenic Target Implosions on OMEGA" (p. 49) describes initial results from direct-drive spherical cryogenic target implosions on the 60-beam OMEGA laser system. These experiments are part of the scientific base leading to direct-drive ignition implosions planned for the NIF. Results shown include neutron yield, secondary-neutron and proton yields, the time of peak neutron emission, and both time-integrated and time-resolved x-ray images of the imploded core. The experimental values are compared with 1-D numerical simulations. The target with an ice-layer nonuniformity of $\sigma_{rms} = 9$ μm showed 30% of the 1-D predicted neutron yield. These initial results are encouraging for future cryogenic implosions on OMEGA and the NIF.

Precision target fabrication is required for a successful ignition demonstration or quality cryogenic experiments on OMEGA. The development of polyimide shells suitable for inertial confinement fusion (ICF) cryogenic experiments on OMEGA is described in an article on target fabrication research beginning on p. 167. We have also determined the associated mechanical properties needed to define the processing conditions for operating the OMEGA Cryogenic Target Handling System (CTHS). Overall, polyimide targets offer a viable alternative to plasma polymer capsules currently in use. The principal advantages of the polyimide material are its high radiation resistance for tritium application and its excellent mechanical properties, which lessen the demanding specifications for the equipment needed to provide cryogenic targets. The single biggest limitation to using polyimide, based on PMDA-ODA chemistry, is the low permeability of the material at room temperature. Methods to increase the permeability are described.

The effects of textures on hydrogen diffusion in nickel was investigated (p. 125). Deuterium and tritium—isotopes of hydrogen—are the primary fuels for ICF, so determining and controlling their rate of diffusion through containment materials are important to the design of ICF facilities. When polycrystalline metals have texture, the preferential orientation of the metals affects hydrogen absorption and diffusion. Hydrogen permeation results show that there are significant differences among the three main textures of nickel membranes. Plating current density has a strong influence on texture development of nickel deposits. The texture of deposits can be easily manipulated by controlling plating conditions. In the experiments performed, textured Ni membranes were prepared using electrodeposition, and the effects of fabrication on their diffusion rates were determined.

In preparation for cryogenic experiments with tritium, we describe LLE's Tritium Recovery System, which is used to clean up the various exhaust streams and to control tritium activity in the gloveboxes (p. 25). This system is optimized for minimum environmental impact and maximum personnel safety. It uses the best-available technologies to extract tritium from inert gas streams in the elemental form. The rationale for the selection of various technologies is discussed in detail. This approach reduces the volumes of effluent that require treatment to the extent practical and also avoids the need to oxidize HT to HTO with its higher radiotoxicity, thereby contributing to safety.

Laser–plasma interactions (LPI) are potentially damaging sources of loss, conversion, and scattering of laser light on a target. We discuss results from pF3D—a parallel, three-dimensional LPI code developed at LLNL for modeling indirect-drive plasmas, which was recently modified for use under direct-drive conditions (p. 93). Unlike indirect drive, modeling direct drive requires simulation of inhomogeneous supersonic flows and density profiles that include a critical surface. The treatment of the critical surface is particularly problematic in codes employing the paraxial approximation for the light waves. The first results of the modified code included realistic simulations motivated by long-scale-length exploding-foil experiments conducted on LLE's 30-kJ, 351-nm, 60-beam OMEGA laser system and intended to represent future NIF direct-drive conditions.

Other LPI research (p. 181) included a linear model of anomalous stimulated Raman scattering from electron-acoustic waves in laser-produced plasmas. Stimulated Raman scattering (SRS) from heavily Landau-damped plasma waves and from electron-acoustic (EA) waves has recently been attributed to nonlinear Bernstein–Green–Kruskal (BGK) wave modes. These phenomena find a simpler, more comprehensive explanation in terms of linear waves in a locally flattened distribution function. The flattening arises from Landau damping of SRS plasma waves (in the case of anomalous SRS) or from perturbations at the EA phase velocity that are then maintained by SRS. Local flattening allows undamped linear EA waves to propagate, as in the original description of these waves by Stix.

"Time-Integrated Light Images of OMEGA Implosions" (p. 1) describes visible-light photographs of imploding OMEGA targets. These beautiful images are used to communicate LLE's mission to the general public. A closer examination of the images revealed a one-to-one correspondence between he bright spots in the image and each of the 60 laser beams. The intensity of the bright spots has been related to refraction and absorption in the plasma surrounding the imploding target. These photographs are now proving to be the basis of a new laser–plasma interaction diagnostic.

Theoretical work (p. 6) presents an analytical model of the nonlinear bubble evolution of single-mode, classical Rayleigh–Taylor (RT) instability at arbitrary Atwood numbers. The model follows the continuous evolution of bubbles from the early exponential growth to the nonlinear regime when the bubble velocity saturates.

The time dependence of electron thermal flux inhibition in direct-drive laser implosions is described beginning on p. 73. The article reports calculations of the nonlocal electron thermal conduction in direct-drive CH target implosions with square pulses by a one-dimensional Fokker–Planck solver combined with a hydrodynamic code. The results show that the electron thermal flux inhibition at the critical surface is time dependent, confirming that a larger flux limiter must be used for shorter-duration pulses. Also, the growth of the Rayleigh–Taylor instability for short-wavelength perturbations is shown to be smaller due to the longer density scale length.

Drive lasers, with known, single-mode modulations, produce nonuniform shocks that propagate into CH targets. The article beginning on p. 68 describes the perturbation of a target by nonuniformities in the drive laser. An optical probe beam is used to measure the arrival of these modulated shocks at various surfaces in the target. Experiments at moderate laser intensities ($\lesssim 10^{13}$ W/cm^2) exhibit behavior that is predicted by hydrocodes and simple scaling laws. This technique may be used to observe various dynamic effects in laser-produced plasmas and shock-wave propagation.

Experiments that control all aspects of nonuniformities in target manufacture, irradiation, and precision drive conditions are required to prepare for a direct-drive ignition experiment on the NIF. A recent experiment (p. 108) has tested the ability of a direct-drive ICF laser pulse shape to vary the adiabat within a target shell. A picket pulse was added to a pulse shape designed to implode a cryogenic shell of D$_2$ with a ratio α of internal pressure to Fermi-degenerate pressure of 5. The effect of a picket is to strengthen the shock in the outer portion of the shell so that the ablation interface has a large α and the fuel maintains its $\alpha = 5$, resulting in increased stability and improved capsule performance.

Implosion experiments with enhanced beam balance (p. 116) have implemented a new technique that determines the beam peak intensities at target chamber center on a full-power target shot by simultaneously measuring the x-ray flux produced by all 60 beams seen separated on a 4-mm-diam, Au-coated spherical target. Up to nine x-ray pinhole camera images are electronically recorded per shot from which beam-to-beam variations in peak intensity are determined, taking into account view angle and x-ray conversion efficiency. The observed variations are then used to correct the beam energies to produce a more-uniform irradiation. The authors present the results of implosion experiments with enhanced beam balance and comparisons to experiments with standard beam balance.

An investigation of the radial structure of shell modulations near peak compression of spherical implosions (p. 151) required the measurement of the structure of shell modulations at peak compression of implosions using absorption of titanium-doped layers placed at various distances from the inner surface of 20-μm-thick plastic shells filled with D^{3}He gas. The results show that the peak-compression, time-integrated areal-density modulations are higher at the inner shell surface, which is unstable during the acceleration phase of an implosion, than in the central part of the shell. The outer surface of the shell, which is unstable during the acceleration phase of an implosion, has a modulation level comparable to that of the inner shell surface.

Measurements of the neutron emission from ICF implosions provide important information about target performance that can be compared directly with numerical models. For room-temperature target experiments on OMEGA, the neutron temporal diagnostic (NTD), originally developed at LLNL, is used to measure the neutron burn history with high resolution and good timing accuracy. Since the NTD is mechanically incompatible with cryogenic target experiments because of the standoff required to remain clear of the Cryogenic Target Handling System, a new cryogenic-compatible neutron temporal diagnostic (cryoNTD) has been designed for LLE's standard ten-inch-manipulator (TIM) diagnostic inserters (p. 156). The instrument provides high-resolution neutron emission measurements for cryogenic implosions. The first experimental results of the performance of cryoNTD are presented and are compared to NTD measurements of room-temperature direct-drive implosions.

We have inferred the growth of target areal density near peak compression in direct-drive spherical target implosions with 14.7-MeV deuterium–helium^3 (D^{3}He) proton spectroscopy on the OMEGA laser system (p. 133). The target areal density grows by a factor of ~8 during the time of neutron production (~400 ps) before reaching 123 ± 16 mg cm^{-2} at peak compression in an implosion of a 20-μm-thick plastic CH target filled with 4 atm of D^{3}He fuel.

The use of carbon activation as a diagnostic for tertiary neutron measurements is reported beginning on p. 161. The yield of tertiary neutrons with energies greater than 20 MeV has been proposed as a method to determine the areal mass density of ICF targets. Carbon activation is a suitable measurement technique because of its high reaction threshold and the availability of high-purity samples. The isotope ^{11}C decays with a half-life of 20.3 min and emits a positron, resulting in the production of two back-to-back, 511-keV gamma rays upon annihilation. The present copper activation gamma-detection system can be used to detect tertiary-produced carbon activation because the positron decay of ^{11}C is nearly identical to the copper decay used in the activation measurements of 14.1-MeV primary deuterium–tritium (DT) yields. Because the tertiary neutron yield is more than six orders of magnitude lower than primary neutron yield, the carbon activation diagnostic requires ultrapure carbon samples, free from any positron-emitting contamination. Carbon purification, packaging, and handling procedures developed in recent years that reduce the contamination signal to a level low enough for OMEGA are presented. Potential implementation of a carbon activation system for the NIF is also discussed.

Experiments have been performed on OMEGA as part of the Stockpile Stewardship Program to investigate the equation of state of carbonized resorcinol foam, a porous material. A theory that models equation-of-state measurements of porous materials is presented beginning on p. 57. Using the impedance-matching method, the foam Hugoniot was calculated from the well-known equation of state of aluminum and from measured shock speeds over the range of 100 kbar to 2 Mbar.

Laser and Optical Materials Research

A reduced-autocorrelation phase plate design for OMEGA and the NIF has been demonstrated (p. 11). Direct-drive ICF for the NIF requires that the time-averaged rms laser nonuniformity be below the 1% level. The lower spatial frequencies of laser nonuniformity are dangerous to the hydrodynamic stability of the ICF target. A reduced autocorrelation phase design shifts the speckle energy up into the higher spatial frequencies where smoothing by spectral dispersion (SSD) and thermal smoothing in the target corona are most efficient. A novel design method for calculating a reduced correlation phase plate is presented, and the smoothing performance results are compared to a standard phase plate.

We have demonstrated precision spectral sculpting of broadband FM pulses amplified in a narrowband medium (p. 79). Amplification of broadband frequency-modulated (FM) pulses in high-efficiency materials such as Yb^{+3}:SFAP results in significant gain narrowing, leading to reduced on-target bandwidths for beam smoothing and to FM-to-AM conversion. Applying precision spectral sculpting, with both amplitude and phase shaping, before amplifying the broadband FM pulses in narrowband gain media compensated for these effects. The spectral sculpting, for center-line small-signal gains of 10^4, produced amplified pulses that have

both sufficient bandwidths for on-target beam smoothing and temporal profiles that have no potentially damaging amplitude modulation.

A new highly stable, diode-pumped, cavity-dumped, compact Nd:YLF regenerative amplifier (regen) of continuously shaped nanosecond pulses with a gain of ~10^9 for the front-end laser system of OMEGA is discussed beginning on p. 103. High output energy, long-term energy and temporal pulse shape stability, and high-quality beam profile have been demonstrated. Reliability, simplicity, modular design, and compactness are key features of this new diode-pumped regenerative amplifier.

To study the connection between the pulsed-laser energy absorption process and film damage morphology we used a SiO_2-thin-film system with absorbing gold nanoparticles (p. 30). We show that, at low laser fluences (below the threshold where damage can be detected optically), the probability of crater formation and the amount of the material vaporized are almost independent of the particle size. Inhomogeneities in the particle environment are responsible for variances in the observed particle/damage crater correlation behavior. In the proposed damage mechanism, the initial absorption is confined to the nanoscale defect. Energy absorbed by the defect quickly heats the surrounding matrix, changing it from a transparent to an absorbing medium, which creates a positive-feedback mechanism that leads to crater formation.

Advanced Technology

A series of thin, hydrogenated amorphous carbon films have been deposited using the saddle-field deposition configuration (p. 44). These films are a precursor to depositing tritiated films. Smooth, low-porosity films up to 15 μm thick and with densities up to 2 g/cm^3 have been grown. The internal structure of the films is featureless. Operating pressure plays an important role in modulating the film quality, growth rate, and density. Eliminating the substrate bias reduces negative ion incorporation in the films to help increase film density and improve film quality.

A theoretical investigation of a semiconductor quantum dot interacting with a strongly localized optical field, as encountered in high-resolution, near-field optical microscopy, is reported (p. 139). The strong gradients of these localized fields suggest that higher-order multipolar interactions will affect the standard electric dipole transition rates and selection rules. For a semiconductor quantum dot in the strong confinement

limit, Zurita-Sanchez and Novotny have calculated the interband electric quadrupole absorption rate and the associated selection rules, finding that the electric quadrupole absorption rate is comparable with the absorption rate calculated in the electric dipole approximation.

The femtosecond response of a freestanding LT-GaAs photoconductive switch is discussed beginning on p. 88. A novel, freestanding LT-GaAs photoconductive switch has a femtosecond response time. The switch was formed by patterning a 1-mm-thick layer of a single-crystal LT-GaAs into a 5-μm by 15-μm bar. The bar was separated from its GaAs substrate and placed across a gold coplanar transmission line deposited on a Si wafer. The switch was excited with 110-fs-wide optical pulses, and its photoresponse was measured with an electro-optic sampling system. Using 810-nm optical radiation, 470-fs-wide electrical transients (640-GHz bandwidth) were recorded.

An investigation of the electric-field-induced motion of polymer cholesteric liquid crystal flakes in a conductive fluid is described beginning on p. 83. Polymer cholesteric liquid crystal flakes suspended in a fluid with non-negligible conductivity can exhibit motion in the presence of an ac electric field. The platelets have a strong selective reflection, which is diminished or extinguished as the flakes move. Flake motion was seen within a specific frequency bandwidth in an electric field as low as 5 mV$_{rms}$/mm.

New results on the time-resolved dynamics of the superconducting-to-resistive transition in dc-biased epitaxial $YBa_2Cu_3O_{7-x}$ (YBCO) microbridges, excited by nanosecond-long current pulses, are reported beginning on p. 40. The resistive switching was induced by the collaborative effect of both the Cooper-pair bias current and the quasiparticle pulse excitation, which together always exceeded the bridge critical current, forming the supercritical perturbation. The experimental dynamics was analyzed using the Geier and Schön (GS) theory, which was modified to include the dc bias. The resistive state was established after a delay time t_d, in agreement with the GS model, which depended in a nonlinear way on both the excitation pulse magnitude and the bridge dc bias.

A great deal of interest has been generated by the discovery of superconductivity in hexagonal magnesium borides because of not only MgB_2's high critical temperature and current density but also its lower anisotropy, larger coherence length, and higher transparency of grain boundaries to current flow.

We have for the first time fabricated MgB_2 superconducting films on flexible substrates (p. 130). Our process to deposit these films on large-area foils (up to 400 cm^2) and, after processing, cut them into any shapes (e.g., stripes) with scissors or bend them multiple times showed that the films suffer no observed degradation of their superconducting properties.

We describe measurements of the time delay of the resistive-state formation in superconducting NbN stripes illuminated by single optical photons (p. 186). A 65($\pm$5)-ps time delay in the onset of a resistive-state formation in 10-nm-thick, 200-nm-wide NbN superconducting stripes exposed to single photons was measured. This delay in the photoresponse decreased down to zero when the stripe was irradiated by multiphoton (classical) optical pulses. The NbN structures were kept at 4.2 K, well below the material's critical temperature, and were illuminated by 100-fs-wide optical pulses. The time-delay phenomenon is explained within the framework of a model based on photon-induced generation of a hotspot in the superconducting stripe and subsequent, supercurrent-assisted resistive-state formation across the entire stripe cross section. The measured time delays in both the single-photon and two-photon detection regimes agree well with the Tinkham model's theoretical predictions of the resistive-state dynamics in narrow, ultrathin superconducting stripes.

OMEGA System Performance

Increased user demand was met in FY02 by expanding the available shot time during select weeks. Ten weeks were extended to four shot days by shooting one 8-h day, two 12-h days, and one 16-h day. This adjustment raised the total executed shots by 11%—from 1289 in FY01 to 1428 in FY02 (see Table 92.V, p. 193). Shaped-pulse cryogenic implosions highlighted the ongoing development of direct-drive cryogenic capability. A total of 21 spherical cryogenic D_2 targets were shot on OMEGA. Some of the cryogenic target shot time was devoted to characterization and system reliability improvements. Planar cryogenic target capability was also activated, and many shots were executed under LLE's Stockpile Stewardship Program (SSP) campaign. Highlights of other achievements and active projects as of the end of FY02 include the following:

- An IR streak camera with pulse-shape analysis software became a key operational tool to optimize pulse-shape performance. Combined with some changes to the control system for pulse-shape setup and upgrades to the regenerative oscillator hardware, the changes have resulted in dramatic improvements to delivered-pulse-shape performance.

- Infrared amplification occurs across a large variety of gain stages. By far, the highest gain stage is the regenerative (regen) amplifier, with 1×10^5 gain. One of the flash-lamp-pumped laser regens for OMEGA was replaced by a diode-pumped version that operates consistently without feedback stabilization. This diode-pumped laser improves pulse-shape performance. The remaining regens on OMEGA will be changed over to the new design in FY03.

- The distributed polarization rotator (DPR)—one of the key optics for beam smoothing on target—was modified for remote removal and reinstallation. The cassette-style removal system retracts the optic from the UV beamline into a protective housing. Having the capability to insert or remove these components improves flexibility for reconfiguring to indirect-drive setups. The full 60-beam complement of actuators will be completed early in FY03.

- The OMEGA laser is designed to provide a high degree of uniformity and flexibility in target illumination. The ability to impose a controlled asymmetric on-target irradiation pattern was developed and used extensively. This capability is used to benchmark multidimensional hydrodynamic simulations by imposing known nonuniform compression conditions on spherical targets. It is also used to modify laser-irradiation conditions for beam-to-beam x-ray yield balance.

- Modifications to the stage-A alignment sensors on OMEGA have streamlined an item of flexibility frequently exploited by LLE principal investigators. The backlighter driver alignment handoff to the OMEGA beamlines was re-engineered to expedite configuration setups that require the use of this source.

- Scientists and engineers from Lawrence Livermore National Laboratory along with LLE collaborators successfully implemented a green (second harmonic, 527 nm) target irradiation capability on one of the 60 OMEGA beams. This capability utilizes the existing OMEGA frequency-conversion crystals with the tripler detuned so that maximum 527-nm conversion is achieved.

- A revised set of direct-drive phase plates was designed and is being fabricated to further optimize irradiation uniformity for spherical implosions. These optics are going to be available in mid-FY03 and are expected to have improved smoothing characteristics in the mid-spatial-frequency range.

**National Laser Users' Facility
and External Users' Programs**

FY02 was a record year for external user activity on OMEGA. As reported in the section beginning on p. 194, a total of 698 target shots were taken on OMEGA for external users' experiments in FY02. This is the highest number of target shots ever taken by external users on OMEGA in a single year and represents a 16% increase in external user shots over FY01. The external user shots accounted for 49% of the total OMEGA target shots in FY02. External users' experiments were carried out by eight collaborative teams under the National Laser Users' Facility (NLUF) Program as well as collaborations led by scientists from Lawrence Livermore National Laboratory (LLNL), Los Alamos National Laboratory (LANL), Sandia National Laboratory (SNL), the Nuclear Weapons Effects Testing (NWET) Program, and the Commissariat à l'Énergie Atomique (CEA) of France.

1. NLUF Programs

FY02 was the second of a two-year period of performance for the eight NLUF programs approved for FY01–FY02 experiments. The eight NLUF campaigns received a total of 118 target shots on OMEGA in FY02.

The Department of Energy (DOE) issued solicitations in mid-FY02 for NLUF proposals to be carried out in FY03–FY04. DOE raised the NLUF funding allocation to $800,000 for FY03 and is expected to increase it to $1,000,000 for FY04 to accommodate the high level of interest shown in the use of OMEGA to carry out experiments of relevance to the National Nuclear Security Agency (NNSA) Stockpile Stewardship Program.

A total of 13 NLUF proposals were submitted to DOE for consideration for FY03–FY04 support and OMEGA shot allocation. An independent DOE Technical Evaluation Panel reviewed the proposals and recommended that up to nine of the proposals be approved for partial funding and shot allocation during FY03–FY04. Table 92.VI (p. 195) lists the successful proposals.

2. FY02 NLUF Experiments

The eight NLUF programs carried out in FY02 included

- *Atomic Physics of Hot, Ultradense Plasmas*

- *Determination of Temperatures and Density Gradients in Implosion Cores of OMEGA Targets*

- *Studies of the Fundamental Properties of High-Energy-Density Plasmas*

- *High-Spatial-Resolution Neutron Imaging of Inertial Fusion Target Plasmas Using Bubble Neutron Detectors*

- *Examination of the "Cone-in-Shell" Target Compression Concept for Asymmetric Fast Ignition*

- *Supernova Hydrodynamics on the OMEGA Laser*

- *Studies of the Dynamic Properties of Shock-Compressed FCC Crystals by* In-Situ *Dynamic X-Ray Diffraction*

- *Optical Mixing of Controlled Stimulated Scattering Instabilities (OMC SSI) on OMEGA*

3. FY02 LLNL OMEGA Experimental Program

The LLNL program on OMEGA in FY02 totaled 406 target shots for target ignition physics, high-energy-density science, and NWET (Nuclear Weapons Effects Testing). This represents a 30% increase over the target shots taken by LLNL on OMEGA in FY01. Highlights of these experiments include laser–plasma interactions, cocktail hohlraums, x-ray Thomson scattering, albedo experiments, hot hohlraums, gas-filled radiation sources, dynamic hohlraums, nonideal implosions, double-shell implosion experiments, charged-particle spectrometry in indirect-drive implosions, and IDrive.

4. FY02 LANL OMEGA Experimental Program

The LANL program on OMEGA in FY02 comprised a total of 132 target shots in support of cylindrical mix (CYLMIX) experiments; the Stockpile Stewardship Program; asymmetric direct-drive implosions; double-shell implosions; hydrodynamic jet experiments in collaboration with AWE, LLNL, and LLE; shock-breakout measurements in collaboration with SNL; and development of phase-2 nuclear diagnostics for the NIF.

5. FY02 SNL OMEGA Programs

SNL carried out a total of 24 target shots on the OMEGA laser in FY02 and also participated in several of the campaigns led by other laboratories. The SNL-led campaigns included indirect-drive ablator shock coalescence; indirect-drive ablator shock velocity at 50 Mbar; indirect-drive ablator x-ray burnthrough measurements; and time- and spatially resolved measurements of x-ray burnthrough and re-emission in Au and Au:Dy:Nd foils.

6. CEA

CEA had four half-day dedicated shot opportunities on OMEGA during FY02. A total of 19 target shots were provided for experiments including tests of the LMJ three-ring symmetry and other aspects of indirect-drive targets. In addition, CEA participated in collaborative experiments on imaging the neutron core emission using the CEA-provided neutron-imaging system (NIS).

Education at LLE

As the only major university participant in the National ICF Program, education continues to be an important mission for the Laboratory. Graduate students are using the world's most powerful ultraviolet laser for fusion research on OMEGA, making significant contributions to LLE's research activities. Twenty-four faculty from five departments collaborate with LLE's scientists and engineers. Presently 57 graduate students are pursuing graduate degrees at the Laboratory, and LLE is directly funding 38 University of Rochester Ph.D. students through the Frank J. Horton Fellowship Program. The re-search includes theoretical and experimental plasma physics, high-energy-density plasma physics, x-ray and atomic physics, nuclear fusion, ultrafast optoelectronics, high-power-laser development and applications, nonlinear optics, optical materials and optical fabrications technology, and target fabrication. Technological developments from ongoing Ph.D. research will continue to play an important role on OMEGA.

One hundred fifty-four University of Rochester students have earned Ph.D. degrees at LLE since its founding. An additional 81 graduate students and 23 postdoctoral positions from other universities were funded by NLUF grants. The most-recent University of Rochester Ph.D. graduates and their thesis titles are

Thomas Gardiner *Astrophysics Stellar Evolution*

Andrei Kanaev *Propagation of Laser Beams Smoothed by Spectral Dispersion in Long-Scale-Length Plasmas*

Feng-Yu Tsai *Engineering Vapor-Deposited Polyimides*

Approximately 46 University of Rochester undergraduate students participated in work or research projects at LLE this past year. Student projects include operational maintenance of the OMEGA laser system; work in laser development, materials, and optical-thin-film coating laboratories; programming; image processing; and diagnostic development. This is a unique opportunity for students, many of whom will go on to pursue a higher degree in the area in which they gained experience at the Laboratory.

In addition, LLE directly funds research programs within the MIT Plasma Science and Fusion Center, the State University of New York (SUNY) at Geneseo, and the University of Wisconsin. These programs involve a total of approximately 18 graduate and 23 undergraduate students from other universities.

For the past 12 years LLE has run a Summer High School Student Research Program (p. 190) in which this year 15 high school juniors spent eight weeks performing individual research projects. Each student is individually supervised by a staff scientist or an engineer. At the conclusion of the program, the students make final oral and written presentations on their work. The reports are published as an LLE report.

In 2002, LLE presented its sixth William D. Ryan Inspirational Teacher Award to Mr. James Keefer, a physics and chemistry teacher at Brockport High School. Alumni of our Summer High School Student Research Program were asked to nominate teachers who had a major role in sparking their interest in science, mathematics, and/or technology. This award, which includes a $1000 cash prize, was presented at the High School Student Summer Research Symposium. Mr. Keefer was nominated by Ms. Priya Rajasethupathy, a 2000 participant in the program.

Robert L. McCrory
Director

Time-Integrated Light Images of OMEGA Implosions

Introduction

Beginning in the spring of 2001, a series of remarkable photographs were taken that clearly show spherical target implosions as they might appear to the naked eye. Not surprisingly, the spherical target itself is not visible. The dominant feature in the photographs is the reflection of the laser beams hitting the target. These reflections appear as bright spots of light, organized in a very symmetric pattern.

These first experimental photographs, taken with aesthetics in mind more than quantitative measurement, were part of a series of visually appealing photographs of the inside of the target chamber. They represent a time-integrated picture of the target shot, from beginning to end (Fig. 89.1).

Upon closer scrutiny these photographs are found to contain useful and interesting information about the interaction of the laser beams with the plasma. The location and brightness of the spots as well as the number that are visible raised some questions, and the explanations were not intuitively obvious.
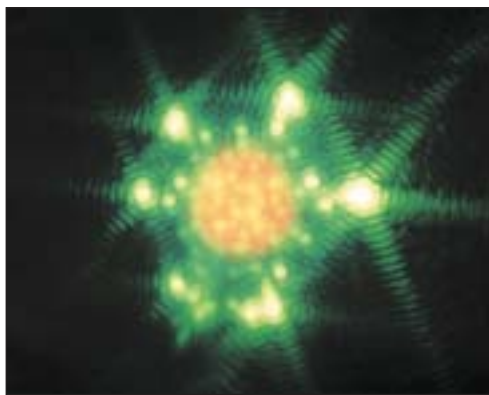
E11509

Figure 89.1
A time-integrated photograph showing a spherical target implosion. Beam reflections dominate the image and provide useful information about laser–plasma interactions. The concentric rings and spokes around each spot are camera artifacts. Note that almost 60 spots are visible, despite this being a picture of only one side of the target.

In light of this, an effort was made to make the photographs more quantitative. A UV transmission filter was added to the camera, and the film was switched from color to monochromatic, which allows a quantitative evaluation of the images. The filter passed 351-nm light, corresponding to the incident laser wavelength (Fig. 89.2).

E11510
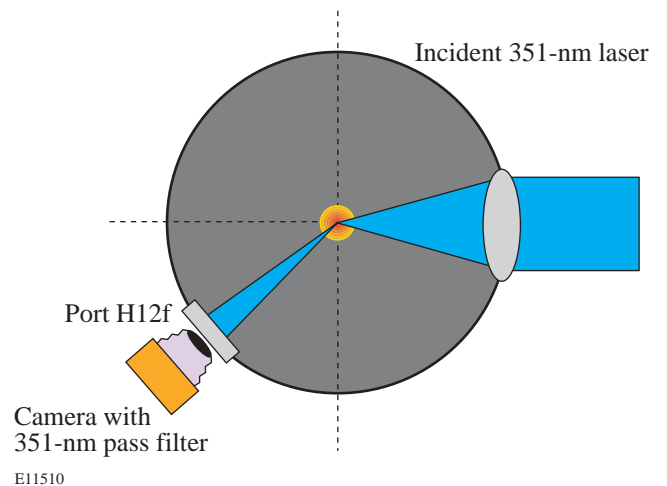
Figure 89.2
A rough layout of the experiment. Laser beams enter the target chamber and strike the spherical target. Reflections from the beams are seen and recorded by the camera in port H12f.

At the same time, in an effort to simulate the images, a program was written that performs ray tracing and absorption on the simulated laser beams. This program is designed to show whether the usual physical assumptions about laser–plasma interactions can explain the main features of the photographs. The simulation also adds time resolution to the images, explaining the photographs in a new light.

Experiment

The first photographs (Fig. 89.1) were taken on color film by a camera mounted on a port outside of the target chamber. This port is slightly off center from a symmetry axis and contributes to a small asymmetry in the photographs. The

camera is operated in an unconventional way by adding a number of magnifying objective lenses in series. This makes it difficult to know precisely what the actual *f* number and focal length are, particularly since the objectives were not designed for 351-nm light.

Several qualitative features, however, are apparent immediately, the most important being that each spot is very distinct and corresponds to one particular laser beam. The outer spots appear to be larger and brighter than the inner spots, and the target itself is washed out. The origin of the soft circular glow in Fig. 89.1 cannot be easily identified, but it does not accurately portray the size of the target. When color film is used, the area appears red. This may be light scattered from the quarter-critical surface due to either Raman scattering or the two-plasmon-decay instability.

Perhaps the most-interesting feature is that all 60 beam spots are visible, which, considering that the photograph shows only one side of the target, was not expected. It means that the beams behind the target are visible as well as the beams incident on the front of the target. This is especially striking considering that the target turns opaque long before the laser pulse reaches its maximum.

The addition of the UV filter and monochromatic film changed the look of the photographs (Fig. 89.3). The spots are much smaller and well defined, and several features are now

E11511

Figure 89.3
A UV photograph of the target implosion. This picture shows precise, small, clearly defined beam reflection spots. The outer spots suffer from over-exposure and camera artifacts, masking some important details.
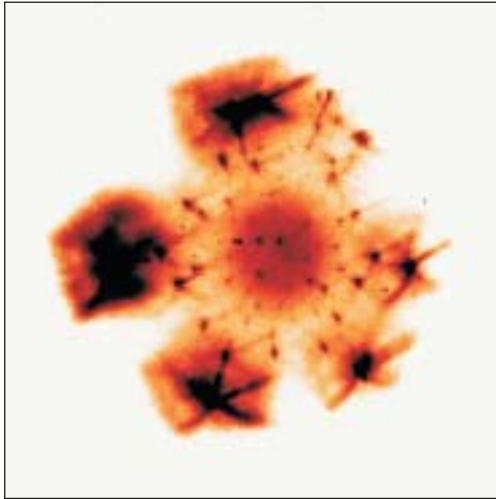
visible that had been obscured. Most notable is the streaking of the outer spots, indicating that, over the course of the shot, these spots move appreciatively from their original position in the radial direction. These outer spots also overexposed the film, showing that they contain much more energy than the inner spots, which are barely visible in places.

These monochromatic photographs were digitized for direct comparison to the output of the simulation.

Theory and Simulation

The index of refraction[1] of a plasma depends on the electron density, as shown in Eq. (1):

$$\mu = \sqrt{1 - n_e/n_c}\,, \tag{1}$$

where μ is the index of refraction, n_e is the electron density, and n_c is the critical density where the local plasma frequency equals the incident light frequency. A beam of light entering a region where $n_e > n_c$ will be reflected and/or absorbed at the critical-density surface. A ray of light passing through a plasma of density $n_e < n_c$ can be bent by refraction. Refraction depends on the direction of the ray and the direction and magnitude of the plasma density gradient.

This introduces the possibility that the laser beams striking the back of the target are refracted through the plasma into the camera lens. This is particularly likely since each laser spot is focused to be slightly bigger than the spherical target, with about 5% of the incident laser energy passing around the original target sphere. The beams striking the front of the target may be refracted and reflected as they approach the critical surface, again having their path bent into the camera lens. In this way, all 60 beams can become visible in the photograph.

The path of a ray through a medium of varying index of refraction is given by[2]

$$\frac{d}{ds}\left(\mu \frac{d\mathbf{x}}{ds}\right) = \nabla\mu \quad \text{(Snell's law)}, \tag{2}$$

where *s* is the path taken by the ray and **x** is the position vector along the path.

This equation can be rewritten in a form suitable for numerical simulation:

$$\mathbf{x}_{i+1} = \mathbf{x}_i + \frac{d\mathbf{x}_i}{ds}\,ds, \tag{3}$$

$$\mu_{i+1}\frac{d\mathbf{x}_{i+1}}{ds} = \mu_i\frac{d\mathbf{x}_i}{ds} + \nabla\mu(\mathbf{x})\,ds. \tag{4}$$

Given the plasma density as a function of position, Eqs. (1), (3), and (4) are sufficient to trace the path of a ray through a plasma.

The simulation takes as input a *LILAC*, 1-D plasma density profile, which gives density as a function of radius. One density profile is given for each time step of 100 ps. The plasma is assumed to be stationary while the light passes through it. Once the density is read in, the index of refraction and its gradient are calculated as a function of radius.

Rays are then traced through this plasma by incrementing *ds* in small steps. Each laser beam is assumed to be focused in such a way that it is slightly wider than the target and composed of many parallel rays. Because the beams are slightly wider than the target, some rays strike the target center and are reflected straight back, some miss and go straight by, and the rest are scattered through the 180° between those two extremes.

Rather than tracing every possible path, the program iteratively throws away all the rays that do not land on the camera lens. After identification of the exact region of the laser that strikes the lens, this region is traced with many rays, yielding higher resolution.

The ray tracing can be done in two dimensions since any single ray remains in its plane of incidence. This plane is then rotated to trace out the full shape of the spot in the image. This process is then repeated for each laser beam. The position of the camera and the position of each beam are read in from a text file, making it easy to switch the parameters for different target shots.

The result of this ray tracing is translated into image space by taking into account the angle at which each ray strikes the camera lens. By rotating each beam and taking into account the geometry of the tank, the full 2-D photograph is reconstructed (Fig. 89.4).

This process is repeated in 100-ps steps until 1200 ps = 1.2 ns have passed. By this point the laser beam has switched
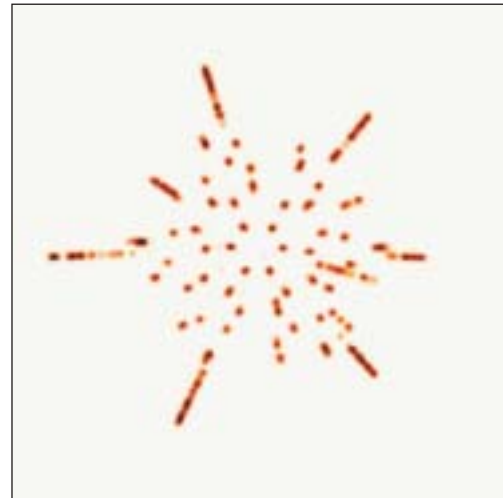
E11512

Figure 89.4
A simulated time-integrated image of an imploding target in the light of the 60 OMEGA beams driving it. This image shows the apparent locations of each beam reflection as seen from port H12f.

off and no longer contributes to the image. The separate time-resolved images are saved and compiled into one time-integrated image to compare with the experimental data.

The simulations also allow for laser light absorption, via inverse bremsstrahlung in the plasmas:

$$\frac{dI}{ds} = -kI, \tag{5}$$

where the absorption coefficient[3]

$$k = \frac{16\pi\,Z^2 n_e n_i e^6 \ln\Lambda(\upsilon)}{3c\upsilon^2\left(2\pi\,m_e k_b T\right)^{3/2}\left(1-\upsilon_p^2\big/\upsilon^2\right)^{1/2}}. \tag{6}$$

The radial intensity distribution of the beam is approximated with a gaussian, yielding data about the beam power as it strikes the camera lens.

Results

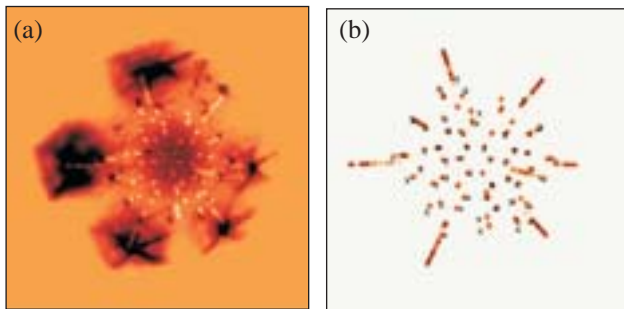The simulations are in good agreement with the experimental photograph (Fig. 89.5). The spots appear in the same symetrical pattern and show roughly the same relative levels of brightness.

The time resolution of the simulated images explains many of the features seen in the photograph. It is now apparent that most of the image is formed in the first 300 ps as a reflection from the solid sphere, with only a very thin plasma corona around it. As the plasma expands and fully forms, absorption takes over and the reflected intensity drops significantly. The outer beam spots seen in Figs. 89.1–89.4 are due to beams behind the target and their spill-over past the target. They suffer the least absorption as they are refracted into the camera. They are still clearly visible even at the end of the laser pulse, which explains the overexposure these spots produced on the film, as well as the outward radial displacement with time (Fig. 89.6).

Conclusion and Discussion

The simulation appears to explain most of the main features of the experimental photographs. The time resolution yields further information that was not available from the time-integrated photographs.

A careful comparison of the simulated images with the experimental photographs is limited by the setup of the camera. The camera has several objective lenses, making it difficult to know the exact path of the light through them. Port H12f of the target chamber is also not completely centered within the six beams surrounding it, leading to asymmetry in the photographs, which is duplicated in the simulation.

More importantly, however, an overall scaling problem was found with the camera. The exact scale of the experimental photographs is not completely certain. The photographs, taken on film, must be digitized in order to compare them with computer simulation.

In light of this, work has begun on a new camera designed to take quantitative digital photographs. This camera will be constructed of reflective optics, and the exact path of the light through it will be known. The simulation will be improved as well. When higher-quality images become available, it will be useful to add effects like plasma velocity and Doppler shifting to the code.

Further development of these ideas will likely address the potential of the new apparatus as a diagnostic for cryogenic target shots. The centering of the target, pointing of the beams, and early power-balance nonuniformities can all potentially be examined using this diagnostic. Further work will be devoted to determining the limits of the simulation and the experimental photographs.

E11513

Figure 89.5
The remarkable agreement between simulated and actual photographs is apparent in the overlay of the simulations on the experimental image. Small disagreements in position and intensity are expected since the simulation is based on a 1-D plasma profile. In (b) small x's have been drawn on the simulated image corresponding to experimental spot position. Several predicted spots seem to be obscured on the experimental photograph. It is expected that with better camera equipment and filtering, these spots will be visible.

E11514

Figure 89.6
A series of simulated photographs showing the image seen by the camera at (a) 100 ps, (b) 400 ps, (c) 800 ps, and (d) 1100 ps. Reflection dominates until ~300 ps, when absorption in the plasma grows to almost 100%. From this point on, beams that refract from behind the target form most of the image.

ACKNOWLEDGMENT

REFERENCES

1. F. F. Chen, *Introduction to Plasma Physics and Controlled Fusion*, 2nd ed., Vol. 1 (Plenum Press, New York, 1984).

2. M. Born and E. Wolf, in *Principles of Optics: Electromagnetic Theory of Propagation, Interference and Diffraction of Light*, 4th ed. (Pergamon Press, New York, 1970), pp. 121–123.

3. T. W. Johnston and J. M. Dawson, Phys. Fluids **16**, 722 (1973).

Analytical Model of Nonlinear, Single-Mode, Classical Rayleigh–Taylor Instability at Arbitrary Atwood Numbers

An interface between two fluids subject to an external force pointing from the heavier to the lighter fluid is hydrodynamically unstable[1] [Rayleigh–Taylor (RT) instability]. This instability plays an important role in astrophysics and inertial confinement fusion.[2] In the limit of small perturbation amplitudes η ($k\eta << 1$, where k is the perturbation wave number), the perturbations grow exponentially[1] $\eta \sim \eta_0 e^{\gamma t}$ with the growth rate $\gamma = \sqrt{A_T k g}$, where $A_T = (\rho_h - \rho_l)/(\rho_h + \rho_l)$ is the Atwood number, ρ_h and ρ_l are the densities of heavier and lighter fluids, respectively, g is the interface acceleration, and η_0 is the initial amplitude. As the amplitude becomes large enough ($k\eta \sim 1$), the interface can be divided into the spikes of the heavier fluid penetrating into the lighter fluid and bubbles of the lighter fluid rising into the heavier fluid. The exponential growth of the bubble amplitude changes to the linear-in-time growth[3–8] $\eta \sim U_b t$, where U_b is the bubble velocity. Such a transition is commonly referred to as a "nonlinear saturation," although, strictly speaking, only the bubble velocity saturates, not the amplitude. To describe the evolution of the perturbation after the saturation, two analytical approaches have been proposed in the past.[3–8] The weakly nonlinear theories[5] (up to the third-order accuracy in $k\eta$) capture only the initial slowing down of the exponential growth. The other approach uses an expansion of the perturbation amplitudes and conservation equations near the tip of the bubble[3,4,7,8] (or spike[8]) up to the second or higher order in the transverse coordinate. In the past, the second approach has been applied only to the fluid–vacuum interfaces ($A_T = 1$)[3,4,6–8] and has been shown to be in good agreement with numerical simulations and experimental data. In this article, the Layzer's theory will be extended to include finite density of the lighter fluid ($A_T \le 1$). We also report an exact solution of conservation equations (valid at the tip of the bubble) in the form of a convergent Fourier series.

First, we consider two irrotational, incompressible, inviscid fluids in two-dimensional (2-D) geometry. The fluids are subject to an external acceleration g pointing from the heavier to the lighter fluid. The y axis is chosen in the direction of the density gradient. The velocity potential ϕ in the absence of viscosity and thermal conduction obeys the Laplace equation

$$\Delta\phi = \partial_x^2\phi + \partial_y^2\phi = 0. \tag{1}$$

In addition, the function ϕ must satisfy the following jump conditions at the fluid interface $y = \eta(x,t)$:

$$\partial_t\eta + v_x^h\partial_x\eta = v_y^h, \tag{2}$$

$$[[v_y - v_x\partial_x\eta]] = 0, \tag{3}$$

$$\left[\left[\rho\left(\partial_t\phi + \frac{1}{2}v^2 + g\eta\right)\right]\right] = f(t), \tag{4}$$

where $[[Q]] = Q^h = Q^l$ (superscripts h and l denote the heavy- and light-fluid variables, respectively) and $f(t)$ is an arbitrary function of time. Equations (2) and (3) are derived from the mass-conservation equation and continuity condition for the velocity component normal to the fluid interface, and Eq. (4) is the Bernoulli's equation. Following Ref. 4, we expand Eqs. (2)–(4) and the interface amplitude η near the tip of the bubble [localized at the point $\{x,y\} = \{0,\eta(0,t)\}$] to the second order in x, $\eta = \eta_0(t) + \eta_2(t)x^2$. The function $\eta_2(t)$ is related to the bubble curvature R as $R = -1/(2\eta_2)$. To satisfy boundary conditions (2)–(4) (six equations), we need six unknowns. Thus, in addition to the functions $\eta_0(t)$, $\eta_2(t)$, and $f(t)$, the velocity potential must contain three unknowns. We write the velocity potential near the bubble tip in the following form:

$$\phi^h = a_1(t)\cos(kx)e^{-k(y-\eta_0)}, \tag{5}$$

$$\phi^l = b_1(t)\cos(kx)e^{k(y-\eta_0)} + b_2(t)y. \tag{6}$$

The form of the light-fluid potential [Eq. (6)] will be verified later using the results of numerical simulations. Substituting Eqs. (5) and (6) into the boundary conditions (2)–(4) and

expanding the latter near the bubble tip gives

$$\dot{\eta}_2 = -\dot{\eta}_0 \frac{k}{2}(k + 6\eta_2), \tag{7}$$

$$\ddot{\eta}_0 \frac{k^2 - 4A_T k\eta_2 - 12A_T \eta_2^2}{2(k - 6\eta_2)}$$

$$+ \dot{\eta}_0^2 k^2 \frac{(4A_T - 3)k^2 + 6(3A_T - 5)k\eta_2 + 36A_T \eta_2^2}{2(k - 6\eta_2)^2}$$

$$+ A_T g\eta_2 = 0. \tag{8}$$

Equation (7) can be integrated directly. The result, assuming initial sinusoidal perturbation with amplitude $\eta_0(0)$, takes the form

$$\eta_2 = -\frac{k}{6} + \left[\frac{k}{6} - \eta_0(0)\frac{k^2}{2}\right]e^{-3k[\eta_0 - \eta_0(0)]}. \tag{9}$$

Furthermore, substituting Eq. (9) into Eq. (8), the latter can be integrated to give an analytic expression for the bubble velocity. This expression is very lengthy, however, and will be reported elsewhere. In practice, one can easily calculate the bubble amplitude by solving the system (7)–(8) using, for example, the *Mathematica* software package.[9] Next, we obtained an asymptotic solution for the bubble velocity by taking the limit of $t \to \infty$ in Eqs. (9) and (8). This gives

$$\eta_2 \to -\frac{k}{6}, \quad U_b \to \sqrt{\frac{2A_T}{1 + A_T}\frac{g}{3k}}. \tag{10}$$

The last equation agrees with the prediction of the drag–buoyancy model.[6] Solution of Eq. (8) provides a continuous bubble evolution from the linear to the nonlinear regime, while the drag–buoyancy model calculates only the asymptotic behavior.

Next, we verify the choice of the velocity potential in the light fluid [Eq. (6)] by comparing the velocity profiles obtained from Eq. (6) and full numerical simulation. For such purpose, we first calculate the coefficients b_1 and b_2 as functions of time:

$$b_1 = \dot{\eta}_0 \frac{6\eta_2 + k}{k(k - 6\eta_2)}, \quad b_2 = \frac{12\dot{\eta}_0 \eta_2}{6\eta_2 - k}. \tag{11}$$

Since $\eta_2(t \to \infty) = -k/6$, then $b_1 \to 0$ and $b_2 \to \dot{\eta}_0$. Then, substituting Eq. (11) into the definition of the light-fluid velocity,

$$v_x^l = -b_1 k \sin(kx)e^{k(y - \eta_0)}$$

and

$$v_y^l = b_1 k \cos(kx)e^{k(y - \eta_0)} + b_2,$$

we find that asymptotically, the light-fluid velocity component parallel to the acceleration becomes flat near the tip of the bubble (no x or y dependence), and the transverse velocity component in that region goes to zero. To confirm this result, we performed a 2-D simulation using an incompressible, inviscid Eulerian code. Figure 89.7 shows the velocity profiles (v_x and v_y) at two different times, calculated using results of simulations for the fluid interface with $A_T = 0.4$ and the initial amplitude of velocity perturbation $v_0 = 0.01\sqrt{g\lambda}$, where λ is the perturbation wavelength. The vertical lines show the interface between the heavier and lighter fluids (the heavier fluid is on the right side of the lines). Velocity v_y is plotted at the position of the bubble center ($x = 0$), and the transverse velocity v_x is plotted at $x = 0.02\lambda$ [$v_x(x = 0) = 0$ at all times]. When the
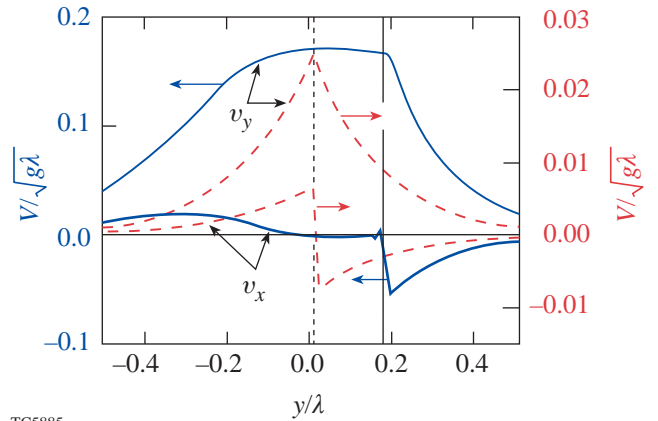
TC5885

Figure 89.7
Velocity profiles at two different times calculated using results of a 2-D simulation. Dashed lines represent profiles in the linear regime, and solid lines correspond to velocities in the nonlinear regime.

perturbations are in the linear regime ($k\eta_0 \ll 1$), the velocity decays exponentially from the interface toward the lighter and heavier fluids (dashed lines). As the bubble amplitude becomes nonlinear ($k\eta_0 > 1$), the longitudinal velocity v_y in the light fluid flattens out near the bubble tip and the transverse velocity goes to zero (solid lines), in agreement with the results of Eq. (11).

Applying the model to the Richtmyer–Meshkov (RM) instability, we take the limit of $g \to 0$ in Eq. (8). The asymptotic bubble velocity in this case becomes

$$U_{RM} \to \frac{3 + A_T}{3(1 + A_T)} \frac{1}{kt}. \tag{12}$$

In his original paper,[4] Layzer takes only the first harmonic as a solution of the Laplace equation (1). Later, several attempts have been made to construct an exact solution for the case of $A_T = 1$ near the tip of the bubble, writing the solution of Eq. (1) as a Fourier series:[3]

$$\phi = \sum_{l=1}^{\infty} a_l e^{ilkx - lky}. \tag{13}$$

It can be shown,[3] however, that keeping the first two terms in the expansion and applying the boundary conditions up to the fourth order in x leads to an imaginary component in the solution for the asymptotic bubble velocity. To overcome this difficulty, Refs. 3 have suggested keeping the bubble curvature R as a free parameter of the problem, limiting the values of R by the convergence condition of series (13). We propose a different approach to construct an exact solution that is valid near the bubble tip. It can be shown that writing the velocity potential in the form

$$\phi^h = \sum_{l=0}^{\infty} a_{2l+1} \cos[(2l+1)kx] e^{-(2l+1)k(y-\eta_0)}, \tag{14}$$

$$\phi^l = \sum_{l=0}^{\infty} b_{2l+1} \cos[(2l+1)kx] e^{(2l+1)k(y-\eta_0)} + b_2 y \tag{15}$$

leads to a real value of bubble velocity in all approximation orders. Such an expansion requires no additional free parameters to provide convergence for the solution. Figure 89.8 shows plots of the first four coefficients a_{1-7} as functions of

time for the case of $A_T = 1$. Observe that coefficients a_l decay exponentially with l, satisfying the convergence condition. Next, we calculate asymptotic values of η_2 and U_b using solution (14)–(15). The result is

$$\eta_2(t \to \infty) = -\frac{k}{4.88}, \quad U_b(\infty) = 1.025 \sqrt{\frac{2 A_T}{1 + A_T} \frac{g}{3k}}. \tag{16}$$

The convergence of solution (14)–(15) is very fast. Keeping only two terms in each sum in ϕ^h and ϕ^l gives the solution for η_2 and U_b within 99.5% accuracy. Remarkably, the values given in Eq. (16) are in agreement with the results of Ref. 3 (for $A_T = 1$), where the authors introduced a free parameter R. This parameter was chosen at the edge point of the region where the Fourier series (13) converges.
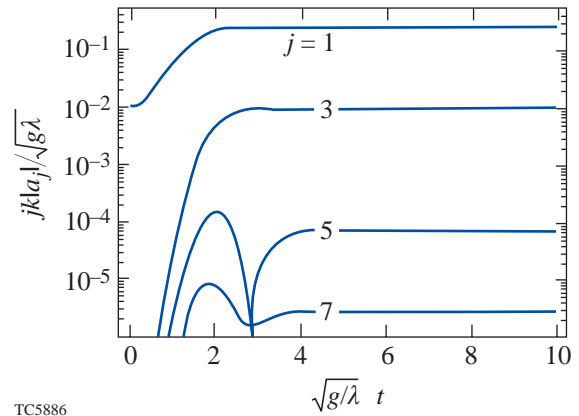
Figure 89.8
Coefficients a_1–a_7 of the Fourier series (14) for $A_T = 1$.

To validate the analysis described above, we compare the results of the model with numerical simulations. Figure 89.9 shows the bubble evolution for the case of $A_T = 0.1$ and $A_T = 0.4$. We start the simulation by imposing a velocity perturbation with amplitude $v_0 = 0.01\sqrt{g\lambda}$. Solid lines represent the solution of Eq. (8); solid dots ($A_T = 0.4$) and solid squares ($A_T = 0.1$) correspond to the results of simulations. Good agreement between theory and simulations confirms the accuracy of the model. Next, we comment on a possibility of applying the Layzer-type analysis to study evolution of the spikes. Reference 8 has shown that such an analysis gives quite a reasonable agreement with simulations for the case of $A_T = 1$. The appropriate velocity potential for the spikes at $A_T < 1$ in the Layzer-type model has the form

$$\phi^h = a_1 \cos(kx)e^{-k(y-\eta_0)} + a_2 y,$$

$$\phi^l = b_1 \cos(kx)e^{k(y-\eta_0)}.$$

Substituting the above expressions into Eqs. (2)–(4) and expanding the latter until the second order in x gives the evolution equations that can be obtained from Eqs. (7) and (8) by substituting $\eta \to -\eta$, $A_T \to -A_T$, and $g \to -g$. Taking the limit of $t \to \infty$, the asymptotic spike velocity becomes

$$U_s = \sqrt{2A_T/(1-A_T)(g/3k)}.$$

The last formula agrees with the prediction of the drag–buoyancy model.[6] Simulations, however, show that the spike velocity for the interfaces with $A_T > 0.1$ does not saturate to a constant value. Figure 89.9 shows the spike amplitudes calculated using the simulation (open circles for $A_T = 0.4$ and open squares for $A_T = 0.1$) and the results of the model (dashed lines). As seen from the results of the simulations, the spike velocity for $A_T > 0.1$ keeps growing linearly in time, even after perturbations become nonlinear. This is caused by the formation of vortices in the proximity of the spike tip. If the Atwood number is not too small, vortices move with the spike, modifying its velocity field and accelerating the spike into the light fluid. Thus, to describe the spike in the nonlinear regime, the velocity potential must be modified to include evolution of the vortices. This is a subject of current research.

TC5887
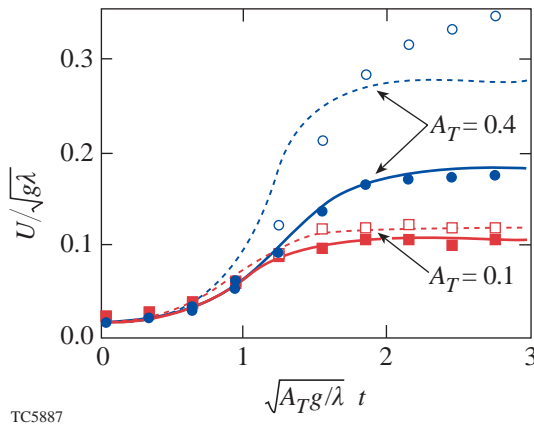
Figure 89.9
Bubble (solid lines, solid circles and squares) and spike (dashed lines, open circles and squares) velocities calculated using the potential model (lines) and numerical simulation (circles and squares).

The procedure described above for the 2-D flow can be applied to analyze the bubble evolution in 3-D geometry. Taking the z axis in the direction of the density gradient and assuming cylindrical symmetry of the bubble, the velocity potential in the heavy and light fluids takes the form $\phi^h = a(t)J_0(kr)e^{-kz}$, $\phi^l = b_1(t)J_0(kr)e^{kz} + b_2(t)z$, where $J_0(x)$ is the Bessel function of zero order. Expanding the velocity potential and the jump conditions across the fluid interface up to the second order in r yields the following system:

$$\eta_2 = -\frac{k}{8} + \left[\frac{k}{8} + \eta_2(0)\right]e^{-2k[\eta_0-\eta_0(0)]}, \qquad (17)$$

$$\ddot{\eta}_0 \frac{k^2 - 4A_T k\eta_2 - 32A_T\eta_2^2}{4(k-8\eta_2)}$$

$$+ \dot{\eta}_0^2 k^2 \frac{(5A_T-4)k^2 + 16(2A_T-3)k\eta_2 + 64A_T\eta_2^2}{8(k-8\eta_2)^2}$$

$$+ A_T g\eta_2 = 0. \qquad (18)$$

The asymptotic bubble velocity and η_2 derived from the system (17)–(18) take the form

$$\eta_2(t \to \infty) = -k/8,$$

$$U_b^{3\text{-D}}(\infty) = \sqrt{2A_T/(1+A_T)(g/k)}.$$

For the RM case ($g = 0$), the asymptotic bubble velocity becomes $U_{\text{RM}}^{3\text{-D}} = 2/(1+A_T)/(kt)$. Repeating calculations by keeping higher harmonics in the expansion

$$\phi^h = \sum_{l=0}^{\infty} a_{2l+1} J_0\big[(2l+1)kr\big]e^{-(2l+1)kz},$$

$$\phi^l = \sum_{l=0}^{\infty} b_{2l+1} J_0\big[(2l+1)kr\big]e^{(2l+1)kz} + b_2 z,$$

the asymptotic bubble velocity converges to

$$U_b^{3\text{-}D} \sim 1.02 \sqrt{\frac{2\,A_T}{1+A_T}\frac{g}{k}}, \quad \eta_2 \to -\frac{k}{6.7}. \tag{19}$$

For $A_T = 1$, these values are close to the results of Ref. 3, where authors have found the following values: $U_b = 0.99\sqrt{g/k}$ and $\eta_2 = -k/6.4$.

In summary, the nonlinear analytical model of the classical single-mode RT instability at arbitrary Atwood numbers was developed. The model gives a continuous bubble evolution from the exponential growth to the nonlinear regime, where the bubble velocity saturates at

$$U_b^{2\text{-}D} = \sqrt{2\,A_T/(1+A_T)(g/3k)}$$

and

$$U_b^{3\text{-}D} = \sqrt{2\,A_T/(1+A_T)(g/k)}.$$

The results of the model agree very well with the numerical simulations and predictions of the drag–buoyancy model.[6]

ACKNOWLEDGMENT

REFERENCES

1. Lord Rayleigh, in *Scientific Papers* (Cambridge University Press, Cambridge, England, 1900), Vol. II.

2. B. A. Remington *et al.*, Phys. Plasmas **7**, 1641 (2000); J. D. Lindl, *Inertial Confinement Fusion: The Quest for Ignition and Energy Gain Using Indirect Drive* (Springer-Verlag, New York, 1998).

3. N. A. Inogamov and S. I. Abarzhi, Physica D **87**, 339 (1995); S. I. Abarzhi, Phys. Rev. E **59**, 1729 (1999).

4. D. Layzer, Astrophys. J. **122**, 1 (1955).

5. G. B. Whitham, *Linear and Nonlinear Waves*, Pure and Applied Mathematics (Wiley, New York, 1974), p. 473; J. W. Jacobs and I. Catton, J. Fluid Mech. **187**, 329 (1988); M. J. Dunning and S. W. Haan, Phys. Plasmas **2**, 1669 (1995).

6. D. Oron *et al.*, Phys. Plasmas **8**, 2883 (2001); U. Alon *et al.*, Phys. Rev. Lett. **74**, 534 (1995); G. Dimonte, Phys. Plasmas **7**, 2255 (2000); G. Dimonte and M. Schneider, Phys. Fluids **12**, 304 (2000).

7. K. O. Mikaelian, Phys. Rev. Lett. **80**, 508 (1998).

8. Q. Zhang, Phys. Rev. Lett. **81**, 3391 (1998).

9. S. Wolfram, *The Mathematica Book*, 3rd ed. (Wolfram Media/Cambridge University Press, 1996).

A High-Pass Phase Plate Design for OMEGA and the NIF

Introduction

The direct-drive configuration utilized in inertial confinement fusion (ICF)[1,2] driven by high-powered lasers requires target illumination with a high degree of uniformity, especially in the lower spatial-frequency modes. Nonuniformity in laser irradiation seeds the Rayleigh–Taylor hydrodynamic instability, which consequently degrades target performance.[3–9] Various techniques, such as two-dimensional (2-D) smoothing by spectral dispersion (SSD),[10–13] distributed phase plates (DPP's),[14,15] polarization smoothing (PS),[16–22] and multiple beam overlap, are employed on the OMEGA laser[16,23,24] and will be employed on the National Ignition Facility (NIF) to improve the on-target irradiation uniformity and reduce the laser imprint. The nonuniformity in the lower frequencies (or spherical-harmonic ℓ modes) is particularly dangerous in ICF implosions due to hydrodynamic instabilities that develop during the longer imprinting periods associated with these modes. In addition, these low-order modes are also the most difficult to smooth with the aforementioned methods.

Reduced-autocorrelation phase plates were proposed to reduce the power spectrum of the low-ℓ modes and were designed with discrete phase elements of fixed spatial aperture.[25] These phase plates were calculated by changing selected phase elements in order to minimize the local autocorrelation function of the near-field phase term; hence the name. The reduced-autocorrelation phase plates, calculated by this method, were able to reduce the nonuniformity in the lower-ℓ modes by only a modest average factor of 2 without any near-field phase aberrations. In addition, due to the discrete nature of the phase plate elements, the envelope of the far-field intensity pattern was not controllable (except by changing the shape/size of the discrete phase elements).

The novel and improved design technique presented in this article calculates continuous versions of these specialized phase plates by directly manipulating the power spectrum of the far-field intensity pattern. These new designs are dubbed "high-pass phase plates" to distinguish them from their predecessors and to emphasize the method of directly manipulating

the spectrum. The novel phase plate design technique calculates continuous phase plates that produce well-defined far-field intensity envelopes with a high degree of azimuthal symmetry and a controllable power spectrum. The high-pass phase plates are able to reduce the nonuniformity in the lower-ℓ modes by average factors of 4 to 10 (depending on the type of high-pass filter employed) without any near-field phase aberrations. The novel plate design technique presented can also be applied to standard phase plates because it requires no control of the far-field power spectrum. In addition, this technique is computationally efficient, and the calculation speeds are improved by two orders of magnitude over current methods.

The performance of high-pass phase plates is significantly affected by any near-field phase aberrations present on a high-powered ICF laser beam. If the phase aberration is strong enough, the resultant far-field intensity's power spectrum tends toward that produced by a standard continuous phase plate. Simulations of the far-field intensity pattern with applied phase aberrations (either measured or simulated), using the code *Waasikwa'*,[24] shows that the lower-ℓ-mode range can still benefit from these high-pass phase plates. High-pass phase plate designs for both OMEGA and the NIF can realize a reduction of about a factor of $\sqrt{2}$ to 2 in nonuniformity over the lower-ℓ-band range ($11 \leq \ell \leq 25$) in the presence of typical laser system phase aberrations.

In the following sections, an overview of the novel phase plate design technique will be presented. Next, standard phase plate designs will be compared to high-pass designs for both OMEGA and the NIF. The affect of near-field phase aberrations will then be discussed followed by the improvement realized in the lower-ℓ-band range in the presence of near-field phase aberrations.

A Novel Phase Plate Design Technique

A novel phase plate design technique was developed to calculate continuous phase plates that produce a well-defined far-field intensity envelope with a high degree of azimuthal symmetry and a controllable power spectrum and is incorpo-

rated in a code called *Zhizhoo'*.[26] *Zhizhoo'* can be configured to calculate a continuous near-field phase plate that produces a speckled far-field spot who's envelope matches almost any well-behaved function and has the ability to control the power spectrum of the far-field intensity in order to produce a speckled pattern with reduced nonuniformity in the low-order modes. A phase plate that reduces the nonuniformity in the low-order modes is referred to as a high-pass phase plate. The technique is computationally efficient and can complete a calculation in 10 to 20 min running on an SGI Origin 2000 machine with eight parallel processors.

The goal of the novel phase plate design technique is to produce a diffractive phase optic that varies slowly across the whole beam aperture and possesses no sharp discontinuities or phase anomalies. Simulated annealing is the current technique used at LLE to calculate continuous phase plates, but it tends to be computationally inefficient and takes tens of hours to complete a calculation.[14,15] The novel phase plate design technique wraps an additional iterative process around a standard phase-retrieval technique that is able to control the spatial and spectral properties of the speckled far-field intensity pattern while calculating a continuous phase plate. Two user-supplied design functions drive the algorithms to produce the required phase plate: the near-field beam intensity $\left|E_0(x_{nf}, y_{nf})\right|^2$ and the far-field intensity envelope target $I_{ff_{target}}(x_{ff}, y_{ff})$, where (x_{nf}, y_{nf}) and (x_{ff}, y_{ff}) are the near-field and far-field coordinate systems, respectively.

1. Standard Phase-Retrieval Technique

The core or central algorithm of the novel phase plate design technique presented here is based on a standard phase-retrieval technique known as the error-reduction scheme; the error is guaranteed to never increase after every iteration.[27,28] The standard phase-retrieval algorithm employs the property of Fourier optics that connects the complex near- and far-field quantities via the Fourier transform,[29] where the far field is at the focal plane of the final lens in the long laser chain in OMEGA and the NIF, viz.,

$$\tilde{E}(x_{ff}, y_{ff}) = \iint E(x_{nf}, y_{nf})$$

$$\exp\left\{-i\frac{2\pi}{\lambda_{UV}f}[x_{ff}x_{nf} + y_{ff}y_{nf}]\right\} dx_{nf} dy_{nf}$$

$$= \mathfrak{F}\{E(x_{nf}, y_{nf})\}, \tag{1}$$

$$E(x_{nf}, y_{nf}) = \frac{1}{(\lambda_{UV}f)} \iint \tilde{E}(x_{ff}, y_{ff})$$

$$\exp\left\{+i\frac{2\pi}{\lambda_{UV}f}[x_{ff}x_{nf} + y_{ff}y_{nf}]\right\} dx_{ff} dy_{ff}$$

$$= \mathfrak{F}^{-1}\{\tilde{E}(x_{ff}, y_{ff})\}, \tag{2}$$

where λ_{UV} = 351 nm is the UV laser wavelength, f is the focal length of the final focusing lens (f = 1.8 m for OMEGA and f = 7.7 m for the NIF), and operators $\mathfrak{F}\{\cdot\}$ and $\mathfrak{F}^{-1}\{\cdot\}$ define the 2-D spatial Fourier transform and its inverse, respectively, that map the complex-valued electric field from the near-field coordinates (x_{nf}, y_{nf}) to the far-field coordinates (x_{ff}, y_{ff}) and vice versa. The magnitudes of the near-field or input beam shape

$$E_0(x_{nf}, y_{nf}) = \left|E(x_{nf}, y_{nf})\right| \tag{3}$$

and the speckled far-field objective pattern

$$\tilde{E}_0(x_{ff}, y_{ff}) = \left|\tilde{E}(x_{ff}, y_{ff})\right| \tag{4}$$

are known *a priori* before the iterative procedure is initiated. During the iterative procedure, the known input beam shape replaces the calculated amplitude of the near field and the far-field objective pattern replaces the calculated amplitude of the far field, while the calculated phase of both complex fields is retained.[28] A diagram of this iterative procedure is illustrated in Fig. 89.10. This algorithm converges quickly and accurately to almost any desirable far-field envelope; the main restrictions are that the envelope be square integrable and possess no sharp discontinuities, i.e., a well-behaved function.[31] The phase calculated during this standard technique is bounded by $\pm\pi$ due to the inherent range of the *arctangent* function used to calculate the phase based on the real and imaginary parts of the complex field quantities.

Bounding the phase in this manner results in many sharp 2π-phase discontinuities that theoretically will not scatter energy; however, a realistic device will scatter energy out of the desired far-field envelope because this boundary is not exactly reproduced due to limitations in the manufacturing process.[32] The

standard phase-retrieval technique can also produce phase anomalies that have sharp π-phase discontinuities (accurately referred to as phase dislocations[33] or phase vortices and imprecisely called phase poles or spiral phase singularities), which scatter additional light when they are illuminated (because a field value of zero is expected at phase dislocations) and are not due to a manufacturing limitation, although manufacturing limitations can exacerbate the scatter. A π-phase discontinuity occurs independently of the direction that the phase dislocation is traversed,[31] and a total of 2π phase is accumulated on a line integral path encircling a phase dislocation of order 1.[34] Both of these scattering sources limit the usefulness of the standard phase technique.

The sharp 2π-phase discontinuities can be removed by a number of different phase-unwrapping algorithms.[35] The phase anomalies pose a much more insidious problem because not only do they inhibit many phase-unwrapping algorithms, they also are one of the main reasons that the standard phase-retrieval technique stagnates or fails to converge.[36] If one attempts to artificially remove the phase discontinuities, they will simply reappear later in another location during the standard phase retrieval's iteration process.[31] Using the standard phase-retrieval technique alone renders the phase dislocations irremovable.

The number of phase anomalies can be reduced by initializing the standard phase technique with distributions that do not inherently contain phase anomalies[34] (which can frequently occur in random distributions); however, some problems benefit equally as well from a random distribution.[36] Another method attempts to remove pairs of phase dislocations by smoothing over the region containing them and then restricting the degree of freedom in that region during further iterations. This method, however, results in a rather tedious and

complicated algorithm that requires searching for and identifying pairs of phase dislocations that may not even reside on the current computational grid.[34]

Phase dislocations are associated with zeros of complex functions.[37–42] If a phase dislocation exists, a complex zero exists (although the opposite is not necessarily true). One source of phase dislocations in the near field is hard clipping or aggressive attenuation of the spatial spectrum (or far field).[31] If a near-field object's spectrum extends beyond the computational domain of the far field or extends into a region where the far-field target is zero, hard clipping can occur. Alternatively, aggressive attenuation of the spatial frequencies can occur during the application of the far-field constraints, i.e., applying a far-field target function that falls rapidly toward zero in regions where the near-field object's spectrum has significant values. Both of these mechanisms can occur when the near-field phase possesses large gradients, which will introduce complex zeros into the near field during the phase-retrieval procedure. It can also be shown, however, that if a near-field object has a spectrum with compact or finite support (i.e., a band-limited function), a near-field phase without phase dislocations can be found.[31]

2. Initial Guess and Construction of the Far-Field Objective

Both the standard phase retrieval and novel phase plate design techniques require an initial guess of the near-field phase. Through a judicious choice, the algorithms can be given a jump-start on convergence that helps prevent stagnation (as mentioned in the previous section). A random initial guess whose values take on any phase in the interval $0 \le \phi \le 2\pi$ can be a useful generic starting point for many applications where phase dislocations are not that much of a concern. This random pattern, however, is not a prudent starting point for continuous phase plate designs.

Figure 89.10
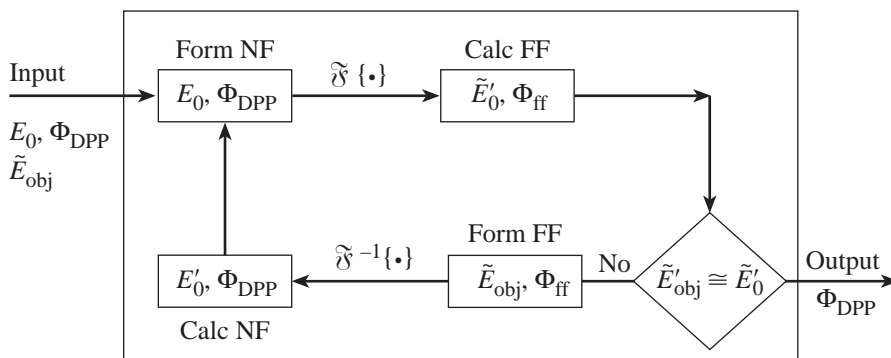A flow diagram depicting the iterative process employed in the standard phase-retrieval technique. The idea behind this technique has a long history dating back to Wolf[30] in 1962. Gerchberg, Saxton, and Fienup extended this idea to two dimensions, and the basic error-reduction scheme is shown in this figure.[27,28] This iterative technique is at the core of the novel phase plate design technique.

TC5912

The best choice for a continuous phase plate design is one whose phase is already continuous and produces a far-field pattern that adequately covers the targeted region. A scaled, colored-noise (see Carslon,[41] pp. 153–154) phase pattern is suitable for this purpose and is given by a Fourier filter operation:

$$\hat{\Phi}_{\text{DPP}}(x_{\text{nf}}, y_{\text{nf}}) = a \cdot \mathfrak{R}\left\{\mathfrak{F}^{-1}\left\{\mathfrak{F}\{\zeta(x_{\text{nf}}, y_{\text{nf}})\}\right.\right.$$

$$\left.\left.\exp\left[-\ln(2)\cdot\left(\frac{k_{\text{nf}}}{k_{0_{\text{DPP}}}}\right)^{20}\right]\right\}\right\}, \qquad (5)$$

where a is the scaling constant, $\zeta(x_{\text{nf}}, y_{\text{nf}}) \in [-1,1]$ is a random number field, $k_{\text{nf}} \equiv \left(k_{x_{\text{nf}}}^2 + k_{y_{\text{nf}}}^2\right)^{1/2}$ is the radial wave number of the near-field coordinate system, $k_{0_{\text{DPP}}} = 360$ rad/m is the FWHM filter point, and $\mathfrak{R}\{\cdot\}$ is the real operator. When the color-noise phase pattern, given by Eq. (5), is used, the resultant far-field speckle pattern possesses a simple Gaussian envelope. The scaling constant a is used to effectively spread out the resultant far-field speckle pattern to cover the targeted area (the value used in this article is $a = 50$ rad for both OMEGA and the NIF). It is important for the constant a to be large enough to encompass the targeted area of the far field but not so large that it extends beyond the computational region of the far field (otherwise, aliasing effects can play havoc on the algorithm).

Once the initial phase $\hat{\Phi}_{\text{DPP}}(x_{\text{nf}}, y_{\text{nf}})$ is chosen, manipulating the initial speckled far-field pattern produced by the initial phase generates the first far-field objective pattern. The initial speckled far-field pattern is given by

$$\hat{\tilde{E}}_0(x_{\text{ff}}, y_{\text{ff}}) = \left|\mathfrak{F}\left\{E_0(x_{\text{nf}}, y_{\text{nf}})\cdot\exp\left\{i\hat{\Phi}_{\text{DPP}}(x_{\text{nf}}, y_{\text{nf}})\right\}\right\}\right|. \qquad (6)$$

First, the envelope of the initial speckled far-field intensity pattern is found by using an optimal filter technique (described in detail in the following section):

$$I_{\text{ff}_{\text{env}}}(x_{\text{ff}}, y_{\text{ff}}) = \mathfrak{R}\left\{\mathfrak{F}^{-1}\left\{\tilde{\Psi}_{\text{opt}}\left(k_{x_{\text{ff}}}, k_{y_{\text{ff}}}\right)\right.\right.$$

$$\left.\left.\mathfrak{F}\left\{\left|\hat{\tilde{E}}_0(x_{\text{ff}}, y_{\text{ff}})\right|^2\right\}\right\}\right\}, \qquad (7)$$

where $\tilde{\Psi}_{\text{opt}}\left(k_{x_{\text{ff}}}, k_{y_{\text{ff}}}\right)$ is the optimal filter. Next a transformation function $\Lambda(x_{\text{ff}}, y_{\text{ff}})$ is defined as

$$\Lambda(x_{\text{ff}}, y_{\text{ff}}) \equiv \begin{cases} \left[\dfrac{I_{\text{ff}_{\text{target}}}(x_{\text{ff}}, y_{\text{ff}})}{I_{\text{ff}_{\text{env}}}(x_{\text{ff}}, y_{\text{ff}})}\right]^{1/2} & ; \quad I_{\text{ff}_{\text{env}}}(x_{\text{ff}}, y_{\text{ff}}) \neq 0 \\ \\ 0 & ; \quad \text{otherwise} \end{cases}, \qquad (8)$$

where $I_{\text{ff}_{\text{target}}}(x_{\text{ff}}, y_{\text{ff}})$ is the far-field target intensity envelope. The function $\Lambda(x_{\text{ff}}, y_{\text{ff}})$ transforms the initial far-field pattern as

$$\tilde{E}_{\text{obj}}(x_{\text{ff}}, y_{\text{ff}}) = \Lambda(x_{\text{ff}}, y_{\text{ff}}) \cdot \hat{\tilde{E}}_0(x_{\text{ff}}, y_{\text{ff}}), \qquad (9)$$

where $\tilde{E}_{\text{obj}}(x_{\text{ff}}, y_{\text{ff}})$ yields the first speckled far-field objective based on the initial far-field pattern $\hat{\tilde{E}}_0(x_{\text{ff}}, y_{\text{ff}})$. The importance of Eq. (9) is both subtle and critical to the convergence to a continuous phase plate; the initial phase $\hat{\Phi}_{\text{DPP}}(x_{\text{nf}}, y_{\text{nf}})$ is correlated to the generated speckle pattern. If this correlation is not maintained, convergence can be lost and the resultant phase pattern tends to produce a speckled far field with a Gaussian-shaped envelope and, under extreme cases, a high central peak develops. The transformation function $\Lambda(x_{\text{ff}}, y_{\text{ff}})$ may contain anomalously high values where $I_{\text{ff}_{\text{env}}}(x_{\text{ff}}, y_{\text{ff}}) \sim 0$. These values are eventually suppressed during the enhancement procedure described in the next section.

3. Wrapper Algorithm: Phase Continuity and Convergence
   Enhancement
   The continuity of the calculated phase is controlled using a two-step process: a 2-D phase-unwrapping procedure is applied to the phase map, calculated using the standard phase-retrieval method, followed by a low-pass filter that removes any residual high frequencies. The 2-D phase-unwrapping problem can be expressed in the form of Poisson's equation. The 2-D phase-unwrapping algorithm implemented in *Zhizhoo'* directly solves Poisson's equation on the whole computational grid using cosine transforms and does not need to painstakingly iterate around the grid as in other methods.[35] The cosine transform technique acts globally on the phase function and therefore is relatively immune to any local phase anomalies in that it tends to smooth over discontinuities, which is a highly desirable feature in the design of continuous phase plates.

Initially, when there are a number of phase anomalies, some residual high-frequency artifacts that remain after the 2-D phase-unwrapping operation need to be additionally smoothed. A simple, smooth, low-pass filter is used to remove the high-frequency artifacts, where the filter is a super-Gaussian:

$$\tilde{\Psi}_\Phi\left(k_{x_{\mathrm{nf}}}, k_{y_{\mathrm{nf}}}\right) = \exp\left\{-\ln(2)\left(\frac{k_{\mathrm{nf}}}{k_{0_{\mathrm{DPP}}}}\right)^{20}\right\}, \quad (10)$$

where $k_{0_{\mathrm{DPP}}} = 1270$ rad/m is the FWHM filter point. Note that the filtering function used here is the same as that implemented in the initial guess of the phase except that the quantity $k_{0_{\mathrm{DPP}}}$ is larger. The filtering is implemented as

$$\Phi_{\mathrm{DPP}}(x_{\mathrm{nf}}, y_{\mathrm{nf}}) = \Re\left\{\tilde{\mathfrak{F}}^{-1}\left\{\tilde{\Psi}_\Phi\left(k_{x_{\mathrm{nf}}}, k_{y_{\mathrm{nf}}}\right)\right.\right.$$

$$\left.\left. \mathfrak{F}\left\{\Phi'_{\mathrm{DPP}}(x_{\mathrm{nf}}, y_{\mathrm{nf}})\right\}\right\}\right\}, \quad (11)$$

where $\Phi'_{\mathrm{DPP}}(x_{\mathrm{nf}}, y_{\mathrm{nf}})$ is the unwrapped phase, $\Re\{\cdot\}$ is the real operator, and the coordinate transformations $k_{x_{\mathrm{nf}}} = 2\pi x_{\mathrm{ff}}/(\lambda_{\mathrm{UV}} f)$ and $k_{y_{\mathrm{nf}}} = 2\pi y_{\mathrm{ff}}/(\lambda_{\mathrm{UV}} f)$ are required to use the definitions in Eqs. (1) and (2).

The speckled far field must be recalculated to account for any changes that occur due to the updated phase plate $\Phi_{\mathrm{DPP}}(x_{\mathrm{nf}}, y_{\mathrm{nf}})$ after continuity is corrected by the unwrapping and filtering process. This speckled far field becomes the current speckled far-field objective and is represented as $\tilde{E}'_{\mathrm{obj}}(x_{\mathrm{ff}}, y_{\mathrm{ff}})$. At first, the resultant unwrapped and filtered phase mapping does not produce a speckled far-field pattern whose envelope matches the target envelope. The whole procedure is then repeated until the continuous phase mapping converges and produces the targeted far-field envelope or reaches a fixed number of iterations. A flow diagram of the complete *Zhizhoo'* design process including the standard phase-retrieval technique is illustrated in Fig. 89.11.

An additional feature is also implemented to encourage fast and accurate convergence before the whole wrapper algorithm is repeated; the far-field target objective is "enhanced" or "emphasized" to compensate for any shortcomings of the current phase mapping, i.e., any azimuthal asymmetries or spurious peaks and valleys in the current far-field intensity envelope are corrected by modifying the 2-D far-field objective to dampen the peak-to-valley variation. This idea is similar to the input/output algorithm described by Fienup.[28] The emphasis is a critical step in the algorithm because it maintains the correlation between the current phase plate and the speckle pattern that it generates. Without this step the algorithm would diverge.
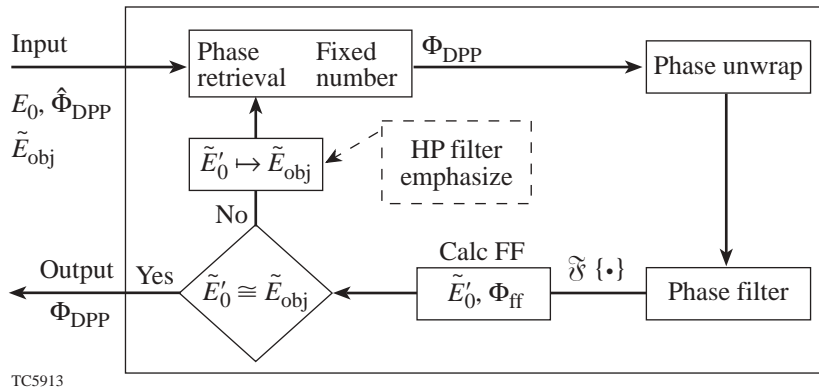
Figure 89.11
A flow diagram depicting the iterative process employed in the novel phase plate design technique and used in the code *Zhizhoo'*. Initialized near-field phase and far-field objective functions are fed into the iterative process. The standard phase-retrieval block (see Fig. 89.10) is executed first, followed by the 2-D phase unwrap and phase filter. Next, the speckled far field $\tilde{E}'_{\mathrm{obj}}(x_{\mathrm{ff}}, y_{\mathrm{ff}})$ is recalculated based on the latest unwrapped and filtered phase plate. Finally, the updated far field $\tilde{E}'_{\mathrm{obj}}(x_{\mathrm{ff}}, y_{\mathrm{ff}})$ is compared to the far-field objective $\tilde{E}_{\mathrm{obj}}(x_{\mathrm{ff}}, y_{\mathrm{ff}})$ to test for convergence and maximum number of iterations reached to determine whether or not to proceed. If proceeding, then the far-field objective functions are modified to maintain correlation with the latest iteration of the near-field phase. The modifications include a convergence enhancement, which is applied to the far-field objective. The second optional modification alters the far-field objective's power spectrum by high-pass filtering before continuing back into the standard phase-retrieval block. The dashed box denotes optional blocks.

The emphasis function requires the envelope of the far-field intensity to make these corrections. The far-field envelope is calculated using either a low-pass or an optimal filter technique.[42] The low-pass method uses a super-Gaussian filter

$$\tilde{\Psi}_{ff}\left(k_{x_{ff}}, k_{y_{ff}}\right) = \exp\left\{-\ln(2)\left(\frac{k_{ff}}{2k_{env}}\right)^{10}\right\}, \qquad (12)$$

where $k_{ff} \equiv \left(k_{x_{ff}}^2 + k_{y_{ff}}^2\right)^{1/2}$ is the radial wave number of the far-field coordinate system and k_{env} defines the approximate frequency where the envelope power spectrum and the speckle spectrum intersect ($k_{env} = 43.2 \times 10^3$ rad/m for OMEGA and $k_{env} = 5.88 \times 10^3$ rad/m for the NIF). The optimal filter uses the far-field power spectrum and a model of the power spectrum of the speckle:

$$\tilde{\Psi}_{opt}\left(k_{x_{ff}}, k_{y_{ff}}\right) = \frac{\left|\tilde{I}_{ff}\left(k_{x_{ff}}, k_{y_{ff}}\right)\right|^2 - \Xi\left(k_{x_{ff}}, k_{y_{ff}}\right)}{\left|\tilde{I}_{ff}\left(k_{x_{ff}}, k_{y_{ff}}\right)\right|^2}, \qquad (13)$$

where $\left|\tilde{I}_{ff}\left(k_{x_{ff}}, k_{y_{ff}}\right)\right|^2$ defines the power spectrum of the far-field intensity and $\Xi\left(k_{x_{ff}}, k_{y_{ff}}\right)$ represents the power spectrum of the speckle intensity, which is given by the autocorrelation of the near-field intensity.[43] The optimal filter is the best method of obtaining the envelope; however, it is not compatible with the design of the high-pass phase plate because a model for the far-field power spectrum is not known for this case *a priori*. The far-field intensity envelope $I_{ff_{env}}\left(x_{ff}, y_{ff}\right)$ is calculated by applying a Fourier-filtering technique similar to Eq. (7) to the far-field intensity $I_{ff}\left(x_{ff}, y_{ff}\right)$ while using one of the filters in Eq. (12) or (13). The emphasis function may now be calculated as

$$\Lambda_{emp}\left(x_{ff}, y_{ff}\right) = \alpha \cdot \Lambda\left(x_{ff}, y_{ff}\right), \qquad (14)$$

where $\Lambda\left(x_{ff}, y_{ff}\right)$ is defined in Eq. (8) and α is an enhancement factor that can be used to hasten convergence by overcompensating for the distortions in the envelope function and is defined as

$$\alpha = \begin{cases} \alpha_{>1}; & \Lambda\left(x_{ff}, y_{ff}\right) > 1 \\ 1; & \Lambda\left(x_{ff}, y_{ff}\right) = 1 \\ \alpha_{<1}; & \Lambda\left(x_{ff}, y_{ff}\right) < 1 \end{cases}. \qquad (15)$$

Care must be taken in selecting the constants $\alpha_{>1}$ and $\alpha_{<1}$ because amplifying oscillations may occur that lead to loss of control and convergence failure. The values found to yield adequate convergence that avoids oscillations are $\alpha_{>1} = 1.1$ and $\alpha_{<1} = 0.9$. The emphasis function $\Lambda_{emp}\left(x_{ff}, y_{ff}\right)$ modifies the current far-field objective before the next trial of the standard phase-retrieval technique as

$$\tilde{E}_{obj}\left(x_{ff}, y_{ff}\right) = \Lambda_{emp}\left(x_{ff}, y_{ff}\right) \cdot \tilde{E}'_{obj}\left(x_{ff}, y_{ff}\right), \qquad (16)$$

where $\tilde{E}'_{obj}\left(x_{ff}, y_{ff}\right)$ represents the current objective and $\tilde{E}_{obj}\left(x_{ff}, y_{ff}\right)$ represents the new trial. Eventually the emphasis function decays toward unity as the continuous phase mapping converges; therefore the emphasis function is similar to a merit function. The emphasis function is 2-D, which enables *Zhizhoo'* to compensate for any azimuthal asymmetries or other distortions in the far-field intensity envelope.

The number of iterations or sets of the wrapper algorithm that are executed in *Zhizhoo'* may end when either a convergence criterion is reached or a maximum number of sets has occurred. The convergence criterion used in *Zhizhoo'* is a simple rms error of the calculated far field relative to the design specification, viz.

$$\sigma_{ff} = \left\{\frac{\iint\limits_{\forall space} \left[\tilde{E}'_{obj}\left(x_{ff}, y_{ff}\right) - \tilde{E}_{obj}\left(x_{ff}, y_{ff}\right)\right]^2 dx_{ff}\,dy_{ff}}{\iint\limits_{\forall space} \left[\tilde{E}_{obj}\left(x_{ff}, y_{ff}\right)\right]^2 dx_{ff}\,dy_{ff}}\right\}^{1/2}, \qquad (17)$$

where $\tilde{E}'_{obj}\left(x_{ff}, y_{ff}\right)$ represents the objective produced by the current realization of the phase plate and $\tilde{E}_{obj}\left(x_{ff}, y_{ff}\right)$ represents the objective prior to the emphasis function modifications. At the completion of all the sets, the calculated continuous phase plate produces a speckled far-field intensity pattern whose envelope matches the objective function extremely well without any azimuthal asymmetries or distortions. In addition, the phase discontinuities or complex zeros of the near field are removed.

4. High-Pass Phase Plate

The ability to control the far-field intensity's power spectrum and produce a high-pass phase plate is merely an extension to the novel phase plate design technique; a step, which is

added to the algorithm, revises the power spectrum of the far-field objective during the iterative process. This step becomes part of the wrapper algorithm, as indicated in Fig. 89.11, and modifies the far-field objective by high-pass filtering its power spectrum. The high-pass filtering must be done as part of the wrapper algorithm because it is necessary to maintain the correlation between the speckle pattern produced by the current phase plate (i.e., after the 2-D phase unwrapping and filtering process) just as in the application of the emphasis function. The current implementation applies the high-pass filtering before the emphasis function modifications. As the continuous-phase mapping converges, it will produce a far-field intensity envelope that matches the targeted objective as well as produce speckle with dramatically reduced power in the lower-ℓ modes. The amount of power that can be removed depends on the type of filter used. A sharp-cutoff, wideband filter can achieve about a factor-of-10 reduction in the power spectrum across the whole requested band, whereas a slowly varying filter envelope can realize as much as a factor-of-100 reduction in the lowest-ℓ modes.

After 2-D phase unwrapping and filtering, the current phase-plate realization yields an intensity speckle field $\left| E'_{\text{obj}}(x_{\text{ff}}, y_{\text{ff}}) \right|^2$ comprised of a unity-mean, uniformly random speckle field, which is modulated by the far-field envelope. The far-field envelope must be removed so that the high-pass filter does not affect the targeted envelope but primarily so that the high-pass filter operates directly on the random speckle field. Separating the unity mean from the uniformly random speckle field and modulating its sum by the envelope function, constructs a model for this speckle field:

$$\left| E'_{\text{obj}}(x_{\text{ff}}, y_{\text{ff}}) \right|^2 = I_{\text{ff}_{\text{env}}}(x_{\text{ff}}, y_{\text{ff}})\left[1 + \text{spec}'(x_{\text{ff}}, y_{\text{ff}})\right], \quad (18)$$

where $I_{\text{ff}_{\text{env}}}(x_{\text{ff}}, y_{\text{ff}})$ is the slowly varying envelope function obtained by low-pass filtering the speckle field and $\text{spec}'(x_{\text{ff}}, y_{\text{ff}})$ is a zero-mean speckle field. The low-pass filter used to calculate $I_{\text{ff}_{\text{env}}}(x_{\text{ff}}, y_{\text{ff}})$, for this case, is given by Eq. (12) except with a super-Gaussian of order 5. The high-pass filter operates on the zero-mean speckle field $\text{spec}'(x_{\text{ff}}, y_{\text{ff}})$.

Let $E'_{\text{obj}}(x_{\text{ff}}, y_{\text{ff}})$ be the far-field objective function produced by the current realization of the phase plate after 2-D phase unwrapping and filtering, which is fed into the speckle model to yield the current zero-mean speckle field $\text{spec}'(x_{\text{ff}}, y_{\text{ff}})$. The high-pass-filtered speckle is then given by

$$\text{spec}(x_{\text{ff}}, y_{\text{ff}})$$

$$= \Re\left\{ \widetilde{\mathfrak{F}}^{-1}\left\{ \Psi_{\text{HP}}\left(k_{x_{\text{ff}}}, k_{y_{\text{ff}}}\right) \cdot \widetilde{\mathfrak{F}}\left\{ \text{spec}'(x_{\text{ff}}, y_{\text{ff}}) \right\} \right\} \right\}, \quad (19)$$

where $\Psi_{\text{HP}}\left(k_{x_{\text{ff}}}, k_{y_{\text{ff}}}\right)$ represents any type of high-pass filter. In this article, the sharp-cutoff filter is given by

$$\Psi_{\text{HP}}\left(k_{x_{\text{ff}}}, k_{y_{\text{ff}}}\right) = \begin{cases} 1; & k_{\text{ff}} > 200/r_{\text{fuel}} \\ 0; & k_{\text{ff}} \leq 200/r_{\text{fuel}} \end{cases}, \quad (20)$$

or the slowly varying filter is given by

$$\Psi_{\text{HP}}\left(k_{x_{\text{ff}}}, k_{y_{\text{ff}}}\right) = \exp\left\{ -\ln(2)\left(\frac{r_{\text{fuel}} k_{\text{ff}}}{200} \right)^{2.25} \right\}, \quad (21)$$

where $r_{\text{fuel}} = 500 \ \mu\text{m}$ is the fuel pellet radius for OMEGA. After high-pass filtering, the zero-mean speckle field is then substituted back into the speckle model to form the new far-field objective $E_{\text{obj}}(x_{\text{ff}}, y_{\text{ff}})$, viz.,

$$E_{\text{obj}}(x_{\text{ff}}, y_{\text{ff}}) = \left\{ I_{\text{ff}_{\text{env}}}(x_{\text{ff}}, y_{\text{ff}})\left[1 + \text{spec}(x_{\text{ff}}, y_{\text{ff}})\right] \right\}^{0.5}. \quad (22)$$

The new far-field objective $E_{\text{obj}}(x_{\text{ff}}, y_{\text{ff}})$ would then be modified further by the emphasis function as described in the previous section.

Phase Plate Design Results

Two types of continuous phase plates were designed using *Zhizhoo'* for each laser: OMEGA and the NIF. The first type of phase plate is referred to as a standard phase plate to distinguish it from the second type, a high-pass phase plate. The standard phase plate is used as the basis of comparison to measure the ability of the high-pass phase plate to reduce the power in the lower-ℓ modes.

1. OMEGA Phase Plate Designs

The targeted far-field intensity envelope for the first OMEGA phase plate design is a super-Gaussian of order 8 (sg = 8) and an intensity-full-width-at-half-maximum (IFWHM) radius of $r_0 = 432 \ \mu\text{m}$:

$$I_{ff_{target}}\left(x_{ff}, y_{ff}\right) = \exp\left\{-\ln(2)\left(\frac{r_{ff}}{r_0}\right)^{sg}\right\}, \tag{23}$$

where $r_{ff} \equiv \left(x_{ff}^2 + y_{ff}^2\right)^{1/2}$ is the radius in the far-field coordinate system. This far-field intensity envelope target defines a 95% enclosed energy contour with a diameter of $D_{95} = 925\ \mu$m and was chosen to demonstrate the ability of *Zhizhoo'* to produce a far-field envelope of high super-Gaussian order. The near-field clear aperture is round and has a diameter of 27.5 cm. The simulation space for the near field was a 1024 × 1024 grid spanning 55.0 cm, and the corresponding far field covered 1.18 mm on a 1024 × 1024 grid.

Zhizhoo' was run with these design parameters to calculate a continuous standard phase plate with a continuous random initial guess for the phase, which was filtered with a super-Gaussian filter of order 20 and filter cutoff parameter $k_{0_{DPP}} = 360\ \text{rad/m}$. The internal standard phase-retrieval code was set to run five iterations, the wrapper algorithm was set at a fixed number of 50 iterations, and emphasis was enabled. *Zhizhoo'* ran in parallel on eight processors on the SGI Origin 2000 for 15 min, which ended with a rms far-field error of $\sigma_{ff} = 5.8\%$. A plot of the azimuthally averaged far-field intensity is compared to the far-field target envelope in Fig. 89.12. The agreement between the resultant far field and the target far-field envelope is excellent even for this high-order super-Gaussian. This level of agreement is achieved mainly due to the combined capabilities of the emphasis function and continuity control to keep the standard phase-retrieval method from stagnating; the error-reduction algorithm is guaranteed to never increase the error upon every iteration, and, if stagnation can be controlled, the calculated phase will converge to the correct answer with no complex zeros in the near field, i.e., no phase dislocations. These results should be compared to the relatively poor results achieved in Refs. 15, 32, and 44. The novel phase plate design technique is also able to control any azimuthal asymmetries of the far field through the application of a 2-D emphasis function. This is illustrated in Fig. 89.13 by plotting the far-field intensity contours that result from applying 1-THz, 2-D SSD and PS in the asymptotic limit.[23,24]

Zhizhoo' was then run to design both a continuous standard and high-pass phase plate with a super-Gaussian far-field target of order 3 (sg = 3) and an IFWHM radius of $r_0 = 325\ \mu$m, which defines a 95% enclosed energy contour with a diameter of $D_{95} = 970\ \mu$m. This super-Gaussian envelope is chosen since it produces ample uniformity on the spherical OMEGA target.

The high-pass function used was a wideband, sharp filter that attempted to attenuate all modes $0 < \ell \leq 200$ and pass all others. *Zhizhoo'* completed the high-pass design in parallel in 20 min

TC5890
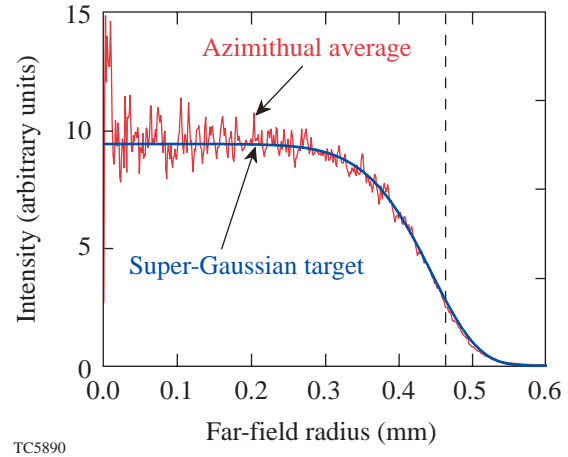
Figure 89.12
The azimuthally averaged far-field intensity (red line) is plotted against the far-field target envelope (blue line). The far-field target envelope has design parameters sg = 8 and $r_0 = 432\ \mu$m. The red line is very noisy near the origin due to the limited number of points that were available to average. The dashed vertical line indicates the 95% enclosed energy contour, which is at $r = 463\ \mu$m. 2-D SSD, PS, and phase aberrations are not applied.

TC5891
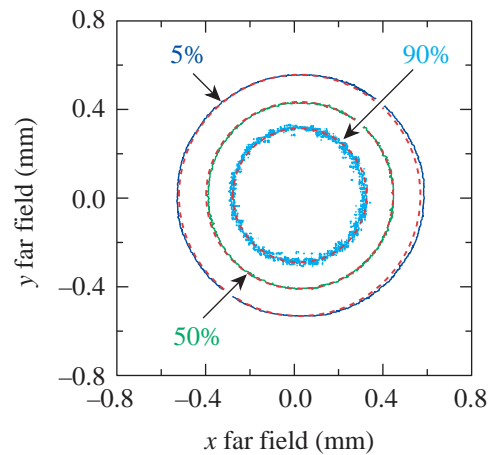
Figure 89.13
The plotted contours correspond to the 5%, 50%, and 90% of the envelope peak of the far-field intensity that result from applying 2-D SSD and PS in the asymptotic limit. The corresponding contours for the target envelope are plotted as dashed lines. The solid contours show excellent agreement to the target with very little azimuthal asymmetry. Phase aberrations have not been applied.

(it takes longer than the standard phase plate because of the additional filtering calculations) using the same fixed number of iterations as before, which ended with a rms far-field error of $\sigma_{ff} = 5.5\%$; the standard phase plate design completed with $\sigma_{ff} = 2.8\%$. The resultant far-field envelopes match the target function very well. The larger σ_{ff} parameter for the high-pass phase plate is due to the inability of the phase plate to reproduce the exact filtered speckle, even though the envelope is very close to the target, i.e., the objective function has less power in the low-ℓ modes compared to the resultant.

The high-pass phase plate's ability to attenuate the power spectrum in the low-order modes is illustrated in Fig. 89.14 for a single beam with and without 2-D SSD and PS. The high-pass phase plate is able to attenuate the power spectrum by a factor of ~10 over a range that doesn't include the far-field envelope $10 < \ell \leq 200$. When all of the 60 OMEGA laser beams are calculated and projected onto the target sphere, the effect of the far-field envelope is removed and the high-pass phase plate is observed to attenuate the mode amplitudes over the full range $0 < \ell \leq 100$ by a factor of $\sim \sqrt{10}$, as illustrated in Fig. 89.15.
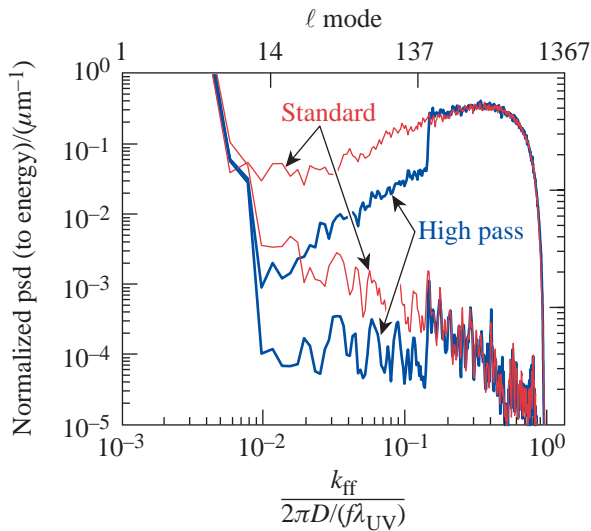
TC5894

Figure 89.14
The azimuthally integrated, single-beam far-field power spectrum (normalized to the total energy) resulting from the high-pass phase plate (thick lines) for OMEGA is compared to the power spectrum of the standard phase plate (thin lines). The upper lines represent the instantaneous speckled far field without SSD or PS applied, and the lower lines represent the smoothed power spectrum that results from 1-THz, 2-D SSD with PS in the asymptotic limit. Phase aberrations have not been applied.

A second high-pass phase plate, also designed with *Zhizhoo*', attempted to slowly reduce the far-field power spectrum over the range $0 < \ell \leq 200$. The goal here was to make the greatest reduction in the lower-ℓ-mode range of $0 < \ell \leq 20$. As illustrated in Fig. 89.16, the power spectrum was, on average, attenuated by nearly a full factor of 100 across the whole band $\ell < 200$ with most of the benefit occurring at the lower-ℓ modes.
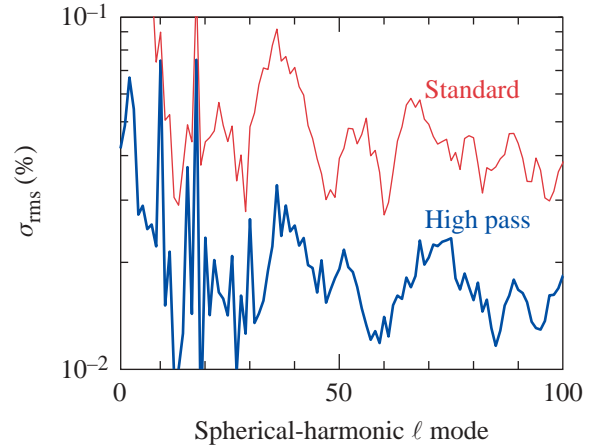
TC5893

Figure 89.15
The ℓ-mode spectrum of an OMEGA 60-beam projection onto a target sphere resulting from the high-pass phase plate (blue line) is compared to the ℓ-mode spectrum of the standard phase plate (red line). These spectra result from 1-THz, 2-D SSD with PS in the asymptotic limit. The target sphere had a diameter of 950 μm. Note that these data are spectral amplitudes. The strong spectral peaks in the low-ℓ-mode range are due to the combined effect of the envelope shape and the target sphere radius, e.g., $\ell = 10$.

2. NIF Phase Plate Designs

The design process for the NIF is very similar to that of OMEGA except that the near field is square and the dimensions are different. The targeted far-field intensity envelope for both NIF phase plate designs is a round super-Gaussian of order 8 (sg = 8) and an IFWHM radius of $r_0 = 1.26$ mm. This far-field intensity envelope target defines a 95% enclosed energy contour with a diameter of $D_{95} = 2.7$ mm. The higher super-Gaussian order was chosen in this case for the NIF because the faster roll-off fits better in the simulation space; a lower order would require a larger grid to provide adequate sampling of the far field (which will be done for production-quality designs). This sg = 8 still provides insight into the high-pass designs, even though it does not provide the best
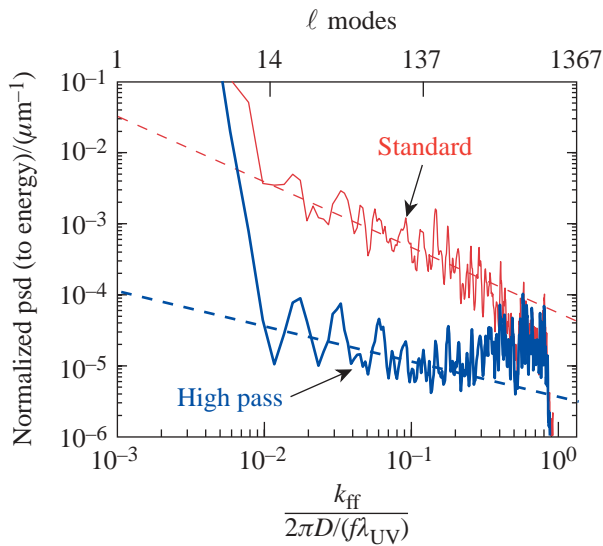
TC5892

Figure 89.16
The azimuthally integrated, single-beam far-field power spectrum (normalized to the total energy) resulting from the second high-pass phase plate (blue line) is compared to the ℓ-mode spectrum of the standard phase plate (red line). These spectra result from 1-THz, 2-D SSD with PS in the asymptotic limit. The slower filter used reduced the power in the ℓ modes in the range of $0 < \ell \leq 200$ by nearly a factor of 100 with most of the reduction occurring in the lower-ℓ modes. The two dashed lines represent the approximate average level of the power spectra and are intended as a guide.

spherical-target illumination. The near-field clear aperture is square and has a width of 35.1 cm in each direction. The simulation space for the near field was a 1024×1024 grid spanning 70.2 cm, and the corresponding far field covered 3.94 mm on a 1024×1024 grid.

Zhizhoo' was then run to design both a continuous standard and a high-pass phase plate to match this super-Gaussian far-field target. The high-pass function used was a wideband, sharp filter, which attempted to attenuate all modes $0 < \ell \leq 200$ and pass all others. *Zhizhoo'* completed the high-pass design using the same fixed number of iterations as before, which ended with a rms near-field error of $\sigma_{ff} = 6.5\%$; the standard phase plate design completed with $\sigma_{ff} = 3.1\%$. As with the OMEGA designs, the resultant far-field envelopes match the target function very well.

Figure 89.17 illustrates the performance of the high-pass phase plate relative to the standard phase plate when all of the 192 NIF laser beams are calculated and then projected onto the target sphere. The high-pass phase plate is able to reduce the amplitudes by a factor of $\sim \sqrt{10}$ for modes over the range $0 < \ell \leq 200$.


TC5914
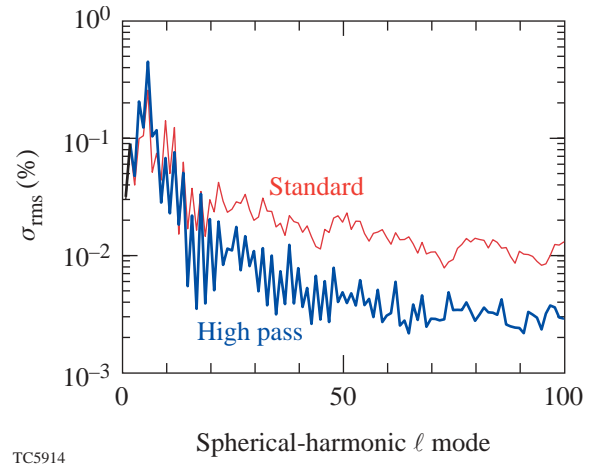
Figure 89.17
The ℓ-mode spectrum of a NIF 192-beam projection onto a target sphere resulting from the high-pass phase plate (blue line) is compared to the ℓ-mode spectrum of the standard phase plate (red line). These spectra result from 1-THz, 2-D SSD with PS in the asymptotic limit. The target sphere had a diameter of 3 mm. Note that these data are spectral amplitudes. A sharp-cutoff, wideband high-pass filter was used to attenuate the ℓ modes in the range of $0 < \ell \leq 200$ and was able to reduce them by a factor of $\sim \sqrt{10}$ over this range.

Effects of Near-Field Phase Aberrations

A near-field phase aberration can have a profound effect on the performance of the high-pass phase plates. The phase of the aberration modifies the way in which near-field elements interfere in the far field to produce the speckle pattern. The complex near field has a specific autocorrelation due to the phase pattern of the high-pass phase plate; viz., the Fourier transform of the far-field intensity is equivalent to the autocorrelation of the complex near field, i.e., the autocorrelation theorem (see Ref. 29). An aberration affects the autocorrelation of the near field and disrupts the specific relationship that was developed during the iteration process. If the aberration is strong enough, it acts like a randomizer, and the resultant far-field power spectrum tends toward that of the standard phase plate; i.e., speckle statistics that behave like those due to a phase plate with circular Gaussian statistics are simply the autocorrelation of the near-field intensity (plus a delta function at the origin).[43] If the phase aberration is not too strong, the resultant power spectrum is a hybrid of the two and lies somewhere in between.

The spatial frequency of the phase aberration affects different spatial frequencies of the far-field intensity. For example, a high-spatial-frequency phase aberration will affect the long-wavelength features in the far-field intensity and vice versa.

Since typical phase aberrations have a spatial spectrum whose spectrum follows a basic inverse power law in order that the high spatial frequencies will have less power than the lower spatial frequencies, one would expect short-wavelength features of the far-field intensity to be affected first.

The near-field phase aberration, which was measured on OMEGA, corresponds to a beam that is 12× diffraction limited. This phase aberration is used in two ways: (1) as an amplitude spectrum that is calculated and fit to an inverse power law to model phase aberrations of varying strength; and (2) as a fixed phase aberration used in *Waasikwa'* far-field simulations. The azimuthally averaged amplitude spectrum of the measured phase aberration is shown in Fig. 89.18 along with the inverse power law model, which is fit to the data. The model used to fit the azimuthally averaged amplitude spectrum of the measured near-field phase aberration is

$$\tilde{\Phi}\left(k_{\mathrm{nf}}\right) = 2\pi a \left(\frac{k_{\mathrm{nf}}}{2\pi}\right)^{b}, \qquad (24)$$

where a defines the magnitude and b defines the power. For the measured near-field phase aberration, $a = 2.45$ and $b = -2.22$. It is assumed that the power law can be scaled by varying the magnitude parameter a while keeping the power b constant. In this way, different far-field simulations can be run with a varying degree of phase aberration. A measure of the strength of the phase aberration is given by the ratio

$$\beta = \frac{D_{95}}{D_{\mathrm{DL}}}, \qquad (25)$$

where D_{95} is the diameter of the 95% enclosed energy contour of the far-field spot due to a phase-aberrated beam relative to the 95% enclosed energy contour for a diffraction-limited beam D_{DL}. For OMEGA the diffraction-limited far-field spot diameter is $D_{\mathrm{DL}} = 6.25\ \mu\mathrm{m}$ and, for the NIF, $D_{\mathrm{DL}} = 23.1\ \mu\mathrm{m}$. When the parameters for the model of the power spectrum given in Eq. (24) are $a = 2.45$ and $b = -2.22$, this yields $\beta = 12$, i.e., 12× diffraction limited using the definition of Eq. (25). The phase-aberration amplitude spectrum model given in Eq. (24) can be used to generate a random phase perturbation that matches the power spectrum model, i.e., colored noise (see Ref. 41, pp. 153–154):

$$\Phi_{\mathrm{aber}}\left(x_{\mathrm{nf}}, y_{\mathrm{nf}}\right) = \Re\left\{\mathfrak{F}^{-1}\left\{\tilde{\Phi}\left(k_{\mathrm{nf}}\right) \exp\left[i\zeta\left(k_{x_{\mathrm{nf}}}, k_{y_{\mathrm{nf}}}\right)\right]\right\}\right\}, \quad (26)$$

where $\zeta\left(k_{x_{\mathrm{nf}}}, k_{y_{\mathrm{nf}}}\right) \in [0, 2\pi]$ is a random number field and defined at Eq. (11). A random phase aberration of varying strength β can be generated using the model given by Eq. (26) by holding the power $b = -1.23$ constant and changing the value of the amplitude a.

The effect that the phase-aberration strength has on the ℓ-mode spectrum of the far-field intensity for multiple-beam projections is shown in Fig. 89.19. The strength parameter β is increased, and the amplitude spectrum begins to change the shorter-wavelength features initially. This is due to the nature of the power spectrum of the phase aberration; the longer wavelengths have more power than the shorter wavelengths. The longer wavelengths of the phase aberration affect the shorter wavelengths of the far-field intensity, i.e., the autocorrelation of the complex near field is disrupted. When the strength parameter β is large enough, e.g., $\beta > 12$, it is difficult to tell the difference between the aberrated far field and the far-field intensity power spectrum due to the standard phase plate.

A benefit from the high-pass phase plates can still be realized in the lower-ℓ modes in the presence of typical near-field phase aberrations. The multiple-beam projection of the far-field intensity onto the target sphere becomes necessary to

TC5794

Figure 89.18
The azimuthally averaged power spectrum of a near-field phase aberration measured on OMEGA. An inverse power law model is shown as a fit to this data; fit parameters are $a = 2.4$ and $b = -2.22$ for the model in Eq. (24).

TC5895
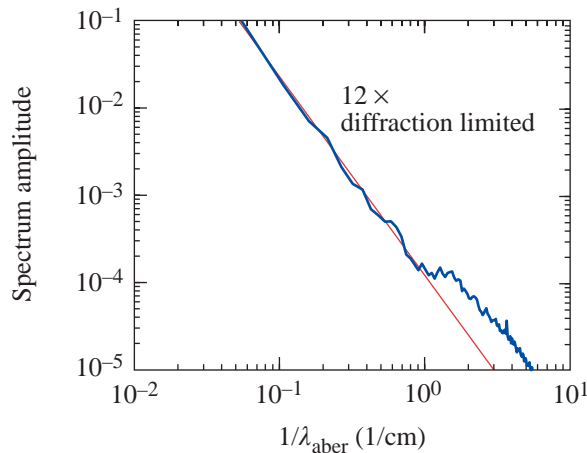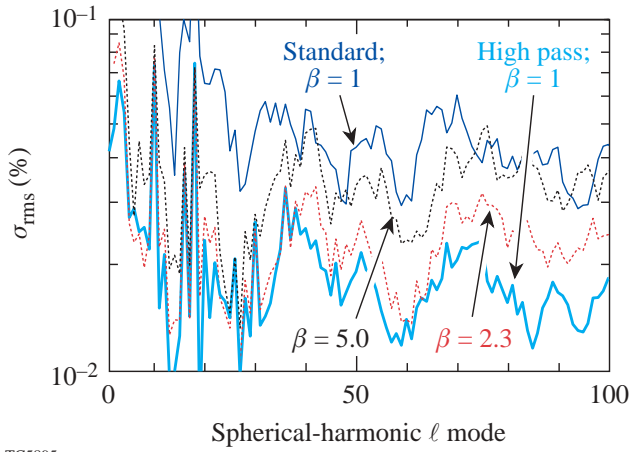
Figure 89.19
The ℓ-mode spectrum of an OMEGA 60-beam projection onto a target sphere due to the standard (upper thin line) and the high-pass (lower thick line) phase plate without phase aberrations is plotted for reference; these are the same traces that correspond to the single-beam spectra in Fig. 89.14. The ℓ-mode spectra of the far-field intensity due to the high-pass phase plate with varying degrees of phase aberration ($\beta = 2.3$ and $\beta = 5.0$) using the models in Eqs. (24) and (26) are shown (dashed lines). As the strength parameter β increases, the power spectrum tends toward that produced by the standard phase plate beginning with the shorter wavelengths. The shorter wavelengths of the far field are disrupted by the longer wavelengths of the phase aberration where the aberration has the strongest spectral amplitude (see Fig. 89.18).

gather this information because the envelope power overwhelms the power spectrum for the single beam for modes $\ell < 20$. A measure of the benefit gained from the high-pass phase plate is given by the ratio of the nonuniformity due to the high-pass phase relative to the standard phase plate summed over the desired ℓ-mode range, viz.,

$$\Gamma = \left[\frac{\sum_{\ell=\ell_{\min}}^{\ell_{\max}} \gamma_\ell^2}{\sum_{\ell=\ell_{\min}}^{\ell_{\max}} \widehat{\gamma}_\ell^2} \right]^{1/2}, \qquad (27)$$

where γ_ℓ and $\widehat{\gamma}_\ell$ are the amplitudes of the spherical ℓ-mode decomposition for the high-pass and standard phase plates, respectively. The amount of benefit that can be realized becomes a function of the ℓ-mode range covered because of (1) the aforementioned effect of the shape of the phase aberration power spectrum and (2) the stationary modes on the target sphere that develop from the shape of the far-field envelope.

The high-pass benefit function Γ (for the high-pass phase plate designed with the wideband sharp filter) is plotted in Fig. 89.20 for the OMEGA laser as a function of the phase-aberration strength β for four different ℓ-mode ranges. The lower-ℓ-mode range $11 \leq \ell \leq 25$ realizes the largest benefit ($\Gamma = 1.6$ for typical system aberration of $\beta = 12$) because the shortest-wavelength features of the phase aberration are not strong enough to totally disrupt the high-pass phase plate. The high-pass phase plate that was designed with the slower filter also achieves an $\Gamma \sim \sqrt{2}$ even though the non-aberrated performance is much higher than that of the first high-pass phase plate. The results for the NIF high-pass phase plate are very similar and are shown in Fig. 89.21. A scaled model of the near-field phase aberration is used for the NIF calculations since the actual aberration is not currently known.

As a final look at the performance of the high-pass phase plates on OMEGA, two *Waasikwa'* far-field simulations were run for a square pulse shape with 1-THz, 2-D SSD and PS: one with the standard phase plate and one with the high-pass phase plate. *Waasikwa'* has the ability to perform multiple-beam projections onto a target sphere: 60 beams are projected onto a target sphere with a diameter of 950 μm. The nonuniformity, covering the ℓ modes $12 \leq \ell \leq 25$, of far-field intensity due to the standard phase plate is plotted in Fig. 89.22 against that due to the high-pass phase plate. The full benefit of the high-pass phase plate is not realized until after 300 ps. This occurs
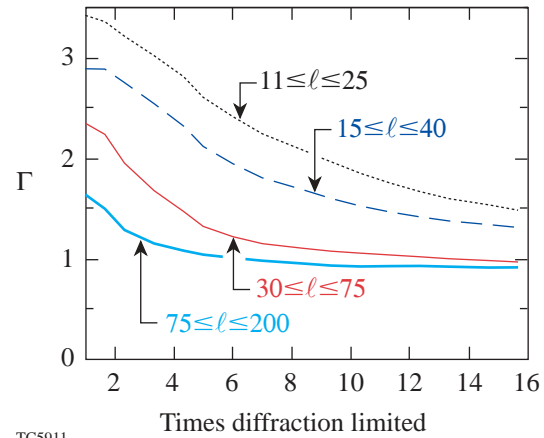
TC5911

Figure 89.20
The benefit realized by the high-pass phase plate [given by Eq. (27)] is plotted as a function of the phase-aberration strength β for the OMEGA laser. The smoothing applied is 1-THz, 2-D SSD in the asymptotic limit with PS. Four different ℓ-mode ranges are covered (as labeled on the plot): $11 \leq \ell \leq 25$, $15 \leq \ell \leq 40$, $30 \leq \ell \leq 75$, and $75 \leq \ell \leq 200$.

because early in time the phase imparted by the 2-D SSD system disrupts the specific autocorrelation of the complex near field in the same way that a phase aberration does. In contrast to the static phase aberration, the phase due to 2-D SSD moves across the near field at a constant rate.[45] This
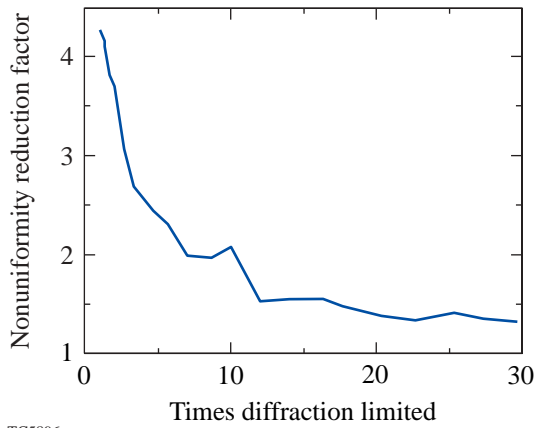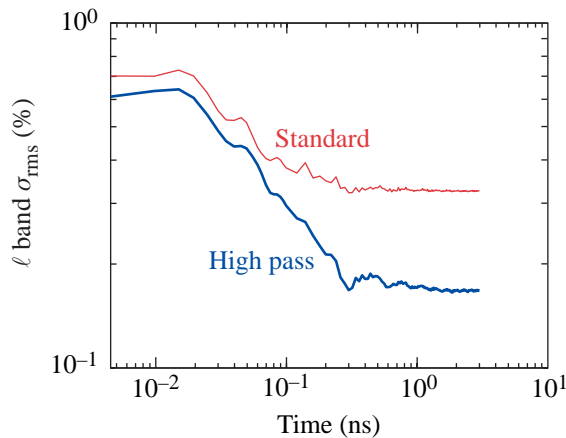

TC5896

Figure 89.21
The benefit realized by the high-pass phase plate [given by Eq. (27)] is plotted as a function of the phase-aberration strength β for the NIF laser. The smoothing applied is 1-THz, 2-D SSD in the asymptotic limit with PS. A single ℓ-mode range is covered: $20 \leq \ell \leq 60$.

TC5797

Figure 89.22
The nonuniformity of the far-field intensity over the ℓ-mode range of $12 \leq \ell \leq 25$ due to the standard phase plate is plotted against that due to the high-pass phase plate for the OMEGA laser. The data represent the results of *Waasikwa'* far-field simulations for a square pulse shape and 1-THz, 2-D SSD with PS. The measured near-field phase aberration was applied to both cases. The full benefit of the high-pass phase plate is not achieved until after 300 ps, when the slowest modulator ($\nu_m = 3.3$ GHz) has completed one full cycle.

movement over time effectively averages the phase due to 2-D SSD after the duration of the slowest phase modulator. In the case of the current 1-THz, 2-D SSD system, the slowest modulator is 3.3 GHz, which yields a cycle time of ~300 ps.

Conclusion

A novel phase plate design technique, based on the standard phase-retrieval algorithm, has been introduced and is able to generate continuous phase plates with outstanding control of the far-field intensity envelope, azimuthal asymmetries, and the far-field power spectrum. This new technique is able to overcome many of the difficulties associated with the standard phase-retrieval algorithm (namely, stagnation) and is able to capitalize on the computational efficiency of this method.

The novel phase plate design technique was incorporated into a code called *Zhizhoo'*, which is used to calculate a number of continuous phase plates for both OMEGA and the NIF. A standard phase plate was designed and employed as a reference to the high-pass phase plates in order to measure the performance when the power in the low ℓ-mode range is reduced. Without near-field phase aberrations, large benefit factors of $\Gamma \sim \sqrt{10}$ or even $\Gamma \sim 10$ are obtained, depending on the manner in which the far-field power spectrum is filtered during the iterative calculations carried out in *Zhizhoo'*. Near-field phase aberrations were shown to have a deleterious affect on the performance of the high-pass phase plates. It was found that a reasonable benefit is still realized, $\Gamma \sim 2$ for the ℓ-mode range $12 \leq \ell \leq 25$, even in the presence of typical near-field phase aberrations. A benefit for both OMEGA and the NIF in the lower and more-dangerous ℓ modes is anticipated by using the high-pass phase plates for direct-drive ICF experiments.

REFERENCES

1. C. P. Verdon, Bull. Am. Phys. Soc. **38**, 2010 (1993).

2. S. E. Bodner, D. G. Colombant, J. H. Gardner, R. H. Lehmberg, S. P. Obenschain, L. Phillips, A. J. Schmitt, J. D. Sethian, R. L. McCrory, W. Seka, C. P. Verdon, J. P. Knauer, B. B. Afeyan, and H. T. Powell, Phys. Plasmas **5**, 1901 (1998).

3. D. K. Bradley, J. A. Delettrez, and C. P. Verdon, Phys. Rev. Lett. **68**, 2774 (1992).

4. J. Delettrez, D. K. Bradley, and C. P. Verdon, Phys. Plasmas **1**, 2342 (1994).

5. J. D. Kilkenny, S. G. Glendinning, S. W. Haan, B. A. Hammel, J. D. Lindl, D. Munro, B. A. Remington, S. V. Weber, J. P. Knauer, and C. P. Verdon, Phys. Plasmas **1**, 1379 (1994).

6. R. Epstein, J. Appl. Phys. **82**, 2123 (1997).

7. V. A. Smalyuk, T. R. Boehly, D. K. Bradley, V. N. Goncharov, J. A. Delettrez, J. P. Knauer, D. D. Meyerhofer, D. Oron, and D. Shvarts, Phys. Rev. Lett. **81**, 5342 (1998).

8. F. J. Marshall and G. R. Bennett, Rev. Sci. Instrum. **70**, 617 (1999).

9. F. J. Marshall, J. A. Delettrez, V. Yu. Glebov, R. P. J. Town, B. Yaakobi, R. L. Kremens, and M. Cable, Phys. Plasmas **7**, 1006 (2000).

10. S. Skupsky, R. W. Short, T. Kessler, R. S. Craxton, S. Letzring, and J. M. Soures, J. Appl. Phys. **66**, 3456 (1989).

11. Laboratory for Laser Energetics LLE Review **69**, 1, NTIS document No. DOE/SF/19460-152 (1996). Copies may be obtained from the National Technical Information Service, Springfield, VA 22161.

12. S. Skupsky and R. S. Craxton, Phys. Plasmas **6**, 2157 (1999).

13. J. E. Rothenberg, J. Opt. Soc. Am. B **14**, 1664 (1997).

14. T. J. Kessler, Y. Lin, J. J. Armstrong, and B. Velazquez, in *Laser Coherence Control: Technology and Applications*, edited by H. T. Powell and T. J. Kessler (SPIE, Bellingham, WA, 1993), Vol. 1870, pp. 95–104.

15. Y. Lin, T. J. Kessler, and G. N. Lawrence, Opt. Lett. **21**, 1703 (1996).

16. T. R. Boehly, D. L. Brown, R. S. Craxton, R. L. Keck, J. P. Knauer, J. H. Kelly, T. J. Kessler, S. A. Kumpan, S. J. Loucks, S. A. Letzring, F. J. Marshall, R. L. McCrory, S. F. B. Morse, W. Seka, J. M. Soures, and C. P. Verdon, Opt. Commun. **133**, 495 (1997).

17. Y. Kato, unpublished notes from work at LLE, 1984.

18. K. Tsubakimoto *et al.*, Opt. Commun. **91**, 9 (1992).

19. K. Tsubakimoto *et al.*, Opt. Commun. **103**, 185 (1993).

20. Laboratory for Laser Energetics LLE Review **45**, 1, NTIS document No. DOE/DP40200-149 (1990). Copies may be obtained from the National Technical Information Service, Springfield, VA 22161.

21. T. E. Gunderman, J.-C. Lee, T. J. Kessler, S. D. Jacobs, D. J. Smith, and S. Skupsky, in *Conference on Lasers and Electro-Optics*, Vol. 7, 1990 OSA Technical Digest Series (Optical Society of America, Washington, DC, 1990), p. 354.

22. J. E. Rothenberg, J. Appl. Phys. **87**, 3654 (2000).

23. S. P. Regan, J. A. Marozas, J. H. Kelly, T. R. Boehly, W. R. Donaldson, P. A. Jaanimagi, R. L. Keck, T. J. Kessler, D. D. Meyerhofer, W. Seka, S. Skupsky, and V. A. Smalyuk, J. Opt. Soc. Am. B **17**, 1483 (2000).

24. J. A. Marozas, S. P. Regan, J. H. Kelly, D. D. Meyerhofer, W. Seka, and S. Skupsky, J. Opt. Soc. Am. B **19**, 7 (2002).

25. R. Epstein and S. Skupsky, J. Appl. Phys. **68**, 924 (1990).

26. Inspired by Anishinaabe words *zhizhoo'* meaning "spreads someone using something" and *zhizhoo'an* "spreads something using something" just as the phase plate spreads out the diffraction-limited, far-field spot to match the far-field objective. Resource: J. D. Nichols and E. Nyholm, *A Concise Dictionary of Minnesota Ojibwe* (University of Minnesota Press, Minneapolis, 1995).

27. R. W. Gerchberg and W. O. Saxton, Optik **35**, 237 (1972).

28. J. R. Fienup, Appl. Opt. **21**, 2758 (1982).

29. J. W. Goodman, *Introduction to Fourier Optics* (McGraw-Hill, New York, 1988).

30. E. Wolf, Proc. Phys. Soc. **80**, 1269 (1962).

31. F. Wyrowski and O. Bryngdahl, J. Opt. Soc. Am. A **5**, 1058 (1988).

32. Y. Lin, T. J. Kessler, and G. N. Lawrence, Opt. Lett. **20**, 764 (1995).

33. B. Ya. Zel'dovich, N. F. Pilipetsky, and V. V. Shkunov, in *Principles of Phase Conjugation*, edited by J. M. Enoch *et al.*, Springer Series in Optical Sciences (Springer-Verlag, Berlin, 1985), Sec. 3.5, Vol. 42, pp. 79–84.

34. H. Aagedal *et al.*, J. Mod. Opt. **43**, 1409 (1996).

35. D. C. Ghiglia and M. D. Pritt, *Two-Dimensional Phase Unwrapping: Theory, Algorithms, and Software* (Wiley, New York, 1998).

36. J. R. Fienup and C. C. Wackerman, J. Opt. Soc. Am. A **3**, 1897 (1986).

37. E. C. Titchmarsh, Proc. London Math. Soc. **25**, 283 (1926).

38. M. S. Scivier and M. A. Fiddy, J. Opt. Soc. Am. A **2**, 693 (1985).

39. M. S. Scivier, T. J. Hall, and M. A. Fiddy, Opt. Acta **31**, 619 (1984).

40. N. B. Baranova and B. Ya. Zel'dovich, Sov. Phys.-JETP **53**, 925 (1981).

41. A. B. Carlson, *Communication Systems: An Introduction to Signals and Noise in Electrical Communication*, McGraw-Hill Electrical and Electronic Engineering Series (McGraw-Hill, New York, 1968), pp. 153–154.

42. W. H. Press, *Numerical Recipes in C: The Art of Scientific Computing* (Cambridge University Press, Cambridge, England, 1988).

43. J. W. Goodman, in *Laser Speckle and Related Phenomena*, edited by J. C. Dainty, Topics in Applied Physics (Springer-Verlag, Berlin, 1984), Chap. 2, Vol. 9, pp. 9–75.

44. Laboratory for Laser Energetics LLE Review **64**, 170, NTIS document No. DOE/SF/19460-99 (1995). Copies may be obtained from the National Technical Information Service, Springfield, VA 22161.

45. Laboratory for Laser Energetics LLE Review **78**, 62, NTIS document No. DOE/SF/19460-295 (1999). Copies may be obtained from the National Technical Information Service, Springfield, VA 22161.

Advanced Tritium Recovery System

Introduction

As part of the U.S. Inertial Confinement Fusion Program, LLE plans to implode deuterium–tritium (DT)–charged microspheres. These microspheres are filled with high-pressure deuterium and tritium gas under cryogenic conditions. The spheres are then stored and transferred as needed to the target chamber (located in an adjacent room) under vacuum and at temperatures near 20 K. LLE is licensed to handle up to 10,000 Ci of tritium, but site release target is less than 1 Ci per year.

LLE is currently upgrading the systems used to produce, transfer, store, and implode these targets. As part of this upgrade, extensive efforts are being made to ensure staff safety and to limit the radioactive effluent that can be released to the environment. Two independent tritium recovery systems (TRS), currently under construction, will capture any tritium that comes from the various sources. One system will serve Room 157, which houses the production, characterization, and storage of targets, and the other system will serve the target chamber, where the targets are imploded. The exhaust emissions from the process streams, from the gloveboxes that house the streams, and from equipment outgassing will have to be collected and treated to remove any tritium present. This article provides an overview of the requirements and describes the technologies that were considered for the decontamination of the process streams and glovebox-cleanup systems for Room 157.

TRS Design Considerations

1. General Constraints and Considerations

To maximize personnel safety and minimize site emission, the following factors were considered as part of the decontamination systems' design:

(a) Critical components and large inventories have secondary or tertiary containment.

(b) No single component failure results in a release of tritium to the room or to the stack.

(c) Systems containing tritium are designed for high integrity, having all stainless components, with either welded connections or leak-tight (VCR) fittings and a minimum of elastomer seals.

(d) Complex operations are typically automated or, if manual, are covered by detailed procedures.

(e) Protective systems that are poised are designed to be tested regularly to ensure their operability.

(f) Active components are designed to allow easy maintenance.

In addition to the design considerations, the operating staff is technically knowledgeable and extensively trained in handling tritium.

While the system has been designed to limit the likelihood of accidental emissions to a very low probability, additional features are included to minimize chronic releases. These can be summarized as follows:

(a) Since the radiotoxicity of HTO is about 10^4 times greater than that of HT, every effort is made to avoid oxidizing any HT present to HTO.

(b) Mixing of exhaust streams having different gases or tritium concentrations is minimized to limit the quantities of effluent to be decontaminated.

(c) All exhaust streams are monitored and controlled.

(d) All accessible areas are well ventilated to avoid potential tritium buildup due to outgassing from contaminated equipment.

2. Room 157 Functional Requirements

To achieve the above objectives, the Room 157 effluent gases are divided into the following four categories:

– DT high-pressure-system (DTHPS) secondary containment (SC) cleanup
– Glovebox (GB) cleanup (low Y, inert)
– Helium vacuum exhaust cleanup [high temperature (high T), inert]
– Air vacuum exhaust cleanup [low temperature (low T), air]

The relationships between the streams and the subsystems that release these streams are provided in Fig. 89.23.

This sorting was done in order to select the best technology for each type of stream and, as a result, achieve the best performance (i.e., lowest emissions) at a reasonable cost.

The DTHPS handles pure DT under high pressure, so it has its own secondary containment, which, in turn, has its own tritium-scavenging system to collect any DT that escapes from the DTHPS. This DTHPS secondary containment and its DT scavenging system are housed inside the DTHPS glovebox. For these reasons, it is impractical to combine its effluent with any of the other systems.

The second category consists of the gloveboxes that have helium atmospheres. Three process trains exist: one for the DTHPS glovebox atmosphere, one for the FTS (fill transfer station) and TFS (tritium fill station) glovebox atmospheres,

and one that acts as a backup to either. Each train consists of a circulating pump, a drier, and, finally, an HT removal bed. Interconnections are provided to allow various combinations of pumps, driers, and HT removal beds. The driers serve primarily to remove any moisture that permeates into the gloveboxes in order to avoid excess loading of the tritium scavengers, but the driers will also remove any HTO that may be present.

The rationale for further splitting the glovebox-cleanup function is that the DTHPS has its own internal containment and the DTHPS glovebox represents a tertiary containment. It will normally have no or very low levels of tritium, so it will require essentially no cleanup on an ongoing basis. The FTS and TFS gloveboxes have comparable levels of tritium activity, so mixing these will have no significant effect on cleanup. Another factor is the potential for dilution. Since the effectiveness of cleanup is to some extent driven by the initial concentration of tritium, mixing essentially clean streams with contaminated streams actually decreases the tritium concentration in the contaminated stream, resulting in reduced capture efficiencies in some devices.

The third category consists of the vacuum systems that service the helium processes. Again, a further subdivision of this group separates the "clean" sources, specifically the FTS base, dome and cooling loop, permeation cell seal, stalk
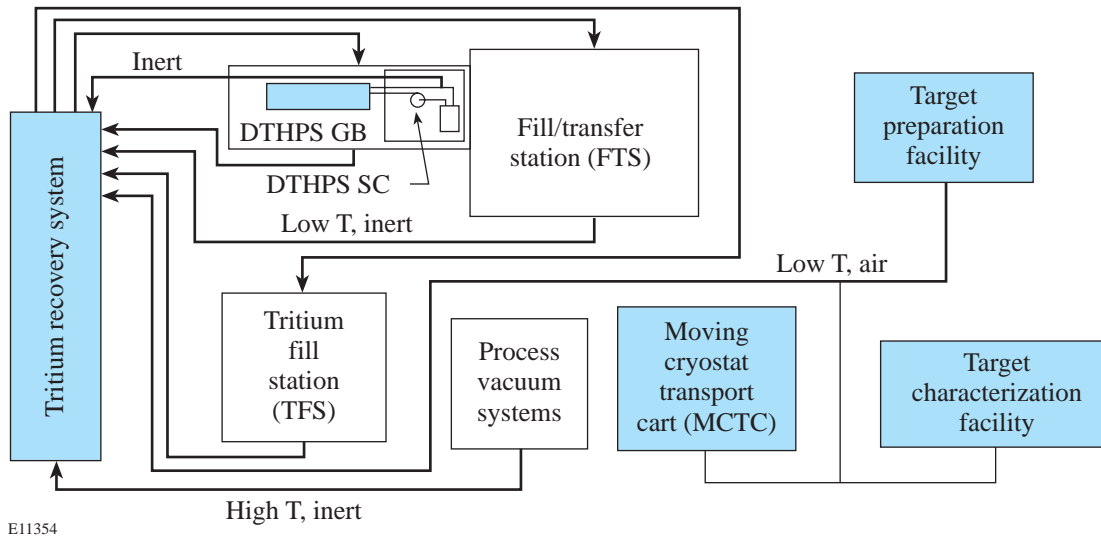

E11354

Figure 89.23
The Room 157 Tritium Recovery System must deal with air and inert gas streams from a variety of sources.

aligner, and borescope, from potentially contaminated sources. Using a monitor to confirm the absence of tritium, the exhaust is routed directly to the stack. If tritium activity is detected, the stream is combined with the other helium vacuum exhaust streams for treatment.

All other helium vacuum exhaust steams are combined into a collection tank. A pump circulates the gas through a drier to remove any HTO, a Ni catalyst bed cracks any organically bound tritium, and finally a scavenger bed removes the product HTO. The subsystem pressure is capped by a relief valve that discharges to a second tank, which can also recirculate any effluent through a second scavenger. The gas in this second loop should be essentially tritium free and should be releasable to the environment. Any discharged gas is nevertheless monitored, and, if it requires further decontamination, it can be routed to the air vacuum exhaust for additional processing.

The final category comprises air vacuum exhaust streams. These streams are not subdivided since they are all normally active, so they will require a routine processing. The stream is initially passed through a drier bed to remove any tritium that might be present as HTO. This may be sufficient to allow the exhaust to be released to the stack, so the stream is monitored at this point and, if possible, sent to stack. If the level of tritium activity is still above the release criteria, the stream is routed to a catalytic oxidizer to convert any tritium that may be present as HT or organically bound tritium (OBT) to HTO. This effluent is then passed through a condenser and another drier bed before going to stack. The final effluent is once more monitored for compliance purposes.

The catalytic reactor most suitable for the LLE application is palladium-coated alumina operated at high temperature (~450°C) and sized to give a residence time of about 4 s. The reactor is followed by a chiller to cool the exhaust before it goes into a drier bed. The catalytic reactor, chiller, and drier beds used in this application are designed for high flow and low resistance to minimize the need for additional pumps to move the gas through the detritiation loops.

All the tritium removal beds have provision for *in-situ* regeneration to eliminate the need for routine bed removal. The regeneration of the HT scavenging beds is accomplished by heating the bed and using a helium carrier flow to accumulate the released HT on a cryogenic molecular sieve before it is transferred to a transportable U-bed for eventual removal from the system. Thus, any captured HT will remain in the elemental form throughout the entire tritium cycle.

The drier beds are also heated for regeneration, releasing the HTO, which is carried by an N_2 gas carrier to a chiller followed by a condenser to remove the bulk of the moisture. The gas then flows to a polishing drier bed, is monitored, and finally released to stack. The recovered moisture, including HTO, is collected in liquid form for interim storage, pending final disposal. Regeneration of driers is by reverse flow to counteract HTO tailing in the drier beds. Hot, dry nitrogen gas is used as a carrier to achieve dew points below −100°C. This allows an extended operating cycle while still maintaining the low outlet tritium concentration needed to meet emission targets.

Tritium Removal Technologies

A number of viable options are available for removing HT from inert gas streams, and given the number of helium-based streams at LLE, every effort was made to use this capability to minimize the production of HTO. The following section examines the technologies that were applicable to the LLE Tritium Removal System.

1. Uranium Beds

Uranium reacts exothermically with hydrogen at room temperature, forming UH_3. Uranium has a high storage capacity for hydrogen (up to 300 scc/g U) and uniform reaction kinetics over a very large H/U ratio. The decontamination factor varies depending on flow and tritium concentration, but a practical minimum effluent concentration of $\leqslant 2$ mCi/m^3 is achievable.[1]

The hydriding reaction is reversible, and by heating the hydride to ~400°C, the hydrogen is released, restoring the bed to its original state. Varying the amount of heat applied can control the hydrogen release rate. However, uranium reacts not only with hydrogen, but also reacts strongly with oxygen and somewhat with nitrogen at room temperatures. Both the oxidation and nitriding are exothermic and become more vigorous at elevated temperatures. When purged with air, U-beds will release stored tritium.

For this reason, uranium can be used only for tritium removal from inert gas streams. It will remove large amounts of tritium with high efficiency and will do so for considerable carrier gas flow rates. Its affinity for oxygen and, to some extent, other gases serves to purify the tritium since only the hydrogen isotopes are released when uranium is heated, although at the cost of irreversibly reacting with the uranium. U-beds have been extensively used, and a very large experience base exists to support this application.

Uranium is not recommended for inert glovebox atmosphere cleanup since the practical decontamination level of ~2 mCi/m^3 is higher than desired. It is best used where large quantities of tritium must be removed and where the effluent will not be released to stack.

2. Zirconium-Iron (ZrFe) Beds

The ZrFe alloy known as ST-198 can also scavenge tritium from inert gas streams since it forms a stable tritide that can be reversibly decomposed.[2] It has a rather modest storage capacity for tritium (0.8 scc/g alloy yields a 1-mCi/m^3 vapor present over the alloy) but can decontaminate to μCi/m^3 levels if tritium inventory of the alloy is kept sufficiently low. Although it requires a substantial residence time (>3 s) to achieve good detritiation, it is an excellent tritium scavenger for glovebox decontamination and for polishing exhaust streams before stacking. Since ST-198 reacts very slowly with nitrogen at room temperature, it can be used to scavenge HT from nitrogen streams.[3] It does not react with organics (CH$_4$), so it will not scavenge tritiated organics from a gas stream unless the stream has been preconditioned with a nickel catalyst to crack the organics to produce HT.[4,5] While ST-198 can be regenerated by heating, it degrades during this process and consequently has a limited lifetime.

Like uranium, ST-198 reacts with oxygen at room temperature and with nitrogen at elevated ($\geq$450°C) temperatures. Both reactions will release stored tritium. ZrFe is best where quantities of hydrogen isotopes are limited, but where the effluent tritium concentration must be suitable for release to the environment.[6,7]

3. Cryogenic Molecular Sieves

Cryogenic molecular sieves can scavenge hydrogen isotopes from a helium carrier by adsorbing the hydrogen molecules. Depending on the partial pressure of hydrogen that is acceptable, molecular sieves operating at liquid nitrogen (LN) temperatures can have a high capacity for hydrogen isotopes. However, the tritium is not firmly bound in the molecular sieve at 77 K, so the tritium residence time in the bed is finite. The residence time is a function of both flow and geometry in that longer beds and lower flows yield a longer time to breakthrough. Warming the molecular sieve slightly above LN temperatures (i.e., to ~100 K) will release the stored hydrogen isotopes. At these temperatures, all other gases will remain firmly adsorbed, thus allowing the recovery of pure-hydrogen

isotopes. These gases can, however, be desorbed by heating the molecular sieve to 350°C, regenerating the molecular sieve to its original condition.

These characteristics make cryosorption an excellent technique to scavenge tritium from helium gas streams. Low exhaust levels of tritium activities can be achieved by limiting the amounts of tritium in the molecular sieve and by monitoring for impending breakthrough. When breakthrough becomes evident, the bed needs to be valved out of service so it can be unloaded. The unloading process proceeds rapidly since the bed needs to be warmed to only 100 K for complete HT unloading.

Figure 89.24 illustrates the efficacy of a cryogenic mole sieve bed to remove HT from a helium stream containing up to 800 mCi/m^3. During this test, the activity downstream of the bed remains below 0.3 mCi/m^3 until breakthrough occurs.
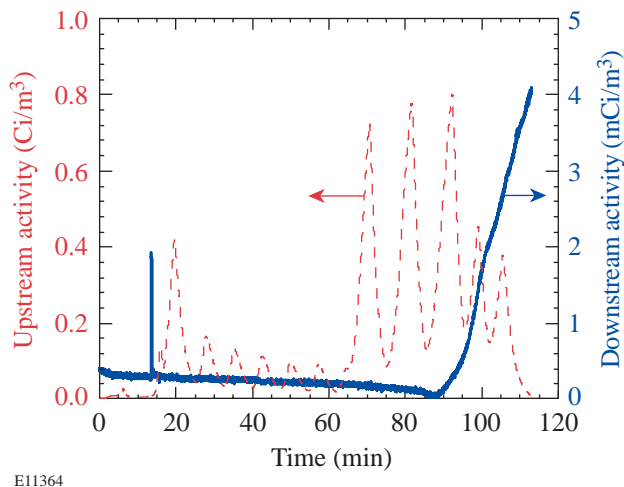
E11364

Figure 89.24
Transfer of tritium from 800-g ST198 bed to cryogenic mole sieve bed with a 28 sLPM helium carrier until tritium breakthrough is observed.

The chief disadvantage of cryosorption is that it requires liquid nitrogen temperatures to retain the hydrogen isotopes on the molecular sieve. This means that a loss of cryogenics could result in the inadvertent release of hydrogen. This capture technology is not passively safe. In addition, the complexity of cryogenic handling is costly and requires techniques and skills that are not commonplace. An example is the need for regenerative heat exchangers as part of any cryotrap to obtain high utilization of liquid nitrogen inventories.

System Configuration

A comprehensive tritium removal system (presented schematically in Fig. 89.25) has been designed and is being built so that LLE can perform its research program and still meet tritium emission targets. To ensure that this system can provide the desired detritiation performance and also provide the highest practical degree of staff safety, all relevant technologies were extensively reviewed. Based on this review, ZrFe scavenger beds are used to reduce tritium levels to low values, cryogenic molecular sieves are used to concentrate tritium, and uranium flow-through beds are used to capture large amounts of tritium. Nickel catalysts are used to crack organics, Pd on alumina is used to oxidize any tritium compounds in air systems, and 5A molecular sieve driers were selected to remove HTO. The technologies selected for the final design were those judged most suitable based on demonstrated robustness, effectiveness, and real-life operating experience.

REFERENCES

1. W. T. Shmayda and N. P. Kherani, Fusion Eng. Des. **10**, 359 (1989).

2. W. T. Shmayda, N. P. Kherani, B. Wallace, and F. Mazza, Fusion Technol. **21**, 616 (1992).

3. K. J. Maynard, N. P. Kherani, and W. T. Shmayda, Fusion Technol. **28**, 1546 (1995).

4. N. P. Kherani, W. T. Shmayda, and R. A. Jalbert, Fusion Eng. Proc. **2**, 1239 (1987).

5. A. B. Antoniazzi and W. T. Shmayda, Fusion Technol. **30**, 879 (1996).

6. A. G. Heics and W. T. Shmayda, Fusion Eng. **1**, 65 (1994).

7. A. G. Heics and W. T. Shmayda, Fusion Technol. **28**, 1509 (1995).
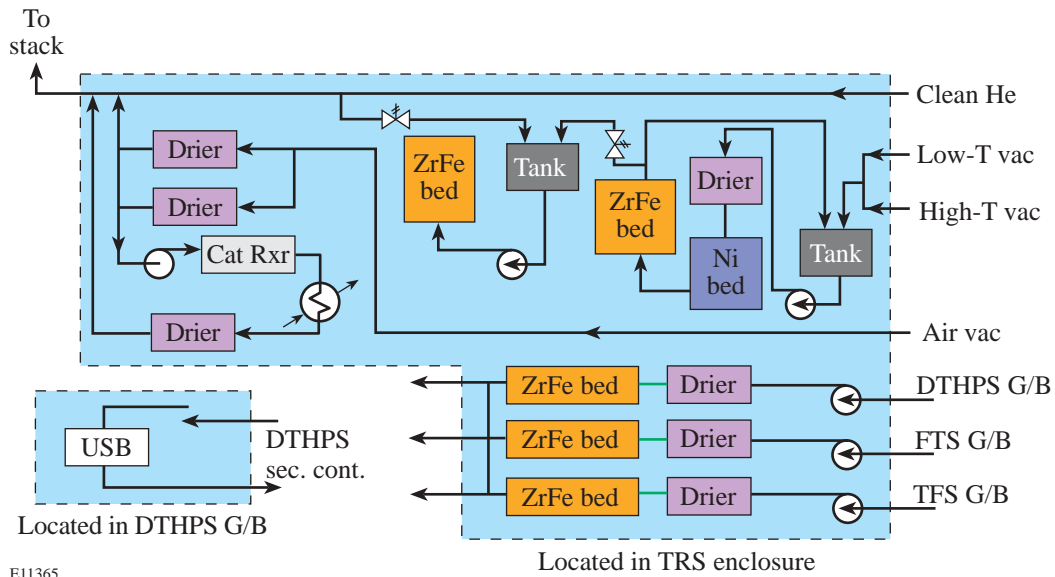
Figure 89.25
Schematic of the Room 157 Tritium Recovery System.

Establishing Links Between Single Gold Nanoparticles Buried Inside SiO₂ Thin Film and 351-nm Pulsed-Laser-Damage Morphology

Introduction

Over the past several years research has indicated that nanoscale defects, dispersed inside thin films with relatively low abundance, are a major laser-damage-initiation source in the UV spectral range.[1–4] The extreme difficulties in characterizing these defects virtually stalled the experimental effort to identify the laser-damage mechanism. This situation led to a proposed model SiO_2-thin-film system[5] with artificially introduced gold nanoparticles serving as well-characterized absorbing defects.

Advantages of such a system include high intrinsic-damage resistance of SiO_2 thin film—which allows artificially-introduced-defect–driven damage to be separated from the intrinsic damage—and the possibility to control the location and size of the nanoparticles. Optical parameters of gold nanoparticles are well documented in scientific literature,[6] and different-sized particles, with narrow size distributions, are available in the form of gold colloids.

Our previous work[5] focused on comparative atomic force microscopy (AFM) investigation of the nanoparticle and 351-nm damage-crater areal density statistic. The results provided the first experimental evidence of the laser energy absorption process spreading from the defect into the thin-film matrix during the laser pulse. The process starts with an absorption in a particle. As the temperature rises, energy transfer from the particle (via UV radiation, thermionic emission, heat conduction, etc.) to the surrounding matrix causes its effective conversion to an absorptive medium and, consequently, damage.

The next step in this work is to establish a direct link between a single nanoparticle buried inside a SiO_2 thin film at a particular location and the film morphology changes caused by pulsed-laser irradiation. The AFM mapping of the film surfaces after particle deposition and laser-irradiation steps opens the possibility of finding, for each detected damage crater, the corresponding nanoparticle, initiating crater formation. As a result, a key question is addressed—How does the damage scale (crater depth and lateral size) correlate with the particle size? Surprisingly, the correlation appears to be very weak, which is explained by the peculiarities of nanoscale defect/host matrix interaction in the inhomogeneous thin-film medium.

The nanoparticle/damage crater correlations also allow direct comparisons of energy deposited in a particle and energy required for crater formation. The results confirm damage mechanism, considering absorption initiation in a particle with subsequent growth of the absorbing volume within the surrounding film matrix on the later laser-pulse stages.

The same correlations reveal crater formation probabilities as a function of the local laser fluence. By extrapolating a probability curve to zero value, one can find the laser fluence at which only limited matrix melting and no crater formation occur, which, later in this article, will be referred to as "nanoscale" damage threshold. Experimental damage thresholds derived this way allow a more-meaningful comparison with theories that consider matrix melting as a damage onset.

Experimental

1. Damage-Test Sample

   Sample preparation involves several steps:

   (a) Fused-silica glass 7980 is cleaved to ~14 × 7 × 6-mm pieces to provide a virgin unprocessed surface (14 × 6 mm) for SiO_2 thin-film deposition.

   (b) The sample is taken to the AFM (Nanoscope III, Digital Inst./Veeco) equipped with a nano-indenting diamond tool, which is used to produce small, ~1-μm-lateral-size, 100-nm-deep indentations organized in a square-type pattern with ~20-μm sides. This pattern is later used as a reference to help find the AFM-mapped areas on the sample surface.

(c) The 120-nm-thick SiO_2 coating is prepared by conventional *e*-beam deposition (base pressure 1.3×10^{-6} Torr; deposition rate 26 nm/min).

(d) Gold nanoparticles in the form of gold colloid are diluted in isopropanol (to achieve an average areal density of 0.3 to 3 μm^{-2}) and deposited by a micropipet onto a SiO_2-coated surface. Three particle sizes are used (5.2-nm, 8.4-nm, and 14.3-nm average diameter) but only one size is used for each experiment. The particle-size distributions provided by the supplier (Ted Pella, Inc.) are presented in Fig. 89.26.

(e) After solvent evaporation (special attention is paid here to the solution-drying protocol to prevent *particle agglomeration*), the sample surface is mapped by the AFM at several locations (each map covers $\sim 6 \times 6$-μm area) in the vicinity of the indentations. Only a few agglomerated particles, mostly in the form of duplets, can be found at each location. Their portion is less than 10% of the total particle population.

(f) As a final step, the sample is taken a second time to the coating chamber and coated with an additional 60-nm layer of SiO_2.

The SiO_2 thin-film sample resulting from this procedure is 180 nm thick and contains gold nanoparticles at a well-defined depth of 60 nm (Fig. 89.27).

An additional sample, not containing particles, is prepared for each experiment, following the above protocol, to make available an undoped SiO_2 damage-test reference.

2. Damage Testing and Sample Irradiation Conditions

The 351-nm, 0.5-ns pulses from a Nd-doped glass laser are used for 1-on-1 damage-threshold evaluation. Laser-beam spot size ($\sim 400\,\mu m$) and fluence distribution are obtained from images captured by a CID (charge-injection device) camera in a sample equivalent plane. Damage onset is detected by means of 110×-magnification dark-field microscopy and, since optical tools are used to determine damage threshold, it will be referred to as an "optical" damage threshold. The "nanoscale" damage threshold, associated with the onset of crater formation and derived from the *AFM investigation* of the post-irradiated coating morphology, will be introduced later in this article. The maximum laser fluence level, used to irradiate the AFM-mapped sites, is varied 10% to 70% above the optical damage threshold. Under these conditions, laser-damage
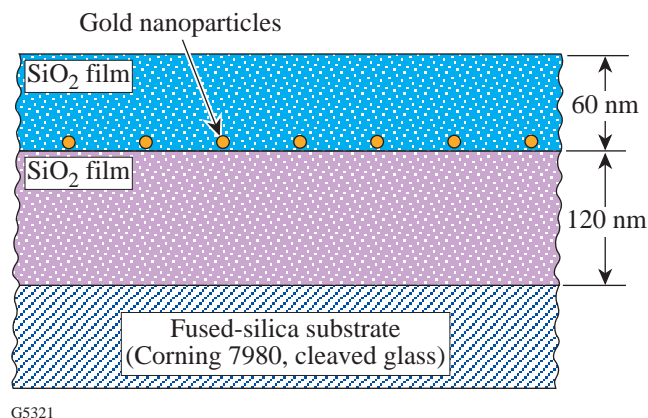
G5321

Figure 89.27
Schematic presentation of the SiO_2 sample with embedded gold nanoparticles.
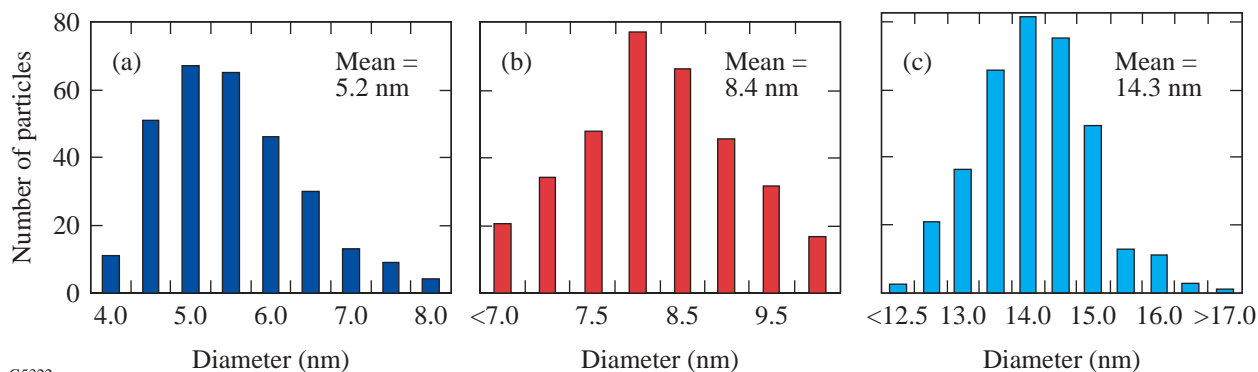
G5322

Figure 89.26
Nanoparticle-size distributions provided by the supplier (Ted Pella, Inc.): (a) 5.2-nm, (b) 8.4-nm, and (c) 14.3-nm average diameter.

morphology is represented by submicrometer-scale craters (Fig. 89.28). The laser-beam spot usually covers several mapped sites, which ensures that different damage levels at different mapped sites will be achieved.
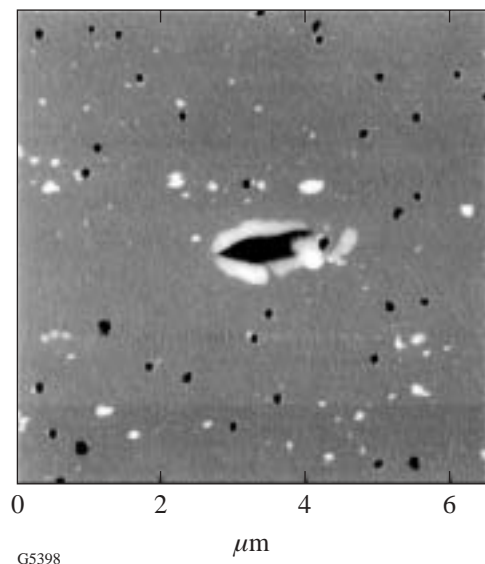
Figure 89.28
The AFM map of a SiO$_2$ coating containing 8.4-nm gold particles and irradiated by a laser pulse with 4.6-J/cm^2 fluence. The indentation in the center of the map serves as a site identification.

3. AFM Mapping

The very small particle size (up to ~4 nm) limits the maximum AFM scan size during particle mapping. Due to tip-sample convolution effects, a 5-nm-diam particle is typically imaged as a feature with ~20- to 25-nm lateral size. Note that modest convolution does not affect the *vertical* scale, which gives a true particle diameter provided that the pedestal is reasonably flat. Bearing this in mind, 2×2-μm or 3×3-μm AFM scans for 5.2-nm and 8.4-nm particles, correspondingly, were performed. The highest-available, 512×512-pixel image resolution ensures at least five to six data points (pixels) per particle diameter. This requires performing six or seven over-lapping, 2×2-μm scans to create a map with a sufficient number of particles for size-effect studies and analyses. The AFM was operated in a tapping mode and employed Si probes with tip radii typically better than 10 nm and apex (last 200 nm) cone angles better than 20°, ensuring ~10-nm lateral resolution. A crater vertical wall slope up to 70° was imaged without convolution along the scan's x axis (along cantilever beam) and up to 80° along the y axis. Typical particle and crater cross-sectional profiles obtained from AFM images are presented in Fig. 89.29.

Results and Discussion

1. Damage Thresholds

The damage-threshold measurement results are summa-rized in Table 89.I. The introduction of gold nanoparticles causes a dramatic reduction in damage threshold. For the

Figure 89.29
Cross-sectional profiles taken through (a) 8.4-nm particles and (b) a typical damage crater.

smallest, 5.2-nm particles, a 4.4-fold reduction, compared to the undoped reference sample, is observed. An even larger threshold drop was found in our previous experiment[5] using the same 5.2-nm particles. It is attributed to particle agglomeration, which is all but eliminated in this work.

The damage-threshold fluence plotted in Fig. 89.30 as a function of the average particle size can be approximated by

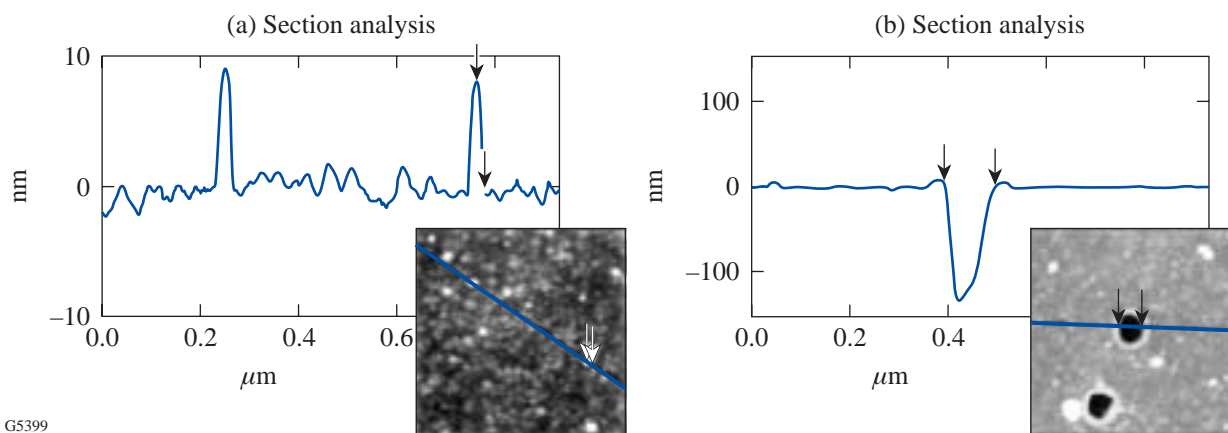$$F_{th} \sim 1/R^t , \qquad (1)$$

where R is the particle radius and $t \sim 0.4$ to 1.0.

An extrapolation of this dependence (Fig. 89.30) to the intersection with the threshold value for the undoped reference sample $F_{th} = 27.1$ J/cm² allows rough estimates for the absorptivity of the intrinsic absorbing defects. By fitting Eq. (1) to the experimental data with their designated error bars, one finds that the possible range for x intercepts lies between 0.1 nm and 1.4 nm.
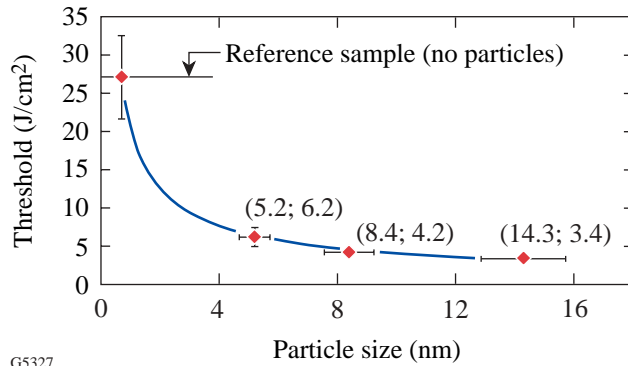
Figure 89.30
Damage threshold as a function of the average particle size. The solid line is the best fit using $F_{th} \sim 1/R^t$ approximation. Numbers in brackets indicate particle size and threshold values, respectively.

It implies that intrinsic defect absorptivity should be similar to the absorptivity of gold particles with a size ≤1.4 nm. Considering Si clusters in SiO₂ film as prime candidates for the intrinsic nanoabsorber role and using Si cluster absorptivity[7] and bandgap/cluster size dependence[8] data, an estimate for the cluster diameter gives values of 1.3 nm ≤ D ≤ 2 nm.

2. Mechanism of Laser-Energy Deposition Inside Thin Film
In all experiments with 5.2-nm and 8.4-nm particles and laser fluences from 2 to 7 J/cm², craters were found exclusively at the positions where particles were lodged during deposition (Fig. 89.31). This proves that (1) particles adhere to the SiO₂ film and are not displaced during deposition of the 60-nm capping layer, and (2) absorbing gold defects alone contribute to the damage process at threshold laser fluences.

This one-to-one link between each nanoparticle and the laser-induced local changes in film morphology has a great advantage over other, nonlocal approaches. For instance, energy absorbed by the individual nanoparticle can be compared with energy required to produce a crater at this location. The calculation of energy absorbed by the particle is based on a simple formula:

$$E_{abs} = F \sigma_{abs} , \qquad (2)$$

where F is the experimentally determined laser-fluence value and σ_{abs} is the Mie[9] absorption cross section.

In the small nanoparticle approximation $2R \ll \lambda$, fully applicable for particle sizes used in this work, according to the Mie theory,[9] the cross section of this process is dominated by dipolar absorption:

$$\sigma_{abs}(\omega) = 9 \frac{\omega}{c} \varepsilon_m^{3/2} V_0 \frac{\varepsilon_2(\omega)}{\left[\varepsilon_1(\omega) + 2\varepsilon_m\right]^2 + \varepsilon_2(\omega)^2} , \qquad (3)$$

Table 89.I: Damage thresholds of SiO₂ film containing gold nanoparticles.

Nanoparticle Average Size (nm)	Damage Threshold (J/cm²)
5.2	6.2±0.2
8.4	4.2±0.1
14.3	3.4±0.2
Reference sample (no particles)	27.1±3.0

Figure 89.31
AFM images of ~2 × 2-μm surface area containing six nanoparticles: (a) nanoparticle map, (b) same area after 60-nm SiO₂ overcoat and irradiation. The craters are formed at exactly the nanoparticle locations.
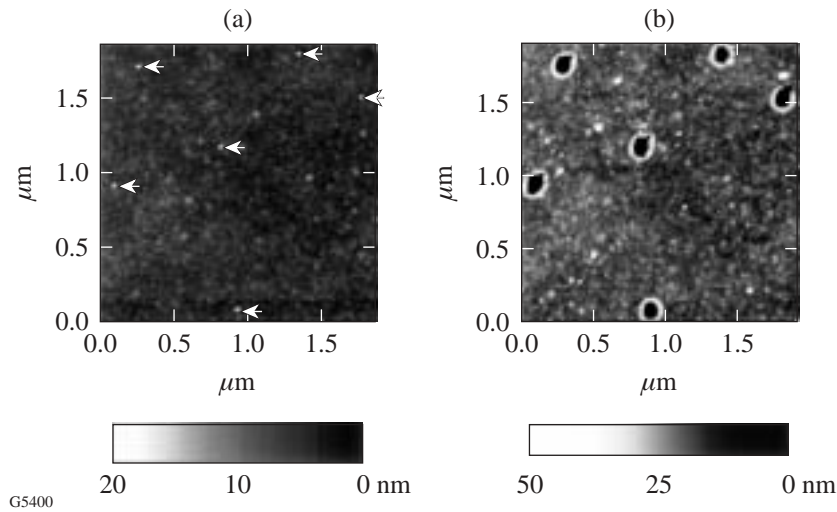
G5400

where V_0 is the particle volume [$V_0 = (4/3)\,\pi R^3$], ε_m is the dielectric function of the medium (SiO₂), $\varepsilon_1(\omega)$ and $\varepsilon_2(\omega)$ are the real and imaginary parts, respectively, of the particle dielectric function, and ω is the laser frequency. The calculation was done for particle sizes ranging from 4 nm to 12 nm, $\varepsilon_m = 2.19$ for SiO₂, and data for ε_1 and ε_2 are taken from Kreibig et al.[6]

The energy required to produce a crater can be estimated by assuming that the material within the crater volume is heated up to the boiling point with subsequent vaporization. The presence of the melting stage is supported by the crater morphology. The glassy, structureless walls and a rim elevated above average surface level [Fig. 89.29(b)] are missing the characteristic granular structure of the surrounding film, which provides clear evidence for melting and resolidification into the glass-type structure during the cooling stage.

Assuming this mechanism, the energy required for crater formation is expressed as

$$E_{cr} = V_{cr}\left[C\rho\left(T_b - 293\,\mathrm{K}\right) + H_{fus} + H_{vap}\right], \qquad (4)$$

where V_{cr} is the crater volume, C is the silica heat capacity, ρ is the density, T_b is the boiling point, and H_{fus} and H_{vap} are the heat of fusion and heat of vaporization, respectively. Values of the parameters used for the calculation of E_{cr} are $C = 741$ J/kg K, $\rho = 2200$ kg/m³, $T_b = 2503$ K, $H_{fus} = 3.12 \times 10^8$ J/m³, and $H_{vap} = 7.6 \times 10^9$ J/m³.

C and ρ are considered independent of temperature for a lack of available high-temperature data (>2000 K). Taking into account that the heat capacity for most glasses increases over the temperature interval of 1 K to 1900 K would result in an ~16% increase in the E_{cr} value calculated from Eq. (4). V_{cr} is derived from AFM data.

The results of calculations for E_{abs} and E_{cr} for eight selected nanoparticles and corresponding craters are presented in Table 89.II, which clearly shows that, considering that the energy absorption process is localized inside the particle, the amount of energy absorbed cannot provide crater formation since $E_{abs} < E_{cr}$ for all but one particle (last row).

This conclusion is valid not only for a chosen set of particles and corresponding craters but also for the majority of such pairs from Fig. 89.32 and all particle/crater pairs from Figs. 89.33(b) and 89.33(c). One must also keep in mind that the energy balance considerations, presented above, are simplified. It implies that all of the energy absorbed inside the particle is used to form a crater. It does not take into account the heating of the volume surrounding the crater and particle, as well as radiative losses. The former contribution can be quite significant since the temperatures in the immediate particle vicinity are much higher than at the sample surface.

These additional dissipation channels cause the energy deficit between E_{abs} and E_{cr} to widen, confirming earlier[5] findings that *absorption initiated in the gold nanoparticle spreads out to the surrounding matrix during the laser pulse*. The conversion of the transparent matrix into an absorptive medium involves energy transfer from the particle heated to a high (up to ~10^4 K) temperature.[10] The possible channels include ionization by thermal UV radiation,[10] electron injection through thermionic emission, and thermal ionization via

conductive heat transfer.[11] The modeling of absorbing volume (plasma ball) growth by Feit *at al.*[12] pointed to exponential behavior of this process as a function of laser fluence.

3. Nanoparticle Size/Damage-Crater-Depth Correlations

The next question to be addressed is how damage-crater scale (depth, lateral size) correlates with particle size. Since the crater's lateral size and depth showed qualitatively similar behavior as a function of particle size, the crater depth is used here for illustration purposes. It is useful to mention here that the intuitive expectation that the crater depth should be the well-defined depth (60 nm) at which particles are lodged is not supported by the experimental results. In fact, craters with depths ranging from 10 to 160 nm are produced for 5.2-nm- and 8.4-nm-average-size particles at different laser fluences (see Figs. 89.32 and 89.33). If energy deposited in the absorbing volume is low, only partial evaporation of the material above the particle takes place and shallow craters with depths <<60 nm are formed. In the other limit, with increasing energy, the absorbing volume is also growing and craters with depths exceeding 60 nm can be formed. In the first approximation [Eq. (3)], the absorption cross section for small particles is proportional to the particle volume V_0. Accordingly, one might expect fairly strong crater-size/particle-size dependence. Experimental findings showed two distinctively different cases, represented in Figs. 89.32 and 89.33.

Table 89.II: Energy absorbed by the particle and energy required for crater formation.

| Particle Size (nm) | σ_{abs} (cm²) | F (J/cm²) | E_{abs} (J) | Crater | | |
				Depth (nm)	Lateral Size* (nm)	E_{cr} (J)
4.0	2.2×10^{-14}	3.2	7.0×10^{-14}	60	47	4.0×10^{-13}
5.3	4.9×10^{-14}	4.0	2.0×10^{-13}	72	53	6.1×10^{-13}
6.3	7.1×10^{-14}	4.0	2.8×10^{-13}	86	64	1.1×10^{-12}
8.1	1.7×10^{-13}	4.0	6.8×10^{-13}	88	63	1.1×10^{-12}
9.2	2.5×10^{-13}	4.6	1.2×10^{-12}	120	83	2.5×10^{-12}
10.4	3.4×10^{-13}	4.6	1.6×10^{-12}	124	95	3.4×10^{-12}
11.8	5.2×10^{-13}	4.6	2.4×10^{-12}	130	112	4.9×10^{-12}
10.0	3.2×10^{-13}	2.3	7.4×10^{-13}	54	50	4.1×10^{-13}

*The lateral size is measured at the average level of the film surface [see Fig. 89.29(b)].
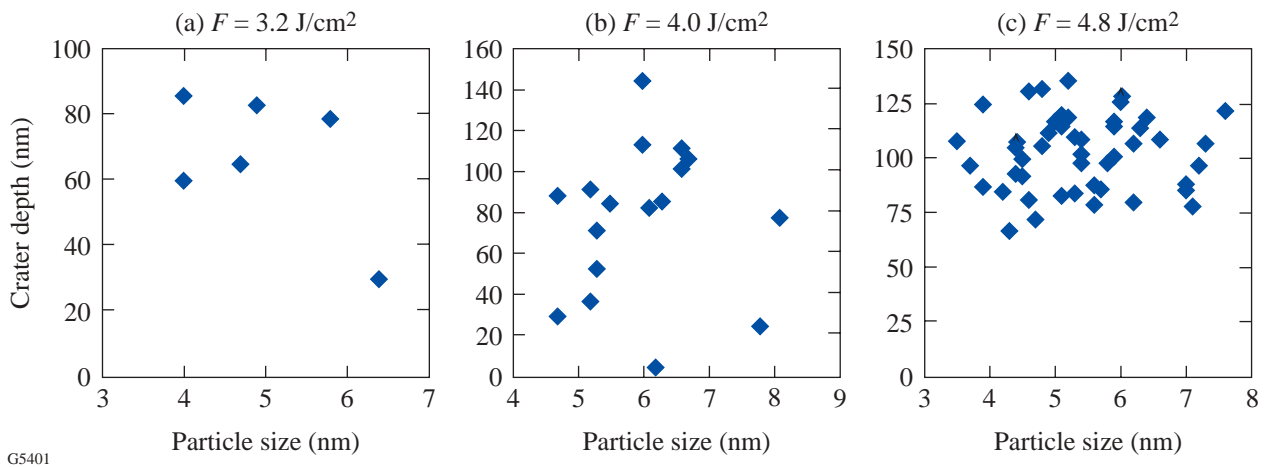

G5401

Figure 89.32
Crater depth as a function of the particle size for 5.2-nm-average-size particles and laser fluence (a) 3.2 J/cm², (b) 4.0 J/cm², and (c) 4.8 J/cm².

In the first case, described by laser fluences of less than 70% of the optical damage threshold, almost *no correlation* is found between particle size and crater depth [Figs. 89.32(a), 89.32(b), and 89.33(a)]. Moreover, at these low laser fluences, when a minor fraction of particles gives rise to crater formation, a situation is frequently encountered where small particles form craters but a larger particle located within a distance of ~1 μm does not. At a constant laser fluence for both particles, the strong influence of the inhomogeneous local particle environment inside the SiO$_2$ film becomes apparent for the laser-energy absorption process and the dissipation channels.

In agreement with a model that considers the effective growth of the absorbing volume caused by particle/matrix interaction during the laser pulse, two factors define the effectiveness of laser-energy deposition:

a. Absorption of laser-pulse energy by the particle itself. In a porous thin-film medium, the nanoparticle's physical contact with the host matrix is not perfect (Fig. 89.34), which results in the effective dielectric function ε_{eff}:

$$\varepsilon_m \geq \varepsilon_{eff} \geq \varepsilon_{air} = 1. \qquad (5)$$

Taking data from the literature[6] on ε_i (351 nm) for nanoparticles with size $2R = 5$ nm ($\varepsilon_1 = -0.8$, $\varepsilon_2 = 6.2$) and ε_m (SiO$_2$) $= 2.19$, we obtain from Eq. (3)

$$\sigma_{abs}(SiO_2)/\sigma_{abs}(air) = 2.5.$$

This result reveals the potential for significant variation in the effectiveness of damage initiation depending on the local physical environment of each gold nanoparticle.

b. Absorption by the matrix modified via energy transfer from the heated particle. Energy transfer from a particle heated to a high temperature in the early stages of the laser pulse to the surrounding film matrix is an essential part of the damage process. To achieve absorption in the particle-surrounding matrix, the energy should be transferred in a time scale of laser pulse length. Any air voids between particle and matrix (Fig. 89.34) will dramatically reduce the rate of such processes as either heat transfer by thermal conductivity or injection of electrons through thermionic emission. The same voids of the order of particle radius, due to geometrical factor, will reduce fluence of the UV radiation coming from the heated particle and consequently matrix ionization rate.
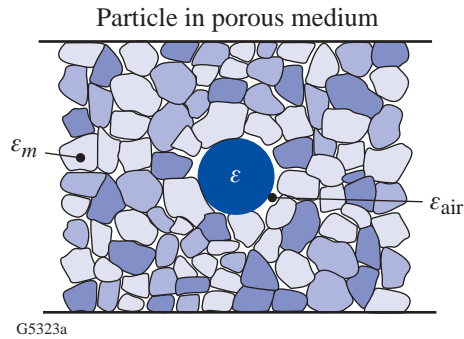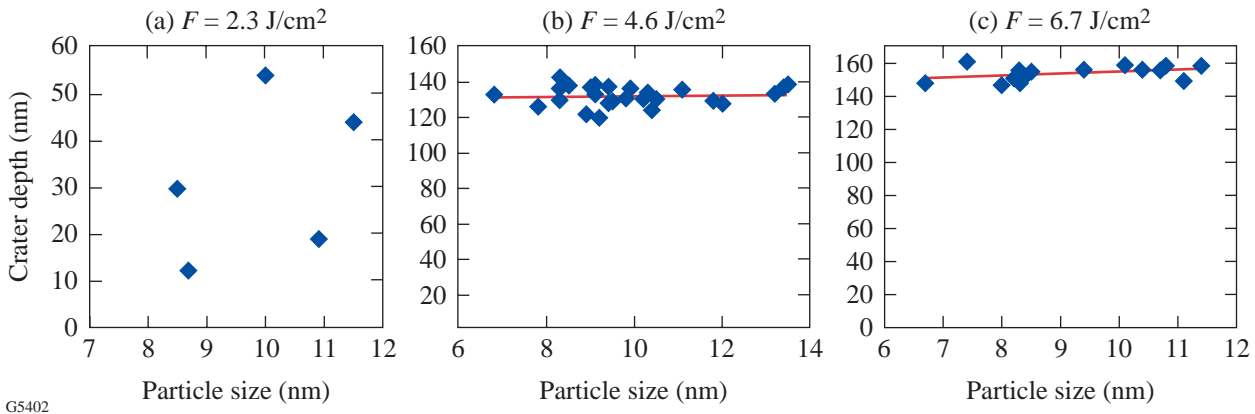
Particle in porous medium

G5323a

Figure 89.34
Schematic presentation of the particle embedded in the porous medium.

G5402

Figure 89.33
Crater depth as a function of the particle size for 8.4-nm-average-size particles and laser fluence (a) 2.3 J/cm^2, (b) 4.6 J/cm^2, and (c) 6.7 J/cm^2.

As a conclusion, effectiveness of the energy transfer from the particle to the surrounding matrix, facilitating growth of the absorbing volume and energy acquisition from the laser pulse, is a strong function of the local particle environment.

In summary, randomness in the local particle environment in the inhomogeneous thin-film medium introduces random variations in crater size and the probability of crater formation. These variations, at laser fluences below optical damage threshold, dominate particle-size effects as long as the size variation is modest, i.e., ±25%. An interesting implication from the above considerations is that porous thin films with large voids might be more damage resistant than dense films, provided that nanoscale absorbers remain the same. High UV damage thresholds of sol-gel–derived coatings,[13] characterized by large free volume, provide additional support for such a hypothesis.

The second case is characterized by very slow linear behavior of crater-depth/particle-size dependence at laser fluences *exceeding* the threshold by 20% to 70% [Figs. 89.33(b) and 89.33(c)]. At these laser-fluence conditions, all gold nanoparticles, mapped by the AFM, give rise to crater formation (100% probability), yet craters show surprisingly narrow depth distributions. Such a trend provides an indication that, with increasing pulse energy, the influence of initial conditions (local environment; particle-size variation) on the final result—crater formation—becomes less important. This can be explained by assuming that the ionized matrix in the particle vicinity starts taking on the dominant absorber role. In this case, the effective absorbing volume of the matrix should be much larger than the particle volume. The radius of this matrix volume should be several times larger than both the particle radius and the average void diameter. Such an increase in effective absorbing volume allows averaging over many local inhomogeneities, resulting in a significant reduction in random variation of the crater depth.

An example of the intermediate case for 5.2-nm particles is presented in Fig. 89.32(c), where crater-depth variation is reduced compared to the low fluence data in Figs. 89.32(a) and 89.32(b), but still significantly larger than for the above-threshold fluence data presented in Figs. 89.33(b) and 89.33(c).

To summarize results on particle/crater correlations: At laser fluences below the optical-damage threshold, effects caused by ±25% variations in particle size are obscured by strong local influence of the inhomogeneous thin-film medium on the crater-formation process. With increasing laser fluence, the probability of crater formation also increases, while the

crater-depth variation is reduced due to the averaging effect caused by the larger absorption volume.

4. Crater-Formation Probability and "Nanoscale" Damage Thresholds

The possibility of detecting laser-induced morphological changes in thin film at each mapped nanoparticle location allows one to investigate the probability of crater formation for an ensemble of particles confined to a small area (typically ~6 × 6 μm), within which the laser fluence can be considered constant.

The probability of crater formation can be defined as the ratio of the number of particles giving rise to crater formation to the total number of particles within the mapped area. Taking into account that craters are detected only at particle locations, this is also the ratio of the number of craters to the total number of particles within the area. The probabilities calculated in this way for 5.2-nm- and 8.4-nm-average-diam particles are presented in Fig. 89.35 as a function of laser fluence. An extrapolation of the crater-formation probability curve to zero probability level allows one to define a laser-fluence value at which only localized melting and no vaporization of the material are observed.
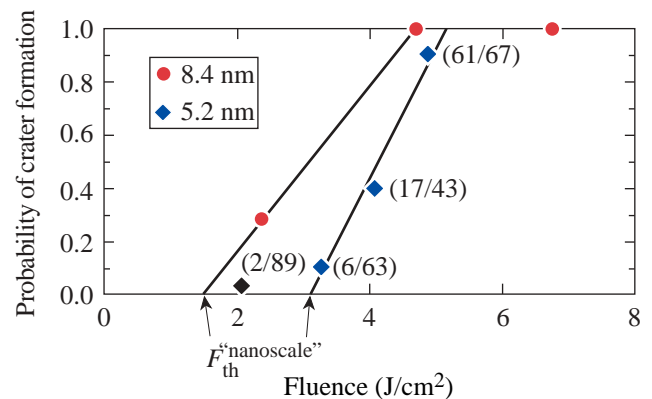
G5328

Figure 89.35
Probability of crater formation as a function of laser fluence. Numbers in brackets indicate crater/particle ratio for each mapped site. Nanoscale damage thresholds are derived from an extrapolation to zero probability.

Defined this way, *nanoscale* damage thresholds are derived as ~3.0 J/cm² and ~1.5 J/cm² for 5.2-nm and 8.4-nm particles, respectively. These are more than a factor of 2 lower than the ones obtained through optical microscopy observation. The introduction of such a threshold establishes a basis for more-meaningful comparison between theory and experiment, since

the majority of theoretical approaches consider damage onset to occur when the film material reaches the melting temperature.

Recent theoretical work by P. Grua and H. Bercegol[14] applied the Mie theory to a similar system of gold nanoparticles embedded in a glass matrix. The gold particle reaching the melting temperature was chosen as a damage criterion for calculating damage threshold. For 3.6-eV photon energy (photon energy of 351-nm radiation = 3.53 eV), 0.5-ns pulses, and particles of $2R$ = 6-nm size, the calculated damage threshold becomes ~0.4 J/cm^2. This value is much lower than ~3-J/cm^2 nanoscale threshold for 5.2-nm-average-size particles obtained in this work and associated with the matrix melting. The difference may be attributed partially to the fact that gold's melting temperature T_{Au} = 1336 K is much lower than silica's melting temperature T_{SiO_2} = 1986 K, which again points to the importance of using similar damage criteria for both theory and experiment. In the work of F. Bonneau et al.,[15] the simulations of nanometer-scale-inclusion–driven laser damage of fused silica indicated that damage onset occurred when the SiO$_2$ matrix reached the melting point. For 10-nm-diam Al nanoparticles and irradiation conditions identical to this work (351 nm, 0.5 ns), the calculated threshold was F_{th} ~ 2 J/cm^2. The fact that this article reports nanoscale threshold of 1.5 J/cm^2 for similar-sized, 8.4-nm gold particles unfortunately does not indicate an agreement between theory and experiment. Taking into account the difference in the absorption cross section and other relevant parameters for aluminum and gold results in a significant reduction in the calculated threshold value when substituting Al particles with Au. This points to the necessity for further theoretical and experimental investigation of the damage mechanisms.

Conclusions

- Introduction of gold nanoparticles into an SiO$_2$ thin film leads to a significant reduction in 351-nm damage thresholds. An extrapolation of damage threshold versus particle size curve to the intersection with undoped sample threshold allows one to estimate the size of intrinsic nanoscale absorbers (presumably Si clusters) as 1.3 to 2 nm.

- AFM mapping shows excellent correspondence between particle and crater location, indicating that absorption by gold particles is solely responsible for the damage initiation.

- Numerical estimates of energy absorbed by gold particles and energy required to melt and evaporate material within the crater volume confirm that laser-energy absorption cannot be confined inside the particle, but rather starts in the particle and then, upon temperature rise, spreads out to the surrounding matrix.

- The particle/crater correlations show peculiarities that can be explained by the influence of thin-film inhomogeneities. At laser fluences below damage threshold, the probability of crater formation and damage extent (crater depth) strongly depends on the local particle environment—effective dielectric constant, void geometry, etc. When laser fluence exceeds the optical damage threshold, the crater-depth/ particle-size dependence approaches very slow linear behavior. This is explained by the dominating role of absorption by the defect-surrounding matrix, the volume of which is much larger than both the volume of the particle and characteristic film inhomogeneity.

- The observed strong influence of the thin-film structure on UV-damage initiation indicates that thin-film damage resistance can benefit from higher film porosity.

- Crater formation probability as a function of laser fluence allows one to define conditions when absorption by the particle is causing only limited melting in the surrounding matrix without significant vaporization (crater formation). A laser fluence corresponding to these conditions is introduced as a nanoscale damage threshold, which should facilitate a more-meaningful comparison with theoretical predictions using the onset of the matrix melting as a damage benchmark.

REFERENCES

1. S. Papernov, A. W. Schmid, J. Anzelotti, D. Smith, and Z. R. Chrzan, in *Laser-Induced Damage in Optical Materials: 1995*, edited by H. E. Bennett et al. (SPIE, Bellingham, WA, 1996), Vol. 2714, pp. 384–392.

2. J. Dijon et al., in *Laser-Induced Damage in Optical Materials: 1995*, edited by H. E. Bennett et al. (SPIE, Bellingham, WA, 1996), Vol. 2714, pp. 416–419.

3. J. Dijon, T. Poiroux, and C. Desrumaux, in *Laser-Induced Damage in Optical Materials: 1996*, edited by H. E. Bennett et al. (SPIE, Bellingham, WA, 1996), Vol. 2966, pp. 315–325.

4. S. Papernov and A. W. Schmid, J. Appl. Phys. **82**, 5422 (1997).

5. S. Papernov, A. W. Schmid, R. Krishnan, and L. Tsybeskov, in *Laser-Induced Damage in Optical Materials: 2000*, edited by G. J. Exarhos *et al.* (SPIE, Bellingham, WA, 2001), Vol. 4347, pp. 146–154.

6. U. Kreibig and M. Vollmer, *Optical Properties of Metal Clusters*, Springer Series in Materials Science, Vol. 25 (Springer-Verlag, Berlin, 1995).

7. K. Kohno *et al.*, Jpn. J. Appl. Phys. 1, Regul. Pap. Short Notes **33**, 6616 (1994).

8. L. Patrone *et al.*, J. Appl. Phys. **87**, 3829 (2000).

9. G. Mie, Ann. Phys. **25**, 377 (1908); C. F. Bohren and D. R. Huffman, *Absorption and Scattering of Light by Small Particles* (Wiley, New York, 1983).

10. Yu. K. Danileiko, A. A. Manenkov, and V. S. Nechitailo, Sov. J. Quantum Electron. **8**, 116 (1978).

11. L. B. Glebov, in *Laser-Induced Damage in Optical Materials: 2000*, edited by G. J. Exarhos *et al.* (SPIE, Bellingham, WA, 2001), Vol. 4347, pp. 343–358.

12. M. D. Feit *et al.*, in *Laser-Induced Damage in Optical Materials: 1997*, edited by G. J. Exarhos *et al.* (SPIE, Bellingham, WA, 1998), Vol. 3244, pp. 350–355.

13. H. A. McInnes *et al.*, in *Laser-Induced Damage in Optical Materials: 2000*, edited by G. J. Exarhos *et al.* (SPIE, Bellingham, WA, 2001), Vol. 4347, pp. 118–126.

14. P. Grua and H. Bercegol, in *Laser-Induced Damage in Optical Materials: 2000*, edited by G. J. Exarhos *et al.* (SPIE, Bellingham, WA, 2001), Vol. 4347, pp. 579–587.

15. F. Bonneau *et al.*, in *Laser-Induced Damage in Optical Materials: 2000*, edited by G. J. Exarhos *et al.* (SPIE, Bellingham, WA, 2001), Vol. 4347, pp. 308–315.

Resistive Switching Dynamics in Current-Biased Y-Ba-Cu-O Microbridges Excited by Nanosecond Electrical Pulses

The response of a superconductor to the injection of current pulses depends directly on the quasiparticle dynamics[1] since the carriers injected from the external circuit are normal (unpaired) electrons that disturb the quasiparticle–Cooper-pair dynamical equilibrium. Most commonly, a current pulse with an amplitude higher than the sample critical current I_c is used (supercritical perturbation), leading to a collapse of the superconducting state and resulting in the resistive response. This phenomenon was first investigated in metallic superconducting thin films by Pals and Wolter[2] and has been recently observed by Jelila *et al.*[3] in superconducting $YBa_2Cu_3O_{7-x}$ (YBCO) microbridges. In both cases, a resistive (voltage) response induced by the supercritical current was reported to have a certain time delay t_d, defined as the delay between the arrival of the input current pulse and the appearance of the voltage signal. The t_d was directly related to t_D, the time required to achieve collapse of the superconductor order parameter D. Jelila *et al.*[3] successfully interpreted the t_d dependence on the supercritical pulse magnitude, using the theory developed by Tinkham.[1]

The supercritical perturbation in a superconducting bridge can also be achieved by a suitable combination of the excitation-pulse magnitude I_{pulse} and the bias current level I_{dc}. In fact, a two-dimensional space of the supercritical perturbations exists, limited only by the conditions $I_{total} = I_{pulse} + I_{dc} > I_c$ and $I_{dc} < I_c$. Together, the bias current (dc) and the pulsed current (time dependent) represent simultaneous injection of *both* Cooper pairs and quasiparticles into a superconductor, allowing us to study a full range of the quasiparticle–Cooper-pair dynamics from very weak [$(I_{pulse} \gtrsim I_c$ and I_{dc} ^{a} 0) or $(I_{pulse}$ ^{a} 0 and $I_{dc} \lesssim I_c)$] to very strong ($I_{pulse} >> I_c$ and $I_{dc} > 0$) perturbations.

The aim of this work is to present our studies on superconducting-to-resistive switching of dc-biased epitaxial YBCO microbridges, subjected to nanosecond electrical pulses in the supercritical perturbation regime. Our studies confirm the existence of a substantial t_d, which depends in a complicated way on both the magnitude of $I_{pulse}(t)$ and the value of I_{dc}

biasing the microbridge. Our measurements were interpreted using a modified Geier and Schön (GS) theory,[4] which, contrary to the Tinkham model,[1] allowed for the incorporation of the dc bias of a superconductor and its relation with t_d. We have also demonstrated that for perturbations much longer than the electron–phonon time $t_{e–ph}$, the dynamics of the current-induced resistive state is limited by the bolometric process and t_D reduces to the phonon escape time t_{es}.

When a long strip of a superconductor is subjected to supercritical perturbation, injected quasiparticles destroy the system equilibrium, resulting in the formation of phase-slip centers, which, in turn, lead to the collapse of D in a characteristic time t_D and the development of a resistive hot spot across the strip's weakest link. At the early, nonequilibrium, or "hot-electron," stage, the quasi-particle relaxation dynamics is governed by inelastic electron–phonon scattering, while the later resistive hot-spot-formation stage is a bolometric process. Thus, t_D should initially follow $t_{e–ph}$ and later be limited by t_{es}. The nonequilibrium process is, of course, measurable only if the width of $I_{pulse}(t)$ is of the order of $t_{e–ph}$ or shorter. The t_d, which determines the appearance of a macroscopic resistive state, is related not only to t_D but also to the sample reduced temperature T/T_c and to the magnitudes of both I_{pulse} and I_{dc} with respect to I_c.

Even though the earlier YBCO experiments by Jelila *et al.*[3] were successfully interpreted using the Tinkham theory,[1] we choose to use the GS theory[4] since it is the only approach that incorporates the dynamics of both Cooper pairs and quasiparticles. The GS model allows the study of the supercurrent-induced response in both the hot-electron and bolometric regimes. It considers a one-dimensional homogeneous superconducting microbridge in which Cooper pairs coexist with quasiparticles. The Cooper-pair dynamics is described by the time-dependent Ginzburg–Landau equation,[5] while the quasiparticle distribution is given by the Boltzmann equation.[6] The main feature in the GS theory is the equation for the conservation of current between the superfluid (Cooper pair) and normal fractions of electrons, and it allowed us to introduce, in

a natural way, the bias I_{dc} in addition to the quasiparticle perturbation $I_{pulse}(t)$. In our approach to the GS model,[7] the three aforementioned differential equations are first solved for a constant subcritical current (the dc bias), resulting in equilibrium values for the parameters of the system at a time $\gg t_{es}$. Next, those equilibrium parameters are used as initial conditions to solve the GS equations for I_{total} constituted of the same I_{dc} and a varying transient $I_{pulse}(t)$. The t_d is defined as the time needed by the normal current component to rise to 50% of the total current through the bridge.

Figure 89.36 presents our GS model simulations of t_d dependence on the reduced bias current $i_{dc} = I_{dc}/I_c$ and on the reduced current pulse $i_{pulse} = I_{pulse}/I_c$. The t_d dependence on the supercritical perturbation forms a surface, which exponentially diverges to infinity at the $i_{dc} + i_{pulse} = 1$ boundary and very rapidly drops toward zero at $i_{dc} = 1$. This behavior is expected. In the $i_{dc} + i_{pulse} < 1$ range, the perturbation is subcritical and the bridge always remains in the superconductive state (only the kinetic-inductive response is possible), while for $i_{dc} > 1$, the bridge remains in the resistive state irrespective of the value of the i_{pulse} perturbation. What is unexpected is the nonlinear $t_d(i_{dc})$ dependence for a constant i_{pulse}. From our solution of the GS model, shown in Fig. 89.36, it is obvious that i_{dc} is not just a scaling parameter in the $i_{pulse} > 1 - i_{dc}$ switching criterion. The magnitude of the bridge bias plays the critical role in the switching dynamics not only for
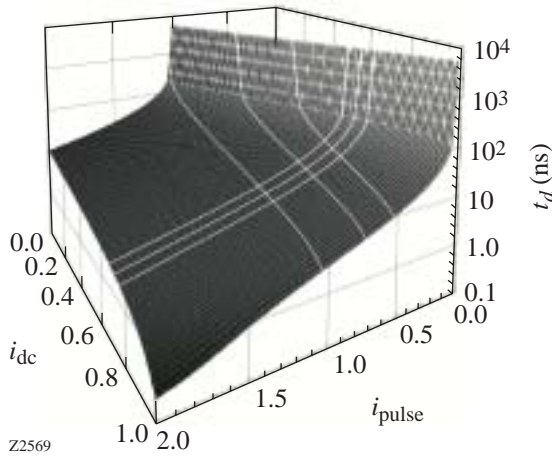
$i_{pulse} < 1$ but also for supercritical i_{pulse}'s, as i_{dc} approaches 1. Finally, we mention that the white lines, shown on the t_d surface in Fig. 89.36, correspond to our experiments and will be discussed below.

Our experimental samples consisted of 200-nm-thick epitaxial YBCO films deposited on MgO substrates and patterned into 8-mm-long, 150-mm-wide coplanar strips (CPS's) with a single 25-mm-wide by 50-mm-long microbridge, placed across the CPS. The bridges were characterized by a zero-resistance transition temperature $T_{c0} = 82.5$ K and a critical current density $J_c > 1$ MA/cm^2 at 77 K. For experiments, the samples were mounted on a copper cold finger inside a temperature-controlled nitrogen cryostat. Nanosecond-wide electrical pulses from a commercial current-pulse generator were delivered to the bridge via a high-speed, semirigid coaxial cable wire-bonded directly to the test structure. The dc bias was provided from an independent source and combined with the current pulse through a broadband microwave bias-tee. A 14-GHz-bandwidth sampling oscilloscope was used to monitor the microbridge response. The oscilloscope was connected to the sample via a second semirigid cable wire-bonded to the output contact pads of the CPS.

Figure 89.37 shows a series of waveforms of the time-resolved resistive switching dynamics of our YBCO microbridge subjected to a 20-ns, 130-mA current pulse at different I_{dc} levels. Since the I_c of the microbridge was 125 mA, the I_{pulse} itself was supercritical, which, when superimposed on the dc bias, resulted in I_{total} well above I_c. From the bottom waveform with no biasing to the second waveform from the top with $I_{dc} = 0.76\,I_c$, the resistive response is seen as the onset and growth of the plateau region after the initial kinetic-inductive peak. The time evolution of the voltage response starts with the small inductive peak, as the still-superconducting microbridge appears as an inductive element and differentiates the ~0.5-ns-wide rising edge of the input current pulse.[7] Later, since I_{total} is supercritical, the superconducting state starts to collapse, as discussed earlier, giving rise to the resistive response after the delay time t_d. The top (thick line) waveform in Fig. 89.37 corresponds to $I_{dc} > I_c$ or, alternatively stated, to the YBCO microbridge in the normal state. We note that in this case, the measured output pulse is just the input current pulse, slightly distorted due to resistive loss of the YBCO CPS. A voltage due to the flux-creep effect can be observed before the inductive peak, as the small offset of the waveform, when I_{dc} increases toward I_c. A similar plateau can also be isolated between the inductive and resistive responses, when $t_d > 20$ ns. Plotting the I_{dc}-V curve in both cases permitted us to identify a shift

Figure 89.36

The time delay t_d surface as a function of both the reduced bias current i_{dc} and the reduced current pulse i_{pulse}. The t_d dependence on the supercritical perturbation was calculated using a modified GS theory for the parameters ($T/T_c = 0.96$ and $t_D = 17$ ns) directly corresponding to our experimental conditions (white lines).

corresponding to I_{pulse} and, therefore, allowed us to compute the actual amplitude of the input pulse across the microbridge.

From a series of data sets analogous to Fig. 89.37, but collected under different experimental conditions, we extracted the t_d values as the time delay between the onset of the inductive peak (instantaneous with the arrival of the input pulse) and the half-point of the rising edge of the resistive region of the voltage response. Our experimental t_d values along with the GS theory are shown in Fig. 89.38. Figure 89.38(a) presents t_d as a function of i_{dc}, for three different values of i_{pulse} = 0.53, 0.74, and 1.04, while Fig. 89.38(b) shows t_d as a function of i_{pulse}, for i_{dc} = 0.68, 0.72, and 0.76, respectively. The GS simulated curves in Fig. 89.38 are the same as the white lines outlined on the t_d surface in Fig. 89.36. The selected levels of supercritical perturbations were $I_{total}/I_c > 1.2$, corresponding to the excitation range where the GS, Tinkham, and Pals and Wolter theories start to disagree.[7] We note that the t_d data points agree very well with the GS theory. The best fit to all our experimental data was obtained for t_D = 17 ns. This latter value is exactly the same as the t_{es} for our YBCO-on-MgO films,[8] calculated as t_{es} = $(4d)/(Kn)$ = 17 ns, where d = 200 nm is the YBCO film thickness, $K = 0.020$ is the average phonon transparency of the YBCO/MgO interface,[9] and n = 2.8 km/s is the velocity of

sound in YBCO averaged over the three acoustic modes. Thus, we can conclude that for current excitations that are much longer than t_{e-ph}, the resistive transition in YBCO films is governed by the bolometric (equilibrium) process and its time-resolved dynamics is limited by t_{es}. This latter observation agrees very well with both theoretical[9] and experimental[10] studies of the response of YBCO films exposed to optical perturbations. It is also consistent with earlier pulse perturba-

(a)
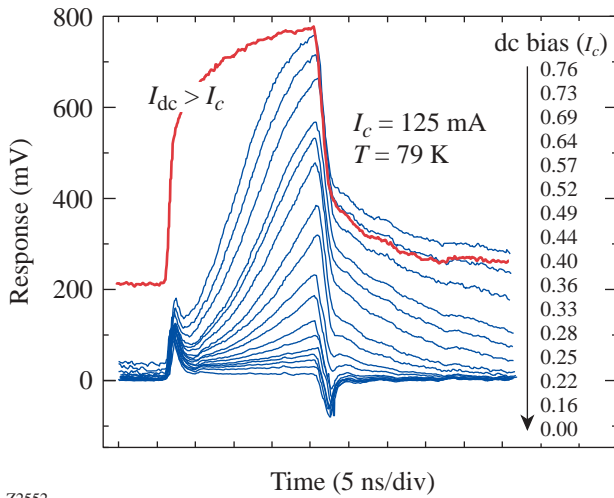
Figure 89.37

Time-resolved YBCO microbridge response to a 20-ns, 130-mA current pulse for the various bridge bias levels at 79 K. T_{c0} = 82.5 K; I_c = 125 mA. For the top (bold) waveform, the bridge was in the normal state ($I_{dc} > I_c$); note the large voltage offset that is representative of the resistive state of the bridge.
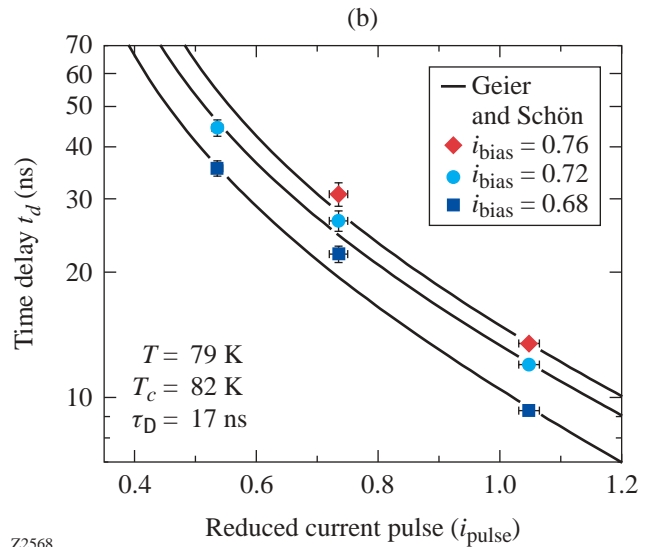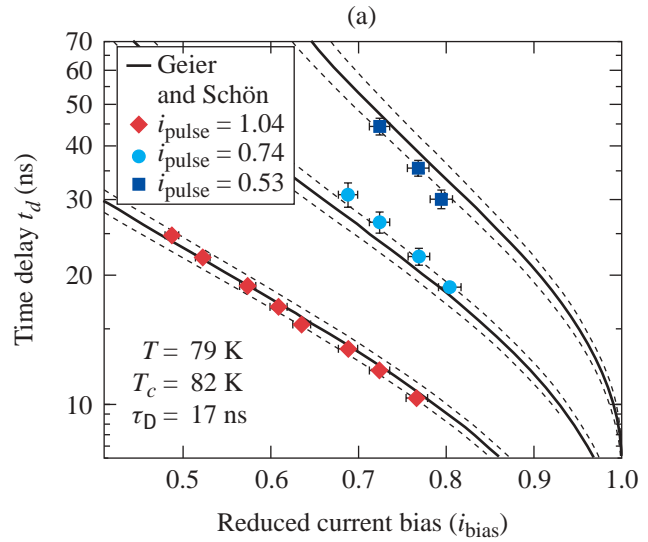
Figure 89.38

The measured t_d as a function of (a) the reduced bias current i_{dc} and (b) the reduced current pulse i_{pulse}. The solid lines represent the GS theory and correspond to the white lines in Fig. 89.36. The dashed lines in (a) define the error range in the amplitude of the current pulse applied the bridge. Note that the t_d scales are logarithmic.

tion experiments, since the literature data[11] seem to show that t_D is proportional to the film thickness and its value is consistent with the experimental determination of t_{es} for YBCO deposited on MgO, which is $t_{es} = 0.085$ ns/nm.

In conclusion, we have presented a study of dc-biased YBCO microbridges excited by nanosecond-long current pulses, which led to supercritical perturbations and resulted in resistive switching, occurring after a certain delay time t_d. The t_d depends roughly exponentially on both the amplitude of the current pulse and the film dc bias current, in a manner consistent with the GS theory. The duration of the superconducting-to-resistive response is, in our case, governed by the equilibrium dynamics of quasiparticles in the film and is limited by t_{es}, with no need to introduce the special t_D relaxation time. We can also predict that t_d could be shortened by using either thinner YBCO films or better acoustically matched substrates. The resistive response of YBCO bridges exposed to picosecond-long perturbations should be limited by the nonequilibrium t_{e-ph} interaction time.

ACKNOWLEDGMENT

REFERENCES

1. M. Tinkham, in *Nonequilibrium Superconductivity, Phonons, and Kapitza Boundaries*, edited by K. E. Gray (Plenum Press, New York, 1981), Chap. 8, pp. 231–262.

2. J. A. Pals and J. Wolter, Phys. Lett. A **70A**, 150 (1979).

3. F. S. Jelila *et al.*, Phys. Rev. Lett. **81**, 1933 (1998).

4. A. Geier and G. Schon, J. Low Temp. Phys. **46**, 151 (1982).

5. See, e.g., M. Tinkham, *Introduction to Superconductivity*, 2nd ed., International Series in Pure and Applied Physics (McGraw-Hill, New York, 1996).

6. A. Schmid and G. Schon, J. Low Temp. Phys. **20**, 207 (1975).

7. G. J. A. Sabouret, "Time Response of High-Temperature Superconducting Microbridge Structures Perturbed by Ultrafast Electrical Current Pulses," M.S. thesis, University of Rochester, 2001.

8. A. V. Sergeev and M. Yu. Reizer, Int. J. Mod. Phys. B **10**, 635 (1996).

9. J.-P. Maneval, K. P. Hong, and F. Chibane, Physica C **235–240**, 3389 (1994).

10. A. D. Semenov, G. N. Gol'tsman, and R. Sobolewski, Supercond. Sci. Technol. **15**, R1 (2002).

11. I. Harrabi, F. Ladan, and J.-P. Maneval, Int. J. Mod. Phys. B **13**, 3516 (1999).

Properties of Amorphous Carbon Films

Introduction

The properties of hydrogenated amorphous carbon (a-C:H) films have been studied over the past decade. A broad spectrum of applications ranging from carbon-based semiconductors, to wear-resistant coatings, to corrosion-resistant surfaces, to coatings on microspheres for inertial confinement targets has been identified. Plasma-based deposition systems use several approaches to decompose the feed gas and grow the carbon films: radio frequencies,[1] direct currents,[2] hot filaments,[3] glow discharges, and saddle fields.[4] In saddle-field plasmas, electrons oscillate between two electrodes to ionize the feed gas. Ions are drawn from the plasma by a gentle axial field and are delivered to a substrate beyond the transparent electrodes. Ions, radicals, and neutrals participate in the film growth process.

The underlying strength of the saddle-field plasma configuration rests in the ability to control several plasma parameters independently over a broad range of operating conditions and to deposit films outside the plasma region. The ion flux and energy, the ratio of the charged particles to neutral particles leaving the plasma, the temperature of the substrate, and the chemical species being deposited on the substrate can be tailored to optimize film properties for specific applications. Adjusting these parameters can alter the film density, the hydrogen content, the intrinsic stress within the films, the porosity, and the surface morphology.

To understand how deposition conditions influence the film properties—stress, density, and growth rate—a series of thin films were grown on flat glass and Pyrex™ plates. The correlation between film stress and deposition condition was measured by coating 0.1-mm-thick glass substrates with a-C:H and measuring the resultant curvature of the bilayer. Density and growth rate were measured by depositing films on thick Pyrex™ plates that were masked with stainless steel covers with an 18.9-mm-diam hole near the center. Subsequently, films were grown on polyalpha-methylstyrene (P*a*MS) and glow discharge polymer (GDP) microspheres using the conditions established for flat plates. One motivation for this work was to establish a protocol for coating microspheres with thick,

smooth, high-density hydrogenated amorphous carbon films for the inertial confinement energy program as a precursor to growing tritiated films. This paper summarizes the film properties that were obtained and discusses their dependence on deposition conditions.

Film Properties

The deposition chamber used in this work is a right cylinder. Stainless steel was the construction material of choice. A transparent anode grid divides the deposition chamber in half. Transparent grid cathodes are located 15 cm from the anode at either end of the cylinder. Electrically floated end plates are positioned approximately 7 cm beyond the cathodes. The grid open area is approximately 80%. Substrates to be coated are fixed to the end plates.

Each substrate was cleaned and degreased in an ultrasonic bath using trichloroethylene, acetone, and methanol in sequence. The substrates were then rinsed with de-ionized water, dried, and fixed on the end plate. All depositions were carried out at or near room temperature. Internal components in the vacuum chamber were inspected, removed, and cleaned before each run. Immediately following a deposition, the film thickness and the radius of curvature of the coated thin substrate were measured using a profilometer. The surface morphology was examined under an optical microscope. The films were subsequently stored in air for more detailed examination. Surfaces were inspected daily under the optical microscope for changes. The structure of the film was examined by breaking the coated substrates to view its cross section under a high-resolution scanning electron microscope (SEM). Thickness was measured using both profilometry and SEM. Film density was estimated from profilometry and SEM data.

Surface Condition

The surface smoothness of films bonded to Pyrex™ substrates depended on the deposition conditions but did not change with time once the deposition was completed. In general, particulate deposition increased with increasing methane pressure. The roughest films were produced at 27 Pa, the

smoothest at 1.3 Pa. Film smoothness could be further enhanced with hydrogen dilution of the methane plasma.

Films deposited on P*a*MS microspheres tended to detach from the underlying structure over the course of several days. Figure 89.39 illustrates typical ridges that evolved and stabilized on a P*a*MS shell over 28 days. No deposition conditions for pure methane plasmas could be found to increase the film–substrate bonding to the level that prevented film detachment on P*a*MS shells. Detachment, however, was never observed on GDP microspheres or Pyrex™ substrates even in pure methane plasmas.
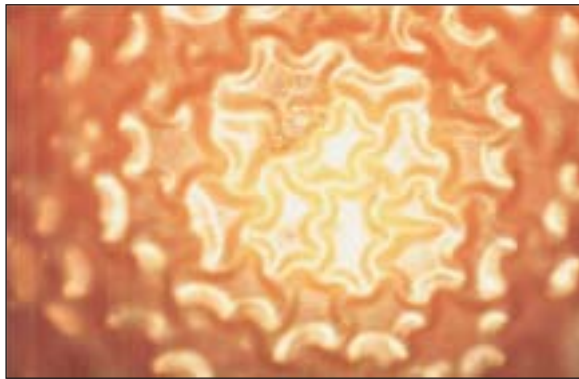
E11444

Figure 89.39
Surface morphology on a P*a*MS microsphere 28 days after deposition; methane pressure: 5.3 Pa, flow rate: 3.5 sccm, anode current: 30 mA, floated substrate.

Film Cross Sections

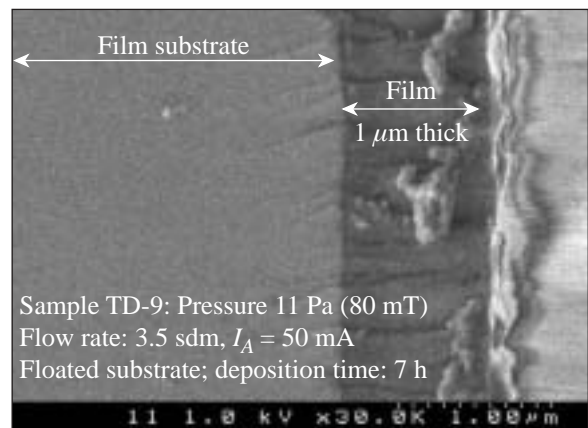A typical film cross section using SEM is provided in Fig. 89.40. The film, on the right-hand side of the picture, is intimately bonded to the Pyrex™ substrate. The body of the film is devoid of any microstructure, even at SEM resolutions on the 10-nm scale; these films are amorphous. As the deposition proceeds, the film grows with the agglomeration of matter on the surface coalescing into the uniformly dense and featureless layer seen in this figure. Several types of particles are involved in the growth process: fragmented methane comprising neutrals and radicals with varying CH atom ratios, including C and H atoms; more-complex CH chains that have polymerized in the plasma; and solid particles that have dislodged from chamber surfaces and attached to the film surface. The relative contributions of these components condensing on the surface to the film growth dynamics depend more on

hydrogen dilution of the methane plasma than on the operating methane pressure. Films grown in pure methane plasmas exhibit surface roughness and porosity that are unacceptable for microsphere applications. Surface smoothness improves, however, when the methane is diluted with hydrogen, and increasing dilution increases surface smoothness.

Hydrogen dilution has additional effects. Plasma stability improves with dilution. There is a notable lack of carbonaceous deposition on the grids and chamber walls. Undiluted methane plasmas are responsible for particulate agglomeration in the gas phase and particle production that eventually find their way to the film surface.

E11373

Figure 89.40
Typical film cross section using SEM; methane pressure: 11 Pa, flow rate: 3.5 sccm, anode current: 50 mA, floated substrate.

Internal Stress

The relative intrinsic stress within the films can be estimated from the radius of curvature of the coated thin wafers.[5,6] The larger the curvature of radius, the lower the relative intrinsic film stress. The relative stress dependence on fill pressure and methane concentration for several films is provided in Figs. 89.41 and 89.42, respectively. All data have been scaled to a uniform film thickness of 1 *m*m for this comparison.

Figure 89.41 indicates that roughly doubling the deposition gas pressure from 2.7 Pa to 5.3 Pa reduces the relative stress approximately fivefold. At an operating pressure of 25 Pa, film stress approaches zero. At the higher operating pressures, plasma particles impinging on the film surface have lower impact energies. They are less likely to embed into the film

bulk. Under these conditions, films grow by particle condensation on the surface rather than by implantation into the bulk. These films can readjust during the growth process to reduce internal stress.

Figure 89.42 illustrates that stress in films increases as the fraction of hydrogen in H_2/CH_4 plasmas decreases and exceeds values for films grown in undiluted methane plasmas. The transition to lower stress values in pure methane plasmas most likely reflects the difference in the plasma composition between diluted and undiluted plasmas.

Methane concentration: 100%
Flow rate: 3.5 sccm
Anode current: 30 mA
Substrate: floating

E11375
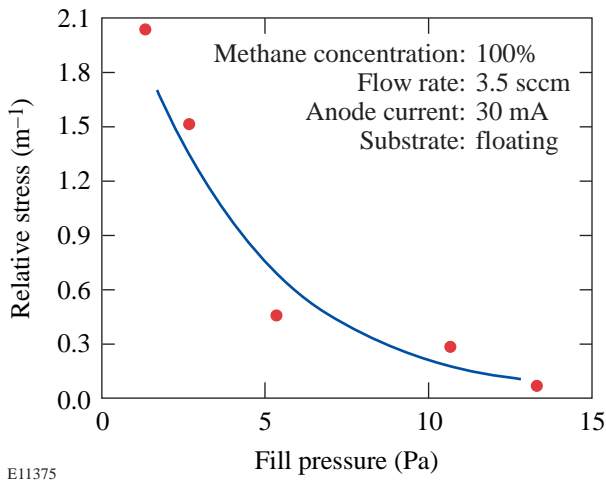
Figure 89.41

Stress in hydrogenated films decreases with increasing methane pressure.
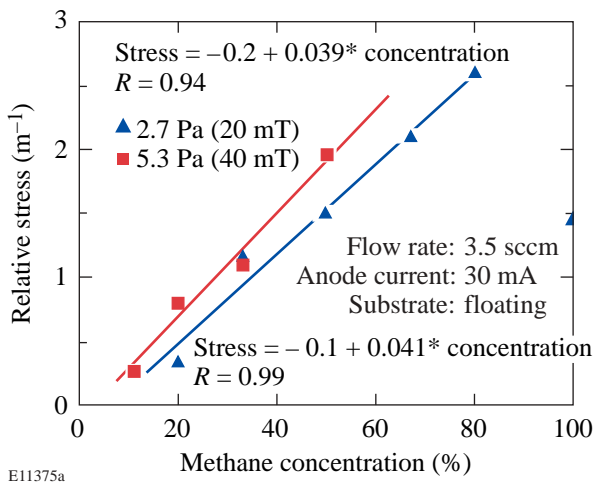
Thickness and Density

Densities are derived from the thickness of the film deposited on the substrate through a stainless steel mask and the film weight determined by weighing each substrate before and after deposition. Film thickness has been measured using both profilometry and SEM. A variation in the film thickness across the diameter of the mask resulting from a shadowing effect by the mask has been included in the density calculation. The film thickness along the border of the mask is smaller than in the center of the opening. Thickness and density estimates based on SEM data are considered to be more reliable and consequently used throughout this discussion.

Figure 89.43 illustrates that film density is strongly dependent on pressure, decreasing with increasing neutral pressure. At lower neutral pressures the electron temperature in the plasma is higher. Higher-energy electrons decompose a larger proportion of the feed gas into smaller neutrals, radicals, and ions. When these particles condense on the substrate, they tend to form higher-density, diamond-like films rather than lower-density, polymeric-like films.

Figure 89.44 demonstrates that film density is also weakly dependent on methane concentration in the plasma, in general increasing with decreasing hydrogen dilution. Increasing the methane concentration in the plasma for a fixed neutral pressure increases the carbon flux to the substrate relative to the hydrogen flux and leads to higher-density films. At 20%

Stress = $-0.2 + 0.039*$ concentration
$R = 0.94$

▲ 2.7 Pa (20 mT)
■ 5.3 Pa (40 mT)

Flow rate: 3.5 sccm
Anode current: 30 mA
Substrate: floating

Stress = $-0.1 + 0.041*$ concentration
$R = 0.99$

E11375a

Figure 89.42

Stress in hydrogenated films increases with decreasing dilution of the methane plasma.

CH$_4$ concentration: 100%
Flow rate: 3.5 sccm
Anode current: 30 mA
Substrate: floating
Density = $2.1 - 0.05*$ pressure
$R = 0.95$

E11374

Figure 89.43

Hydrogenated film density decreases with increasing methane pressure in the deposition chamber.

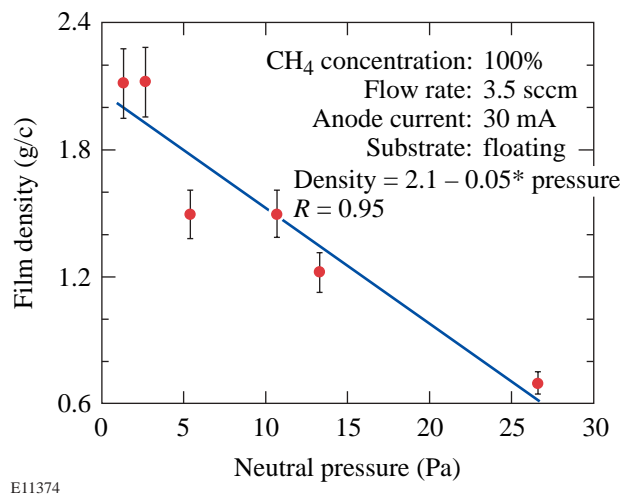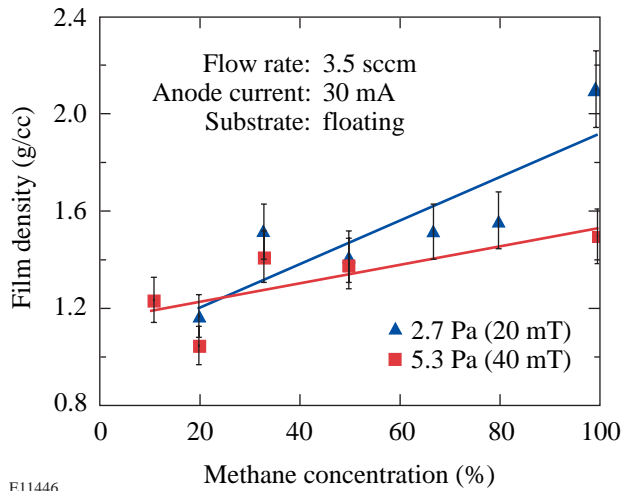methane, the atom C/H ratio is 8%; at 80% that ratio increases to 22%. The plasma is predominantly a hydrogen plasma with an increasing minority constituent as the methane concentration increases. It is noteworthy that up to 80% methane concentration, film densities for both neutral pressures are similar, suggesting that the plasma properties are similar for the two cases. At 100% the C/H ratio is 25%; however, the lower operating pressure, 2.7 Pa, yields a film with a significantly higher density than for the 5.3-Pa case, suggesting that the plasma properties for that case are very different.

Figure 89.46 illustrates the film's growth rate dependence on methane concentration at a fixed neutral pressure. Fixing neutral pressure fixes the extraction field. Increasing the carbon species number density within the plasma by increasing the methane concentration also increases the number of particles available for extraction. The extraction rate and consequently the growth rates are seen to increase with methane concentration in this figure as expected.

Figure 89.44
Film's density's dependence on hydrogen dilution of the methane.
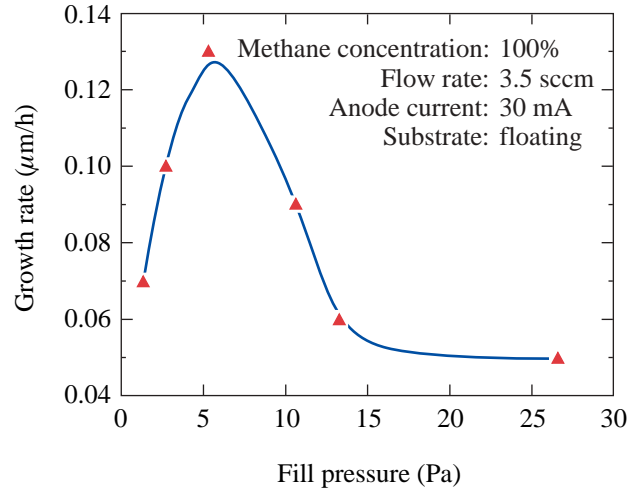
Figure 89.45
Growth rate dependence on neutral pressure.

Growth Rate

Growth rate depends on the operating pressure, as illustrated in Fig. 89.45. It peaks near 5 Pa and decreases at both lower pressures and higher fill pressures. At pressures below 5 Pa, the number of carbon atoms present in the plasma limits the film's growth rate. The extraction rate is fixed by the electric field within the plasma sheath, so the film can grow only at the rate that carbon species enter the sheath from the plasma side. The carbon particle density is determined by the fill pressure. Increasing the fill pressure increases the number of carbon species available for film growth, as the figure illustrates. At pressures above 5 Pa the growth rate is reduced because the extraction field strength is reduced at the higher fill pressures. While the carbon species density in the plasma is high, most of these particles are not available for film growth. The peak near 5 Pa represents the optimum balance between available carbon species in the plasma and their extraction rate for this system.

Figure 89.46
Growth rate increases with increasing methane content in the plasma.

Conclusions

The surface morphology of films depends on the operating gas pressure and the hydrogen concentration in the gas mixture. Surface smoothness improves with decreasing gas pressure and increasing hydrogen dilution. Gross features on the surfaces, such as lumps and pits, are attributed to particulate transport from the plasma to the film surface. Film chips detached from the chamber walls are the most likely source of these particles. The presence of hydrogen reduces the production or existence of larger-chained molecules in the plasma. Consequently the deposition of these particles on the films, the grids, and the walls is strongly suppressed. Fine structure on the film surface is attributed to the deposition conditions— the energy of the impacting particles, the ratio of the atom/ neutral/radical fluxes, and the magnitude of the carbon flux— and is most likely related to gas phase polymerization within the plasma.

Hydrogen dilution also improves plasma performance. Long-term plasma stability improves because the grids are not progressively coated with carbonaceous material.

The key deposition parameter responsible for residual stress in the film is the pressure of the precursor gas. Decreasing the pressure from 27 Pa to 1.3 Pa increases the residual stress in the films. Increasing the pressure of the precursor gas decreases the anode potential and increases the substrate self-bias, thereby changing the energy distribution of the particle flux involved in the deposition process.

Deposition of films on P*a*MS microspheres showed that stress generated during the growing process can drastically change the topology of the coated surface over time. In some cases changes began within a few hours of deposition, while in other cases the films were unaltered for several weeks. In addition to these time-dependent manifestations, all films exhibited a granular surface.

Operating pressure also plays an important role in modulating density and growth rate. Film density depends on the gas pressure. Film density increases with decreasing gas pressure to reach a maximum of 2 g/cc at 2.7 Pa in methane plasmas. Diluting the methane with hydrogen decreases the film density.

Growth rates up to 0.13 *m*m/h have been achieved. These tests provide the deposition conditions for growing tritiated amorphous carbon films.

REFERENCES

1. S. R. P. Silva *et al.*, Diam. Relat. Mater. **4**, 977 (1995).

2. D. S. Whitmell and R. Williamson, Thin Solid Films **35**, 255 (1976).

3. E. N. Farabaugh *et al.*, in *Applications of Diamond Films and Related Materials: Third International Conference*, edited by A. Feldman *et al.* (NIST, Gaithersburg, MD, 1995), Vol. 1, pp. 361–364.

4. F. Gaspari *et al.*, in *Applications of Diamond Films and Related Materials: Third International Conference*, edited by A. Feldman *et al.* (NIST, Gaithersburg, MD, 1995), Vol. 1, pp. 743–746.

5. J. G. Kim and J. Yu, J. Mater. Res. **13**, 3027 (1998).

6. H. Yamada, O. Tsuji, and P. Wood, Thin Solid Films **270**, 220 (1995).

First Results from Cryogenic Target Implosions on OMEGA

Introduction

The base-line direct-drive ignition target design for the National Ignition Facility (NIF)[1] is a thick cryogenic DT-ice layer enclosed in a thin CH shell.[2,3] In direct-drive inertial confinement fusion (ICF)[4] a spherical target is illuminated by a large number of laser beams to provide a spherically symmetric implosion. Target implosions with cryogenic DT fuel are planned using the 60-beam OMEGA laser system[5] to validate the theoretically determined[3] levels of laser and target uniformity required to achieve direct-drive ignition and gain on the NIF. The OMEGA cryogenic target designs are energy scaled from the NIF ignition designs.[2,3] In particular, the OMEGA cryogenic targets, driven by an energy-scaled ignition pulse, are designed to be as "hydrodynamically equivalent" as possible to the ignition capsule designs. In this context, the constraints placed on the OMEGA cryogenic target designs include peak shell velocities, hot-spot convergence, in-flight aspect ratio, and stability properties similar to those of the NIF designs. To compare igniting and non-igniting target designs, we use the hot-spot convergence ratio, defined as the ratio of the radius containing 90% of the yield when propagating burn was deactivated compared to the initial ice–gas interface. In addition, the principle sources of nonuniformity on OMEGA, which lead to a degradation in target performance, are similar to the NIF. For direct-drive ICF these sources are single-beam nonuniformity ("laser imprint"), drive asymmetry, inner ice surface, and outer-surface roughness.

Ignition with direct-drive ICF relies on the generation of a "spark" in the compressed "hot spot" to begin the nuclear burn.[6] The hot spot is a high-temperature, low-density region surrounded by a low-temperature, high-density region into which the burn wave propagates, leading to significant energy gain. Target and laser illumination nonuniformities lead to distortions in the hot spot due to secular (linear in time) growth of low-order ($\ell \leq 10$) modes, shell breakup, and mix due to the Rayleigh–Taylor (RT)[7,8] growth of high-order ($\ell > 10$) nonuniformities. Previous cryogenic target experiments[9–13] have used ice layers that were formed only by β-layering, but not thoroughly and carefully characterized. The targets generally performed poorly (the reported neutron yields did not exceed 0.2% of the 1-D predictions[10]), and the results could not be used to validate detailed multidimensional numerical simulations because of the missing information on the inner-ice-surface nonuniformity spectrum.

This article describes first experiments with layered and characterized cryogenic targets on OMEGA. These experiments have validated the technology to fill, layer, characterize, and shoot cryogenic targets. The following sections present the OMEGA cryogenic target designs, describe the results of the characterization of the inner-ice-surface quality of the cryogenic targets, review the results from the first cryogenic D_2 campaign on OMEGA, give an outlook on future improvements, and present conclusions.

OMEGA Cryogenic Target Designs

The basis for the OMEGA cryogenic designs is the NIF direct-drive, $\alpha = 3$ ignition design, which consists of a 340-μm-thick DT-ice layer encased in a thin (3-μm) plastic capsule of 1.69-mm outer radius.[3] The laser pulse required for the ignition design is a 9.25-ns shaped pulse consisting of a 10-TW, 4.25-ns foot rising to a 450-TW peak drive for 2.5 ns. Although higher one-dimensional gains can be achieved for lower-adiabat implosions, the highest multidimensional gains for NIF energy and uniformity levels are predicted to be achieved for implosions driven on an adiabat between 3 and 4. One-dimensional hydrodynamic scaling arguments[14] have been used to design the cryogenic targets for OMEGA. It has been shown[14,15] that the energy, time, and laser power scalings are

$$\left(E \sim R^3, \, t \sim R, \text{ and } P \sim R^2 \right).$$

The NIF is designed to provide 1.5 MJ of energy with the $\alpha = 3$ pulse shape, while OMEGA is capable of delivering 30 kJ. Thus, the radius of an OMEGA capsule should be approximately 0.3 times the NIF design, i.e., 0.46 mm, with a 100-μm DT-ice layer inside a 1-μm-thick plastic shell. The equivalent OMEGA $\alpha = 3$ pulse consists of a 0.75-TW foot

rising to a 33-TW peak with an overall pulse length of 2.5 ns. Figure 90.1 shows a comparison between the NIF and OMEGA targets and pulse shapes. One-dimensional hydrocode calculations predict a gain of 45 (neutron yield $Y_n = 2.5 \times 10^{19}$), a hot-spot convergence ratio of 28, and a peak fuel areal density $\rho R_{peak} = 1300$ mg/cm^2 for the NIF ignition design. A neutron yield of $Y_n = 1.8 \times 10^{14}$, a hot-spot convergence ratio of 20, and a peak fuel areal density $\rho R_{peak} = 300$ mg/cm^2 are predicted for the scaled OMEGA cryogenic DT design.[3] The "classical" definition of convergence ratio (the ratio of the minimum to the initial fuel–shell radius) is inappropriate for cryogenic targets since the inner ice layer forms part of the hot spot; therefore we use the hot-spot convergence ratio as defined in the introduction. A detailed analysis[15] shows that the energy-scaled targets exhibit similar 1-D behavior of the shock timing and fuel adiabat as the ignition designs. The shorter density scale length of the OMEGA target leads to a lower laser energy absorption of 40% compared to 60% for the ignition design. Consequently the energy-scaled target has a slightly higher adiabat and a lower hot-spot convergence ratio of 20 compared to 28 in the ignition design.

The RT instability can degrade target performance by breaking the spherical symmetry of the implosion. The RT instability occurs twice during the implosion: at the outer ablation surface as the shell accelerates inward and at the hot spot/main fuel layer interface as the capsule decelerates at the end of the implosion. The RT instability is seeded by single-beam laser nonuniformity, drive asymmetry, feedout from the inner ice surface, and outer-surface roughness. Detailed 2-D *ORCHID* simulations[3] have established the maximum levels of these nonuniformity sources to achieve ignition and gain on the NIF.

The analysis of these results shows that, for an outer-surface roughness of <115 nm and an inner-ice-surface roughness of ≤1 μm rms, individual beam smoothing by two-color-cycle, 1-THz, 2-D SSD with polarization smoothing (PS), and an on-target power imbalance of <2% rms, a gain of 30 is predicted for the NIF (70% of 1-D). The OMEGA design has been shown[3,15] to be more sensitive to the nonuniformity seeds than the NIF. This is attributed to the smaller hot spot in the OMEGA design, which can be more easily disrupted by the penetration of the cold spikes from the main fuel layer. For the same uniformity conditions as described for the NIF, the OMEGA-scaled $\alpha = 3$ design is predicted to give 30% of 1-D yield.[15]

Target Layering and Characterization

To create a 100-μm ice layer, the ~3-μm-thick, high-strength CH shells were filled with ~1000 atm of D_2 in a permeation cell inside the Fill/Transfer Station (FTS).[16] The process of filling these capsules takes ~24 h because the gas pressure can be incremented only in very small steps (0.7 atm/min) to avoid buckling of the thin shell due to the pressure gradient between higher pressure outside and lower pressure inside the targets. The targets are cooled very slowly (~0.1 K/min) to below the triple point of D_2 (18.72 K) to avoid bursting from the higher
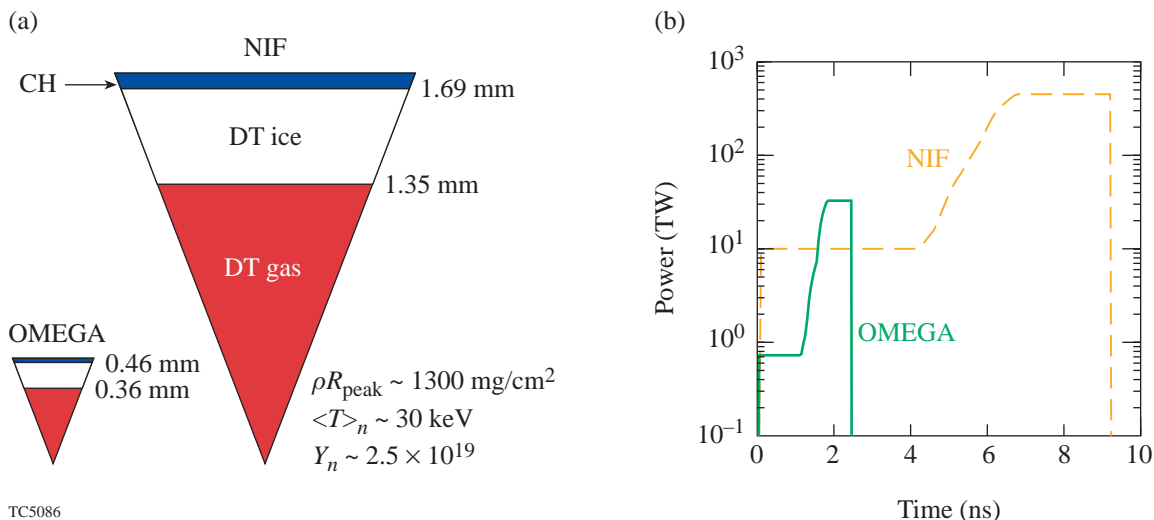

Figure 90.1
The NIF and OMEGA capsule designs (a) and pulse shapes (b). The radius of the OMEGA design is approximately 0.3 times that for the NIF. The pulse duration shrinks from 9.25 ns with a peak power of 450 TW to 2.5 ns with 32-TW peak power.

pressure of the warmer gas inside the targets. After transferring the targets from the FTS to the moving cryostat transfer cart (MCTC), the target assembly is inserted into the characterization station, where the targets are viewed using a high-magnification, high-fidelity optical system during the layering process. The layer is formed and maintained using an IR laser at 3.16-μm wavelength, which is preferentially absorbed in the D_2 ice. This creates a temperature gradient between the cooled layering sphere, which surrounds the target, and the gas/ice interface inside the target. Thicker parts of the ice layer are heated preferentially, increasing the sublimation rate in the hotter parts, while the gas preferentially refreezes at the colder parts of the ice layer. This results in a net layering effect that leads to an equal ice-layer thickness over the entire sphere.

This IR layering scheme uses more than one order of magnitude more heating power than β-layering of DT-filled cryogenic targets can provide, which suggests that active layering might be necessary even for DT targets.

The inner-ice-surface nonuniformities are characterized using a shadowgraphic technique as shown in Fig 90.2. The parallel rays from a light source are refracted at the plastic shell and reflected by total internal reflection from the inner ice surface, thus forming a virtual bright ring. The bright ring in the recorded image is unrolled using the center of the shadow of the plastic shell as a reference point, providing a graph with the distance of the inner ice surface from the center of the shell as a function of angle. The difference in the measured distance of

E11675
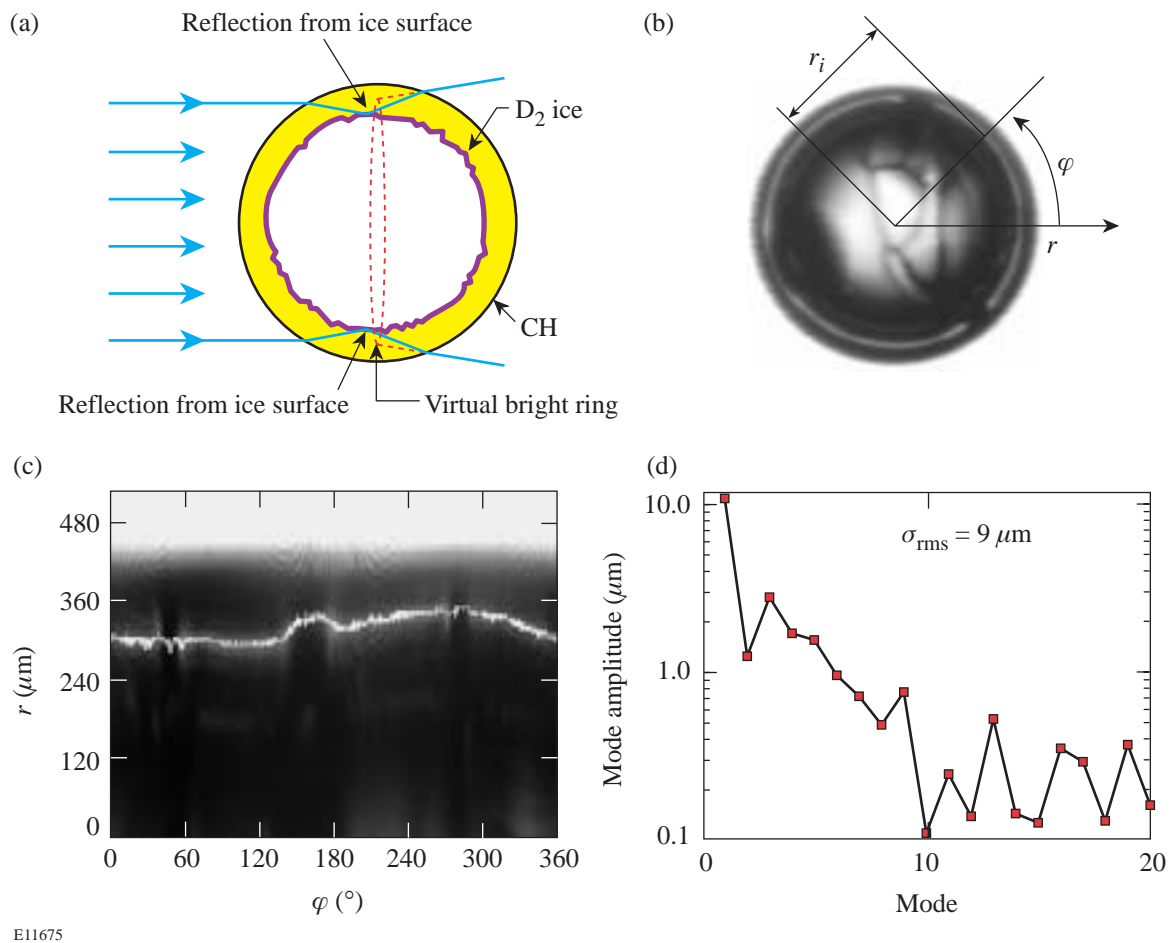
Figure 90.2
Shadowgraphic layer characterization: (a) The target is illuminated by collimated white light. (b) Internal total reflection at the ice/gas surface produces a virtual bright ring in the image. (c) The image is unrolled around its center, mapping the distance of the ice/gas interface as a function of angle around the target. (d) The difference of the measured distance from a perfect circle is decomposed into cosine mode amplitudes.

the ice surface from a perfect circle is then decomposed into cosine modes, resulting in a nonuniformity spectrum of the inner ice surface. These measurements provide only a 2-D representation of the inner-ice-surface nonuniformity along one circular cut through the sphere. Several such measurements, along different lines of sight, can be performed to fully map the 3-D nonuniformity spectrum.

Cryogenic Target Implosions

The cryogenic targets used in these first experiments were ~930-μm-diam, ~3-μm-thick shells of high-strength CH with 100-μm-thick D_2-ice layers. The targets were characterized along one line of sight and showed an inner-ice-surface roughness of $\sigma_{rms} \geq 9$ μm, with the most power (~90%) in the three lowest modes. A 1-ns square pulse at ~24-kJ laser energy was used with the best single-beam smoothing available [distributed phase plates (DPP);[17] polarization smoothing (PS) with birefringent wedges;[18] 2-D, single-color-cycle, 1-THz smoothing by spectral dispersion (SSD)[19]] and optimized energy balance (<3% beam to beam).[20] The calculated time-dependent, on-target overlapped nonuniformity ($\ell = 1 \sim 500$) due to single-beam nonuniformity, assuming perfect beam-to-beam power balance for 1-THz SSD with PS, is less than 1% after 300 ps.[21] When beam overlap on target is included, the on-target nonuniformity due to beam-to-beam energy imbalance is less than 1% ($\ell \leq 12$). This level of single-beam laser nonuniformity and drive asymmetry is close to that specified above; however, the current levels of inner-ice-surface roughness ($\sigma_{rms} \geq 9$ μm) significantly exceed the design goal ($\sigma_{rms} \leq 1$ μm). A 1-ns square pulse was used to make the implosion

less sensitive to instability growth than the $\alpha = 3$ design in Fig. 90.1. This pulse puts the target on an $\alpha = 25$ adiabat and leads to a predicted hot-spot convergence ratio of approximately 10. One-dimensional *LILAC*[22] simulations predict a neutron-averaged areal density of ~40 mg/cm^2, an ion temperature of approximately 2 keV, and a neutron yield of 1.0×10^{11}. Five target shots were successfully performed in a two-week experimental campaign. All targets showed good neutron-yield performance (up to 3.5×10^{10}), ranging from 4% to 30% of the clean yield, denoted as yield over clean (YOC), predicted by 1-D *LILAC* hydrodynamic simulations.

Table 90.I summarizes the performance measured by neutron and particle diagnostics of two target shots, 24089 and 24096, having ice-layer nonuniformities of $\sigma_{rms} = 19$ μm and $\sigma_{rms} = 9$ μm, respectively. The performance is compared with 1-D clean calculations. Secondary in-flight fusion reactions of the tritium (T) and helium (He^3) ions produced in the D_2 fusion reaction can be used to infer fuel areal densities.[23–26] The areal density of the hot neutron-producing core $<\rho R>_{hot}$ ($T_i \geq 0.5$ keV) is inferred using the ratio of the secondary proton to the primary neutron, Y_{2n}/Y_n, from the in-flight fusion of He^3 (Ref. 27). Due to the very short range of He^3 in the colder fuel (<1 mg/cm^2 at $T_e < 0.5$ keV),[28] the secondary proton production is confined to the hot parts of the core, if the electron and ion temperatures are assumed to be equal. This measurement saturates at about 10 mg/cm^2 for a plasma electron temperature close to 3 keV, which is consistent with the measured neutron-averaged ion temperatures $<T_{ion}>_n$. The inferred values of $<\rho R>_{hot} = 5$ mg/cm^2 and $<\rho R>_{hot} = 7$ mg/cm^2 for target shots

Table 90.I: Target performance measured by neutron and particle diagnostics and compared to 1-D clean calculations for the two best-performing target shots: 24089 and 24096.

	1-D	24089	24096
Roughness (μm)		19	9
Neutron yield	1.0×10^{11}	$(1.26\pm0.1) \times 10^{10}$	$(3.05\pm0.1) \times 10^{10}$
Yield compared to 1-D		16%	30%
$<T_{ion}>_n$ (keV)	2.1	2.9±0.5	3.5±0.5
Bang time (ns)	1.8	1.8±0.1	1.7±0.1
Y_{2n}/Y_n	9.0×10^{-3}	$(8.0\pm0.4) \times 10^{-3}$	$(9.0\pm0.5) \times 10^{-3}$
Y_{2p}/Y_n	1.2×10^{-3}	$(0.6\pm0.1) \times 10^{-3}$	$(0.8\pm0.1) \times 10^{-3}$
$<\rho R>_{hot}$ (mg/cm^2)	14	5±1	7±1
$<\rho R>_{total}$ (mg/cm^2)	40	20–30–58	12–25–38

24089 and 24096, respectively, are well below the saturation level. The predicted areal density of the hot neutron-producing core $<\rho R>_{hot}$ ($T_i \geq 0.5$ keV) at peak neutron production in the 1-D clean calculations is 14 mg/cm^2. The total areal density $<\rho R>_{total}$ is measured using the downshift of the secondary proton spectrum.[27] A relatively large spread is seen in the data, recorded by five proton detectors located in different ports around the target. Table 90.I shows the minimum, average, and maximum values inferred. The predicted 1-D $<\rho R>_{total}$ is given by the neutron-averaged areal density. The measured average total areal densities are more than 60% of the 1-D clean predictions. The ratio of the secondary neutron to the primary neutron, Y_{2n}/Y_n, can also be used to infer the total areal density.[25,27] However, secondary neutron ratios are also sensitive to the temperature profile through the slowing down of the primary triton of the D_2 fusion reaction and the energy-dependent cross section of the reaction. In these experiments it is most probably saturated, given the relatively high $<\rho R>_{total}$ as inferred from the downshift of the secondary proton spectrum. In addition, secondary neutron ratios close to 1×10^{-2} are seen in this model only if all the fuel has a temperature higher than 1 keV,[25,28] which is a highly unlikely scenario in these experiments. The measured and predicted bang times are very

close, indicating that the laser absorption and hydrodynamic response of the cryogenic targets are accurately modeled in the 1-D clean calculations. The experimental data show that the YOC and $<\rho R>_{hot}$ are most sensitive to the inner-ice-surface nonuniformities and improve significantly as the nonuniformity decreases. The neutron-averaged ion temperature and the bang time exhibit little sensitivity to the ice nonuniformity. Figure 90.3 shows static x-ray pinhole camera (XRPC) images and snapshots taken by an x-ray framing camera (XRFC) with an exposure time of 40 ps at peak compression compared with shadowgraphic images taken before the target shot. The XRPC images display the entire implosion from the thin plastic shell lighting up on the outside of the target at the beginning of the pulse to the formation of a core in the center of the image. A comparison of the two experiments clearly shows that shot 24096 starts with lower inner-ice-surface nonuniformities that carry over into a more integral and symmetric core. Neutron data confirm this behavior with shot 24096 achieving 30% YOC while shot 24089 had 16% YOC. This should be compared to noncryogenic implosion experiments on OMEGA that have achieved YOC of ~30% for targets with acceleration-phase-stability properties similar to the future $\alpha = 3$ cryogenic implosions described earlier.[20]

Shot 24089

1 mm	1 mm	100 μm

Shot 24096

Target shadowgram | Time-integrated x-ray pinhole camera image | X-ray framing camera snapshot

E11249
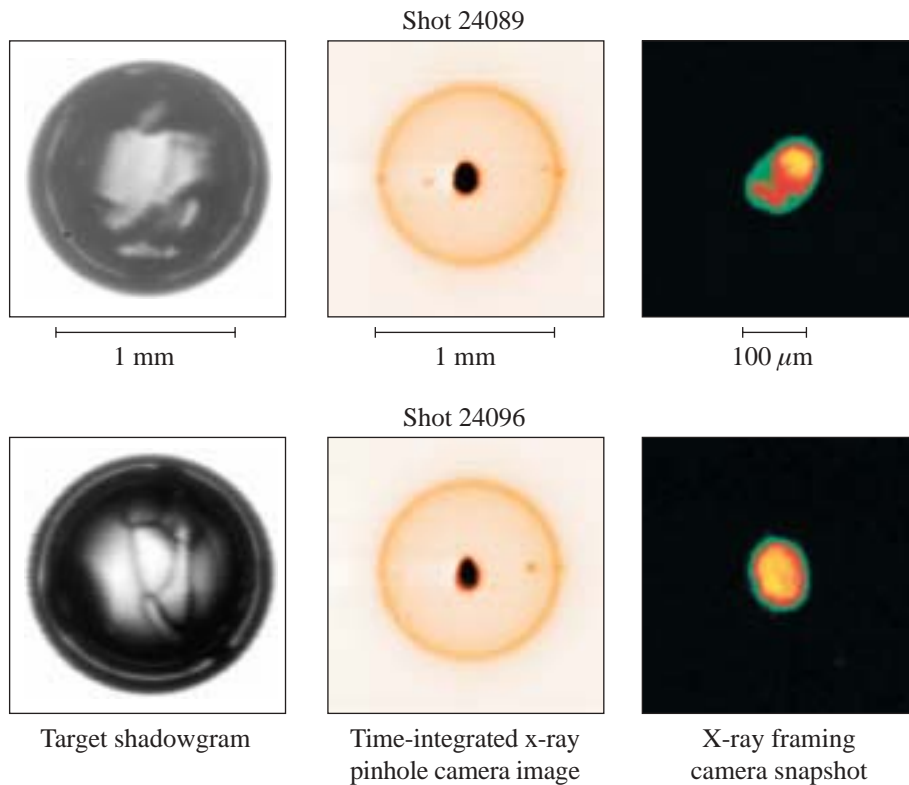
Figure 90.3
Shadowgraphic images of the targets for shots 24089 and 24096 shown in comparison with static x-ray pinhole camera (XRPC) images and x-ray framing camera (XRFC) snapshots. The XRPC images show the lighting up of the thin plastic shell on the outside of the target and the formation of a core in the center of the image. The XRFC images are recorded at peak compression with an exposure time of 40 ps. A clear correlation of the layer quality in the shadowgraphic images and the core quality in the XRPC and XRFC images can be seen.

Both the nuclear and x-ray data indicate that at the present level of inner-ice-surface nonuniformity, the target performance as measured by the YOC, the areal density of the hot neutron-producing core, and the integrity and symmetry of the x-ray core image are strongly affected by the quality of the inner ice layer. The other nonuniformity sources including laser imprint and drive asymmetry, which did not vary significantly during the experimental campaign, appear to be less important in these experiments.

Near-Term Developments

Recent layering studies have produced a much better layer quality ($\sigma_{rms} = 3\ \mu$m), with most of the amplitude in the two lowest-order modes. Figure 90.4 shows a shadowgraphic image of such a layer, together with the mode-amplitude spectrum. If the two lowest-order modes of the inner-ice-surface nonuniformity are caused by nonuniformities in the tempera-

ture profile inside the layering sphere, they are relatively easy to improve by minor changes in the layout of the layering geometry.[29] Other sources of ice-surface nonuniformity, like enhanced thermal resistivity at the plastic/ice interface, are under active investigation. Future experiments will use lower-adiabat pulse shapes like the ramp-to-flat pulse shown in Fig. 90.5 together with targets with recently improved ice layers, to achieve higher areal densities. When the layer quality reaches the design goal of $\sigma_{rms} \leq 1\ \mu$m, low-adiabat pulses like the $\alpha = 3$ pulse will be used to obtain peak areal densities of more than 200 mg/cm^2 using D_2-ice layers. Table 90.II summarizes the calculated clean 1-D performance and adiabat for the three different pulse shapes. Future cryogenic experiments using DT-ice layers, which are more massive than pure-D_2 layers, should extend the accessible parameter space to peak areal densities of ~300 mg/cm^2.

(a)　　　　　　　　(b)
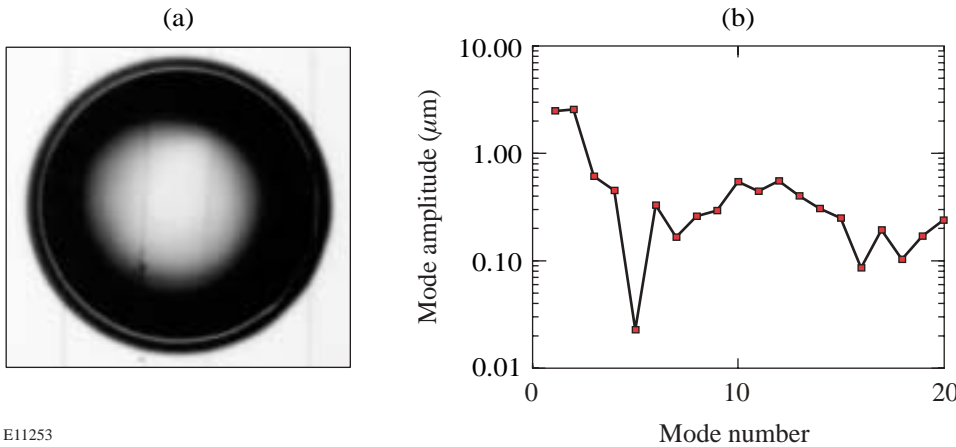
Figure 90.4
Shadowgraphic image (a) of a cryogenic target shown together with the mode-amplitude spectrum (b) of the inner-ice-surface nonuniformities and demonstrating as low as 3-μm rms ice roughness.

E11253

Table 90.II: Calculated clean 1-D performance of D_2 cryogenic target for three pulse shapes with different predicted fuel adiabats. The hot-spot convergence ratio is defined as the ratio of the radius containing 90% of the yield compared to the initial ice interface when propagating burn was deactivated.

Pulse	Adiabat	Energy (kJ)	$\langle\rho R\rangle_{peak}$ (mg/cm^2)	D_2 yield	Hot-spot CR
1-ns square	27	24	43	1.0×10^{11}	10
Ramp to flat	17	18	63	1.2×10^{11}	11
$\alpha = 3$	3	30	212	8.8×10^{11}	20

TC5714a
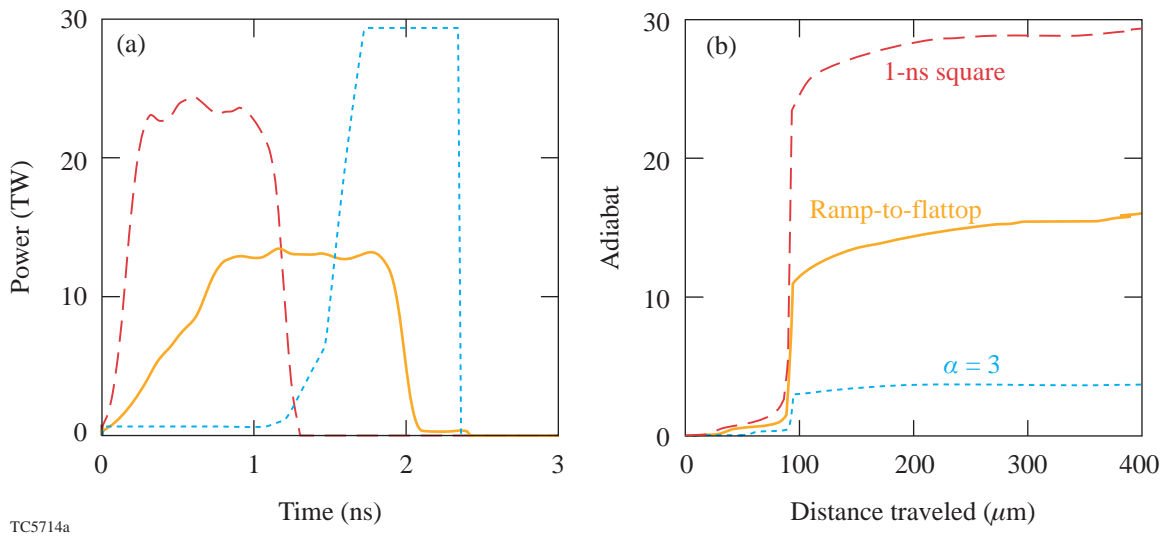
Figure 90.5
Laser power history (a) for three different OMEGA pulse shapes and (b) the corresponding fuel-adiabat trajectories.

Conclusion

The first experiments with the recently commissioned OMEGA Cryogenic Target Handling System have been described. The cryogenic target design is energy scaled from the direct-drive ignition designs for the NIF. The major goal of these experiments is to study the various sources of nonuniformity and their influence on target performance. Similar one-dimensional behavior and stability properties of the OMEGA and NIF cryogenic target designs will facilitate the extrapolation of the cryogenic target studies on OMEGA to NIF targets. In particular, NIF direct-drive ignition targets will be less sensitive to instability growth because the hot spot in the NIF design is bigger than in the OMEGA cryogenic targets. The first cryogenic targets, using 1-ns square pulses, achieved 30% of 1-D yield and more than 60% of the predicted neutron-averaged areal density with an inner-ice-surface nonuniformity of $\sigma_{rms} = 9\,\mu$m. At the present level of inner-ice-surface nonuniformity, the target performance is strongly affected by the quality of the inner ice layer. Recent improvements in the layering technique make it possible to produce much better ice layers, $\sigma_{rms} = 3\,\mu$m, with the prospect of achieving the design goal of 1 μm in the near future. Targets with improved inner-ice-surface quality will be used with lower-adiabat pulses to substantially increase the fuel areal density. In summary, these very encouraging initial results are a major step on the path leading to high-density compressed cores in direct-drive target implosions on OMEGA and to direct-drive ignition on the National Ignition Facility.

REFERENCES

1. J. A. Paisner, E. M. Campbell, and W. J. Hogan, Lawrence Livermore National Laboratory, Livermore, CA, UCRL-JC-117397 (1994).

2. C. P. Verdon, Bull. Am. Phys. Soc. **38**, 2010 (1993).

3. P. W. McKenty, V. N. Goncharov, R. P. J. Town, S. Skupsky, R. Betti, and R. L. McCrory, Phys. Plasmas **8**, 2315 (2001).

4. J. Nuckolls *et al.*, Nature **239**, 139 (1972).

5. T. R. Boehly, D. L. Brown, R. S. Craxton, R. L. Keck, J. P. Knauer, J. H. Kelly, T. J. Kessler, S. A. Kumpan, S. J. Loucks, S. A. Letzring, F. J. Marshall, R. L. McCrory, S. F. B. Morse, W. Seka, J. M. Soures, and C. P. Verdon, Opt. Commun. **133**, 495 (1997).

6. J. D. Lindl, *Inertial Confinement Fusion: The Quest for Ignition and Energy Gain Using Indirect Drive* (Springer-Verlag, New York, 1998), Chap. 6, pp. 61–82.

7. Lord Rayleigh, Proc. London Math Soc. **XIV**, 170 (1883).

8. G. Taylor, Proc. R. Soc. London Ser. A **201**, 192 (1950).

9. T. M. Henderson and R. R. Johnson, Appl. Phys. Lett. **31**, 18 (1977).

10. F. J. Marshall, S. A. Letzring, C. P. Verdon, S. Skupsky, R. L. Keck, J. P. Knauer, R. L. Kremens, D. K. Bradley, T. Kessler, J. Delettrez, H. Kim, J. M. Soures, and R. L. McCrory, Phys. Rev. A **40**, 2547 (1989).

11. R. R. Johnson *et al.*, Phys. Rev. A **41**, 1058 (1990).

12. Y. Kitagawa *et al.*, Phys. Rev. Lett. **75**, 3130 (1995).

13. K. A. Tanaka *et al.* Phys. Plasmas **2**, 2495 (1995).

14. K. A. Brueckner and S. Jorna, Rev. Mod. Phys. **46**, 325 (1974).

15. Laboratory for Laser Energetics LLE Review **82**, 49, NTIS document No. DOE/SF/19460-344 (2000). Copies may be obtained from the National Technical Information Service, Springfield, VA 22161.

16. Laboratory for Laser Energetics LLE Review **81**, 6, NTIS document No. DOE/SF/19460-335 (1999). Copies may be obtained from the National Technical Information Service, Springfield, VA 22161.

17. T. J. Kessler, Y. Lin, J. J. Armstrong, and B. Velazquez, in *Laser Coherence Control: Technology and Applications*, edited by H. T. Powell and T. J. Kessler (SPIE, Bellingham, WA, 1993), Vol. 1870, pp. 95–104.

18. T. R. Boehly, V. A. Smalyuk, D. D. Meyerhofer, J. P. Knauer, D. K. Bradley, R. S. Craxton, M. J. Guardalben, S. Skupsky, and T. J. Kessler, J. Appl. Phys. **85**, 3444 (1999).

19. S. Skupsky, R. W. Short, T. Kessler, R. S. Craxton, S. Letzring, and J. M. Soures, J. Appl. Phys. **66**, 3456 (1989).

20. D. D. Meyerhofer, J. A. Delettrez, R. Epstein, V. Yu. Glebov, V. N. Goncharov, R. L. Keck, R. L. McCrory, P. W. McKenty, F. J. Marshall, P. B. Radha, S. P. Regan, S. Roberts, W. Seka, S. Skupsky, V. A. Smalyuk, C. Sorce, C. Stoeckl, J. M. Soures, R. P. J. Town, B. Yaakobi, J. D. Zuegel, J. Frenje, C. K. Li, R. D. Petrasso, D. G. Hicks, F. H. Séguin, K. Fletcher, S. Padalino, M. R. Freeman, N. Izumi, R. Lerche, T. W. Phillips, and T. C. Sangster, Phys. Plasmas **8**, 2251 (2001).

21. S. Skupsky and R. S. Craxton, Phys. Plasmas **6**, 2157 (1999).

22. M. C. Richardson, P. W. McKenty, F. J. Marshall, C. P. Verdon, J. M. Soures, R. L. McCrory, O. Barnouin, R. S. Craxton, J. Delettrez, R. L. Hutchison, P. A. Jaanimagi, R. Keck, T. Kessler, H. Kim, S. A. Letzring, D. M. Roback, W. Seka, S. Skupsky, B. Yaakobi, S. M. Lane, and S. Prussin, in *Laser Interaction and Related Plasma Phenomena*, edited by H. Hora and G. H. Miley (Plenum Publishing, New York, 1986), Vol. 7, pp. 421–448.

23. T. E. Blue *et al.*, J. Appl. Phys. **54**, 615 (1983).

24. H. Azechi *et al.*, Appl. Phys. Lett. **49**, 555 (1986).

25. H. Azechi, M. D. Cable, and R. O. Stapf, Laser Part. Beams **9**, 119 (1991).

26. M. D. Cable and S. P. Hatchett, J. Appl. Phys. **62**, 2233 (1987).

27. Laboratory for Laser Energetics LLE Review **83**, 130, NTIS document No. DOE/SF/19460-357 (2000). Copies may be obtained from the National Technical Information Service, Springfield, VA 22161.

28. F. H. Séguin, C. K. Li, D. G. Hicks, J. A. Frenje, K. M. Green, R. D. Petrasso, J. M. Soures, D. D. Meyerhofer, V. Yu. Glebov, C. Stoeckl, P. B. Radha, S. Roberts, C. Sorce, T. C. Sangster, M. D. Cable, S. Padalino, and K. Fletcher, Phys. Plasmas **9**, 2725 (2002).

29. E. L. Alfonso, I. Anteby, and D. R. Harding, Fusion Technol. **38**, 149 (2000).

Equation-of-State Measurements of Porous Materials on OMEGA: Numerical Modeling

Introduction

The equation of state (EOS) of materials at high densities and pressures is of wide interest to inertial confinement fusion (ICF), planetary physics, and astrophysics. The EOS at these conditions often involves a mixture of atomic, ionic, and molecular species, making *ab initio* theoretical modeling prohibitive. Experiments to constrain EOS models have been performed using static methods such as diamond-anvil cells[1] and at higher pressures using dynamic methods, such as shocks generated by light-gas guns,[2] lasers,[3] and even nuclear explosions.[4,5] Of these methods, laser-driven shocks currently provide the best method available for not only accessing the high pressures of interest, but performing accurate measurements necessary to determine the EOS.

The Hugoniot of a material is the set of thermodynamic states, e.g., pressure and density, that can be reached after the propagation of shock waves of various strengths through the material. The measurement of a Hugoniot represents only a finite number of points along a single line through pressure–density space. While this by no means uniquely determines the EOS, it may constrain it. If the experimental data are determined to a great enough precision, they may even (as is hoped for in the impedance-matching measurements of deuterium) rule out competing EOS models.[6] Even though Hugoniot data may not constrain all regions of the EOS, the principal and secondary Hugoniots are of primary interest in applications relevant to ICF, since the gain of target designs is sensitive to the timing of two shocks for most direct-drive designs and as many as four shocks for indirect-drive designs.

Foams play a key role in the so-called above-ground experiments of the Stockpile Stewardship Program (SSP).[7] In support of the SSP, a series of experiments designed to study the EOS of foams began in the past year at LLE. In addition, high-gain, direct-drive ICF target designs have been proposed that use foams, making their properties of interest in ICF as well. For instance, in the designs of Colombant *et al.*,[8] foam is used as ablator material, in conjunction with an outer layer of a high-atomic-number material such as Au. In these designs, the foam is preheated by radiation from the outer layer and has substantially higher ablation velocities, resulting in a more stable outer surface. In other "wetted-foam" designs,[9] the higher atomic number of the foam results in greater absorption and increased laser energy coupled into the target, allowing more fuel to be used, producing higher gain. The models of both Colombant[8] and Skupsky[9] use foam to increase the target performance, in contrast to earlier foam designs, which proposed the use of foam only as a matrix to contain liquid DT or as a means to reduce imprint.[10,11] Direct-drive ICF target designs usually use a pulse that drives two main shocks into the target. The performance of these targets depends in part on the timing of these shocks, making determination of the wetted-foam EOS essential.

Several laser-driven shock experiments have been performed to determine the Hugoniot of foams of various densities and constituent materials. Benuzzi *et al.*[12] and Batani *et al.*[13] determined the shock speed and post-shock pressure as a function of initial foam average density for values from 5 to over 1000 mg/cc, for TMPT [trimethylol propane triacrylate $(C_{15}H_{20}O_6)$]. Koenig *et al.*[14] subsequently determined the pressure as a function of density for a range of initial TMPT foam densities, comparing their results to a Hugoniot calculated with the *SESAME* EOS, and inferring the amount of preheat necessary for agreement. The experiments performed at LLE complement these by focusing on carbonized resorcinol aerogel foam (CRF), a carbonized derivative of resorcinol formadlehyde (RF).[15] Aerogels are generally of interest because of their ultrafine cell and pore sizes (smaller than 1000 Å; by comparison, TMPT has pore sizes ~1 μm). Also, the carbonized derivative CRF has the benefit of greater material strength. CRF is being studied specifically because of its use in the Stockpile Stewardship Program. Unlike RF, CRF is optically opaque, potentially complicating the characterization that is necessary for application in ICF wetted-foam targets. For this reason, RF, TMPT, CH, and other foams similar to TMPT (such as divinyl benzene and ethyleneglycol dimethacrylate) are of potential interest for ICF target designs.

Because of their porosity, shocked foams exhibit behaviors not found in continuous materials: For example, if the porosity is large enough, it is possible for the shocked foam to have a lower density than that of its composite material. Probing the properties of shocked foams provides the potential for greater understanding of the structural physics of porous materials.

This article describes ongoing efforts at LLE to investigate the properties of CRF at high pressures and densities, focusing on the theoretical design of the experiments. In the following section the method used to determine the Hugoniot of foam samples is described as well as the resulting sensitivity to experimental uncertainty. Following that, the procedure used to calculate the Hugoniot is presented. The simulations used to design the experiments are then described, as well as the requirements placed on the target and pulse for a high-accuracy Hugoniot measurement experiment. These are followed by a discussion of the results.

The Impedance-Matching Method

When a sound wave encounters an interface between two materials, the strength and properties of the reflected and transmitted waves are determined by the *acoustic impedance* ρc, where ρ is the density and c the sound speed, in the two materials: if the acoustic impedance is continuous across the interface, the wave travels from one material to the other without changing speed; otherwise a wave is reflected as well as transmitted. As a sound wave is essentially a weak shock wave traveling at the sound speed, the behavior for a strong shock is similar: The acoustic impedance is replaced by the product of the density with the shock speed, ρU_s. If the shock encounters an increase in this quantity at a material interface between two materials, a shock is reflected back into the first material as well as transmitted into the second; otherwise a shock is transmitted and a rarefaction wave reflected. (A rarefaction wave is a propagating region that grows in time, in which the density and pressure drop as the material is accelerated.)

The *impedance-matching method*[16] uses the interaction of a shock wave with an interface between materials of different "hardness" (ρU_s) to determine a material's Hugoniot using the EOS of a reference material. A shock is sent through a layer of material of known EOS into a layer of the material under study (e.g., foam) in contact with the known material. Al is used as a reference material since it has been well characterized in previous studies at the pressures of interest here.[17] In these experiments the shock is generated by laser-driven ablation. The Rankine–Hugoniot (RH) jump equations for pressure and

density provide two equations for the post-shock conditions (pressure p and density ρ) in the foam in terms of the known initial conditions (pressure p_0 and density ρ_0), the shock speed U_s, and the post-shock particle speed U_p. These conditions are applied across the shock front in both the Al and the foam, giving four equations in eight unknowns. Assuming that no gap forms between the Al and the foam, the pressure and the post-shock speed are continuous across that interface, providing an additional two constraints. Thus, measurement of the shock speeds in the two materials is sufficient to fully describe the system. (The shock speed is assumed to be equal to the average shock speed.) Measurement of the shock-breakout times from the Al and foam using the VISAR interferometer[18] allows determination of the average shock speed in each layer. The particle speed in the foam is inferred from the measured average shock speed in the Al, combined with knowledge of the Al EOS. This process is described in detail in the next section.

The reason the impedance-matching method was chosen for these experiments can be seen by examination of alternate methods. Other methods that have been used to determine a material's Hugoniot include the following: (1) The symmetric method, involving colliding two planar samples, where both the sample speed before contact and the resulting shock speed are measured. This method has the advantage of not relying upon knowledge of the EOS of a standard material. It requires, however, that the material speed be measured, for instance with side-on radiography. It also requires that the sample withstand being driven by the laser without bowing or loss of structural integrity. (2) The reshock method, which is similar to the impedance-matching method, except that the shock is sent first through the unknown sample, and subsequently into the material of known EOS. As in impedance matching, measurement of the shock speeds in both materials allows determination of the shocked state of the material of unknown EOS, given knowledge of the EOS of the standard. Because the former is shocked twice, this method allows access to higher pressures than the impedance-matching method. Computation of the Hugoniot, however, is less accurate. (3) A modification of the impedance-matching method has been suggested[19] in which a foot pulse is used to raise the entire target to a higher initial pressure (given by the ablation pressure) after which the intensity is increased and a main shock is launched and tracked using side-on x-ray radiography. This method allows access to still higher pressures but also requires that the laser pulse be sufficiently long for pressure equilibrium to be reached, which may be prohibitively long. (These methods and other methods

for experimentally ascertaining EOS properties without determining the Hugoniot are discussed in Refs. 16 and 20.)

In addition to the standard impedance-matching method, the experiments on OMEGA will explore the *direct* method, in which both the shock speed and the (post-shock) particle speed are measured using side-on radiography (e.g., see Ref. 21). This method replaces the error introduced by using a known EOS to determine the particle speed with the uncertainty, which may be lower, of determining the interface position from side-on radiography.

Calculation of the Hugoniot and Sensitivity to Measurement Uncertainty

As mentioned above, the Hugoniot of the foam is calculated using the known Hugoniot and isentrope of the reference material. For the data shown here, a quotidian-equation-of-state (QEOS)[22] table for Al was used.[23] In principle, any reference EOS may be used to determine the conditions (pressure, density, fluid speed) in the foam after the passage of the primary shock. When the primary shock enters the foam from the Al (which has a higher acoustic impedance), a rarefaction wave (RW) is sent back into the Al. This RW has the effect of equalizing the pressure and velocity in the Al and foam. This is shown schematically in Fig. 90.6, which contain plots of the pressure and density near the Al/foam interface (the dashed line in Fig. 90.6) before [(a) and (b)] and after [(c) and (d)] the shock has passed from the Al into the foam. Assuming there are no gaps between the Al and the foam, the velocity and pressure on either side of the interface (that is, regions *i* and *ii*) must be equal. Thus, the post-shock pressure and velocity in the foam are equal to the values in the Al after the passage of the RW. In Fig. 90.6(c) and 90.6(d) this is shown by the continuity of the pressure across the interface. Since the EOS of the Al is known, these conditions (in region *ii*) may be used to determine the conditions in the Al before the RW, but after the passage of the primary shock (i.e., region *iii*).

This process is shown graphically in Fig. 90.7. The RH jump conditions for mass, pressure, and energy are given by, respectively,

$$\rho\left(U_s - U_p\right) = \rho_0\left(U_s - U_0\right),$$

$$p - p_0 = \rho_0\left(U_s - U_0\right)\left(U_p - U_0\right),$$

$$E - E_0 = \frac{1}{2}\left(p + p_0\right)\left(V_0 - V\right),$$

where ρ is the density, p is the pressure, E is the internal energy, $V = 1/\rho$, zero subscripts refer to pre-shock values, U_s is the shock speed, and U_p is the post-shock speed.[16] The Al standard EOS is used in a form tabulated by isotherms. The states that lie on the Hugoniot may be determined for a given isotherm using the RH equation for energy. For the strong shocks considered here, the initial pressure and energy are much smaller than their post-shock values and may be taken to be zero. Combining the RH equations for mass and momentum, and setting $U_0 \rightarrow 0$ (as is the case in the experiment), the shock speed is given along the Hugoniot by

$$U_s^2 = \frac{p - p_0}{\rho - \rho_0} \times \frac{\rho}{\rho_0}.$$

The point along the Hugoniot (the solid line in Fig. 90.7) corresponding to the state of the Al just after the passage of the primary shock is that for which U_s is given by the measured shock speed U_{Al}.

TC5915
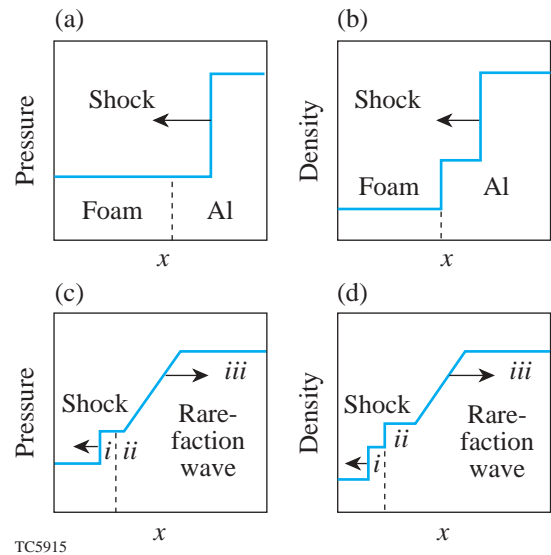
Figure 90.6
A schematic representation of the pressure and density near the Al/foam interface (represented by a dashed line) before [(a) and (b)] and after [(c) and (d)] passage of the shock from the foam into the Al. When the shock passes into the foam, a rarefaction wave is sent back into the Al, equalizing the pressure and velocity in the two materials. Notice that while the density changes across the interface, the pressure is continuous.

Assuming radiative losses are insignificant, the RH equations are satisfied, and the states reached by the RW lie along the release isentrope (the dashed line in Fig. 90.7) intersecting the shocked Al state determined above. The release isentrope may be calculated simply by finding, for each isotherm, the states for which the entropy is unchanged. The entropy change is given in terms of temperature and density changes by

$$ds = c_v \frac{dT}{T} - \frac{dp}{dT}\bigg|_\rho \frac{d\rho}{\rho^2}$$

(see, e.g., Ref. 24). The particle speed along the release isentrope is computed using the relation (see, e.g., Ref. 20)

$$U_p = \int_{\rho_0}^{\rho} c_s(\rho)\, d\ln\rho = -\int_{V_0}^{V} \left(-\frac{\partial p}{\partial V}\right)_s^{1/2} dV.$$

The final state along the isentrope reached by the RW is that intersected by the Rayleigh line given by the RH momentum equation in the foam (again, where $U_0 = 0$), $p = \rho_0 U_{\text{foam}} U_p$.

Finally, once the post-shock pressure and particle speed in the foam are calculated, the post-shock foam density may be found from the RH mass equation

$$\rho_{\text{foam}} = \rho_0 U_{\text{foam}} / (U_{\text{foam}} - U_p).$$

Uncertainty in the calculated Hugoniot is due to both the uncertainty in the measurement of the shock speeds and the calculation of the post-shock pressure and density in the foam. The final uncertainty δP in the pressure, for instance, given the measured uncertainties δU_{Al} and δU_{foam} in the shock speeds, is given by

$$\delta P = \sqrt{\left(\frac{\partial P}{\partial U_{\text{Al}}} \delta U_{\text{Al}}\right)^2 + \left(\frac{\partial P}{\partial U_{\text{foam}}} \delta U_{\text{foam}}\right)^2},$$

and likewise for the uncertainty δU_p in the foam post-shock particle speed. The necessary partial derivatives are calculated numerically by calculating $\Delta P(\Delta U_{\text{Al}}, \Delta U_{\text{foam}})$, in the limit that $\Delta U_{\text{Al}} \to 0$ or $\Delta U_{\text{foam}} \to 0$. The values of the calculated partial derivatives are required to converge in these limits in order to calculate the final uncertainty. The uncertainty $\delta\rho$ in the density is given by the chain rule:

$$\delta\rho_{\text{foam}} = \frac{\partial\rho_{\text{foam}}}{\partial U_p} \delta U_p = \frac{\rho_0 U_{\text{foam}}}{\left(U_{\text{foam}} - U_p\right)^2} \delta U_p.$$

As can be seen from this expression, the closer the shock speed is to the particle speed in the foam, the more uncertain the determination of the foam post-shock density. For example, consider an experiment with shock speeds of 28 μm/ns in the Al and 40 μm/ns in the foam. The corresponding post-shock
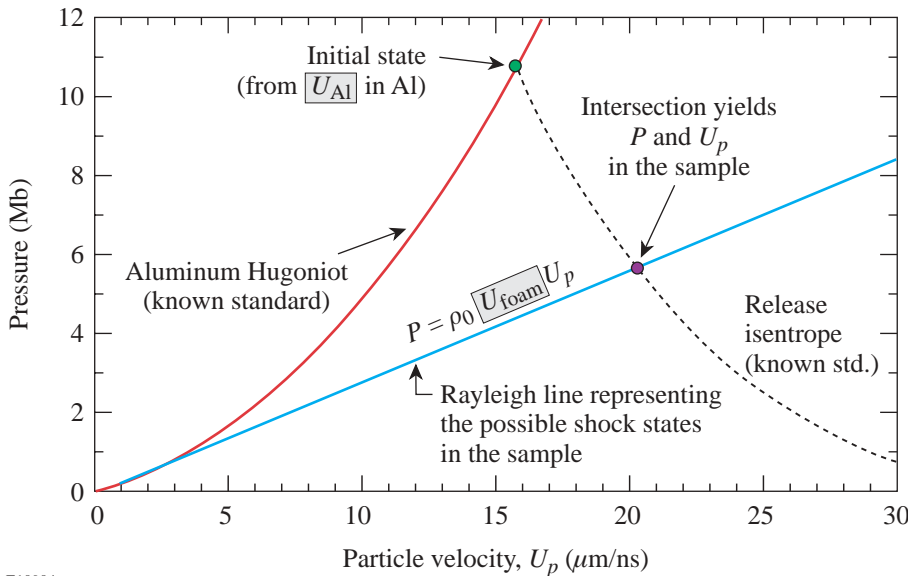

Figure 90.7
A graphical representation of the process used to determine the foam Hugoniot from the measured shock speeds.

E10904a

conditions in the foam are $\rho = 0.59$ g/cc and $p = 1.3$ Mbar. To achieve an uncertainty of even 0.1 g/cc (17%) in the calculated density, the measured uncertainty in the shock speeds (assuming they are equal) must be less than ~2%. The corresponding uncertainty in the pressure is ~13%.

The preceding procedure to determine the Hugoniot may be performed, for purposes of estimation, entirely analytically if a linear relationship is assumed between the shock and particle speeds in the Al, $U_{Al} \approx C + sU_p$ (see, e.g., Ref. 20). For the Al *SESAME* table[25] these constants are given approximately by $C \sim 5.35$ km/s, $s \sim 1.34$ for shock speeds between 10 and 30 km/s. In this case the uncertainties may also be estimated analytically.[26,27]

Target Design

As described above, only *average* shock speeds are measured experimentally. To accurately determine the Hugoniot, the target and pulse must be designed so that the shock is steady. The primary shock will remain steady in the Al and CRF only if it is not overtaken by secondary rarefaction waves and shocks generated by the passage of the primary shock between different material layers.

At least three other factors constrain the design of the target: First, the uncertainty in the measured average shock speed is less for a thicker layer, since it is based on a determination of the breakout time of the shock. Second, at the end of the laser pulse a rarefaction wave (RW) is sent into the target. It can be shown[28] that the RW always moves faster than the primary shock because the post-shock fluid speed plus the sound speed in the post-shock material is greater than the shock speed. The duration of the pulse must be sufficient so that the RW does not reach the primary shock before it breaks out of the target. (For a single-layer target, the RW catches the primary shock at about a time equal to twice the pulse duration.[29]) Third, the ablator layer(s) must be of a sufficient optical thickness to prevent radiation from the corona from preheating the sample layers. Preheat not only changes the initial conditions seen by the shock but nonuniformly alters the temperature and density, affecting shock steadiness. The effects of radiative preheat are discussed further in the next section. (For a further discussion of preheat effects see Ref. 30.)

Figure 90.8 shows a space–time diagram from a *LILAC* simulation[31] of a sample target. (All *LILAC* simulations described here use the *SESAME* EOS.[32]) A schematic of the target is shown in Fig. 90.9. The 1-D simulation represents a slice parallel to the *x* axis, which cuts through the thin side of

the Al step and the foam. The locations of the shocks and RW's in Fig. 90.8 are determined from the local variations in inverse pressure scale length $|L^{-1}| \equiv |\partial \ln p/\partial x|$ (in μm^{-1}), where p is the pressure and x is the distance into the target. For clarity in identification of shocks and RW's, the target in this simulation is driven by a steady 3.5-ns, 200-TW/cm^2 laser pulse. The RW launched from the ablation surface at the end of the laser pulse may be seen in the neighborhood of 3.6 ns, 100 μm. Note that the reflected RW from the Al/CRF interface results in a second, inward-traveling shock when it reaches the ablation surface.

To predict shock steadiness and compare the results of simulations with experimentally measured shock speeds, the shock position and velocity must be determined from *LILAC* simulations. The former is found by determining the location of the local maxima of L^{-1}. These correspond to abrupt changes in the pressure, due to both shocks and material interfaces. Some of these maxima may be ruled out by requiring that $L > 0$. Two additional criteria aid in locating the shock: First, since the global maximum of L^{-1} is often the rear surface (farthest from the laser) of the foam, the local maximum closest to the front (or laser side), in most targets, corresponds to the shock. Second, the shock may also be identified as the maximum nearest to a local maximum in the derivative dT_e/dt of the electron temperature T_e with respect to time t, allowing the shock position to be unambiguously identified numerically.

Once the cell containing the position of the shock is determined as a function of time, the shock speed is computed: the location of the shock within a cell is approximated by fitting a parabola to $L^{-1}(x)$, using the value of L^{-1} in the cell, combined with $\partial L^{-1}/\partial x$ in the two neighboring cells. Due to the finite time resolution of the simulation, the shock velocity determined by differentiating the shock position is noisy. The noise has a time scale comparable to $\Delta z/U_s$ and, by choosing grid spacing Δz, can be made much smaller than the time scale for physical changes in U_s (due to, for instance, secondary shocks and rarefaction waves, and temperature and density gradients due to preheat). This noise is then removed by performing a linear regression at each time using n previous and subsequent values of the velocity. This least-squares fit acts as a low-pass filter, removing fluctuations in the shock speed having frequencies higher than $f \sim (2n\Delta t)^{-1}$, where Δt is the time interval for simulation output. (Note that Δt is typically much larger than the simulation time step.) As a result, the time interval for simulation output must be chosen to ensure that no hydrodynamic behavior of interest is removed during the smoothing process. A plot of the shock speed versus time for a typical target is shown in Fig. 90.10.
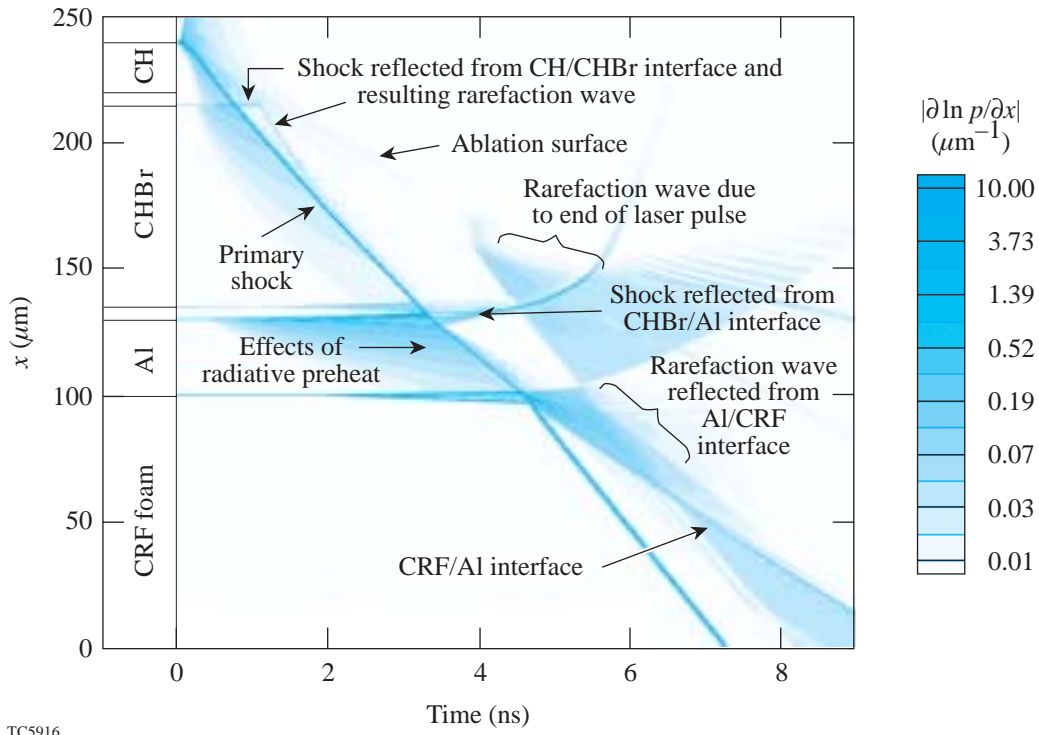
TC5916

Figure 90.8
A space–time diagram from a *LILAC* simulation of a standard target. The location of the shocks and rarefaction waves (RW's) are determined from the local variations in inverse pressure scale length $\left|\partial\ln p/\partial x\right|$ (in μm^{-1}), where p is the pressure and x is the distance into the target. Note the RW's and secondary shocks that are generated when the primary shock reaches each material interface.
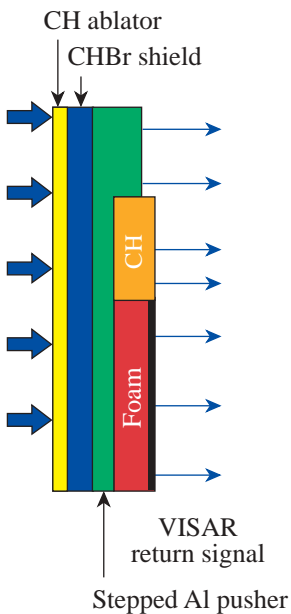
Shot 23860
E11040b

Figure 90.9
The structure of a standard target used in the EOS experiments on OMEGA. The target consists of a CH ablator, a CHBr radiation shield, a stepped Al layer, and a foam layer. Some of the targets also have a "witness plate" of, for instance, plastic, which is transparent to the VISAR laser.
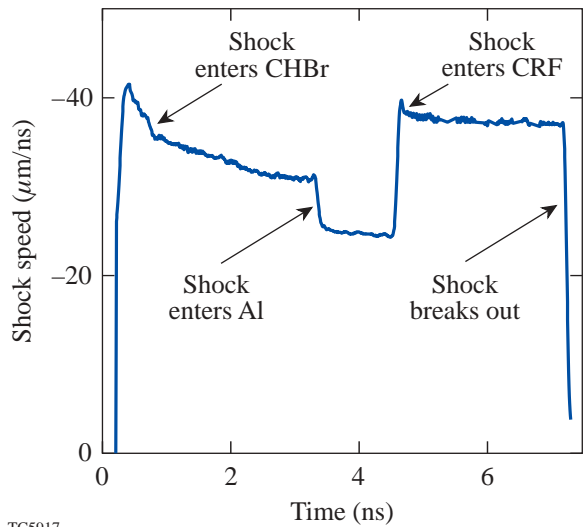
TC5917

Figure 90.10
The primary shock speed as calculated from the *LILAC* simulation corresponding to Fig. 90.6. The rapid drop in the calculated shock speed at 7.2 ns corresponds to the breakout of the shock from the CRF. In this and other shock plots in this article, oscillations with periods of tens of picoseconds are due to numerical noise.

The targets used in these experiments initially consisted of a 20-μm-thick CH ablator, a 30-μm-thick Al layer (and 100 μm on the thick side of the Al step), and a 100-μm-thick foam layer. The resulting shock speed was found to be less steady than desired. Following Glendinning *et al.*,[33] an 80-μm-thick brominated-plastic layer was added after the CH ablator to serve as a radiation shield to prevent preheat. Radiative preheat causes a continuous change in the pre-shock temperature, density, and pressure. The speed of the primary shock changes as a result of the varying pre-shock conditions. In Fig. 90.11 a comparison of the computed shock speeds shows the improved shock steadiness when the CHBr radiation preheat shield is used. The steadiness of the shock may be measured by the standard deviation of the shock speed. (The steadiness σ is then given by a time-weighted average of the steadiness in the Al and the foam.) Without the CHBr preheat shield, $\sigma \sim 1.75$ μm/ns, and with the shield, $\sigma \sim 0.37$ μm/ns.
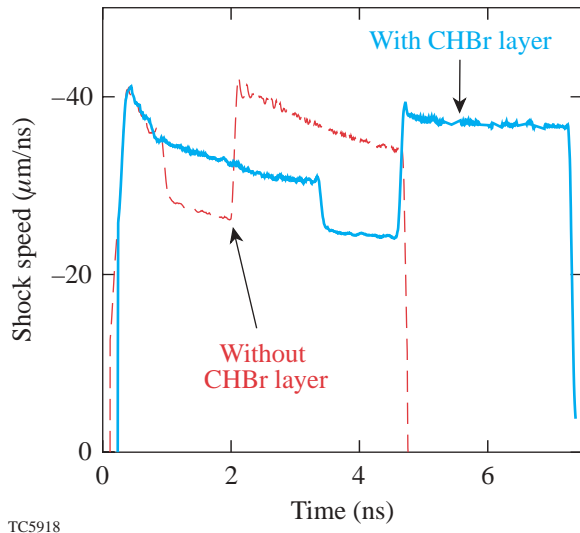

TC5918

Figure 90.11
The shock speed for targets with (solid) and without (dashed) an 80-μm CHBr preheat shield, showing its effectiveness at reducing radiative preheat and the resulting increase in shock steadiness.

In addition to affecting shock steadiness, even a small amount of preheat may alter the Hugoniot for moderate and low pressures. Figure 90.12 shows the Hugoniot for CRF as calculated from QEOS, assuming 0.0252-eV (room temperature), 0.4-eV, and 1-eV initial temperatures. The room-temperature curve show a well-documented feature of porous materials, namely a Hugoniot that curves to lower densities

for higher shock pressures. This behavior occurs because, for strong shocks in this regime, the thermal pressures produced in crushing the foam can become very large, resulting in lower densities. Note that while the final density ρ is lower than that of the constituent ($\rho_c \sim 1$ g/cc for a CH foam, for instance), it is still higher than the average initial foam density ρ_f, so that $\rho_f < \rho < \rho_c$. This anomalous behavior is described in Ref. 16 and has been observed in other materials as well.[5] This anomalous behavior is not seen in the 0.4-eV and 1-eV curves, indicating that at small preheat values the foam begins to behave more like a continuous solid. Impedance-matching experiments by Koening *et al.*[14] also found that agreement between the experimental and theoretical EOS's could be obtained only by assuming a small amount of preheat.

TC5919
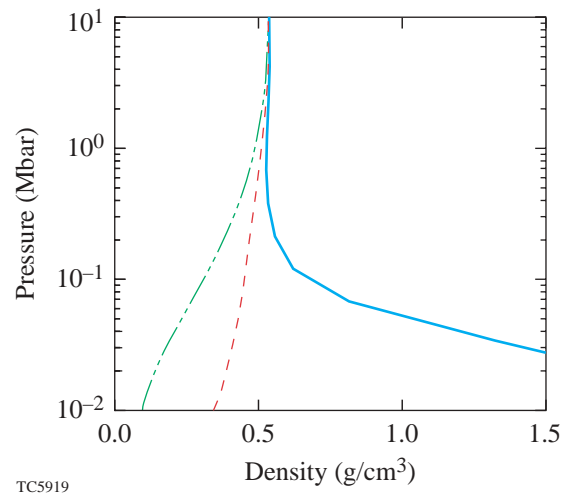
Figure 90.12
The Hugoniot calculated from the QEOS, for a room-temperature CRF foam (solid), a 0.4-eV foam (dashed), and a 1-eV foam (dashed–dotted). Notice that the Hugoniots for the heated foams do not show the anomalous behavior of decreasing density with increasing pressure.

Because the ablation pressure scales with the laser intensity as $p \propto I^\alpha$, where $\alpha \approx 2/3$ (Ref. 34) and because the pressure is proportional to the square of the shock speed for strong shocks, a temporal intensity perturbation would be expected to result in a shock speed perturbation of $\delta U/U_0 \approx (1/3)\delta I/I_0$. However, the laser drive is coupled to the post-shock target material through the conduction zone. As a result, the system behaves like a driven, damped harmonic oscillator, and perturbations in the drive of sufficiently high frequency have no significant effect on the primary shock. This may be seen in the shock speeds from simulations of a typical target in which 10%

amplitude modulations with 250-ps and 1-ns periods are imposed on a flattop pulse (see Fig. 90.13). (These pulses include a 100- to 200-ps rise and fall taken from a typical measured pulse.) These periods were chosen as characteristic of the time scales for variations observed in typical shots on OMEGA. The amplitude modulations launch a sequence of shocks (alternated with rarefaction waves) into the target, causing jumps in the shock speed when they catch up to the primary shock. For a 20-TW/cm^2 pulse, which produces a 440-kbar shock in the foam, the 1-ns modulation results in $\sigma \sim 3.7\%$, while the 0.25-ns modulation perturbs the shock speed in the foam by only $\sigma \sim 1\%$.

TC5920

Figure 90.13
Shock speed for three simulations: one with a perfectly flat pulse (thick solid) and two with 10%-amplitude-modulated pulses with periods of 250 ps (thin solid) and 1 ns (dashed). All three pulses have a realistic 100- to 200-ps rise and fall taken from a typical measured pulse. Pressure modulations from the modulate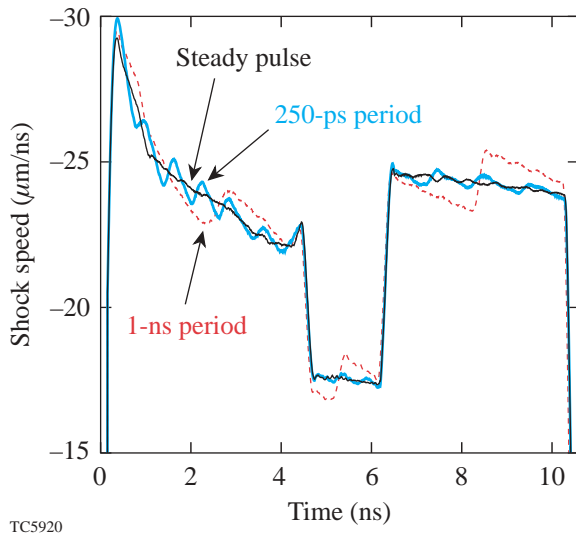d pulse steepen into distinct shocks by the time they reach the primary shock, resulting in abrupt jumps in shock speed, as at 8 ns.

The σ for a range of perturbation periods and amplitudes is shown in Fig. 90.14. These data were computed using an array of *LILAC* simulations, with periods of 250 ps, 0.5 ns, …, 3.5 ns; amplitudes of 5% (1 TW/cm^2), 10%, 15%, 20%; and compared to a simulation with a flattop pulse.

Because the shock speed as a function of time in the Al and foam is not steady, it is possible (though unlikely) for a perturbed pulse to result in decreased standard deviation of the shock speed about the mean. For this reason, we have

also computed the standard deviation σ_f not about the mean, but with respect to the shock speed of a flattop pulse (see Fig. 90.15).

For comparison, the discrete Fourier transforms of 32 pulses, with a range of average intensities from 4 TW/cm^2 to almost 100 TW/cm^2, from two experimental campaigns performed on OMEGA in October and November 2001, were computed (see Fig. 90.16). The contour lines associated with an average spectrum (heavy solid curves) as well as a best and worst (dashed curves) (using linear interpolation for non-integral mode numbers) for this set of shots are shown in Figs. 90.14 and 90.15. These figures show that for a typical OMEGA pulse, the unsteadiness of the shock may be expected, from 1-D simulations, to be below 1.5%.
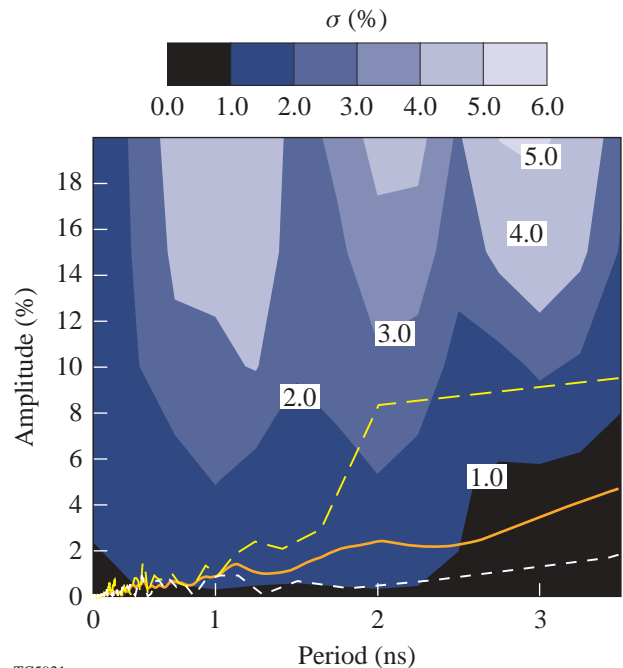
TC5921

Figure 90.14
The standard deviation σ about the mean of the shock speed, during the shock transit through the Al and foam. The steadiness is shown as a fraction (in %) of the mean shock speed. For comparison, the average discrete Fourier transform of 32 shots from two EOS experiments is also shown (solid), as well as a best and worst spectrum (dashed). The sharpness of the contour lines reflects the finite number of simulations used. Note that because the period of the perturbations can be comparable to the hydrodynamic time scale, the phase of the perturbations can be important for larger amplitudes, creating the local extrema in σ [and in σ_f in Fig. 90.15 (see below)].
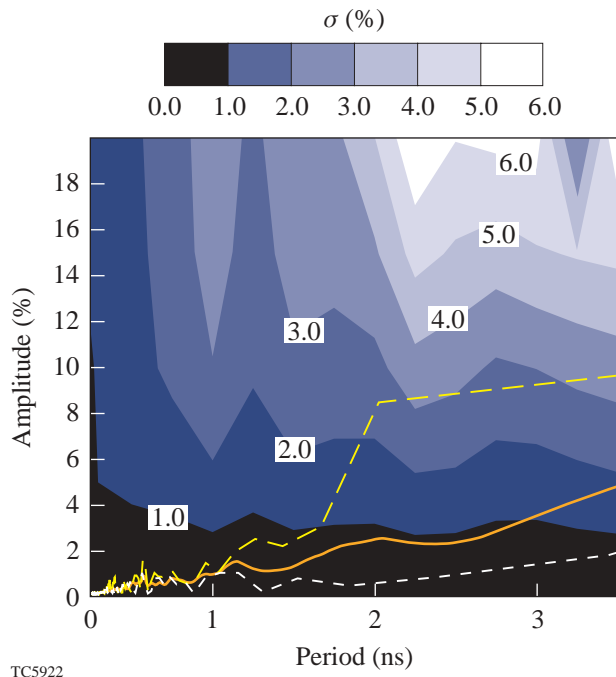
TC5922

Figure 90.15
The standard deviation, as in Fig. 90.14, but computed with respect to the shock speed for a steady pulse, rather than with respect to the mean.

The preceding conclusion is based on the assumption that, since the amplitudes of the modulations are small, the modes remain linear. An additional simulation that was performed using an average pulse shape (of the normalized measured pulses) resulted in a pulse unsteadiness σ of 1.44%, to be compared to the 0.95% of the perfectly flattop pulse. This supports the conclusion that the typical pulse steadiness on OMEGA will in general, for this intensity, result in shock steadiness of less than ~1.5%.

Due to 2-D effects, such as shock curvature and transverse radiative transport,[35] defocusing of the beam by the corona,[33] and lateral plasma flow,[36] 1-D simulations systematically overestimate the shock speed. Fortunately, determining the foam Hugoniot requires only the EOS of Al, along with the measured shock speeds, and does not depend on precise agreement between the simulated and measured shock-breakout times. A comparison of experimental results with 1-D simulated shock speeds, in which the intensity was reduced to account for 2-D effects, is shown in Fig. 90.17. For this shot (27174) a 20% reduction was needed. In general, a sufficient margin is built into the 1-D target designs to allow for the systematic decrease in shock speed due to 2-D effects.

TC5923

Figure 90.16
The pulses used in the comparisons shown in Figs. 90.14 and 90.15. Before computing the Fourier transforms, the rise and fall of the pulses were removed (dotted).

E11614
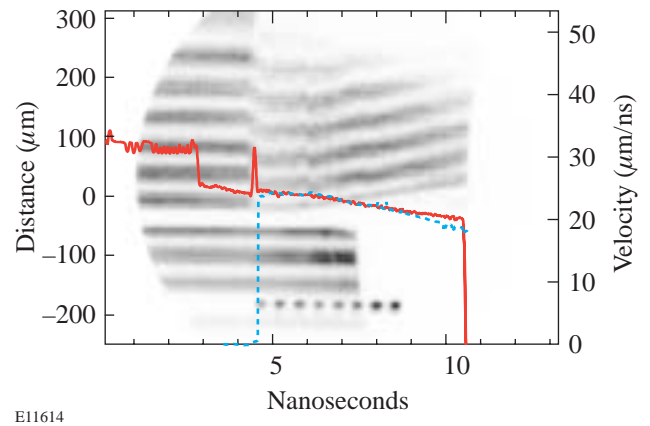
Figure 90.17
A comparison of the measured (dashed) and simulated (solid) shock speeds for shot 27174. To model 2-D effects, the intensity of the measured pulse was uniformly decreased by 20%. This target consisted of 20 μm CH, 5 μm glue (modeled by CH), 80 μm CHBr, 5 μm glue, 40 μm Al, and 140 μm quartz. The transparent quartz layer was used to determine shock speed as a function of time, for comparison with simulation. Because the density of quartz is close to that of Al, it also provides an indication of the typical shock speeds in the thick portion of the Al step. The measured shock speed was determined from the motion of the ASBO/VISAR fringes, which are also shown. The simulation and experiment were synchronized to the time of shock breakout into the quartz.

Discussion and Conclusions

A description of the theoretical tools used in the design of targets has been presented here, including the constraints presented by the requirement of minimal radiation preheat and shock steadiness. Even a small amount (0.4 eV) of preheat can alter the Hugoniot at pressures of less than 1 Mbar for 100-mg/cc CRF foam, potentially constraining the amount of allowable preheat. It has also been shown that the pulse steadiness of typical pulses on OMEGA is sufficient to ensure, on average, shock steadiness of less than 1.5% (for a typical 20-TW/cm^2, 3.5-ns pulse). If the measured shock speeds have an error of 1.5%, the resulting uncertainty in the density and pressure will be ~6.6% and ~2.4%, respectively, for a shock generated by laser illumination of this intensity. While this result does not rule out the effects of pulse steadiness, it suggests that other aspects of the experiment should be improved as well. Future experiments will also focus on the use of the "direct method," in order to reduce the uncertainty in the computed density by providing a direct measure of target compression.

REFERENCES

1. R. J. Hemley and H. K. Mao, Phys. Rev. Lett. **61**, 857 (1988).

2. A. H. Jones, W. M. Isbell, and C. J. Maiden, J. Appl. Phys. **37**, 3493 (1966).

3. C. G. M. van Kessel and R. Sigel, Phys. Rev. Lett. **33**, 1020 (1974).

4. L. V. Al'tshuler *et al.*, Sov. Phys.-JETP **34**, 606 (1958).

5. R. F. Trunin, *Shock Compression of Condensed Materials* (Cambridge University Press, Cambridge, England, 1998).

6. G. W. Collins *et al.*, Science **281**, 1178 (1998).

7. R. Jeanloz, Phys. Today **53**, 44 (2000); *High-Energy-Density Physics Study Report*, National Nuclear Security Administration, U.S. Department of Energy, Washington, DC (6 April 2001).

8. D. G. Colombant *et al.*, Phys. Plasmas **7**, 2046 (2000).

9. S. Skupsky, R. Betti, T. J. B. Collins, V. N. Goncharov, D. R. Harding, R. L. McCrory, P. W. McKenty, D. D. Meyerhofer, and R. P. J. Town, "High-Gain, Direct-Drive Target Designs for the National Ignition Facility," to be published in the *Proceedings of the 2nd International Conference on Inertial Fusion Sciences and Applications*.

10. L. M. Hair *et al.*, J. Vac. Sci. Technol. A **6**, 2559 (1988).

11. M. Desselberger *et al.*, Phys. Rev. Lett. **74**, 2961 (1995).

12. A. Benuzzi *et al.*, Phys. Plasmas **5**, 2827 (1998).

13. D. Batani *et al.*, Plasma Phys. Control. Fusion **40**, 1567 (1998).

14. M. Koenig *et al.*, Phys. Plasmas **6**, 3296 (1999).

15. R. W. Pekala and F-M. Kong, Lawrence Livermore National Laboratory, Livermore, CA, UCRL-99846 (1988).

16. Ya. B. Zel'dovich and Yu. P. Raizer, in *Physics of Shock Waves and High-Temperature Hydrodynamic Phenomena*, edited by W. D. Hayes and R. F. Probstein (Academic Press, New York, 1966).

17. J. H. Campbell *et al.*, Laser Part. Beams **15**, 607 (1997).

18. L. M. Barker and R. E. Hollenbach, J. Appl. Phys. **43**, 4669 (1972).

19. J. W. Bates and A. N. Mostovych, Bull. Am. Phys. Soc. **46**, 43 (2001).

20. G. R. Gathers, *Selected Topics in Shock Wave Physics and Equation of State Modeling* (World Scientific, Singapore, 1994).

21. R. Cauble *et al.*, Phys. Plasmas **4**, 1857 (1997).

22. R. M. More *et al.*, Phys. Fluids **31**, 3059 (1988).

23. D. A. Young, Lawrence Livermore National Laboratory, private communication (2001).

24. F. Reif, *Fundamentals of Statistical and Thermal Physics* (McGraw-Hill, New York, 1965).

25. S. P. Marsh, ed. *LASL Shock Hugoniot Data*, Los Alamos Series on Dynamic Material Properties (University of California Press, Berkeley, CA, 1980).

26. N. C. Holmes, Rev. Sci. Instrum. **62**, 1990 (1991).

27. A. C. Mitchell and W. J. Nellis, J. Appl. Phys. **52**, 3363 (1981).

28. R. Courant and K. O. Friedrichs, *Supersonic Flow and Shock Waves*, Pure and Applied Mathematics, v. 1 (Interscience, New York, 1948), p. 141.

29. R. J. Trainor and Y. T. Lee, Phys. Fluids **25**, 1898 (1982).

30. J. J. Honrubia *et al.*, J. Quant. Spectrosc. Radiat. Transf. **61**, 647 (1999).

31. M. C. Richardson, P. W. McKenty, F. J. Marshall, C. P. Verdon, J. M. Soures, R. L. McCrory, O. Barnouin, R. S. Craxton, J. Delettrez, R. L. Hutchison, P. A. Jaanimagi, R. Keck, T. Kessler, H. Kim, S. A. Letzring, D. M. Roback, W. Seka, S. Skupsky, B. Yaakobi, S. M. Lane, and S. Prussin, in *Laser Interaction and Related Plasma Phenomena*, edited by H. Hora and G. H. Miley (Plenum Publishing, New York, 1986), Vol. 7, pp. 421–448.

32. S. P. Lyon and J. D. Johnson, Los Alamos National Laboratory, Los Alamos, CA, Report LA-UR-92-3407 (1992).

33. S. G. Glendinning, D. K. Bradley, R. C. Cauble, M. J. Edwards, H. Louis, J. C. Moreno, S. J. Moon, B. A. Remington, E. J. Turano, T. R. Boehly, R. S. Craxton, and R. Town, Bull. Am. Phys. Soc. **45**, 199 (2000).

34. R. E. Kidder, Nucl. Fusion **8**, 3 (1968).

35. D. Braun *et al.*, Bull. Am. Phys. Soc. **46**, 44 (2001).

36. M. Temporal *et al.*, Il Nuovo Cimento **19D**, 1839 (1997).

Observations of Modulated Shock Waves in Solid Targets Driven by Spatially Modulated Laser Beams

Introduction

Shock waves produced by laser-driven ablation are an important part of studies of inertial confinement fusion (ICF),[1,2] the equation of state of materials (EOS),[3–5] laboratory astrophysics,[6,7] and other high-energy-density sciences. In ICF, nonuniformities in the drive laser can produce nonuniform shocks that create mass perturbations in the target.[2] These perturbations can be amplified by the Rayleigh–Taylor (RT)[1] instability to a sufficiently large enough level to disrupt the implosion and reduce its performance. The propagation of these modulated shocks is determined by the physics of the laser-interaction region and stabilization processes;[8,9] hence, their measurement provides information about the intervening processes. Modulations in drive intensity can also be used to verify the scaling of shock strength (velocity) with drive intensity to better understand coupling efficiency and its scaling with intensity.

This article reports on novel experiments in which targets are driven with a laser beam having a single-mode, spatial-intensity modulation. The resultant ablation-pressure modulations produce shocks with spatially varying strengths (and velocities). The arrival times of the shock at various surfaces in the target are used to infer differences in the shock velocities and therefore the pressures produced by the modulated drive intensity. By placing an embedded layer within the target, the shock arrival at two surfaces is measured, thereby providing an added opportunity to observe the evolution of the modulated shock as it traverses the target. This evolution can be used to study dynamic effects in laser-produced plasmas, namely stabilization by dynamic overpressure.[9]

Experimental Results

In these experiments, 20-μm-thick CH ($\rho = 0.92$ g/cm^2) targets were irradiated with 351-nm laser light at average intensities of 6×10^{12} W/cm^2. A 0.5-μm-thick Al layer was embedded at the center (10 μm deep) of the target. This layer provided an intermediate surface where the shock arrival was detected. Modulations in drive intensity of ~5:1 produced ~3:1 modulations in shock pressure. Hydrodynamic simulation of these experiments is in good agreement with the average shock speeds, their modulations, and the resultant breakout times.

These experiments were conducted on the OMEGA[10] laser using a single drive beam having a distributed phase plate (DPP)[11] that produces a modulated intensity pattern at its focal spot. The phase plate was designed and fabricated to produce a one-dimensional irradiance distribution on a flat target placed in the quasi far field of the OMEGA laser beam. One-quarter of the Talbot cycle (the transition from only phase modulation to only intensity modulation) was used to achieve a sinusoidal irradiance distribution, with flat phase, from a sinusoidal phase distribution, with flat irradiance, in the near field of the laser. Photolithographic and ion-etching techniques were used to place a surface relief in fused silica.[11] As the laser beam traverses the etched-glass plate, it acquires the needed phase distribution from the etched pattern to produce a sinusoidal intensity distribution at the focal plane. The focusing lens was positioned to obtain a spatial wavelength of 60 μm at the target plane.

This beam was incident on the target at an angle of 23°. The modulations were oriented so that obliquity distortions were negligible in the modulation direction. The arrival of the shock front at the rear and embedded surfaces was detected using the active-shock-breakout (ASBO) diagnostic.[12] It uses a 532-nm (doubled Nd:YAG) probe laser directed onto the back of the experimental targets to detect shock velocity or breakout times.

Figure 90.18 shows the experimental arrangement with the UV drive laser incident from the left onto the front of the target and the ASBO probe laser incident from the right, probing the rear side of the target. The ASBO diagnostic normally uses the time-resolved displacement of VISAR (velocity interferometer system for any reflector) fringes[12,13] to detect shock velocity. In the case of opaque materials, the ASBO probe beam does not detect the shock wave within the material but records the disruption of the rear-surface reflectivity produced there by the arrival of the shock. (The release of the rear surface
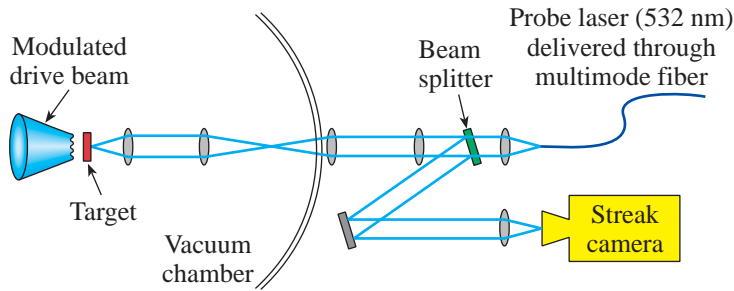
E11493

produces an expanding plume of material that quickly absorbs the laser energy.) The shock speeds are deduced from the known material thickness and the shock transit time as measured by this breakout.

Figure 90.19(a) shows an optical image of the drive-laser intensity distribution obtained with a charge-coupled-device (CCD) camera placed at an equivalent target plane[14] for the OMEGA laser. The distributed phase plate described above produced the modulations in the laser focal spot. The focal position was chosen to produce modulations with a wavelength of ~60 μm; the resultant spot was about 800 μm in diameter.

Figure 90.19(b) is a plot of the intensity distribution in the vertical direction along the center of the image. The intensity modulations range between 5:1 and 3:1, depending on which area of the focal spot is analyzed. This variation occurs because the nonuniformities in phase and irradiance of the laser beam are comparable to those that produce the sinusoidal pattern. (These effects can be compensated for in future designs.) The absolute values for the on-target intensity were obtained by normalizing the total distribution of intensities to the incident laser power for shot 24569.

Figure 90.20 is a pinhole-camera image of the x rays emitted from an Au target irradiated by this beam [Fig. 90.19(a)] at an average intensity of ~10^{14} W/cm^2. This intensity is higher than that used to drive the targets but is used to produce sufficient x rays for imaging purposes. At this intensity the x rays are predominately from n-shell Au emission. The lower apparent modulation amplitude results from the nonlinear conversion of the UV to x-ray energy.

The opaque layer (0.5 μm of Al) embedded in the target provides an internal surface at which the shock arrival is detected. The depth of that imbedded layer was 10 μm from the irradiated surface; another 10 μm of CH was coated on the rear

side. The heat front did not penetrate the front 10 μm of CH to the Al layer while the laser was on.

Figure 90.21 shows the time-resolved ASBO data for two shots, depicting the signal reflected from targets irradiated by the intensity distribution shown in Fig. 90.19. (The series of

E11494

dots across the bottom of the figures are temporal fiducial pulses, each separated by 0.548 ns.) For these experiments, one leg of the VISAR interferometer was blocked, producing a simple probe beam, giving a continuous spatial record of the shock-breakout time. The ASBO probe beam penetrates the rear portion of the target (10 μm of transparent CH) and reflects
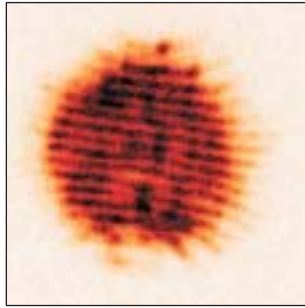
E11495

Figure 90.20
An x-ray pinhole-camera image of the x rays emitted from a Au target irradiated by the beam shown in Fig. 90.19(a).
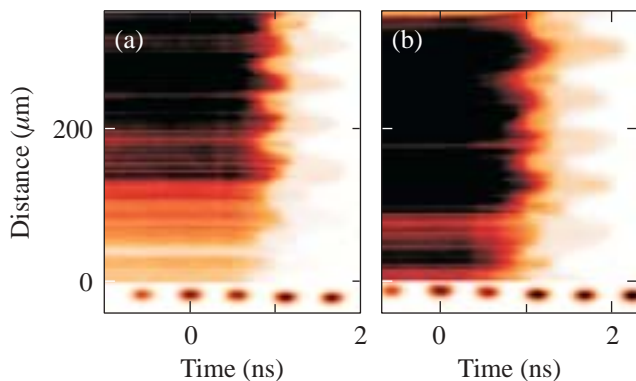
E11496

Figure 90.21
Streak records of probe beam reflection from (a) shot 24566 and (b) shot 24569. The dark signal from approximately −1 ns to +1 ns is the probe beam reflection off the unshocked Al layer within the target. The transition to the lighter area occurs when the shock arrives at the Al layer, reducing its reflectivity. The cessation of that light area (later in time) is caused by the arrival of the shock at the rear surface. The modulations in each of these transition regions result from different arrival times of the modulated shock in the target.

off the embedded Al layer. This reflection is seen as the dark portion of the image that extends from less than –1 to ~1 ns. (The horizontal streaks seen in these signals are due to the spatial speckle of the probe laser.) The drive laser began at 0 ns. At about +1 ns, the shock arrives at the Al layer and changes the layer's reflectivity, signaling the arrival of the shock at that surface. At that point, the signal to ASBO decreases but does not completely disappear. This reduction in signal results from either reduced reflectivity of the Al or reduced transmissivity of the rear CH section. Both are caused by the shock's arrival at the Al layer. The contour of change in reflectivity (dark to light transition) is modulated at the same spatial frequency as the incident laser modulations. The earlier occurrences of this transition represent the arrival of faster portions of the shock (shorter transit times) and later occurrences the slower portions (longer transit times). The lighter region persists until about 1.5 to 2 ns, then it disappears completely. This total loss of signal occurs when the shock arrives at the rear surface and that surface unloads, no longer reflecting the probe laser. Note that the extinction time of this light area is also modulated and it is in phase with the dark-to-light transition at ~1 ns. These transitions in target reflectivity mark the arrival of the shock front at each surface and can therefore be used to infer shock velocities and modulations in those velocities.

Analysis

Figure 90.22 shows a plot (solid curves) of the shock arrival times (at the Al layer and the rear surface) as a function of space as deduced from Fig. 90.21(b). Using these data and the thickness of the intervening target material, the shock speed as a function of space can be inferred. In the lower curve, the earliest times (corresponding to intensity peaks) occur at ~0.97 ns, and the latest times (intensity troughs) occur at ~1.15 ns. The respective times for the upper curves are 1.47 ns and 1.95 ns, where $t = 0$ is the start of the laser pulse. Each of these values represents the average of three peaks or troughs. (The trend to later times at the right end of these plots likely results from the finite size of the laser spot. Its edges have slightly lower intensity and hence produce slower shocks that arrive at the surfaces later in time.) Using the 10-μm distance for transit times at the peak and trough of the modulated shock, we find that the minimum shock speed is 12.5 μm/ns and the maximum is 20 μm/ns. The errors in velocity are expected to be ≤5% and arise mainly from uncertainties in target thickness (±0.1 μm) and determination of shock arrival time (~ ±10 ps). Using the Hugoniot data for CH from *SESAME* tables,[15] these shock velocities correspond to pressures of 2.85 and 0.97 Mb, respectively. In a similar shot with an identical target, the

shock speeds were slightly higher but the modulations of similar size. Table 90.III lists the results for the two shots. The breakout times (t_P and t_T for peaks and troughs) at either $10\,\mu m$ or $20\,\mu m$ in the target were averaged over three spatial periods. V_- is the shock velocity given by the distance ($10\,\mu m$) divided by the difference between later breakout times (troughs of shock); V_+ is the velocity associated with the earlier breakout times (peaks of shock). The pressures P_- and P_+ are inferred from the shock velocities V_- and V_+ using the *SESAME* equation-of-state tables. I_+/I_- is the ratio of intensity calculated from the pressure ratio P_+/P_- using the intensity scaling for pressure as given below.
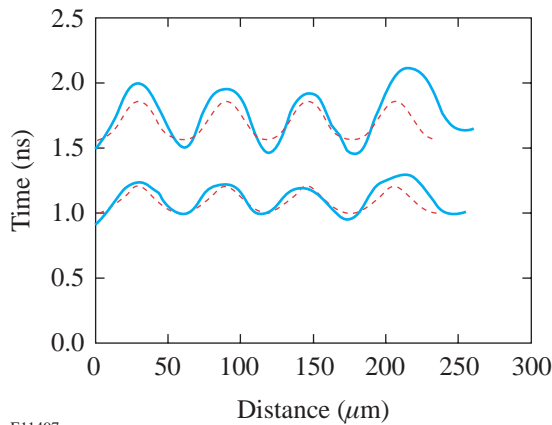
E11497

Figure 90.22
The shock arrival times versus space for shot 24566 [Fig. 90.21(b)]. The upper curve represents the contour of the shock arrival time at the rear surface; the lower curve for the arrival at the Al layer embedded at $10\,\mu m$. The dashed lines are the simulated arrival times of the shock at those surfaces.

The dependence of pressure on intensity has been established by considerable ICF research as $P(\text{Mbar}) = 40\,(I/\lambda)^{2/3}$ (Refs. 16–18), where λ is the laser wavelength in μm and I is laser intensity in $10^{15}\,\text{W/cm}^2$. It is expected that for the intensities in these experiments, plasma instabilities are not important and this scaling law should be valid. At $6 \times 10^{12}\,\text{W/cm}^2$, the pressure should be ~2.7 Mb; a factor-of-5

reduction in intensity should produce a 0.9-Mb shock. These numbers are in good agreement with the observed pressure changes as inferred from the modulations in shock velocity, as shown in Table 90.III. Note that the pressure modulations are similar for the two shots, despite the differences in absolute pressure. This is because the sinusoidal intensity distribution was the same for both shots. The absolute pressure is different because the laser power (pulse shape and laser energy) was different (by a factor of ~5) for the two shots: $6 \times 10^{12}\,\text{W/cm}^2$ and $1.5 \times 10^{12}\,\text{W/cm}^2$.

Figure 90.23 shows a contour plot depicting density from a 2-D hydrodynamic simulation of this experiment using the computer code *ORCHID*.[19] The laser is incident from the left, and the shock (propagating to the right) can be seen as the first contour. A portion of the embedded AL layer (indicated in the figure) has been displaced by the shock. The laser intensity was $6 \times 10^{12}\,\text{W/cm}^2$ (average) in a sinusoidal intensity distribution with 60-μm wavelength and intensity modulation (peak-to-
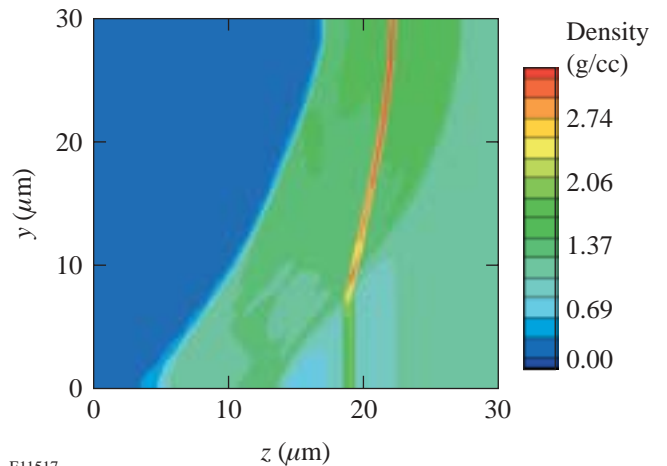
E11517

Figure 90.23
Density contours (at 1.39 ns) in a 2-D hydrocode (*ORCHID*) simulation of these experiments with an embedded Al layer as shown. The modulated laser (1/2 cycle of the sinusoidal modulation is shown) is incident from the left. The curved shock propagates to the right.

Table 90.III: Experimental results.

Shot #	(W/cm²)	Trough		Peak		Velocity		Pressure		Modulation	
		t_{T20}	t_{T10}	t_{P20}	t_{P10}	V_-	V_+	P_-	P_+	P_+/P_-	I_+/I_-
24566	6×10^{12}	1.62	1.06	1.15	0.813	17.8	29.6	2.18	6.45	2.96	5.09
24569	1.4×10^{12}	1.95	1.15	1.47	0.973	12.5	20.1	0.97	2.85	2.94	5.04

valley) of 5:1. The predicted arrival time of the shock at the embedded layer and the rear surface is shown as dashed curves in Fig. 90.22.

Conclusion

These experiments have demonstrated a technique for observing modulated shocks in solid targets. Modulations in the drive intensity produce shocks with spatially varying speeds. The arrival of these shocks at surfaces of the target was detected with an optical probe beam. The transit times of the shocks through the targets provide the velocities at various points along the shock front and detect the modulations in shock velocity. These velocities were used to infer the resultant pressure modulations produced by modulations in drive intensity. The experimental results are consistent with established models for the intensity scaling of ablation pressure. The 2-D hydrocode *ORCHID* modeled the observed breakout times and modulations accurately. This technique will be useful for studying dynamic overpressure where ablation dynamics may alter the amplitude of shock modulations as it propagates through a target. In addition, these results confirm established scaling laws for ablation pressure with drive intensity.

REFERENCES

1. J. D. Lindl, Phys. Plasmas **2**, 3933 (1995).

2. S. E. Bodner, D. G. Colombant, J. H. Gardner, R. H. Lehmberg, S. P. Obenschain, L. Phillips, A. J. Schmitt, J. D. Sethian, R. L. McCrory, W. Seka, C. P. Verdon, J. P. Knauer, B. B. Afeyan, and H. T. Powell, Phys. Plasmas **5**, 1901 (1998).

3. G. W. Collins *et al.*, Science **281**, 1178 (1998).

4. R. Cauble *et al.*, Phys. Plasmas **4**, 1857 (1997).

5. G. W. Collins *et al.*, Phys. Plasmas **5**, 1864 (1998).

6. B. A. Remington *et al.*, Science **284**, 1488 (1999).

7. B. A. Remington *et al.*, Phys. Plasmas **7**, 1641 (2000).

8. V. N. Goncharov, "Self-Consistent Stability Analysis of Ablation Fronts in Inertial Confinement Fusion," Ph.D. thesis, University of Rochester, 1998.

9. V. N. Goncharov, S. Skupsky, T. R. Boehly, J. P. Knauer, P. McKenty, V. A. Smalyuk, R. P. J. Town, O. V. Gotchev, R. Betti, and D. D. Meyerhofer, Phys. Plasmas **7**, 2062 (2000).

10. T. R. Boehly, D. L. Brown, R. S. Craxton, R. L. Keck, J. P. Knauer, J. H. Kelly, T. J. Kessler, S. A. Kumpan, S. J. Loucks, S. A. Letzring, F. J. Marshall, R. L. McCrory, S. F. B. Morse, W. Seka, J. M. Soures, and C. P. Verdon, Opt. Commun. **133**, 495 (1997).

11. T. J. Kessler, Y. Lin, J. J. Armstrong, and B. Velazquez, in *Laser Coherence Control: Technology and Applications*, edited by H. T. Powell and T. J. Kessler (SPIE, Bellingham, WA, 1993), Vol. 1870, pp. 95–104.

12. P. M. Celliers *et al.*, Appl. Phys. Lett. **73**, 1320 (1998).

13. L. M. Barker and R. E. Hollenbach, J. Appl. Phys. **43**, 4669 (1972).

14. S. P. Regan, J. A. Marozas, J. H. Kelly, T. R. Boehly, W. R. Donaldson, P. A. Jaanimagi, R. L. Keck, T. J. Kessler, D. D. Meyerhofer, W. Seka, S. Skupsky, and V. A. Smalyuk, J. Opt. Soc. Am. B **17**, 1483 (2000).

15. B. I. Bennett *et al.*, Los Alamos National Laboratory, Report LA-7130 (1978).

16. C. E. Max, *Physics of Laser Fusion, Vol. I*, Lawrence Livermore National Laboratory, Livermore, CA, UCRL-53107, Rev. 1 (1982).

17. W. M. Manheimer, D. G. Colombant, and J. H. Gardner, Phys. Fluids **25**, 1644 (1982).

18. S. M. Pollaine and J. D. Lindl, Nucl. Fusion **26**, 1719 (1986).

19. R. L. McCrory and C. P. Verdon, in *Inertial Confinement Fusion*, edited by A. Caruso and E. Sindoni (Editrice Compositori, Bologna, Italy, 1989), pp. 83–124.

Time-Dependent Electron Thermal Flux Inhibition in Direct-Drive Laser Implosions

Electron thermal conduction plays an important role in inertial confinement fusion (ICF):[1] it transports the laser energy absorbed near the critical surface into the overdense region and therefore directly affects the ablation process, the laser absorption, and implosion dynamics. The flux-limited Spitzer–Härm (SH) model[2] has been widely used to calculate the electron thermal conduction. In this model, the flux limiter f (typical value is 0.06)[3] is introduced to limit the SH electron thermal flux[4] and is given by

$$q_e = \min\left(f q_{FS}, q_{SH}\right), \qquad (1)$$

where q_e is the electron thermal flux, q_{FS} is the free-streaming thermal flux defined as $q_{FS} = n_e T_e \left(T_e / m_e\right)^{1/2}$, n_e is the electron number density, T_e is the electron temperature in energy units, m_e is the electron mass, and f is the flux limiter, respectively; q_{SH} is the SH electron thermal flux.[4] Because the flux limiter is empirically determined from the comparison between the numerical simulations and the experimental results,[5] it depends on the experimental conditions and the experimental uncertainties.

More-general approaches to calculating the electron thermal transport include a Monte Carlo method[6] and solving the Fokker–Planck (FP) equation. Many authors have reported that nonlocal electron thermal conduction is important, leading to a flux inhibition in laser-produced plasmas.[7–12] This article shows that the flux inhibition is time dependent for square pulses, which affects CH target implosions.

When the mean free path of the electrons is greater than the typical temperature and gradient scale lengths in the plasma, the transport is nonlocal. To calculate the nonlocal thermal conduction and to study its effect on the target implosions, a FP code was developed and combined with a one-dimensional hydrodynamic code ($LILAC$[13]). In our code, the electron velocity distribution function is expanded up to the $\ell = 3$ mode by Legendre polynomials of the direction cosines of the velocity vectors:[14]

Zeroth order:

$$\frac{\partial f_0}{\partial t} + \frac{1}{3}\left\{\frac{v}{\eta x^2}\frac{\partial}{\partial x}\left(x^2 f_1\right) - \frac{a_x}{v^2}\frac{\partial}{\partial v}\left(v^2 f_1\right)\right\}$$

$$- \frac{2}{15 v^2}\frac{\partial U}{\partial x}\frac{\partial}{\partial v}\left(v^3 f_2\right) = C_{ee} + S_0 ; \qquad (2)$$

First order:

$$\frac{\partial f_1}{\partial t} + v\frac{\partial f_0}{\partial x} - a_x\frac{\partial f_0}{\partial v}$$

$$+ \frac{2}{5}\left\{\frac{v}{x^2}\frac{\partial}{\partial x}\left(x^2 f_2\right) - \frac{a_x}{v^3}\frac{\partial}{\partial v}\left(v^3 f_2\right)\right\}$$

$$- \frac{\partial U}{\partial x}\cdot f_1 - \left\{\frac{2}{5}\frac{\partial U}{\partial x} + \frac{1}{5x^2}\frac{\partial}{\partial x}\left(x^2 U\right)\right\} v^2 \frac{\partial}{\partial v}\left(\frac{f_1}{v}\right)$$

$$= -\nu_{ei} f_1 ; \qquad (3)$$

Second order:

$$\frac{\partial f_2}{\partial t} + v\frac{\partial f_1}{\partial x} - \frac{v}{3x^2}\frac{\partial}{\partial x}\left(x^2 f_1\right) - \frac{2}{3}a_x v\frac{\partial}{\partial v}\left(\frac{f_1}{v}\right)$$

$$+ \frac{3}{7}\left\{v\frac{\partial f_3}{\partial x} - \frac{a_x}{v^4}\frac{\partial}{\partial v}\left(v^4 f_3\right)\right\} + \frac{1}{7}\left\{\frac{2}{x^2}\frac{\partial\left(x^2 U\right)}{\partial x} - 4\frac{\partial U}{\partial x}\right\}f_2$$

$$- \left\{\frac{\partial U}{\partial x} - \frac{1}{3x^2}\frac{\partial\left(x^2 U\right)}{\partial x}\right\}v\frac{\partial f_0}{\partial x}$$

$$- \frac{1}{21}\left\{8\frac{\partial U}{\partial x} + \frac{3}{x^2}\frac{\partial\left(x^2 U\right)}{\partial x}\right\}v\frac{\partial f_2}{\partial v}$$

$$= -3\nu_{ei} f_2; \tag{4}$$

Third order:

$$\frac{\partial f_3}{\partial t} + \frac{3}{5}\left\{v\frac{\partial f_2}{\partial x} - a_x v^2\frac{\partial}{\partial v}\left(\frac{f_2}{v^2}\right)\right\} = -6\nu_{ei} f_3; \tag{5}$$

where f_0, f_1, f_2, and f_3 are the $\ell = 0$ (isotropic part), 1, 2, and 3 modes of the distribution function, respectively. For the closure of these coupled equations, we use the simplified f_3 equation without the correction terms for hydrodynamic motion and nonplanar geometry; f_3 is reset to 0 at the beginning of every time step because $f_3 \ll f_2$ but $\Delta f_3 \neq 0$.

In the above equations, C_{ee} is the electron–electron collision operator,[15] which is determined from the interaction of f_0 with itself only; ν_{ei} is the electron–ion collision frequency[12] given by

$$\nu_{ei} = \phi 4\pi n_e Z^* e^4 \ln\Lambda / m_e^2 v^3,$$

which effectively includes the corrections of higher-order terms neglected in the electron–electron collision operator,

$$\phi = \left(Z^* + 4.2\right)/\left(Z^* + 0.24\right).$$

The effective charge Z^* is defined by $Z^* = \langle Z^2\rangle/\langle Z\rangle$, where $\langle Z^2\rangle, \langle Z\rangle$ are the square of the charge and charge averaged over the ion species, respectively; e is the electron charge; $\ln\Lambda$ is the Coulomb logarithm,[16] and U is the ion velocity. The acceleration term is defined as $a_x = eE_x/m_e$, where the electric field E_x is obtained from the current-free condition $j = 4\pi e/3 \int_0^\infty dv v^3 f_1 = 0$. S_0 is a source term that accounts for the change in the Maxwell distribution function

$$f_M = n_e\left(m_e/2\pi T_e\right)^{3/2}\exp\left(-m_e v^2/2T_e\right),$$

i.e., $S_0 = \delta(f_M)$, due to changes in the electron density and temperature from ionization, radiation transport, laser absorption, and PdV work calculated by the hydrodynamic code before the FP calculation. The friction term η limits the temperature change due to the thermal conduction according to the real gas heat capacity per electron c_{ve}. For a real gas, η is given by $\eta = 2c_{ve}/3$, where c_{ve} is obtained from the hydrodynamic code. After the FP calculation, the effective electron temperature, defined as $T_{eff} = 2\pi/m_e \int_0^\infty f_0 v^4 dv$, is returned to the hydrodynamic code. This is equivalent to solving the electron energy equation in the hydrodynamic equations.

We simulated the implosion of a polystyrene CH shell of 900-μm diameter and 20-μm thickness filled with 15 atm of D_2 gas. The 0.35-μm-wavelength laser pulse was a 1-ns-duration square starting at $t = 200$ ps with a rise time (0 to maximum) of 200 ps and a constant power of 25 TW from 0.4 ns to 1.4 ns. The irradiation intensity on the target was 9×10^{14} W/cm^2. Figure 90.24(a) shows the laser profile and the calculated electron thermal flux at the critical surface,

$$q_{FP} = 2\pi m_e/3 \int_0^\infty v^5 f_1 dv,$$

normalized by the free-streaming thermal flux at the critical surface, q_{FS}. The ratio q_{FP}/q_{FS} can be defined as the flux-inhibition factor f if q_{FP} is assumed to be q_e, the "actual" flux when $f q_{FS} \leq q_{SH}$ in Eq. (1). We observe that f increases until 400 ps and then decreases with time. This shows the time dependence of the flux-inhibition factor in an ICF implosion. This time dependence of the flux inhibition is explained by the properties of the SH model and the nonlocal nature of the transport.

For the first explanation, we consider the time dependence of the relation between q_{FS} and q_{SH}, described by the SH model. At the critical surface q_{FS} is a function of the electron

temperature only, and q_{SH} is written in terms of λ_0/L_T and the free-streaming flux as $q_{SH} = 16\sqrt{2}\,\pi^{-1/2}(\lambda_0/L_T)\,q_{FS}$, where λ_0 is the electron mean free path for 90° collision scattering[5] given by

$$\lambda_0 = v_{th}^4 \Big/ \Big[4\phi\pi n_e Z^* \big(e^2/m_e\big)^2 \ln\Lambda \Big],$$

where v_{th} is the thermal velocity defined by $v_{th} = (2\,T_e/m_e)^{1/2}$. L_T is the temperature gradient scale length defined as $T_e/(\partial T_e/\partial x)$. Figure 90.24(b) shows λ_0/L_T and electron thermal fluxes q_{FS}, q_{SH}, and q_{FP} at the critical surface. λ_0/L_T increases during the rise time of the laser pulse when T_e increases rapidly. It then decreases as L_T increases faster than λ_0 after 400 ps, at which time the constant laser pulse starts. Also, q_{FS} increases gradually with time in Fig. 90.24(b) as the

electron temperature increases gradually. This leads to q_{SH} being almost constant after 400 ps since the increase in q_{FS} and the decrease in λ_0/L_T cancel each other in contributing to q_{SH}.

The relation between q_{SH} and q_{FP} is determined by the nonlocal transport. As seen in Fig. 90.24(b), the FP flux has a trend similar to that of the SH flux: the ratio q_{FP}/q_{SH} stays between 0.5 and 0.6 during the constant laser power. Yet, during that time, because λ_0/L_T decreases with time, we would expect the flux to be less constrained. The fact that the ratio q_{FP}/q_{SH} stays constant indicates that flux inhibition from the SH flux due to the nonlocality of the electron transport increases with time.

From the time development of the flux-inhibition factor f and the absorbed laser power I_A, the absorbed laser power–averaged flux-inhibition factor, $\langle f \rangle = \int f I_A dt / \int I_A \, dt$, is estimated to be 0.075 for the sharp-cutoff flux-limited SH formula of Eq. (1). We also calculated $\langle f \rangle$ with the harmonic mean flux-limited SH model, which is given by

$$q_e^{-1} = \big(f q_{FS}\big)^{-1} + q_{SH}^{-1}.$$

For this model, $\langle f \rangle$ is 0.15.

The validity of our Fokker–Planck calculation is checked by comparing the calculated neutron burn history with both experimental results and results of the flux-limited SH model. The experiments were performed on the 60-beam OMEGA laser system[17] with the best smoothing conditions.[18] The neutron burn history was measured with the neutron temporal detector, which has a temporal accuracy of ±50 ps.[19] All the calculations were carried out with the real laser pulse and target conditions. In Fig. 90.25(a), we show three neutron rates calculated by FP and by SH with flux limiters of 0.07 and 0.06. These results are for 15-atm-D_2 gas pressure and 20-μm shell thickness irradiated by a 1-ns-duration square pulse. The results of both FP and SH with a flux limiter of 0.07 show good agreement with the experimental result. The results shown in Fig. 90.25(b) for a fuel gas pressure of 3 atm also agree well with the experimental result for a flux limiter of 0.07. The difference in amplitude between the theoretical and experimental observed rate of neutron production or the reduced burn history is believed to be caused by the shell–fuel mix during the deceleration phase due to the Rayleigh–Taylor (RT) instability.[18] Results in Figs. 90.25(a) and 90.25(b) are consistent with the previous results shown in Fig. 90.24(a), where FP calculation gives $\langle f \rangle$ of 0.075. In Fig. 90.25(c), we show the
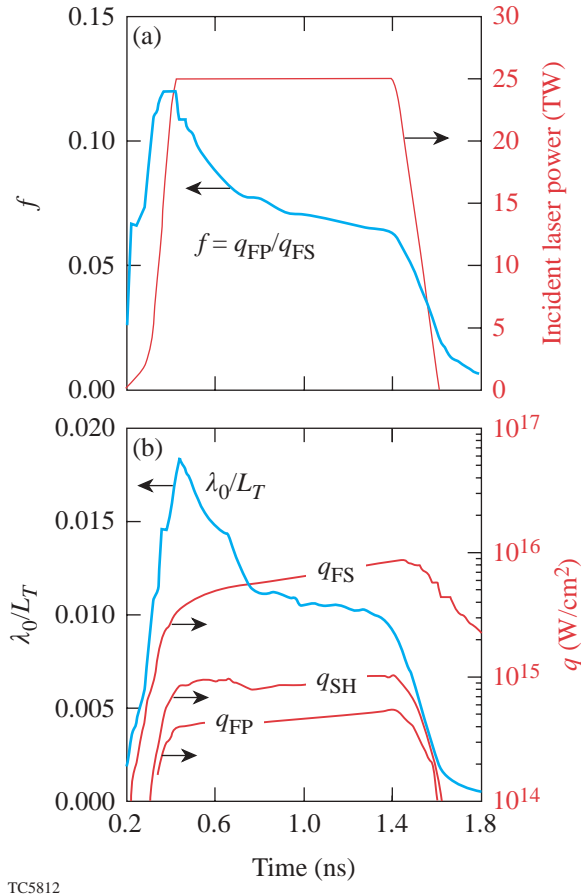
TC5812

Figure 90.24
(a) Ratio of the q_{FP} and q_{FS} measured at the critical surface; (b) ratio of λ_0 and L_T. q_{FS} and q_{SH} are calculated from the n_e and T_e obtained by FP calculation.

TC5888
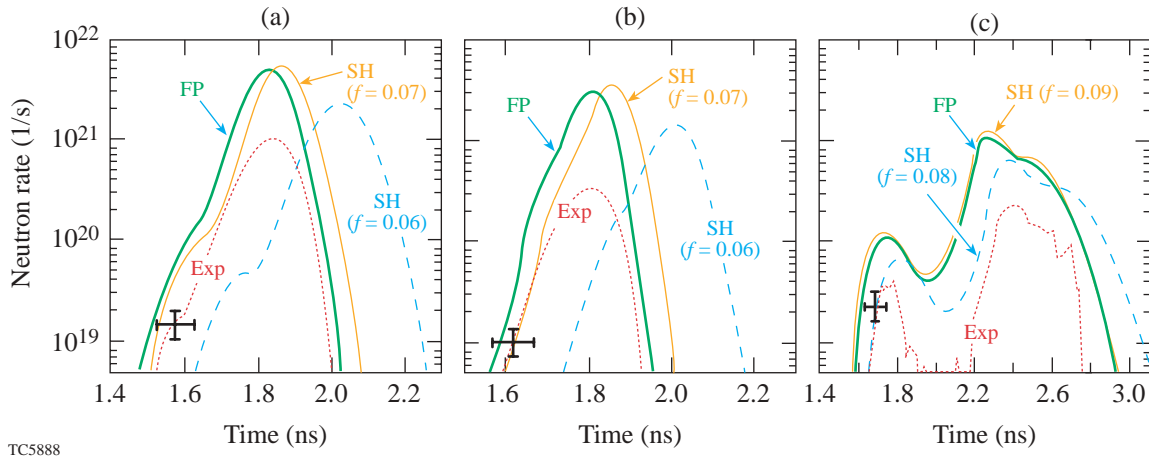
Figure 90.25

Comparison of the calculated neutron rate with results from the experiment for FP and SH with a flux limiter of 0.07 and 0.06: (a) 15 atm of D_2 fuel gas and 1-ns square pulse; (b) 3 atm of D_2 fuel and 1-ns square pulse; (c) 20 atm of DT fuel and 0.4-ns square pulse.

neutron rate for the case of a 0.4-ns square pulse (20 atm of DT in a similar target). In this case, the FP bang time agrees with that of the flux-limited SH for a flux limiter of 0.09. The experimental bang time is between SH with a flux limiter of 0.08 and FP. This indicates that a larger flux limiter is needed for short-pulse cases. In this case, $\langle f \rangle$ was found to be 0.087, which is larger than 0.075 for the 1-ns square pulse. This is consistent with the fact that a large flux-inhibition factor is needed to match the flux-limited SH flux to FP early in the pulse, as shown in Fig. 90.24(a). For all the cases shown in Figs. 90.25(a)–90.25(c), FP gives neutron temporal profiles about 50 ps ahead of these experiments. This discrepancy is within the experimental error bar. A stricter treatment of S_0 and η in Eq. (2) might reduce this discrepancy.

Next, we show the effects of the time dependence of the flux-inhibition factor on the absorption and the stability of the shell during the implosion. Due to the larger flux-inhibition factor early in the pulse, FP gives a larger thermal flux than SH with a flux limiter of 0.07, as shown in Fig. 90.24(a), resulting in a larger electron-density scale length, $L_n = n_e/(\partial n_e/\partial x)$, at the critical surface as seen in Fig. 90.26, where we also show that FP and SH with $f = 0.07$ give almost the same electron temperature T_e at the critical surface. The larger density scale length of FP at the critical surface early in the pulse gives rise to a larger absorption fraction by inverse bremsstrahlung than in the SH case as shown in Fig. 90.27, where we plot the temporal evolution of the laser absorption calculated by FP and by SH with flux limiters of 0.07 and 0.06. The laser absorption for FP is larger early in the pulse, while later in the pulse, FP

gives a lower laser absorption than SH with a flux limiter f of 0.07. The total absorption fraction is 0.83 for FP and 0.76 and 0.68 for SH with f of 0.07 and 0.06, respectively. FP gives a larger laser absorption fraction than that of the SH with 0.07 and 0.06 by about 7% and 15%, respectively.

The effect of the FP transport on the growth of the RT instability during the acceleration phase was investigated using the Betti–Goncharov formula.[20] In the acceleration

TC5814a
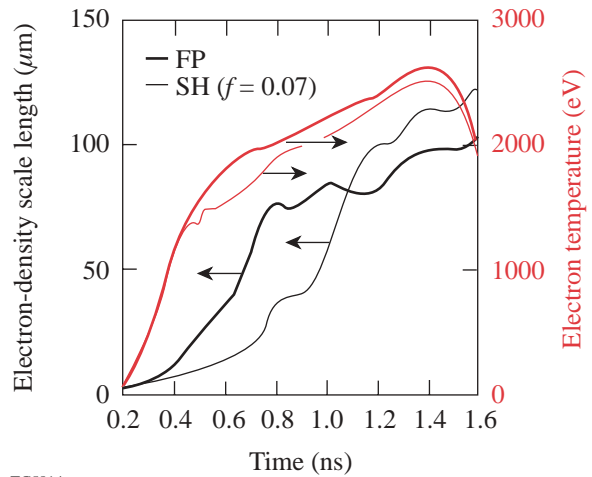
Figure 90.26

L_n and T_e for FP and SH with a flux limiter of 0.07, measured at the critical surface.

TC5815
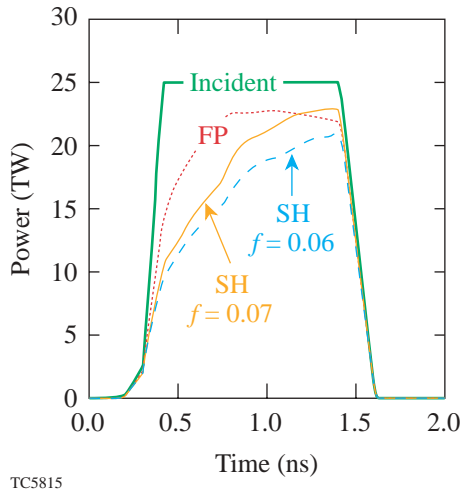
Figure 90.27
The absorbed laser power for FP and SH with flux-limiter values of 0.07 and 0.06. For reference, the incident power is also shown.

phase, the averaged ablation density $\langle \rho_a \rangle$ and the averaged mass ablation rate $\langle \dot{m} \rangle$ are 3.3 g/cm^3 and 1.35×10^6 g/cm^2 s for FP and 3.9 g/cm^3 and 1.53×10^6 g/cm^2 s for SH with a flux limiter of 0.07, respectively. Here, FP gives $\langle \rho_a \rangle$ and $\langle \dot{m} \rangle$ about 15% lower than that for SH. The averaged minimum density-gradient scale length $\langle L_m \rangle$ is 1.47 μm for FP and 1.06 μm for SH. This larger $\langle L_m \rangle$ in FP leads to stabilization of the growth of the RT instability of short-wavelength perturbations during the acceleration phase. The obtained α and β in the Betti–Goncharov formula[20] are 0.90 and 1.5, which are almost the same for both FP and SH.

Conclusion

Flux inhibition for square-pulse CH implosions has been shown to be time dependent. The thermal flux at the critical surface early in the pulse in the FP simulation is larger than in the flux-limited SH with a flux limiter equivalent to the averaged value calculated from the FP calculation. This was confirmed by comparing the neutron burn history from FP simulations with the experimental measurements for different fuel gas pressure and laser pulse durations. A larger flux limiter is required in simulations of implosions driven by shorter-duration pulses. The increase in the density scale length at the critical surface increases the laser absorption. The longer scale length at the ablation region also leads to a slight stabilization of the Rayleigh–Taylor growth by short-wavelength perturbations.

REFERENCES

1. J. Nuckolls *et al.*, Nature **239**, 139 (1972).

2. R. C. Malone, R. L. McCrory, and R. L. Morse, Phys. Rev. Lett. **34**, 721 (1975).

3. R. L. McCrory, J. M. Soures, C. P. Verdon, P. Audebert, D. Bradley, J. Delettrez, R. Hutchison, S. D. Jacobs, P. Jaanimagi, R. Keck, H. Kim, T. Kessler, J. Knauer, R. Kremens, S. Letzring, F. Marshall, P. McKenty, M. C. Richardson, A. Simon, R. Short, S. Skupsky, and B. Yaakobi, in *High Intensity Laser-Matter Interactions*, edited by E. M. Campbell and H. Baldis (SPIE, Bellingham, WA, 1988), Vol. 913, pp. 40–58.

4. L. Spitzer, Jr. and R. Härm, Phys. Rev. **89**, 977 (1953).

5. D. Shvarts, J. Delettrez, R. L. McCrory, and C. P. Verdon, Phys. Rev. Lett. **47**, 247 (1981).

6. R. J. Mason, Phys. Rev. Lett. **47**, 652 (1981).

7. A. R. Bell, R. G. Evans, and D. J. Nicholas, Phys. Rev. Lett. **46**, 243 (1981).

8. J. P. Matte and J. Virmont, Phys. Rev. Lett. **49**, 1936 (1982).

9. J. R. Albritton, Phys. Rev. Lett. **50**, 2078 (1983).

10. J. P. Matte, T. W. Johnston, J. Delettrez, and R. L. McCrory, Phys. Rev. Lett. **53**, 1461 (1984).

11. A. Nishiguchi *et al.*, Phys. Fluids B **4**, 417 (1992).

12. E. M. Epperlein, Laser Part. Beams **12**, 257 (1994).

13. M. C. Richardson, P. W. McKenty, F. J. Marshall, C. P. Verdon, J. M. Soures, R. L. McCrory, O. Barnouin, R. S. Craxton, J. Delettrez, R. L. Hutchison, P. A. Jaanimagi, R. Keck, T. Kessler, H. Kim, S. A. Letzring, D. M. Roback, W. Seka, S. Skupsky, B. Yaakobi, S. M. Lane, and S. Prussin, in *Laser Interaction and Related Plasma Phenomena*, edited by H. Hora and G. H. Miley (Plenum Publishing, New York, 1986), Vol. 7, pp. 421–448.

14. I. P. Shkarofsky, T. W. Johnston, and M. P. Bachynski, *The Particles Kinetics of The Plasmas* (Addison-Wesley, Reading, MA, 1966).

15. E. M. Epperlein, J. Comput. Phys. **112**, 291 (1994).

16. S. Skupsky, Phys. Rev. A **36**, 5701 (1987).

17. T. R. Boehly, D. L. Brown, R. S. Craxton, R. L. Keck, J. P. Knauer, J. H. Kelly, T. J. Kessler, S. A. Kumpan, S. J. Loucks, S. A. Letzring, F. J. Marshall, R. L. McCrory, S. F. B. Morse, W. Seka, J. M. Soures, and C. P. Verdon, Opt. Commun. **133**, 495 (1997).

18. D. D. Meyerhofer, J. A. Delettrez, R. Epstein, V. Yu. Glebov, V. N. Goncharov, R. L. Keck, R. L. McCrory, P. W. McKenty, F. J. Marshall, P. B. Radha, S. P. Regan, S. Roberts, W. Seka, S. Skupsky, V. A. Smalyuk, C. Sorce, C. Stoeckl, J. M. Soures, R. P. J. Town, B. Yaakobi, J. D. Zuegel, J. Frenje, C. K. Li, R. D. Petrasso, D. G. Hicks, F. H. Séguin, K. Fletcher, S. Padalino, M. R. Freeman, N. Izumi, R. Lerche, T. W. Phillips, and T. C. Sangster, Phys. Plasmas **8**, 2251 (2001).

19. R. A. Lerche, D. W. Phillion, and G. L. Tietbohl, Rev. Sci. Instrum. **66**, 933 (1995).

20. R. Betti, V. N. Goncharov, R. L. McCrory, and C. P. Verdon, Phys. Plasmas **5**, 1446 (1998).

Precision Spectral Sculpting of Broadband FM Pulses Amplified in a Narrowband Medium

Solid-state laser systems envisioned for inertial fusion energy (IFE) applications will require both high efficiency and high single-beam, on-target uniformity. High efficiency is achieved by diode pumping, and on-target uniformity is achieved by beam-smoothing techniques. One of the most-promising gain media for these high-efficiency lasers is ytterbium-doped strontium fluorapatite (Yb^{+3}:SFAP).[1] While this material is ideal for efficient diode pumping, its gain bandwidth is relatively narrow. This has implications for the amount of on-target beam smoothing that can be achieved with techniques such as smoothing by spectral dispersion (SSD),[2] which requires bandwidths of the order of 1 THz in the ultraviolet[3] or roughly 0.333 THz (330 GHz) in the infrared part of the system.[4] Since this bandwidth is comparable to the gain bandwidth of Yb^{+3}:SFAP, significant gain narrowing can be expected in the laser system.

Gain narrowing in this case does more than limit the amount of on-target bandwidth available for beam smoothing. The technique of SSD impresses frequency-modulated (FM) bandwidth on the laser and disperses it with gratings in order to smooth speckle on target. Gain narrowing modifies this FM spectrum, leading to amplitude modulation (AM) or FM-to-AM conversion in the temporal profile of the pulse. The AM occurs primarily at the high-peak-power output of the laser system, significantly increasing the risk of laser damage.

In this article, the application of spectral sculpting to FM pulses is presented. Specifically, spectral sculpting is used to precompensate the effects of gain narrowing in narrowband solid-state amplifiers. The technique of spectral sculpting has previously been used to compensate the effects of gain narrowing in ultrafast amplifiers by spectrally shaping the input pulse prior to amplification[5] or by the use of an intra-amplifier spectral filter.[6] In these examples, the primary goal was to increase the width of the amplified output spectrum. For FM pulses, however, any modification to the original spectrum leads to AM; thus the effects of gain narrowing must be *precisely* compensated to ensure that the amplified output spectrum matches exactly the original, unamplified FM spec-trum. We experimentally demonstrate complete gain-narrowing compensation for small-signal, center-line gains of the order of 10^4 and FM bandwidths that are comparable to the linewidth of the amplifying medium.

The concept of spectral sculpting is illustrated in Fig. 90.28. The spectrum of an FM pulse and its corresponding smooth temporal profile are shown in Fig. 90.28(a). As illustrated in Fig. 90.28(b), a spectral mask that attenuates the line-center sidebands, which experience high gain, and wholly transmits the distant low-gain sidebands is applied to the pulse at the input to the laser system. After spectral sculpting, this low-energy input pulse no longer has a purely FM spectrum and is thus heavily amplitude modulated [Fig. 90.28(b)]. As the pulse is amplified through the system, the sculpted spectrum evolves toward a purely FM spectrum. At the output of the
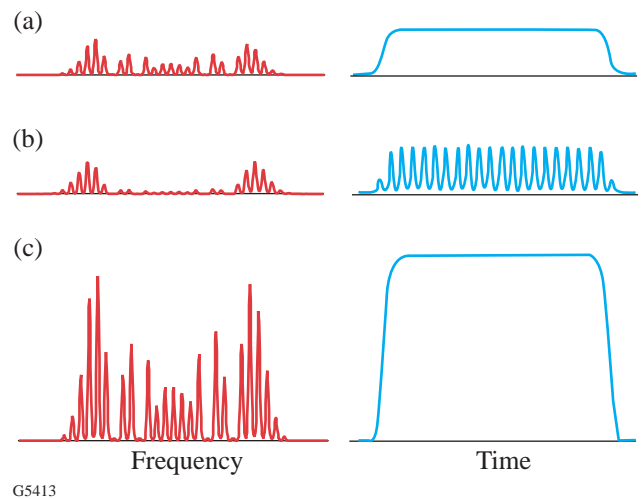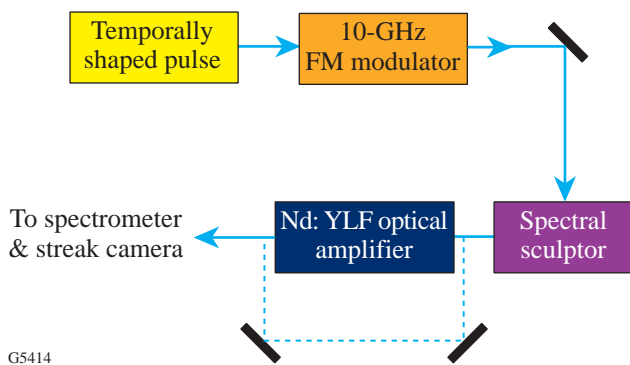

Figure 90.28

(a) Unamplified FM spectrum and associated smooth temporal profile. (b) Sculpted, unamplified FM spectrum. The associated temporal profile shows significant AM. (c) Sculpted, amplified FM spectrum. The amplified output has the original FM spectrum and a smooth temporal profile.

system, precisely where the energy, fluence, and concomitant damage risk are highest, the purely FM spectrum is recovered, with no AM [shown in Fig. 90.28(c)].

A schematic of the experimental setup is shown in Fig. 90.29. The FM bandwidth was generated by double passing a monochromatic, temporally shaped pulse through a $LiNbO_3$ phase modulator.[7] This pulse then entered the spectral sculptor. After sculpting, the pulse was injected into a narrowband, cavity-dumped, multipass Nd:YLF amplifier. Nd:YLF's narrower gain transition serves as a surrogate for the Yb^{+3}:SFAP with a proportional reduction in input bandwidth. The total number of round-trips through the cavity, and thus the overall gain experienced by the pulse, was adjustable. After amplification, the spectral profile of the sculpted, amplified pulse was measured with a custom-built spectrometer with a resolution of ~0.1 Å. To assess the magnitude of post-amplification AM, the temporal profile of these pulses was characterized with an LLE-built streak camera with a 15- to 20-ps temporal resolution.

The design of the spectral sculptor is based on a configuration known as a *zero-dispersion pulse compressor with a pulse-shaping mask*.[8] In this configuration, the sidebands of the FM-modulated incident pulse are first angularly dispersed by a gold-coated diffraction grating. A lens then transforms the angular dispersion of the sidebands into a spatially separated array of individual sidebands located at the back focal (Fourier) plane of the lens. A mask, placed in this plane, performs the actual sculpting. The second half of the sculptor is a mirror image of the first part, producing a spectrally sculpted pulse whose individual FM sidebands are overlapped in space.

The specific layout of a particular Fourier-plane mask dictates the optical design of the sculptor. Many types of both fixed and programmable masks might be used to shape the spectrum of a pulse.[9] The programmable mask used here (from Cambridge Research Inc.) is based on the liquid-crystal-modulator (LCM) light valve developed by Wefers and Nelson.[10] The discrete nature of the FM spectrum is ideally suited to this pixelated light valve, and thus our sculptor was designed so that the spatial separation between each sideband in the Fourier plane matched exactly the LCM pixel separation. For a grating groove density of 1740 grooves/mm, a center wavelength of 1.053 μm, an FM sideband spectral separation of 10.384 GHz, and a LCM pixel separation of 100 μm, the required focal length of the lenses was 775 mm. Since the required focal length was so long, each lens in the sculptor was replaced with a three-lens, telephoto system (designed by D. Weiner), resulting in a 60% reduction in the overall length of the sculptor.

The LCM light valve provides control of both the transmission and relative optical phase of each FM sideband. This is done by applying a computer-controlled voltage to each of two liquid crystal layers in each LCM pixel. The sculpting mask can thus be tailored to compensate a variety of conditions in the amplifier. An algorithm was developed that adjusts the transmission of each LCM pixel until the power spectrum of the amplified, sculpted pulse matches a given, desired reference spectrum.

The reference spectrum, which is the original pure FM spectrum generated by the phase modulator, was measured by sending the output of the sculptor, with the transmission of each LCM pixel set to 100%, directly to the spectrometer (see the dashed line in Fig. 90.29). Once the reference spectrum was taken, the unsculpted pulse was then amplified in the Nd:YLF amplifier and sent into the spectrometer. The power spectrum of the amplified pulse is given by

$$\left|E_{amp}(l)\right|^2 = \left|E_{in}(l)\,g(l)\right|^2, \tag{1}$$

where $\left|E_{in}(l)\right|^2$ is the spectrum of the unamplified, unsculpted pulse (the reference spectrum) and $\left|g(l)\right|^2$ is the gain spectrum of the Nd:YLF amplifier. Given this measurement of the amplified power spectrum, a compensating mask function $M(l)$ was then calculated and sent to the LCM. When the LCM is used only as a transmission mask, this mask function can be expressed as

Temporally shaped pulse → 10-GHz FM modulator

Nd: YLF optical amplifier ← Spectral sculptor

To spectrometer & streak camera

G5414

Figure 90.29
Schematic of the spectral sculpting setup.

$$M(I) = \frac{\left|E_{\text{in}}(I)\right|^2}{\left|E_{\text{amp}}(I)\right|^2} = \frac{1}{\left|g(I)\right|^2}. \tag{2}$$

The now-sculpted pulse was amplified, and the resulting spectrum was again measured and compared to the reference spectrum. This procedure was repeated until the amplified, sculpted spectrum matched the original reference spectrum $\left|E_{\text{in}}(I)\right|^2$. This comparison of spectra was accomplished by calculating the relative difference in energy between corresponding sidebands in the reference and amplified spectra. When the rms average difference among all of the sidebands was less than 4%, the spectra were considered to be equivalent and the sculpting procedure ended.

Figure 90.30(a) shows the measured reference FM spectrum, containing ~29 sidebands with a bandwidth of ~220 GHz. Since the spectral width of the Nd:YLF gain curve is approximately two-thirds the width of that of Yb^{+3}:SFAP, we used an FM bandwidth that was two-thirds of that required for a Yb^{+3}:SFAP-based IFE laser system using SSD for beam smoothing. The pulse temporal profile corresponding to the reference spectrum in Fig. 90.30(a), as measured with the streak camera, is shown in Fig. 90.30(b). Without precompensation, as shown in Fig. 90.30(c), the amplified (gross small-signal, center-line gain ~9100) FM pulse spectrum is significantly narrowed. The temporal profile of this gain-narrowed, amplified FM pulse shows nearly 100% AM [Fig. 90.30(d)]. Due to the fact that gain narrowing leads to a symmetric distortion of the original FM spectrum, the predominant frequency of the AM is ~20 GHz, which is twice the phase-modulation frequency.

Beginning with the unsculpted, amplified spectrum in Fig. 90.30(c), the sculpting algorithm iterated, as described above, until the sculpted, amplified spectrum matched the reference spectrum. For gains of ~10^4, four to five iterations were typically required. The resulting amplified and sculpted spectrum is shown in Fig. 90.30(e). This power spectrum shows that precompensating the effects of gain narrowing produces an amplified spectrum that matches the original unamplified FM power spectrum, thus providing the necessary bandwidth for on-target smoothing. As discussed above, the sculpting technique must also produce amplified pulses with a minimum amount of AM. As can be seen in Fig. 90.30(f), the applied spectral sculpting mask used to generate the spectrum

in Fig. 90.30(e) has significantly reduced the AM at the amplifier output; however, some residual 20-GHz AM remains.

To better understand the source of this residual AM, a model that uses the experimentally measured power spectra to calculate the expected temporal pulse profile was developed. These simulations showed that the relative amplitude errors in the sidebands (which were typically of the order of a few percent) were not sufficient to cause the observed residual AM. It was thus concluded that the sculpting algorithm successfully produced the correct amplified FM power spectrum, and that the residual AM was not caused by errors in the sculpted amplitudes of the individual amplified sidebands.

The simulations described above were then expanded to include the effects of errors in the phase relationship among the sidebands that comprise the amplified FM spectra. Two primary sources of phase error in the experiment were material

G5415

Figure 90.30

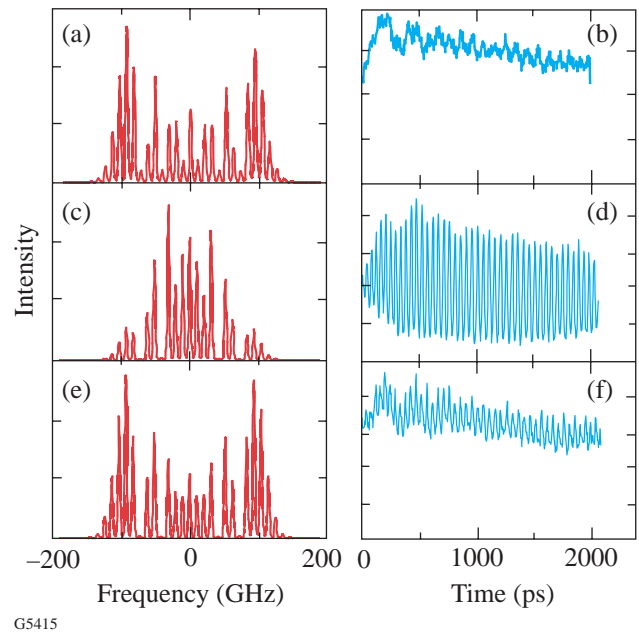(a) Unamplified FM pulse spectrum (reference spectrum); (b) streak camera measurement of the temporal profile of the pulse whose spectrum is shown in (a); (c) gain-narrowed, amplified FM spectrum; (d) temporal profile corresponding to the gain-narrowed spectrum shown in (c); (e) amplified, sculpted FM spectrum; (f) temporal profile corresponding to the amplified, sculpted spectrum shown in (e).

dispersion and imaging errors in the sculptor. These sources primarily produce a spectral phase whose magnitude varies as the square of the frequency difference among the sidebands. Introducing this quadratic spectral phase dependence into our simulations produced FM pulses with amplitude modulation at the fundamental modulation frequency (i.e., 10 GHz). While a small amount of 10-GHz modulation can be observed in our data, the primary residual modulation frequency was 20 GHz.

Another source of spectral phase error in this setup is that associated with the narrowband Nd:YLF gain transition. Assuming that the gain profile of Nd:YLF is Lorentzian in shape, the spectral phase associated with this transition can be expressed as[11]

$$f(w) = \frac{G_{\mathrm{dB}}(w_c)}{8.68} \frac{2(w - w_c)/Dw}{1 + [2(w - w_c)/Dw]^2}, \qquad (3)$$

where $G_{\mathrm{dB}}(w_c)$ is the center-line gain in decibels, w_c is the center frequency of the Nd:YLF transition, and Dw is its spectral FWHM. Simulations showed that the addition of a phase function of this form to an FM spectrum, using parameters that matched our experimental conditions, produced 20-GHz temporal modulation with an amplitude similar to that observed in the data.

Using our LCM sculptor, the amplitude mask used to produce the FM spectrum in Fig. 90.30(e) was combined with a phase mask whose functional form is the inverse of the function described by Eq. (3), with the overall gain, transition center frequency, and transition width being adjustable parameters. These parameters were iterated to minimize the amplitude modulation in the streak camera measurements. The resulting experimental temporal profile is shown in Fig. 90.31. Comparing this figure with Fig. 90.30(f), it is clear that by using phase compensation in addition to amplitude shaping, the residual AM in the amplified temporal pulse can be completely eliminated.

Conclusion

This article has presented what is believed to be the first demonstration of spectral sculpting applied to the amplification of broadband FM pulses in a narrowband gain medium. Because of FM-to-AM conversion, spectral sculpting for these pulses requires both precision amplitude and phase compensation of narrowband gain effects. Spectral sculpting for narrowband, center-line small-signal gains of 10^4 has been
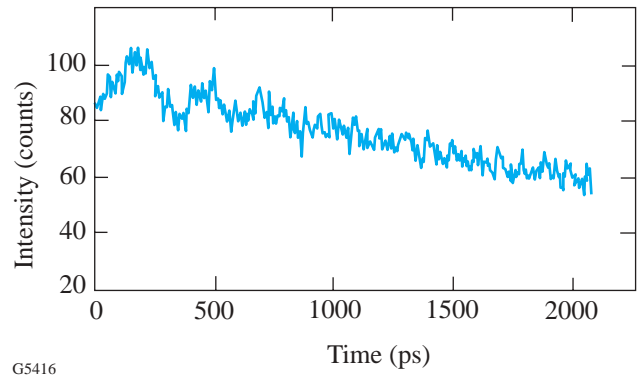
Figure 90.31
Temporal profile of an amplified FM pulse whose spectrum was both phase sculpted and amplitude sculpted.

demonstrated, producing amplified pulses that have both sufficient bandwidth for on-target beam smoothing and temporal profiles with no potentially damaging AM.

REFERENCES

1. C. D. Marshall *et al.*, IEEE J. Quantum Electron. **32**, 650 (1996).

2. S. Skupsky, R. W. Short, T. Kessler, R. S. Craxton, S. Letzring, and J. M. Soures, J. Appl. Phys. **66**, 3456 (1989).

3. J. E. Rothenberg *et al.*, presented at the 1999 Fusion Summer Study Workshop, Snowmass, CO, 12–23 July 1999.

4. D. Eimerl *et al.*, Opt. Lett. **22**, 1208 (1997).

5. F. Verluise *et al.*, Opt. Lett. **25**, 575 (2000).

6. C. P. J. Barty *et al.*, Opt. Lett. **21**, 219 (1996).

7. Laboratory for Laser Energetics LLE Review **78**, 53, NTIS document No. DOE/SF/19460-295 (1999). Copies may be obtained from the National Technical Information Service, Springfield, VA 22161.

8. A. M. Weiner, J. P. Heritage, and E. M. Kirschner, J. Opt. Soc. Am. B **5**, 1563 (1988).

9. A. M. Weiner, Rev. Sci. Instrum. **71**, 1929 (2000).

10. M. M. Wefers and K. A. Nelson, Opt. Lett. **20**, 1047 (1995).

11. A. E. Siegman, *Lasers* (University Science Books, Mill Valley, CA, 1986), p. 283.

Electric-Field-Induced Motion of Polymer Cholesteric Liquid Crystal Flakes in a Moderately Conductive Fluid

Polymer cholesteric liquid crystals (pCLC's) are commonly limited to passive applications as thin films reflecting a specific wavelength and polarization of light due to their inherent selective reflection properties. Some pCLC's in the state above their glass transition temperature can be used for active applications, but due to their high viscosity, switching times are long compared to low-molar-mass liquid crystals with a similar structural composition. New possibilities for pCLC applications emerged in 1994 when Faris proposed fracturing pCLC films with Grandjean texture (the helical axis of the molecular structure is normal to the film surface) into tiny particles called "flakes."[1] Initial research on pCLC flakes, performed by Korenic *et al.*, focused on cyclic polysiloxanes[2] exhibiting selective reflection in the visible. The flaking process was refined, and passive optical effects were studied. By characterizing the selective reflection effect for both films and flakes, Korenic showed that bulk properties were preserved. Colorimetry of pCLC flakes in various drying binders (e.g., glues and adhesives) leads to the development of new paint and pigment concepts for potential applications in both the decorative arts and document security.[3,4] Optimization of the vivid selective reflection effect for passive applications was found to depend on particle concentration, the use of a restricted particle size range (e.g., ~90 to 180 μm), and immersion in a drying binder with comparable refractive index (~1.6).

The use of an electric field to control the motion of particles has been investigated for decades. The prospect of electrophoretic image displays[5] replacing cathode ray tubes was very realistic in the early 1970s until liquid crystal displays took the lead in development. Particle displays remained a novelty until recent advances involving particle encapsulation and the novel concept of a mechanically flexible display that emerged from work with polymer-dispersed liquid crystal technology in the 1980s.[6] An electrophoretic display based on the encapsulation of hundreds of micron-sized charged particles that migrate back and forth inside a 50- to 200-μm capsule is being developed by E-Ink®.[7] A second leading particle display technology, Gyricon®,[8] relies on individually encapsulated bichromal, 25- to 200-μm spheres with oppositely charged hemispheres

that rotate with the application of a suitable electric field. Response times for these technologies, currently ~200 to 300 ms, are judged to be sufficient for applications such as electronic books, commercial advertising signs, or personal data assistants (PDA's). Achieving color with these technologies is complex and requires the addition of color filters or the development of multichromal spheres,[9] respectively. A new concept that involves ~10-μm birefringent polymer nematic liquid crystal spheres[10] may also have applications in particle display technology. These spheres were shown to reorient within 100 to 200 μs in an electric field due to the negative dielectric anisotropy of the polymer nematic material. Crossed polarizers would be necessary to observe optical effects.

Here we report an extension of the pCLC flake technology from entirely passive optical applications to an investigation of motion in an electric field.[11,12] Commercial polycyclosiloxane flakes,[13] typically 6 μm thick, with an arbitrary shape and a selective reflection peak at $\lambda_0 = 520$ nm (green) were sieved and dried[2] to obtain batches with sizes between 20 and 50 μm [Fig. 90.32(a)]. The pCLC flakes were suspended in propylene carbonate (PC) (Aldrich, 99.7% HPLC grade), a host fluid that is transparent, chemically compatible with the pCLC material, of a comparable density, and has a non-negligible conductivity of ~5×10^{-6} siemens/cm (Table 90.IV). Test cells were constructed using pairs of 25 $\times$ 25 $\times$ 3-mm indium tin oxide (ITO)-coated glass substrates.[14] A mixture of 41±3-μm-diam soda lime glass spheres (Duke Scientific Corp.) dispersed in a UV-curing epoxy (Masterbond UV 15-7TK1A) was applied in four corners of one substrate to set the cell gap. Cells were then filled by capillary action and sealed with epoxy (Devcon 5-Min®). Basic observations were made using a polarizing microscope (Leitz Orthoplan). A digital camera (Panasonic Digital 5100) with a timer was used to record flake motion with a time resolution of 100 ms. Data on flake motion occurring on a sub-second timescale was obtained by detecting the light reflected from the rotating flake surface using a photomultiplier tube (PMT) (Hamamatsu R905) coupled to the microscope ocular by means of a fiber optic mounted in a precision fiber coupler (Newport Corp.). The PMT signal was displayed

(a)

(b)

Field off

Glass   ITO   Host fluid   Flake

(c)

Field on

G5408
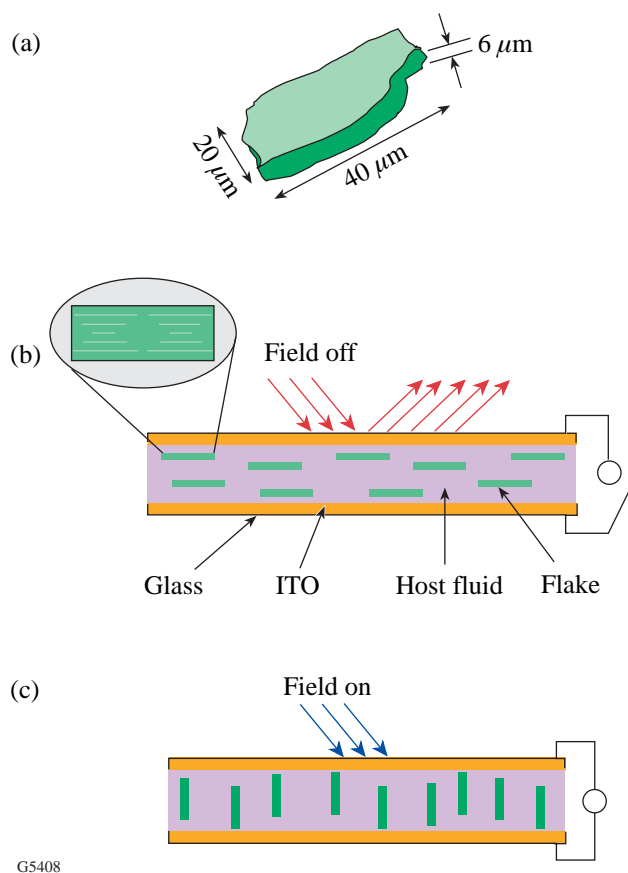
on one channel of an oscilloscope (HP 54520A) and directly compared with the field applied to the cell displayed on the second channel. A function generator (Stanford Research Systems DS345) provided the sinusoidal driving voltage for ac fields. Flake motion was observed as a function of the waveform's magnitude and frequency. Rotational behavior was easily detected under near-normal illumination through a 10× objective (N.A. = 0.2). Brightly reflecting flakes lying in the plane defined by the substrates [Fig. 90.32(b)] darkened substantially after reorienting [Fig. 90.32(c)].

Experiments concentrated on investigating ac sine wave–driven devices. Using the polarizing microscope and the digital camera to track flake motion, we found that pCLC flakes responded to electric fields by rotating approximately

Figure 90.32
Dimensions of a typical irregularly shaped pCLC flake are depicted in (a). Flakes lie approximately parallel to cell substrates when no electric field is applied (b) and appear green due to selective reflection caused by the helical molecular structure of cholesteric liquid crystals, as depicted by the enlarged flake. Flakes reorient with one long axis parallel to the applied field (c). They appear dark since light is no longer reflected off their flat surfaces.

Table 90.IV: Properties of CLC520 flakes and host fluid.

Property at 20°C	Wacker polysiloxanes CLC520	Propylene Carbonate[d]
Index of refraction @ 589 nm	1.573* (Ref. 4)	1.422[c]
Dielectric permittivity @ 1 kHz	~ 3[a]	69[d]
dc conductivity (S/cm)	–	~ 5×10^{-6}
Dynamic viscosity (Pa·s)	Solid	$2.9 \times 10^{-3[c]}$
Density (g/cm³)	~1.1[b]	1.189[c]
All materials were used as received without further processing. *Average index of refraction. [a]Measured with an impedance meter (253 Electro Scientific Instruments) [b]Measured by a water displacement technique [c]Sigma-Aldrich-Fluka Catalog (2000) [d]High Purity Solvent Guide, Baxter Diagnostics Inc., Burdick & Jackson Division (1990)		

90° about one axis, typically the longest one [Fig. 90.32(c)]. Flake motion was seen in electric fields as low as 5 mV$_{rms}$/μm (0.21 V$_{rms}$) within a specific frequency bandwidth defined as the range where the flake response time increased by a factor of 3 from the fastest response detected. In a typical set of data for one flake (shown in Fig. 90.33) the flake's fastest response at 5 mV$_{rms}$/μm required 47 s at 130 Hz. The frequency bandwidth extended from 45 Hz to 500 Hz for this very low magnitude field. As the magnitude of the driving field increased to 30 mV$_{rms}$/μm, the frequency range for motion broadened to extend from approximately 25 Hz to 1000 Hz. This sixfold increase in voltage greatly reduced the reorientation time for the flake to less than 1 s. Many other flakes were seen to behave in a similar manner.

G5409
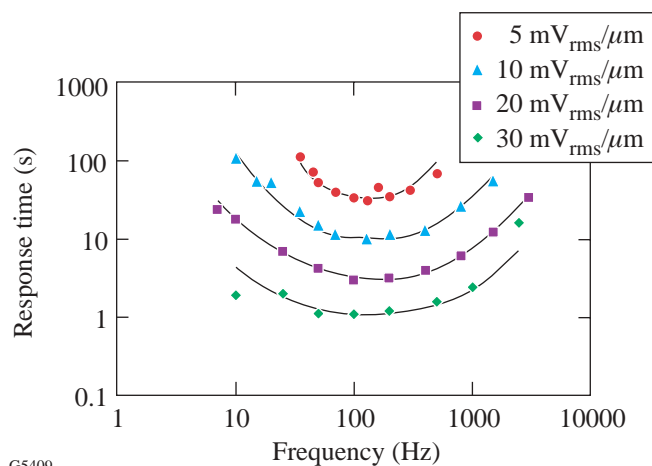
Figure 90.33
The characteristic time response of a representative pCLC flake as a function of frequency at specific electric field values. Lines are drawn to guide the eye. Similar behavior was observed for dozens of flakes.

The reorientation times of flakes in the field of view imaged onto the digital camera (2 mm × 1 mm) were examined as a function of incremental voltage increases of a 50-Hz electric field. Attention was directed to two types of flakes: (1) "small" flakes with the largest dimension of the order of 25 μm (typically square or triangular) and (2) "large" flakes with a 35- to 50-μm dimension that tended to be rectangular. The small flake's response curve in Fig. 90.34 shows an inverse quadratic dependence on the field ($R^2 \approx 0.98$); however, for fields larger than approximately 30 mV$_{rms}$/μm (1.3 V$_{rms}$) the large flakes consistently reoriented more quickly than the small flakes. Inertial terms are small enough to be neglected in this system, so it is possible that at higher voltages these flakes carried a

proportionally larger induced dipole moment due to their size and (typically) rectangular shape, thereby causing these flakes to reorient more quickly than smaller flakes.

G5410
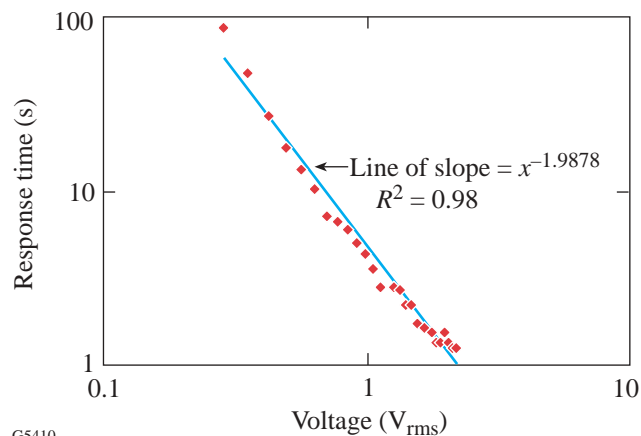
Figure 90.34
The average response time of several flakes has an inverse quadratic dependence on the applied voltage. The standard deviation of 10% is of the order of the size of the data points.

Using the signal from the PMT to detect light reflected from a single typical flake, we found that the actual time necessary for a flake to rotate was less than the reorientation time measured with the digital camera through the microscope eyepiece (Fig. 90.35). In the presence of a 40-mV$_{rms}$/μm (1.7 V$_{rms}$, 100 Hz) field there was a delay time D_t of 420 ms for the flake to initiate movement after the field was first applied. The flake then completed the full reorientation, as determined by its reflectivity shifting from a maximum to a minimum value, with a fall time R_t of 560 ms. The total reorientation time was therefore just under 1 s. (Here we define the reorientation time of a flake as the sum of the D_t and the R_t). We attribute D_t to the time necessary for an insulating pCLC flake to acquire a dipole moment.

The motion of pCLC flakes was not bistable, but this system showed "memory" or hysteresis. Flakes relaxed to their initial position in the plane of the cell several minutes after the driving field was turned off. There was also a gradual, approximately linear increase in response time for suspended flakes in the PC host for over 48 h.

Electrophoresis can be discounted as a possible mechanism because pCLC flakes are not charged initially, but acquire an

G5411
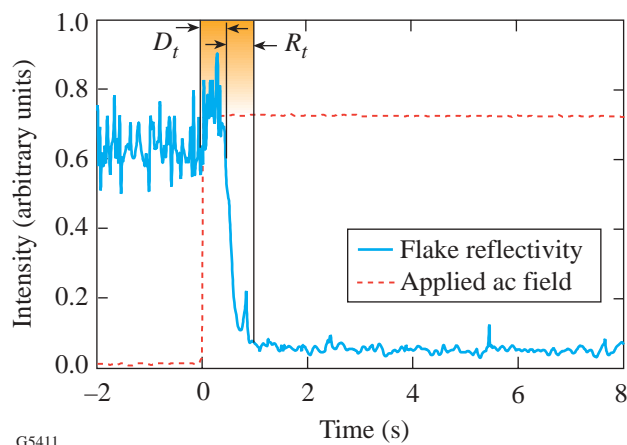
Figure 90.35

Flake motion in a 40-mV$_{rms}$/μm (1.72-V$_{rms}$) field at 100 Hz was studied with a PMT detecting light reflected from the flake surface. Initially, the flake reflected brightly but little light was detected upon reorientation. The resulting contrast ratio, with no attempt to eliminate light from other flakes and sources of scatter, was approximately 15:1.

induced polarization that is presumed to come from migrating charges. Since the electric fields applied to test cells were uniform to within ±3%, dielectrophoresis, which requires an electric field gradient, can also be eliminated as a possible effect contributing to flake motion. The mechanism leading to flake reorientation in host fluids with non-negligible conductivity is most likely the orientational effect described by Jones.[15] This effect is caused by an induced dipole, with a quadratic dependence on the electric field, brought about by the difference in the conductivity and dielectric constant between the flake and the host fluid. The response time for flake motion is determined by solving the equation of motion for the system, which includes the torques due to the induced dipole and the viscous retardation, while the moment of inertia is neglected. Calculations show that the flake response time will have an inverse quadratic dependence on the electric field, as was experimentally observed. A closed-form solution in two dimensions was obtained, and time response calculations corresponded well with the experimental observations in Fig. 90.33. A numerical solution, based on Okagawa's work,[16] was found for flake motion in three dimensions.

Summary

In summary, we have observed the reorientation of pCLC flakes suspended in propylene carbonate, a moderately conductive host fluid. Flakes align with one axis parallel to the electric field. Motion has been observed in applied fields as low as 5 mV$_{rms}$/μm. Reorientation time decreased, while the frequency range for motion increased with the applied voltage. We have observed 90° flake rotation in times R_t as short as hundreds of milliseconds. We envision much faster response times in device geometries where the flake rotation is restricted to a few degrees. The response time, which has a inverse quadratic dependence on the applied field, is also dependent upon flake shape and size as well as various material characteristics. Though flake motion is not bistable, it has a memory effect that needs to be explored further. Controlling flake orientation can lead to both commercial and scientific applications. Display applications with the capability for color are envisioned, as well as optical filters, polarizers, and spatial light modulators.

REFERENCES

1. S. M. Faris, U.S. Patent No. 5,364,557 (15 November 1994).

2. E. M. Korenic, S. D. Jacobs, S. M. Faris, and L. Li, Mol. Cryst. Liq. Cryst. **317**, 197 (1998).

3. R. L. van Renesse, in *Optical Document Security*, edited by R. L. van Renesse (Artech House, Boston, 1994), Chap. 13, pp. 263–280.

4. E. M. Korenic, "Colorimetry of Cholesteric Liquid Crystals (Polysiloxane, Polarizing Paints)," Ph.D. thesis, University of Rochester, 1997.

5. I. Ota, J. Ohnishi, and M. Yoshiyama, Proc. IEEE **61**, 832 (1973).

6. J. L. Fergason, in *1985 SID International Symposium, Digest of Technical Papers*, edited by J. Morreale (Pallisades Inst. Res. Services, New York, 1985), pp. 68–70.

7. B. Comiskey *et al.*, Nature **394**, 253 (1998).

8. N. K. Sheridon *et al.*, J. Soc. Inf. Disp. **7**, 141 (1999).

9. N. K. Sheridon and G. G. Robertson, U.S. Patent No. 5,767,826 (16 June 1998).

10. D. R. Cairns, M. Sibulkin, and G. P. Crawford, Appl. Phys. Lett. **78**, 2643 (2001).

11. L. Li, Reveo, Inc., private communication (1998).

12. K. L. Marshall, T. Z. Kosc, S. D. Jacobs, S. M. Faris, and L. Li, World Patent No. WO 01/88607 A1 (22 November 2001); T. Z. Kosc, K. L. Marshall, S. D. Jacobs, and B. Klehn, presented at the Novel Optical Materials and Applications Meeting, Cetraro, Italy, 20–27 May 2001.

13. Wacker-Chemie, Consortium für Electrochemische Industrie GmbH, Zielstattstrasse 20, D-81379 München, Germany.

14. Thin Film Devices, Inc., Anaheim, CA 92807. The ITO is sputter coated 750 Å thick onto a soda lime float glass substrate with a rms surface roughness of 3 to 4 Å (Zygo NewView™ 5000, 20× Mirau, areal over 250 μm × 350 μm; Zygo Corporation, Middlefield, CT 06455). It has a resistivity of 100 Ω/sq and <88% transmission in the visible.

15. T. B. Jones, *Electromechanics of Particles* (Cambridge University Press, New York, 1995).

16. A. Okagawa, R. G. Cox, and S. G. Mason, J. Colloid Interface Sci. **47**, 536 (1974).

Femtosecond Response of a Freestanding LT-GaAs Photoconductive Switch

The use of semiconductor photoconductive devices to generate picosecond and subpicosecond electrical signals has been the subject of intense research for the last two decades, primarily motivated by the fast-growing demand for ultrafast, integrated optoelectronic photoswitches and photodetectors. Photoconductive devices based on ion-implanted InP,[1,2] ion-implanted silicon-on-sapphire,[3] amorphous silicon, low-temperature-grown GaAs (LT-GaAs),[4–7] as well as metal-semiconductor-metal diodes,[8] have been studied thoroughly. Unfortunately, due to either their nonstandard active material or the need for nanolithography, it is difficult to integrate any of the above devices into advanced optoelectronic systems or high-performance digital electronics circuits (conventional or superconducting) fabricated on Si substrates. The existing semiconductor photoswitches usually require hybrid integration, which drastically reduces their intrinsic multigigahertz bandwidth.

This article reports on a new method of making a freestanding LT-GaAs photoconductive switch that can be placed at virtually any point on any circuit containing a coplanar strip (CPS) transmission structure. Our device is characterized by <0.5-ps response time and ~23-V/W responsivity (typical for Si or GaAs photodetectors) for 810-nm radiation.

The fabricating process of freestanding LT-GaAs photoconductive devices is described in detail elsewhere.[9] Briefly, 1-μm-thick LT-GaAs films were grown by molecular beam epitaxy on semi-insulating GaAs substrates covered with a layer of AlAs, at a temperature range of 200°C to 250°C and at a growth rate of 1 μm/h.[10] The 0.5-μm-thick AlAs etch-stop interlayer was grown first to enable the separation of the LT-GaAs film from the substrate. After the growth, wafers with LT-GaAs layers were annealed *in situ* at 600°C for 10 min under local As overpressure.

The multiple-step process was used to lift and transfer the LT-GaAs layer from the GaAs substrate.[9–11] First, LT-GaAs was covered with a photoresist, and the photoswitch structures, approximately 5 μm wide and 15 μm long, were defined by photolithography. Next, the wafer was placed into the diluted HF solution (HF:H_2O = 1:9) for selective AlAs etching, which led to separation of the LT-GaAs film from the substrate. The separated LT-GaAs switch was then placed gently on a predetermined spot on the Si substrate. Special care was taken to ensure that the contacting surfaces were exceptionally clean so the LT-GaAs would adhere to the Si through molecular bonding. In the final step, the 10-nm/300-nm-thick, Ti/Au CPS lines were fabricated on top of the switch, resulting in the structure shown in the inset in Fig. 90.36. The final two steps could be easily reversed, i.e., in many fabrication runs the Ti/Au CPS lines were fabricated first, and the switch was placed on top of them, again attached by molecular forces.

The femtosecond response of our LT-GaAs photoconductive switches was measured with an electro-optic (EO) sampling system,[12] using a LiTaO$_3$ total-internal-reflection (TIR) probe,[4,13,14] as shown in Fig. 90.36. The TIR configuration allowed us to position the excitation and sampling spots only ~10 μm away, eliminating the signal distortion caused by propagation effects and enabling the measurement of close-to-intrinsic electrical transients. A commercial Ti:sapphire laser with a repetition rate of 82 MHz was used to generate 110-fs-wide, 810-nm-wavelength optical pulses. Both the excitation and sampling beams were focused to ~5-μm spots with a single 10×, long-focal-length microscope objective. The same objective also collected the sampling beam reflected by the TIR probe.[4,13,14]

The time-resolved photoresponse signals of our freestanding LT-GaAs photoconductive switch, dc biased at 30 V and illuminated by the average optical excitation power P_{ex} of 2.7 mW, 3.2 mW, 3.9 mW, and 4.6 mW, respectively, are shown in Fig. 90.37. The transient amplitudes were normalized to demonstrate that although measurements for each P_{ex} were optimized separately, the response was very reproducible, with a 470-fs full-width-at-half-maximum (FWHM) pulse width, a rise time (10% to 90%) of 340 fs, and a fall time (90% to 10%) of 460 fs. Small ripples on top of the ~5-ps-long shoulder after the main peak were also present in each measurement.

Following Ref. 14, we believe that these ripples were caused by electrical signal reflections of the interfaces of our >50-μm-thick LiTaO$_3$ crystal at the bottom of the TIR probe. The latter was confirmed by measuring the transients when the sampling spot was moved ~100 μm. In this case, the measured pulse was broadened to a FWHM of 1.1 ps (due to the CPS dispersion), and post-pulse ripples were shifted in time with the respect of main pulse.

The electrical transient generated by the photoconductive device results from the temporary increase of conductivity due to photogenerated free carriers in the illuminated region of the semiconductor. The signal's intrinsic rise time is limited by how fast the optical energy is delivered, which corresponds to the integral of the laser pulse (in our case, ~120 fs). Our measured, 340-fs rise time is broadened by the EO system time response τ_s, which includes such factors as the finite spot size of the sampling beam, the thickness of the LiTaO$_3$ crystal, and the equivalent lumped-element circuit parameters.[7] The value of τ_s can be estimated as

$$\tau_s = \sqrt{340^2 - 120^2} \approx 320 \text{ fs}.$$

Owing to the existence of a very large concentration of deep-level traps in LT-GaAs, which originated in the fabrication procedure, the signal's fall time is limited by the free-carrier lifetime. Knowing that the measured fall time is 460 fs and taking into account τ_s, we can derive the carrier lifetime as

$$\tau = \sqrt{460^2 - 320^2} \approx 330 \text{ fs}.$$

Z2571

Z2572

Figure 90.36
Schematics of the electro-optic TIR probe placed on top of the Au CPS line fabricated on a Si wafer (the figure is not to scale). The inset shows the micrograph of an actual LT-GaAs freestanding switch and the positions of the excitation and sampling beams.
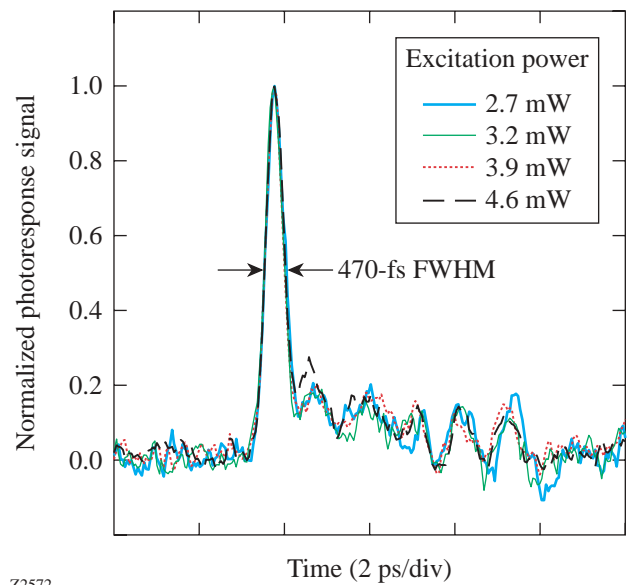
Figure 90.37
A 470-fs FWHM electrical photoresponse of our freestanding LT-GaAs photoconductive switch biased at 30 V and excited by 810-nm radiation, for several values of the optical excitation power. The optical power was measured at the sample plane, including all the optics and the TIR probe.

This latter value fits very well with the literature data on LT-GaAs, measured using the EO systems, e.g., $\tau < 400$ fs reported by Gupta *et al*.[6] We note that the all-optical, pump/probe experiments tend to give much shorter, $\tau \approx 150$ fs, values.[15] We must remember, however, that for all-optical experiments, the probe beam tests dynamics of very hot carriers, at much higher optical frequencies, as compared to the voltage response, measured by the EO sampling.

Figure 90.38 shows the dependence of the photoresponse amplitude on P_{ex} when the bias voltage V_b was set at 30 V. We observe a linear dependence for moderate P_{ex} values with a slope of ~23 V/W, which can be interpreted as the voltage responsivity of our photoconductive device. For $P_{ex} > 4.5$ mW, the signal amplitude saturates. The photoresponse amplitude versus V_b, measured at $P_{ex} = 4.6$ mW, is also linear (inset in Fig. 90.38), with a few volts offset at low biases, apparently, due to nonohmic contacts at the Au/LT–GaAs interface.

The photoswitch behavior presented in Fig. 90.38 is expected. With no light incident on the device, the resistance of the LT-GaAs bar is above 40 MΩ; thus, we can safely assume that the measured signal is entirely due to photogenerated carriers inside our 1-μm-thick sample (optical penetration depth of 810-nm photons is 0.86 μm). The background signal recovered to 0 V after each pulse, which indicated that the underlying Si substrate with its long recombination time was not being excited. With the gradual increase of P_{ex}, more and more electron-hole pairs are generated, increasing conductivity and leading to the proportional increase of the electrical response. Above a certain excitation level, however, all available carriers (for a given photon energy) are excited, so the further increase in P_{ex} does not produce more carriers and the signal reaches saturation. Similarly, for a given P_{ex}, the increase of the switch V_b leads to the linear (due to the Ohm's law) increase of the amplitude of the photocurrent.

To provide more quantitative interpretation and to check if our experimental data are consistent with theoretical predictions, we calculated the amplitude of the photocurrent pulse generated in our experiment as $I_s = V_s/Z_0$, where V_s is the voltage pulse amplitude and $Z_0 = 30$ Ω is the CPS characteristic impedance. For $P_{ex} = 3.9$ mW, the measured V_s is 70 mW, leading to $I_s = 2.33$ mA. Taking into account that the signal FWHM is 470 fs, the total number of carriers involved in the transient photocurrent pulse is $N \approx 7 \times 10^3$. This value can be inserted into the theoretical formula,[7] which returns the number of carriers generated in a semiconductor by a laser pulse and collected by the photoswitch electrodes, to see if the measured data is consistent with reasonable values of the quantum efficiency:

$$N = \eta(1 - R)E_0[1 - \exp(-\alpha d)]\frac{1}{\hbar\omega}\mu\tau\frac{V_b}{l^2}, \qquad (1)$$

where η is the quantum efficiency, R is the reflectivity, E_0 is the laser energy per pulse of $\hbar\omega$ photons impinging on the LT-GaAs layer, α is the optical absorption coefficient at the excitation wavelength, d is the thickness, μ is the mobility of the LT-GaAs layer, and l is the spacing between the CPS electrodes. Substituting into Eq. (1) parameters relevant for our experimental situation, namely, $E_0 = 68$ pJ (corresponding to $P_{ex} = 3.9$ mV), $V_b = 30$ V, $l = 10$ μm, α (810 nm) = 1.16 μm^{-1}, $d = 1$ μm, $\tau = 330$ fs, and estimating $R \approx 0.4$ and $\mu \approx 100$ cm^2/V-s, we finally obtain $\eta \approx 0.1$. We also note that Eq. (1) predicts experimentally observed (Fig. 90.38) linear dependences for both P_{ex} ($P_{ex} \sim E_0$) and V_b. For $P_{ex} = 4.6$ mW, the number of photogenerated carriers corresponds to a total carrier density of ~10^{18} cm^{-3}, which is a reasonable value for LT-GaAs near the saturation (see Fig. 90.38).
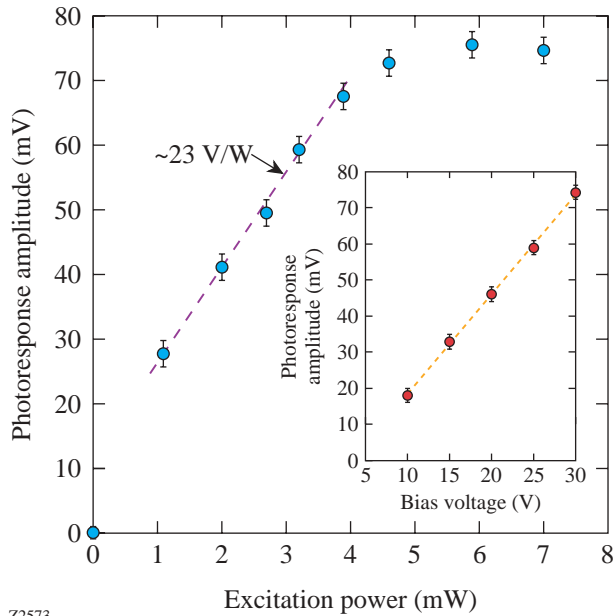
Z2573

Figure 90.38
The amplitude of the photoresponse signal as a function of P_{ex} for the fixed, 30-V switch bias. The inset shows the signal amplitude versus the bias voltage for $P_{ex} = 4.6$ mW.

Conclusion

In conclusion, a freestanding LT-GaAs photoconductive device has been successfully fabricated and demonstrated to have a femtosecond time resolution, voltage responsivity of ~23V/W, and a quantum efficiency of the order of 10%. The time-resolved, 470-fs FWHM of our pulses corresponds to ~640-GHz, 3-dB bandwidth for the photodetector. For moderate P_{ex} and V_b, the photoresponse signal was found to increase linearly, in very good agreement with theoretical predictions. The LT-GaAs excess carrier lifetime was measured to be 330 fs, in agreement with the literature data. The freestanding photoswitch is best suited for hybrid optoelectronic and ultrafast electronic systems since it can be placed at virtually any point on the test circuit.

REFERENCES

1. A. G. Foyt, F. J. Loeonberger, and R. C. Williamson, Appl. Phys. Lett. **40**, 447 (1982).

2. P. M. Downey and B. Schwartz, Appl. Phys. Lett. **44**, 207 (1984).

3. M. B. Ketchen *et al.*, Appl. Phys. Lett. **48**, 751 (1986).

4. U. D. Keil and D. R. Dykaar, Appl. Phys. Lett. **61**, 1504 (1992); D. H. Auston, in *Picosecond Optoelectronic Devices*, edited by C. H. Lee (Academic Press, Orlando, 1984), pp. 73–117.

5. F. W. Smith *et al.*, Appl. Phys. Lett. **54**, 890 (1989).

6. S. Gupta *et al.*, Appl. Phys. Lett. **59**, 3276 (1991).

7. S. Gupta, J. F. Whitaker, and G. A. Mourou, IEEE J. Quantum Electron. **28**, 2464 (1992).

8. M. Y. Liu, S. Y. Chou, T. Y. Hsiang, S. Alexandrou, and R. Sobolewski, J. Vac. Sci. Technol. B **10**, 2932 (1992); C.-C. Wang, S. Alexandrou, D. Jacobs-Perkins, and T. Y. Hsiang, Appl. Phys. Lett. **64**, 3578 (1994).

9. R. Adam, M. Mikulics, M. Siegel, P. Kordos, X. Zheng, Y. Xu, and R. Sobolewski, "Fabrication and Optical Response of LT-GaAs Freestanding Photoconductive Devices," in preparation.

10. P. Kordos *et al.*, Appl. Phys. Lett. **71**, 1118 (1997); P. Kordos *et al.*, Electron. Lett. **34**, 119 (1998).

11. A. Sasaki *et al.*, J. Electrochem. Soc. **146**, 710 (1999).

12. J. A. Valdmanis and G. Mourou, IEEE J. Quantum Electron. **QE-22**, 69 (1986).

13. S. Alexandrou, R. Sobolewski, and T. Y. Hsiang, IEEE J. Quantum Electron. **28**, 2325 (1992).

14. M. Y. Frankel *et al.*, IEEE Microw. Guid. Wave Lett. **1**, 60 (1991).

15. M. Mikulics, M. Marso, R. Adam, A. Fox, D. Buca, A. Förster, P. Kordos, Y. Xu, and R. Sobolewski, in *2001 International Symposium on Electron Devices for Microwave and Optoelectronic Applications* (IEEE, Piscataway, NJ, 2001), pp. 155–159.

Modeling Laser–Plasma Interaction Physics Under Direct-Drive Inertial Confinement Fusion Conditions

Introduction

Laser–plasma interaction (LPI) processes taking place in indirect- and direct-drive targets differ significantly in several ways. Plasma electron densities n_e in hohlraum targets are typically a few percent of the critical density $n_c = m_e \, \omega_0^2 / 4\pi e^2$, so that the main instability mechanisms are stimulated Raman and stimulated Brillouin scattering (SRS and SBS, respectively), which typically have very large predicted linear gains due to the long scale lengths of near-uniform plasma.[1] The theoretical challenge here is to understand the nonlinear saturation mechanisms that are responsible for the small, observed reflectivities. In direct-drive targets the plasma is inhomogeneous, with the linear gain for parametric instabilities often limited by the inhomogeneity of the plasma, rather than by damping of the unstable waves. In direct-drive targets, all electron densities up to critical ($n_c \sim 8 \times 10^{21}$ cm^{-3} for 0.351-μm light) can be accessed by the laser. As a consequence of the dispersion relations of the participating waves, SBS can take place anywhere in the underdense region $n_e < n_c$, and SRS can take place anywhere below the quarter-critical surface $n_e \leq n_c/4$. At the quarter-critical surface SRS is in competition with two-plasmon decay (TPD), a particularly dangerous instability because of its low threshold and its ability to produce hot electrons that preheat the target. Complicated physics is expected at the critical surface itself, including but not limited to resonance absorption, profile modification, instability, and surface rippling.[2] Interactions in the underdense plasma corona are further complicated by the crossing of multiple beams. These beams can interact parametrically via common decay waves, excited simultaneously by several beams, or via electromagnetic seeding involving specular or parametric reflections at or near the critical-density surface. The need to take into account such complications means that simple theoretical models are of rather limited use. One must adopt multidimensional simulation tools that are able to model the necessary physical processes on a large scale in order to have a hope of interpreting current experimental data and making predictions for future experiments.

While modeling LPI in *indirect-drive*-relevant plasmas has received a great deal of attention, and several semipredictive simulation codes have been developed,[3,4–6] the same cannot be said for direct drive. Recently pF3D, a three-dimensional, parallel LPI interaction code developed by LLNL, has been modified at LLE for use in direct-drive conditions. The significant advantage of pF3D[3] over the code *HARMONHY*[4] is its efficient parallelization using message passing, which has been exploited using Hydra, a 64-processor SGI Origin. This article describes recent developments in this regard, and in addition to some background on pF3D and similar codes, shows some of the first results that have modeled long-scale-length OMEGA multibeam experiments.

This article is organized as follows: The next section gives the background behind the modeling of large-scale LPI experiments and includes a discussion of the physical effects that make such simulations especially challenging. The section on **Simulations** gives details specific to the simulation of OMEGA experiments, including the treatment of the expanding plasma, the critical surface, and collisional absorption. It also contains the first pF3D results in direct-drive geometry, including simulations of SBS backscatter for a range of laser intensities. Simulations exhibiting self-smoothing of laser light are also presented. The final section explains the relevance of these simulations not only to present, but also to future OMEGA and National Ignition Facility (NIF) experiments. Further advances expected in the near future are also explored.

The Physics of Large-Scale Modeling

One of the reasons for the complexity of LPI, and indeed plasma physics in general, is the mixing between disparate length scales. In LPI, the plasma response at scales around a fraction of the laser wavelength λ_0 is generally not independent of those taking place at the much larger hydrodynamic scale length of the target, l_h. For NIF-scale targets irradiated by 0.351-μm light, this ratio can be very large:

$l_h/\lambda_0 \sim 10^3$ to 10^4 (an example of this is the onset of large-scale flow due to SBS momentum deposition[7]). In recent years one advance in simulations that has made large-scale simulations possible has been the use of wave-envelope methods[3,4,8] that attempt to surmount these problems.

Another major complication for LPI is the complexity of the plasma response. Typical experimental scales of interest to laser fusion (both direct and indirect drive) are lengths of the order of 1 mm and times of 1 ns. It is quite impossible to model the plasma over these scales using any first principles model, such as particle-in-cell (PIC), Vlasov, or Fokker–Planck. One must necessarily deal with a reduced description, the simplest being the plasma fluid, where the only information retained from the single particle distribution function is its hydrodynamic moments. Although fluid models are the simplest (though still containing a host of nonlinearities), one cannot often neglect linear and nonlinear kinetic effects. Advances have been made in combining both linear wave–particle interaction (Landau damping),[9] electron kinetic effects such as nonlocal electron transport,[4] and nonlinear frequency shifts[10] into fluid codes.

1. Wave-Envelope Methods and the Paraxial Approximation

The basic idea in wave-envelope methods is to take advantage of the fact that it is often possible to write the transverse electric field of the laser as a sum of components that are each well characterized by a given frequency and wave number and also well separated from one another (spectrally). By enveloping around, and hence explicitly removing, the characteristic spatial and temporal frequency of each component, one arrives at equations where only the slow variation of the envelope needs to be followed. This leads to a relaxation of numerical constraints, coarser grids, and larger simulation volumes. An example of this is the paraxial approximation where one needs only to resolve the Rayleigh length and not the wavelength of the light. In the paraxial approximation, the constraint that the envelope function be slowly varying in space restricts the model to describe only light propagating within a range of wave numbers and frequencies not too far from the characteristic frequencies. Experience shows that an angular $\pm 30°$ can be tolerated, but this is often good enough for practical purposes.[11] Complications are that the plasma responds to the ponderomotive force and ohmic heating, which are quadratic in the electric field. Hence there are ponderomotive and thermal sources at the beat frequencies, both spatial and temporal, of all the transverse components. To retain the advantage, the plasma response must likewise be harmonically decomposed around each frequency present, taking into ac-

count nonlinear couplings between each,[7] as is done in both pF3D[3] and *HARMONHY*,[4] i.e., it is through the plasma response that the transverse electromagnetic components are nonlinearly coupled.

To make these general statements more concrete, we will describe how the above procedure applies to SBS (both near-backward and near-forward) in the simulation codes pF3D and *HARMONHY* (although the algorithms differ between the two codes, the general approach is essentially the same in each). Raman scattering can be treated in a similar way, but for simplicity we will consider only Brillouin here. Consider a transverse electromagnetic wave characterized by its amplitude $\tilde{\mathbf{E}}$. The time-enveloped amplitude $\mathbf{E}$ is defined by the equation $\tilde{\mathbf{E}} = \mathbf{E}\exp(-i\omega_0 t) + \text{c.c.}$, and it satisfies the time-enveloped Maxwell equation:

$$\left\{ 2i\partial_t + \frac{c^2}{\omega_0}\nabla^2 + \omega_0\left[1 - \frac{n_e}{N_c}\left(1 - i\,v_{ei}/\omega_0\right)\right]\right\} \mathbf{E} = 0, \quad (1)$$

where $\mathbf{E}$ is assumed to vary on time scales much greater than ω_0^{-1}. We have ignored here the term proportional to $\nabla(\nabla \cdot \mathbf{E})$, but we have retained the damping of electromagnetic waves, usually neglected in underdense plasma, since it is important close to the critical surface in direct-drive plasmas. Motivated by physical arguments, we expect the electric field to contain two spectral features, one corresponding to transverse waves propagating in the general direction of the laser axis and another propagating in the near-backward direction (SBS in the underdense region is expected to be reasonably well collimated in the backward direction as the longitudinal correlation length of the laser is greater than in the transverse direction by a large multiple of the f number). Hence, we write

$$\mathbf{E}(\mathbf{x},t) = \mathbf{E}_+(\mathbf{x},t)\exp\left[i\int_0^z k_0(z')dz'\right]$$

$$+ \mathbf{E}_-(\mathbf{x},t)\exp\left[i\int_z^L k_0(z')dz'\right]. \quad (2)$$

Here the axially dependent wave number $k_0(z)$ must satisfy the linear dispersion relation for transverse waves $k_0(z) = \omega_0/c\sqrt{1 - N_{e,\text{sec}}/N_c}$, and the electron density $N_{e,\text{sec}}$ is defined later in Eqs. (4) and (6). The slowly varying envelopes then satisfy the equations

$$\left(\partial_t + V_g \partial_z + \frac{1}{2}\partial_z V_g + \frac{\nu_{ei}}{2}\right)\mathbf{E}_+ - \frac{ic^2}{2\omega_0}\left(\varepsilon_{\mathrm{par}}\partial_z^2 + \nabla_\perp^2\right)\mathbf{E}_+$$

$$= -i\frac{\omega_0}{2N_c}\left(n_0\mathbf{E}_+ + n_1\mathbf{E}_-\right), \tag{3a}$$

$$\left(\partial_t - V_g \partial_z - \frac{1}{2}\partial_z V_g + \frac{\nu_{ei}}{2}\right)\mathbf{E}_- - \frac{ic^2}{2\omega_0}\left(\varepsilon_{\mathrm{par}}\partial_z^2 + \nabla_\perp^2\right)\mathbf{E}_-$$

$$= -i\frac{\omega_0}{2N_c}\left(n_0\mathbf{E}_- + n_1^*\mathbf{E}_+\right), \tag{3b}$$

where $V_g = c^2 k_0(z)/\omega_0$ is the magnitude of the group velocity of the light and $\nu_{ei} = 4/3\sqrt{2\pi}\,\ln\lambda e^4 Z n_e m_e^{-1/2} T_e^{-3/2}$ is the electron-ion collision frequency, which is responsible for the collisional damping of the electromagnetic waves. The parameter $\varepsilon_{\mathrm{par}}$ has been introduced, and it takes on the values $\varepsilon_{\mathrm{par}} = 0$ or 1, corresponding to the paraxial approximation and the unapproximated wave equation, respectively. Notice that the paraxial approximation assumes that $\partial/\partial z \ll k_0$.

2. Plasma Response

The presence of the high-frequency beat terms between E_+ and E_- in the ponderomotive force,

$$F_{\mathrm{pond}} = \nabla U = e^2/\left(4m_e\omega_0^2\right)\nabla|\mathbf{E}|^2,$$

motivates a decomposition of all the fluid variables in the same fashion as outlined here for the electron density n_e:

$$n_e = N_0 + \left[n_1 \exp i\psi(z) + \mathrm{c.c.}\right]. \tag{4}$$

In this decomposition, n_1 is the (complex) amplitude of the ion-acoustic wave (IAW) driven by the backward SBS process, whose phase $\psi(z)$ is given by

$$\psi(z) = \int_0^z k_0(z')dz' - \int_z^L k_0(z')dz',$$

so that $\partial_z\psi(z) = k_{\mathrm{IAW}}(z)$, where $k_{\mathrm{IAW}} = 2k_0$ denotes the local wave number of the SBS-driven IAW. The amplitude satisfies

$$\left(\frac{d}{dt} + 2ik_0 u_z + \nu_{\mathrm{ia}}\right)^2 n_1 + \left(\omega_a - 2ik_0 C_a^2\frac{\partial}{\partial z} - C_a^2\nabla^2\right)n_1$$

$$= -k_0^2\frac{Zm_e}{m_i}N_0 E_+ E_-^* + S_a, \tag{5}$$

where

$$d/dt = \partial/\partial t + u\cdot\nabla$$

is the convective derivative, $C_a = \sqrt{(ZT_e + 3T_i)/m_i}$ is the IAW sound speed, ν_{ia} is the ion-acoustic damping rate, and S_a is the thermal Cherenkov source of ion waves. (We have changed the notation slightly from Ref. 3.) In Eq. (4), N_0 denotes the slowly varying part of the electron density for which the quasi-neutral limit is correct. For use in Eqs. (3), the slowly varying part N_0 must itself be decomposed into a sum of a secular piece, $N_{e,\mathrm{sec}}$, and a quasi-static, large-scale perturbation n_0,

$$N_0 = N_{e,\mathrm{sec}} + n_0. \tag{6}$$

The secular piece of the background equilibrium electron density is the part that varies over the interaction region, due to hydrodynamic expansion of the target, and whose phase has been taken into account by allowing k_0 to be a function of z in the usual WKB (Wentzel, Kramers, Brillouin) manner. Its value at a particular axial location is equal to the transverse spatial average of N_0. The quasi-static, large-scale perturbation n_0 is related to flow generation caused by momentum transfer, self-focusing/filamentation, and forward-scattering processes.

The slowly varying plasma-hydrodynamic quantities satisfy a nonlinear set of equations,

$$\partial_t\rho + \nabla\cdot\left(\rho\mathbf{u}_i\right) = 0, \tag{7a}$$

$$\partial_t\left(\rho\mathbf{u}_i\right) + \nabla\cdot\left(\rho\mathbf{u}_i\mathbf{u}_i\right)$$

$$= -\nabla\left(P_i + P_e\right) - \left\langle\rho\nabla U\right\rangle_0 - 2\nu_F\rho\mathbf{u}_i, \tag{7b}$$

$$\frac{3}{2}\left[\partial_t P_i + \nabla \cdot \left(\mathbf{u}_i P_i\right)\right] + P_i \cdot \mathbf{u}_i = \nabla_\perp \cdot \left(\kappa_i \nabla_\perp T_i\right) + Q_i, \quad (7c)$$

$$\frac{3}{2}\left[\partial_t \delta T_e + \nabla \cdot \left(\mathbf{u}_i \delta T_e\right)\right] + \delta T_e \nabla \cdot \mathbf{u}_i$$

$$= \nabla_\perp \cdot \left(\kappa_{e,\mathrm{NL}} \nabla_\perp T_e\right) + Q_e. \quad (7d)$$

Here, $\rho = m_i N_0 / Z$ is the ion mass density, Z is the average ion charge, $P_e = N_0 T_e$ and $P_i = \left(\rho/m_i\right) T_i$ are the electron and ion pressures, respectively, Q_e and Q_i are the electron and ion heating rates, κ_i and $\kappa_{e,\mathrm{NL}}$ are the ion and (possibly nonlocal) electron thermal conductivities, and the quantity ν_F denotes the damping operator describing Landau damping and ion–ion collisions (see Ref. 12).

Most efforts have concentrated on hohlraum conditions, where no critical surface is present, but we are now applying pF3D, solving Eqs. (3), (5), and (7) to OMEGA direct-drive experiments.

Simulations of Long-Scale-Length OMEGA Experiments

Experimental OMEGA campaigns have addressed LPI conditions that closely resemble NIF direct-drive ignition targets at the start of the main pulse using single, staggered multiple-beam irradiation of solid, planar CH targets. Full-aperture backscatter stations (FABS) have measured the time-integrated, time-resolved SBS as well as SRS back-scatter energy and spectra. In the present work, we discuss SBS and make comments about TPD only. In general terms, the level of observed SBS backscatter for single-beam, normal incidence increases exponentially with laser intensity up to intensities of about 2×10^{14} W/cm^2, with corresponding reflectivities of ~1%, after which it begins to saturate with reflectivities greater than, or around, 10%. This level can be reduced significantly by the addition of SSD (smoothing by spectral dispersion) bandwidth (0.5 or 1 THz experimentally) and by polarization smoothing (PS), both of which seem to be more efficient at removing the frequency upshifted (blue) part of the backscattered spectrum than the downshifted (red), and leads to reflectivities of a fraction of a percent. Similar behavior is also seen in the case of multiple-beam irradiation.

The SBS spectra (features near $\lambda_0 \sim 351$ nm) consistently show two distinct features. One feature (referred to as the "blue feature") has a shift to shorter wavelengths that increases in time up to a maximum experimentally observed spectral shift of $\delta\lambda = \lambda_0^2 / (2\pi c)\,\delta\omega \sim 1$ nm. This is due to SBS in the underdense plasma corona where the flow velocity due to target expansion is supersonic and $\left|\mathbf{u}_i\right| > C_a$. The other spectral feature is shifted to longer wavelengths (the "red feature") and is seen predominantly in the specular direction, i.e., if the beam is not normally incident and there is no opposing beam that could specularly reflect light into the FABS, then this feature is absent. This feature must arise from interactions very close (tens of microns) to the critical surface and is presumably seeded by specular reflection. The blue component is observed only in the backscatter direction and is seen regardless of the angle between the laser axis and the target normal. The temporal duration of the blue feature also differs between multibeam and single-beam irradiation, but this is likely due to the different hydrodynamics between the two targets. It then seems that the two spectral features have their origins in two well-separated regions in the plasma. Based on the expected hydrodynamic profile, from *SAGE* simulations,[13] the red feature must come from a region separated by only tens of microns from the critical surface, whereas the blue feature comes from a region hundreds of microns out into the corona. The critical region is not currently modeled in a self-consistent manner in pF3D and will not be addressed in detail here. (The actual details on how the critical surface is presently treated will be detailed below.) Work is under way to study this region separately using a full-wave code that does not assume the paraxial approximation and uses the pF3D simulations to provide the necessary boundary conditions.

Detailed understanding of the experiment is necessary for confident predictions and future NIF/OMEGA experiments. Before proceeding with our simulations relevant to the current OMEGA experiments, we will discuss in detail the modeling of both the inhomogeneous plasma profile and the critical surface.

1. Modeling the Hydrodynamic Expansion of the Target

Hydrodynamic evolution of the target during the nanosecond laser pulse is significant, and previous experience with experiments conducted at LULI has shown that this must be modeled accurately for close agreement with experimental data.[14] The predictive value of *SAGE* has been verified over several experimental campaigns, so we have chosen to initialize our plasma hydrodynamics using data provided by *SAGE*. Figure 91.1 shows the initial conditions, taken from *SAGE*, corresponding to the z component of the expansion velocity $\mathbf{u}_i$ and the plasma electron density N_0 for various times relative

to the start of the interaction pulse. This flow velocity gives a spatially dependent Doppler shift to IAW, and its gradient localizes the three-wave SBS interaction, which are all essential features of the experiment.

TC5979
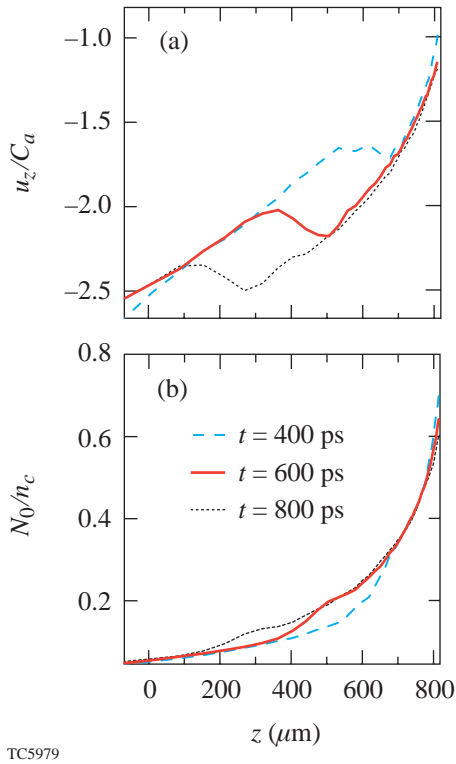
Figure 91.1
The component of the plasma expansion velocity (normalized to C_a for hydrogen at 1 keV) in the direction of the target normal, and electron plasma density as a function of the axial coordinate z. The gradient in the expansion velocity limits the resonance region for backward stimulated Brillouin scattering due to the detuning of the three-wave coupling via a flow-induced Doppler shift in the IAW frequency. The important feature is the plateau that provides a more-favorable region for SBS growth, which moves outward toward the laser and lower electron plasma densities in time. The three curves (dashed, solid, dotted) correspond to the times 400, 600, and 800 ps after the start of the interaction pulse, respectively.

2. Modeling the Critical Surface

To relax the numerical constraints in the electromagnetic part of the problem, we previously used the paraxial approximation by setting $\varepsilon_{\mathrm{par}} = 0$ in Eq. (3). This causes difficulty near the critical surface, however, since the local wave vector $k_0(z)$ there is smaller and vanishes, $k_0(z_t) = 0$, at the turning point $z = z_t$, invalidating our approximation. One approach is to retain the second derivative in Eqs. (3) in a region surrounding the critical surface. We currently adopt a simpler method: Fig. 91.2 shows a typical simulation volume having its z axis

along the target normal and with the plasma density increasing with the axial coordinate due to target expansion. The length of the simulation box is chosen so that $n_e(z = 0) \sim 0.1\, n_c$ and $n_e(L_z) \sim 0.7$–$0.8\, n_c$, which implies a standoff of approximately 10 μm from the end of the simulation volume and the UV critical surface. Appropriate DPP boundary conditions must be provided for E_+ at $z = 0$ (see Fig. 91.3). The boundary conditions for E_- at $z = L_z$ are obtained by treating the end of the simulation volume as a partially reflecting mirror by setting

$$E_-\left(\vec{x}_\perp, L_z\right) = \sqrt{R(t)}\, E_+\left(\vec{x}_\perp, L_z\right),$$

TC5980
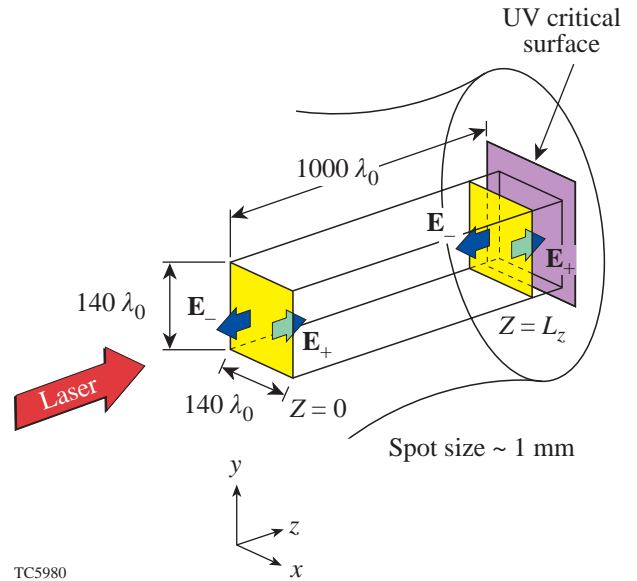
Figure 91.2
The typical geometry used in simulating direct-drive LPI experiments. The solid target is assumed to have its outward normal along the z axis (pointing to the left), with the UV critical surface as indicated. The laser is incident from the left. The simulation volume is smaller than the envelope of the beam as indicated; DPP and SSD are modeled by applying the appropriate boundary condition (i.e., amplitude and phase) for the complex electric-field envelope E_+ at $z = 0$ (see Fig. 91.3). This gives rise to the characteristic speckle pattern in the box as it propagates to the end of the box at $z = L_z$. The region between $z = L_z$ and the UV critical surface is not modeled in pF3D, but the reflection from the critical surface is accounted for by setting $\mathbf{E}_- = \sqrt{R}\mathbf{E}_+$ at $z = L_z$, where R is the reflectivity arising from the stand-off region as calculated from the *SAGE* hydrodynamic profile. The envelope $\mathbf{E}_-$ then propagates backward through the box, exiting at $z = 0$, where the plasma reflectivity can be measured. Typically, the simulation volume is reduced to two dimensions with backward SBS present due to numerical constraints.

TC5970
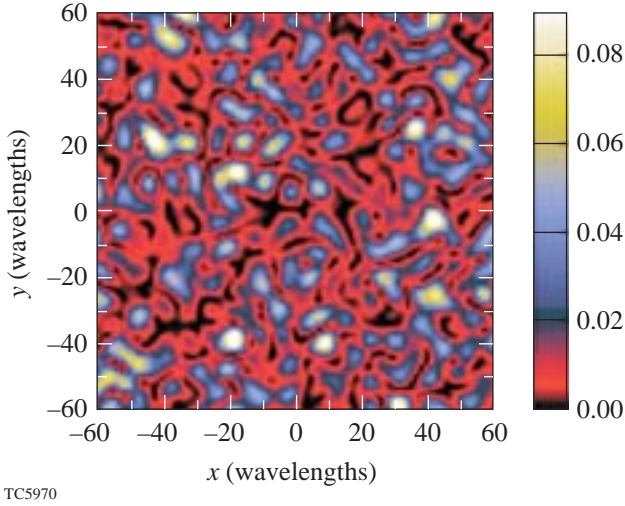
Figure 91.3
An example of the electric-field density, normalized to the average intensity, taken on the entrance plane of the box $z = 0$. This was created assuming the cylindrical top-hat model (in three dimensions)[21] corresponding to an $f/6$ DPP.

TC5982a
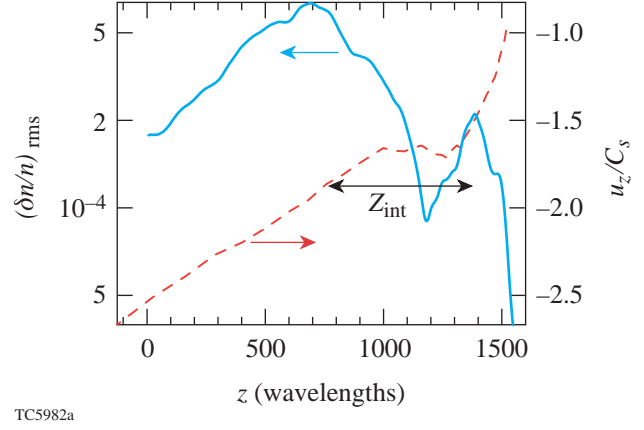
Figure 91.4
IAW amplitudes n_1 [see Eq. (5)] averaged over the transverse extent of the simulation box, and plasma expansion velocity as a function of the axial coordinate z. Notice that there are two regions of significant IAW amplitude, one around the sonic point, where IAW's are resonantly driven by specularly reflected light, and the other corresponding to the shelf in plasma expansion velocity, where backward SBS gain is high.

with the reflectivity coefficient given by

$$ R = \exp\left[2\int_{L_z}^{z_t} \kappa_{ab}(z',t)\,dz' \right], $$

where $\kappa_{ab} = \nu_{ei}/V_g$. Typical values near the peak of the interaction pulse are $R \sim 0.6$. In this way, the electromagnetic (EM) backscatter seed has at least the proper intensity for the corresponding *SAGE* profile (if nonlinear interactions are negligible). The phase is not correct, although this is not expected to be important. Changes to this model will be made as our understanding regarding the nonlinear interactions near critical is improved. Angular and frequency broadening will be modeled if it is found to be important. We will incorporate a full-wave solver near the turning point if necessary.

3. SBS Backscatter Signal in Simulation and Experiment

As in the experiment, simulations show a blue feature in the spectrum of backscattered light due to SBS coming from a flat region of expansion velocity. Indeed, examination of the plasma expansion velocity profile (Figs. 91.1 and 91.4) shows that there is a preferred location for SBS growth, the flat "shelf" of uniform velocity, which has a characteristic size of ~ 200 μm. In all other parts of the profile, the inhomogeneity scale length is short. This shelf is swept further downstream (toward the laser) with time, so that at later times the local

plasma density at the shelf falls rapidly (see Fig. 91.1). Based on an estimate of the expected SBS intensity gain in the shelf region, we may also be able to explain simply the early "quenching" of the SBS signal seen in the multibeam experiments.[15] Assuming the strong damping limit, and a uniform expansion velocity, the convective intensity gain in practical units is given by $I_{SBS} = I_{seed} \exp(G)$, with $G = z_{int}/L_G$, and

$$ L_G^{-1} = 0.045 \frac{1}{\nu_i} \frac{\omega_0}{c} \frac{n_e/n_c}{\sqrt{1-n_e/n_c}} I_{15}\lambda_{\mu m} \frac{1}{T_{keV}}. \tag{8} $$

Taking z_{int} to be ~ 200 μm (as Fig. 91.1 shows to be the length of the shelf), $\nu_{ia}/2k_0C_a = 0.1$, $I_{15} = 0.4$, $\lambda_{\mu m} = 0.351$, and $T_{keV} = 2.2$, we arrive at a gain G that as a function of the plasma density, $G \sim 100(n_e/n_c)/\sqrt{1-n_e/n_c}$, drops from a value of $G = 30$ to 10 as the plasma density drops from $n_e/n_c = 0.25$ to 0.1. This factor-of-3 reduction in the gain as the shelf moves to lower density (Fig. 91.1) explains why the SBS signal drops when the laser intensity is at its peak. This gain will be achieved after a time, τ_{SBS} given approximately by $\tau_{SBS} \sim G/\nu_{ia}(2k_0) < 30$ ps. Figure 91.5 shows actual power reflectivities, taken from recent pF3D simulations, at various times in the pulse (to gain a picture of the interaction over the whole laser pulse, some approximations have been made[16]).
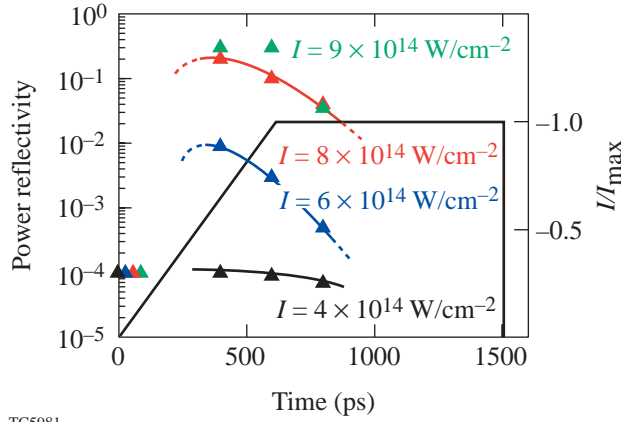
TC5981

Figure 91.5
Laser power reflectivity, as a function of time, taken from simulations corresponding to a range of maximum average laser intensities between $I = 4 \times 10^{14}$ W/cm^2 and $I = 9 \times 10^{14}$ W/cm^2. The laser pulse was turned on at $t = 0$ and then ramped linearly to maximum intensity in 500 ps after which it was held fixed for an additional 1 ns, as in typical OMEGA experiments. Notice that the reflectivity peaks early in the pulse.

Currently we are investigating the more complicated, and less easily predicted, effects of EM seeding from the critical surface and the effects of multiple-beam irradiation and quantifying the ability of SSD bandwidth to suppress SBS.

a. EM seeding of backward SBS. The EM seeding of Brillouin backscatter in the strongly underdense region is affected by the plasma inhomogeneity. Each frequency component of the backscattered light can be resonant with ion waves only in a spatially narrow region such that the frequency-matching conditions are satisfied locally and $\omega_0 - \omega_1 = \omega_{IAW}[1 - M_\parallel(z)]$, where ω_1 is the frequency of the backscattered radiation and $\omega_{IAW} = |\mathbf{k}_{IAW}| C_a$ is the IAW frequency for a sound wave with wave number $\mathbf{k}_{IAW}$. The spatial extent of this resonance region is determined by the width of the ion-acoustic resonance $\sim v_{ia}^{-1}$ and the scale length of the flow Mach number $\mathbf{M}$. The wave-number-matching conditions $\mathbf{k}_0 = \mathbf{k}_1 + \mathbf{k}_{IAW}$ are determined by the scattering geometry only since the magnitude of the wave vector of scattered light is essentially unchanged, $|\mathbf{k}_1| \approx |\mathbf{k}_0| = \omega_0/c\sqrt{1 - n_e/n_c}$, because the shift by the ion-acoustic frequency $\omega_0 - \omega_1$ is very small compared to ω_0.

It has been suggested that the sonic point is of special importance because light specularly reflected by the critical surface with little or no spectral shift[17] will be resonant with the IAW at this point and may drive them to large amplitude.

This effect is evident in Fig. 91.4. The resonance may be less important, however, if the reflected light is not monochromatic and is spread in angle and frequency due to nonlinear interactions near the critical surface. In addition, experimental evidence indicates that the absorption is much greater than predicted by Eq. (10), and the backscattering seed at the sonic point may be substantially less than is shown in Fig. 91.4. We would not expect specularly reflected light to provide an efficient seed for SBS occurring in the supersonic region due to the large frequency mismatch.

In summary, the parametric reflections from other beams (in multibeam geometries) are expected to be more important than specular reflection for seeding the blue part of the scattered light spectrum, and there is much experimental evidence for synergy between the beams, while interactions near the sonic point are influenced by both specular and parametric reflections in both single and multibeam geometries. The region near the critical surface associated with the red feature in the spectrum of reflected light is the most complicated and best investigated with a code capable of solving the full wave equation.

b. Anomalous absorption. In the absence of parametric reflections, at low intensity, one would expect the laser absorption η to be due to classical inverse Bremsstrahlung only. Integrating the equations for laser intensity [obtained from Eq. (3)],

$$\frac{\partial}{\partial z}\left(V_g |E_\pm|^2\right) = \mp \frac{v_{ei}}{V_g}\left(V_g |E_\pm|^2\right), \qquad (9)$$

over *SAGE* density and temperature profiles, one obtains the reflectivity $R = 1 - \eta$, where

$$R = \exp\left[-2\int_0^{z_t} \kappa_{ab}(z')\,dz'\right], \qquad (10)$$

$\kappa_{ab} = v_{ei}/V_g$ is a function that depends on the density and temperature, and z_t is the turning point for the transverse waves, defined by $1 - n_e(z_t)/n_c - \sin^2(\theta) = 0$. For a *SAGE* profile at $t = 400$ ps, the above formula predicts $R = 0.025$ (for $\theta = 0°$). This lower bound on the reflectivity is larger than the experimentally observed reflectivity by approximately two orders of magnitude.

Possible explanations for this serious discrepancy include inaccuracies in the *SAGE* profiles near the critical surface, where most of the absorption occurs, and where it is especially sensitive to temperature through the electron-ion collision frequency,

$$\nu_{ei} \sim 8.16 \frac{\ln\Lambda}{10} Z_{\text{eff}} \frac{n_e}{n_c} \left(\frac{0.351}{\lambda_{0,\mu m}} \right)^2 T_{e,\text{keV}}^{-3/2} \text{ ps}^{-1}, \quad (11)$$

a factor that appears in the exponent of the equation for the reflectivity, Eq. (10). Other possible explanations are the geometric effect of diffuse scattering through a rough critical surface (although a scattering into 2π radians would be required, and this can be ruled out experimentally) and increased collisionality brought about by ion turbulence. A close investigation of the backscatter spectrum, together with pF3D simulations, might be the best route to resolving this outstanding problem and offers the possibility of providing a diagnostic for laser absorption.

4. Self-Focusing Instability and Self-Smoothing

Another area where pF3D simulations are expected to provide insight is the investigation of so-called plasma-induced self-smoothing of laser light. This is a mechanism in which the spatial and temporal correlation length of the laser can be dramatically reduced, as a result of nonlinear plasma response related to the self-focusing (SF) instability and forward SBS. Although this is presently a very active area of research, with strong experimental evidence showing its importance to backward SBS in underdense plasmas,[18–20] effects likely of importance to direct drive such as laser imprint and saturation of TPD have not been investigated either experimentally or theoretically (including through simulation).

The onset of self-smoothing is related to the SF instability and has a threshold which, in practical units, is given by

$$p \sim 0.39 \frac{I_{15} \lambda_{\mu m}^2}{T_{e,\text{keV}}} f_\#^2 \left(\frac{n_e}{n_c} \right) > 1, \quad (12)$$

where the factor of order unity (0.39 here) comes from assuming a cylindrical top-hat DPP (distributed phase plate) spectrum in 3-D.[21] For relevant parameters, it is seen that SF might become important at higher intensities, nearing 1×10^{15} W/cm². This is demonstrated in Fig. 91.6, which shows

a longitudinal slice of the electric-field intensity of a DPP beam. Notice the reduction in the size of the laser speckle pattern, which is also associated with a reduction in the laser coherence time.

The increased incoherence of the laser beam can disrupt and reduce the level of coherent parametric instabilities, which is beneficial for inertial confinement fusion (ICF). Regarding SBS, the shelf in the expansion velocity makes the OMEGA experiments quite different from previous investigations of SBS in inhomogeneous plasmas, where there was no preferential region for growth. Competition between self-smoothing and SBS can be revealed by the spatial location of SBS ion waves, as reported for LULI experiments using a Thomson-scattering diagnostic.[18] A close examination of

Cross section of electric-field intensity

TC5983
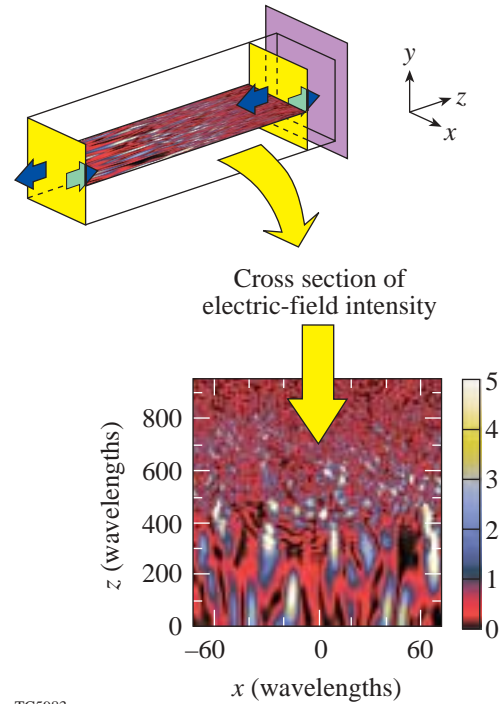
Figure 91.6

At laser intensities nearing $I = 1 \times 10^{15}$ W/cm², the threshold for the self-focusing instability [Eq. (12)] is exceeded in the intense laser speckles. This leads to a reduction in the transverse correlation length of the laser light and frequency broadening. This effect, which has become known as plasma self-induced smoothing, could have an impact on parametric processes such as the two-plasmon-decay instability. This figure illustrates this by showing a longitudinal cross section of the laser intensity (in real space), normalized to the average intensity. The light propagates along the z axis, from bottom to top in the figure. The quarter-critical surface is just beyond the region where the self-smoothing has set in. This could have a saturating effect on the two-plasmon-decay instability.

the SBS signal at high laser intensity may then give valuable information on self-smoothing. This is of broad significance because the incoherence generated by filament instability that is responsible for self-smoothing will affect all resonant parametric processes.

Self-smoothing could have important consequences for the TPD instability since the observed behavior of TPD electrons seems to suggest saturation near 10^{15} W/cm^2, which is similar to the threshold of SF. The TPD instability, as inferred from fast electrons, is also dependent on SSD bandwidth. This dependence seems consistent with a reduction of filamentation at higher SSD bandwidth. The addition of SSD bandwidth is assumed to suppress SF/filamentaion,[22,23] but this has not been studied in the present context.

Discussion

We began by discussing the importance of large-scale simulations in the interpretation and understanding of LPI in ICF fusion experiments and the differences between the indirect- and direct-drive approaches. We also outlined the difficulties and challenges that these types of simulations present and indicated that LPI in direct-drive plasmas has received comparatively little attention. We have set out to remedy this situation and have, in collaboration with LLNL, begun to modify the interaction code pF3D for use in modeling direct-drive plasmas.

The first pF3D results of backward SBS scattering using a realistic inhomogeneous plasma profile, as predicted by the code *SAGE* for recent LPI interaction experiments, have been presented. These simulation results have been used to interpret the experimental backscatter data and have reproduced the behavior of the blue spectral feature observed. Future work will carefully examine the effect of SSD bandwidth and polarization smoothing.

The narrow region near critical is currently treated in a rather simple way. This region is being studied with a separate code for solving the full wave equation. These two codes could be integrated in the future if necessary.

A large discrepancy was found in the level of absorption due to inverse bremsstrahlung between that calculated from *SAGE* and the value obtained experimentally. The level of ion-acoustic fluctuations near the sonic point is dependent on the plasma reflectivity and may potentially be used as a diagnostic for absorption. The pF3D code may be used in conjunction with experiments to resolve this problem.

Finally, it was demonstrated that self-smoothing will become important at higher laser intensities, which will impact all parametric processes including SBS, SRS, and TPD. It will also modify the laser imprint. Due to the potential importance of all these processes, the newly modified pF3D will be used to address these issues in the very near future.

REFERENCES

1. J. D. Lindl, Phys. Plasmas **2**, 3933 (1995).

2. E. J. Valeo and K. G. Estabrook, Phys. Rev. Lett. **34**, 1008 (1975).

3. R. L. Berger *et al.*, Phys. Plasmas **5**, 4337 (1998).

4. J. Myatt, D. Pesme, S. Huller, A. Maximov, W. Rozmus, and C. E. Capjack, Phys. Rev. Lett. **87**, 255003 (2001).

5. V. V. Eliseev *et al.*, Phys. Plasmas **3**, 3754 (1996).

6. S. Huller, Ph. Mounaix, and V. T. Tikhonchuk, Phys. Plasmas **5**, 2706 (1998).

7. D. Pesme, presented at the LLNL Workshop on Saturation of Simulated Raman and Brillouin Instabilities, Livermore, CA, 3–5 April 2002.

8. H. A. Rose, Phys. Plasmas **4**, 437 (1997).

9. H. A. Rose, Phys. Plasmas **3**, 1709 (1996).

10. L. Divol *et al.*, Bull. Am. Phys. Soc. **46**, 293 (2001).

11. A. Maximov, Laboratory for Laser Energetics, private communication (2001).

12. H. A. Rose, Phys. Plasmas **3**, 1709 (1996).

13. R. S. Craxton and R. L. McCrory, J. Appl. Phys. **56**, 108 (1984).

14. V. T. Tikhonchuk, J. Fuchs, C. Labaune, S. Depierreaux, S. Huller, J. Myatt, and H. A. Baldis, Phys. Plasmas **8**, 1636 (2001).

15. Laboratory for Laser Energetics LLE Review **87**, 128, NTIS document No. DOE/SF/19460-397 (2001). Copies may be obtained from the National Technical Information Service, Springfield, VA 22161.

16. We have adopted the following methodology that assumes that there are no correlations that live longer than several tens of picoseconds. To put this in perspective, the damping time of an ion wave with wave number given by $2\omega_0/c$ is approximately 1 ps, and only ten times larger for forward SBS at 5°. The time for SBS to reach its asymptotic state, τ_{SBS} can be crudely approximated as $\tau_{SBS} \sim G/v_{ia}(2k_0)$, which is less than 10 ps. At the chosen starting time the

hydrodynamic profile is initialized with *SAGE* and the laser turned over a few picoseconds to the appropriate intensity. When an asymptotic state is reached, the SBS is expected to be representative of that occurring.

17. The linear phase modulation due the motion of the critical surface imparts a negligible frequency shift.

18. C. Labaune, presented at the LLNL Workshop on Saturation of Simulated Raman and Brillouin Instabilities, Livermore, CA.

19. A. J. Schmitt and B. B. Afeyan, Phys. Plasmas **5**, 503 (1998).

20. A. V. Maximov *et al.*, Phys. Plasmas **8**, 1319 (2001).

21. H. A. Rose, Phys. Plasmas **2**, 2216 (1995).

22. R. L. Berger *et al.*, Phys. Rev. Lett. **75**, 1078 (1995).

23. R. L. Berger *et al.*, Phys. Plasmas **6**, 1043 (1999).

Highly Stable, Diode-Pumped, Cavity-Dumped Nd:YLF Regenerative Amplifier for the OMEGA Laser Fusion Facility

Introduction

The OMEGA facility is LLE's 60-beam, 30-kJ (UV) laser system for performing inertial confinement fusion (ICF) experiments. One of the main features of the OMEGA laser is a flexible optical pulse–shaping system[1] that produces 0.1- to 5-ns, complex-shaped, low-energy pulses that must be amplified to ~1-mJ level before being injected into power amplifiers. Regenerative amplifiers (regens) are well suited for this application, which requires high energy stability and output-beam quality, including low (<1%) beam ellipticity.

High output-pulse-energy stability was achieved on OMEGA with a negative-feedback system in a flashlamp-pumped regen.[2] This system establishes a stable prelase before the energy in the cavity starts to build up; however, this feedback system can cause dramatic pulse-shape distortion,[3] which is difficult to compensate for. A sophisticated negative-feedback system that does not distort the input-pulse shape was developed for the flashlamp-pumped OMEGA regen.[4,5] The only pulse-shape distortion in this regen results from gain saturation in the regen's active element.

This article presents the design and test results of a new highly stable, diode-pumped, cavity-dumped, compact Nd:YLF regenerative amplifier that does not use a negative-feedback system and thus has reduced system complexity.

Regenerative Amplifier Concept

The regenerative amplifier is the key component of the OMEGA laser driver line. The following tight requirements on regen stability and beam quality must be met:

- output-pulse energy > 0.2 mJ,
- high long-term energy stability (<1% rms fluctuation),
- high temporal pulse shape stability (<1% rms deviation),
- high beam quality (TEM$_{00}$; ellipticity <1%),
- wavelength tunability to match gain peak to seed-pulse wavelength, and
- OMEGA operational availability >90% with reliability and compactness.

Two major factors affect regen output-pulse-energy stability: gain fluctuations and injected-pulse-energy fluctuations.

Gain fluctuations change the energy and timing of the intracavity peak pulse; hence, they dramatically affect the regen's output-pulse energy when cavity dumping occurs at a given time. Diode pumping, due to its high stability, makes gain fluctuations negligible, contributing to output-pulse-energy stability. Stable gain also provides high temporal pulse-shape stability because the distortion caused by gain saturation is constant. The end-pump geometry of diode pumping significantly improves beam quality.

Injected-pulse-energy fluctuations primarily change the intracavity peak pulse timing, which causes output-pulse-energy variations when the regen is cavity dumped at a fixed time. In our case, the injected pulse energy changes because of (1) fluctuations in the pulse-shaping system and (2) different input-pulse shapes that present significantly different input-pulse energies. Earlier studies[6,7] have shown that output-pulse-energy fluctuations due to injected-pulse-energy fluctuations are minimized when the gain-over-loss ratio is high. We have developed a fast and simple regen simulation model that corresponds very well to our experimental results. The rate-equation regen model described in Ref. 6 has been simplified by treating the regen's active element as a thin gain layer. The input pulse is sliced in time. Gain and level populations in the active element are recalculated after each slice propagation using recurrence relations for fluence, gain coefficient, and gain-recovery coefficient. According to our calculations, the energy of the regen intracavity peak pulse depends weakly on the injected pulse energy for a broad range of injected energies, which is in agreement with results obtained in Ref. 7. Also, our calculations show that the peak of the intracavity energy dynamics is relatively flat and the peak pulse energy for different injected energies stays constant for several round-trips. These considerations make the concept of building a highly stable regen without a negative-feedback system viable.

Regenerative Amplifier Design

A cavity-dumped Nd:YLF regen with a 220-cm-long linear cavity has been developed to accommodate shaped pulses of up to 7-ns duration. The regen layout is shown in Fig. 91.7.

The choice of Nd:YLF as an active medium is required to match the gain peak of the Nd:phosphate-glass OMEGA amplifiers. The regen cavity is semiconfocal, formed by high-reflective mirrors—one flat and the other with a 4-m radius of curvature. An $8 \times 8 \times 20$-mm Nd:YLF active element was placed near the middle of the cavity to avoid pulse-overlap effects during long-pulse amplification. The regen gain center wavelength can be tuned to the injected-pulse wavelength by adjusting the temperature of an active element placed on the Peltier element.

Two 25-W, fiber-coupled diode arrays operating at 805 nm were used for regen pumping. The regen was pumped at a 5-Hz repetition rate, although a higher repetition rate should be possible. An 800-μs pump-pulse duration was found to be optimal. The 0.6-mm pump fiber core was re-imaged into a 0.9-mm spot in the center of the active element. The cavity mode diameter inside the active element was calculated to be ~1 mm, so the pumped volume diameter was smaller than the

mode diameter, allowing it to serve as an intracavity gain aperture. An additional intracavity aperture was installed for tighter beam-quality control.

Regen reliability is provided by a simple cavity design: a no-feedback-system, cavity-dumped linear resonator. A small, 15-in. $\times$ 38-in. regen footprint is provided by folding the cavity. A high gain/loss ratio in the cavity-dumping regime provides output-pulse-energy stability, while a thermostabilized solid-aluminum block design contributes to the overall regen parameter stability (Fig. 91.8).

Experimental Results

To test the regen performance, square optical pulses of various durations and energies produced by our pulse-shaping system[1] were used. First of all, we wanted to demonstrate that our regen simulation model adequately describes regen dynamics. We calculated and measured intracavity regen dynamics [Fig. 91.9(a)] and square-pulse distortion of the regen peak pulse [Fig. 91.9(b)] when a 4-ns FWHM, ~170-pJ square pulse was injected. It is evident that our regen model agrees well with experimental results. (In practice, energies of ~10 to 100 pJ are used.)
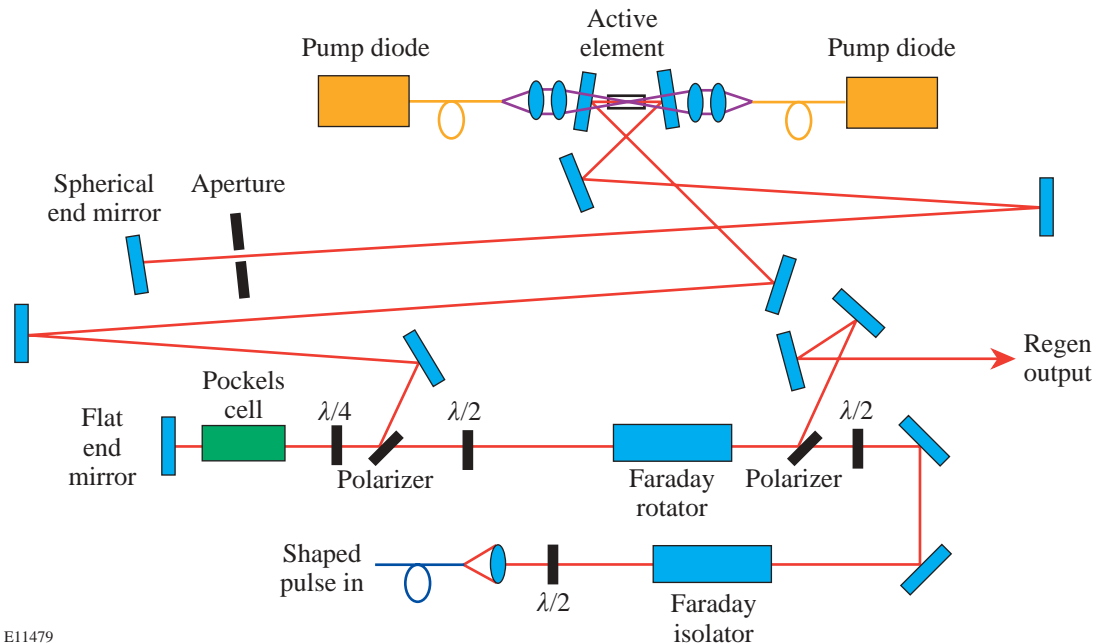
E11479

Figure 91.7
Layout of the diode-pumped, cavity-dumped Nd:YLF regen, which is able to amplify shaped pulses of up to 7-ns duration.
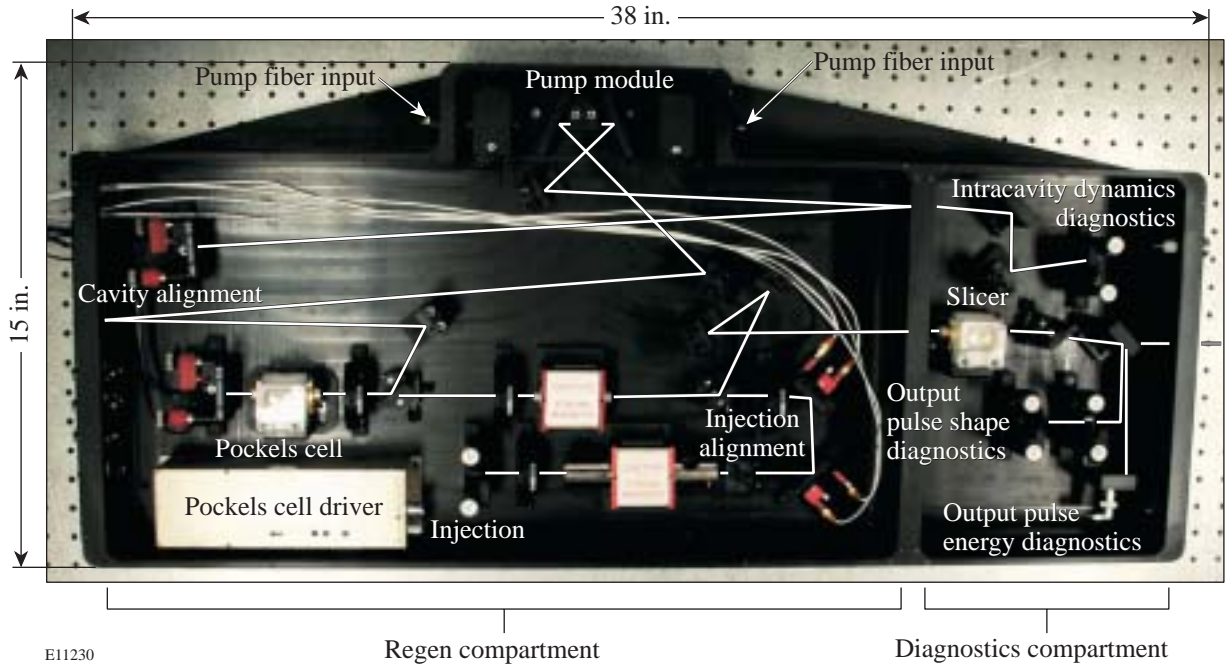
Figure 91.8
OMEGA diode-pumped regen design. Regen enclosure is made of a solid-aluminum block and includes regen and diagnostics compartments. The regen footprint is 15 in. × 38 in., including an optical diagnostics compartment.
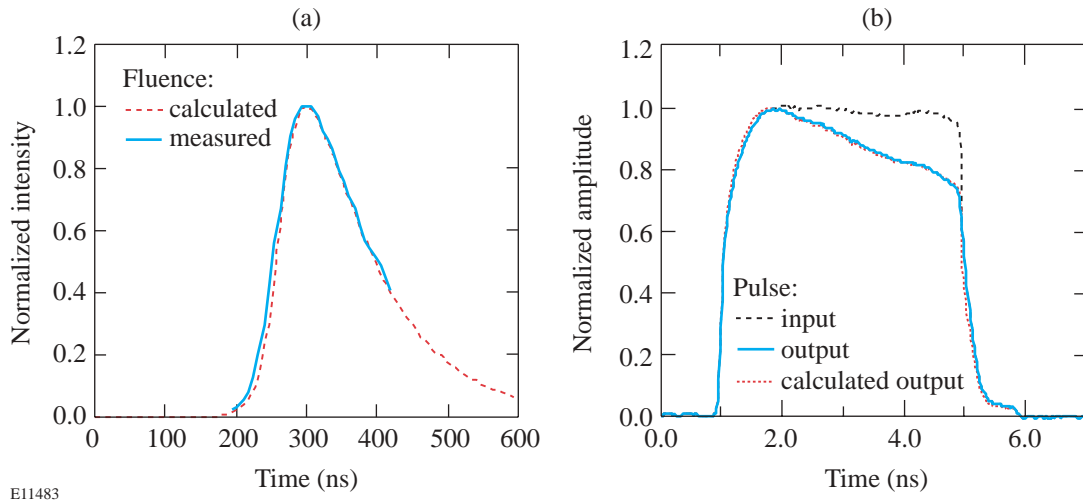
Figure 91.9
(a) Regen intracavity dynamics and (b) peak square-pulse distortion calculated and measured for a 4-ns injected square pulse.

To demonstrate regen insensitivity to an injected-pulse energy, we changed the injected square pulse width (energy) and measured the cavity-dumped output-pulse energy [Fig. 91.10(a)]. The output energy stays within a 1% range when injected energy changes by 600%. A decrease in the gain/loss ratio makes the regen more sensitive to injected energy variations [Fig. 91.10(b)].

We were able to inject pulses with energy as low as several picojoules, which yielded an ~10^9 regen overall gain. Regen energy stability was excellent: <0.9% rms fluctuations over a 24-h period [Fig. 91.11(a)]. It is worth noting that output-pulse-energy stability is higher at lower output energies [Fig. 91.11(b)].

We also measured the long-term stability of the output temporal pulse shape (Fig. 91.12). Temporal-pulse-shape variations did not exceed 1% rms over 5 h of operation. Temporal-pulse-shape stability is an extremely important driver-line parameter for OMEGA operations.

The regen beam profile was measured with an IR scientific-grade CCD camera with more than 1000:1 dynamic range and corresponded to a TEM_{00} mode. The beam ellipticity over the beam above the 0.001 level was computed using a second-moment calculation method was 1.5% with no intracavity aperture and <1% with the intracavity aperture that supported the TEM_{00} mode.

Conclusion

A highly stable, diode-pumped Nd:YLF regen for use in the OMEGA front-end laser system has been developed. This regen produces shaped optical pulses of up to 7-ns duration with low, <0.9% rms energy fluctuations for further amplification on OMEGA. Excellent temporal-pulse-shape stability and beam quality are the main advantages in comparison to previous designs.

ACKNOWLEDGMENT
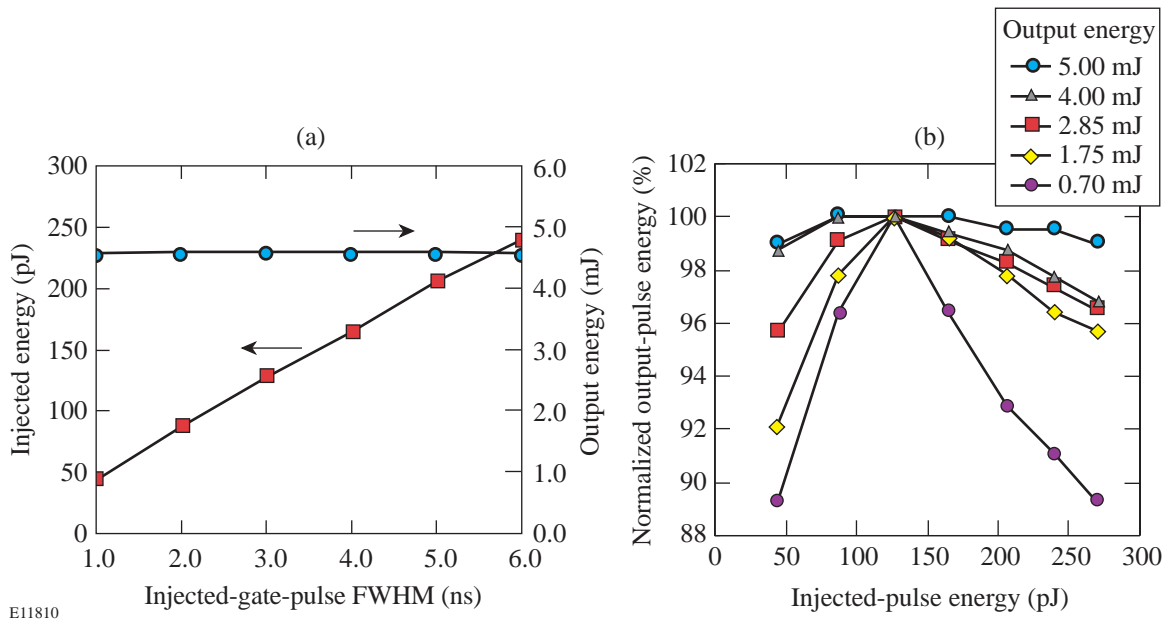
Figure 91.10
Regen output-pulse energy does not change with variations of injected-pulse energy, when (a) gain/loss ratio is high, and (b) becomes more sensitive to injected-pulse energy with decreasing gain/loss ratio. Note that the vertical scale of (b) is expanded to show the variation with input energy.

E11488
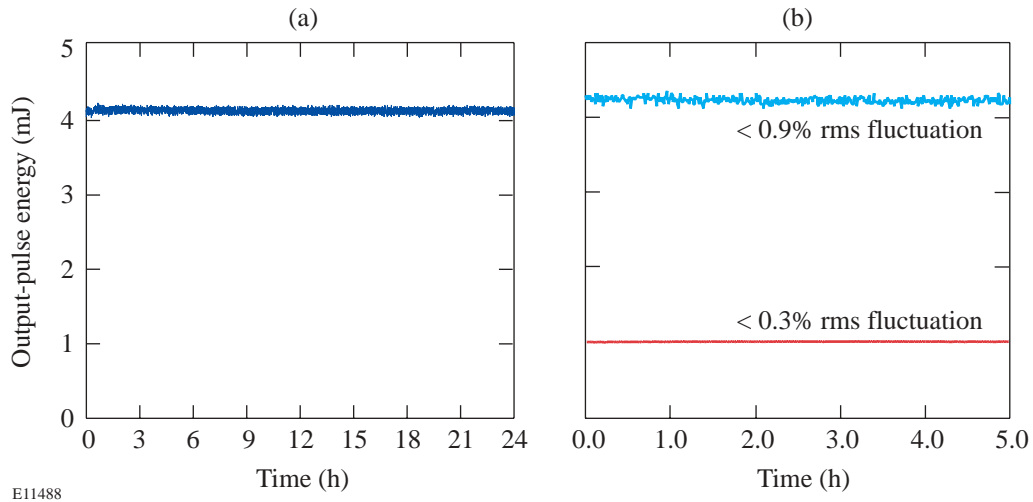
Figure 91.11

(a) Regen output-pulse-energy stability is <0.9% rms over 24 h; (b) regen stability is higher at lower output energies.

E11489b
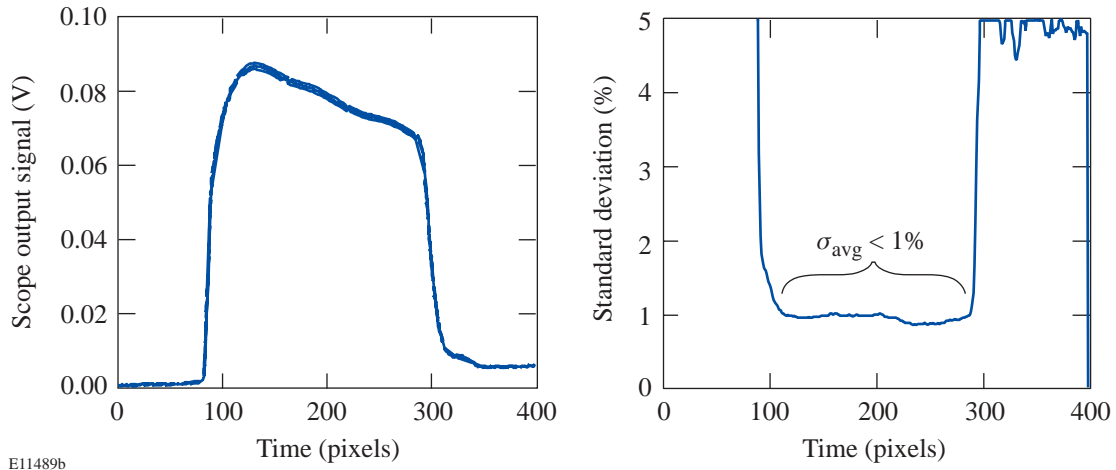
Figure 91.12

Regen output-temporal-pulse-shape stability is excellent: pulse shape standard deviation is <1% over 5 h.

REFERENCES

1. A. V. Okishev, M. D. Skeldon, R. L. Keck, and W. Seka, in *Advanced Solid State Lasers*, edited by H. Injeyan, U. Keller, and C. Marshall, OSA Trends in Optics and Photonics Series (Optical Society of America, Washington, DC, 2000), Vol. 34, pp. 112–115.

2. D. L. Brown, I. Will, R. G. Roides, C. K. Merle, M. D. Skeldon, and W. Seka, in *1993 Optical Society of America Annual Meeting*, 1993 OSA Technical Digest Series, Vol. 16 (Optical Society of America, Washington, DC, 1993), p. 250.

3. A. Okishev, M. D. Skeldon, S. A. Letzring, W. Seka, and I. Will, in *OSA Proceedings on Advanced Solid-State Lasers*, edited by B. H. T. Chai and S. A. Payne (Optical Society of America, Washington, DC, 1995), Vol. 24, pp. 274–276.

4. M. D. Skeldon, A. Babushkin, W. Bittle, A. V. Okishev, and W. Seka, IEEE J. Quantum Electron. **34**, 286 (1998).

5. A. Babushkin, W. Bittle, S. A. Letzring, M. D. Skeldon, and W. Seka, in *Third International Conference on Solid State Lasers for Application to Inertial Confinement Fusion*, edited by W. H. Lowdermilk (SPIE, Bellingham, WA, 1999), Vol. 3492, pp. 124–130.

6. W. H. Lowdermilk and J. E. Murray, J. Appl. Phys. **51**, 2436 (1980).

7. J. E. Murray and W. H. Lowdermilk, J. Appl. Phys. **51**, 3548 (1980).

Improved Performance of Direct-Drive Implosions with a Laser-Shaped Adiabat

Introduction

The minimum energy required for ignition of the imploding capsule in inertial confinement fusion is a strong function of the fuel adiabat (the ratio of the shell pressure to the Fermi-degenerate pressure) α_{stag} at the time of maximum compression: $E_{min} \sim \alpha_{stag}^3$. Thus, to minimize the energy, the shell must be driven on the lowest possible adiabat. The performance of low-adiabat implosions is limited by hydrodynamic instabilities that tend to disrupt the shell during the acceleration phase. The most important instability is the Rayleigh–Taylor[1,2] (RT) instability seeded by single-beam non-uniformities and surface roughness. The main mechanism that reduces the RT growth is mass ablation from the target surface,[3] characterized by the ablation velocity V_a. The ablation velocity, in turn, increases with the adiabat α in the ablation region as $V_a \propto \alpha^{3/5}$. As the shell accelerates, the RT instability takes place at the outer part of the shell, which ablates during the implosion. Thus, one can satisfy the requirements of the lower-adiabat fuel at the maximum compression and the higher-adiabat ablation region by shaping the adiabat inside the shell.

Experiments have been done in both planar[4–8] and convergent[9,10] geometries to understand the evolution of perturbations at the ablation surface during acceleration of a planar foil or implosion of a cylinder or hemisphere. The ablation surface and the shell–fuel surface are coupled in that perturbations on the shell–fuel interface can "feed out"[11] to the ablation surface and perturbations that grow on the ablation surface can "feed through"[12] to the shell–fuel interface.

Interface perturbations grow exponentially $\left(a = a_0\, e^{\gamma t}\right)$ during the "linear" phase of the RT instability and reach a saturation phase (when $a \sim \lambda/10$) where the growth continues at a reduced rate.[13] Here, a is the amplitude of the perturbation, a_0 is the initial perturbation amplitude (the seed), γ is the growth rate, and λ is the wavelength of the perturbation.

A great deal of effort has gone into reducing the seeds (a_0) due to illumination nonuniformities (imprinting) and target imperfections. The effect of imprinting has been reduced by a number of beam-smoothing techniques, including distributed phase plates (DPP's),[14] polarization smoothing (PS) with birefringent wedges,[15,16] smoothing by spectral dispersion (SSD),[17] and induced spatial incoherence (ISI).[18] The effect of the RT instability can also be reduced by lowering the RT growth rate. It has been shown that the ablation-surface RT growth rate is reduced by the ablation process.[3] Subsequent theoretical work that includes the effect of thermal transport[19] and experiments with planar targets[8] shows that the dispersion formula for a CH target is given by

$$\gamma = 0.98\sqrt{\frac{kg}{1+kL}} - 1.7 \cdot kv_a,$$

where k is the perturbation spatial wave number, g is acceleration, L is density scale length, and V_a is ablation velocity.

The ablation velocity term not only reduces the growth rate but stabilizes the interface for perturbation wavelengths shorter than the cutoff wavelength λ_c, where

$$\lambda_c = \frac{4\pi L}{\sqrt{1 + 4\left(\frac{0.98}{1.7}\right)^2 \times \frac{Lg}{V_a^2}}},$$

which, in the limit that $k \times L \ll 1$, is

$$\lambda_c = 2\pi\left(\frac{1.7}{0.98}\right)^2 \times \frac{V_a^2}{g}.$$

The ℓ mode of a perturbation on a spherical target is given approximately by the circumference of the target $(2\pi r)$ divided by the perturbation wavelength, so that the cutoff ℓ mode $\ell_c \sim 2\pi r/\lambda_c$. A capsule is stable for modes equal to or larger than ℓ_c.
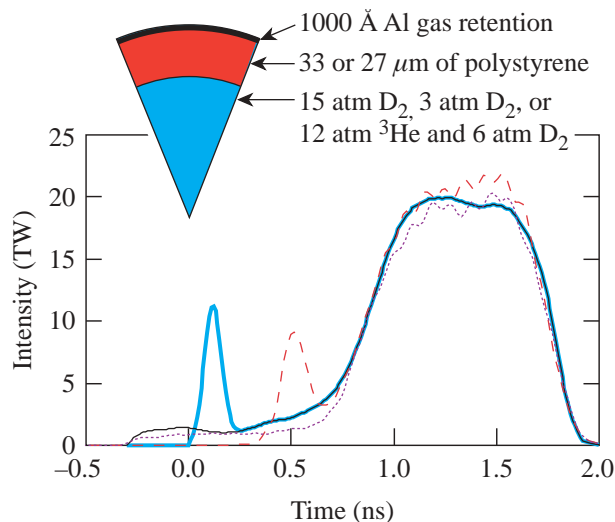
The ablation velocity is defined as the velocity at which the ablation surface moves into the target. This is given by the mass

ablation rate (the rate at which material is removed from the ablation surface) divided by the density of the same material. The mass ablation rate is determined by the intensity of the incident radiation onto the target; therefore, decreasing the density of material at the ablation surface can increase the ablation velocity.

Two techniques—radiation preheat[20] and driving a decaying shock wave[21]—have been proposed to decrease the density at the ablation surface by raising its temperature and causing the shell to decompress. Decreasing the density at the ablation surface increases the ablation velocity, the entropy of the ablation surface, and thus the adiabat. One must be careful, however, to increase the shell adiabat at the ablation surface only and not the whole shell or the fuel. The entropy of the fuel must be minimally affected by these techniques so that the target will continue to be compressed efficiently.

Adiabat Shaping in Spherical Implosions

An experiment was designed to test the technique of launching a decaying shock wave into a spherical shell, setting the adiabat of the shell high at the ablation surface and low at the fuel–shell interface. This was accomplished by adding a narrow picket pulse to the beginning of a laser pulse shape designed to implode a target with a low shell adiabat as shown by the thick solid curve of Fig. 91.13. The picket pulse initiates a shock wave in the shell that becomes unsupported in that the pressure at the ablation surface is decreased, resulting in the generation of a rarefaction wave the propagates toward the shock wave. The rarefaction wave overtakes the shock wave, and the resultant shock wave decays as it propagates through the shell. The laser-irradiation pulse shape is designed so that the shock wave affects the ablation interface with minimal change at the shell–fuel interface.

The experiment was designed around a D_2-filled polystyrene shell, 33 μm thick and 905 μm in diameter filled to a pressure of 15 atm. Two pulse shapes (shown in Fig. 91.13) were used to compress this shell with a low adiabat ($\alpha = 2$) at the fuel–shell interface. The main drive pulse, shown as the thin solid curve, has a 2-TW, 700-ps-long foot followed by a power law rise[22] to a peak intensity of 20 TW on target. The foot pulse drives a shock wave that is fully supported throughout the implosion and changes the entropy of the shell and fuel. The dotted curve in Fig. 91.13 shows an actual pulse shape used during the experiments.

The optimum picket pulse is one that will raise the adiabat of the ablation surface without affecting, or minimally affecting, the fuel–shell interface adiabat. It was found by one-dimensional (1-D) hydrodynamic simulations that this optimum pulse for the implosions with a picket pulse was comprised of a narrow, 100-ps-FWHM (full width at half maximum), Gaussian picket combined with the main drive pulse described above. This combined pulse, shown as the thick solid curve in Fig. 91.13, has a picket 750 ps before the half-maximum intensity point of the power-law rise of the drive pulse. The narrowest picket pulse available on OMEGA for these experiments had a FWHM of 120 ps. The experiment was designed with a pulse using a 120-ps picket placed at 340 ps before the half-maximum point of the compression pulse shown as the dashed curve in Fig. 91.13. The total laser energy on target is 19 kJ with 0.9 kJ in the picket pulse.

Figure 91.13
(Inset: Types of targets used to study the effect of a picket pulse on the implosion of a spherical gas-filled shell. Targets with either a 33-μm- or 27-μm-thick polystyrene shell were filled with either 15 atm of D_2, 3 atm of D_2, or a mixture of 12 atm of ^{3}He and 6 atm of D_2.) Pulse shape used to measure the effect of a picket pulse before a drive pulse on the performance of an implosion. The drive pulse was designed to implode a spherical cryogenic DT target on an isentrope. This pulse shape implodes a gas-filled CH shell as an $\alpha = 2$ isentrope. This pulse shape is shown as the thin solid curve (which is covered by the thick solid curve after 0.25 ns). The actual pulse shape delivered by the laser is shown as the dotted curve. The optimum picket pulse has an intensity of 55% of the drive pulse intensity, is 100 ps wide between the half-intensity points, and precedes the compression pulse by 750 ps. This pulse shape is shown as the thick solid curve. The actual picket was 120 ps wide so it had to be positioned 340 ps ahead of the drive pulse with an amplitude of 40% of the drive pulse. The actual picket and drive pulse combination used is shown as the dashed curve.

E11794

The effect of the picket on the implosions is shown in Figs. 91.14 and 91.15. Stability was calculated using the output from the 1-D hydrodynamics simulation code *LILAC*.[23] The calculation uses *LILAC* output to determine values for the shell's physical quantities, an assumed initial perturbation spectrum at the ablation surface, and a model for RT growth[12] to determine the amplitude of perturbations at the ablation surface during an implosion. The initial perturbation is a quadrature sum of the illumination nonuniformity as calculated by a two dimensional (2-D) hydrodynamics simulation and the measured target outer-surface roughness.[24] The amplitude of the inner peak, or bubble, of the perturbation divided by the shell thickness is shown in Fig. 91.14. It is assumed that the perturbation disrupts the shell when this value is equal to 1. For

the case of the pulse shape without a picket (shown as the thick solid curve), this occurs at the peak of the compression pulse at 1.28 ns. The thin solid curve in Fig. 91.14 shows the result when a picket is added to the beginning of the compression pulse. The bubble-to-shell thickness ratio stays below 1 during the entire time that the laser irradiates the target, reaching a maximum value of 0.7 near the end of the compression pulse. This analysis indicates that the shell driven with a picket pulse is more stable during the acceleration phase of the implosion than one driven without a picket.

Figure 91.15 shows the simulated shell density and adiabat as functions of radius at the time of maximum acceleration for two separate implosions. Densities are plotted as solid curves,
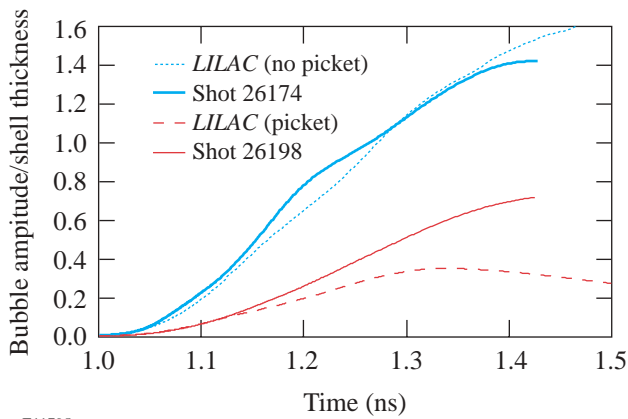
Figure 91.14

Bubble amplitude divided by the shell thickness calculated by a stability postprocessor applied to the output from the 1-D hydrodynamic simulation *LILAC*. The thick and dotted curves indicate the laser pulse without a picket. The thin and dashed curves indicate pulse shapes with a picket. The dashed and dotted curves indicate the ideal pulse shape for a 15-atm-D_2-filled, 33-μm-thick polystyrene shell. The thick and thin curves are calculated for the actual pulse shapes delivered onto the target.
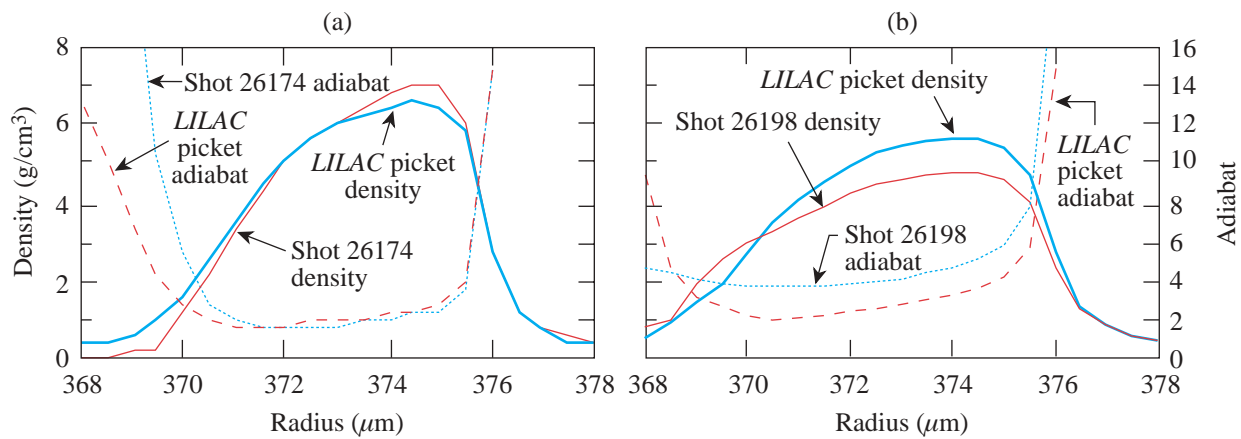
Figure 91.15

The density and adiabat versus position at the time of peak acceleration calculated from *LILAC*. In (a) with the drive pulse only, the density is plotted as solid lines, and the adiabat is plotted as broken lines. In (b) the density and adiabat are plotted with a picket pulse added to the compression pulse. The thick and dashed lines in both (a) and (b) are calculated from *LILAC* for the optimum laser pulse shapes. The thin and dotted lines are calculated for the pulse shape used in the experiment.

and the adiabats are plotted as dashed curves. Figure 91.15(a) shows the results for illumination without a picket for both the ideal and actual pulse shapes, and Fig. 91.15(b) shows the results for pulses with a picket, again for both the ideal and actual pulse shapes. The ablation surface is at the position of 376 μm, where the density is 2.5 g/cm^3. The value of the adiabat at the ablation surface without a picket is 3.9 and with a picket is 5.6. The fuel–shell interface is at a position of 372 μm for the pulse shape without a picket and 370 μm for illumination with a picket. The value of the adiabat is 1.7 for pulses without a picket and 2.1 for pulses with a picket.

Experimental Results

The OMEGA[25] laser system was used to implode spherical targets with the above pulse shapes. Sixty beams of 351-nm radiation were incident onto the target. All beams had polarization smoothing, 1-THz bandwidth, 2-D SSD, and DPP's with an intensity envelope given by a third-order super-Gaussian to minimize the illumination nonuniformities imposed by the laser. The targets used for these measurements are shown as the inset in Fig 91.13. The shells were made of polystyrene either 33 or 27 μm thick and filled with three gas-fill conditions: 15 atm of D_2; 3 atm of D_2; and a mixture of 12 atm of ^{3}He and 6 atm of D_2. All targets had a 1000-Å layer of aluminum to act as a gas-retention barrier. The laser pulse shapes were optimized for an outer diameter of 906 μm, and the delivered targets had diameters that ranged from 901 to 923 μm.

Both x-ray and fusion particle (neutron and proton) diagnostics were used to measure and quantify the implosions. X-ray framing cameras[26] were used to measure the time and spatially dependent x-ray emission during the implosion. X-ray microscopes[27] were used to study the final core spatial

shapes. Neutron yields and spectra were measured with scintillator time-of-flight counters[28–30] at 3.5 and 7 m from the center of the target chamber. Protons from fusion processes were detected with range filters[31] designed to determine both their yield and energy spectrum.

It is important that the 1-D hydrodynamic simulation calculate the implosion dynamics correctly when a model is used to determine the growth of perturbations. Two x-ray framing cameras were used to measure the radius of the imploding shell as a function of time. The data for all 15-atm-gas-filled, 33-μm-thick CH shells are plotted in Fig. 91.16. These data are from 15-atm-D_2-filled and 12-atm-^{3}He/6-atm-D_2-filled targets. The experimental data are the value of the peak x-ray emission radius of a two-dimensional image and are plotted as crosses. The *LILAC*-calculated position of the outer and inner shell surfaces are plotted as solid and dashed lines. The inner and outer shell radii are determined by radii at which the density is 1/*e* times the peak density of the shell. Data for laser irradiation without the picket pulse are plotted in Fig. 91.16(a), and data for laser irradiation with the picket are plotted in Fig. 91.16(b). The *LILAC* calculations agree reasonably well with the experimental data. This indicates that the motion of the imploding target is calculated correctly.

X-ray images of the core emission from a Kirkpatrick–Baez (KB) microscope are shown in Fig. 91.17. These images are integrated in time; however, most of the x-ray emission from the core comes during the peak compression of the target. The image from an implosion without a picket pulse is shown in Fig. 91.17(a), and the image from an implosion with a picket pulse is shown in Fig. 91.17(b). The images show a more-intact fuel mass when a picket pulse is added to the main compres-
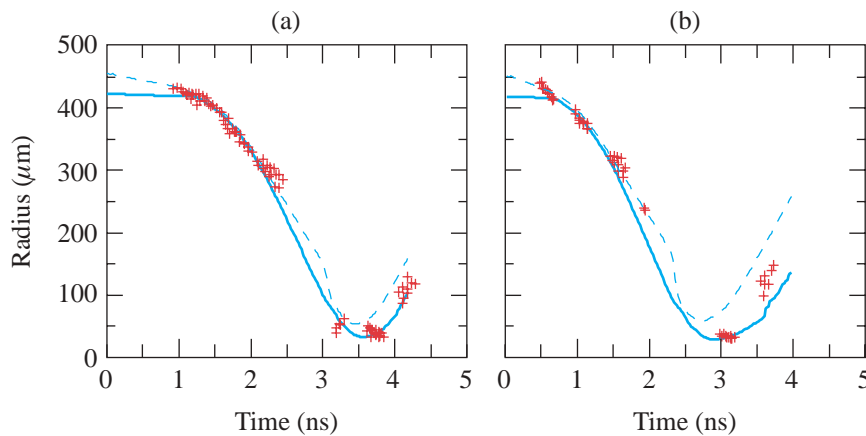
Figure 91.16
Radius versus time for all 15-atm-filled, 33-μm-thick CH shell targets. The plot in (a) shows data for laser irradiation using the compression pulse without a picket pulse. Averages for *LILAC*-calculated position of the inner and outer shell radius are plotted as solid and dashed lines, and the experimental data as measured with two x-ray framing cameras are plotted as crosses. The plot in (b) shows data taken with a picket pulse. The solid and dashed curves are averages of the *LILAC*-calculated positions of the inner and outer shell radius. The experimental data as measured with x-ray framing cameras are plotted as crosses.

E11797

sion pulse. Lineouts along the lines shown in the images are plotted in Fig. 91.17(c). The lineout of the image without a picket pulse is plotted as a dashed curve. Lineout data from the image with a picket pulse are plotted as the solid line. Figure 91.17(c) shows that the lineout from the implosion with a picket is typical of that from a "limb-brightened" image and shows that the implosion was more stable than the implosion without a picket.

Results from the fusion-product-yield measurements for three shots for each target and pulse shape are shown in Table 91.I. It can be seen from the data that for the 15-atm-D_2-filled, 33-μm-thick shell, there is a factor-of-3 increase in the number of 3-MeV neutrons from the target irradiated with a picket pulse than that from the target without a picket. The experiment was optimized for the 33-μm-thick shells; the improvement for the 27-μm-thick shells is only 50%. Both the 3-atm-D_2-filled and the ^{3}He-D_2-filled, 33-μm-thick shells show an improved fusion yield by a factor of 2. The ratio of the measured primary neutron yield to the neutron yield predicted by the hydrodynamics simulation [usually referred to as yield-over-clean (YOC)] for the 15-atm-D_2-filled, 33-μm-thick shells improves from 0.03 to 0.19. In all cases, the YOC can be seen to improve significantly.
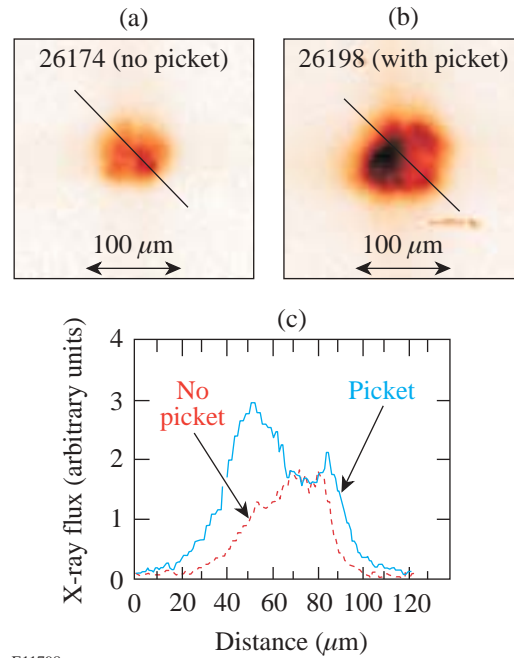
Figure 91.17
X-ray microscope images of target cores formed from a 33-μm-thick CH shell filled with 15 atm of D_2; (a) with only the main compression pulse used; (b) when a picket pulse was added to the compression pulse. Lineouts through the images are shown in (c). The dashed line is the lineout without a picket pulse; the solid line is the lineout with a picket pulse.

Table 91.I: Summary of fusion-product measurements and simulation output. The first column describes the composition, shell thickness (mm, in square brackets), and fill pressure (atm, in parentheses) of the target.

Target	Experimental Measurements			LILAC Simulation Output		
	Yield (D_2)	Yield (DT)	Yield (D^{3}He)	Yield (D_2)	Yield (DT)	Yield (D^{3}He)
Without picket						
D_2(15)CH[33]	4.14×10^9	7.99×10^6	2.96×10^6	1.17×10^{11}	3.04×10^8	1.66×10^8
D_2(3)CH[33]	1.06×10^9	8.00×10^5	1.83×10^6	4.17×10^{10}	9.51×10^7	6.34×10^7
^{3}He(12)D_2(6)CH[33]	9.32×10^8	9.30×10^5	2.94×10^6	1.54×10^{10}		
D_2(15)CH[27]	1.98×10^{10}	3.89×10^7	1.83×10^7	2.50×10^{11}	6.60×10^8	4.18×10^8
With picket						
D_2(15)CH[33]	1.27×10^{10}	3.57×10^7	7.26×10^6	6.60×10^{10}	1.20×10^8	8.12×10^7
D_2(3)CH[33]	1.98×10^9	1.83×10^6	1.88×10^6	1.19×10^{10}	1.36×10^7	1.15×10^7
^{3}He(12)D_2(6)CH[33]	1.44×10^9	1.77×10^6	5.75×10^6	8.20×10^9		
D_2(15)CH[27]	2.96×10^{10}	5.22×10^7	2.96×10^7	1.94×10^{11}	4.15×10^8	3.05×10^8

Neutron-production rates for the 15-atm-D_2-filled, 33-μm-thick shell, measured (open symbols) and predicted (solid curves), are shown in Fig. 91.18. The thin curve and open square plots are data from the implosion without a picket. The thick curve and open circle plots are from the matching implosion using a picket. The experimental data were measured with the "neutron temporal diagnostic" (NTD).[32] The temporal offsets needed to compare experimental and simulation data were determined by maximizing the cross-correlation of the drive portion of the pulse as a function of a temporal shift relative to the laser pulse without a picket. This aligned the leading edges of the main drive pulse for all of the data. It is assumed that the neutron production is determined by the compression of the target by the drive pulse. An additional time shift was introduced to align the position of the shock neutron production calculated by *LILAC* for shapes without and with the picket pulse. The experimental data and the output from hydrodynamic simulations were processed in this manner so that the timing could be compared for all data. The temporal error for the relative times of emission is estimated to be of the order of 30 ps. The measured neutron burn rate divided by the calculated neutron burn rate from *LILAC* is plotted in Fig. 91.19. The data from implosions without a picket are plotted as open squares, and the data from implosions with a picket are plotted as open circles. The ratio of burn rates peaks

at 0.35 for implosions with a picket pulse, while the ratio without a picket pulse peaks at 0.2. The neutron-burn-rate ratios show that the duration of neutron emission is longer for implosions with a picket pulse. Comparing the experimental data with predictions indicates that the implosions using a picket not only attain higher absolute yields than the implosions without a picket, they also return, as was stated earlier, a larger fraction of the 1-D yield. This suggests more-stable implosions with less mix due to RT growth.

While the experimental results from the neutron diagnostics reported above are encouraging, results from several other diagnostics remain inconclusive. Ion temperatures, inferred from the broadening of the neutron spectra, were reported to be from 2.1 to 2.5±0.5 keV for the 33-μm-thick shells and from 2.6 to 2.8±0.5 keV for the 27-μm-thick shells. There were no appreciable differences between implosions using the laser pulses with or without the picket. Additionally, the downshift of the primary proton energy can be used to measure the total ρR of the target integrated over the time of proton emission. The measured mean energy for the compression yield was 11.3±2.0 MeV for the implosion without a picket and 11.6±1.8 MeV for the implosion with a picket. The total ρR for both of these targets was inferred to be 106±8 and 108±8 mg/cm^2, respectively.
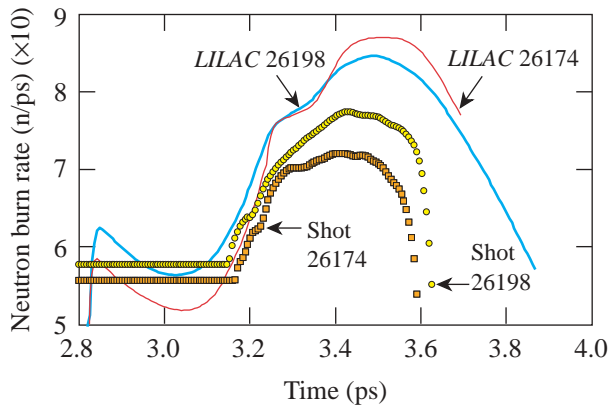
Figure 91.18

Neutron-production rates for a 15-atm-D_2-filled, 33-μm thick polystyrene shell. The thin curve and open squares are data for the pulse without a picket pulse. The thick curve and open circles are data for the pulse with a picket in front. Open symbols are the experimental measurements, and the solid curves are from the 1-D hydrodynamic simulation *LILAC*. Note that these points lie very close together before ~3.2 ns.
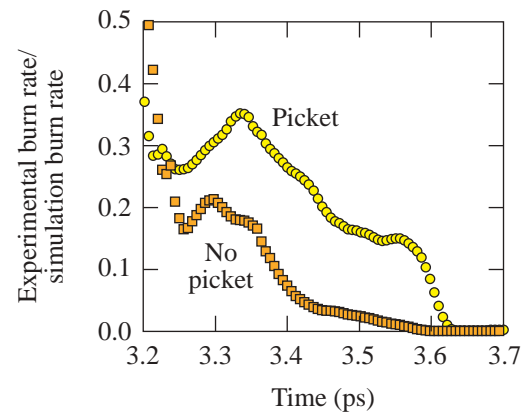
Figure 91.19

Experimental neutron-production rate divided by the neutron-production rate from a 1-D hydrodynamic simulation *LILAC* for a 15-atm-D_2-filled, 33-μm-thick polystyrene shell. The open square points are data for the pulse without a picket pulse, and the open circle points are data for the pulse with a picket in front.

Finally, results from the measurements of the 14.7-MeV proton emitted from the D^3He reaction are shown in Table 91.II. Targets filled with D^3He allowed for the measurement of the primary proton yield from the shock wave convergence at the center of the capsule. The mean energy for the protons was measured as 14.3 MeV for the laser irradiation both without and with a picket pulse. The number of protons from the shock wave is $7.1\pm1.2 \times 10^5$ without a picket pulse and $7.5\pm1.1 \times 10^5$ with a picket pulse as shown in column 2 of Table 91.II. Comparison of these measurements infer that the shock strength of the compression pulse is unaffected by the introduction of a picket. This would indicate that the shock created by a picket decayed in the shell before it had a chance to significantly alter the adiabat of the fuel.

Conclusion

An experiment has been performed to measure the effect of a picket pulse on the implosion of a spherical target. The purpose of this pulse was to initiate a decaying shock wave that lowers the density of the shell at the ablation interface but does not significantly affect the entropy of the shell–gas interface. The yields of fusion products are improved both in terms of the absolute value and in terms of the comparison to 1-D hydrodynamic simulation output. The increase in neutron yield for implosions with a picket pulse is not due to the added energy in the picket since both the absolute and relative neutron yields improved.

Between the two pulse shapes there is little change in either the total target ρR or the ion temperature. The neutron temperature measurement is the neutron-weighted ion temperature. It is possible this weighted measurement will be the same for both types of implosions. The ρR as measured with the protons from the D^3He reaction measures the total ρR of the target and not just the fuel ρR. This measurement is dominated by the thick target shells and is less sensitive to the fuel.

The emission rate for the 3-MeV neutrons compared to the simulation output shows that the start of emission calculated by the simulation compares well with the experimental data. The neutron-burn-rate measurements indicate that the 1-D simulation overestimates the duration of the neutron emission, probably due to the multidimensional effects not included in this type of calculation. The neutron emission from implosions using a picket pulse reaches a higher emission rate and a higher ratio of the experimental neutron burn rate to the *LILAC*-calculated neutron burn rate. Comparing the experimental data with predictions indicates that the implosions using a picket not only attain higher absolute yields than the implosions without a picket, they also return, as was stated earlier, a larger fraction of the 1-D yield. This demonstrates that picket pulses stabilize the implosion, resulting in less mix due to the RT growth at the ablation interface.

Table 91.II: Summary of 14-MeV proton measurements. The first column describes the target as in Table 91.I. The second column is the total number of protons emitted during the compression of the target. Column 3 is the number of protons emitted when the shock wave reaches the center of the target. The downshift of the protons is shown in column 4, and the calculated total ρR of the target is shown in column 5.

	Proton measurements			
Target	Yield (D^3He)	Yield (D^3He)	ΔE	ρR_{total}
Without picket	Compression	Shock	MeV	mg/cm^2
D_2(15)CH[33]	2.96×10^6		3.5 ± 0.3	106 ± 8
He^3(12)D2(6)CH[33]	2.94×10^6	7.11×10^5	3.4 ± 0.3	104 ± 8
D_2(15)CH[27]	1.83×10^7		2.6 ± 0.2	81 ± 6
With picket				
D_2(15)CH[33]	7.26×10^6		3.6 ± 0.3	108 ± 8
He^3(12)D2(6)CH[33]	5.75×10^6	7.51×10^5	3.5 ± 0.2	106 ± 6
D_2(15)CH[27]	2.96×10^7		3.0 ± 0.2	92 ± 6

ACKNOWLEDGMENT

REFERENCES

1. Lord Rayleigh, Proc. London Math Soc. **XIV**, 170 (1883).

2. G. Taylor, Proc. R. Soc. London Ser. A **201**, 192 (1950).

3. S. E. Bodner, Phys. Rev. Lett. **33**, 761 (1974).

4. J. Grun *et al.*, Phys. Rev. Lett. **58**, 2672 (1987).

5. M. Desselberger *et al.*, Phys. Rev. Lett. **65**, 2997 (1990).

6. S. G. Glendinning, S. V. Weber, P. Bell, L. B. Da Silva, S. N. Dixit, M. A. Henesian, D. R. Kania, J. D. Kilkenny, H. T. Powell, R. J. Wallace, P. J. Wegner, J. P. Knauer, and C. P. Verdon, Phys. Rev. Lett. **69**, 1201 (1992).

7. C. J. Pawley *et al.*, Phys. Plasmas **6**, 565 (1999).

8. J. P. Knauer, R. Betti, D. K. Bradley, T. R. Boehly, T. J. B. Collins, V. N. Goncharov, P. W. McKenty, D. D. Meyerhofer, V. A. Smalyuk, C. P. Verdon, S. G. Glendinning, D. H. Kalantar, and R. G. Watt, Phys. Plasmas **7**, 338 (2000).

9. W. W. Hsing *et al.*, Phys. Plasmas **4**, 1832 (1997).

10. C. Cherfils *et al.*, Phys. Rev. Lett. **83**, 5507 (1999).

11. R. Betti, V. Lobatchev, and R. L. McCrory, Phys. Rev. Lett. **81**, 5560 (1998).

12. V. N. Goncharov, P. McKenty, S. Skupsky, R. Betti, R. L. McCrory, and C. Cherfils-Clérouin, Phys. Plasmas **7**, 5118 (2000).

13. S. W. Haan, Phys. Rev. A **39**, 5812 (1989).

14. T. J. Kessler, Y. Lin, J. J. Armstrong, and B. Velazquez, in *Laser Coherence Control: Technology and Applications*, edited by H. T. Powell and T. J. Kessler (SPIE, Bellingham, WA, 1993), Vol. 1870, pp. 95–104.

15. Y. Kato, unpublished notes from work at LLE, 1984.

16. T. R. Boehly, V. A. Smalyuk, D. D. Meyerhofer, J. P. Knauer, D. K. Bradley, R. S. Craxton, M. J. Guardalben, S. Skupsky, and T. J. Kessler, J. Appl. Phys. **85**, 3444 (1999).

17. S. Skupsky, R. W. Short, T. Kessler, R. S. Craxton, S. Letzring, and J. M. Soures, J. Appl. Phys. **66**, 3456 (1989).

18. R. H. Lehmberg and S. P. Obenschain, Opt. Commun. **46**, 27 (1983).

19. R. Betti, V. N. Goncharov, R. L. McCrory, P. Sorotokin, and C. P. Verdon, Phys. Plasmas **3**, 2122 (1996).

20. D. G. Colombant *et al.*, Phys. Plasmas **7**, 2046 (2000).

21. J. D. Lindl and W. C. Mead, Phys. Rev. Lett. **34**, 1273 (1975).

22. R. E. Kidder, Nucl. Fusion **16**, 3 (1976).

23. M. C. Richardson, P. W. McKenty, F. J. Marshall, C. P. Verdon, J. M. Soures, R. L. McCrory, O. Barnouin, R. S. Craxton, J. Delettrez, R. L. Hutchison, P. A. Jaanimagi, R. Keck, T. Kessler, H. Kim, S. A. Letzring, D. M. Roback, W. Seka, S. Skupsky, B. Yaakobi, S. M. Lane, and S. Prussin, in *Laser Interaction and Related Plasma Phenomena*, edited by H. Hora and G. H. Miley (Plenum Publishing, New York, 1986), Vol. 7, pp. 421–448.

24. P. W. McKenty, V. N. Goncharov, R. P. J. Town, S. Skupsky, R. Betti, and R. L. McCrory, Phys. Plasmas **8**, 2315 (2001).

25. T. R. Boehly, D. L. Brown, R. S. Craxton, R. L. Keck, J. P. Knauer, J. H. Kelly, T. J. Kessler, S. A. Kumpan, S. J. Loucks, S. A. Letzring, F. J. Marshall, R. L. McCrory, S. F. B. Morse, W. Seka, J. M. Soures, and C. P. Verdon, Opt. Commun. **133**, 495 (1997).

26. O. L. Landen *et al.*, in *Ultrahigh- and High-Speed Photography, Videography, and Photonics '93*, edited by P. W. Roehrenbeck (SPIE, Bellingham, WA, 1993), Vol. 2002, pp. 2–13.

27. F. J. Marshall and Q. Su, Rev. Sci. Instrum. **66**, 725 (1995).

28. T. J. Murphy *et al.*, Rev. Sci. Instrum. **66**, 930 (1995).

29. R. A. Lerche and T. J. Murphy, Rev. Sci. Instrum. **63**, 4880 (1992).

30. V. Yu. Glebov, D. D. Meyerhofer, C. Stoeckl, and J. D. Zuegel, Rev. Sci. Instrum. **72**, 824 (2001).

31. F. H. Séguin, C. K. Li, D. G. Hicks, J. A. Frenje, K. M. Green, R. D. Petrasso, J. M. Soures, D. D. Meyerhofer, V. Yu. Glebov, C. Stoeckl, P. B. Radha, S. Roberts, C. Sorce, T. C. Sangster, M. D. Cable, S. Padalino, and K. Fletcher, Phys. Plasmas **9**, 2725 (2002).

32. R. A. Lerche, D. W. Phillion, and G. L. Tietbohl, Rev. Sci. Instrum. **66**, 933 (1995).

Direct-Drive Implosion Experiments with Enhanced Beam Balance on OMEGA

Introduction

Laser-driven, direct-drive inertial confinement fusion (ICF) is accomplished by near-uniform illumination of spherical fuel-bearing targets with high-power laser beams.[1–3] A goal of ICF is to achieve thermonuclear ignition and gain, which requires symmetric compression of the fuel to high temperatures ($\gtrsim 4$ keV) and high areal densities ($\gtrsim 0.3$ g/cm^2). Both target imperfections and departures from symmetric laser illumination contribute to degradation of target performance. Low-mode ($\ell \leq 10$) perturbations of the intensity, generally due to beam-to-beam variations, can cause distortions of the core at stagnation; whereas small-scale imperfections in the target layers and in the single-beam intensity profiles contribute to higher-mode ($\ell \geq 10$) perturbations, which lead to Rayleigh–Taylor unstable growth, target breakup, and mixing of material from the shell and from the gas fill. Both can degrade target performance by reducing the peak temperature and areal density of the final fuel region.

Direct-drive ICF implosion experiments are currently being performed on LLE's OMEGA laser system.[4] The goal of these experiments is to attain near-ignition conditions in the compressed fuel region. Implosion experiments are being performed with both surrogate cryogenic targets[5,6] (where the shell acts as the main fuel layer) and actual cryogenic targets[7] (where the shell is principally solid fusion fuel). The cryogenic targets are being prepared by the newly implemented Cryogenic Target Handling System[8] using D$_2$ as the fuel layer. The eventual goal is to demonstrate optimized implosions of cryogenic DT-fuel targets. Studies of the performance of surrogate fuel targets have shown that the smoothness of the individual beams has a measurable effect on target performance;[5,6] however, the effect of beam balance on the target performance has not been quantified.[6]

This article presents a method that measures the beam-to-beam intensity variations at the target and then uses these measurements to correct the beam intensities, thereby minimizing the variations. The beam-to-beam UV intensity variations at the target are inferred from measurements of the x-ray flux produced by each of the 60 beams of OMEGA seen separated on a 4-mm-diam, Au-coated spherical "pointing" target. Up to eight x-ray pinhole camera (XPHC) images are electronically recorded per shot from which variations in intensity are determined, taking into account view-angle effects and x-ray conversion efficiency dependence on intensity. The observed variations are then used to correct the beam intensities to produce more-uniform irradiation (or enhanced beam balance). The enhanced beam balance condition is in contrast to the standard beam balance condition arrived at by balancing the output of the laser as measured by 60 cross-calibrated full-beam calorimeters. As applied to imploding targets, the enhanced balance condition consistently yields improved symmetry of the imploding shell as observed by multiple-view x-ray imaging diagnostics. This is evidence of a more-uniform final fuel layer in the imploding target, an important goal for eventual attainment of ignition and gain.

Measurement of On-Target Intensity Using X-Ray Imaging

To accurately determine the intensity of a beam striking a laser target, it is necessary to be able to measure the full-beam intensity and/or energy before focusing and then to account for all losses incurred in transporting the beam to the target. In addition, the beam profile at its focus must be known. OMEGA uses distributed phase plates and spectrally dispersed frequency modulation to produce a time-averaged intensity pattern at the target, which is smoothed in space [smoothing by spectral dispersion (SSD)].[9] The SSD version currently in use on OMEGA smooths the beam in two dimensions with an effective bandwidth of 1 THz and is enhanced by the use of polarization smoothing (PS).[10] The smoothed beam instantaneously has a so-called super-Gaussian shape given by

$$I_{\mathrm{UV}}(r) = I_{\mathrm{UV}}(0) \times e^{-(r/\sigma_r)^\eta}, \tag{1}$$

where $I_{\mathrm{UV}}(0)$ is the intensity at the beam peak, and r and σ_r are in units of distance from the beam center. Typical values for OMEGA 1-THz-SSD-with-PS beams are $\sigma_r = 300$ μm and $\eta = 2.5$.

Since the integral of Eq. (1) over time and space yields the beam energy, it is easy to see that for beams of equal size (i.e., equal σ_r and η) a measurement of the beam's peak intensity is sufficient to measure the beam energy. Here, advantage is being taken of the high UV-absorption efficiency of Au at high intensities (>90% for intensities below 10^{13} W/cm^2).[11] Inverse-bremsstrahlung-heated Au plasmas reradiate most of their energy in the soft x-ray range (1 to 10 keV), making it possible to image the emission and, with knowledge of the x-ray conversion efficiency, to infer the UV intensity that produced the observed x-ray flux. Phenomenologically, the x-ray flux resulting from an incident intensity I_{UV} can be expressed as

$$I_x = C_{UV-x} \times I_{UV}^{\gamma}, \tag{2}$$

where C_{UV-x} is a constant dependent upon the x-ray band (energy range) and detection method utilized (see Subsection 3).

Spherical targets coated with Au have been used to verify beam alignment on OMEGA since target experimental operations began.[12] This method can determine the beam placement to an accuracy of ~10 μm. It has been noted for some time that although beam energies have been made to be nearly equal at the output of the laser, intensities on target appear to differ significantly. Figure 91.20 shows an x-ray image from a pointing target recorded by a charge-injection-device (CID), x-ray-sensitive camera[13] at the image plane of an x-ray pinhole camera. (The pinhole cameras use 10-μm-diam pinholes at a distance of 164 mm and a magnification of 4.0. The CID cameras have 38.5-μm-sq pixels, giving a resolution at the target of ~12 μm.) The pinholes themselves are covered with a 101.6-μm-thick Be foil with an additional 50.8 μm of Be between the pinhole and the detector acting as a vacuum window and a light shield for the camera. The camera sensitivity and window transmission provide for an effective energy band with a minimum of ~2 keV and falling sensitivity above 4 keV (see Ref. 13 for further details). Two of the beams at the center of the image have been highlighted (beams 4-2 and 4-4), and lineouts through the images are shown. Despite the fact that the beam energies are reported to be nearly equal, the peak x-ray intensities are seen to differ by a factor of ~2. This suggests that either the reported energies are in error or other factors, such as beam size on target or unaccounted-for losses, differ significantly for these two beams. (These two beams were chosen since from this view the beams are at the same angle to the view direction normal; any angular effects on the observed intensity should therefore be equal.) The following method is suggested by images obtained on beam-pointing shots: Measure the beam intensities on target using a set of cross-calibrated x-ray cameras; correct the observed intensities for view-angle effects and conversion-efficiency dependence. The incident-beam-intensity variations can then be determined. Once these corrections are determined, the beam-to-beam intensity differences can then be reduced, resulting in more nearly spherical implosions. This technique and its application and results are the subject of the remainder of this article.

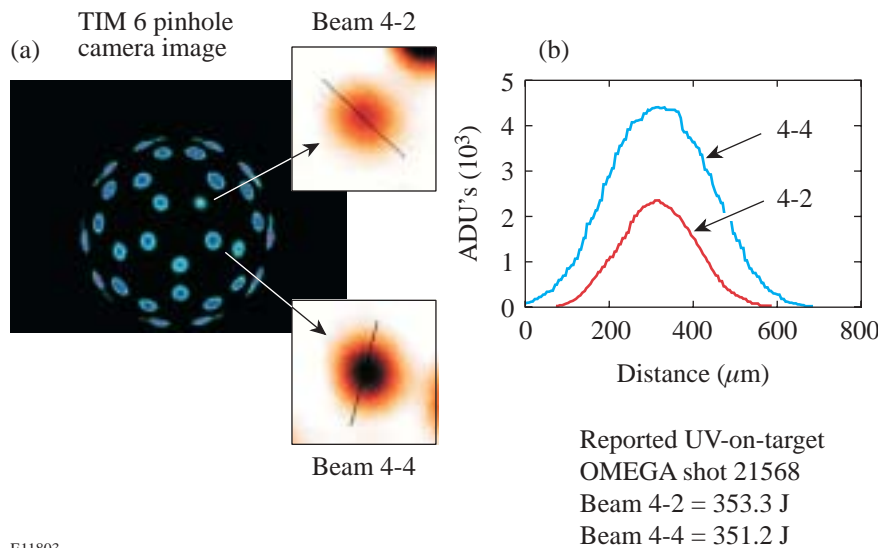Figure 91.20
(a) TIM (ten-inch manipulator)-based pinhole camera image of a 4-mm-diam, Au-coated pointing target taken with a CID camera. Beams 4-2 and 4-4 are shown in enlarged insets. (b) Lineouts through the x-ray beam spots showing the detected intensities in analog-to-digital units (ADU's). Despite nearly equal reported energies, the peak x-ray intensities differ by about a factor of 2.

E11803

1. The View-Angle Effect on the Observed X-Ray Intensity

The effect of view angle on observed intensity has been determined by uniformly illuminating a 1-mm-diam, Au-coated sphere (Fig. 91.21) at an intensity equal to the mean intensity on a pointing shot ($\sim 10^{14}$ W/cm^2). Since all beams now overlap, the individual beam energies are ~ 6 times lower. The azimuthally averaged radial lineout of the x-ray image [Fig. 91.21(b)] is seen to closely match that expected from an optically thin plasma shell, as characterized by

$$I_x(r) = I_x(0) \times (r_0/\Delta r)$$

$$\times \left[\sqrt{(1+\Delta r/r_0)^2 - (r/r_0)^2} - \sqrt{1-(r/r_0)^2} \right], \quad (3)$$

where $I_x(0)$ is the intensity observed at the center of the image (face-on), r is the distance in the target plane from the center of the image, r_0 is the plasma emission radius, and Δr is the plasma thickness. The profile of Fig. 91.21(b) is best fit by values of $r_0 = 500 \ \mu m$ and $\Delta r = 113 \ \mu m$.

2. Camera Cross-Calibration

Up to eight x-ray cameras are used on a pointing shot, producing different views of the beams on target. To compare beam images from two cameras, the view-angle effect must be removed, leaving only the difference in collection solid angle (pinhole area) and camera gain. Figure 91.22 shows one such comparison of beam peak intensities seen from two cameras after correcting for the view-angle effect using Eq. (3) and using the best-fit parameters as determined from the results shown in Fig. 91.21 ($\Delta r = 113 \ \mu m$, whereas $r_0 = 2$ mm for these

targets). The observed intensities follow a straight line with a zero intercept and a slope equal to the ratio of the sensitivity of the two cameras.

E11804
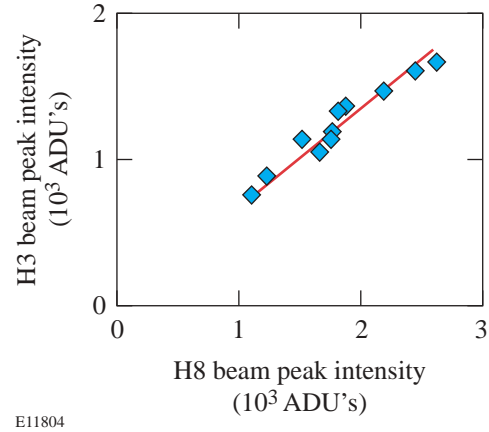
Figure 91.22
View-angle-corrected beam peak intensities as viewed by two x-ray pinhole cameras. The straight-line correlation demonstrates the validity of the view-angle correction and determines the cross-calibration factor for the two cameras.

3. Conversion-Efficiency Dependence and Determination of On-Target Beam-to-Beam Variation

An estimate of the power-law conversion of UV to x rays was determined by varying a single-beam energy, yielding a value of γ in Eq. (2) of ~ 3.7. This preliminary value was then used when fitting values of the observed beam shapes. Combining Eqs. (1) and (2) yields

$$I_x(r) = I_x(0) \times \left[e^{-(r/\sigma_r)^\eta} \right]^\gamma, \quad (4)$$

(a) CID image (H6 view)   (b) Radial profile

1-mm-diam
Au-coated sphere

E11296
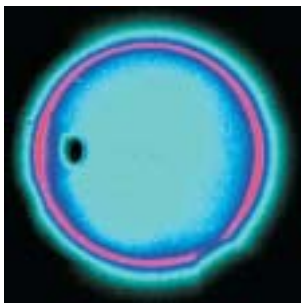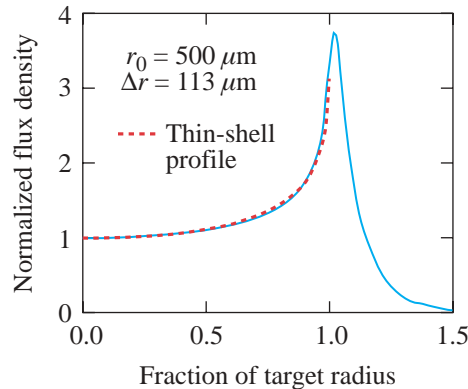
Figure 91.21
(a) An x-ray pinhole camera image of a uniformly illuminated, 1-mm-diam, Au-coated sphere used to determine the angular effect on the observed surface flux density. (b) The azimuthally averaged radial profile of the uniformity target. Regions of the target not covered by gold (at points of support during coating) were excluded from the azimuthal averaging.

where

$$I_x(0) = C_{UV-x} \times \left[I_{UV}(0) \right]^{\gamma}. \qquad (5)$$

Figure 91.23 shows a fit of a single beam (4-4) to Eq. (4). The peak values are determined in this manner for every beam by using up to eight pinhole cameras.
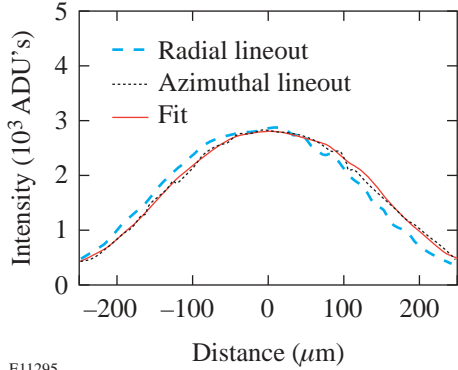
E11295

Figure 91.23
Fit to a single-beam x-ray intensity profile using a super-Gaussian with power-law x-ray conversion efficiency [Eq. (4)].

With a set of cross-calibrated cameras, variations from beam to beam can be determined for all 60 beams of OMEGA. During laser system operation, some beam-energy variation occurs due to variations in amplification and input beam (driver line) energy. System calorimeters [e.g., high-energy diodes (HED's)] are used to account for these variations. If beam-energy variations are accounted for by variations in the HED-measured beam energies, then beam-to-beam variations not due to beam-energy variations should remain the same and show up as differences on target. This is seen in a plot of the ratio of the normalized inferred peak UV intensity I_{UV}^* derived from x-ray imaging to the normalized HED determined UV intensity I_{UV} for all 60 beams on one shot as compared with the average of the same for seven shots (Fig. 91.24). The values are seen to be stable despite large variations in beam energy. Using the average values of these ratios, R_i is given by

$$R_i = I_{UV_i}^* \big/ E_{UV_i}^* , \qquad (6)$$

where $I_{UV_i}^*$ is the normalized x-ray-inferred UV peak intensity and $E_{UV_i}^*$ is the HED-determined normalized UV energy on

target (both for the ith beam). Applying these corrections to the HED-measured energies allows for a more accurate determination of the power-law conversion parameter γ [Eq. (4)]. A best-fit value of $\gamma = 3.42 \pm 0.13$ is seen to fit the observed x-ray to UV variation (Fig. 91.25).
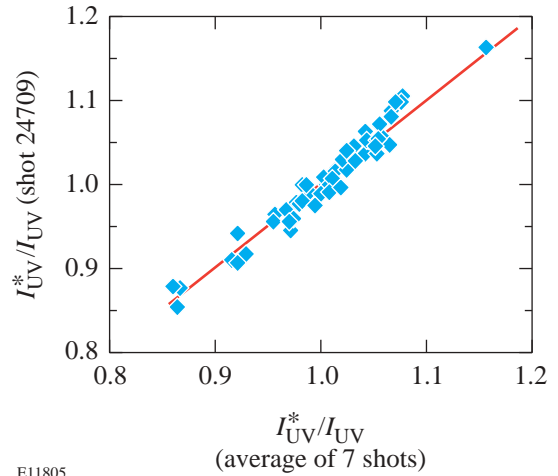
E11805

Figure 91.24
Values of the ratios of the normalized x-ray-inferred beam peak intensities to the normalized HED-inferred beam energies for all 60 beams determined from one pointing shot versus the same values averaged over seven shots. Each data point represents a different beam. The beam energies were purposely varied from ~250 to 440 J, resulting in little change in these ratios despite nearly 100% changes in the peak x-ray intensity.
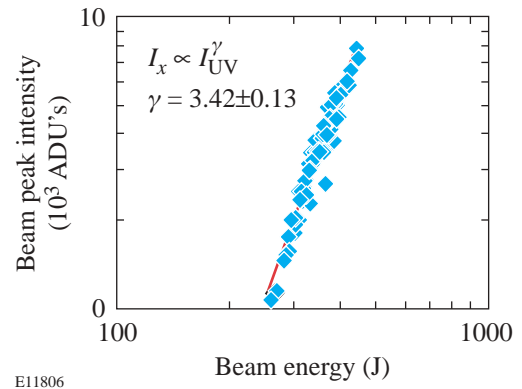
E11806

Figure 91.25
The observed peak x-ray intensities corrected for view-angle effect as a function of the corrected beam energies. The dependence follows a power law of $\gamma = 3.42 \pm 0.13$.

Enhanced On-Target Beam Balance

In the standard balance technique, the gains in the amplifiers by stage, and the losses by stage (primarily in the split regions), are adjusted to produce equal beam energies at the system output calorimeters. The UV energies on target are inferred from continuous-wave (cw) laser measurements of the losses incurred in each beam by the mirrors, lenses, diffracting optics, vacuum windows, and debris shields from the system output calorimeters to the target (i.e., from the transport to the target). Variations of these losses are kept to a minimum by replacement of the poorest-performing elements. In contrast, the enhanced balance technique uses the measured x-ray intensities at the target to determine the gain of the last IR amplifier required to produce equal intensities (x-ray and, hence, by inference UV also) at the target. An algorithm has been developed by which a beam's desired UV energy output can be achieved with a variation in the capacitor-bank voltage of the final disk amplifier.

Using the measured values of R_i, it is possible to further minimize on-target variations by iteration. From Eq. (6) it follows that

$$I^*_{UV_i} = R_i \times E^*_{UV_i} . \tag{7}$$

The normalized beam energies are varied to attempt to make all values of $I^*_{UV_i}$ equal to 1. The adjustments are made by changing the capacitor bank voltage of the last amplifier and by observing the resultant change in output energy. The response follows the equation

$$E_{UV} = E_{IR} \times G_{amp}(V_{bank}) \times \varepsilon_{UV} , \tag{8}$$

where E_{UV} is the inferred UV energy, E_{IR} is the input IR energy, G_{amp} is the gain of the laser amplifier for a capacitor bank voltage of V_{bank}, and ε_{UV} is the efficiency of the UV conversion crystals, which is also a function of G_{amp} and E_{IR}.

Figure 91.26 shows a comparison of a standard balance pointing shot (in which IR variations are minimized) to an enhanced balance pointing shot (in which peak-intensity variations are minimized). The standard balance shot [Fig. 91.26(a)] has a small variation in the HED-determined energies [$\sigma_{rms}(E_{UV}) = 2.8\%$], but a large variation in the inferred normalized UV beam peak intensities [$\sigma_{rms}(I^*_{UV}) = 6.6\%$]. Conversely, the enhanced balance shot [Fig. 91.26(b)] has a larger HED-determined variation [$\sigma_{rms}(E_{UV}) = 6.0\%$], but a

smaller variation in the inferred normalized UV beam peak intensities [$\sigma_{rms}(I^*_{UV}) = 2.2\%$]. The beam-to-beam variations have been reduced by about a factor of 3.
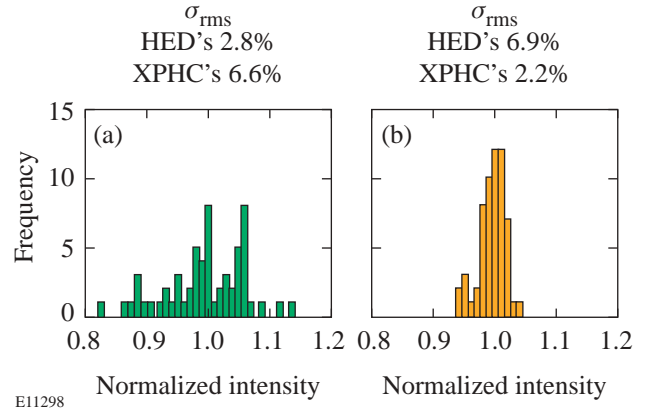
Figure 91.26
The inferred UV beam peak intensity distribution for all 60 beams of OMEGA determined on (a) a standard balance pointing shot and (b) an enhanced balance pointing shot.

Enhanced-Balance Implosion Experiments

With the enhanced-balance-correction constants R_i determined, the beam peak intensities can be inferred from the HED-determined beam energies corrected by the enhanced-correction constants R_i. Figure 91.27 shows x-ray microscope images of a set of implosions performed with standard balance and enhanced balance. Three pairs of targets were used. All were 930-μm-diam, 18.5-μm-thick CH shells filled with 15, 7, and 3 atm of D_2 gas, respectively. A clear difference is seen in the shape of the core apparently due to the change in direct-drive illumination uniformity. [The two cases had average values of $\sigma_{rms}(I^*_{UV}) = 6.0\%$ for the standard balance condition and 2.2% for the enhanced balance condition.] Figure 91.28 shows another comparison of core shape for a different shell thickness (27 μm) and fill pressure (20 atm D_2). All enhanced balance implosions show more-symmetric cores; however, small-scale structure is common to both cases.

Analysis of the angular dependence of the illumination uniformity demonstrates the effect on the implosion. The calculated overlap intensity shown in Fig. 91.29 is displayed in an Aitoff projection for the standard-balance, 15-atm-filled case (shot 24119, see Fig. 91.27). The overlap intensity calculation assumes HED-measured beam energies corrected for by

15-atm-filled   7-atm-filled   3-atm-filled

Standard balance

Enhanced balance

50 μm

CR = 14   CR = 23   CR = 38

E11299
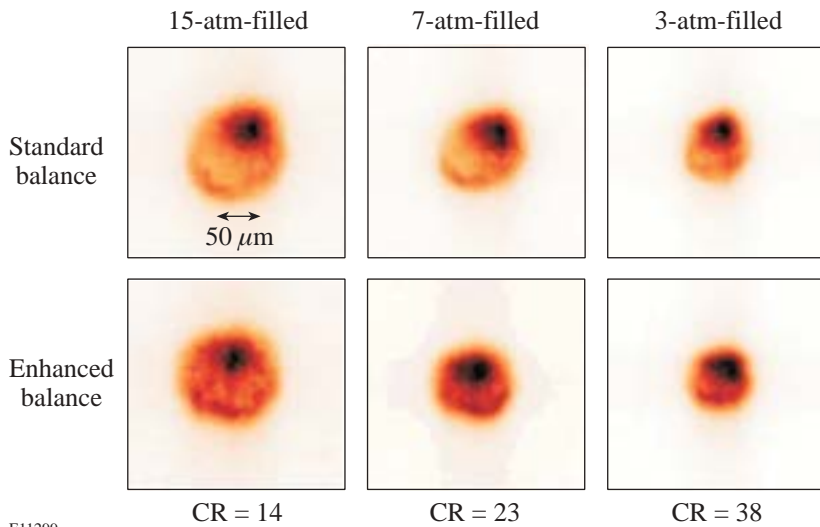
Figure 91.27
Direct-drive implosion experiments performed on OMEGA with 18.5-μm-thick CH shells filled with 15, 7, and 3 atm of D_2 gas. All shots were with ~23 kJ of UV on target in a 1-ns square pulse, using 1-THz SSD with PS. The enhanced balance implosions show a more-uniform spherical stagnation region. The calculated convergence ratios for these implosions (initial fuel–shell interface radius divided by final radius, CR) are indicated.

the enhanced balance analysis [Eq. (7)] with all beams having the same super-Gaussian profile ($r_0 = 300$ μm and $\eta = 2.5$). Absorption is modeled by a simple cosine dependence on the angle the rays make with the target normal. The individual peaks seen are at the overlap of five or six beams and are due to the imperfect overlap of the OMEGA beams with the given target size, number of beams, and beam shape (~1.5% peak to valley for perfect beam balance). Also shown is a lineout through the computed intensity pattern as would impinge on the limb of the target as seen from the x-ray microscope. The intensity pattern has an ~7% peak-to-valley variation with two minima at 40° and 220° and maxima at 120° and 290°, where

the angle referred to is clockwise with respect to the vertical. After applying enhanced balance, the intensity variations due to beam balance are reduced to less than 2%.

(a) $\theta = 0°$

+5

KB3 limb

$\varphi = -180°$ $\varphi = 0°$ $\varphi = 180°$

Intensity (%)

−5

$\theta = 180°$

(b)   Intensity variation on limb of KB3 (%)

+5

0

−5

0   360

Phase angle (°)

E11808

(a)   100 μm   (b)
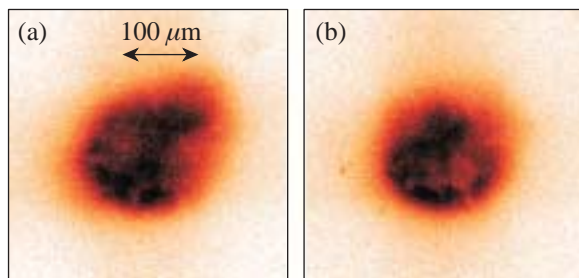
E11807

Figure 91.28
Comparison of KB (Kirkpatrick–Baez) microscope–imaged implosion cores for a pair of 27-μm-thick CH shells filled with 20 atm of D_2, (a) with standard balance and (b) with enhanced balance. The enhanced balance implosion again shows a more spherically shaped core.
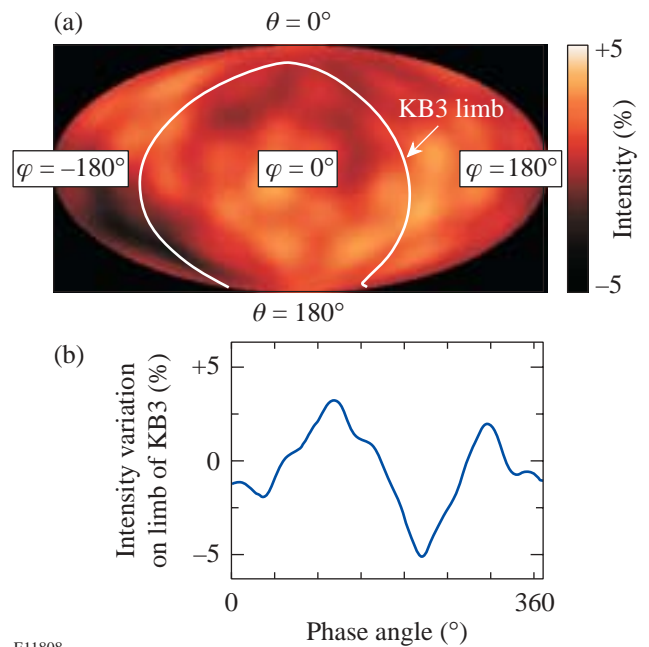
Figure 91.29
(a) The calculated overlap intensity on a standard balance implosion (OMEGA shot 24119) presented as an Aitoff projection of the entire spherical surface. The measurements from the pointing shots infer a peak to valley of 7%. (b) The lineout through the limb of the target as seen from the KB microscope used in Figs. 91.27 and 91.28.

An *ORCHID*[14] 2-D hydrocode simulation was performed using the calculated intensity on the target limb from phase angle 40° to 220° for the axisymmetric laser illumination. Radiation transport is not included in this simulation. The effect of radiation losses, however, was accounted for by lowering the effective incident intensity. By its nature, a 2-D simulation can only simulate axisymmetric flow. Figure 91.30 shows the result of the simulation near the time of maximum shell compression showing a slightly distorted core with an ellipticity $e = 1.08$. Shown as an inset is the observed x-ray image with the axis of the minima in the calculated intensity indicated. The ellipticity of the core image and the simulation are in good agreement, confirming that the main effect is explained by a measurable beam imbalance. Correcting the beam imbalance nearly removes the residual ellipticity as a result of the more-uniform illumination by the 60 beams of OMEGA.

and were filled with 3 or 15 atm of D_2 gas. Figure 91.31(a) shows the ratio of the measured D-D neutron yield to the *LILAC* hydrocode[15]–predicted yield [yield over calculated (YOC)] for these experiments. This measure of target performance is used as a means of comparison to account for differences in energy on target and shell-thickness differences from shot to shot. The enhanced balance target implosions were performed with slightly less energy (typically 21 kJ on enhanced balance shots and 23 kJ on standard balance shots) since after correction for imbalance, some beams could not be raised to sufficiently high levels, necessitating all others to be lowered. The results are seen to follow the included trend lines (dashed) with little obvious difference due to balance condition. Figure 91.31(b) shows the measured ratio of D-T neutron secondary yield to D-D neutron primary yield in these same experiments. [The only difference between the two balance conditions is the apparent larger variation in the standard balance values of the 15-atm-filled target implosions. Despite a definite change to more-symmetric shell stagnations, the primary and secondary neutron yield measurements indicate little dependence of target performance on balance condition (at least

KB3 ellipticity = 1.08

40°

50 μm

OMEGA shot 24119

ORCHID
Isodensity contours
$\tau = 1.9$ ns
Ellipticity = 1.08

E11809

Figure 91.30
Isodensity contours from an *ORCHID* 2-D hydrocode simulation of the implosion of an 18.5-μm-thick, 15-atm-filled CH shell (OMEGA shot 24119). The time of this snapshot is 1.9 ns from the start of the laser pulse (near the time of maximum shell compression). The input intensities used were those calculated for this experiment and occurring on the limb of the target as observed from the KB microscope. The corresponding image is shown as an inset with the symmetry axis of the 2-D simulation indicated.

E11301

Figure 91.31
Measurements of the fusion yield's dependence on balance condition from a set of 3- and 15-atm-D_2-filled CH shell implosions: (a) the ratio of the measured to the simulated primary D-D neutron yield; (b) the ratio of the measured secondary DT neutron yield to the measured primary D-D neutron yield.

The symmetry of the implosions appears to correlate with the beam balance. To determine the effects on other measures of target performance, a series of implosion experiments were performed with 1-THz SSD smoothing with PS and 1-ns square pulses. The targets ranged from 18 to 25 μm in thickness

with these measurements).] Whereas, it has been shown in past experiments that these measurements show a dependence on single-beam smoothing.[5,6,10]

Additional measurements of the directional dependence of the total ρR at the time of peak fusion production have recently been reported by Séguin *et al.*[16] Their measurements are derived from the slowing down of 14.7-MeV D-He^3 fusion reaction-generated protons observed from different directions around the target. They find that the observed ρR asymmetries are significantly different for the two balance conditions reported in this work (standard and enhanced). Although asymmetries still exist, they appear to be lower when the optimum x-ray-inferred enhanced balance condition is imposed.

Conclusions

A method for determining and optimizing the beam-to-beam intensity variation of the 60 beams of the OMEGA laser system, as configured for direct-drive illumination (with 1-THz SSD and polarization smoothing), has been developed. This method infers the beam-to-beam energy balance by direct observation of x rays emitted by Au plasmas produced by OMEGA's focused high-power laser beams. The UV energy balance is determined from the observed x-ray balance by taking into account x-ray conversion efficiency and view-angle effects in a semi-empirical manner. Optimized or enhanced balance is achieved by removing the precisely determined beam-to-beam energy variation by adjusting the gain of the last amplifier. The method has achieved a three-fold reduction in the beam imbalance, from an inferred level of ~6% (rms) to ~2% (rms).

Direct-drive implosions with enhanced beam balance consistently show more spherically shaped stagnation cores. A 2-D hydrocode simulation of an uncorrected (standard balance) implosion shows that the magnitude and direction of the resulting core distortion are consistent with arising from beam imbalance. In contrast there is little effect on the YOC ratio or fuel areal density.

The small differences in beam-to-beam energy (<10%) have not been explained by repeated measurements of transport losses in the mirrors, lenses, diffracting optics, and windows. It is likely that the differences are due to scattering losses not accounted for by the spatially integrating techniques employed to measure transport and can be determined only by a technique, such as described in this work, that measures the intensity at the target with calibrated imaging diagnostics.

REFERENCES

1. J. Nuckolls *et al.*, Nature **239**, 139 (1972).

2. J. D. Lindl, *Inertial Confinement Fusion: The Quest for Ignition and Energy Gain Using Indirect Drive* (Springer-Verlag, New York, 1998), Chap. 6, pp. 61–82.

3. S. E. Bodner, D. G. Colombant, J. H. Gardner, R. H. Lehmberg, S. P. Obenschain, L. Phillips, A. J. Schmitt, J. D. Sethian, R. L. McCrory, W. Seka, C. P. Verdon, J. P. Knauer, B. B. Afeyan, and H. T. Powell, Phys. Plasmas **5**, 1901 (1998).

4. T. R. Boehly, D. L. Brown, R. S. Craxton, R. L. Keck, J. P. Knauer, J. H. Kelly, T. J. Kessler, S. A. Kumpan, S. J. Loucks, S. A. Letzring, F. J. Marshall, R. L. McCrory, S. F. B. Morse, W. Seka, J. M. Soures, and C. P. Verdon, Opt. Commun. **133**, 495 (1997).

5. F. J. Marshall, J. A. Delettrez, V. Yu. Glebov, R. P. J. Town, B. Yaakobi, R. L. Kremens, and M. Cable, Phys. Plasmas **7**, 1006 (2000).

6. F. J. Marshall, J. A. Delettrez, R. Epstein, V. Yu. Glebov, D. R. Harding, P. W. McKenty, D. D. Meyerhofer, P. B. Radha, W. Seka, S. Skupsky, V. A. Smalyuk, J. M. Soures, C. Stoeckl, R. P. Town, B. Yaakobi, C. K. Li, F. H. Séguin, D. G. Hicks, and R. D. Petrasso, Phys. Plasmas **7**, 2108 (2000).

7. C. Stoeckl, C. Chiritescu, J. A. Delettrez, R. Epstein, V. Yu. Glebov, D. R. Harding, R. L. Keck, S. J. Loucks, L. D. Lund, R. L. McCrory, P. W. McKenty, F. J. Marshall, D. D. Meyerhofer, S. F. B. Morse, S. P. Regan, P. B. Radha, S. Roberts, T. C. Sangster, W. Seka, S. Skupsky, V. A. Smalyuk, C. Sorce, J. M. Soures, R. P. J. Town, J. A. Frenje, C. K. Li, R. D. Petrasso, F. H. Séguin, K. Fletcher, S. Padalino, C. Freeman, N. Izumi, R. Lerche, and T. W. Phillips, Phys. Plasmas **9**, 2195 (2002).

8. Laboratory for Laser Energetics LLE Review **81**, 6, NTIS document No. DOE/SF/19460-335 (1999). Copies may be obtained from the National Technical Information Service, Springfield, VA 22161.

9. S. Skupsky, R. W. Short, T. Kessler, R. S. Craxton, S. Letzring, and J. M. Soures, J. Appl. Phys. **66**, 3456 (1989).

10. D. D. Meyerhofer, J. A. Delettrez, R. Epstein, V. Yu. Glebov, V. N. Goncharov, R. L. Keck, R. L. McCrory, P. W. McKenty, F. J. Marshall, P. B. Radha, S. P. Regan, S. Roberts, W. Seka, S. Skupsky, V. A. Smalyuk, C. Sorce, C. Stoeckl, J. M. Soures, R. P. J. Town, B. Yaakobi, J. D. Zuegel, J. Frenje, C. K. Li, R. D. Petrasso, D. G. Hicks, F. H. Séguin, K. Fletcher, S. Padalino, M. R. Freeman, N. Izumi, R. Lerche, T. W. Phillips, and T. C. Sangster, Phys. Plasmas **8**, 2251 (2001).

11. P. D. Goldstone, J. A. Cobble, A. Hauer, G. Stradling, W. C. Mead, S. R. Goldman, S. Coggeshall, M. C. Richardson, P. A. Jaanimagi, O. Barnouin, R. Marjoribanks, B. Yaakobi, F. J. Marshall, P. Audebert, and J. Knauer, in *X Rays from Laser Plasmas*, edited by M. C. Richardson (SPIE, Bellingham, WA, 1987), Vol. 831, pp. 54–61.

12. J. M. Soures, R. L. McCrory, C. P. Verdon, A. Babushkin, R. E. Bahr, T. R. Boehly, R. Boni, D. K. Bradley, D. L. Brown, R. S. Craxton, J. A. Delettrez, W. R. Donaldson, R. Epstein, P. A. Jaanimagi, S. D. Jacobs, K. Kearney, R. L. Keck, J. H. Kelly, T. J. Kessler, R. L. Kremens, J. P. Knauer, S. A. Kumpan, S. A. Letzring, D. J. Lonobile, S. J. Loucks, L. D. Lund, F. J. Marshall, P. W. McKenty, D. D. Meyerhofer, S. F. B. Morse, A. Okishev, S. Papernov, G. Pien, W. Seka, R. Short, M. J. Shoup III, M. Skeldon, S. Skupsky, A. W. Schmid, D. J. Smith, S. Swales, M. Wittman, and B. Yaakobi, Phys. Plasmas **3**, 2108 (1996).

13. F. J. Marshall, T. Ohki, D. McInnis, Z. Ninkov, and J. Carbone, Rev. Sci. Instrum. **72**, 713 (2001).

14. R. L. McCrory and C. P. Verdon, in *Inertial Confinement Fusion*, edited by A. Caruso and E. Sindoni (Editrice Compositori, Bologna, Italy, 1989), pp. 83–124.

15. M. C. Richardson, P. W. McKenty, F. J. Marshall, C. P. Verdon, J. M. Soures, R. L. McCrory, O. Barnouin, R. S. Craxton, J. Delettrez, R. L. Hutchison, P. A. Jaanimagi, R. Keck, T. Kessler, H. Kim, S. A. Letzring, D. M. Roback, W. Seka, S. Skupsky, B. Yaakobi, S. M. Lane, and S. Prussin, in *Laser Interaction and Related Plasma Phenomena*, edited by H. Hora and G. H. Miley (Plenum Publishing, New York, 1986), Vol. 7, pp. 421–448.

16. F. H. Séguin, C. K. Li, J. A. Frenje, S. Kurebayashi, R. D. Petrasso, F. J. Marshall, D. D. Meyerhofer, J. M. Soures, T. C. Sangster, C. Stoeckl, J. A. Delettrez, P. B. Radha, V. A. Smalyuk, and S. Roberts, Phys. Plasmas **9**, 3558 (2002).

Effects of Textures on Hydrogen Diffusion in Nickel

Introduction

The transition metal–hydrogen systems have been intensively researched for many years because of the various applications of these systems. A large hydrogen solubility in some transition metals allows their use for safe and high-capacity hydrogen storage.[1,2] At the other end of the spectrum, hydrogen ingress at low concentrations can induce mechanical degradation of nickel and nickel alloys and compromise the intended application of the metal.[1,3] An understanding of hydrogen adsorption/desorption characteristics on, and hydrogen mobility in, the metals is needed to predict the hydrogen impact on the metal systems.

Both deuterium and tritium are used as fuel for inertial confinement fusion (ICF) energy. In ICF applications, both adsorption on surfaces and permeation through metals are of importance. Hydrogen adsorption and desorption processes intimately control the degree to which surfaces become contaminated and subsequently the extent to which these surfaces can be decontaminated. In general, the smaller the adsorption rate, the shorter the residence time on a surface, and the simpler the structure of the oxide on a surface, the less susceptible that surface is to tritium contamination for a given set of exposure conditions. Contamination can proceed by simple condensation on a surface followed by absorption into the subsurface structure and by beta-activated radical surface reactions that capture mobile tritium atoms on surfaces into more tightly bound tritium-bearing complexes that are difficult to remove.

Surface tritium can also be absorbed into the metal and permeate to the opposite side, from where it can escape the process loop or contaminate a coolant circuit. For example, a nickel-alloy vessel with 1/32-in.-thick walls filled with tritium gas at 1 atm and room temperature will permeate 0.3 pCi/s/cm^2 in steady state, a tolerable release rate in part because the time to attain steady state is 6.3 years. At 300°C, however, this container will reach steady-state permeation within 1.6 h and release tritium at 0.8 μCi/s/cm^2. Such releases are unacceptably high and require intervention to preclude unacceptable releases to the environment or accumulation in cooling cir-

cuits. Permeation-resistant barriers, engineered composites, and low-absorption-coated, textured surfaces can offer relief from these emissions.

Hydrogen molecules dissociate on metal surfaces, dissolve atomically into the substructure, and interact with the microstructure of the metals. The interaction depends not only on the hydrogen concentration in the bulk but also on the prevalent microstructure; i.e., the mixture of crystal defects, grain boundaries, grain size, grain orientation, and phase composition present within the metal matrix. The density and blend of these features depends on the manufacturing and operating history of the metal.

For example, electrodeposition is the preferred approach to fabricate nickel membranes in industry. The texture of the nickel membranes can be controlled by the deposition parameters. Since hydrogen permeation in single-crystal metals is anisotropic, textured polycrystalline metals may exhibit different permeation properties for different textures. While an earlier study[4] has shown that texture can influence hydrogen adsorption and diffusion in metals, to date there has been no systematic investigation of the effect of textures on hydrogen permeation through nickel. In this article, the relationship between hydrogen permeation and grain orientation in nickel membranes is studied. To this end, the following section outlines the experimental procedures used to prepare and characterize the nickel membranes and to measure the permeability of the membrane. Subsequent sections describe the details of the microstructure and its influence on permeation.

Experimental Procedure

Nickel membranes were electroplated in a Watt's bath at 50°C. The electrolyte comprised 300 g/l of NiSO$_4$ • 6H$_2$O, 35 g/l of NiCl$_2$ • 6H$_2$O, and 35 g/l of H$_3$CO$_3$ to make a pH-3 liquid. The electroplating current density was controlled galvanostatically between 0.1 to 0.8 A/cm^2. The anode was pure nickel. A titanium cathode substrate was chosen to support the nickel film during deposition because the nickel membranes could be easily peeled off. The substrate surface

was mechanically polished to minimize imprinting the substrate grain structure on the growing nickel film. Additionally, film thickness usually exceeded 50 μm to further minimize imprinting the substrate orientation on the film's texture in preference for that favored by the electrodeposition parameters. The nickel deposits were then removed from the substrates to measure their grain orientation without any interference from the substrate. The permeability of these membranes were subsequently studied in an electrochemical cell.

The membrane surface texture was measured with a Siemens x-ray diffractometer outfitted with a molybdenum target. Maps of the orientation of the (100), (110), and (111) directions were measured in 5° polar and radial steps up to a maximum tilt of 80°. Orientation distribution functions (ODF) were calculated from these maps, also known as pole figures, according to the procedure described by Bunge[5] with the aid of the software TexTool 3.0.

Hydrogen permeation was measured electrochemically with the aid of two cells separated by the nickel membrane of interest using the configuration shown in the Fig. 91.32. Hydrogen was injected into the membrane on the upstream side at a fixed rate, and the extraction rate was measured on the downstream side.

The electrolyte in both cells was 0.1 N NaOH to yield a pH 13 solution. On the exit (anode) side, a separate Ni/NiO electrode served as a saturated calomel electrode to maintain the membrane at a constant potential of 0.3 V relative to the anode. Prior to any measurements, both compartments were deoxygenated by bubbling nitrogen gas through the solutions. The measurements were carried out at 22°C. Before charging the membrane, an anodic potential 0.3 V was applied for 24 h to extract any residual hydrogen from the membrane and to reduce the background permeation current density. A graphite

cathode on the entry side was polarized galvanostatically to ensure that the singly charged ionic hydrogen flux impinging on the upstream surface was constant and fixed at a current density of 0.1 mA/cm^2. At this current density, the hydrogen flux reaching the membrane is 6×10^{14} particles/s-cm^2. Permeant hydrogen is collected downstream of the membrane as the anodic current flows between the membrane and the anode. Sometime after the initiation of a cathodic current, an anodic current appears downstream and grows in strength to a maximum value. At this time, the hydrogen concentration gradient across the membrane thickness is linear, being highest at the entry side and nearly zero at the exit side. The time integral of the permeation current becomes constant once the linear concentration gradient is established within the membrane. Extrapolating the straight portion of the time-integrated curve back to the time axis yields a unique value known as the lag time (t_L). This time is related to the hydrogen diffusion coefficient (D) for the material[6] by the relation

$$t_L = \frac{x^2}{2D}, \tag{1}$$

where x is the membrane thickness.

The concentration of adsorbed hydrogen on the upstream surface reflects the dynamic equilibrium between particles arriving from the electrolyte and particles disappearing into the metal. If the arrival flux rate far exceeds the absorption flux rate, hydrogen bubbles form on the upstream surface. Hydrogen transport through the metal is the rate-limiting step. If the absorption rate exceeds the arrival rate, the permeant flux is limited by the hydrogen arrival rate at the surface rather than by the adsorption rate into the metal. In this work, hydrogen transport through the metal is the rate-limiting step. In this case, steady-state permeation is described by Fick's First Law, and the concentration of absorbed hydrogen on the input

E11789
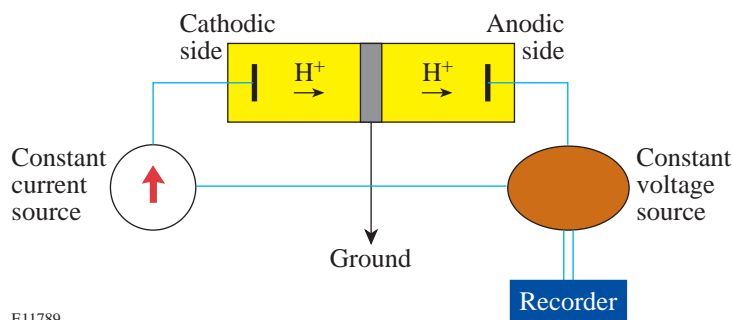
Figure 91.32
Schematic layout of the electrolytic permeation facility.

surface, C_0, is uniquely related to the steady-state anodic current density I_{ss} by the relation

$$C_0 = \frac{I_{ss}x}{FD},\qquad(2)$$

where F is the Faraday constant (= 96,485 Coul/g-atm).

Results and Discussion

1. Microstructure and Texture

The microstructure across the cross section of each nickel deposit comprised three distinct zones. Grains in the vicinity of the film–substrate interface were equiaxed and fine. Immediately above this layer, the structure began to change from equiaxed grains to columnar grains. Beyond that and for the remainder of the film up to the nickel–air interface, the grains were columnar and orientated perpendicular to the substrate for most electroplating conditions.

The orientation of grains, i.e., the texture of the surface, was measured by Bragg diffraction to generate the ODF's. Figure 91.33 illustrates the ODF of the titanium substrate used in this work. This ODF is typical of a cold-rolled titanium plate.[7] A typical ODF for a nickel membrane electrodeposited for the present work is presented in Fig. 91.34. Inspection of these two distribution functions indicates that there has been no textural imprinting by the substrate on the nickel deposit. The nickel texture has been determined solely by the deposition parameters.

Either (100) or (110) fiber textures can been obtained by changing the deposition conditions. At low current density, the (100) fiber texture is preferred. At high current density, the (110) fiber texture dominates. The (111) texture can be derived by annealing deposits with strong <100> texture at 800°C for 1 h.[8]

E11790
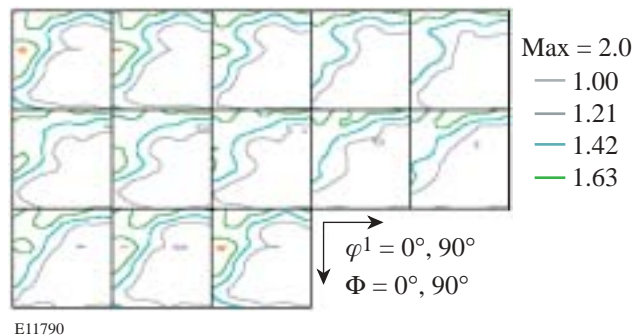
Figure 91.33
Orientation distribution function of the titanium substrate.

E11791
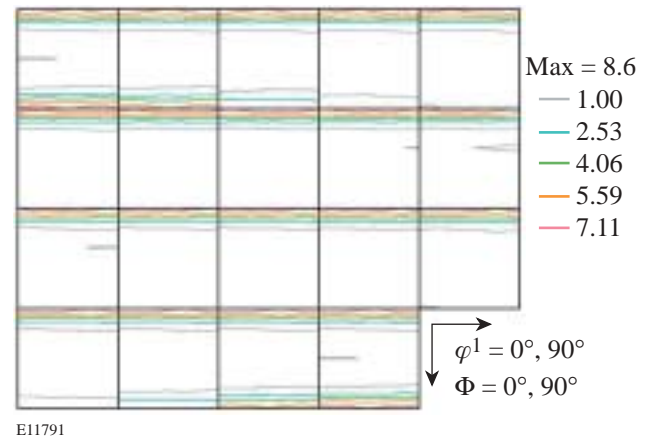
Figure 91.34
Orientation distribution function of nickel deposit.

2. Hydrogen Permeation and Analysis

The temporal behavior of hydrogen permeation through nickel with different textures is shown in Fig. 91.35. The permeation behavior for a nickel sample without any dominant texture has been included for reference. In all cases, the permeation current increases smoothly with increasing charging time to a maximum constant value. There are significant differences, however, among the textured and nontextured membranes. Hydrogen transport through (111) texture is faster than for any of the other textures. The time to attain steady-state permeation is longest in (110) texture nickel. Compared to the sample without any dominant texture, the response time for surfaces with a dominant texture is rapid.

E11792
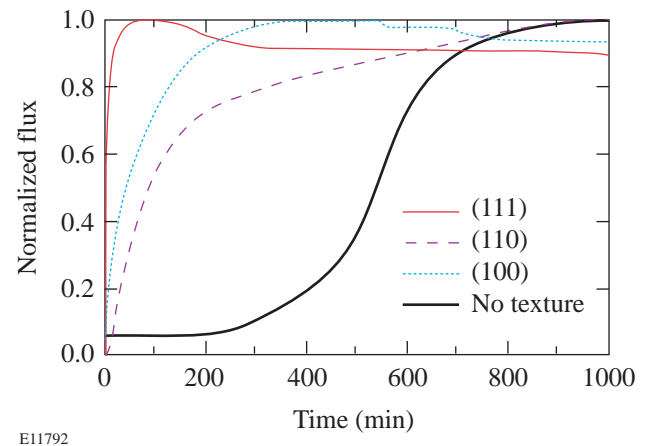
Figure 91.35
Temporal evolution of hydrogen permeation through nickel membrane with differing textures and for a sample without any dominant texture.

Hydrogen diffusivity and near-surface hydrogen concentration have been calculated using Eqs. (1) and (2) for the various nickel membranes and are listed in Table 91.III. Diffusion coefficients for (100) and (110) single-crystal samples have been provided for comparison. The coefficients are seen to increase as one moves toward more-open crystal structures, i.e., from (100) to (110) and then to (111) textured samples. The sample without any dominant texture exhibits the lowest diffusion coefficient of all the samples investigated. Diffusion coefficients for polycrystalline nickel membranes with dominant (100) and (110) textures are respectively higher than for (100) and (110) single-crystal membranes, but both exhibit the same trend when moving toward more-open structures, i.e., from (100) to (110) textures.

The near-surface concentration (C_0) of hydrogen in the sample without any dominant texture is the highest. The concentrations in (111) and (110) textured cases are the lowest of the samples studied and lie within experimental error of each other. This table suggests that the near-surface hydrogen concentration on the upstream side of the membrane is depleted by rapid transport through the membrane. The higher the diffusivity, the lower the subsurface hydrogen concentration.

Hydrogen permeation through a metal membrane in an electrochemical environment involves three steps: hydrogen atom absorption, diffusion across the membrane, and desorption. The molecular dissociation and the atomic association steps on the upstream and downstream sides of the membrane respectively that are normally associated with gas-phase hy-

drogen permeation are not present in this case because the hydrogen arrives and leaves the membrane as ions in the electrolyte. Hydrogen transport is characterized by three interaction energies: absorption, diffusion, and desorption. Typically adsorption and desorption energies are the same for polycrystalline metals without any dominant texture. The diffusion energy tends to be governed by bulk microstructural features, such as grain orientation, grain boundary density, and trap density. Both activation energies can influence the total hydrogen permeation flux and the temporal evolution of that flux.

Hydrogen adsorption energies differ for various crystal planes.[12–14] These have been measured for the three low-index planes: (100), (110), and (111) of nickel.[12] The net adsorption energy of a surface can be estimated from weight-averaged linear combinations of adsorption energies on low-index planes and the preponderance of those planes on a specific surface. Typically, the results are displayed on an inverse pole figure to account for the distribution of the low-index planes in a selected direction in the specimen relative to the crystal axes. Crystals in face-centered cubic metals such as nickel possess higher degrees of symmetry, and the three low-index planes, (100), (110), and (111), are adequate to uniquely specify a surface orientation. Consequently only the unit stereographic triangle needs to be shown. Figure 91.36 displays the net surface adsorption energy dependence of hydrogen on nickel. This figure shows that the adsorption energy is highest for (100) and lowest for (111). Hydrogen is expected to adsorb more easily through (111) planes than either (100) or

Table 91.III: Hydrogen permeation data for nickel with different textural surfaces.

Membrane Surface Structure		D (10^{-9} cm^2/s) ±5%	C_0 (mmol/cm^3) ±10%
Polycrystalline Ni	No texture	2.6	0.38
	(100)	3.4	0.18
	(110)	6.5	0.12
	(111)	8.5	0.13
Single-Crystal Ni	(100)	0.56 (Ref. 9)	
		0.51 (Ref. 10)	
	(110)	0.62 (Ref. 11)	

(110) planes. As a consequence, hydrogen ingress and transport through nickel can be tailored by altering the surface orientation of crystals to favor or suppress the (111) plane.
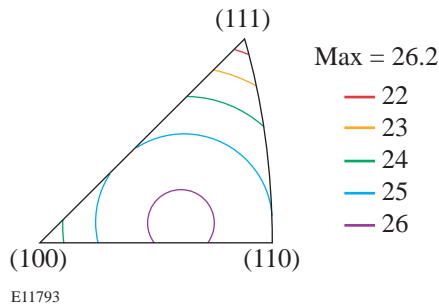

Figure 91.36
Hydrogen absorption energies for the three low-index planes in nickel.

Diffusivity can also be modulated by orientation.[9–11] Table 91.III indicates that hydrogen transport is more rapid in single crystals via (110) than (100) orientations. Polycrystalline membranes are combinations of many single crystals with different orientations. Texturing a polycrystalline membrane provides a method for selecting a dominant orientation with the intent of enhancing or suppressing hydrogen adsorptions and subsequent transport. Hydrogen transport can be modulated by textural control in addition to the bulk microstructural features discussed earlier.

Conclusions

Nickel membranes with differing textures have been grown and analyzed. Deposition parameters that influence the texture during the growing process have been identified. These protocols were implemented to construct membranes for permeation experiments. Electrolytic permeation has been used to study the impact of texture on hydrogen permeation through nickel.

Four conclusions can be derived from this work: First, textured nickel films can be grown on titanium without textural imprinting from the substrate. Plating current density has a strong influence on texture forms of nickel deposits. At low current density, the (100) fiber texture is the dominant component; at high current density, the (110) fiber texture dominates. Annealing at 800°C for 1 h, (100) texture converts to (111) texture. Second, hydrogen permeation through nickel membranes depends on texture. Diffusion coefficients increase as one moves from (100) to (110) to (111) textured samples. The diffusion coefficient of a sample without a dominant texture is smaller than for textured samples. Diffusion coefficients of polycrystalline textured membranes are higher than similar single-crystal membranes, but both sets of membranes exhibit similar trends in behavior. Third, adsorption energies for different orientations have been calculated by using the weight-averaged combinations of the absorption energies for the three basic planes in nickel: (100), (110), and (111). Absorption energies for different orientations are presented. Finally, hydrogen transport in the bulk is expected to depend on texture in addition to the microstructural features such as grain size, traps, and grain boundary density typically discussed in the literature.

REFERENCES

1. H. Wipf and R. G. Barnes, *Hydrogen in Metals III: Properties and Applications*, Topics in Applied Physics, Vol. 73 (Springer, Berlin, 1997).

2. K. Hong, J. Alloys Compd. **321**, 307 (2001).

3. R. M. Latanision and M. Kurkela, Corrosion **39**, 174 (1983).

4. Y. Cao, J. A. Spunar, and W. T. Shmayda, "Microstructure Control Factors of Hydrogen Diffusion Through Palladium and Pd-Ag Membranes," to be published in *Defect and Diffusion Forum*.

5. H.-J. Bunge, *Texture Analysis in Materials Science: Mathematical Methods* (Butterworths, London, 1982).

6. M. A. V. Devanathan and Z. Stachurski, Proc. R. Soc. Lond. A, Math. Phys. Sci. **270**, 90 (1962).

7. H. Inoue and N. Inakazu, in *Eighth International Conference on Textures of Materials (ICOTOM 8)*, edited by J. S. Kallend and G. Gottstein (The Metallurgical Society, Warrendale, PA, 1988), pp. 997–1004.

8. F. Czerwinski and J. A. Szpunar, Corros. Sci. **41**, 729 (1999).

9. A. M. Brass and A. Chanfreau, Acta Mater. **44**, 3823 (1996).

10. Y. Ebisuzaki, W. J. Kass, and M. O'Keeffe, J. Chem. Phys. **46**, 1378 (1967).

11. A. M. Brass, A. Chanfreau, and J. Chene, in *Hydrogen Effects on Materials Behavior*, edited by N. R. Moody and A. W. Thompson (Minerals, Metals, and Materials Society, Warrendale, PA, 1990), pp. 19–31.

12. G. Kresse and J. Hafner, Surf. Sci. **459**, 287 (2000).

13. K. Christmann *et al.*, J. Chem. Phys. **70**, 4168 (1979).

14. G. Kresse, Phys. Rev. B, Condens. Matter **62**, 8295 (2000).

Superconducting Properties of MgB$_2$ Thin Films Prepared on Flexible Plastic Substrates

The recent discovery of superconductivity at 39 K in hexagonal magnesium diborides[1] has stimulated very intensive investigations of the fundamental mechanism of superconductivity in MgB$_2$ as well as the possible practical applications of this new superconductor. In comparison with high-temperature cuprates, MgB$_2$ superconductors have more than two-times-lower anisotropy, significantly larger coherence length, and higher transparency of grain boundaries to the current flow. At the same time, when compared to conventional metallic superconductors (including Nb$_3$Sn or NbN), they have at least two-times-higher critical temperature T_c and energy gap, as well as higher critical current density J_c. As a result, MgB$_2$ superconductors are expected to play an important role for high-current, high-field applications, as well as in cryoelectronics, where they might be the material-of-choice for above-300-GHz clock-rate digital electronics. In addition, MgB$_2$ devices could operate in simple cryocoolers.

The availability of high-quality superconducting thin films with single-crystal-like transport properties[2] is the key to realization of practical MgB$_2$ cryoelectronic devices. Films with high values of T_c and J_c have been prepared on SrTiO$_3$, Al$_2$O$_3$, Si, SiC, and other substrates by various deposition techniques.[3–8] All of the above procedures required post-annealing at temperatures higher than 600°C, and the superconducting properties of the resulting films depended very strongly on the conditions of their annealing. The best reported MgB$_2$ thin films are characterized by $T_c \approx 39$ K and $J_c > 10^7$ A/cm^2 at 4.2 K and 5×10^5 A/cm^2 at 30 K, both at zero external magnetic field.[9] Preparation of MgB$_2$ thin films on unconventional substrates, such as stainless steel[10] or plastic foils, is also desirable. MgB$_2$-on-steel films are interesting for the preparation of low-magnetic shielding and antennas, while plastic foils are very attractive for their bending and shaping abilities.

In this article, we present the preparation and superconducting properties of MgB$_2$ thin films fabricated on flexible substrates (Kapton-E polyamide foil), using three specially designed, rapid annealing processes. Flexible plastic substrates introduce a number of novel aspects to superconducting technology, such as the ability to cut the final structures into desired shapes for, as an example, magnetic shielding. They are also unbreakable and can be rolled into small superconducting coils or form flexible microwave or high-speed digital microstrips and coplanar transmission lines.

Kapton-E foils up to 20×20 cm^2 (limited in size by our deposition apparatus) were cleaned in acetone, ultrasonically washed in ethanol, and air-dried before being placed in our vacuum chamber. Mg-B precursor films 100 nm to 200 nm thick with a nominal composition of 1:2 were prepared on the unheated foil by simultaneous evaporation of Mg (purity 99.8%) and B (purity 99.9%) from separate W and Ta resistive heaters at a vacuum of 8×10^{-4} Pa. After deposition, the Mg-B films were *ex-situ* annealed in a special low-temperature process to avoid overheating the Kapton foil, which had to be kept below its 300°C deformation temperature.

Several rapid annealing procedures have been implemented. Initially, the Mg-B films were placed inside a quartz tube on a thick sapphire plate and introduced for 10 to 300 s into a preheated furnace. The furnace temperature varied from 350°C to 500°C, and the Ar atmosphere could be changed from 3 kPa to 100 kPa in a flow regime. In another approach, the Mg-B films were placed "face down" on a resistive heater and annealed at 500°C to 600°C in pure Ar for 60 to 180 s. For overheating protection, the foil was covered with a sapphire plate and a large Cu block on top. After annealing, the samples were cooled down in approximately 30 s to room temperature. Both of the above annealing methods resulted in superconducting MgB$_2$ with $T_{c,\mathrm{on}}$ up to 33 K and a transition temperature $\Delta T_c \approx 10$ K. The highest $T_{c,\mathrm{on}}$ was obtained after annealing for 180 s at 500°C on a resistive heater. Unfortunately, under such conditions, the color of the Kapton foil changed from yellow to black and it partially lost its flexibility. The maximal J_c was only about 500 A/cm^2 at 4.2 K, suggesting that the damaged foil stressed the MgB$_2$ film.

Much better results were obtained using the third annealing method; thus, the remainder of this work will be devoted to

those films. The Mg-B thin films were radiatively heated with halogen lamps in vacuum; simultaneously, the substrate side of our samples was placed on an external water-cooled radiator to protect the plastic foil. The distance between the samples and the halogen source was 7 cm, and the vacuum chamber was pumped down to a base pressure of 1×10^{-2} Pa to minimize the oxygen content and other gas impurities during annealing. The foil temperature was controlled by a thermocouple located very close to its surface. The duration of the annealing process was 60 to 180 s, and the temperature at the film surface varied from 300°C to 650°C. After annealing, the vacuum chamber was filled with Ar and the films were cooled to room temperature in 20 to 30 s. Even for the highest Mg-B annealing temperature, the Kapton was always kept below 300°C, no deformation or change of color was observed, and the resulting MgB_2 samples were fully flexible.

Figure 91.37 shows the surfaces and the critical temperature parameters of three films annealed under different condi-

tions. For samples annealed for at least 1 min at film surface temperatures of 550°C to 650°C, the film morphology exhibited domains or lamellar structures [Figs. 91.37(a) and 91.37(b), respectively] and their maximal $T_{c,\text{on}}$ was only 20 K and 30 K, respectively. The film presented in Fig. 91.37(b) showed signs of heat-induced substrate damage and its ΔT_c was very wide. After extensive trial-and-error studies, we realized that the best annealing conditions consisted of pre-heating at 300°C and only very brief, 30-s heating at 600°C, followed by post-heating for 60 s again at 300°C. The films produced in this manner were characterized by very smooth surfaces [Fig. 91.37(c)], without domains, cracks, or lamellar structures. X-ray diffraction exhibited no diffraction peaks, indicating an amorphous phase analogous to that of similar post-annealed MgB_2 films prepared on Si and sapphire substrates from Mg-B precursors.[6]
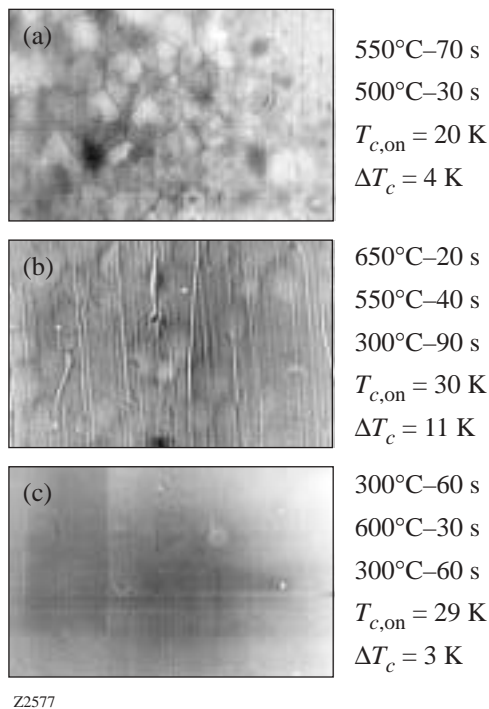
The homogeneity of our thin films was studied by Auger spectroscopy. The Auger spectra (Fig. 91.38) show a strong non-stoichiometry of Mg and B on the film surface, as well as an enhanced content of oxygen and presence of carbon. The damaged surface layer was only ~20 nm thick, however, as estimated by the rate of Mg-B etching and scanning electron microscopy studies. The bulk of the film had a uniform 1:2 stoichiometry ratio, with only small oxygen content, apparently from the residual oxygen in the annealing vacuum chamber.

(a)	550°C–70 s
	500°C–30 s
	$T_{c,\text{on}} = 20$ K
	$\Delta T_c = 4$ K
(b)	650°C–20 s
	550°C–40 s
	300°C–90 s
	$T_{c,\text{on}} = 30$ K
	$\Delta T_c = 11$ K
(c)	300°C–60 s
	600°C–30 s
	300°C–60 s
	$T_{c,\text{on}} = 29$ K
	$\Delta T_c = 3$ K

Z2577

Figure 91.37
Scanning-electron-microscope pictures of three MgB_2 thin films annealed under different conditions in the halogen lamp process. Each picture is identified by the film-annealing temperatures and times, and the resulting $T_{c,\text{on}}$ and ΔT_c. The optimal conditions correspond to the film shown in panel (c).

Z2578

Figure 91.38
The depth profile of an optimally annealed [Fig. 91.37(c)] MgB_2 film, obtained from the Auger measurement.

The films prepared according to the annealing recipe shown in Fig. 91.37(c) also had the best superconducting properties. The maximal $T_{c,\text{on}}$ obtained was 29.3 K, as shown in Fig. 91.39, where we plotted the resistive superconducting transitions for both the stripe cut from a film by scissors and the one patterned by photolithography and Ar-ion etching. The

cut stripe was approximately 1 mm wide and its superconducting properties are representative of our plain MgB$_2$ films, while the patterned bridge was 10 μm wide and 120 μm long. We note that Ar-ion etching resulted in a slight reduction of $T_{c,\text{on}}$; at the same time, however, ΔT_c was decreased to 2 K. The patterned microbridge was also used for J_c measurements. The inset in Fig. 91.39 shows the J_c dependence on temperature, together with the fit based on $J_c(T) = k(1-T/T_c)^\alpha$, where k is a constant and α is a fitting parameter. The fit shown in Fig. 91.39 was obtained for $\alpha = 2$ and indicates that our film is granular with a network of superconductor–normal metal–superconductor (SNS) weak links.[11,12] At 4.2 K, J_c reached a value $>7 \times 10^5$ A/cm^2.

presence of a SNS weak-link network in the films. The Auger measurement showed that besides the ~20-nm-thick film surface, the bulk of the film exhibited a fully stoichiometric composition of Mg and B. Finally, we note that our rapid annealing procedure prevented any substrate degradation and is suitable for high-temperature annealing of thin films prepared on substrates unstable at high temperatures.

REFERENCES

1. J. Nagamatsu *et al.*, Nature **410**, 63 (2001).

2. M. Angst *et al.*, Phys. Rev. Lett. **88**, 167004 (2002).

3. C. B. Eom *et al.*, Nature **411**, 558 (2001).

4. H. Y. Zhai *et al.*, J. Mater. Res. **16**, 2759 (2001).

5. D. H. A. Blank *et al.*, Appl. Phys. Lett. **79**, 394 (2001).

6. W. N. Kang *et al.*, Science **292**, 1521 (2001).

7. A. Plecenik *et al.*, Physica C **363**, 224 (2001).

8. X. H. Zeng *et al.*, Appl. Phys. Lett. **79**, 1840 (2001).

9. H.-J. Kim *et al.*, Phys. Rev. Lett. **87**, 087002 (2001).

10. A. H. Li *et al.*, Physica C **361**, 73 (2001).

11. V. Ambegaokar and A. Baratoff, Phys. Rev. Lett. **10**, 486 (1963).

12. P. G. de Gennes, Rev. Mod. Phys. **36**, 225 (1964).

Z2579

Figure 91.39
Resistance versus temperature characteristics of an optimally annealed MgB$_2$ film (open circles) and the photolithographically patterned MgB$_2$ microbridge (closed circles). The inset shows the $J_c(T)$ dependence measured for a small microbridge, together with the theoretical fit illustrating the SNS, weak-link dependence.

Conclusion

In conclusion, the preparation of superconducting MgB$_2$ thin films on flexible plastic foils has been presented. Our films were amorphous and exhibited a very smooth surface. The films were annealed under optimal conditions, using rapid radiative (halogen lamps) heating of Mg-B and simultaneous water-cooling of the Kapton foil, and were characterized by $T_{c,\text{on}}$ of about 29 K, ΔT_c of about 3 K, and $J_c > 7 \times 10^5$ A/cm^2 at 4.2 K. The measured $J_c(T)$ characteristics indicated the

Time-Resolved Areal-Density Measurements with Proton Spectroscopy in Spherical Implosions

The goal of the inertial confinement fusion (ICF)[1,2] implosion is to achieve high-enough temperature and compression of the fuel to sustain thermonuclear burn. The burn begins with spark ignition of the central hot spot[2] that is created as a result of shock heating and target compression. The burn wave then propagates into the higher-density regions of the compressed shell, releasing energy through the products of thermonuclear reactions.[2] The combination of high temperature and high density–radius product (called areal density or ρR) of the compressed target is necessary to ignite the target and achieve high gain.[1] In the direct-drive ignition target design[3] for the National Ignition Facility (NIF),[2] a 3.4-mm-diam, 350-μm-thick cryogenic deuterium–tritium (DT) shell is imploded with 192 overlapped laser beams with a total energy of 1.5 MJ. The hot-spot areal density must be ~300 mg/cm^2 at a temperature exceeding ~10 keV to ignite. The expected neutron yield of 2.5×10^{19} (corresponding to a gain of ~45) will be achieved at a fuel temperature of ~30 keV and a target areal density of ~1200 mg/cm^2 at peak compression. Areal densities measured so far in cryogenic implosions[4–7] are far below the values necessary for ignition because far-lower laser energy is used and the unstable growth of target perturbations inhibits achieving the desired compression. In recent implosions on the 60-beam, 351-nm OMEGA laser system, areal densities of ~40 mg/cm^2 have been achieved with cryogenic D$_2$ targets and laser energies of ~23 kJ.[7]

Because of the technical complexity associated with cryogenic equipment, most ICF implosions use plastic or glass shells filled with different gases, allowing a large variety of diagnostics to be used in experiments. Indirect-drive implosions on the Nova laser achieved ~15 mg/cm^2 of gas and ~70 mg/cm^2 of shell areal densities, respectively.[8] Recent studies on OMEGA reported up to ~15 mg/cm^2 of gas and ~60 mg/cm^2 of shell areal densities measured with charged-particle diagnostics.[9] Measurements using shell absorption of x rays emitted from the hot core reported[10] shell areal densities up to ~100 mg/cm^2. The highest reported values of areal densities, up to ~1 g/cm^2, are from implosions on the GEKKO XII laser system.[11]

To date, all reported values of target compression are time averaged over the neutron and charged-particle production. During this time, the target areal density is expected to grow by an order of magnitude or more. Time-integrated particle spectra (used to measure average areal densities) clearly show signatures of time evolution. For example, in OMEGA experiments with 24-μm-thick shells filled with 18 atm of D^{3}He gas, primary proton spectra have two distinctive features from shock and compression phases of implosion.[12] These features are produced when target areal densities differ by a factor of ~10, with a corresponding time difference of ~500 ps. This article describes experiments where the measured neutron production histories combined with primary 14.7-MeV proton spectra of D^{3}He fuel allows the first determination of areal-density *growth* during the time of neutron production up to peak compression. These measurements become possible when all other aspects contributing to the shape of the proton spectrum, such as geometrical broadening from the finite size of the proton-production region, broadening from small-scale target nonuniformities, and ion temperature broadening, are taken into account. In this article we not only present for the first time target-areal-density evolution, a fundamental quantity for ICF, but also provide areal-density growth measurements for the study of unstable growth of target perturbations, an area of the utmost importance to the success of ICF.

The experiment consisted of two direct-drive implosions on the 60-beam OMEGA laser system.[13] The targets were ~950-μm-initial-diam, 20-μm-thick plastic CH shells filled with 18 atm (shot 25220) and 4 atm (shot 25219) of D^{3}He gas. Neutron-production histories from the reaction $D + D \rightarrow {}^3He(0.82\ \text{MeV}) + n\ (2.45\ \text{MeV})$ were measured with the neutron temporal diagnostic (NTD).[14] Proton spectra from the reaction $D + {}^3He \rightarrow {}^4He(3.6\ \text{MeV}) + p(14.7\ \text{MeV})$ have been measured with seven wedged-range filters (WRF's)[15] to ensure approximately uniform coverage of the target. The shapes of the time-integrated proton spectra depend primarily on the evolution of the target areal density and the temporal history of proton production (which is approximately proportional to the measured neutron-production history). Implo-

sions of targets with an equivalent mass of D_2 and DT fuels provide values of neutron yield and ion temperature (measured using scintillator detectors), neutron burn width (using the neutron bang-time detector),[14] and average fuel areal density (from detection of knock-on deuterons),[9] which together are used to estimate sizes of particle production and fuel regions at peak neutron production. These sizes are required to determine the extent of geometrical and temperature broadening contributions to the shapes of proton spectra. Results from equivalent implosions with shells having titanium-doped layers provide measurements of areal-density modulations (by means of differential imaging),[16] which also contribute to the widths of the proton spectra. The targets were imploded with a 1-ns square pulse with a total on-target energy of ~23 kJ. All laser beams were smoothed with distributed phase plates,[17] 1-THz, two-dimensional smoothing by spectral dispersion,[18] and polarization smoothing[19] using birefringent wedges. The average beam-to-beam energy imbalance was about 3% to 4%.

Figure 91.40 shows the results of a simulation of shot 21240, which had a 12-atm-D^3He fill, performed with the 1-D hydrocode *LILAC*;[20] these results were used to develop and test a fitting method to determine the areal-density evolution. Protons born in nuclear reactions [Fig. 91.40(a)] are slowed down by the plasma of the gas fuel and plastic shell [the simulated areal-density evolution is shown by a solid curve in Fig. 91.40(b)] on the way out from the target core to the detector. The energies of protons leaving the target are calculated using the Bethe–Bloch stopping power[21] relation, which depends very weakly on the plasma density and temperature. The slowing-down curve shown in Fig. 91.40(c) has been calculated for a fully ionized CH plasma with an electron density of 10^{25} cm^{-3} (corresponding to plastic density of ~35 g/cm^3) and a temperature of 0.5 keV. The proton spectrum [Fig. 91.40(d), solid line] represents the integral of the protons born and slowed down by the target. The resulting proton spectrum is additionally broadened by the core ion temperature of 3.4 keV and geometrical effects, discussed below.

The areal-density evolution is inferred by fitting a constructed spectrum $P_c(E)$ to the measured $P_m(E)$ proton spectrum. The spectrum $P_c(E)$ is constructed using the measured neutron-production rate (assumed to be proportional to the proton-production rate) and the target areal density ρR_t, assumed to have a Lorentzian form as a function of time t:

$$\rho R_t(t) = C_0 \Big/ \Big[(t - C_1)^2 + (C_2/2)^2 \Big].$$

The best fit is achieved using a χ^2 minimization of the deviation between $P_c(E)$ and $P_m(E)$ by varying three fitting parameters C_0, C_1, and C_2. The sensitivity and systematic errors of

Figure 91.40
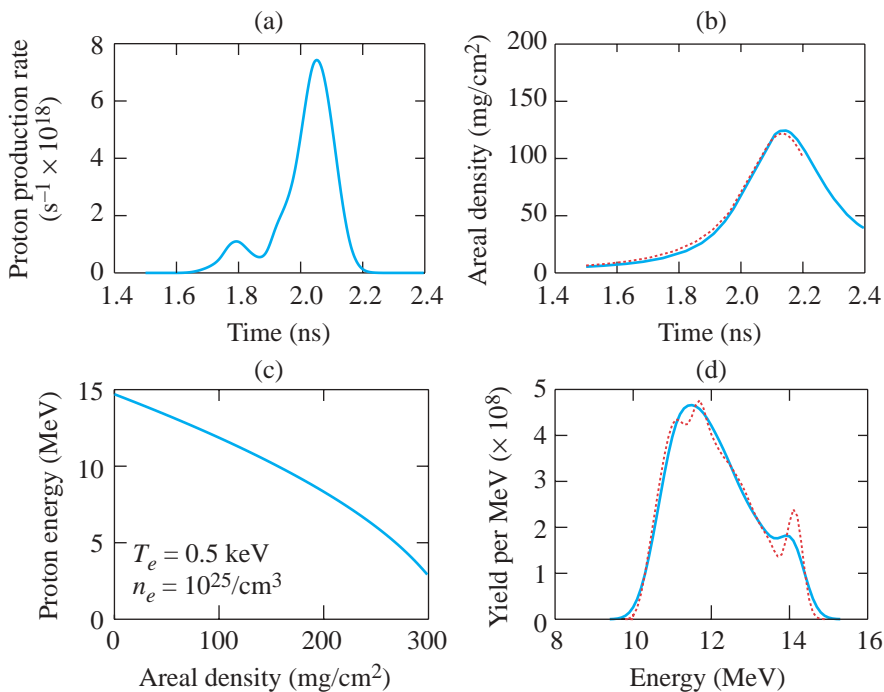The results of 1-D *LILAC* simulations (solid lines) and the calculated fit (dashed lines) for shot 21240: (a) the proton-production history; (b) the target-areal-density evolution; (c) the proton energy versus target areal density calculated using Bethe–Bloch stopping power for an electron density of 10^{25}/cm^3 and a temperature of 0.5 keV; and (d) the proton energy spectra.

E11659

this method have been tested with the simulation results shown in Fig. 91.40 by comparing the fit with the simulated areal-density evolution. The dashed lines in Figs. 91.40(b) and 91.40(d) show that a good fit for the yield is achieved when the fitted areal-density evolution is very close to the actual. This method is very sensitive because even small (10% at ~100 mg/cm^2) variations in areal density result in sizable deviations (~0.5 MeV) in the proton spectrum. The fitting assumes that the ion temperature, size of the core, shell, production region, and stopping power do not change in time. The uncertainties of these approximations are included in the systematic errors discussed below.

Geometrical broadening effects are described schematically in Fig. 91.41(a), and the resulting broadening shapes are shown in Fig. 91.41(b). In these calculations the gas fuel occupies a spherical region of radius R_2 and a proton-produc-
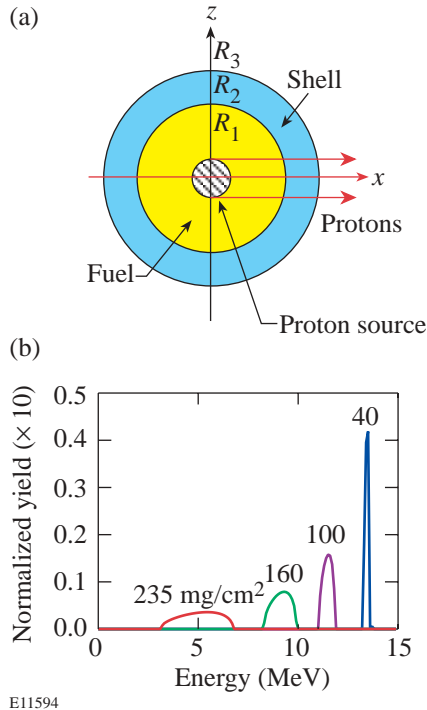

(a)

(b)

E11594

Figure 91.41
The geometrical broadening effects. Panel (a) shows the target schematic. The proton-production region has a radius of R_1, the gas fuel has a radius of R_2, and the shell has a thickness of R_3–R_2. The protons travel to a distant detector in the direction of the x axis. Panel (b) shows the geometrically broadened shapes, as normalized 14.7-MeV proton spectra after passing through shells with areal densities of 40, 100, 160, and 235 mg/cm^2, calculated for $R_1 = 27 \ \mu$m, $R_2 = 33 \ \mu$m, and $R_3 = 63 \ \mu$m.

tion region of radius R_1. On the way to the distant detector, protons lose their energy primarily in the shell of thickness R_3–R_2. Protons that are born on the x axis (which passes through the core center and the detector) always leave the target in a direction normal to the shell, while protons that are born off this axis penetrate the shell at some angle to the shell normal. As a result, even for an undistorted shell, the protons reaching the detector will have an energy spectrum broader than that originally emitted from the production region since the amount of proton energy loss depends on the path length in the shell. Figure 91.41(b) shows spectra of monoenergetic protons after passing a uniform shell of various areal densities for a target with $R_1 = 27 \ \mu$m, $R_2 = 33 \ \mu$m, and $R_3 = 63 \ \mu$m, taken from the _LILAC_ simulation presented in Fig. 91.40. The number of protons reaching the detector in the x direction as a function of coordinate z ($0 \leq z \leq R_1$) have the distribution

$$F(z) = Cz\sqrt{R_1^2 - z^2} \, ,$$

where C is a constant derived using the target geometry shown in Fig. 91.41(a). The effective areal density seen by the protons going to the detector as a function of z is

$$\rho R_{\text{eff}}(z) = \rho \left(\sqrt{R_3^2 - z^2} - \sqrt{R_2^2 - z^2} \right).$$

Substituting z for ρR_{eff} in the expression for $F(z)$ and converting areal density to proton energy using Fig. 91.40(c) results in the geometrically broadened shapes shown in Fig. 91.41(b). The original monoenergetic proton spectrum shifts to lower proton energies and broadens as a result of geometrical effects. For each shot, the parameters R_1, R_2, and R_3 have been calculated using experimental results from a large number of shots with fills having an equivalent mass of D$_2$ and DT. For example, in implosions with 15-atm-D$_2$ fuel (mass equivalent to 18 atm of D^{3}He), $R_2 = 36 \ \mu$m has been calculated using conservation of fuel mass (8.3×10^{-7} g) and measured fuel areal density (~15 mg/cm^2). In order to match the experimental neutron yield of ~1.6×10^{11}, the particle-production volume must have $R_1 = 22 \ \mu$m with a measured ion temperature of ~3.7 keV and a neutron burn width of ~170 ps. In an implosion with 3-atm-D$_2$ fuel (mass equivalent to 4 atm of D^{3}He), radii of $R_1 = 25 \ \mu$m and $R_2 = 32 \ \mu$m were calculated based on the fuel mass of 1.67×10^{-7} g, fuel areal density of ~4 mg/cm^2, neutron yield of ~6.6×10^{10}, ion temperature of ~5 keV, and neutron burn width of ~150 ps. The shell thickness R_3–R_2, the most-insensitive parameter on fitting results, has been taken to be 30 μm for both types of implosions.

Figure 91.42 shows the proton spectrum fitting results for shot 25220 with 18 atm of D^3He gas for seven detectors, which provided approximately uniform coverage of the shell. Inferred areal-density time histories for all seven directions are shown by the solid lines in Fig. 91.42(h) together with the neutron-production history (dotted line). The additional small effect of short-scale (with mode number $\ell > 6$) areal-density nonuniformities on proton spectrum broadening has been corrected by reducing the areal density shown in Fig. 91.42 by 7% with the uncertainty ranging from 0% to 15% included in the error bars: Differential imaging measurements[16] of inner-shell, titanium-doped layers show areal-density perturbation levels of ~15% at peak neutron production. In the whole shell these values are about ~7%, as calculated by 2-D simulations,[16] because the whole shell is more uniform than the inner layer, which is unstable during the deceleration phase of the implosion. The constant correction due to this effect is a good approximation (even though the measured shell modulations grow throughout the implosion) since its contribution to spectral broadening is maximum at peak neutron production and lower at peak compression because of lower amount of protons contributing to it. In experiments, ~70% of total proton spectrum width is due to the areal-density evolution, ~20% is due

to geometrical effects, and the remaining ~10% is due to temperature, short-scale (with mode number $\ell > 6$) areal-density perturbations, and instrumental broadening. A discussion of the experimental error analysis is presented in Appendix A.

Figure 91.43 summarizes the results for shots with (a) 18-atm- and (b) 4-atm-D^3He fills and compares them with 1-D *LILAC* predictions. The more-stable 18-atm-fill shot has a measured peak areal density of 109±14 mg/cm^2 (thick solid line), which is close to the 1-D simulation result (thin solid line); however, the more-unstable 4-atm shot has a measured peak areal density of 123±16 mg/cm^2, much lower than the 1-D simulation result of 230 mg/cm^2. During neutron production (from 1.6 to 2.0 ns), the areal density grows by a factor of ~8 in the 4-atm shot. At peak compression, the areal-density asymmetries with low mode numbers $\ell \leq 6$ are ~10% and ~20% for 18-atm- and 4-atm-fill targets, respectively, as estimated from the measured values in the seven detectors. The measured peak areal density is only about 10% higher for the 4-atm-fill target than that of the 18-atm-fill target. This is consistent with core sizes of $R_2 = 32$ μm and 36 μm, respectively, estimated using neutron and particle measurements.
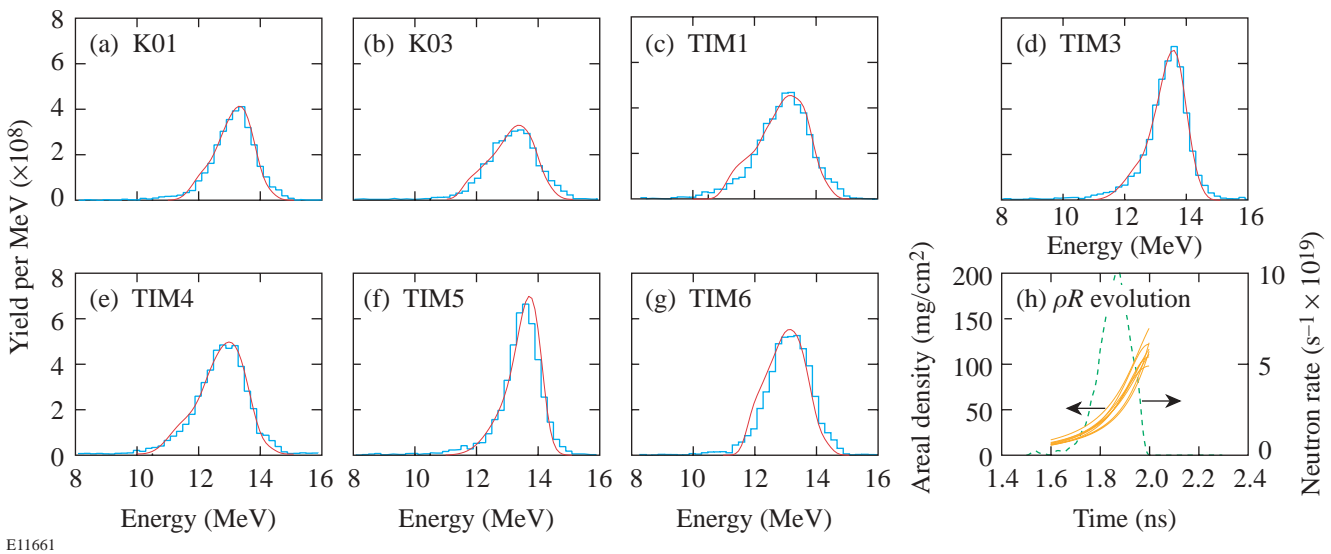

E11661

Figure 91.42

The proton spectra and fitting results (smooth solid lines) for shot 25220 with 18 atm of D^3He gas [(a)–(g)]. (h) Also shown is the inferred areal-density evolution in seven directions (solid lines) and the neutron-production history (dotted line) for this shot.
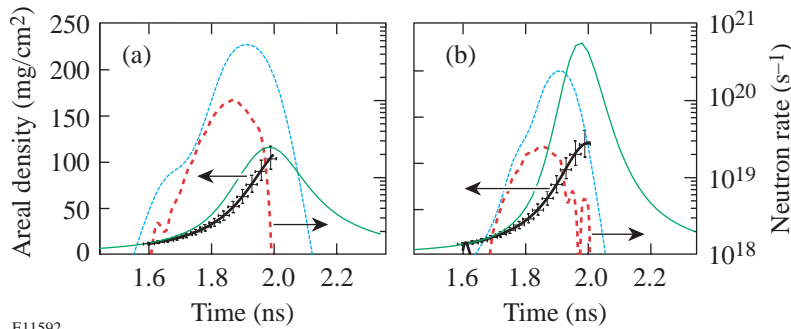
E11592

Figure 91.43
The measured (thick) and simulated (thin) target areal-density evolutions (solid) and neutron-production histories (dashed) for shots with (a) 18-atm and (b) 4-atm gas fills.

In conclusion, the target areal density grows by a factor of ~8 during the time of neutron production (~400 ps) before reaching 123 ± 16 mg/cm^2 at peak compression in the shot with a 20-μm-thick plastic CH target filled with 4 atm of D^{3}He fuel. This value is lower by a factor of ~2 than the 1-D simulation result of 230 mg/cm^2. For the more-stable, 18-atm-fill target, the target areal density reaches 109 ± 14 mg/cm^2 at peak compression, close to the 1-D prediction of 115 mg/cm^2.

ACKNOWLEDGMENT

Appendix A

The errors in the areal-density evolution measurements include systematic errors calculated from the sensitivity analysis of the fitting results and statistical errors of measured proton spectra. The biggest systematic error is the uncertainty in plasma conditions that affect proton stopping power. The relevant error is about ±0.5 MeV at a proton energy of 10 MeV, which translates to an areal-density uncertainty of $\pm10\%$ at 100 mg/cm^2. The use of neutron instead of proton-production history resulted in a 24-ps temporal shift of the areal-density evolution. The assumption that the proton-production size R_1 is constant during proton production gives an uncertainty of ±0.3 MeV at 10 MeV, which translates to an areal-density uncertainty of $\pm6\%$ at 100 mg/cm^2. The uncertainty in the other geometrical parameters R_2 and R_3 are negligibly small in the present analysis. The additional uncertainty due to possible ion-temperature evolution is also calculated to be negligible compared to other errors. The statistical errors due to the noise in the proton spectra, neutron-production history, and the errors in the fitting parameters C_0, C_1, and C_2 have been estimated to be ±0.5 MeV at 10 MeV, which translates to an areal-density uncertainty of $\pm10\%$ at 100 mg/cm^2. Averaging over seven independent measurements makes them even smaller.

REFERENCES

1. J. Nuckolls *et al.*, Nature **239**, 139 (1972).

2. J. D. Lindl, Phys. Plasmas **2**, 3933 (1995).

3. P. W. McKenty, V. N. Goncharov, R. P. J. Town, S. Skupsky, R. Betti, and R. L. McCrory, Phys. Plasmas **8**, 2315 (2001).

4. R. R. Johnson *et al.*, Phys. Rev. A **41**, 1058 (1990).

5. F. J. Marshall, S. A. Letzring, C. P. Verdon, S. Skupsky, R. L. Keck, J. P. Knauer, R. L. Kremens, D. K. Bradley, T. Kessler, J. Delettrez, H. Kim, J. M. Soures, and R. L. McCrory, Phys. Rev. A **40**, 2547 (1989).

6. K. A. Tanaka *et al.*, Phys. Plasmas **2**, 2495 (1995).

7. C. Stoeckl, C. Chiritescu, J. A. Delettrez, R. Epstein, V. Yu. Glebov, D. R. Harding, R. L. Keck, S. J. Loucks, L. D. Lund, R. L. McCrory, P. W. McKenty, F. J. Marshall, D. D. Meyerhofer, S. F. B. Morse, S. P. Regan, P. B. Radha, S. Roberts, T. C. Sangster, W. Seka, S. Skupsky, V. A. Smalyuk, C. Sorce, J. M. Soures, R. P. J. Town, J. A. Frenje, C. K. Li, R. D. Petrasso, F. H. Séguin, K. Fletcher, S. Padalino, C. Freeman, N. Izumi, R. Lerche, and T. W. Phillips, Phys. Plasmas **9**, 2195 (2002).

8. M. D. Cable *et al.*, Phys. Rev. Lett. **73**, 2316 (1994).

9. C. K. Li, F. H. Séguin, D. G. Hicks, J. A. Frenje, K. M. Green, S. Kurebayashi, R. D. Petrasso, D. D. Meyerhofer, J. M. Soures, V. Yu. Glebov, R. L. Keck, P. B. Radha, S. Roberts, W. Seka, S. Skupsky, C. Stoeckl, and T. C. Sangster, Phys. Plasmas **8**, 4902 (2001).

10. F. J. Marshall, J. A. Delettrez, V. Yu. Glebov, R. P. J. Town, B. Yaakobi, R. L. Kremens, and M. Cable, Phys. Plasmas **7**, 1006 (2000).

11. H. Azechi *et al.*, Laser Part. Beams **9**, 193 (1991).

12. R. D. Petrasso, F. H. Séguin, J. A. Frenje, C. K. Li, J. R. Rygg, B. E. Schwartz, S. Kurebayashi, P. B. Radha, C. Stoeckl, J. M. Soures, J. Delettrez, V. Yu. Glebov, D. D. Meyerhofer, and T. C. Sangster, "Measuring Implosion Dynamics through ρR Evolution in Inertial Confinement Fusion Experiments," submitted to Phys. Rev. Lett.

13. T. R. Boehly, D. L. Brown, R. S. Craxton, R. L. Keck, J. P. Knauer, J. H. Kelly, T. J. Kessler, S. A. Kumpan, S. J. Loucks, S. A. Letzring, F. J. Marshall, R. L. McCrory, S. F. B. Morse, W. Seka, J. M. Soures, and C. P. Verdon, Opt. Commun. **133**, 495 (1997).

14. R. A. Lerche, D. W. Phillion, and G. L. Tietbohl, Rev. Sci. Instrum. **66**, 933 (1995).

15. F. H. Séguin, C. K. Li, D. G. Hicks, J. A. Frenje, K. M. Green, R. D. Petrasso, J. M. Soures, D. D. Meyerhofer, V. Yu. Glebov, C. Stoeckl, P. B. Radha, S. Roberts, C. Sorce, T. C. Sangster, M. D. Cable, S. Padalino, and K. Fletcher, Phys. Plasmas **9**, 2725 (2002).

16. V. A. Smalyuk, J. A. Delettrez, V. N. Goncharov, F. J. Marshall, D. D. Meyerhofer, S. P. Regan, T. C. Sangster, R. P. J. Town, and B. Yaakobi, Phys. Plasmas **9**, 2738 (2002).

17. Y. Lin, T. J. Kessler, and G. N. Lawrence, Opt. Lett. **20**, 764 (1995).

18. S. P. Regan, J. A. Marozas, J. H. Kelly, T. R. Boehly, W. R. Donaldson, P. A. Jaanimagi, R. L. Keck, T. J. Kessler, D. D. Meyerhofer, W. Seka, S. Skupsky, and V. A. Smalyuk, J. Opt. Soc. Am. B **17**, 1483 (2000).

19. T. R. Boehly, V. A. Smalyuk, D. D. Meyerhofer, J. P. Knauer, D. K. Bradley, R. S. Craxton, M. J. Guardalben, S. Skupsky, and T. J. Kessler, J. Appl. Phys. **85**, 3444 (1999).

20. J. Delettrez, R. Epstein, M. C. Richardson, P. A. Jaanimagi, and B. L. Henke, Phys. Rev. A **36**, 3926 (1987).

21. T. A. Mehlhorn, J. Appl. Phys. **52**, 6522 (1981).

Multipolar Interband Absorption in a Semiconductor Quantum Dot: Electric Quadrupole Enhancement

Introduction

A quantum dot is an artificially created semiconductor structure in the size range of 5 to 100 nm. As a whole, it behaves like an atom since the quantum effects of the confined electrons are enlarged with respect to the interactions of the electrons inside each atom. Since the conception of quantum dots in the early 1980s, the study of their physical properties continues to be a very active field of research. Quantum dots can now be synthesized by various methods and have a multitude of potential technological applications, which include lasers with high optical gain and narrow bandwidth, and wavelength tunability.[1] Also, dipole–dipole interaction between neighboring quantum dots is being explored for applications in quantum computing.[2] Furthermore, quantum dots are potential single-photon sources, which may be used to create nonclassical electromagnetic states.[3]

Near-field optical techniques have extended the range of optical measurements beyond the diffraction limit and stimulated interests in many disciplines, especially material sciences and biological sciences.[4,5] Spatial resolution is increased by accessing evanescent modes in the electromagnetic field. These modes are characterized by high spatial frequencies and therefore enable the probing of subwavelength structures. Near-field optical techniques have also been employed to study the optical properties and dynamics of charge carriers in artificial nanostructures such as quantum wells, quantum wires, and quantum dots (see, for example, Refs. 6–8).

Nanostructures interacting with optical near fields do not necessarily behave in the same way as nanostructures interacting with far-field radiation. In Ref. 9, for example, the response of a quantum well when excited by the diffracted field of an aperture enhances quadrupole transitions, giving rise to a modified absorption spectrum of the quantum well. Furthermore, absorption properties may also be modified due to nonlocal spatial dispersion as described in Ref. 10. Recently, Knorr *et al*. formulated a general theoretical, self-consistent multipolar formalism for solids. This formalism can even be extended to account for delocalized charges.[11] The spectral response originating from the interaction between semiconductor quantum dots and the optical field generated by a small aperture has been discussed in Refs. 12–14. References 13 and 14 account for the highly inhomogeneous excitation field produced by the subwavelength aperture.

This article focuses on the interaction of a spherical semiconductor quantum dot with a highly confined optical near field. It has been shown that such fields can be generated near laser-illuminated, sharp-pointed tips.[15–17] Here, we adopt this geometry and approximate the fields near the tip by an oscillating electric dipole oriented along the tip axis. In Ref. 18, it has been demonstrated that this is a reasonable approximation and that the dipole moment can be related to the computationally determined field-enhancement factor. Furthermore, our analysis relies only on the field distribution and not on the actual enhancement factor. We will consider a spherical quantum dot in the strong-confinement limit.

The interaction between a quantum dot and the optical near field is described semiclassically using the multipolar expansion. For far-field excitation, the first term in this expansion, the electric dipole term, gives rise to a response that is considerably stronger than the response produced by subsequent terms. This is due to the fact that the physical dimension of the quantum dot is much smaller than the wavelength of optical radiation and also due to the weak spatial variation of the exciting far field. The spatial variations of optical near fields, however, are much stronger, and, as a consequence, it is expected that the contribution of higher terms in the multipolar expansion cannot *a priori* be neglected. In this article, the strength of electric quadrupole absorption compared with the strength of the electric dipole absorption will be analyzed. This study is motivated by two basic questions: (1) To what extent are standard selection rules modified by higher-order multipolar transitions in confined optical fields? and (2) Can optical resolution be improved by selectively exciting higher-order multipole transitions? To keep the analysis as simple as possible, we will neglect the Coulomb interaction between hole and electron as well as the spin of these particles.

The article is organized as follows: In the next section, the semiclassical multipolar Hamiltonian formalism is presented. In the same section, the wave functions for the hole and the electron in an ideal spherical quantum dot are reviewed, and the field operator representation is outlined. In subsequent sections, the absorption rate in the electric dipole approximation is discussed, and the absorption rate arising from the electric quadrupole term in the multipolar expansion is derived. The theory is applied to a quantum dot near a laser-illuminated metal tip. Approximated parameters for GaAs are used to estimate the absorption rate for electric dipole transitions and electric quadrupole transitions. In the last section, results are discussed and conclusions and future work are presented.

Preliminary Concepts

1. The Multipolar Hamiltonian

   A semiclassical approach is used to describe the interaction of a quantum dot with the electromagnetic field. In this approach, the electromagnetic field obeys the Maxwell equations, and the Hamiltonian of the system $\left(\hat{H}\right)$ can be separated into two contributions as

$$\hat{H} = \hat{H}_0 + \hat{H}_I,\qquad(1)$$

where $\hat{H}_0$ and $\hat{H}_I$ are the unperturbed Hamiltonian (absence of fields) and the interaction Hamiltonian, respectively. In the Coulomb gauge, they are defined as

$$\hat{H}_0 = \frac{1}{2m}\hat{\mathbf{p}}^2 + V(\mathbf{r}),\qquad(2)$$

$$\hat{H}_I = -\frac{e}{m}\hat{\mathbf{p}}\cdot\mathbf{A}(\mathbf{r},t) + \frac{e^2}{2m}\mathbf{A}^2(\mathbf{r},t) + e\phi(\mathbf{r},t),\qquad(3)$$

where $V(\mathbf{r})$ is the potential energy, $\hat{\mathbf{p}}$ is the canonical momentum, $\mathbf{A}(\mathbf{r},t)$ is the vector potential, and $\phi(\mathbf{r},t)$ is the scalar potential. The multipolar Hamiltonian is obtained by using the canonical transformation $\hat{U} = \exp(iz/\hbar)$ in which z is given by[19,20]

$$z = \int \tilde{\mathbf{P}}(\mathbf{r})\cdot\mathbf{A}(\mathbf{r},t)d^3r \equiv 0,\qquad(4)$$

where $\tilde{\mathbf{P}}(\mathbf{r})$ is the polarization. If the vector potential $\mathbf{A}(\mathbf{r},t)$ and the scalar potential $\phi(\mathbf{r},t)$ are expanded in a Taylor series

with respect to a reference charge distribution at $\mathbf{R}$ as follows:

$$\mathbf{A}(\mathbf{r},t) = \sum_{n=0}^{\infty}\frac{1}{(n+2)n!}\left[(\mathbf{r}-\mathbf{R})\cdot\nabla\right]^n\mathbf{B}(\mathbf{R},t)\cdot(\mathbf{r}-\mathbf{R}),\qquad(5)$$

$$\phi(\mathbf{r},t) = \sum_{n=0}^{\infty}\frac{-1}{(n+1)!}(\mathbf{r}-\mathbf{R})\left[(\mathbf{r}-\mathbf{R})\cdot\nabla\right]^n\cdot\mathbf{E}(\mathbf{R},t),\qquad(6)$$

then this choice of $\mathbf{A}(\mathbf{r},t)$ and $\phi(\mathbf{r},t)$ satisfies condition (4). By substituting Eqs. (5) and (6) into Eq. (3), we obtain

$$\hat{H}_I = \hat{H}^E + \hat{H}^M + \hat{H}^Q + \dots.\qquad(7)$$

Here $\hat{H}^E$, $\hat{H}^M$, and $\hat{H}^Q$ are the first three terms of the multipolar expansion, namely, the electric dipole, the magnetic dipole, and the electric quadrupole, respectively, which are defined as

$$\hat{H}^E = -\mathbf{d}\cdot\mathbf{E}(\mathbf{r},t)\big|_{\mathbf{r}=\mathbf{R}},\qquad(8a)$$

$$\hat{H}^M = -\mathbf{m}\cdot\mathbf{B}(\mathbf{r},t)\big|_{\mathbf{r}=\mathbf{R}},\qquad(8b)$$

$$\hat{H}^Q = -\nabla_1\cdot\overleftrightarrow{\mathbf{Q}}\mathbf{E}(\mathbf{r}_1,t)\big|_{\mathbf{r}_1=\mathbf{R}},\qquad(8c)$$

where $\mathbf{d}$, $\mathbf{m}$, and $\overleftrightarrow{\mathbf{Q}}$ are the electric dipole moment, the magnetic dipole moment, and the electric quadrupole moment, respectively, with respect to a reference charge distribution at $\mathbf{R}$. The nabla operator ∇_1 acts only on the spatial coordinates $\mathbf{r}_1$ of the electric field. It is important to mention that $\mathbf{m}$ depends on the canonical momentum. For weak fields, however, the canonical momentum can be approximated as the mechanical momentum.

2. The Quantum Dot Wave Functions (Strong Confinement)

   We assume that a spherical quantum dot is made of a direct band-gap semiconductor for which the bulk electric dipole transitions are allowed between the valence band and the conduction band. In a generic manner, we assume that the valence band has p-like character and the conduction band has s-like character. The latter assumption is commonly encountered for several semiconductors such as the GaAs. We consider that an electron and a hole are completely confined in a sphere with radius a by the potential energy

$$V(r) = \begin{cases} 0 & r \le a \\ \infty & r > a \end{cases}, \qquad (9)$$

where r is the radial coordinate. Also, we assume that the electron (hole) has the same effective mass m_e (m_h) as in the bulk material. This consideration is valid if the volume of the sphere is much larger than the volume of a primitive cell in the crystal. Strong confinement is achieved if the Bohr radii of electron (b_e) and hole (b_h) are much larger than the radius of the quantum dot a. By assuming the aforementioned conditions, the wave function of the electron in the conduction band can be expressed as

$$\Psi^e(\mathbf{r}) = \frac{1}{\sqrt{V_0}} u_{c,0}(\mathbf{r}) \zeta^e(\mathbf{r}). \qquad (10)$$

Here $u_{c,0}(\mathbf{r})$ is the conduction-band Bloch function (with lattice periodicity) having the corresponding eigenvalue $k = 0$, and V_0 is the volume of the *unit cell*. Similarly, the corresponding wave function for the hole in the valence band is

$$\Psi^h(\mathbf{r}) = \frac{1}{\sqrt{V_0}} u_{v,0}(\mathbf{r}) \zeta^h(\mathbf{r}), \qquad (11)$$

with $u_{v,0}(\mathbf{r})$ being the valence-band Bloch function with eigenvalue $k = 0$. $\zeta^e(\mathbf{r})$ and $\zeta^h(\mathbf{r})$ are the envelope functions, which vary spatially much slower than $u_{v,0}(\mathbf{r})$ and $u_{c,0}(\mathbf{r})$. Roughly, the energy difference between adjacent electron {hole} energy levels is

$$\left(\hbar^2 / m_e a^2\right) \left[\hbar^2 / \left(m_h a^2\right)\right].$$

If this energy difference is much larger than the Coulomb interaction $e^2 / \left(4\pi\varepsilon_0 \in a^2\right)$, the electron–hole interaction can be neglected. Under this assumption, the envelope function $\zeta^{e(h)}(\mathbf{r})$ for the electron (hole) satisfies the time-independent Schrödinger equation in which the potential energy is given by Eq. (9). The solution in spherical coordinates (r, θ, ϕ) is given by

$$\zeta_{n,l,m}^{e(h)}(r,\theta,\phi) = \Lambda_{nl}(r) Y_{l,m}(\theta,\phi). \qquad (12)$$

Here $Y_{l,m}(\theta, \phi)$ is the spherical harmonics and the radial function $\Lambda_{nl}(r)$ is

$$\Lambda_{nl}(r) = \sqrt{\frac{2}{a^3}} \frac{1}{j_{l+1}(\beta_{nl})} j_l\left(\beta_{nl} \frac{r}{a}\right). \qquad (13)$$

j_l is the lth-order spherical Bessel function, β_{nl} is the nth root of j_l, i.e., $j_l(\beta_{nl}) = 0$. The corresponding energy levels $\varepsilon^{e,h}$ are found to be

$$\varepsilon^e = \varepsilon_g + \frac{\hbar^2}{2m_e}\left(\frac{\beta_{nl}}{a}\right)^2, \qquad (14)$$

$$\varepsilon^h = \frac{\hbar^2}{2m_h}\left(\frac{\beta_{nl}}{a}\right)^2, \qquad (15)$$

where ε_g is the bulk energy band gap. Figure 91.44 shows the resulting level scheme. According to Eqs. (14) and (15), the energy is independent of the quantum number m, thus the energy level nl is ($2l+1$)-fold degenerate.
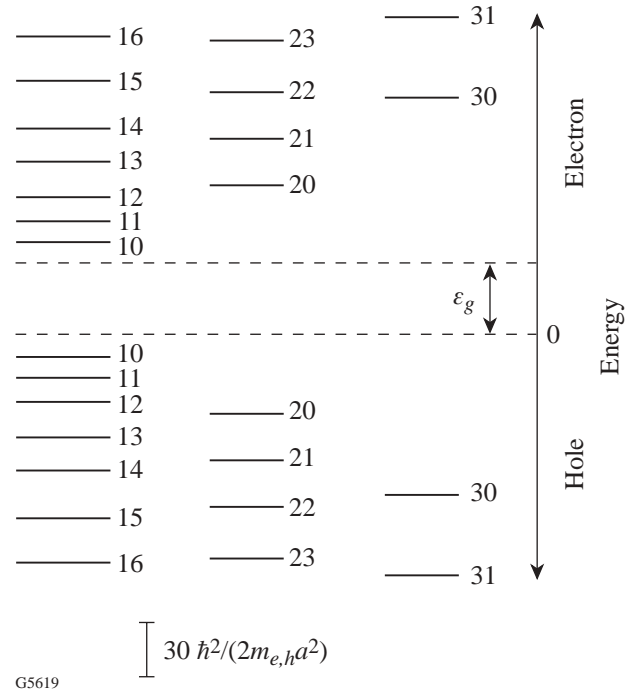

G5619

Figure 91.44
Energy level diagram of a spherical quantum dot according to Eqs. (14) and (15). Each energy level is characterized by the quantum numbers n and l, and its degeneracy corresponds to the quantum number m. Unlike the case of a hydrogen atom, the quantum number n does *not* restrict the number of suborbitals l.

3. Field Operator Representation

The annihilation carrier field operator $\hat{\Psi}$ can be expressed as a linear combination of hole creation operators in the valence band and electron annihilation operators in the conduction band, i.e.,[21,22]

$$\hat{\Psi}(\mathbf{r}) = \sum_{n,l,m}\left[\frac{1}{\sqrt{V_0}}u_{c,0}(\mathbf{r})\zeta_{nlm}^{e}(\mathbf{r})\hat{f}_{nlm}\right.$$

$$\left.+\frac{1}{\sqrt{V_0}}u_{v,0}(\mathbf{r})\zeta_{nlm}^{h}(\mathbf{r})\hat{g}_{nlm}^{\dagger}\right], \quad (16)$$

where $\hat{f}_{nlm}$ is the annihilation operator for an electron in the conduction band with envelope function $\zeta_{nlm}^{e}(\mathbf{r})$. On the other hand, $\hat{g}_{nlm}^{\dagger}$ is the creation operator for a hole in the valence band with envelope function $\zeta_{nlm}^{h}(\mathbf{r})$. The creation carrier field operator $\hat{\Psi}^{\dagger}$ is the adjoint of Eq. (16).

Absorption in the Electric Dipole Approximation

We consider a monochromatic electric field oscillating with frequency ω as

$$\mathbf{E}(\mathbf{r},t) = \tilde{\mathbf{E}}(\mathbf{r})e^{-i\omega t} + \text{c.c.} \quad (17)$$

Here $\tilde{\mathbf{E}}(\mathbf{r})$ is the spatial complex amplitude and "c.c." means complex conjugate. By setting the origin O at the center of the quantum dot and using the rotating-wave approximation, the electric dipole transition rate α^{E} for photon absorption is[21,22]

$$\alpha^{E} = K_e \sum_{nml}\sum_{rst}\tilde{\delta}_{nr}\tilde{\delta}_{ls}\tilde{\delta}_{mt}\ \delta\left[\hbar\omega - \left(\varepsilon_{nl}^{e} + \varepsilon_{rs}^{h}\right)\right], \quad (18)$$

where $\tilde{\delta}$ is the Kronecker delta, δ is the Dirac delta function, and K_e is the absorption strength given by

$$K_e = \frac{2\pi}{\hbar}e^2\left|\tilde{\mathbf{E}}(\mathbf{0})\cdot\mathbf{P}_{cv}\right|^2, \quad (19)$$

and

$$\mathbf{P}_{cv} = \frac{1}{V_0}\int_{\text{UC}}u_{c,0}^{*}(\mathbf{r}')\mathbf{r}'u_{v,0}(\mathbf{r}')d^3r' = -\frac{\hbar}{m_0\omega}\mathbf{m}_{cv}. \quad (20)$$

Here $\mathbf{m}_{cv}$ is defined as

$$\mathbf{m}_{cv} \equiv \frac{1}{V_0}\int_{\text{UC}}u_{c,0}^{*}(\mathbf{r}')\nabla'u_{v,0}(\mathbf{r}')d^3r', \quad (21)$$

with UC denoting the volume of the unit cell. In Eq. (20), we have used the fact that $\hat{\mathbf{r}} \equiv -i\hat{\mathbf{p}}/m_0\omega$ (m_0 and e are the rest mass and the charge of the electron, respectively). From Eq. (18), we notice that the absorption strength (K_e) depends *only* on the bulk material properties of the quantum dot. That is, it depends on the Bloch functions u_{co} and u_{vo} and is not influenced by the envelope functions $\zeta_{nlm}^{e,h}(\mathbf{r})$. Also, Eq. (18) indicates that the allowed transitions are those for which electron and hole have the same quantum numbers, i.e.,

$$n = r \text{ and } l = s \text{ and } m = t.$$

These relationships define the selection rules for electric dipole transitions in a semiconductor quantum dot.

Absorption Arising from the Quadrupole Term

1. Electric Quadrupole Hamiltonian

The electric quadrupole interaction Hamiltonian $\hat{H}^{Q}$ can be represented as

$$\hat{H}^{Q} = \int\hat{\Psi}^{\dagger}(\mathbf{r})H^{Q}(\mathbf{r})\Psi(\mathbf{r})d^3r, \quad (22)$$

$$H^{Q}(\mathbf{r}) = -\nabla_1\cdot\overleftrightarrow{\mathbf{Q}}(\mathbf{r})\mathbf{E}(\mathbf{r}_1,t)\big|_{\mathbf{r}_1=0}, \quad (23)$$

where the $\overleftrightarrow{\mathbf{Q}}(\mathbf{r})$ is the quadrupole moment

$$\overleftrightarrow{\mathbf{Q}}(\mathbf{r}) = \frac{1}{2}e\mathbf{r}\mathbf{r}. \quad (24)$$

Here, and in the following, the subsequent listing of two vectors [as in Eq. (24)] denotes the outer product (dyadic product). The *interband* terms are found by substituting Eq. (16) and its adjoint into Eq. (22), thus

$$\hat{H}^Q = -\nabla_1 \cdot \left[\sum_{nlm} \sum_{rst} \hat{f}^\dagger_{nlm} \hat{g}^\dagger_{rst} \int u^*_{c,0}(\mathbf{r}) \right.$$

$$\times \zeta^{e*}_{nlm}(\mathbf{r}) \overleftrightarrow{\mathbf{Q}}(\mathbf{r}) u_{v,0}(\mathbf{r}) \zeta^h_{rst}(\mathbf{r}) d^3 r \bigg]$$

$$\times \mathbf{E}(\mathbf{r}_1, t)\Big|_{\mathbf{r}_1=0} + \text{h.c.}, \tag{25}$$

where "h.c." denotes the Hermitian conjugate. We calculate the integral of Eq. (25) by decomposing it into a sum of integrals over the volume occupied by each of the unit cells. By applying the coordinate transformation $\mathbf{r}' = \mathbf{r} - \mathbf{R}_q$, where $\mathbf{R}_q$ is a translational lattice vector (the lattice remains unchanged when it is translated by $\mathbf{R}_q$), Eq. (25) becomes

$$\hat{H}^Q = -\nabla_1 \cdot \left[e \sum_{nlm} \sum_{rst} \sum_q \hat{f}^\dagger_{nlm} \hat{g}^\dagger_{rst} \int_{\text{UC}} u^*_{c,0}(\mathbf{r}' + \mathbf{R}_q) \right.$$

$$\times \zeta^{e*}_{nlm}(\mathbf{r}' + \mathbf{R}_q)$$

$$\times \overleftrightarrow{\mathbf{Q}}(\mathbf{r}' + \mathbf{R}_q) u_{v,0}(\mathbf{r}' + \mathbf{R}_q)$$

$$\times \zeta^h_{rst}(\mathbf{r}' + \mathbf{R}_q) d^3 r' \bigg] \mathbf{E}(\mathbf{r}_1, t)\Big|_{\mathbf{r}_1=0} + \text{h.c.} \tag{26}$$

Since $u_{i,0}(\mathbf{r}' + \mathbf{R}_q) = u_{i,0}(\mathbf{r}')$ ($i = c,v$), and the functions $\zeta^h_{nlm}(\mathbf{r}' + \mathbf{R}_q)$ and $\zeta^e_{nlm}(\mathbf{r}' + \mathbf{R}_q)$ are practically constant in each unit cell volume, Eq. (26) can be approximated as

$$\hat{H}^Q \approx -\nabla_1 \cdot \left[e \sum_{nlm} \sum_{rst} \sum_q \hat{f}^\dagger_{nlm} \hat{g}^\dagger_{rst} \zeta^{e*}_{nlm}(\mathbf{R}_q) \zeta^h_{rst}(\mathbf{R}_q) \right.$$

$$\times \left(\frac{1}{2} \mathbf{R}_q \mathbf{P}_{cv} + \frac{1}{2} \mathbf{P}_{cv} \mathbf{R}_q + \overleftrightarrow{\mathbf{Q}}_{cv} \right) \bigg] \mathbf{E}(\mathbf{r}_1, t)\Big|_{\mathbf{r}_1=0} + \text{h.c.} \tag{27}$$

Here $\mathbf{P}_{cv}$ is given by Eq. (20), and $\overleftrightarrow{\mathbf{Q}}_{cv}$ is defined as

$$\overleftrightarrow{\mathbf{Q}}_{cv} = \frac{1}{2V_0} \int_{\text{UC}} u^*_{c,0}(\mathbf{r}') \mathbf{r}' \mathbf{r}' u_{v,0}(\mathbf{r}') d^3 r' . \tag{28}$$

The term containing $\mathbf{R}_q \mathbf{R}_q$ has vanished because of the orthogonality of the Bloch functions, i.e., $\langle u_{i,0} | u_{j,0} \rangle = \hat{\delta}_{ij}$; $j = c,v$. The $\overleftrightarrow{\mathbf{Q}}_{cv}$ vanishes since we are assuming that the valence band is p-like and the conduction band is s-like. Thus, using $\overleftrightarrow{\mathbf{Q}}_{cv} = 0$, and replacing $\Sigma_q \to \int dR$, Eq. (27) becomes

$$\hat{H}^Q = -\nabla_1 \cdot \left[e \sum_{nlm} \sum_{rst} \hat{f}^\dagger_{nlm} \hat{g}^\dagger_{rst} \right.$$

$$\times \left(\frac{1}{2} \mathbf{P}_{cv} \mathbf{D}_{nmlrst} + \frac{1}{2} \mathbf{D}_{nmlrst} \mathbf{P}_{cv} \right) \bigg]$$

$$\times \mathbf{E}(\mathbf{r}_1, t)\Big|_{\mathbf{r}_1=0} + \text{h.c.} \tag{29}$$

Here $\mathbf{D}_{nmlrst}$ is defined as

$$\mathbf{D}_{nmlrst} \equiv \int \zeta^{e*}_{nlm}(\mathbf{R}) \mathbf{R} \zeta^h_{rst}(\mathbf{R}) d^3 R, \tag{30}$$

with the integration running over the volume of the quantum dot. Equation (29) is the final expression for the electric quadrupole Hamiltonian $\hat{H}^Q$. The factor $\mathbf{D}_{nmlrst}$ depends only on the envelope functions. By using the definition of $\zeta^{e,h}_{nlm}(\mathbf{R})$ given by Eq. (12), $\mathbf{D}_{nmlrst}$ becomes

$$\mathbf{D}_{nmlrst} = A_{nlrs} B_{lm} B_{st} \left\{ \frac{C_{st}}{2(2l+1)} \left[\mathbf{n}_x \pm i\mathbf{n}_y \right] \right.$$

$$\times \left\{ \tilde{\delta}_{(m+1)t} \left[\tilde{\delta}_{l(s-1)} + \tilde{\delta}_{l(s+1)} \right] \right.$$

$$+ \tilde{\delta}_{(m-1)t} \left[(l-m+1)(l-m+2) \tilde{\delta}_{l(s-1)} \right.$$

$$\left. - (l+m)(l+m-1)\tilde{\delta}_{l(s+1)} \right] \right\}$$

$$\left. + \mathbf{n}_z C_{lm} \tilde{\delta}_{mt} \left[\frac{l+m+1}{2l+3} \tilde{\delta}_{l(s-1)} + \frac{l-m}{2l-1} \tilde{\delta}_{l(s+1)} \right] \right\}, \qquad (31)$$

where the coefficients A_{nlrs}, B_{lm}, and C_{lm} are given by

$$A_{nlrs} \equiv 2\pi \int_0^a R^3 \Lambda_{nl}(R) \Lambda_{rs}(R) dR, \qquad (32a)$$

$$B_{lm} \equiv \sqrt{\frac{(2l+1)}{4\pi} \frac{(l-m)!}{(l+m)!}}, \qquad (32b)$$

$$C_{lm} \equiv \frac{2(l+m)!}{(2l+1)(l-m)!}. \qquad (32c)$$

2. Electric Quadrupole Selection Rules and Absorption Rate

Using again the Fermi Golden Rule, the electric quadrupole transition rate (α^Q) for photon absorption reads as

$$\alpha^Q = \frac{2\pi}{\hbar} \sum_{nlm} \sum_{rst} \left| \left\langle nml; rst \left| \hat{H}_{\text{int}}^Q \right| 0 \right\rangle \right|^2 \delta \left[\hbar\omega - \left(\varepsilon_{nl}^e + \varepsilon_{rs}^h \right) \right]. \qquad (33)$$

Here $|0\rangle$ is the ground state of the quantum dot. By substituting Eq. (29) into Eq. (33), we obtain that the electric quadrupole transition rate

$$\alpha^Q = \frac{2\pi}{\hbar} e^2$$

$$\times \sum_{nlm} \sum_{rst} \left| \nabla_1 \cdot \left(\frac{1}{2} \mathbf{P}_{cv} \mathbf{D}_{nmlrst} + \frac{1}{2} \mathbf{D}_{nmlrst} \mathbf{P}_{cv} \right) \tilde{\mathbf{E}}(\mathbf{r}_1) \right|_{\mathbf{r}_1=0}^2$$

$$\times \delta \left[\hbar\omega - \left(\varepsilon_{nl}^e + \varepsilon_{rs}^h \right) \right]. \qquad (34)$$

We find that the electric quadrupole absorption rate contains the dyadic product of $\mathbf{P}_{cv}$ and $\mathbf{D}_{nmlrst}$ and vice versa. While $\mathbf{P}_{cv}$ depends on the bulk material properties, $\mathbf{D}_{nmlrst}$ depends on the quantum dot properties [see Eqs. (20) and (31)]. This term implies that the allowed electric quadrupole transitions occur when the quantum numbers l, s, m, and t fulfill

$$m - t = \pm 1 \text{ and } l - s = \pm 1$$

or

$$m - t = 0 \text{ and } l - s = \pm 1.$$

These relationships form the selection rules for the electric quadrupole transitions in a semiconductor quantum dot. Figure 91.45 illustrates the first few allowed quadrupole transi-
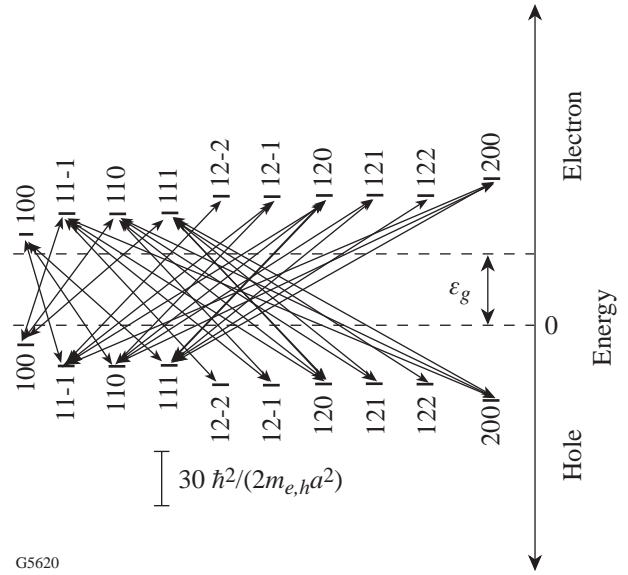

G5620

Figure 91.45
Diagram of the allowed electric quadrupole transitions in a spherical quantum dot. The energy levels are labeled by the quantum numbers nlm (electron) and rst (hole). The selection rules are $l-s = \pm 1$ and ($m-t = \pm 1$ or $m-t = 0$)]. The allowed electric quadrupole transitions exclude the allowed electric dipole transitions.

tions. We find that the quadrupole selection rules exclude any electric dipole allowed transitions. This allows the electric quadrupole transitions to be spectroscopically separated from electric dipole transitions.

Absorption Rates in Strongly Confined Optical Fields

To compare the electric dipole and electric quadrupole absorption rates in strongly confined optical fields, we consider a quantum dot in the vicinity of a laser-illuminated metal tip. This situation is encountered in so-called "apertureless" schemes of near-field optical microscopy. Strongest light confinement is achieved when the metal tip is irradiated with light polarized along the tip axis. For this situation, Fig. 91.46(a) shows the field distribution $\left(|\mathbf{E}|^2\right)$ rigorously calculated by the multiple multipole (MMP) method[23] near a gold tip with 10-nm end diameter and irradiated with $\lambda = 800$-nm light.[24] In MMP, electromagnetic fields are represented by a series expansion of known analytical solutions of Maxwell equations. To determine the unknown coefficients in the series expansion, boundary conditions are imposed at discrete points on the interfaces between adjacent homogeneous domains. The calculated field distribution, for our particular geometry, can be well approximated by the field generated by an electric dipole aligned along the tip axis z and located at the origin of tip curvature. Figure 91.46(b) demonstrates the validity of this dipole approximation: the rigorously calculated field strength

$\left(|\mathbf{E}|^2\right)$ for the metal tip is plotted along the z axis (solid line) and compared with the corresponding field generated by the dipole (dashed line).[18] The only adjustable parameter is the dipole moment $\mathbf{p}_0$, which can be related to the computationally determined field enhancement factor. Because of this very good approximation, we simply replace the laser-illuminated metal tip by a dipole.

The electric field $\mathbf{E}(\mathbf{r})$ generated by an oscillating electric dipole with moment $\mathbf{p}_0$ located at $\mathbf{r}_0$ and oscillating at the angular frequency ω can be represented as

$$\tilde{\mathbf{E}}(\mathbf{r}) = \frac{k_0^2}{\varepsilon_0} \overleftrightarrow{\mathbf{G}}(\mathbf{r}, \mathbf{r}_0, \omega) \mathbf{p}_0. \tag{35}$$

Here, $k_0 = \omega/c$ (c being the vacuum speed of light), and $\overleftrightarrow{\mathbf{G}}(\mathbf{r}, \mathbf{r}_0, \omega)$ is the free-space dyadic Green's function.[25] We consider the situation depicted in Fig. 91.47, where a sharp metal tip illuminated with light polarized along the tip axis (z axis) is substituted by a dipole with magnitude p_0 and oriented in the z direction. The dipole is located at $\mathbf{r}_0 = z_0 \mathbf{n}_z$, and the quantum dot coordinates are $\mathbf{r} = x \mathbf{n}_x + y \mathbf{n}_y$. The quantum dot is scanned in the plane $z = 0$, while the position of the exciting dipole is kept fixed.

G5621
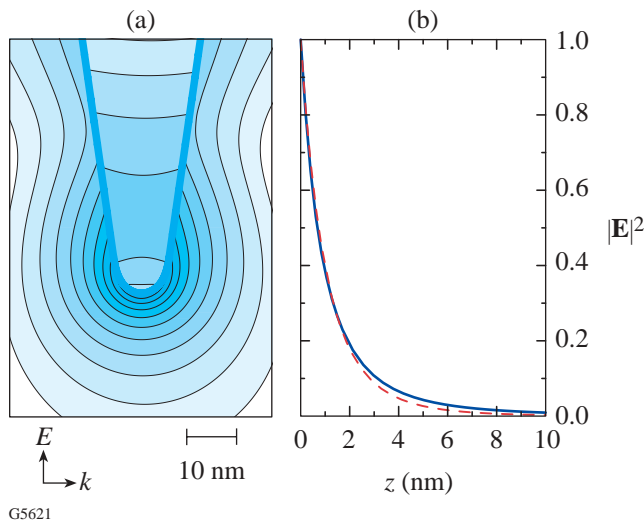
Figure 91.46
(a) Computed field distribution ($|\mathbf{E}|^2$) near a gold tip irradiated by a plane wave polarized along the tip axis. Logarithmic scaling with a factor of 2 between successive contour lines. (b) Comparison of the computed field ($|\mathbf{E}|^2$, solid curve) with the corresponding field of a dipole ($|\mathbf{E}|^2$, dashed curve) oriented along the tip axis and located inside the tip. Both fields are evaluated along the tip axis z with $z = 0$ coinciding with the tip surface.

G5622
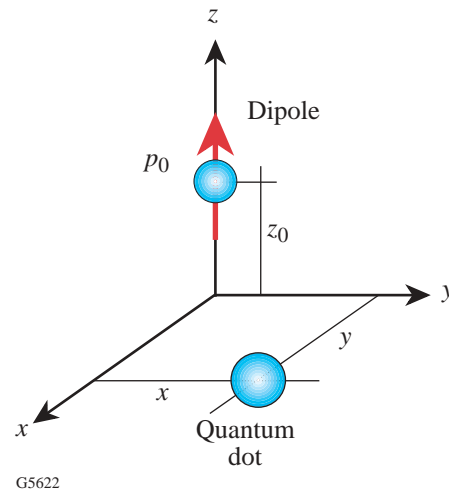
Figure 91.47
Simplified configuration of a quantum dot $\left(\mathbf{r} = x \mathbf{n}_x + y \mathbf{n}_y\right)$ interacting with a laser-illuminated metal tip. The tip is replaced by a vertical dipole $\left(\mathbf{r}_0 = z_0 \mathbf{n}_z\right)$ with moment p_0 and oriented along the z axis.

To calculate the electric quadrupole absorption rate (α^Q) and the electric dipole absorption rate (α^E), we consider Bloch functions for the valence band and conduction band that are similar to those of GaAs. If we ignore spin-orbit coupling and spin degeneracy, the p-like valence band is three-fold degenerate. The Bloch functions are calculated by using the empirical pseudopotential method with parameters taken from Ref. 26. GaAs has a lattice constant of $d = 0.565$ nm, and the effective masses of electron and hole are $m_e = 0.067\ m_0$ and $m_h = 0.080\ m_0$ (light hole), respectively. Inclusion of the heavy hole will only shift the hole energy levels, as long as the heavy-hole Bohr radius is larger than the quantum dot radius.

We consider the lowest-allowed electric dipole transition, i.e., the transition with the lowest-allowed energy difference between initial and final states. During this transition, an electron with quantum numbers (100) and a hole with quantum numbers (100) are created. Since there is *no* preferential coordinate axis, we take the rotational average of Eq. (18). Also, by taking into account the degeneracy of the valence band (three-fold), the averaged electric dipole absorption rate becomes

$$\left\langle \alpha^E \right\rangle = \left\langle K_e \right\rangle \delta\left[\hbar\omega - \left(\varepsilon_{10}^e + \varepsilon_{10}^h\right)\right], \tag{36}$$

where

$$\left\langle K_e \right\rangle = \frac{2\pi}{\hbar} e^2 \left|\tilde{\mathbf{E}}(\mathbf{0})\right|^2 |\mathbf{P}|^2 \tag{37}$$

and

$$|\mathbf{P}| = \left|\mathbf{P}_{cv_1}\right| = \left|\mathbf{P}_{cv_2}\right| = \left|\mathbf{P}_{cv_3}\right|. \tag{38}$$

By computing numerically the integral of Eq. (20) over a *unit cell* of the crystal, we obtain that $|\mathbf{P}| \approx 0.75\ d$.

The lowest-energy-allowed electric quadrupole transition creates a hole with quantum numbers (110), (11-1), or (111) (three-fold degeneracy) and an electron with quantum numbers (100). Again, there is *no* preferential coordinate axis, so the rotational average of Eq. (34) has to be evaluated. Since the electric quadrupole moment is the dyadic product of two vectors with independent orientations, the rotational average of Eq. (34) is obtained in a straightforward manner. After evaluating the average and taking into account the degeneracy

of the valence band and the hole energy level, the averaged electric quadrupole absorption rate becomes

$$\left\langle \alpha^Q \right\rangle = \left\langle K^Q \right\rangle \delta\left[\hbar\omega - \left(\varepsilon_{10}^e + \varepsilon_{11}^h\right)\right]. \tag{39}$$

Here $\langle K^Q \rangle$ corresponds to

$$\left\langle K^Q \right\rangle = \frac{2\pi}{\hbar} \frac{e^2}{2} |\mathbf{P}|^2 |\mathbf{D}|^2$$

$$\times \sum_{i,j} \left[\left|\frac{\partial}{\partial x_i} \tilde{E}_j(\mathbf{0})\right|^2 + \frac{\partial}{\partial x_i} \tilde{E}_j(\mathbf{0}) \frac{\partial}{\partial x_j} \tilde{E}_i^*(\mathbf{0}) \right]. \tag{40}$$

The ith Cartesian coordinate is denoted by x_i and $\tilde{E}_i(\mathbf{r})$ is i^{th} Cartesian component of the electric field $\tilde{\mathbf{E}}_i(\mathbf{r})$. $|\mathbf{D}|$ corresponds to

$$|\mathbf{D}| = |\mathbf{D}_{10010}| = |\mathbf{D}_{100111}| = |\mathbf{D}_{10011-1}|. \tag{41}$$

The integration of Eq. (41) over the quantum dot volume renders a value $|\mathbf{D}| \approx 0.3\ a$.

Discussion of the Near Field–Quantum Dot Interaction

We analyze absorption rates for quantum dots with the two different radii: $a = 5$ nm and $a = 10$ nm. For $a = 5$ nm, the electric quadrupole transition is excited at a wavelength of $\lambda \approx 500$ nm and the electric dipole transition at $\lambda \approx 550$ nm. On the other hand, the quadrupole transition for a quantum dot of radius $a = 10$ nm occurs at $\lambda \approx 615$ nm and the electric dipole transition at $\lambda \approx 630$ nm.

For a quantum dot that is just beneath the exciting dipole ($\mathbf{r} = \mathbf{0}$), Fig. 91.48 shows the ratio of the quadrupole absorption rate and the dipole absorption rate ($\langle \alpha^Q \rangle / \langle \alpha^E \rangle$) as a function of the normalized separation z_0/λ. The vertical dashed line indicates the minimum physical distance between quantum dot and the dipole, i.e., the limit at which the tip and quantum dot would touch (we assume a tip radius of 5 nm).

For the quantum dot with radius $a = 5$ nm and an excitation wavelength of $\lambda = 550$ nm, the normalized minimum distance

is $z_0^{min}/\lambda \approx 0.018$. Similarly, for the quantum dot with radius $a = 10$ nm and a wavelength of $\lambda = 630$ nm, the minimum distance is 15 nm, which corresponds to a normalized distance of $z_0^{min}/\lambda \approx 0.024$. The important finding is that the ratio $(\langle \alpha^Q \rangle / \langle \alpha^E \rangle)$ can be as high as 0.3 for a 5-nm quantum dot [see Fig. 91.48(a)] and even 0.6 for a 10-nm quantum dot [see Fig. 91.48(b)]. These values are roughly three orders of magnitude larger than those obtained by using far-field excitation [for plane wave excitation the ratio is of the order of $(a/\lambda)^2$]. Thus, we find that in the extreme near field ($z_0 < \lambda/10$), quadrupole transitions become important and the electric dipole approximation is not sufficiently accurate!

The plots in Figs. 91.49 and 91.50 are generated by scanning the quantum dot in the x-y plane while keeping the exciting dipole at the constant height z_0. Figure 91.49 shows the electric dipole absorption rate $\langle \alpha^E \rangle$, whereas Fig. 91.50 shows the electric quadrupole absorption rate $\langle \alpha^Q \rangle$. Both plots are symmetrical with respect to the z axis. In the case of $\langle \alpha^E \rangle$, this symmetry is generated by the dominant field component $\tilde{E}_z$, whereas in the case of $\langle \alpha^E \rangle$, the symmetry is due to the strong field gradient $\partial \tilde{E}_z / \partial z$. The electric dipole absorption rate is proportional to the square of the particle dipole moment p_0 and to the square of the lattice constant of the crystal d. On the other hand, the quadrupole absorption rate is also proportional to the square of (a/λ). This is evident in Fig. 91.50 where the ratio a/λ in Fig. 91.50(b) is twice the ratio a/λ in Fig. 91.50(a). A comparison between the widths of the curves in Figs. 91.49 and 91.50 shows that *no* improvement of spatial resolution can be achieved by selectively probing optical quadrupole transitions!

Conclusions

As was mentioned above, laser-irradiated metal tips are used in near-field optical microscopy as miniature light sources.[17] A strongly enhanced and localized optical field is created at the tip apex if proper polarization conditions are used. Using this technique, spectroscopic measurements with spatial resolutions of only 10 to 20 nm have been demonstrated.[17] To date, this is the highest spatial resolution of any optical spectroscopic measurement. This technique will be
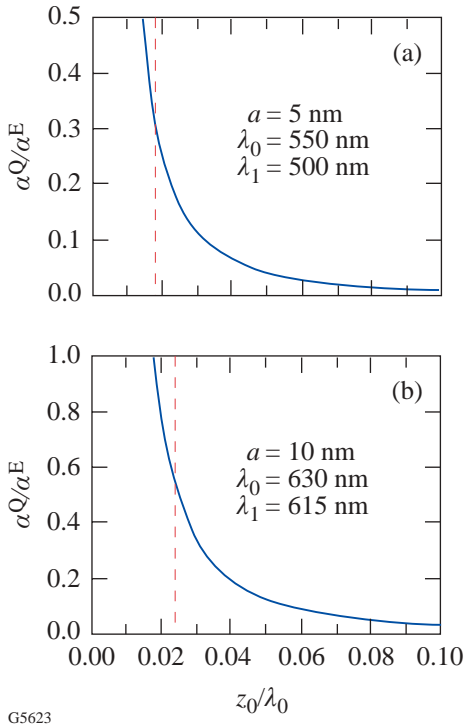

Figure 91.48
Ratio of the electric quadrupole absorption rate $\langle \alpha^Q \rangle$ and the electric dipole absorption rate $\langle \alpha^E \rangle$ as a function of the normalized distance (z_0/λ_0) between excitation dipole ($\mathbf{r}_0 = z_0 \mathbf{n}_z$) and quantum dot center ($\mathbf{r} = \mathbf{0}$). The quantum dot radius is $a = 5$ nm in (a) and $a = 10$ nm in (b). The vertical dashed line indicates the minimum physical separation between the center of the quantum dot and the exciting dipole. This separation corresponds to $a_t + a$, where $a_t = 5$ nm is the radius of curvature of the metal tip.

Figure 91.49
Electric dipole absorption rate $\langle \alpha^E \rangle$ as a function of the normalized lateral coordinates (x/λ, y/λ). The height of the excitation dipole is $z_0 = 0.025\, \lambda$. The vertical axis has units of $(2\pi^2)(edp_0/\epsilon_0)^2 [10^4/(\hbar\lambda^6)] \delta[\hbar\omega - (\varepsilon_{10} + \varepsilon_{10})]$. The symbols e, d, and p_0 denote the elementary charge, the lattice constant, and the dipole moment, respectively.

applied in our future investigations to experimentally verify the quadrupole transitions predicted in this work. Single CdSe quantum dots will be dispersed on a flat substrate, and the quantum dot luminescence will be recorded as a function of excitation wavelength and tip position.

In this work, higher-order multipole interactions between a semiconductor quantum dot and a strongly confined optical field have have analyzed. Expressions have been derived for the electric quadrupole interaction Hamiltonian, the associated absorption rate, and selection rules. It has been assumed that the quantum dot has a p-like valence band and an s-like conduction band. Also, the Bohr radii of electron and hole were assumed to be larger than the sphere radius (strong confinement limit), and *no* Coulomb interactions between hole and electron have been taken into account. Because of their different selection rules, electric dipole and electric quadrupole interband transitions can be separated and selectively excited. The electric quadrupole absorption strength depends on the bulk properties of the material (Bloch functions) as well as on the envelope functions (confinement functions). This differs from the electric dipole absorption strength, which depends only on the bulk properties of the semiconductor. When the quantum dot with radius a interacts with the confined optical

field produced by a sharply pointed tip, the ratio between the electric quadrupole absorption rate and the electric dipole absorption rate can be as high as 0.3 for $a = 5$ nm and even 0.6 for $a = 10$ nm. Electric quadrupole transitions cannot be ignored in the extreme near field, i.e., for separations between tip and quantum dot smaller than $\lambda/10$. The inclusion of electric quadrupole transitions modifies the absorption spectra of quantum dots in the extreme near field. We have shown, however, that *no* improvement in the spatial resolution can be achieved by selective probing of electric quadrupole transitions. Future studies will be directed at electric quadrupole excitonic interactions.

REFERENCES
1. V. I. Klimov *et al.*, Science **290**, 314 (2000).

2. G. K. Brennen, I. H. Deutsch, and P. S. Jessen, Phys. Rev. A, At. Mol. Opt. Phys. **61**, 062309 (2000).
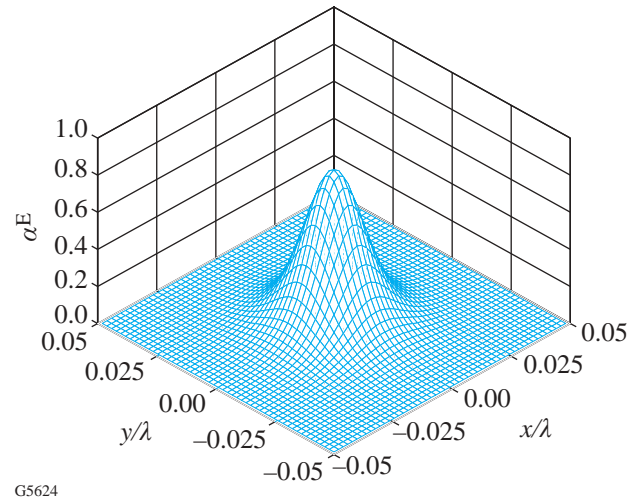
3. P. Michler *et al.*, Science **290**, 2282 (2000).
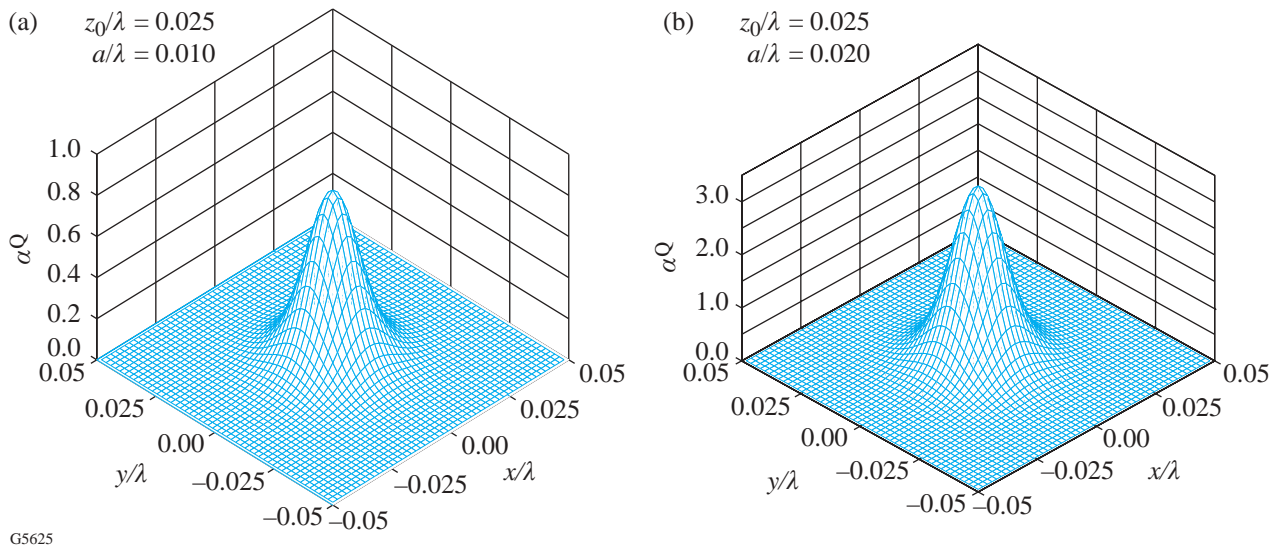
Figure 91.50
Electric dipole absorption rate $\langle \alpha^Q \rangle$ as a function of the normalized lateral coordinates (x/λ, y/λ). The height of the excitation dipole is $z_0 = 0.025\,\lambda$. The symbols e, d, and p_0 denote the elementary charge, the lattice constant, and the dipole moment, respectively. The quantum dot radius is $a = 0.01\,\lambda$ in (a) and $a = 0.02\,\lambda$ in (b). The width of the curve is roughly the same as in Fig. 91.49, which indicates that no improvement of resolution can be achieved by quadrupole transitions. The vertical axis has units of $\left(2\pi^5\right)\left(edp_0/\epsilon_0\right)^2\left[10^4/\left(\hbar\lambda^6\right)\right]\delta\left[\hbar\omega - \left(\varepsilon_{10} + \varepsilon_{11}\right)\right]$.

4. For a recent review, see R. C. Dunn, Chem. Rev. **99**, 2891 (1999).

5. N. Van Hulst, ed., J. Microsc. **202** (1, Pt. 1), 1 (2001).

6. R. D. Grober *et al.*, Appl. Phys. Lett. **64**, 1421 (1994).

7. J. Levy *et al.*, Phys. Rev. Lett. **76**, 1948 (1996).

8. A. Richter *et al.*, Ultramicroscopy **71**, 205 (1998).

9. A. von der Heydt *et al.*, J. Chem. Phys. **112**, 7831 (2000).

10. O. Mauritz *et al.*, Phys. Rev. Lett. **82**, 847 (1999).

11. A. Knorr, S. W. Koch, and W. W. Chow, Opt. Commun. **179**, 167 (2000).

12. B. Hanewinkel *et al.*, Phys. Rev. B, Condens. Matter **55**, 13,715 (1997).

13. G. W. Bryant, Appl. Phys. Lett. **72**, 768 (1998).

14. A. Chavez-Pirson and S. T. Chu, Appl. Phys. Lett. **74**, 1507 (1999).

15. H. F. Hamann *et al.*, J. Chem. Phys. **114**, 8596 (2001).

16. Y. C. Martin, H. F. Hamann, and H. K. Wickramasinghe, J. Appl. Phys. **89**, 5774 (2001).

17. E. J. Sanchez, L. Novotny, and X. S. Xie, Phys. Rev. Lett. **82**, 4014 (1999), and references therein.

18. L. Novotny, in *Near-Field Optics and Surface Plasmon Polaritons, Topics Appl. Phys.*, edited by S. Kawata (Springer-Verlag, Berlin, 2001), Vol. 81, pp. 123–141.

19. R. G. Woolley, J. Phys. B, At. Mol. Phys. **6**, L97 (1973).

20. L. D. Barron and C. G. Gray, J. Phys. A, Math. Gen. **6**, 59 (1973).

21. H. Haug and S. W. Koch, *Quantum Theory of the Optical and Electronic Properties of Semiconductors*, 2nd ed. (World Scientific, Singapore, 1993).

22. L. Banyai and S. W. Koch, *Semiconductor Quantum Dots*, World Scientific Series on Atomic, Molecular, and Optical Physics, Vol. 2 (World Scientific, Singapore, 1993).

23. C. Hafner, *The Generalized Multipole Technique for Computational Electromagnetics* (Artech House, Boston, 1990).

24. L. Novotny, R. X. Bian, and X. S. Xie, Phys. Rev. Lett. **79**, 645 (1997).

25. C. Tai, *Dyadic Green Functions in Electromagnetic Theory*, 2nd ed., IEEE Press Series on Electromagnetic Waves (IEEE Press, Piscataway, NJ, 1994).

26. P. Y. Yu and M. Cardona, *Fundamentals of Semiconductors: Physics and Materials Properties*, 1st ed., corr. print (Springer, Berlin, 1996).

Radial Structure of Shell Modulations Near Peak Compression of Spherical Implosions

Introduction

In inertial confinement fusion (ICF), a spherical target is imploded by either direct illumination of laser beams (direct drive)[1] or x rays produced in a high-Z enclosure (hohlraum).[2] The growth of shell perturbations is the greatest factor limiting target performance in these implosions. Initial nonuniformities in the shell include target imperfections and modulations from laser nonuniformities in the case of direct-drive ICF.[3–8] These modulations initially grow at the shell's outer surface during the laser-driven part of implosions due to the acceleration-phase Rayleigh–Taylor (RT) instability[9–12] and convergent Bell–Plesset (BP) effects.[13] These outer-surface perturbations feed through the shell during their acceleration-phase growth, seeding the deceleration-phase RT instability[14–18] on the inner surface. As the shell starts to decelerate, the outer-shell modulations become stable. The inner surface of the shell, however, is subject to the RT instability during the deceleration phase since the higher-density shell is slowed down by the lower-density gas of the target core.[14–18] As a result, the shell modulations penetrate deep into the gas fuel region causing shell–fuel mixing.[19–21] This mixing inhibits the achievement of high compression and reduces the fuel temperature that is necessary to sustain efficient fuel burn.

The first measurements[18,22] of shell modulations around peak compression were based on differential imaging[22] of core emission with shells having diagnostic titanium-doped layers. At peak compression, when the maximum density and temperature occur, the hot, compressed core and inner surface of the shell produce strong x-ray emission. This emission is used as a backlighter to probe the outer, colder shell.[22] To measure shell integrity, both time-integrated[22] and time-resolved[18] measurements used imaging at photon energies above and below the titanium K edge. Core images at photon energies below the K edge (not absorbed by the shell) provide the spatial shape of the backlighter, while core images at photon energies above the K edge (highly absorbed by the shell's titanium) contain information about the structure of shell-areal-density modulations in the titanium-doped layer.

Earlier experiments[18,22] were limited to measurements of perturbations at the shell's inner surface, where modulations and compression were expected to be the highest. Measurements with titanium-doped layers placed in the central and outer parts of the shell were not sensitive enough to detect perturbations. Differential imaging in the current experiments is extended to the much more sensitive absorption in the titanium $1s$–$2p$ spectral region instead of the absorption above the K edge. Near peak compression, the shell is heated by energy transported from the hot core through thermal conduction and radiation. At temperatures around 0.1 to 1 keV, the shell titanium is partially ionized and is able to absorb core radiation not only at photon energies above the K edge ($\geq$ 4.966 keV) but also in the $1s$–$2p$ absorption line region at photon energies around 4.5 to 4.75 keV. The mass absorption rate of any absorption line from the titanium $1s$–$2p$ spectral region is about one order of magnitude higher than at photon energies above the K edge. As a result, differential imaging can be extended to the central and outer parts of the shell, where the compression and modulations are smaller. In this article the first measurements of the compressed-shell modulation structure away from the inner surface are presented. A similar technique has also been employed for modulation measurements in indirectly driven implosions.[23]

Experimental Conditions

Figure 92.1 shows a schematic of spherical targets and the positions of the titanium-doped layers in the shell used in these experiments and their predicted location at peak compression. Targets with ~450-μm initial radii and 20-μm-thick shells, filled with 18 atm of D^{3}He gas, were imploded by 351-nm laser light using the 60-beam OMEGA laser system[24] with a 1-ns square pulse and a total energy of ~23 kJ. All shots were taken with laser beams smoothed by distributed phase plates (DPP's),[25] 1-THz, two-dimensional smoothing by spectral dispersion (2-D SSD),[26] and polarization smoothing (PS)[27] using birefringent wedges. The average beam-to-beam energy imbalance was ~3% in all implosions. The diagnostic, 1-μm-thick, titanium-doped (~2% by atom) CH layers were offset

from the inner surface by ~1, 5, 7, and 9 μm of pure CH. These layers were expected to determine shell-areal-density modulations at the inner, central, and outer parts of the shell at peak compression. Figure 92.1(b) shows the temperature and density profiles at peak compression of one of the targets calculated by the 1-D code *LILAC*.[28] At peak compression, the diagnostic titanium layer offset by 1 μm is located on the slope of the density profile at the inner shell, where the unstable surface is located. Titanium layers offset by 5 μm and 7 μm are in the central part of the shell, and the layer offset by 9 μm lies in the outer part of the shell at peak compression [see Fig. 92.1(b)].

Core images were measured with a gated monochromatic x-ray imager (GMXI),[29] which was set up for time-integrated (~200-ps) measurements during these experiments. One channel of the GMXI recorded monochromatic (with FWHM of ~30 eV) images at ~4.60 keV in the spectral region of titanium 1*s*–2*p* absorption, while the other channel was set up at ~4.87 keV outside titanium absorption regions or emission lines. Figure 92.2 shows Wiener-filtered images[30] for shots with titanium layers offset by 1, 5, 7, and 9 μm and for one shot without titanium, which was used to estimate the noise level. The Wiener filter used a noise level constructed from the difference of two images $I_{1s-2p}(\mathbf{r})$ and $I_{<K}(\mathbf{r})$ in shot
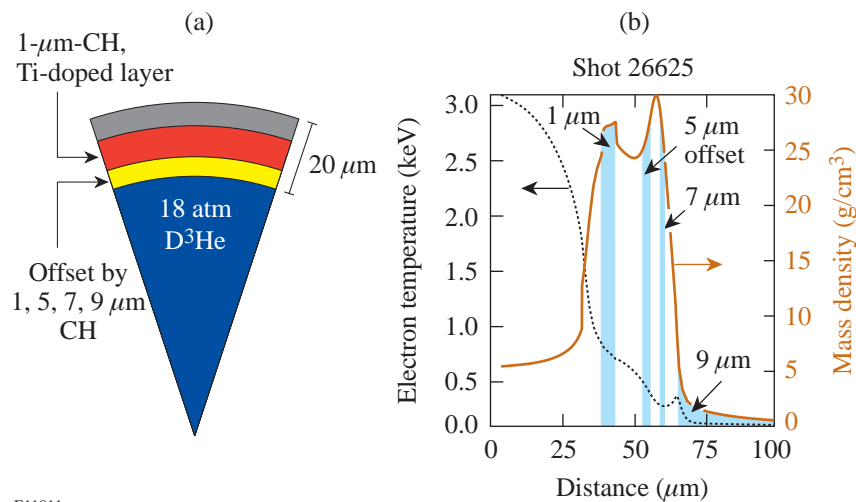
Figure 92.1
(a) Schematic of spherical targets with diagnostic titanium-doped (2% by atom) layers offset by 1, 5, 7, and 9 μm of pure CH from the inner surface. (b) *LILAC*-simulated profiles of target density and temperature at peak compression of the implosion. The locations of titanium-doped layers are shown by the light blue areas.

E11811
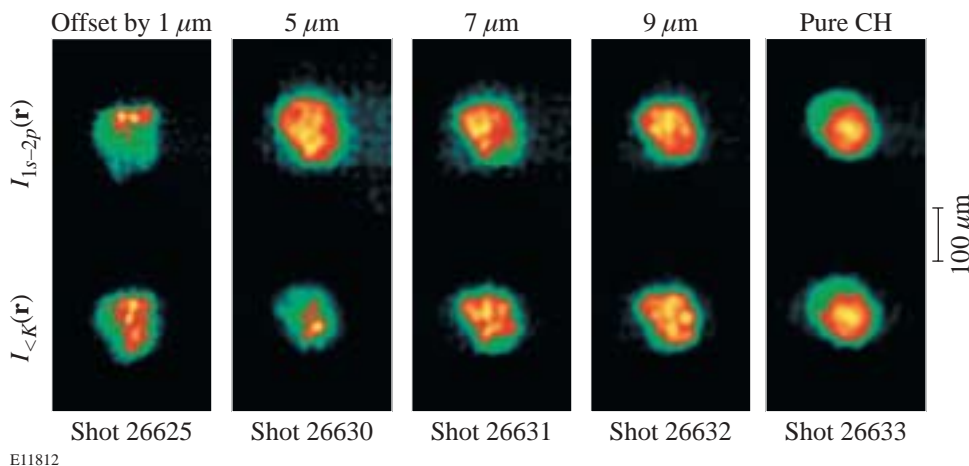
E11812

Figure 92.2
Wiener-filtered core images around peak compression at energies inside (~4.60 keV, upper row of images) and outside (~4.87 keV, lower row of images) the titanium 1*s*–2*p* absorption spectral region for shots with 1-μm- (shot 26625), 5-μm- (shot 26630), 7-μm- (shot 26631), and 9-μm-offset (shot 26632) titanium-doped layers, and for the shot without titanium (26633).

26633 without titanium and the measured GMXI modulation transfer function (MTF).[31] All the details of the image processing are described in Refs. 18, 22, and 30. The shell optical-depth (OD) modulations were calculated using the natural logarithm of the ratio of intensities of the two images at photon energies in the $1s$–$2p$ spectral region (highly absorbed by the shell), $I_{1s-2p}(\mathbf{r})$, and outside the $1s$-$2p$ region, below the K edge (weakly absorbed by the shell), $I_{<K}(\mathbf{r})$:

$$\delta[\text{OD}(\mathbf{r})] = \delta\left\{\ln\left[I_{1s-2p}(\mathbf{r})/I_{<K}(\mathbf{r})\right]\right\}.$$

The spectra of the core emissions were captured on an x-ray streak camera.[32] They were subsequently time integrated and used to infer a spatial average of the OD of the titanium layer in the $1s$–$2p$ spectral region. The red line (shot 26625) in Fig. 92.3(a) shows an example of a measured time-integrated spectrum $S_{\text{meas}}(E)$ as a function of photon energy E. The spectral responses of the GMXI at two channels in $[R_{1s-2p}(E)]$ and out $[R_{<K}(E)]$ of the $1s$–$2p$ absorption spectral region are represented by the dashed and dotted lines, respectively. The thick green line represents the estimated continuum level $S_{\text{con}}(E)$ of core x rays, used to calculate average titanium optical depth $\text{OD} = \ln[S_{\text{con}}(E)/S_{\text{meas}}(E)]$ at a photon energy of $E = 4.6$ keV. The average titanium OD is used to determine the relative OD modulations (which are equal to the relative areal-density modulations), $\delta[\text{OD}(\mathbf{r})]/\text{OD} = \delta[\rho R(\mathbf{r})]/\rho R$, to compare levels of modulations in the different parts of the shell.

In addition, the measured spectra are used to calculate the spatial variations in images due to small variations in the spectral response across the vertical axis of the images. For example, the central part of the image $I_{1s-2p}(\mathbf{r})$ is set up for measurements at a photon energy of $E = 4.60$ keV. The x rays originating at this point of the image are reflected at an angle

of 5.88±0.01° from the GMXI multilayer mirror. The x rays originating from the horizontal line at 100 μm off the image center are reflected from the mirror at a slightly different angle of 5.91±0.01°, corresponding to a photon energy of 4.58 keV. Similarly, the x rays originating at the horizontal line at −100 μm off the center line in the image plane are reflected from the mirror at an angle of 5.85±0.01°, corresponding to a photon energy of 4.63 keV. The resulting image correction functions were calculated for each shot using corresponding spectra. For example, for the images at the $1s$–$2p$ absorption channel, the resulting correction function is proportional to the convolution of the measured spectrum $S_{\text{meas}}(E)$ with the spectral response function $R_{1s-2p}(E)$. Figure 92.3(b) shows correction functions for shot 26625 inside (dashed line) and outside (dotted line) the $1s$–$2p$ absorption channel. For each Wiener-filtered image, the x-ray intensity at the vertical axis was divided by the corresponding correction function to compensate for these spatial variations.

Experimental Results

Figure 92.4 presents the images of optical-depth modulations in the titanium-doped layers offset by 1, 5, 7, and 9 μm from the shell's inner surface. As shown in Fig. 92.1(b), these layers represent different parts of the shell ranging from the inner to the outer surfaces at peak compression. Power-per-mode spectra of these modulations as functions of spatial frequency are presented in Fig. 92.5(a). The amplitudes of modulations are highest at a spatial frequency of ~20 mm^{-1} corresponding to a wavelength of ~50 μm (with a mode number of $\ell \sim 6$). This result is in agreement with previous inner-surface measurements using K-edge imaging. The absolute values of optical-depth modulation σ_{rms} decreased monotonically from 0.30±06 at the inner surface to 0.13±06 at the outer surface as shown by the solid line in Fig. 92.5(b). The relative areal-

(a)

(b)

Fiducial

$1s$–$2p$ absorption

E11813
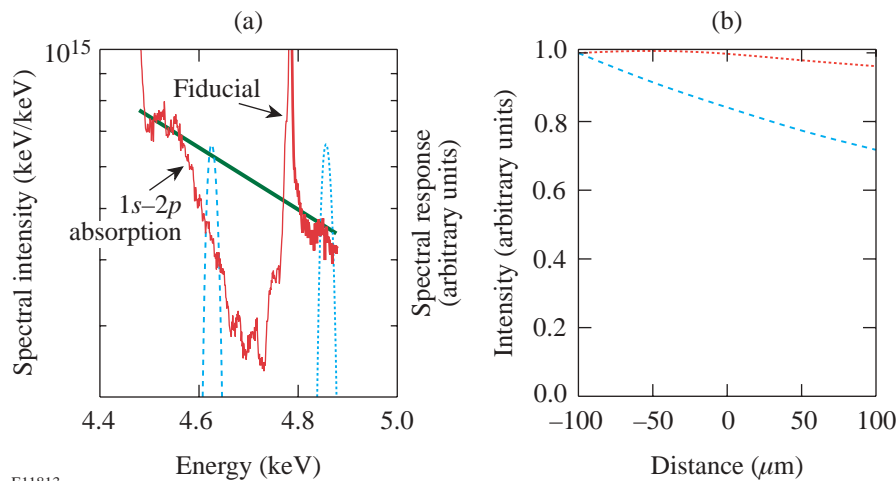
Figure 92.3
(a) Measured time-integrated spectrum $S_{\text{meas}}(E)$ as a function of photon energy for shot 26625 (red line). Estimated continuum level $S_{\text{con}}(E)$ as a function of photon energy (thick green line). The instrumental spectral responses as functions of photon energy of GMXI channels inside $[R_{1s-2p}(E)$, dashed line] and outside $[R_{<K}(E)$, dotted line] the titanium $1s$–$2p$ absorption region. (b) The spatial correction functions as a function of distance in the vertical axis for images inside (dashed line) and outside (dotted line) the titanium $1s$–$2p$ absorption region.

density modulation σ_{rms} is 59±14%, 18±5%, 26±10%, and 52±20% in the layers offset by 1, 5, 7, and 9 μm, respectively, as shown by the dashed line in Fig. 92.5(b). The modulations are highest at the inner surface (in the 1-μm-offset layer), which is unstable during the deceleration phase of implosion near peak compression. As expected, the modulations decrease in the bulk of the shell (in the 5- and 7-μm-offset layers) but then increase at the outer surface (in the 9-μm-offset layer), which was unstable during the acceleration, laser-driven phase of the implosion. The areal-density modulations in the whole shell are dominated by nonuniformities in the inner and central parts of the shell. The contribution of outer shell modulations is small because of the small compression at the outer surface. As shown in Fig. 92.1(b), the 9-μm-offset layer is expected to be outside the compressed shell, and therefore its high modulation level is not very important to the integrity of the whole shell. The measured level of modulation at the inner surface, 59±14%, is in agreement with previous results[22] measured at peak compression. For comparison, at peak neutron production, ~100 ps earlier than the peak compression, previous time-resolved measurements have shown lower modulation levels, about 20% at the inner surface.[18] In the future, experiments will extend the time-integrated measurements of modulations in the central and outer parts of the shell to time-resolved measurements using the same titanium $1s$–$2p$ absorption technique.

Conclusions

This article has presented the first time-integrated measurements of the compressed-shell modulation structure away from the inner surface. The differential imaging technique has replaced previous titanium K-edge imaging with much more sensitive imaging using the titanium $1s$–$2p$ absorption spectral region. As a result, measurements of modulations at central and outer parts of the shell have become accessible. In implosions with the 20-μm-thick shells, the relative areal-density modulation σ_{rms} is 59±14%, 18±5%, 26±10%, and 52±20%, in layers offset by 1, 5, 7, and 9 μm, respectively. The spatial spectra of modulations peaked at a spatial frequency of ~20 mm^{-1} corresponding to a wavelength of ~50 μm (with a mode number of $\ell \sim 6$). The areal-density modulations in the whole shell are dominated by modulations in the inner and central parts of the shell, while the contribution of outer shell modulations is small because of the smaller compression at the outer surface.

Offset by
1 μm   5 μm   7 μm   9 μm

100 μm

Shot 26625   Shot 26630   Shot 26631   Shot 26632

E11814
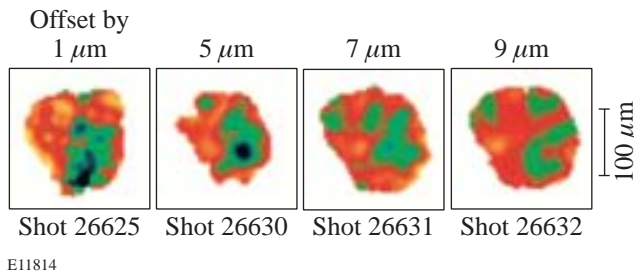
Figure 92.4
Optical-depth-modulation images at peak compression for shots with 1-μm- (shot 26625), 5-μm- (shot 26630), 7-μm- (shot 26631), and 9-μm-offset (shot 26632) titanium-doped layers integrated over ~200 ps of x-ray emission.

E11815
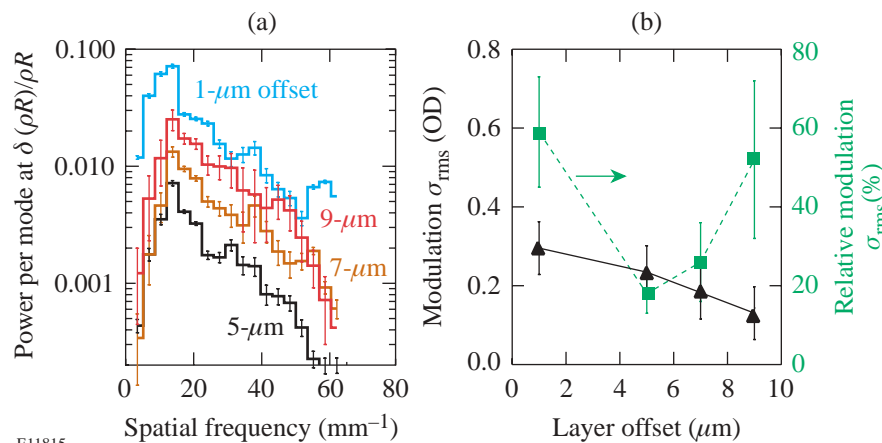
Figure 92.5
(a) Power per mode as a function of spatial frequency of relative areal-density modulations at peak compression for shots with 1-, 5-, 7-, and 9-μm-offset titanium-doped layers. (b) Peak compression optical-depth modulation σ_{rms} (solid line) and relative areal-density modulation σ_{rms} (dashed line) as functions of the layer offset.

REFERENCES

1. J. Nuckolls *et al.*, Nature **239**, 139 (1972).

2. J. D. Lindl, *Inertial Confinement Fusion: The Quest for Ignition and Energy Gain Using Indirect Drive* (Springer-Verlag, New York, 1998), Chap. 6, pp. 61–82.

3. C. J. Pawley *et al.*, Phys. Plasmas **6**, 565 (1999).

4. H. Azechi *et al.*, Phys. Plasmas **4**, 4079 (1997).

5. R. J. Taylor *et al.*, Phys. Rev. Lett. **76**, 1643 (1996).

6. D. H. Kalantar, M. H. Key, L. B. Da Silva, S. G. Glendinning, B. A. Remington, J. E. Rothenberg, F. Weber, S. V. Weber, E. Wolfrum, N. S. Kim, D. Neely, J. Zhang, J. S. Wark, A. Demir, J. Lin, R. Smith, G. J. Tallents, C. L. S. Lewis, A. MacPhee, J. Warwick, and J. P. Knauer, Phys. Plasmas **4**, 1985 (1997).

7. V. A. Smalyuk, T. R. Boehly, D. K. Bradley, V. N. Goncharov, J. A. Delettrez, J. P. Knauer, D. D. Meyerhofer, D. Oron, and D. Shvarts, Phys. Rev. Lett. **81**, 5342 (1998).

8. T. R. Boehly, V. N. Goncharov, O. Gotchev, J. P. Knauer, D. D. Meyerhofer, D. Oron, S. P. Regan, Y. Srebro, W. Seka, D. Shvarts, S. Skupsky, and V. A. Smalyuk, Phys. Plasmas **8**, 2331 (2001).

9. S. G. Glendinning, S. N. Dixit, B. A. Hammel, D. H. Kalantar, M. H. Key, J. D. Kilkenny, J. P. Knauer, D. M. Pennington, B. A. Remington, R. J. Wallace, and S. V. Weber, Phys. Rev. Lett. **78**, 3318 (1997).
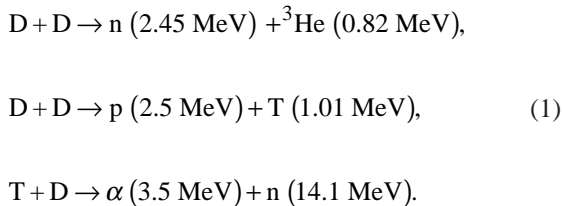
10. K. S. Budil *et al.*, Phys. Rev. Lett. **76**, 4536 (1996).

11. K. S. Budil *et al.*, Phys. Plasmas **8**, 2344 (2001).

12. J. P. Knauer, R. Betti, D. K. Bradley, T. R. Boehly, T. J. B. Collins, V. N. Goncharov, P. W. McKenty, D. D. Meyerhofer, V. A. Smalyuk, C. P. Verdon, S. G. Glendinning, D. H. Kalantar, and R. G. Watt, Phys. Plasmas **7**, 338 (2000).

13. M. S. Plesset and T. P. Mitchell, Q. Appl. Math. **13**, 41 (1956).

14. H. Sakagami and K. Nishihara, Phys. Rev. Lett. **65**, 432 (1990).

15. R. P. J. Town and A. R. Bell, Phys. Rev. Lett. **67**, 1863 (1991).

16. M. C. Herrmann, M. Tabak, and J. D. Lindl, Phys. Plasmas **8**, 2296 (2001).

17. R. Betti, K. Anderson, V. N. Goncharov, R. L. McCrory, D. D. Meyerhofer, S. Skupsky, and R. P. J. Town, Phys. Plasmas **9**, 2277 (2002).

18. V. A. Smalyuk, J. A. Delettrez, V. N. Goncharov, F. J. Marshall, D. D. Meyerhofer, S. P. Regan, T. C. Sangster, R. P. J. Town, and B. Yaakobi, Phys. Plasmas **9**, 2738 (2002).

19. S. P. Regan, J. A. Delettrez, F. J. Marshall, J. M. Soures, V. A. Smalyuk, B. Yaakobi, V. Yu. Glebov, P. A. Jaanimagi, D. D. Meyerhofer, P. B. Radha, W. Seka, S. Skupsky, C. Stoeckl, R. P. J. Town, D. A. Haynes, Jr., I. E. Golovkin, C. F. Hooper, Jr., J. A. Frenje, C. K. Li, R. D. Petrasso, and F. H. Séguin, Phys. Rev. Lett. **89**, 085003 (2002).

20. D. D. Meyerhofer, J. A. Delettrez, R. Epstein, V. Yu. Glebov, V. N. Goncharov, R. L. Keck, R. L. McCrory, P. W. McKenty, F. J. Marshall, P. B. Radha, S. P. Regan, S. Roberts, W. Seka, S. Skupsky, V. A. Smalyuk, C. Sorce, C. Stoeckl, J. M. Soures, R. P. J. Town, B. Yaakobi, J. D. Zuegel, J. Frenje, C. K. Li, R. D. Petrasso, D. G. Hicks, F. H. Séguin, K. Fletcher, S. Padalino, M. R. Freeman, N. Izumi, R. Lerche, T. W. Phillips, and T. C. Sangster, Phys. Plasmas **8**, 2251 (2001).

21. P. B. Radha, J. Delettrez, R. Epstein, V. Yu. Glebov, R. Keck, R. L. McCrory, P. McKenty, D. D. Meyerhofer, F. Marshall, S. P. Regan, S. Roberts, T. C. Sangster, W. Seka, S. Skupsky, V. Smalyuk, C. Sorce, C. Stoeckl, J. Soures, R. P. J. Town, B. Yaakobi, J. Frenje, C. K. Li, R. Petrasso, F. Séguin, K. Fletcher, S. Padalino, C. Freeman, N. Izumi, R. Lerche, and T. W. Phillips, Phys. Plasmas **9**, 2208 (2002).

22. B. Yaakobi, V. A. Smalyuk, J. A. Delettrez, F. J. Marshall, D. D. Meyerhofer, and W. Seka, Phys. Plasmas **7**, 3727 (2000).

23. J. Koch, Lawrence Livermore National Laboratory, private communication (2002).

24. T. R. Boehly, D. L. Brown, R. S. Craxton, R. L. Keck, J. P. Knauer, J. H. Kelly, T. J. Kessler, S. A. Kumpan, S. J. Loucks, S. A. Letzring, F. J. Marshall, R. L. McCrory, S. F. B. Morse, W. Seka, J. M. Soures, and C. P. Verdon, Opt. Commun. **133**, 495 (1997).

25. Y. Lin, T. J. Kessler, and G. N. Lawrence, Opt. Lett. **20**, 764 (1995).

26. S. P. Regan, J. A. Marozas, J. H. Kelly, T. R. Boehly, W. R. Donaldson, P. A. Jaanimagi, R. L. Keck, T. J. Kessler, D. D. Meyerhofer, W. Seka, S. Skupsky, and V. A. Smalyuk, J. Opt. Soc. Am. B **17**, 1483 (2000).

27. T. R. Boehly, V. A. Smalyuk, D. D. Meyerhofer, J. P. Knauer, D. K. Bradley, R. S. Craxton, M. J. Guardalben, S. Skupsky, and T. J. Kessler, J. Appl. Phys. **85**, 3444 (1999).

28. J. Delettrez, R. Epstein, M. C. Richardson, P. A. Jaanimagi, and B. L. Henke, Phys. Rev. A **36**, 3926 (1987).

29. F. J. Marshall and J. A. Oertel, Rev. Sci. Instrum. **6**, 735 (1997).

30. V. A. Smalyuk, T. R. Boehly, L. S. Iwan, T. J. Kessler, J. P. Knauer, F. J. Marshall, D. D. Meyerhofer, C. Stoeckl, B. Yaakobi, and D. K. Bradley, Rev. Sci. Instrum. **72**, 635 (2001).

31. F. J. Marshall, M. M. Allen, J. P. Knauer, J. A. Oertel, and T. Archuleta, Phys. Plasmas **5**, 1118 (1998).

32. D. H. Kalantar *et al.*, Rev. Sci. Instrum. **72**, 751 (2001).

A TIM-Based Neutron Temporal Diagnostic
for Cryogenic Experiments on OMEGA

Introduction

In inertial confinement fusion[1] experiments, shells filled with deuterium (D_2) or a deuterium–tritium (DT) mixture are heated by either direct laser illumination or soft x-ray radiation in a laser-heated hohlraum. The target is compressed to conditions under which thermonuclear fusion occurs. The most-promising target designs consist of a layered cryogenic D_2 or DT shell enclosed by a very thin shell of plastic, which is ablated very early and does not contribute significantly to the dynamics of the implosion.[2,3] During the plasma confinement time, which is of the order of 100 ps, fuel atoms undergoing fusion release energetic charged particles, photons, and neutrons. The fusion reactions of interest are

$$D + D \rightarrow n\ (2.45\ \text{MeV}) + {}^3\text{He}\ (0.82\ \text{MeV}),$$

$$D + D \rightarrow p\ (2.5\ \text{MeV}) + T\ (1.01\ \text{MeV}), \qquad (1)$$

$$T + D \rightarrow \alpha\ (3.5\ \text{MeV}) + n\ (14.1\ \text{MeV}).$$

The particle energies are shown in parentheses. While most of the charged particles are slowed down in the plasma and stopped, or "ranged out," before they leave the target, most neutrons escape the fuel without collision. As a result, the time history of neutrons arriving at an external diagnostic represents the burn history of the target fuel. Measurements of the neutron burn history provide important information about target performance that can be compared directly with numerical models. The time of peak neutron emission—the "neutron bang time"—is very sensitive to the details of the energy absorption and the equation of state used to describe the plasma. The neutron burn history contains valuable information about the plasma evolution close to the peak of compression. Target and laser illumination nonuniformities can feed through to the inner surface of the shell by the deceleration phase. Amplified by the Rayleigh–Taylor growth, these nonuniformities can severely disrupt the hot, neutron-pro-

ducing region of the target, leading to a strongly distorted neutron burn history. Several detectors measuring the neutron bang time[4–8] are described in the literature, but only the streak-camera–based neutron temporal diagnostic[9] (NTD) is capable of resolving the details of the neutron burn history with a resolution of ~50 ps for DD neutrons and ~25 ps for DT neutrons. The NTD is currently installed on LLE's OMEGA laser. NTD is a highly successful instrument,[10] but the size of the cryogenic target shroud system prevents placing the scintillator of the NTD system at its optimum location close to the target. This makes it too insensitive to record the burn history of the current D_2 cryogenic target experiments. Furthermore, Doppler broadening of the neutron spectrum severely compromises the time resolution of NTD at larger distances.[9] These mechanical constraints motivated the development of new cryogenic-compatible neutron temporal diagnostic (cryoNTD), which fits into LLE's standard ten-inch manipulator (TIM) diagnostic inserters, to provide high-resolution neutron emission measurements for cryogenic implosions. This article describes the setup of cryoNTD and first experimental results compared to NTD on room-temperature direct-drive implosions and on cryogenic implosions.

Setup of the Detector System

The cryoNTD system, shown schematically in Fig. 92.6, is based on a fast plastic scintillator (Bicron BC422[11]), which converts the kinetic energy of the neutrons into light. A light collection and transfer system (Fig. 92.7) transports the light from the scintillator to the input plane of a fast (<15-ps) optical streak camera.[12] The front end of the optical system is mounted in the TIM and inserted close to the target. An optical fiducial is used to time the neutron signals relative to the incident laser pulse. The size of the scintillator is that required to record high-quality burn histories at a yield comparable to 10^{10}, which is the performance of the early cryogenic D_2 target implosions on OMEGA.[3] A simple scaling from the sensitivity of NTD with a 6-mm-diam scintillator at 2 cm from the target to the required standoff distance of 9 cm shows that a 30-mm-diam scintillator is sufficient. Due to the limited size of the photocathode of the streak camera, a demagnifying optical system
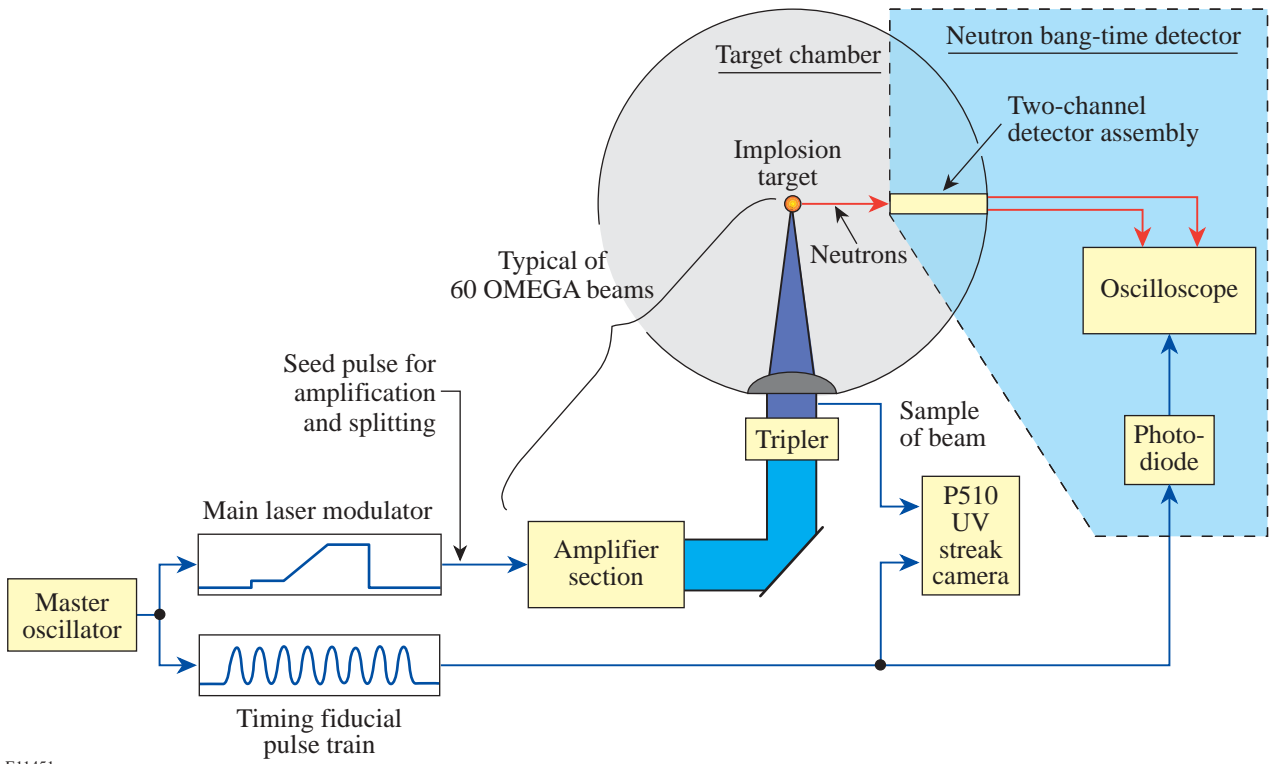
E11451

Figure 92.6
A block diagram of the cryoNTD detector system integrated into the OMEGA facility. The fiducial system provides cross timing between the neutron signals and the incident laser pulse, which is recorded on the P510 UV streak camera.
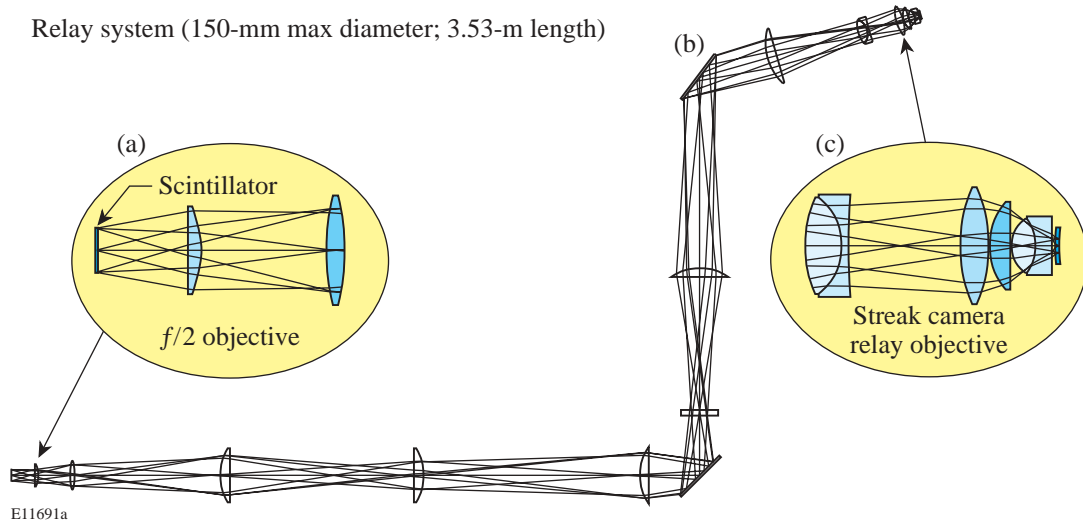
E11691a

Figure 92.7
A fast scintillator converts the neutron kinetic energy into light, which is collected by a fast $f/2$ optic (a). An optical system (b) transports the light to the input plane of a fast optical streak camera with 3:1 demagnification though an $f/0.67$ final lens system (c).

with a 3:1 ratio is used. A fast $f/2$ lens collects the light from the scintillator with high efficiency [Fig. 92.7(a)]. An optical system consisting of 11 lenses and 2 mirrors relays the image of the scintillator though the TIM and the vacuum window along a 3.5-m optical path to the streak camera [Fig. 92.7(b)]. The 3:1 demagnification in combination with the fast $f/2$ lens leads to a very demanding $f/0.67$ final lens system, which maximizes the transmission of the optical system [Fig. 92.7(c)]. The 527-nm light from the OMEGA fiducial system is delivered via an optical fiber collimated and imaged onto the streak camera through the final lens assembly. The OMEGA fiducial consists of a series of eight pulses spaced 548 ps apart and is synchronized to the shaped OMEGA laser pulse with a jitter of less than 20 ps. The optical fiducial is amplified separately from the main laser pulse, split, and distributed to various diagnostic instruments for precision timing. The fiducial pulse train is also recorded on the P510 ultraviolet streak camera,[13] which measures the laser pulse shape. The common optical fiducial serves as a reference for both the neutron signal and the laser pulse, thus enabling very accurate timing of the cryoNTD signals.

The low light levels from the scintillator, the fast collection and transport optic, and the TIM design make it necessary to install a sophisticated system of shields and light baffles to avoid any scattered laser light from entering the optical system. Figure 92.8(a) shows a sample image from a cryogenic D_2 implosion with a yield of 3.17×10^{10} recorded on the CCD camera attached to the optical streak camera. The fiducial is seen on top of the image and the scintillator output in the center. The "wings" seen on either side of the scintillator signal are most probably produced by the spatially nonuniform transmission of the optical system. Figure 92.8(b) shows image exposure versus time averaged across the central portion of the scintillator signal. The streak camera flat-field and geometric distortions are included in the signal processing. The time history of the scintillator signal is the convolution of the neutron temporal distribution with the scintillator response. The scintillator has a very fast rise time of <20 ps and a decay time of ~1.2 ns. Consequently the burn history information is encoded in the leading edge of the pulse due to the much longer decay of the scintillator compared to the burnwidth.

Data Analysis and Calibration

The actual neutron burn history is obtained by deconvolving the effect of the long scintillator decay from the recorded signal. A "physical modeling" approach is used for the deconvolution, where the neutron signal n_i at the pixel location i is given as the recorded signal s_i minus the sum of all

earlier neutron signals, which are decaying exponentially at the scintillator fall time τ:

$$n_i = s_i - \sum_{j=0}^{i-1} n_j \exp\left[\frac{(i-j) \times \Delta t_p}{\tau} \right]. \tag{2}$$

In this equation, Δt_p is the time separation of two pixels. This method is fast and deterministic and is very stable against noise on the streak camera signal. The neutron signal is broadened by several different mechanisms. The thermal broadening of the neutron energy spectrum leads to an arrival time spread in the scintillator of[9]

$$\Delta t_T^{DD} = 778 \frac{\text{ps}}{m \, \text{keV}^{1/2}} \sqrt{T} \times d \tag{3}$$

(a)

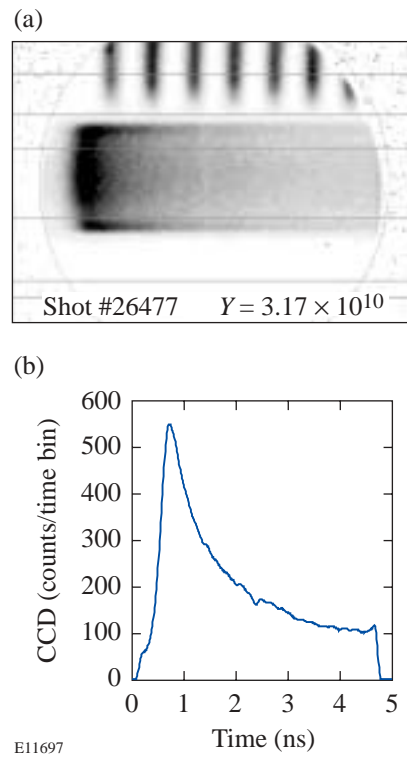Shot #26477 $Y = 3.17 \times 10^{10}$

(b)

E11697

Figure 92.8
A streak camera image (a) of the neutron signal from a D_2 cryogenic implosion with a yield of 3.17×10^{10}. The fiducial seen on the top of the image is used for timing the neutron signal to the incident laser pulse. The image exposure versus time (b) is averaged across the central portion of the scintillator signal.

for DD neutrons, where Δt_T is the FWHM in ps, d is the target-to-detector distance in meters, and T is the neutron-averaged ion temperature in keV. For the 9-cm standoff distance of cryoNTD, this effect limits the time resolution to ~70 ps at 1 keV. The finite neutron transit time through the scintillator $\Delta t_s = \Delta x / v_n$ broadens the signal by $\Delta t_s^{DD} = 44$ ps with a 1-mm-thick scintillator using a neutron speed of $v_n = 2.16$ cm/ns. Adding both effects in quadrature gives an estimate of ~80 ps for the time resolution of cryoNTD. Figure 92.9 shows a comparison of the neutron burn histories obtained by NTD and cryoNTD on a room-temperature direct-drive OMEGA plastic target filled with 15 atm of D_2. The signals are aligned in time for best correlation to allow a better comparison. Although the effects of the limited time resolution of cryoNTD compared to NTD, which has a time resolution of ~50 ps for DD neutrons, can be seen, the burn histories compare very favorably.

Absolute timing is established using the OMEGA fiducial system. The recorded fiducial pulse is fitted by a pulse train of eight Gaussian pulses spaced apart at the well-characterized period of $d_t = 548$ ps:

$$\text{fidu}(t) = \sum_{i=0}^{7} a_i \, \exp\left\{-\left[t - (t_0 + i \times dt)\right]^2 \middle/ 2\sigma^2\right\} \qquad (4)$$

to the recorded signal. Here a_i is the amplitude of each fiducial peak, t_0 is the time of the first fiducial pulse, and σ is

the standard deviation of an individual fiducial pulse. This reduces the influence of noise on the determination of the timing reference. CryoNTD has been calibrated against NTD using a series of room-temperature plastic targets filled with D_2. The bang times measured by cryoNTD are very close to the bang times from NTD (Fig. 92.10), showing only 40-ps rms spread. Figure 92.11 shows a comparison of neutron burn histories from a direct-drive cryogenic target with a low-nonuniformity ice layer[3] and a cryogenic target with a very poor layer quality, both irradiated by a 1-ns, square, 23-kJ laser

E11699
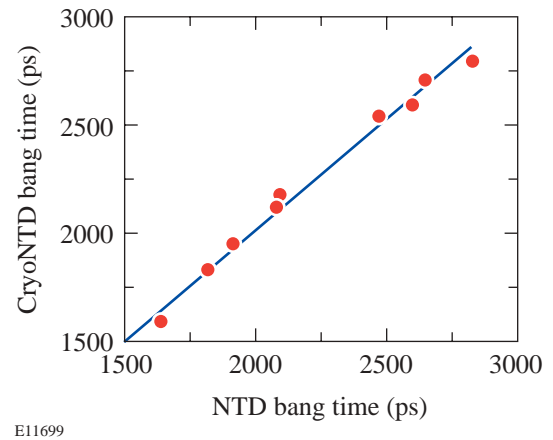
Figure 92.10
The bang times measured by the NTD compared to those of the cryoNTD for a series of room-temperature plastic targets.

E11698

Figure 92.9
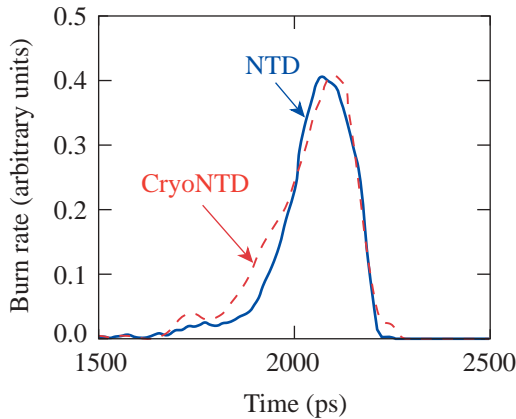A comparison of the neutron burn histories recorded by the cryoNTD and the NTD from a room-temperature plastic target filled with 15 atm D_2 at a yield of 2×10^{10}.

E11700

Figure 92.11
A comparison of neutron burn histories from direct-drive cryogenic targets with a good ice layer (solid line) and a poor ice layer (dashed line). Both targets are driven by a 1-ns square laser pulse.

pulse. The temporal shape of the laser pulse is shown for comparison. Even though the neutron yield of both implosions is relatively close—1.5×10^{10} for the poor capsule and 3.1×10^{10} for the good capsule—the neutron burn history shows dramatic differences.

Summary and Outlook

A cryogenic-compatible neutron temporal diagnostic (cryoNTD) has been developed for OMEGA to allow the high-resolution measurement of the neutron burn history on early direct-drive D_2 cryogenic targets. The scintillator and the front end of the optical system are mounted in a TIM and inserted close to the target. The back end of the optical system containing the optical streak camera to record the light emitted from the scintillator is mounted outside the vacuum of the target chamber. The OMEGA fiducial system is used to cross-time the neutron signals to the incident laser pulse. This instrument is able to measure the neutron burn history at yields $>10^9$ DD neutrons with a resolution of ~80 ps. An absolute timing accuracy of 40 ps has been demonstrated using cross-calibration to the NTD. The time resolution of the cryoNTD is sufficient to resolve the important features of the reaction rate history of cryogenic implosions with high absolute timing accuracy. Future optimized cryogenic targets will generally show higher neutron yields,[3] allowing the use of a thinner scintillator (<0.5 mm), which will improve the time resolution of the instrument. Neutral density filters can be inserted in the light path to accommodate even the highest predicted yields, which will be comparable to 10^{12}.

ACKNOWLEDGMENT

REFERENCES

1. J. H. Nuckolls, Phys. Today **35**, 24 (1982).

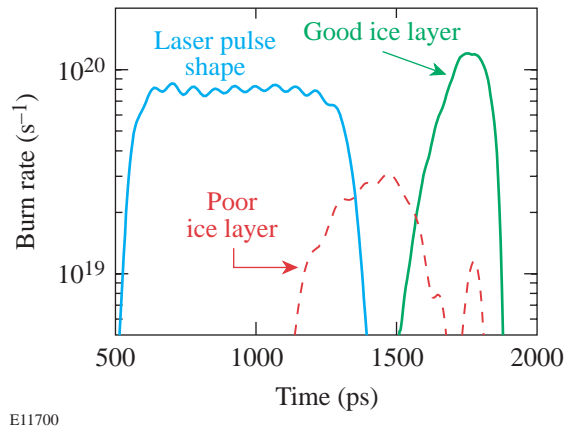2. S. Skupsky, R. Betti, T. J. B. Collins, V. N. Goncharov, D. R. Harding, R. L. McCrory, P. W. McKenty, D. D. Meyerhofer, and R. P. J. Town, in *Inertial Fusion Sciences and Applications 2001*, edited by K. Tanaka, D. D. Meyerhofer, and J. Meyer-ter-Vehn (Elsevier, Paris, 2002), pp. 240–245.

3. C. Stoeckl, C. Chiritescu, J. A. Delettrez, R. Epstein, V. Yu. Glebov, D. R. Harding, R. L. Keck, S. J. Loucks, L. D. Lund, R. L. McCrory, P. W. McKenty, F. J. Marshall, D. D. Meyerhofer, S. F. B. Morse, S. P. Regan, P. B. Radha, S. Roberts, T. C. Sangster, W. Seka, S. Skupsky, V. A. Smalyuk, C. Sorce, J. M. Soures, R. P. J. Town, J. A. Frenje, C. K. Li, R. D. Petrasso, F. H. Séguin, K. Fletcher, S. Padalino, C. Freeman, N. Izumi, R. Lerche, and T. W. Phillips, Phys. Plasmas **9**, 2195 (2002).

4. R. A. Lerche *et al.*, Rev. Sci. Instrum. **59**, 1697 (1988).

5. N. Miyanaga *et al.*, Rev. Sci. Instrum. **6**, 3592 (1990).

6. R. A. Lerche, M. D. Cable, and D. W. Phillion, Rev. Sci. Instrum. **61**, 3187 (1990).

7. T. J. Murphy and R. A. Lerche, *ICF Quarterly Report* **3**, 35, Lawrence Livermore National Laboratory, Livermore, CA, UCRL-LR-105821-93-1 (1992).

8. R. A. Lerche, D. W. Phillion, and G. L. Tietbohl, in *Ultrahigh- and High-Speed Photography, Videography, and Photonics '93*, edited by P. W. Roehrenbeck (SPIE, Bellingham, WA, 1993), Vol. 2002, pp. 153–161.

9. R. A. Lerche, D. W. Phillion, and G. L. Tietbohl, Rev. Sci. Instrum. **66**, 933 (1995).

10. D. D. Meyerhofer, J. A. Delettrez, R. Epstein, V. Yu. Glebov, V. N. Goncharov, R. L. Keck, R. L. McCrory, P. W. McKenty, F. J. Marshall, P. B. Radha, S. P. Regan, S. Roberts, W. Seka, S. Skupsky, V. A. Smalyuk, C. Sorce, C. Stoeckl, J. M. Soures, R. P. J. Town, B. Yaakobi, J. D. Zuegel, J. Frenje, C. K. Li, R. D. Petrasso, D. G. Hicks, F. H. Séguin, K. Fletcher, S. Padalino, M. R. Freeman, N. Izumi, R. Lerche, T. W. Phillips, and T. C. Sangster, Phys. Plasmas **8**, 2251 (2001).

11. Bicron Newbury, Newbury, OH 44065-9577.

12. R. A. Lerche, in *Ultrahigh- and High-Speed Photography, Videography, Photonics, and Velocimetry '90*, edited by P. A. Jaanimagi, B. T. Neyer, and L. L. Shaw (SPIE, Bellingham, WA, 1991), Vol. 1346, pp. 376–383.

13. W. R. Donaldson, R. Boni, R. L. Keck, and P. A. Jaanimagi, Rev. Sci. Instrum. **73**, 2606 (2002).

Carbon Activation Diagnostic for Tertiary Neutron Measurements
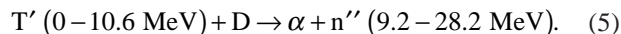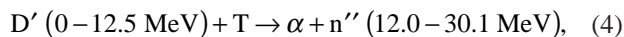
Introduction

In inertial confinement fusion (ICF)[1] implosions, nuclear reactions in the fusion fuel produce energetic neutrons and a variety of charged particles. The primary reaction for DT fuel is

$$D + T \rightarrow \alpha + n \ (14.1 \text{ MeV}). \qquad (1)$$

In a secondary reaction, a small percentage of 14.1-MeV neutrons will scatter elastically from D or T ions in the fuel (prime notation indicates a scattered particle):

$$n + D \rightarrow n' + D' \ (0-12.5 \text{ MeV}), \qquad (2)$$

$$n + T \rightarrow n' + T' \ (0-10.6 \text{ MeV}). \qquad (3)$$
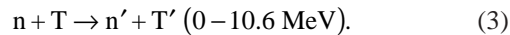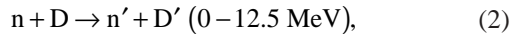
As these scattered ions pass through the fuel, some will undergo tertiary, in-flight fusion reactions:

$$D' \ (0-12.5 \text{ MeV}) + T \rightarrow \alpha + n'' \ (12.0-30.1 \text{ MeV}), \quad (4)$$

$$T' \ (0-10.6 \text{ MeV}) + D \rightarrow \alpha + n'' \ (9.2-28.2 \text{ MeV}). \quad (5)$$

The yield of these high-energy tertiary neutrons is proportional to $(\rho R)^2$ for small values of ρR, where ρR is the areal density of the DT fuel, and to ρR for large values of ρR (Ref. 2) and is about 10^{-6} of the primary 14.1-MeV neutron yield.

The fuel areal density ρR is a fundamental parameter that characterizes the performance of an ICF implosion. For high areal densities ($\rho R > 0.3$ g/cm^2), which will be realized in implosion experiments at the National Ignition Facility (NIF)

and Laser Megajoule Facility (LMJ), the target areal density exceeds the stopping range of charged particles, and ρR measurements with charged-particle spectroscopy will be difficult. In this region, an areal-density measurement using tertiary neutrons is one of the alternative methods. The use of tertiary neutrons for measurements of high areal densities in ICF implosions has been proposed by several authors[2–4] in the past. This article describes the experimental development of a tertiary neutron diagnostic using carbon activation and the 30-kJ, 60-beam OMEGA laser system.[5]

Carbon as an Activation Material

The use of carbon as a threshold activation material was proposed many years ago.[3] There are three main reasons why carbon is a good activation material for tertiary neutron measurement. First, the ^{12}C(n,2n)^{11}C reaction has a Q value of 18.7 MeV, well above the 14.1-MeV primary DT neutron energy. Thus, the reaction ^{12}C(n,2n)^{11}C will occur only from interactions with the high-energy tertiary neutrons. The experimental cross section of the ^{12}C(n,2n)^{11}C reaction shown in Fig. 92.12 was measured in several experiments and can be used to calculate a tertiary neutron signal in a carbon sample.

The second attractive feature of carbon is the properties of its decay. The isotope ^{11}C decays to ^{11}B with a half-life of 20.39 min and emits a positron, resulting in the production of two back-to-back, 511-keV gamma rays upon annihilation. The ^{11}C half-life is advantageous since it is compatible with the experimental conditions on OMEGA. The OMEGA laser fires at approximately one-hour intervals, and it takes a few minutes to remove the disk from the target chamber and carry it to the gamma-detection system after the laser has been fired. Thus, if the half-life were much shorter, a significant amount of information would be lost during transfer. If it were considerably longer, there would not be enough time to record all of the decays between shots. The positron decay of ^{11}C is nearly identical to the ^{62}Cu decay used in the copper activation measurements of 14.1-MeV primary DT yields; therefore, the well-developed copper activation gamma-counting system[6,7] can be used.
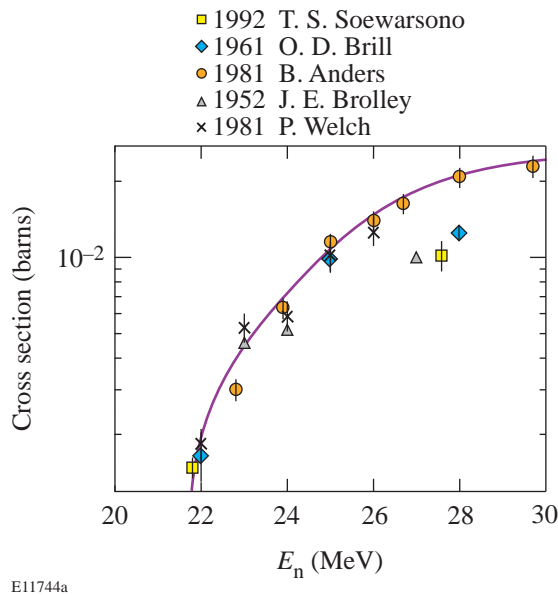
□ 1992 T. S. Soewarsono
◆ 1961 O. D. Brill
● 1981 B. Anders
△ 1952 J. E. Brolley
× 1981 P. Welch

E11744a

Figure 92.12
Experimentally measured cross section σ for the reaction $^{12}C(n,2n)^{11}C$. The solid line is the fit used for calculations in the **Carbon Activation for OMEGA and the NIF** section.

The third reason carbon was chosen is the availability of high-purity samples. The purity of the activation sample is very important for tertiary activation diagnostic, as will be discussed in the **Contamination Signal in Carbon Activation** section below. Carbon is also a nontoxic, nonflammable, inexpensive, and safe material. These properties give carbon a big advantage over sodium, which has also been proposed.[3]

OMEGA Carbon Activation System

The activation samples with a 7.6-cm diameter and a different thickness can be inserted with a pneumatic retractor into a reentrant tube installed on the OMEGA target chamber. Before a shot, the activation samples are manually installed in the retractor holder and inserted into the target chamber at 42 cm from the target. Immediately after a laser shot, the activated sample is automatically extracted from the chamber and dropped through a plastic tube to the pickup basket in a room under the OMEGA Target Bay. The operator delivers the activated sample to the gamma-detection system in the counting room. Generally, this process takes 1.5 to 3 min. Since the space in the OMEGA target chamber is very limited, the same pneumatic retractor is used for both copper and carbon activation diagnostics.

The OMEGA gamma-detection system consists of two 7.6-cm-diam, 7.6-cm-thick NaI(Tl) scintillation detectors separated by 0.89 cm or 1.78 cm and associated electronics. Each detector has an ORTEC 460 delay linear amplifier and an ORTEC 551 single-channel analyzer (SCA), which perform pulse-height discrimination. The time coincidence between two detectors is established by an ORTEC 418A universal coincidence module followed by an ORTEC 974 quad counter/ timer module that counts time, single counts from each detector and two detectors coincidence. The 974 counter is read by a PC-based data acquisition program every 5 s and recorded for future analysis. The window of each SCA is set between 426 keV and 596 keV in order to detect 511-keV gammas from positron annihilation. The energy scale of each SCA is calibrated with a ^{22}Na radioactive source before each set of measurements. The NaI detectors are shielded from all sides with 7.6 cm of lead to reduce cosmic ray background. As a result of the shielding, the background coincidence count rate is about 18 counts/hour. To isolate the NaI detectors from direct activation by 14.1-MeV neutrons produced during high-yield OMEGA shots, the gamma-detection system is placed at a distance of 120 m from the target. Dedicated experiments have shown that the gamma-detection system records no coincidence for yields up to 7×10^{13}.

Contamination Signal in Carbon Activation

Any material that produces a positron emitter by interaction with 14.1-MeV neutrons will add a contamination signal in the carbon activation diagnostic. The most-dangerous contaminants for carbon activation are copper and nitrogen, which produce positron emitters in reactions $^{63}Cu(n,2n)^{62}Cu$, $^{65}Cu(n,2n)^{64}Cu$, and $^{14}N(n,2n)^{13}N$. Each of these reactions has a threshold below 14 MeV. The nitrogen cross section for a 14.1-MeV neutron is 6.5 mb and is comparable to the carbon cross section for tertiary neutrons. The ^{63}Cu cross section for 14.1-MeV neutrons is about 100 times larger than the carbon cross section for tertiary neutrons. Since the primary 14.1-MeV neutron yield is about 10^6 times larger than the tertiary yield, the contamination in the carbon sample must be less than one part per million (ppm) for nitrogen and 0.01 ppm for copper.

In the development of the carbon activation diagnostic, graphite disks from Bay Carbon[8] were used. Bay Carbon carefully selects their graphite for its physical and chemical compositions and performs chemical vapor purification (CVP) of the graphite. Bay Carbon purity is defined as follows: No more than three elements may be present (other than carbon), no single element may exceed one part per million

(ppm), and the total impurity level may not exceed two ppm in the graphite.

In addition to the purity of the sample material itself, proper packaging and handling procedures are very important. To keep the graphite disks clean before a shot, the disks are shrink-wrapped in plastic before being placed into the retractor and delivered to the gamma-detection system. The plastic is removed and discarded before counting. This procedure prevents surface contamination of the graphite disks. This is especially important on OMEGA because the same retractor is used for both copper and carbon activation. The graphite disks without shrink wrap showed a contamination signal of about 1000 coincidences per hour of counting. The shrink-wrapping procedure protects the graphite disks from surface contamination but leads to other forms of contamination.

The shrink-wrap plastic contains hydrogen. When bombarded by 14.1-MeV neutrons, the hydrogen atoms can produce elastically scattered protons with energies up to 14 MeV. These protons interact with carbon in the graphite disks and produce positron-emitting nitrogen via reaction $^{12}C(p,\gamma)^{13}N$. This source of contamination was eliminated through the use of graphite foils (thinner pieces of graphite) placed on both sides of the disk between the disk and the shrink wrap. The graphite foils act as protective barriers for the protons from the plastic. This combination of the disk and two foils is called a "sandwich." The foils are made from the same graphite as the disks in order to keep the disks clean. The foils are 2.5 mm thick, enough to completely stop the protons originating in the plastic and prevent their penetrating the graphite disk. All contamination from such protons is restricted to the graphite foils, which are removed and discarded before counting.

Because the graphite porosity is about 20%, the graphite disks can absorb and store ^{14}N nitrogen from the air. The 14.1-MeV neutrons can produce positron-emitting nitrogen ^{13}N via the reaction $^{14}N(n,2n)^{13}N$. To remove air from the graphite disks, a special purification facility was developed at the SUNY Geneseo.

The first step in the purification process is to remove the nitrogen and other contaminant gases from within the graphite disks and replace them with an inert gas such as argon that cannot be activated by 14.1-MeV neutrons. To do this, a large three-zone tube furnace is employed. This furnace is composed of a 7-ft-long, 7-in.-diam quartz tube. The graphite disks are inserted into the oven using a 5-ft-long rod. The oven is then brought to vacuum, heated to 1000°C, and maintained at that

temperature for several hours. After cooling to room temperature, the quartz tube is flooded with high-purity (0.99995) argon. The disks stay in this environment for several hours. They are extracted from the quartz tube by placing a large glove bag over one end of the tube, filling it to positive pressure with argon gas, and then using a rod to remove the disks from the quartz tube into the glove bag. Graphite foils are fit to both sides of the disk, and the disks are then placed into small vacuum bags, which are immediately vacuum sealed. The disks can remain in the vacuum-sealed bag for at least six months without contamination.

In earlier experiments, the disks were taken out of the vacuum bags immediately before the shot and quickly sealed in shrink wrap, which was left on during the shot. In later experiments, the disks were shot in the vacuum bags, never being exposed to air contaminants.

Experimental Results

The main goal of the diagnostic development was to minimize the contamination signal in carbon samples. Several iterations of the purification, packaging, and gamma-detection system were made until the system described above was developed. In this section, results obtained in 2001–2002, after major improvements to the system, are presented.

Tests of the carbon activation system were carried out on the 30-kJ, 60-beam OMEGA laser system[5] in direct-drive implosions. A 1-ns square laser pulse shape with 28-kJ to 31-kJ energy was used to implode glass microballoons with shell thicknesses from 2.5 to 4 μm filled with 20 atm of DT. These targets have a very low ρR and should produce no measurable tertiary neutrons. Thus, any signal in these experiments was a contamination signal. The primary DT neutron yield was measured by an absolutely calibrated time-of-flight scintillating counter located 20 m from the target. The neutron yields in these experiments ranged from 4×10^{13} to 9.6×10^{13}.

In the experiments on OMEGA, the cosmic ray background for the empty gamma-detection system was measured, fitted to a linear function, and subtracted from the coincident counts for each carbon disk. The results from the graphite disks were then normalized to a yield of 7.4×10^{13}, which was the average neutron yield for this series of measurements. The carbon disks without shrink wrap produced a contamination signal of about 1000 counts; disks in shrink wrap produce about 80 to 100 counts; and disks packaged as a sandwich in shrink wrap produce a contamination signal of only about 30 to 50 counts. The results for the carbon disks irradiated in sealed vacuum bags

are shown in Fig. 92.13. The two shots with carbon disks in vacuum bags without foils show a higher contamination signal than from a sandwich, demonstrating the importance of shielding from the protons originating in the plastic. The six sandwich results include four shots from June 2001 and two "consistency check" shots from June 2002. All of them show a similar contamination signal of 30 to 50 coincidence counts for 7.4×10^{13} primary neutron yield.
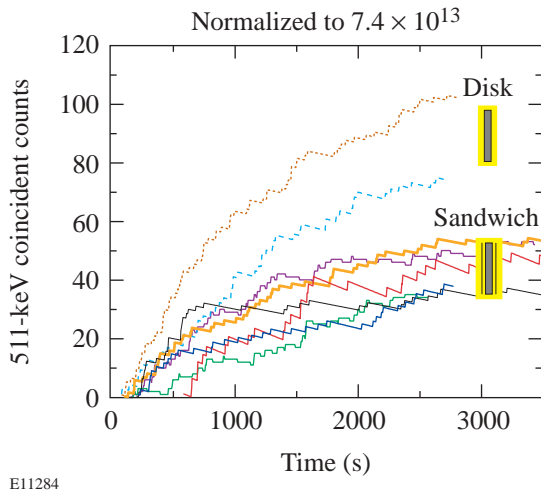

E11284

Figure 92.13
Coincidence counts in the gamma-detection system as a function of time after a shot for 0.89-cm-thick disks and "sandwiches."

The 0.89-cm carbon disk thickness originates from a copper disk thickness optimized for 511-keV gamma absorption in copper. Since the absorption length of 511-keV gammas in carbon is about five times larger than in copper, the carbon disk thickness can be increased. In June 2002 we tested on OMEGA carbon disks with a thickness of 1.78 cm. The results of these tests normalized to the same 7.4×10^{13} primary neutron yield are shown in Fig. 92.14. The contamination signals from the thicker disks are similar to the thinner disks, suggesting that contamination is mostly a surface-related effect. In the thicker disks the tertiary signal will increase by a factor of 2, and the efficiency of the gamma-detection system decreases for the thicker disk by approximately 20%; the thicker disk has a 1.8 gain in sensitivity. Monte Carlo calculations for the optimal carbon disk thickness are in progress.

Consistent, repeatable results in two sets of measurements one year apart, which include the manufacture of new carbon disks, show stability and reproducibility of the carbon activation diagnostic chain—from manufacturing the disk to the purification and handling system.

E11741
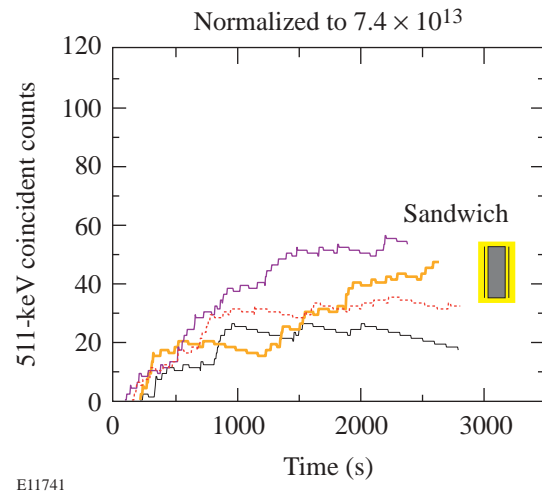
Figure 92.14
Coincidence counts in the gamma-detection system as a function of time after a shot for 1.78-cm-thick sandwiches.

Carbon Activation for OMEGA and the NIF

Direct-drive spherical DD cryogenic target implosions[9] are routinely carried out on the 60-beam OMEGA laser system, and implosions with cryogenic DT fuel are planned for the near future. The OMEGA cryogenic DT design and expected laser pulse shape with an intensity picket are shown in Fig. 92.15. The intensity picket shapes the adiabat of the main fuel and ablator, reducing both the seeds and the growth rate of Rayleigh–Taylor instability.[10] A one-dimensional $LILAC$[11] simulation calculates a neutron yield of $Y_n = 6.0 \times 10^{14}$ and a neutron-averaged fuel areal density $\langle \rho R \rangle = 245$ mg/cm^2 for the design shown in Fig. 92.15. The $IRIS$[12] postprocessor to $LILAC$ was used to calculate the spectrum of all neutrons emerging from an OMEGA cryogenic DT target. Figure 92.16 shows the calculated tertiary/primary neutron spectrum and the same spectrum multiplied by the cross section of the ^{12}C(n,2n)^{11}C reaction approximated by the solid line in Fig. 92.12.

The target design from Fig. 92.15 and tertiary spectrum from Fig. 92.16 were used to estimate the expected signal from a carbon activation sample in OMEGA cryogenic DT experiments. A 7.6-cm-diam, 0.89-cm-thick carbon disk at 40 cm from the target subtends solid angle 2.25×10^{-3}. The integral of the tertiary/primary neutron spectrum multiplied by the carbon cross section in Fig. 92.16 is about 3×10^{-5} mb/primary neutron. The 80-g carbon disk will receive 1.2×10^{-7} activations for each incident primary neutron or 2.7×10^{-10} activations for each primary neutron produced in the

target. The gamma-detection system has an efficiency of 20%, thus the measured coincidence counts per produced primary neutron will be 5.4×10^{-11}. At a primary DT yield $Y_n = 6.0 \times 10^{14}$, we expect 3.2×10^4 coincidence counts from tertiary neutrons in the gamma-detection system. A similar calculation

for the implosion quenched at a $\langle \rho R \rangle = 150$ mg/cm^2 and neutron yield $Y_n = 9.2 \times 10^{13}$ gives about 400 coincidence counts in the gamma-detection system. With the achieved level of contamination signal, the present carbon activation system can be used for areal-density measurements of OMEGA cryogenic DT targets.

Tertiary neutron measurements by carbon activation are an inexpensive, well-developed diagnostic that can be easily deployed on the NIF for areal-density measurements. All major diagnostic development problems have already been solved on OMEGA. Purified carbon packages are good for at least six months; consequently, they can be prepared in the already-existing purification facility at SUNY Geneseo and shipped to the NIF as needed. The carbon activation diagnostic will require a rapid transport system similar or identical to the yield activation system on the NIF because of the relatively short half-life of carbon.

The only problem that must be solved on the NIF for carbon activation is background in the gamma-detection system itself generated by the neutrons from a NIF implosion. Such a background-induced problem was observed on OMEGA when the gamma-detection system was located 40 m from the target. In Fig. 92.17 the background coincidence counts of an empty gamma-detection system are shown as a function of time. After a shot with a neutron yield of 7.35×10^{13}, a jump of 42 coincidence counts was recorded. Additionally the background stays high for about 1 h after the shot and then returns to the normal cosmic ray level. On OMEGA this background prob-

E11873

Figure 92.15
The OMEGA cryogenic capsule design (a) and pulse shape with an intensity picket (b).
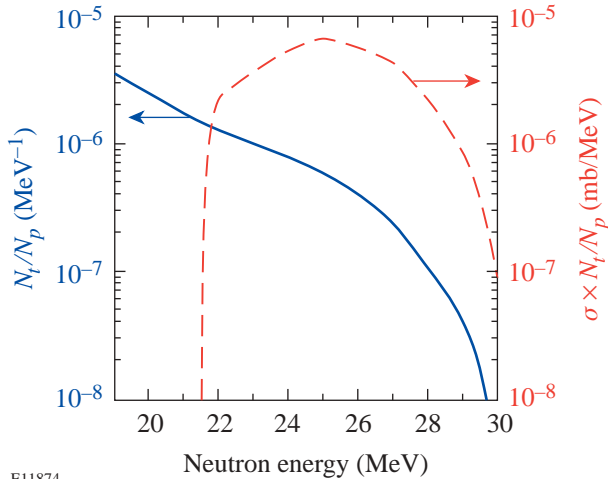
E11874

Figure 92.16
Ratio of tertiary N_t to the primary N_p neutrons per energy interval (MeV) as a function of tertiary neutron energy and the same ratio multiplied by the carbon cross section σ in mb.
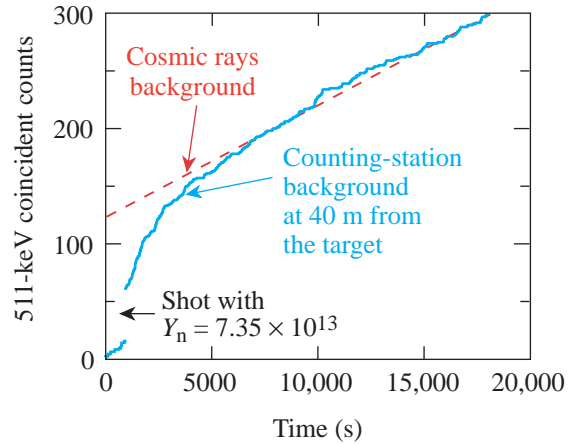
E11689

Figure 92.17
Background coincidence counts of an empty gamma-detection system at 40 m from the target during an OMEGA shot with a neutron yield of 7.35×10^{13}.

lem was solved by moving the gamma-detection system much farther from the target. Since neutron yield on the NIF will be about 10^5 times higher than on OMEGA, a judicious choice of neutron shielding and location of the gamma-detection system will be required. Background measurements during the shot will also be needed. Two identical gamma-detection systems could be implemented—one for signal and another for the background measurement.

Conclusions

This article has described the experimental development of the carbon activation diagnostic for tertiary neutron measurements performed on the 60-beam OMEGA laser system. We have created a purification facility and have developed packaging and handling procedures that significantly reduce the contamination signal in the carbon samples. Experiments on OMEGA in 2001–2002 have shown very good reproducibility of the contamination signal from the carbon samples.

The present carbon activation system is ready for areal-density measurements of DT cryogenic targets on OMEGA. The same carbon activation diagnostic can be implemented on the NIF, although the neutron-induced background issues in the gamma-detection system need to be solved for the NIF.

REFERENCES

1. J. D. Lindl, *Inertial Confinement Fusion: The Quest for Ignition and Energy Gain Using Indirect Drive* (Springer-Verlag, New York, 1998).

2. Laboratory for Laser Energetics LLE Review **69**, 46, NTIS document No. DOE/SF/19460-152 (1996). Copies may be obtained from the National Technical Information Service, Springfield, VA 22161.

3. D. R. Welch, H. Kislev, and G. H. Miley, Rev. Sci. Instrum. **59**, 610 (1988).

4. H. Azechi, M. D. Cable, and R. O. Stapf, Laser Part. Beams **9**, 119 (1991).

5. T. R. Boehly, D. L. Brown, R. S. Craxton, R. L. Keck, J. P. Knauer, J. H. Kelly, T. J. Kessler, S. A. Kumpan, S. J. Loucks, S. A. Letzring, F. J. Marshall, R. L. McCrory, S. F. B. Morse, W. Seka, J. M. Soures, and C. P. Verdon, Opt. Commun. **133**, 495 (1997).

6. F. C. Young, J. Golden, and C. A. Kapetanakos, Rev. Sci. Instrum. **48**, 432 (1977).

7. R. J. Leeper *et al.,* Nucl. Instrum. Methods Phys. Res. B **B24**, 695 (1987).

8. Bay Carbon Inc., Bay City, MI 48706.

9. C. Stoeckl, C. Chiritescu, J. A. Delettrez, R. Epstein, V. Yu. Glebov, D. R. Harding, R. L. Keck, S. J. Loucks, L. D. Lund, R. L. McCrory, P. W. McKenty, F. J. Marshall, D. D. Meyerhofer, S. F. B. Morse, S. P. Regan, P. B. Radha, S. Roberts, T. C. Sangster, W. Seka, S. Skupsky, V. A. Smalyuk, C. Sorce, J. M. Soures, R. P. J. Town, J. A. Frenje, C. K. Li, R. D. Petrasso, F. H. Séguin, K. Fletcher, S. Padalino, C. Freeman, N. Izumi, R. Lerche, and T. W. Phillips, Phys. Plasmas **9**, 2195 (2002).

10. V. N. Goncharov, "Improved-Performance of Direct-Drive ICF Target Designs with Adiabat Shaping Using and Intensity Picket," presented at the 44th Annual Meeting of the APS Division of Plasma Physics, Orlando, FL, 11–15 November 2002; to be published in Physics of Plasmas.

11. M. C. Richardson, P. W. McKenty, F. J. Marshall, C. P. Verdon, J. M. Soures, R. L. McCrory, O. Barnouin, R. S. Craxton, J. Delettrez, R. L. Hutchison, P. A. Jaanimagi, R. Keck, T. Kessler, H. Kim, S. A. Letzring, D. M. Roback, W. Seka, S. Skupsky, B. Yaakobi, S. M. Lane, and S. Prussin, in *Laser Interaction and Related Plasma Phenomena*, edited by H. Hora and G. H. Miley (Plenum Publishing, New York, 1986), Vol. 7, pp. 421–448.

12. Laboratory for Laser Energetics LLE Review **86**, 68, NTIS document No. DOE/SF/19460-393 (2001). Copies may be obtained from the National Technical Information Service, Springfield, VA 22161.

The Properties of Polyimide Targets

In 1996 LLE began a research effort to make spherical capsules from polyimide material for use in direct-drive inertial confinement fusion (ICF) experiments. Previously, ICF capsules were made exclusively from glass, polystyrene, or an amorphous carbon–hydrogen solid solution referred to as "plasma polymer" or "glow-discharge polymer."[1] Polyimide was first proposed as a potential material for a target wall in 1995 because of its appreciable strength;[2] however, no viable method for making these capsules was identified. Following a five-year development project, a process for making polyimide capsules was developed and demonstrated, and the technology transferred to General Atomics—the ICF target fabricator—for production. As part of the project, polyimide shells with various properties relevant to ICF were developed. Those properties will be presented and compared in this article.

The fabrication method and associated properties of the different direct-drive polyimide targets have been reported previously.[3–5] This article summarizes and compares those properties that are important for producing cryogenic targets. Furthermore, issues that are unique to providing cryogenic targets, which impose stringent demands on performance from the shell material, are explained.

The properties of polyimide of importance to direct-drive ICF experiments are those that will increase the survivability of the shell during the process used to make cryogenic deuterium–tritium targets: specifically, the mechanical and permeation properties and the resistance of the material to embrittlement in a radioactive (tritium) environment. The rationale for choosing polyimide as a candidate material is that the polyimide chemical structure is one of the strongest polymeric materials, and among the most radiation resistant polymers,[6] and it should have the greatest likelihood of surviving demanding processing conditions.

Shells used for direct-drive ICF experiments need to be as robust as possible to withstand the inherent pressure gradients present when equipment has to operate over a wide pressure and temperature range. Shells are typically ~900 to 950 μm in diameter with the wall as thin as possible (1 to 3 μm) to minimize Raleigh–Taylor (RT) instabilities. The shell becomes an ICF target when it contains a nominal 100-μm layer of deuterium ice, which will include tritium in future experiments. The ice layer is achieved by first permeating gas at room temperature (or greater) into the shell and then cooling the shell and gas to below the triple point (for deuterium) at 18.73 K. The challenge in this process is caused by the fragility of the shell, which because of its large aspect ratio (diameter to wall thickness) can withstand only a very small pressure differential. This limits the driving force for permeation: it can take many days to fill the capsule with the sizeable gas inventory required to yield a 100-μm ice layer, and a well-controlled thermal environment is required to prevent the target from bursting or buckling.

During the permeation filling cycle, which can occur at temperatures from 270 to 500 K, and the subsequent cooling process to 18 K, the radioactive tritium gas decays with a half-life of 12.3 years and releases an electron with a mean energy of 6 keV. These high-energy electrons rupture chemical bonds, thereby weakening the capsule material. This creates a self-limiting cycle where increasingly long filling/cooling times de-rate the capsule's strength, which in turn requires even longer filling/cooling times. It has yet to be established that high-aspect-ratio shells can even be filled with tritium to the desired pressure without rupturing.

Finally, there is a requirement to minimize the processing time (filling and cooling cryogenic targets) as tritium decay produces a helium atom that will affect the convergence, and hence performance, of an imploding target. Given the tritium decay rate (0.015% conversion of T to ^{3}He per day), the desired duration for filling and cooling cryogenic targets is less than three days.

The sections that follow discuss (1) the mechanical properties of polyimide shells; (2) the techniques for changing the

shell's permeability by controlling the composition and microstructure of the polyimide; (3) the cooling of targets; and (4) the effects of radiation on shell properties.

The Structural Behavior and Properties of Polyimide Shells

1. The Mechanics of a Shell's Response to a Pressure Differential

A pressure differential across a shell's wall generates a uniform hydrostatic load within the wall that is resisted by in-plane forces (tension, compression, and shear) (see Fig. 92.18).[7] The magnitude of the induced forces can be analyzed solely by force-equilibrium equations (membrane theory) as long as the shell does not deform under the applied load, i.e., it is statically determined. Once the shell deforms, bending theory is needed to fully quantify the stress distribution in the shell and hence determine the maximum pressure differential a shell can withstand.
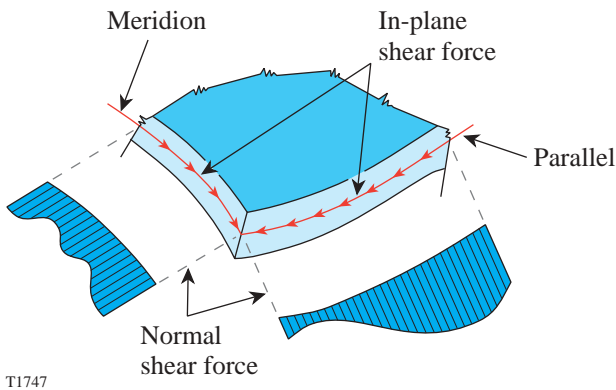

T1747

Figure 92.18
Schematic of the in-plane membrane forces present in a uniformly strained shell.

Direct-drive shells are classified as thin-walled shells; shells where the ratio of the wall thickness to the shell radius is less than 0.05 are categorized as "thin wall" and shells where the ratio is greater than 0.05 are "thick wall." This category of shell is unable to resist even small out-of-plane bending moments that easily deflect the wall. Once the shell is deformed, the intrinsic strength of the spherical geometry is compromised and the shell either shatters if it is brittle or collapses intact if it is elastic. Thicker-wall shells, such as indirect-drive shells, have a twofold strength advantage over thin-wall shells: first, the load-bearing capacity of the shell is greater, and second, once a shell begins to deflect to out-of-plane moments, the wall

more effectively resists the bending moment. Calculating the strength of thick-wall shells is also more complex since the bending theory is now an effective secondary reinforcement mechanism (membrane theory describes the primary mechanism) for resisting the applied load.

The buckle pressure is defined as that uniform load where the shell wall is at its maximum in-plane compression and shear stress, and any infinitesimal increase in pressure will cause the shell wall to deform. Increasing the pressure subjects the shell wall to bending moments, and at a critical pressure—the collapsing pressure—the shell collapses. The shells of interest in direct-drive ICF are all thin-wall (<5-μm) polymers with little resistance to out-of-plane forces, so the collapsing pressure is equal to the buckling pressure. The buckling pressure P_{buckle} is determined by the dimensions of the shell and the intrinsic properties of the material:[7]

$$P_{buckle} = \frac{2E}{\sqrt{3\left(1-v^2\right)}}\left(\frac{w}{r}\right)^2, \tag{1}$$

where E is the elastic modulus, σ is the tensile strength, v is Poisson's ratio (0.34), w is the wall thickness, and r is the radius.

The bursting pressure P_{burst} is analogous to the buckling pressure except that the internal pressure is greater than the external pressure and the in-plane forces are tensile (σ) and shear:

$$P_{burst} = 2\sigma\left(w/r\right). \tag{2}$$

ICF targets are not perfectly spherical, although the sphericity is excellent (0.5 ± 0.2 μm out-of-round). This lack of sphericity decreases the buckling pressure from what would be expected for a perfectly spherical shell: At the region where the shell departs from perfect sphericity, the radius of curvature changes. Here the in-plane compressive stress acquires a shear component. This stress deflects the shell wall out-of-plane; the magnitude of the deflection and the affected area of the shell depend on the shear and flexural moduli, respectively. Thin-wall shells have little resistance to this out-of-plane force, so once the applied in-plane load can no longer be supported by in-plane compression, the strength of the spherical shape is compromised and the shell buckles. Shells where the radius of curvature changes abruptly, and that also have low shear and flexural moduli, will buckle at lower loads than rounder shells with greater stiffness.

Two phenomena combine to make thinner shells substantially more fragile: First, thinner-wall shells are more out-of-round than moderately thicker shell walls, a consequence of the shell fabrication process; second, as discussed above, thinner walls are inherently less resistant to bending moments than are moderately thicker shell walls. Experimentally it was observed that as the thickness of the shell wall decreases below $4\,\mu$m, the elastic modulus [Eq. (1)] becomes a weaker predictor of the maximum buckling pressure that a shell can withstand: There is a greater variation in the observed buckle pressure of a large sample of very thin wall shells (1 μm) compared to thicker shells. This behavior is not adequately explained by possible variations in the elastic modulus and Poisson ratios of different shells, which are intrinsic material properties independent of thickness; these properties depend upon the materials' microstructure, and supporting x-ray diffraction data show a similar microstructure for thick and thin films.[8,9] A more probable explanation for the greater variation in the buckle pressure of thin-wall shells is a greater variation in the roundness of the shells.

In the future, each shell will have to meet a specification for the maximum-allowable out-of-roundness to maximize the shell's survivability during processing. This will require the sphericity and uniformity of the wall thickness of each thin-wall shell to be quantified.

2. Fabrication of Thin-Wall Spherical Shells

Two effects can reduce the sphericity of the shell: First, there is the inherent out-of-roundness of the mandrel on which the polyimide shell is formed. Typically this value increases as the mandrel diameter increases. Second, a consequence of the polyimide-shell manufacturing is that additional out-of-roundness can be introduced during fabrication. Typically, this contribution is greater for thinner shell walls.[9]

The fabrication technique is summarized in Figs. 92.19 and 92.20. First, polyamic acid is deposited on a mandrel. The coated mandrel is then heated to convert polyamic acid into polyimide and simultaneously depolymerize the poly-α methyl-styrene mandrel. This depolymerization of the 30-μg mandrel would generate a burst pressure of 140 atm in the absence of permeation. Permeation does occur, however, and if the depolymerization rate is kept at or below the permeation rate, the polyimide shell will inflate only marginally and without exploding. Shells with walls as thin as 0.9 μm have been fabricated in this manner.[5,9] Shells can be made more out-of-round (beyond the limit established by the mandrel) during the depolymerization phase where expansion of the shell

stresses the plastic: If the shell material is strained beyond the yield point, it will plastically deform in those areas where the wall is thinnest. This nonuniform and nonrecoverable expansion will cause the shell to lose its sphericity when the internal pressure is reduced.[9]

While it is possible to make polyimide shells with the desirable strength and modulus properties, strict quality control will be required to select only the best geometries. Otherwise the greater mechanical properties of polyimide will not be realized.
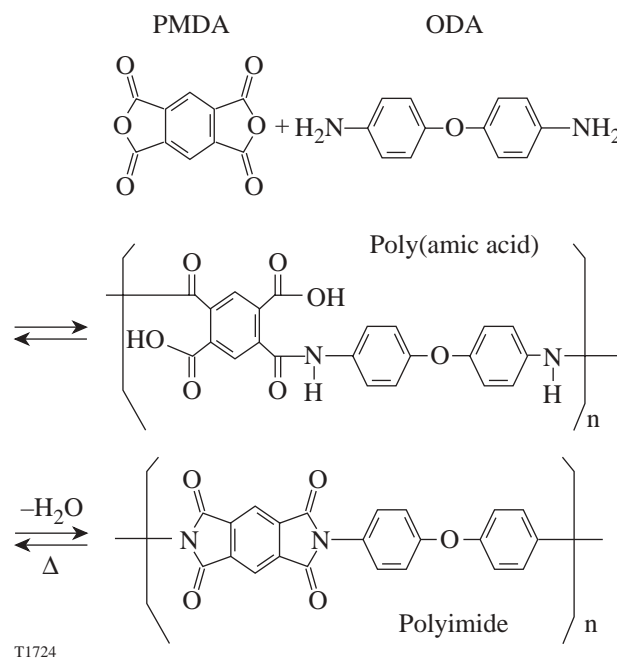
Figure 92.19
Schematic of the chemical process used to make polyimide shells using the vapor-deposition technique.

3. Stiffness, Strength, and Elasticity of Polyimide Shells

The physical properties of polyimide shells are listed in Table 92.I; the properties of plasma polymer shells are also listed for comparison. Generally, polyimide has greater physical properties than plasma polymer and, in addition, has a higher density, radiation resistance, and lower permeability, so the selection of one of these materials over the other as the optimal shell material is not immediately apparent. The implications of these other properties (permeability and radiation resistance) on the selection of polyimide or plasma polymer as a target material are expanded upon later.
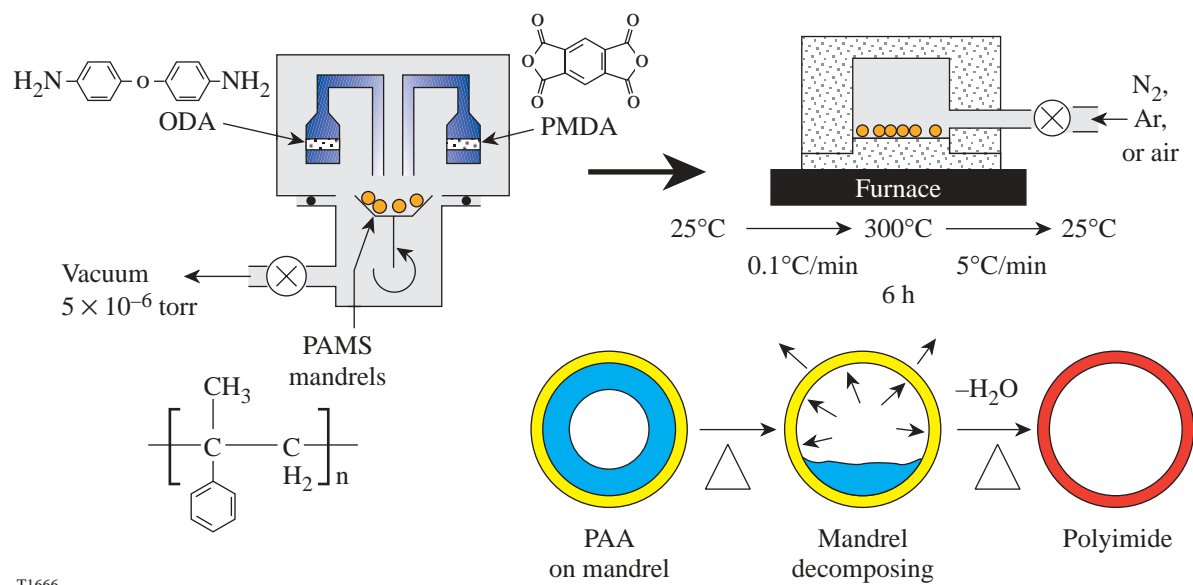
Figure 92.20
Sequence of operations used to make polyimide shells.

The elastic modulus of vapor-deposited polyimide shells [calculated from Eq. (1)] was marginally larger than the literature-reported values for the same chemical formulation made using liquid processing: 3.2 GPa and 3.0 GPa, respectively.[10,11] There is a difference, however, in the method used to measure these values: using overpressure to buckle shells measures a biaxial compressive elastic modulus, whereas literature values for a commercial polyimide, Kapton™, are measured using American Standards and Testing Materials (ASTM) procedures with uniaxial tensile loading. The elastic modulus for vapor-deposited polyimide was also measured using an accepted nano-indentation method and was determined to be 4.0 GPa.[9]

The tensile strength of the polyimide was calculated from Eq. (2) by changing the pressure on either side of the shell and measuring the commensurate change in the diameter of the shell.[9,10] Vapor-deposited polyimide shells are appreciably stronger than solution-cast films, with ultimate strengths of 280±20 MPa and 170 MPa, respectively. The greater strength of the vapor-deposited polyimide material is attributed to the preferential alignment of the crystalline lattice in polyimide shells (discussed in detail later). Similar to the elastic-modulus measurements, pressure testing a shell to determine the tensile strength is a measure of the biaxial tensile stress–strain behav-ior (in the plane of the shell), which is different from a uniaxial strength test of an ASTM-dimensioned measurement.

It is important to note that all testing of both polyimide and plasma polymer shells was to determine the optimal process-ing conditions as measured by each material's inherent stiff-ness, strength, and plasticity. No effort was intentionally made to preselect an underlying mandrel within a particular round-ness and wall thickness specification. (This would have made the study too large, expensive, and intractable.) Therefore, the variation in the mandrels' sphericity is included in the statisti-cal variation of the polyimide shells. This has the biggest effect on the reported elastic-modulus values of the shells, which are most susceptible to out-of-roundness effects. The possibility remains that future optimization and strict quality control of the underlying mandrels will improve the mechanical proper-ties of both polyimide and plasma polymer shells.

The importance in ICF applications of having a higher-strength shell material is to improve the ability of the shell to (1) resist buckling pressures during permeation filling, (2) resist bursting and buckling pressures that develop within the permeation cell when a filled target is cooled to 20 K, and (3) resist bursting when the target is transferred (inside a cryostat) from the permeation cell to a cryostat.[12] This requires

Table 92.I: Comparison of the physical properties and chemical composition of available ICF shell materials.

Polymer Material	Elastic Modulus (GPa)	Ultimate Strength (MPa)	Elongation (%)	Chemical Composition	
				Atomic fraction (%)	
Polyimide (PMDA-ODA formulation) 1.42 gm/cm^3	3.2±0.1	280±12	27±2	C H N	56 26 5
Polyimide (6FDA-ODA formulations) 1.42 gm/cm^3	2.6±0.1	221±15	15±2	C H N O F	54 24 3 9 13
Plasma polymer[13] (high-density/ strength version) 1.18 gm/cm^3	2.7±0.2	88±10		C H	54 46
Plasma polymer[13] (baseline) 1.04 gm/cm^3	1.6±0.4	80±5		C H	43 57
Deuterated plasma polymer[13] (high-strength/ density version) 1.11 gm/cm^3	2.0±0.1	82±5		C D	61 39
Deuterated plasma polymer[13] 1.09 gm/cm^3	0.9±0.2			C D	59 41

that the elastic modulus and strength of the shell material be known over a wide temperature range (at least from 295 K to 18 K and more desirably from 573 K to 18 K to allow for higher-speed permeation at elevated temperatures). Typically, the room-temperature strength of the material is the most commonly reported value. The measured temperature dependences of the strength and elastic modulus are reported in Fig. 92.21. The elastic modulus is measured to increase by a factor of 2.5 over the temperature range 300 K to 130 K.

Polymers become stronger at lower temperatures, which increases the survivability of polymers in cryogenic applications. In ICF applications, however, use of only this value can be deceptive, since a plastically strained shell may have too high a permeability, which renders it useless, so the yield strength, below which a material behaves elastically, must also

be known. Once a shell exceeds the yield strength, the change in the diameter in response to the applied stress is determined by the coefficient of hardening (the slope of the stress–strain curve in the plastic regime). This value is typically much smaller than the elastic modulus. A small stress in this regime can create a sizeable strain that will cause the shell to expand significantly and not recover its original dimensions. More-over, the shell can deform (i.e., change in roundness) if the walls are not uniformly thick. By reason of this behavior the stress–strain relationship of the polyimide ideally should be known over the entire temperature range of interest (18 K to 573 K). This will allow the cryogenic target handling equip-ment to be designed to minimize the time required to provide ICF cryogenic targets (to limit the buildup of He^3). Obviously, equipment to handle cryogenic targets can be designed without detailed knowledge of the shell's behavior, but the design will

necessarily be conservative to ensure that the target survives processing, which is counter to the need to process targets as rapidly as possible.
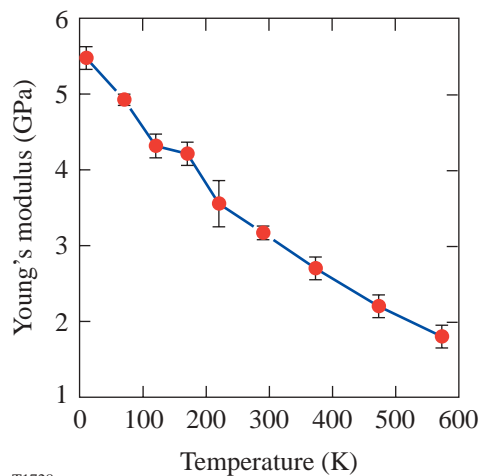
T1728

Figure 92.21
The temperature-dependent elastic modulus of polyimide from 12 K to 573 K.

4. Effects of Plastically Deforming Polyimide Shells

X-ray diffraction data of polyimide shells indicate the presence of a crystalline phase.[8] The crystal lattice plane is aligned perpendicular to the circumference of the shell as the polymer chain preferentially lies in the plane of the shell (see Fig. 92.22). This configuration gives the polyimide shell its strength and stiffness in compression/buckling, due to the stiffness of the lattice structure to out-of-plane forces, and also in tension/bursting, due to the alignment of the polymer backbone within the plane of the circumference.

When a polyimide shell is over-tensioned, as occurs when the internal pressure in the shell exceeds the yield stress of the material, the polyimide plastically deforms and the mechanical properties of the shell decrease: the buckle pressure decreases by 55%, which is attributed to the elastic modulus decreasing as the crystallinity of the material decreases,[9,10] and the shell becomes more nonspherical, which lowers the in-plane compressive and shear loads that the shell can withstand.

Of particular interest and relevance to ICF applications is the effect that plastically deforming polyimide has on the permeability of the material. A large sample of 120 polyimide shells were over-pressurized to determine the effect of strain

on the permeability of the material to deuterium. The effect fell into one of two categories: the permeability changed either enormously (three orders of magnitude) or only slightly (from no change to a quadrupling). The biggest change occurred in 30% of the shells. Importantly, the gas transport mechanism remained permeation, where the gas must dissolve in the plastic material, since heating the capsule to 300°C completely recovered the initial permeation and strength/modulus properties. The alternative gas transport mechanism is Knudsen diffusion, which would occur if pinholes or voids were created. These features would allow a gas/gas-surface diffusion process where gas can pass through a membrane without being absorbed into the material. This would be unacceptable since the shell would remain permeable at cryogenic temperatures, allowing the low-viscosity gas and liquid to easily pass out of the shell; as a result, the target would be unable to retain the deuterium fill.

When polymers are cooled, the activation energy for permeation increases and the permeability of the material decreases (more detail later in this article); however, an internal overpressure within the shell strains the wall and counteracts the decrease in permeability. This phenomenon was observed in 0.9-mm-diam plasma polymer shells filled with liquid deuterium (~51 μg) at 20 K (which equates to 1000-atm pressure at room temperature). When the shell was allowed to warm gradually, the internal pressure increased and the gas permeated out of the shell. Following this observation, the perme-
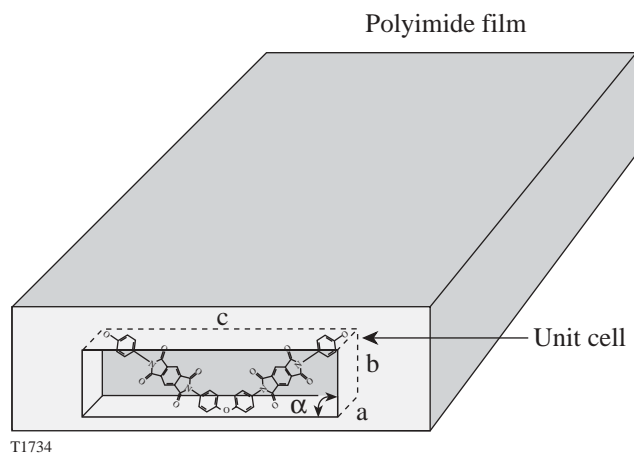
T1734

Figure 92.22
Schematic of the orientation of a polyimide crystal unit cell within the wall of a shell: $a = 6.31$ Å, $b = 3.97$ Å, $c = 32$ Å, and $\alpha = 90°$. The shaded planes of the unit cell represent the *00l* and *l00* lattice planes.

ation time constant for the shells at room temperature was measured and found to be unchanged. The only explanation for the shells not exploding when warmed gradually is that the permeability of the material changed as the shell expanded. By contrast, shells warmed rapidly explode as expected.

Once a thin-wall shell succumbs to an overpressure and bends, the intrinsic property of the material determines what happens next: brittle (plasma polymer, polystyrene) shells lack ductility and fracture into shards; polyimide, which is extremely elastic (typically tolerating up to 27% elongation), either collapses intact or tears apart, depending upon whether the overpressure is inside or outside the shell.

5. Surface Roughness of Polyimide Shells

Throughout this development program no effort has been made to optimize the smoothness of polyimide shells. This was considered a secondary priority, which would be addressed once the processing conditions and associated fundamental mechanical properties of the shell were accurately known.

Surface-roughness profiles of polyimide targets were acquired to establish a "typical" roughness power spectrum. Typically the roughness ranged from 0.5 to 1 μm with significant power throughout the spectrum. The low-order roughness was partially attributed to the quality of the mandrel on which the shell was formed; there had deliberately been no attempt to screen the quality of the mandrels for the smoothest and most-round ones because a large number of mandrels were required for the statistical study and the cost of analysis would have been prohibitive at that stage. The high-frequency roughness was corroborated with electron microscope images (Fig. 92.23) of the shells that showed "bumps" on the surface with lateral dimensions of 2 to 8 μm.
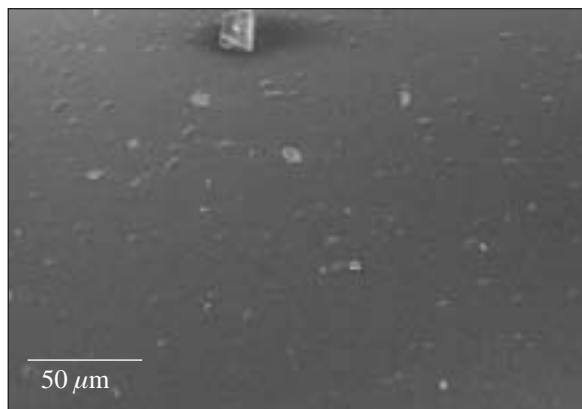
Issues Regarding Shells Specific to Processing Cryogenic Targets

1. Permeating Gas into Shells

The permeation coefficient (P) is the product of the diffusion coefficient (D) for a gas through a material and the solubility coefficient (S) of the gas in the material, where

$$P = S \times D = (\text{quantity of permeant})$$
$$\times (\text{wall thickness})/[(\text{area}) \times (\text{time})$$
$$\times (\text{pressure drop across shell})]. \qquad (3)$$

(The diffusivity has dimensions of area/time, and solubility has dimensions of molar-volume/pressure.)

The permeation time constant is an empirical figure of merit measured for all ICF capsules; it is the time required for 63% of the gas inside the shell to permeate out of the shell. This value depends on the wall thickness and the surface area and is independent of the pressure differential across the shell. Combining the time constant with the allowable buckling-pressure differential [Eq. (1)] gives the maximum rate at which a shell can be filled:

$$\text{Fill rate}(\text{atm/s})$$
$$= (\text{buckling} \times \text{pressure})/(\text{permeation} \times \text{time} \times \text{constant}).$$

Figure 92.23
Scanning electron micrograph of the surface of a 5-μm-wall PMDA-ODA shell. The overall surface is moderately smooth with the lateral dimensions of "bumps" below 10 μm. The larger particulates that are visible on the surface but removable are a consequence of the targets not being handled exclusively in a clean-room environment.

T1718a

Direct-drive targets for experiments on the National Ignition Facility (NIF) are scaled versions of OMEGA targets and possess the same theoretical buckle pressures and time constants, so both types of shells can be filled at comparable rates. (Practically, larger-diameter targets are less spherical than smaller targets so the effective buckling pressure is marginally lower than would be expected by scaling smaller shells.) The larger diameter of a NIF target and the 350-μm-thick ice layer, however, will require 15 times more gas than an OMEGA target to achieve a scaled-thickness ice layer. A 100-μm ice layer for OMEGA targets requires approximately 1000 atm of gas at room temperature. (A 0.95-mm-diam shell at 295 K requires a fill pressure of 1027 atm to yield a 100-μm ice layer.) Filling targets at higher temperatures requires a higher pressure (1296 atm at 100°C for a 0.95-mm shell) since the gas density decreases with increasing temperature.

2. Effect of Temperature on the Permeability

Increasing the temperature not only increases the permeation rate but also decreases the elastic modulus (see Fig. 92.21), albeit less significantly, making permeation at elevated temperatures desirable. Table 92.II lists the time required to fill OMEGA and NIF direct-drive targets by permeation using different shell materials and different temperatures. Clearly, there is a major time benefit if shells can be filled at the maximum allowable temperatures. The maximum allowable temperature for the polyimide target is 400°C, which would require a fill pressure of 2210 atm, and the fill time would be reduced from 300 h to less than 10 h.

The temperature dependency of the permeability coefficient is given by

$$P = P_0 \exp\left(-E_p/RT\right),$$

where P_0 is the pre-exponential value [7×10^{-28} mol m/(m s Pa) for polyimide] and E_p (16.9 to 20.3 kJ/mol, depending upon the processing conditions) is the activation energy for permeation. The temperature dependency of the permeability of polyimide shells is reported from 130 K to 300 K[8,9] (Fig. 92.24) and for polyimide film to 523 K.[11]

3. Effect of Crystallinity on Permeability

The permeability of polyimide varies moderately according to the processing conditions and is affected by the crystallinity of the material. Permeation proceeds through a mechanism that requires polymeric chains to move over a very localized area to accommodate the movement of dissolved gas molecules through the plastic; this is referred to as the "segmental

Table 92.II: Calculated minimum time required to fill targets by permeation. The targets are (1) a 0.95-mm-diam shell with a 1-μm wall and a 100-μm ice layer for cryogenic experiments on OMEGA; and (2) a 3.4-mm-diam shell with a 3-μm wall and a 350-μm ice layer for cryogenic experiments on the NIF. Different permeation temperatures are presented where the mechanical and permeation properties are known. The ^{3}He density increases at a rate of 0.02 mg/cm^3/day.

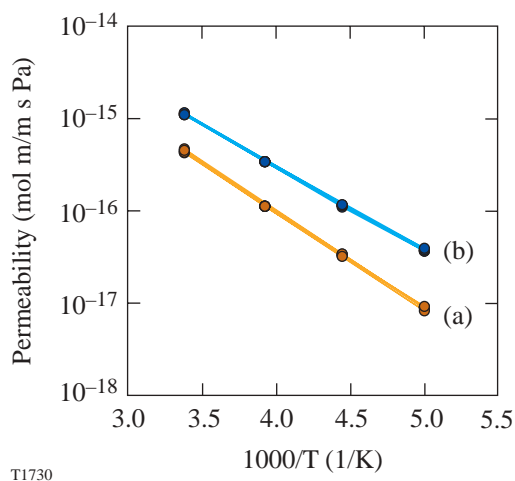| Target	Permeation Time Constant (s)	Required Fill Pressure (atm)	Fill Time (h)
Plasma polymer at 295 K (OMEGA)	10	1027	25.4
Plasma polymer at 373 K (OMEGA)	2.7	1296	8.5
Plasma polymer at 295 K (NIF)	106.8	101	375
Plasma polymer at 373 K (NIF)	28.5	1263	126
Polyimide (PMDA-ODA formulation) at 295 K (OMEGA)	184	1027	320
Polyimide (PMDA-ODA formulation) at 573 K (OMEGA)	1.8	1925	10.2

Figure 92.24

The temperature-dependent helium permeability of polyimide processed in nitrogen (a) is lower than when it is processed in air (b) due to the increased crystallinity and stiffness of the polymer.

Figure 92.25

Comparison of transmission-mode x-ray diffraction patterns of polyimide shells imidized at increasing rates (a) 0.1 C/min, (b) 1 C/min, and (c) 5 C/min, together with integrated 2θ plots. The increased intensity of the *002* peaks at 5.7°. 2θ indicated greater crystallinity and is associated with lower permeability.

mobility" of the polymer. Amorphous material predictably is more permeable than crystalline material since the crystallinity increases the rigidity of the polymer chain. Another consideration is the scale length of the crystal: materials with similar overall crystallinity are more permeable if the crystalline regions are larger and more sparsely distributed than if there is a greater number of smaller, more-distributed regions—a channeling effect.[8,9]

The effect of changing an important processing variable—the imidization rate—is to change the size and distribution of crystals without changing the overall degree of crystallinity. Polyimide shells that are formed using a rapid imidization process (5 C/min) show more-intense, narrower 002 x-ray diffraction peaks than do polyimide shells that are made using a gradual imidization rate (0.1 C/min) (Fig. 92.25). The peaks of the rapidly imidized material are better aligned in the plane of the shell, as shown by grazing-angle x-ray diffraction data.[8,9] Finally, the material that was rapidly imidized has larger-scale, better-oriented crystalline regions that are more dispersed throughout the amorphous material, and this morphology corresponds to a more-permeable material.

By changing a second processing condition and imidizing polyimide shells in an air rather than a nitrogen atmosphere, the degree of crystallinity was reduced and the permeability of the material increased by 20%.

4. Effect of Mechanical Strain on the Permeability

Stressing polyimide beyond the yield stress—80 MPa at 3% strain—plastically deforms the material. (The ultimate yield stress of the vapor-deposited polyimide is 280 MPa at a biaxial strain of 27%.) As the polyimide shell is cooled inside the Cryogenic Target Handling System's (CTHS's) permeation pressure vessel, it is strained; the tensile and compressive nature of the strain varies over the entire temperature range as a complex function of the properties of the gas and materials at different temperatures. Given the exceptionally low buckling strength of the shell compared to the burst strength, it is desirable to maintain the shell in a regime where there is a net tensile (burst) force. This increases the risk that the stress may exceed the yield stress and the polyimide wall will be plastically deformed. The diameter of the shell will then increase, and the thickness of the ice layer will decrease proportionally, adding uncertainty to the dimensions of the target when it is shot. A maximum strain limit of 3% in the shell is the recommended design point for establishing the thermal performance of the permeation cell. Temperature gradients within the permeation cell, during either steady state or unsteady state, that translate into pressure gradients exceeding the 3% limit across the shell wall are unacceptable.

A consequence of biaxially straining polyimide shells be-yond a 15% level is a change in the permeability of the material. As described above, approximately 1/3 of all shells strained to this level have an ~1000-fold increase in permeabil-ity. There are two intriguing aspects to this behavior: first, that the increased permeability is so sizeable, and second, that the behavior is stochastic. An explanation for this behavior is that strain introduces a microstructural change to the material. Supporting evidence is that the elastic modulus (stiffness) decreases by 56% (to 1.5 GPa) when strained and the crystal-linity decreases substantially (see Fig. 92.26).[5,9,10] It is pre-sumed that the statistical nature to the change in magnitude of the permeability is in the random initial distribution of crystal-line and amorphous phases in the material, and the response of the material to the strain. Doubtlessly, strain changes the morphology; however, permeation will increase only if there is a contiguous alignment of highly mobile polymer chains through the shell wall—and this eventuality is statistical. Very important for confirming that this phenomenon is a micro-structural event is the observation that the original elastic modulus and permeability values are returned when a strained and highly permeable shell is heated to 300°C. At the high temperature the plastic becomes more fluid and the strain-induced morphological change is reversed.

T1671a
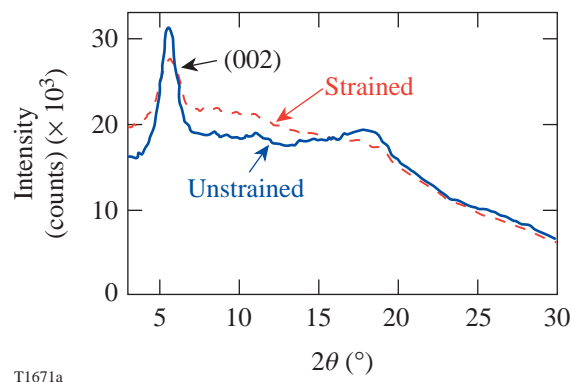
Figure 92.26
Comparison of transmission-mode x-ray diffraction patterns of polyimide shells for unstrained and mechanically biaxially strained polyimide shells showing appreciably greater crystallinity present in the unstrained shell.

5. Effect of Chemical Modification to the Polyimide on the Permeability

An alternative way to modify the segmental mobility of the polymer chain to enhance the permeability is to add flexible chemical units into the backbone of the polymer. Figures 92.19 and 92.27 compare the chemical formulation of two vapor-deposited polyimide shells: (a) the original PMDA-ODA–based polyimide discussed in detail here and (b) a 6FDA-ODA formulation that adds a flexible fluorine-based linkage to the polymer chain, respectively.[13,14]
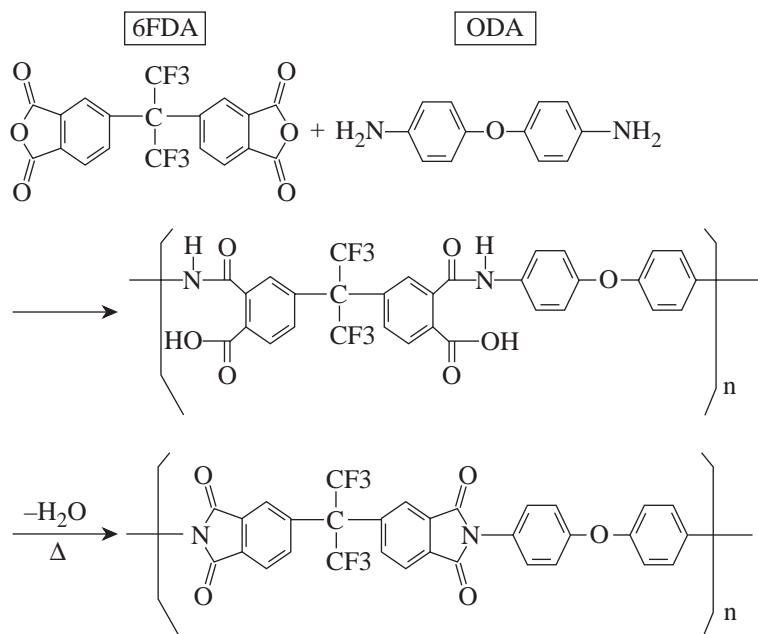
T1716

Figure 92.27
Structural and elemental composition of a permeable fluorinated-polyimide formulation.

The disadvantage of using the fluorinated polyimide for ICF experiments is the presence of fluorine (10 at. %) and the consequent x-ray preheat that will occur during an implosion. The advantages are numerous: The deuterium permeability is 50× greater than traditional PMDA-ODA–based polyimide, while the elastic modulus is only 18% lower. This reduces the time required to fill the shell with 1000 atm of deuterium at room temperature from 333 h to 8.8 h. (Note that this compares the fluorinated polyimide against the nonmechanically strained PMDA-ODA polyimide.)

The second advantage of using the polyimide based on 6FDA-ODA chemistry is the lower activation energy from permeation compared to polyimide made using PMDA-ODA chemistry, 12.3 versus 20.1 kJ/mol[12] (see Fig. 92.28). This will allow the fluorinated polyimide to retain higher permeability as the capsule is cooled (discussed in detail in the next section) to alleviate pressure differentials across the shell due to temperature gradients within the permeation pressure vessel.

6. Evaluation of Different Treatment Processes on the
   Processing Time Required to Fill Cryogenic Targets
   by Permeation

The critical parameters and the associated time required to fill OMEGA- and NIF-scale cryogenic shells are listed in Table 92.III for four different types of shells: (1) a standard plasma polymer shell, (2) a standard polyimide shell, (3) a
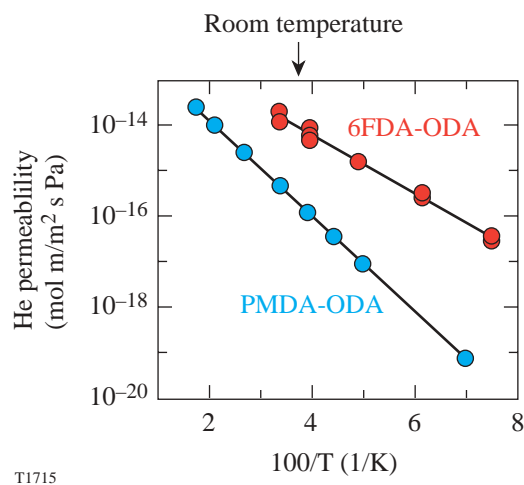
Figure 92.28
Arrhenius plot comparing the permeability of polyimide formulations: PMDA-ODA and 6FDA-ODA, over a wide temperature range.

polyimide shell structurally modified to enhance the permeability, and (4) a polyimide shell chemically modified to enhance the permeability. There is a clear time advantage, from a processing perspective, to using the more recently developed mechanically and chemically modified polyimide shells; however, these shells have other disadvantages when considering the processability of the target or the implosion performance of the target.

Table 92.III: Calculated minimum time to fill by permeation three different types of polyimide shells and a plasma polymer shell for OMEGA and the NIF. Target dimensions, respectively, are 0.95-mm-diam, 1.0-μm wall and 100-μm ice layer; and 3.5-mm-diam, 3.0-μm wall and 350-μm ice layer. The temperature is 295 K.

Polyimide Material	Fill Time (h) (OMEGA)	Fill Time (h) (NIF)
Baseline polyimide (PMDA-ODA formulation)	320	205 days
Mechanically strained polyimide (PMDA-ODA formulation)	0.66	21
Fluorinated polyimide (6FDA-ODA formulation)	8.0	121
High-density CH plasma polymer	25.4	375

Cooling Targets

Once the permeation cycle is complete, the pressure inside the shell is equal to the pressure outside the shell. The entire pressure vessel is then cooled to 26 K. During this process the vessel must be cooled uniformly to minimize the pressure gradient that develops across the shell. Inevitably a thermal gradient will develop along the internal perimeter of the permeation pressure vessel and also between the perimeter and the center where the shell is located. This is the most-precarious phase for the survival of the target: while transient temperature gradients during cooling do not induce pressure gradients within the gas on the time scale of interest, a pressure gradient does develop across the shell wall.

The ideal shell material would be one with the highest-possible stiffness, strength, and yield strength (in both compression and tension) to resist the pressure difference, and the highest-possible permeability over the widest temperature range down to 30 K to alleviate the pressure differential. Finally, permeation must be negligible at 26 K, the temperature where the liquid/gaseous deuterium outside the shell is removed, leaving a shell containing 51 μg of liquid deuterium with a vapor pressure of ~2 atm. One last desirable property is that the material resists damage from electron radiation when tritium gas is used.

At the beginning of the cooling cycle, at temperatures where polyimide is still permeable, any pressure gradient is minimized by permeation. As the temperature decreases, the permeability of the shell also decreases. At lower temperatures, slower cooling rates are required to allow longer periods for the pressure gradient across the shell to be reduced. When the shell becomes impermeable, the survival of the shell depends on whether any further thermally induced pressure gradient exceeds the shell's buckle or burst strengths. If the thermally induced pressure gradients remain too high, the only remedy is to improve the thermal uniformity of the permeation pressure vessel.

Thermal modeling of the permeation cell in the OMEGA CTHS reveals that a 1-K temperature change at the perimeter induces a 0.5-atm pressure differential across the shell wall at 295 K and a 0.9-atm pressure differential at 60 K. At these densities the thermal diffusivity is moderately low, and the thermal time constant is ~30 s. This pressure differential creates a bursting force since the perimeter of the permeation vessel is colder and hence denser than the center of the vessel where the shell is located. This load is in addition to other phenomena such as the thermally induced contraction of the shell (which generates a net bursting pressure) and the temperature of the gas in the plumbing that connects the permeation vessel to a valve at room temperature (which creates a net buckling pressure). Depending on the cooling rate, the thermal uniformity of the permeation cell, and the temperature-dependent permeability of the polyimide, the shell can pass from a buckle to burst regime and back as the temperature decreases.

The weakest failure mode for shells is buckling, and the buckling strength of a thin-wall polyimide shell (nominal 1-μm wall) is 0.13 atm. The burst strength for a 1-μm wall shell is ~4 atm, whereas the yield strength is ~1 atm. A practical constraint in the design of the equipment is the accuracy of the silicon diode temperature sensor used to regulate the temperature ramp: in practice, the accuracy is ±0.5 K at 300 K. This value, the long thermal time constant for the permeation vessel, and the shorter thermal time constant for the gas to respond to temperature gradients combine to limit the value of using active temperature control over the temperature environment to minimize the likelihood of bursting/buckling the shell. Clearly the thermal environment within the pressure vessel has to be engineered to remain as constant as possible over a wide temperature and pressure range: from 18 K to 573 K and 1000 atm to a maximum of 2200 atm (33,000 psi), respectively.

The OMEGA Cryogenic Target Handling System has demonstrated that it is possible to process 0.95-mm-diam shells with walls as thin as 2.5 μm at room temperature over a period of three days. With the design goal being to process a 0.95-mm-diam shell with a 1-μm wall in less than two days, advanced shell materials and improved thermal engineering of the equipment are required. Greater strength will provide greater margin for the design of the permeation cell and will also offset possible strength degradation from radiation damage.

The future use of tritium adds two complications to the process: (a) hydrogen embrittles many metals, limiting the selection of available alloys for making the pressure vessel, and (b) the potential radioactive hazard requires heightened safeguards.

Radiation Effects

The decay of a triton produces an electron with a mean energy of 6 keV and an energy range of 2 to 18 keV.[6] The effect of this electron on a polymer is to rupture chemical bonds and weaken the material.[6] Given the high DT density in a target (0.11 gm/cm^3 for pressurized gas and 0.25 gm/cm^3 for ice), the stopping power of the medium is appreciable and the 1/e

penetration distance is less than 30 μm. Consequently, only tritium dissolved in the plastic wall and the tritium immediately adjacent to the plastic wall damage the plastic.

During the processing of cryogenic targets there are three phases where tritium decay is an issue: (1) during the pressure ramp, (2) during the cooling cycle, and (3) during layering. During the pressure ramp (0.05 atm/min for a 1-μm-wall shell) the dose from the tritium dissolved in the wall (assuming 10% solubility at 1 atm scales linearly with increasing pressure) will be approximately 50 MGy. Added to this is the contribution from tritium adjacent to the shell wall, which is less than 2 MGy. During cooling at a rate of 0.1 K/min, the dose will be 6 MGy, the majority coming from gas dissolved in the plastic and less than 1 MGy from the adjacent gas volume. When ice has formed and layered, the dose, primarily from the adjacent ice layer, will be 0.3 MGy/h. This contribution is smaller since the 1/e penetration distance is only 9 μm at ice density and the amount of tritium dissolved in the wall is negligible. Allowing 36 h to layer and deliver a target, the total dose to the shell material may be expected to be of the order of 70 MGy. These radiation doses are estimates based on the penetration distance of 6-keV electrons at discrete temperatures and densities. A rigorous analysis would be considerably more complex and require more-detailed information than is available. The purpose of this analysis was to estimate the dosage for subsequent radiation-induced damage experiments.

In an effort to quantify the effect that radiation damage from tritium decay may have on polyimide, polyimide shells were irradiated with an electron beam from a scanning electron microscope. The electron energy was 8 keV, and the current flux calculated to be 7 mA/m^2. The total integrated dose was 60 and 120 MGy. The results are summarized as follows: the elastic modulus showed no change with exposure; the tensile strength decreased from 280 MPa (initially) to 266 MPa at the 60-MGy dose and 240 MPa at the 120-MGy dose; and the permeability did not change with dose. The property that showed the biggest change was the elasticity/plasticity of the system: the maximum elongation that polyimide can withstand is 27%. Exposure to 60 MGy reduces this to 20%, and exposure to an additional 60 MGy further reduces this to 14%. None of these performances will impair polyimide sufficiently to affect the likely survivability of the shell, but two important issues remain: any impairment to the yield strain was not determined, and any change in the transparency of the material was not investigated.

The observed radiation resistance is an important consideration when evaluating polyimide material as a potential shell material. Literature values for the performance of polystyrene (which possesses a chemical composition similar to plasma polymer) suggest that the mechanical properties are considerably more impaired than for heavily conjugated organic structures such as polyimide.[6]

Conclusions

Polyimide shells suitable for ICF cryogenic experiments on OMEGA were developed, and the associated mechanical properties were determined to define the processing conditions for operating the OMEGA Cryogenic Target Handling System. Overall, polyimide targets offer a viable alternative to plasma polymer capsules currently in use. The greatest virtue for the polyimide material is its high radiation resistance (for tritium application) and its excellent mechanical properties, which lessen the demanding specifications for the equipment needed to provide cryogenic targets.

The single biggest limitation to using the most thoroughly developed and characterized polyimide, based on PMDA-ODA chemistry, is the low permeability of the material at room temperature. This increases the processing time and exacerbates the deleterious effect of ^{3}He production on the performance of the implosion. Importantly, there are solutions to this problem, but each has its own implications: (1) The permeation time can be reduced substantially by filling shells at elevated temperature (up to 300°C), but this adds to the complexity of the cryogenic system needed to provide these targets. (2) The permeability can be dramatically increased by mechanically straining polyimide to modify the crystalline microstructure of polyimide, which achieves the shortest-possible fill time. The technique has not been thoroughly developed, however, and cannot yet be relied upon for routine production: the yield is low and the magnitude and effect of the shell deformation during the process remain too variable and not fully determined. The production aspects for this process have to be developed further. (3) The final option for increasing the permeability of polyimide is the most promising: change the chemical formulation to add flexibility to the polymer chain. Not only does this increase the permeability at room temperature, but it also increases the permeability of the material over a broad temperature range—a property that will increase the survivability of thin-wall targets during processing. The disadvantage of this approach is the presence of fluorine in the polymer and the effect fluorine has on the implosion physics.

REFERENCES

1. S. A. Letts *et al.*, Fusion Technol. **28**, 1797 (1995).

2. J. J. Sanchez and S. A. Letts, Fusion Technol. **31**, 491 (1997).

3. E. L. Alfonso, S. H. Chen, R. Q. Gram, and D. R. Harding, J. Mater. Res. **13**, 2988 (1998).

4. F.-Y. Tsai, E. L. Alfonso, S. H. Chen, and D. R. Harding, Fusion Technol. **38**, 83 (2000).

5. F.-Y. Tsai, D. R. Harding, S. H. Chen, T. N. Blanton, and E. L. Alfonso, Fusion Sci. Technol. **41**, 178 (2002).

6. *Safe Handling of Tritium: Review of Data and Experience*, Technical Reports Series No. 324 (IAEA, Vienna, 1991).

7. E. H. Baker, L. Kovalevsky, and F. L. Rish, *Structural Analysis of Shells* (McGraw-Hill, New York, 1972).

8. F.-Y. Tsai, T. N. Blanton, D. R. Harding, and S. H. Chen, "Temperature Dependency of the Properties of Vapor-Deposited Polyimide," to be published in the Journal of Applied Physics.

9. F.-Y. Tsai, "Engineering Vapor-Deposited Polyimides," Ph.D. thesis, University of Rochester, 2002.

10. F.-Y. Tsai, E. L. Alfonso, D. R. Harding, and S. H. Chen, J. Phys. D: Appl. Phys. **34**, 3011 (2001).

11. *Polyimides: Fundamentals and Applications*, edited by M. K. Ghosh and K. L. Mittal, Plastics Engineering, Vol. 36 (Marcel Dekker, New York, 1996).

12. Laboratory for Laser Energetics LLE Review **81**, 6 and 21, NTIS document No. DOE/SF/19460-335 (1999). Copies may be obtained from the National Technical Information Service, Springfield, VA 22161.

13. A. Nikroo, General Atomics, private communication (2002).

14. F.-Y. Tsai, D. R. Harding, S. H. Chen, and T. N. Blanton, "High-Permeability Fluorinated Polyimide Microcapsules by Vapor-Deposition Polymerization," to be published in Polymer.

Anomalous Stimulated Raman Scattering and Electron Acoustic Waves in Laser-Produced Plasmas: A Linear Model

Stimulated Raman scattering (SRS), an instability in which light is scattered by and amplifies electron plasma waves, has long been a concern in laser-fusion research because of its potential to reduce absorption and implosion efficiency. This concern is enhanced by the unsatisfactory state of the theory, particularly in accounting for the prevalence of anomalous SRS—scattering from plasma waves that according to conventional theory should be very heavily Landau damped.[1–5] Furthermore, scattering from waves satisfying the electron-acoustic (EA) dispersion relation (see below), which according to conventional theory should also be very heavily damped, has recently been identified.[2,4] These observations imply that Landau damping in laser-produced plasmas is often lower by an order of magnitude than would be predicted by the conventional linear theory of waves in a Maxwellian plasma.[5]

Since nonlinear Berstein–Green–Kruskal (BGK)[6] waves are undamped and under some conditions satisfy the EA dispersion relation,[7] they have recently been invoked to account for these phenomena.[2,4,8] However, the observed EA wave scattering (as well as much of the anomalous SRS) is at low levels, so that the fundamental question is how the associated plasma waves are amplified from small amplitudes (noise) despite prohibitive linear damping, rather than how they behave at large amplitudes. While nonlinear analysis has a place in modeling large-amplitude processes such as saturation, it seems appropriate to seek a linear explanation of the small-amplitude aspects of anomalous SRS and EA waves.

We begin by observing that the undamped nature of BGK waves stems not from their nonlinearity but rather from the fact that they represent a local flattening of the distribution function at the wave phase velocity (since the trapped distribution must be an even function of velocity in the wave frame). Our model of anomalous SRS posits a local flattening of the distribution function resulting from Landau damping of thermal noise driven by SRS. We shall see that such a locally flattened distribution function (LFDF) supports linear waves with reduced damping and enhanced SRS growth. Flattening resulting from Landau damping is a well-known process and

represents a nonlinear modification of the original Maxwellian but does not imply the formation of BGK waves. In fact the evolution of the flattening is usually analyzed using so-called quasi-linear (that is, nonlinear only in the sense that it involves products of linear wave quantities) theory,[9] as a result of the damping of a continuum of linear waves. For our purposes the significant properties of the flattening (its location, width, etc.) can be ascertained from linear theory, and a detailed nonlinear analysis of the dynamics of the flattening process is unnecessary. We first demonstrate that a LFDF arbitrarily close to a Maxwellian supports linear undamped plasma waves. We take a model LFDF of the form

$$f(u) = f_0(u) + f_1(u) + f_2(u), \tag{1a}$$

where

$$f_0(u) = \frac{1}{\sqrt{\pi}} e^{-u^2}, \tag{1b}$$

$$f_1(u) = -f_0'(u_0)(u-u_0) e^{\frac{(u-u_0)^2}{(\Delta u)^2}}, \tag{1c}$$

and

$$f_2(u) = \frac{1}{3}\left[\beta - f_0''(u_0)\right]\left[(u-u_0)^2 - \frac{1}{2}(\Delta u)^2\right] e^{\frac{(u-u_0)^2}{(\Delta u)^2}}. \tag{1d}$$

Velocities are normalized to $\sqrt{2}v_T$, where v_T is the electron thermal velocity. The model thus comprises a Maxwellian that has been "flattened" near $u_0 = v_0/(\sqrt{2}v_T)$ over the range Δu, so that $f'(u_0) = 0$ and $f''(u_0) = \beta$, an arbitrary parameter. Note that $\int_{-\infty}^{\infty} f(u)\,du \equiv 1$ and that $f(u)$ is an analytic function of u that becomes arbitrarily close in L_p norm to the Maxwellian $f_0(u)$ as Δu is made small.

The corresponding dielectric function for waves of frequency ω and wave number k is given by

$$\varepsilon(k,\omega) = 1 - \frac{1}{2(k\lambda_D)^2} \int_{-\infty}^{\infty} \frac{f'(u)}{u - \frac{\omega}{\sqrt{2}kv_T}} \, du. \qquad (2)$$

Substituting (1a)–(1d) into (2) gives

$$\varepsilon(k,\omega) = 1 + \frac{1}{(k\lambda_D)^2}\left[1 + \Omega Z(\Omega)\right]$$

$$+ \frac{u_0 e^{-u_0^2}}{(k\lambda_D)^2}\left[2y + \left(2y^2 - 1\right)Z(y)\right]$$

$$+ \frac{\Delta u}{(k\lambda_D)^2}\left[\frac{\sqrt{\pi}}{2}\beta + \left(1 - 2u_0^2\right)e^{-u_0^2}\right]$$

$$\times \left[\frac{2}{3}\left(y^2 - 1\right) + \left(\frac{2}{3}y^3 - y\right)Z(y)\right], \qquad (3)$$

where Z denotes the plasma dispersion function, $\Omega \equiv \omega/\left(\sqrt{2}kv_T\right)$, and $y \equiv \left(\Omega - u_0\right)/\Delta u$. The first two terms on the right of (3) give $\varepsilon_0(k,\omega)$ the dielectric function for a Maxwellian.

For each value of $k\lambda_D$ there are an infinite number of roots of (3). For the Maxwellian case, the least-damped root is usually referred to as "the" electron plasma wave; the other roots are very heavily damped and have little physical significance.[10] The flattening in the LFDF case introduces a new set of roots corresponding to waves with phase velocities near u_0. The least damped of these has much smaller damping than the plasma wave for large $k\lambda_D$. It is of interest to determine the conditions under which the damping of this root vanishes. In that case Ω is real, and

$$Z(\Omega) = i\sqrt{\pi}e^{-\Omega^2} - 2\,\mathrm{Daws}(\Omega),$$

where the Dawson function is defined as

$$\mathrm{Daws}(x) \equiv e^{-x^2}\int_0^x e^{t^2}\,dt = \frac{1}{2}\sqrt{\pi}e^{-x^2}\,\mathrm{erfi}(x).$$

Then for $\Omega = u_0$ we see from (3) that $\mathrm{Im}(\varepsilon) = 0$, and the condition for a root as $\Delta u \to 0$ is

$$1 + \left[1 - 2\Omega\,\mathrm{Daws}(\Omega)\right]/(k\lambda_D)^2 = 0,$$

which is just the dispersion relation for electron-acoustic waves in a Maxwellian plasma. Electron-acoustic modes were proposed in 1962 by Stix,[11] who speculated that a particular relative drift velocity of electrons and ions might cancel $\mathrm{Im}\left[\varepsilon(\omega,k)\right]$ and allow such modes to exist. As this seemed rather contrived, EA modes attracted little interest and were dropped from the second edition of Stix's book.[12] The experimental observation of scattering from EA waves[4] therefore came as somewhat of a surprise, and at first they were not recognized as such.[13] We will return to EA waves after investigating anomalous SRS in a LFDF.

We combine in the usual way[14] the electromagnetic equations for the pump and scattered light waves with the dielectric function for the plasma waves (3) to obtain the dispersion relation for SRS backscatter:

$$D(k,\omega) \equiv \varepsilon(k,\omega)\left[(\omega - \omega_0)^2 - (k - k_0)^2 c^2 - \omega_p^2\right]$$

$$- \left[1 - \varepsilon(k,\omega)\right]\frac{k^2 v_{\mathrm{osc}}^2}{4} = 0. \qquad (4)$$

Here k_0 and ω_0 are the wave number and frequency of the pump (laser) wave, ω_p is the electron-plasma frequency (a homogeneous plasma and fixed ions are assumed), and $v_{\mathrm{osc}} \equiv eE_0/m\omega_0$ is the electron quiver velocity in the laser field E_0.

We begin by studying a Maxwellian (unflattened) plasma, substituting $\varepsilon_0\,(k,\omega)$ in (4). Temporal growth rates of the SRS instability are found by solving (4) for ω as a function of k. The growth rate is a maximum at the resonance where both factors of the first term in (5) are small. Figure 92.29 shows normalized growth rates $\gamma/\left(\sqrt{2}\,kv_T\right)$ for a laser intensity of 10^{15} W/cm^2, temperature of 4 keV, and various values of the normalized electron-plasma density $n/n_c = \omega_p^2/\omega_0^2$, where n_c is the critical density. In the absence of damping, the growth

rate would be $\gamma_0 / (\sqrt{2} k v_T) \sim 10^{-2}$, so it is evident that Landau damping has substantially decreased the growth rate. Note that the resonant value of $k\lambda_D$ increases and the resonance becomes broader as the density decreases.
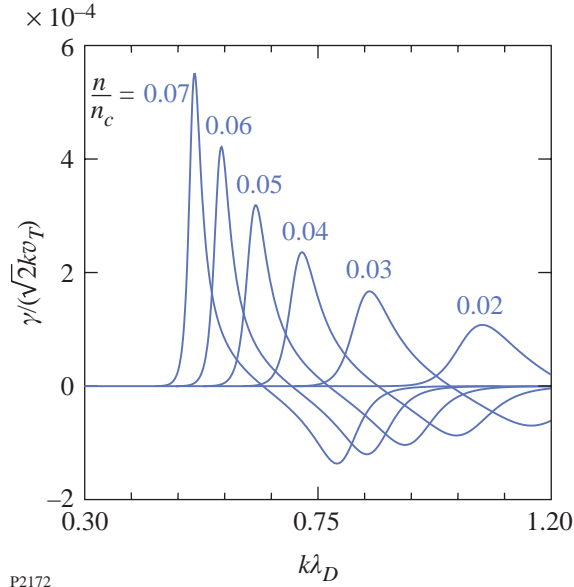

P2172

Figure 92.29

The SRS growth rates in a Maxwellian plasma with an incident laser intensity of 10^{15} W/cm^2 and an electron temperature of 4 keV.

Since monotonic distribution functions support only damped waves, we may expect the localized distortion of the distribution function resulting from damping of the SRS-driven plasma waves to continue until there is a point of inflection at the wave phase velocity. Such a situation can be represented by a LFDF with $\beta = 0$. To model the flattening effect of SRS we choose the flattening velocity $u_0 = \text{Re}(\Omega_{\max})$, where $\Omega_{\max}$ is the root corresponding to the peak growth rates in Fig. 92.29. The effects of interest are insensitive to Δu as long as it is small, so we take $\Delta u = 0.1$. Results for a density of $n/n_c = 0.05$ are shown in Fig. 92.30(a). The upper line represents the electromagnetic mode, effectively undamped in hot, low-density plasma, and the lower curve represents the least-damped plasma mode. In the absence of the pump these two modes would propagate independently, but the coupling due to the pump produces the SRS instability near the resonance at $k\lambda_D \cong 0.63$. Owing to the reduced Landau damping of the plasma mode resulting from the flattening, the peak SRS growth rate is larger than in Fig. 92.29 for the same plasma conditions by a factor of ~3. Note that the flattening has also resulted in an undamped electron-acoustic mode at $k\lambda_D \cong 0.5$. This mode does not satisfy the wave-vector-matching conditions for Raman scattering, however, so it is not driven.

While substantially reduced by the flattening, the Landau damping of the SRS plasma mode in Fig. 92.30(a) is still significant. This damping will continue the net transfer of particles from velocities below u_0 to velocities above u_0 until the wave is undamped. We may thus expect the flattening to overshoot, resulting in a small secondary maximum of the distribution function near u_0. This situation can be modeled by a nonzero value of β; the value of β giving an undamped plasma wave at the SRS matching wave vector is

$$\beta = \frac{3}{\sqrt{\pi}} \left[\frac{1 + (k\lambda_D)^2 - 2u_0 \, \text{Daws}(u_0)}{\Delta u} + \frac{2}{3} \left(2u_0^2 - 1 \right) e^{-u_0^2} \right].$$

For the parameters of Fig. 92.30, $\beta \cong 2.54$, and the resulting plot is seen in Fig. 92.30(b). The reduction in damping of the plasma mode has increased the peak SRS growth rate as seen at $k\lambda_D \cong 0.63$ in Fig. 92.30(b) by a factor of ~3 over the SRS growth rate in Fig. 92.30(a). Note however that, owing to the secondary maximum of the distribution function, the EA mode has now become unstable, with an even larger growth rate than the SRS. This suggests that the EA wave may quickly grow to large amplitudes and disrupt the SRS process. Such a quench-
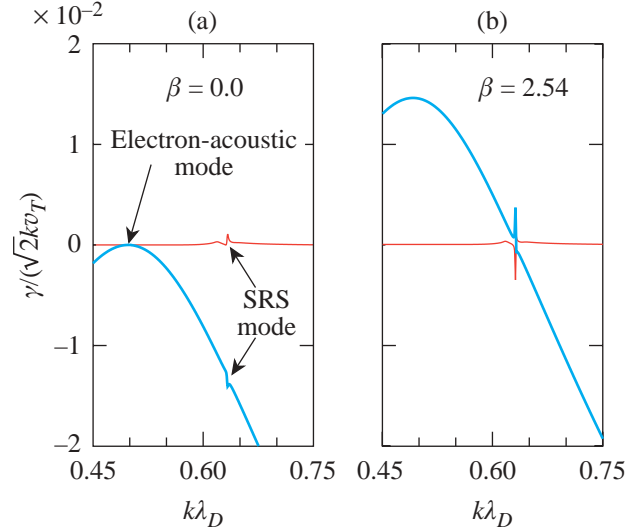
P2173

Figure 92.30

(a) The imaginary parts of the two least-damped roots of the SRS dispersion relation for a flattened distribution with $u_0 = 1.71$, corresponding to the peak of the SRS growth curve in Fig. 92.29 for $n/n_c = 0.05$. (b) The same distribution function, but with β increased to give zero damping of the plasma mode at the SRS resonance.

ing mechanism may be related to the intermittent interruptions in the SRS reflectivity seen in simulations [Fig. 1(a) of Ref. 15] and may help to explain why anomalous SRS reflectivities saturate at much lower levels than standard (small $k\lambda_D$) SRS reflectivities, though both have similar initial growth rates (see, e.g., Fig. 4 of Ref. 5). It is also noteworthy that the SRS growth rate peak in the $\beta = 0$ case is much narrower than in the original Maxwellian and consists of a sharp peak with a smaller subsidiary peak at slightly smaller $k\lambda_D$; this strongly resembles the form of the plasma-wave spectrum seen in SRS simulations [Fig. 1(b) of Ref. 15].

This analysis of anomalous SRS has been based on a locally flattened Maxwellian, an idealization capturing the essential aspects of a distribution function modified by Landau damping while remaining mathematically tractable. However, the Maxwellian itself represents an idealization; in a real plasma, thermal and other fluctuations are continually causing local, temporary distortions in the form of the distribution function. In particular, we may expect that such local distortions will on occasion result in a reduction or elimination of the slope of the distribution function. As noted above, such a distortion may represent an arbitrarily small deviation from the Maxwellian and still allow propagation of undamped EA waves. As the slope of the distribution function relaxes back to its equilibrium value, such a wave would ordinarily become heavily Landau damped and disappear. However, if it satisfies the frequency and wave-number-matching conditions for SRS, it will be driven just as the plasma wave in the case of anomalous SRS, resulting in amplification of the EA wave, maintenance of the local flattening by Landau damping, and the production of scattered light.

Such scattering has recently been seen at low levels in experiments,[4] though it was attributed to a nonlinear EA-like BGK mode. In fact, Refs. 4 and 8 suggest that such waves are the source of anomalous SRS and, on that basis, propose limiting SRS reflectivities in NIF targets by modifying plasma parameters so that $k\lambda_D > 0.53$ for the SRS-driven BGK wave (such waves are limited to $k\lambda_D < 0.53$). However, experiments in which SRS originates from low densities indicate that this nonlinear interpretation is implausible. To see this it is useful to combine the EA dispersion relation with the SRS resonance conditions to obtain a relation between the scattered light wavelength and the density at which scattering occurs. This relation is shown in Fig. 92.31 for the plasma parameters of the experiments in Ref. 3 (laser wavelength 351 nm, electron temperature $T_e \cong$ keV). Note that EA-wave scattering does not occur at densities below 0.08 critical; this is related to the $k\lambda_D$

< 0.53 restriction (at lower densities the Debye length becomes too large to satisfy this condition for the SRS k). At higher densities there are two possible scattered wavelengths; the upper solution corresponds to plasma-wave scattering and the lower to EA-wave scattering.

Two types of experiments are described in Ref. 3. In the first, an interaction beam is focused on a relatively homogeneous plasma formed by an exploding foil; the density in the interaction region is (from hydro simulations) about 0.2 critical. From Fig. 92.31 it is seen that plasma waves at this density produce scattered light at about 650 nm, and that is what is seen in the experiment. No EA-wave scattering (at about 450 nm) is detected. In the second type of experiment, however, the interaction beam is focused on a plasma derived from a solid target, so that a full range of densities down to vacuum is represented in the interaction region. The SRS spectrum in these experiments extends from 420 to 540 nm, indicating that low densities are necessary to produce scattering at these wavelengths. The absence of SRS at higher densities is likely due to the steeper density gradients there that hydro simulations show in the solid-target experiments; such gradients would equally rule out EA waves at these densities as the source of the scattering. The scattering is, however, consistent with anomalous SRS from plasma waves in densities ≤0.04 critical. At such densities and temperatures (~4 keV) EA
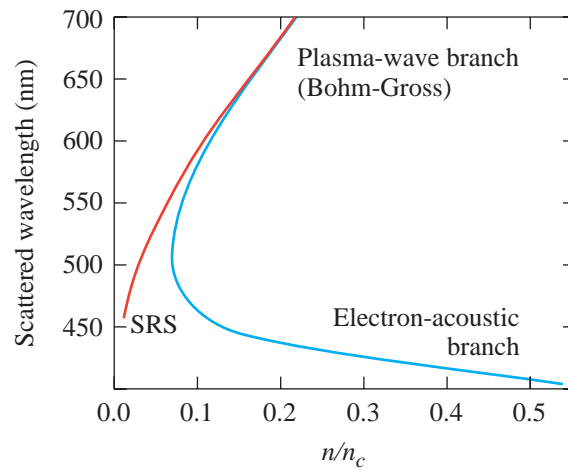
P2175

Figure 92.31
The scattered wavelength as a function of density for incident laser wavelength 351 nm for EA scattering and SRS. At long scattered wavelengths both waves approach the Bohm-Gross dispersion relation but diverge at shorter wavelengths (larger $k\lambda_D$).

scattering does not exist, and reduced damping of the SRS plasma wave ($k\lambda_D \sim 1$) is required to account for the dominance of these wavelengths in the observed spectrum. Local flattening of the distribution function as described above therefore seems the most satisfactory explanation for these results.

In summary, the model presented here shows that linear waves in a locally flattened distribution function can account for both anomalous SRS and EA-wave observations. Several predictions of the linear model differ qualitatively from those of the nonlinear approach. Among these: the linear model accommodates coexistence of SRS and EA waves, as seen in Refs. 4 and 13, and the occurrence of SRS at very low densities, as in Ref. 3. The linear model also suggests that proposals[2,4,8] to eliminate SRS in the NIF by altering plasma parameters so that $k\lambda_D > 0.53$ may not be successful.

ACKNOWLEDGMENT

REFERENCES

1. A. Simon, W. Seka, L. M. Goldman, and R. W. Short, Phys. Fluids **29**, 1704 (1986) and references therein.

2. D. S. Montgomery *et al.*, Phys. Plasmas **9**, 2311 (2002).

3. S. P. Regan, D. K. Bradley, A. V. Chirokikh, R. S. Craxton, D. D. Meyerhofer, W. Seka, R. W. Short, A. Simon, R. P. J. Town, B. Yaakobi, J. J. Caroll III, and R. P. Drake, Phys. Plasmas **6**, 2072 (1999).

4. D. S. Montgomery *et al.*, Phys. Rev. Lett. **87**, 155001 (2001).

5. J. C. Fernandez *et al.*, Phys. Plasmas **7**, 3743 (2000).

6. I. B. Bernstein, J. M. Greene, and M. D. Kruskal, Phys. Rev. **108**, 546 (1957).

7. J. P. Holloway and J. J. Dorning, Phys. Lett. A **138**, 279 (1989); J. P. Holloway and J. J. Dorning, Phys. Rev. A **44**, 3856 (1991).

8. H. A. Rose and D. A. Russell, Phys. Plasmas **8**, 4784 (2001).

9. E. M. Lifshitz and L. P. Pitaevskifi, *Physical Kinetics*, 1st ed., Course of Theoretical Physics, Vol. 10 (Pergamon Press, Oxford, 1981), pp. 199–205.

10. These correspond to the alternative definition of electron-acoustic modes; see Ref. 11.

11. T. H. Stix, *The Theory of Plasma Waves* (McGraw-Hill, New York, 1962), p. 218. The term "electron-acoustic wave" is also often used to refer to the infinite set of solutions to the Landau dispersion relation other than the least-damped one [e.g., D. C. Montgomery, *Theory of the Unmagnetized Plasma* (Gordon and Breach, New York, 1971), p. 69]. Since in the past all these modes were usually mentioned only to be dismissed, many authors confuse or conflate the two definitions; our usage conforms to that of Stix.

12. T. H. Stix, *Waves in Plasmas* (American Institute of Physics, New York, 1992).

13. J. A. Cobble *et al.*, Phys. Plasmas **7**, 323 (2000).

14. J. F. Drake *et al.*, Phys. Fluids **17**, 778 (1974).

15. H. X. Vu, D. F. DuBois, and B. Bezzerides, Phys. Plasmas **9**, 1745 (2002).

Time Delay of the Resistive-State Formation in Superconducting Stripes Excited by Single Optical Photons

Recently proposed superconducting single-photon detectors (SSPD's), based on ultrathin, submicrometer-width NbN superconducting stripes, are characterized by picosecond response times, high quantum efficiency, broadband single-photon sensitivity, and extremely low dark counts.[1,2] The devices have immediately found a variety of applications ranging from noninvasive testing of very-large-scale integrated (VLSI) circuits[3] to quantum cryptography.[4,5] Their single-photon-counting ability has been interpreted within a phenomenological hot-electron photoresponse model proposed in Ref. 1 and elaborated in Ref. 6. The model describes the formation of a hotspot,[7] right after the single-photon absorption event, followed by in-plane growth of a resistive hotspot area due to the high efficiency of the excited quasiparticle multiplication process in NbN films.[8] During this stage, however, the resistive state does not appear across the superconducting stripe because the size of a single normal hotspot, created by an optical photon, is significantly smaller than our stripe width.[2] The resistive state appears due to a supplementary action of the device's bias current density j, which should be close to the stripe's critical current density j_c. After the supercurrent is expelled from the normal hotspot region, the bias current density in the stripe's "sidewalks" j_{sw} exceeds j_c [see Fig. 92.32(c)], resulting in the penetration of the electric field in the sidewalk areas of the stripe.[6] As a result, we observe a voltage pulse that reflects the initial act of photon capture.

The resistive-state development process presented above should lead to an experimentally observable time delay in the superconducting stripe's resistive photoresponse.[9] This delay, in turn, if measured, would give direct confirmation of a supercurrent-enhanced, hotspot-induced photoresponse mechanism of our SSPD.[1]

The dynamics of the resistive-state formation in a photon-illuminated, two-dimensional (2-D) superconducting stripe depends on the radiation flux density incident on the device and the bias current density, as is schematically illustrated in Fig. 92.32. At relatively high (macroscopic) incident photon fluxes, a large number of hotspots are simultaneously formed in our superconducting stripe [Fig. 92.32(a)]. In this case, the hotspots overlap with each other across a cross section of the stripe. Since the stripe thickness d is comparable with coherence length ξ, we can assume that for overlapping hotspots, a resistive barrier is instantaneously formed across the NbN stripe and, as a result, a voltage signal is generated within an electron thermalization time of 6.5 ps.[10] When the photon flux is decreased, the hotspots become isolated [Fig. 92.32(b)]. Finally, for the flux containing one or less than one absorbed photon per pulse, we can expect that, at best, only one resistive
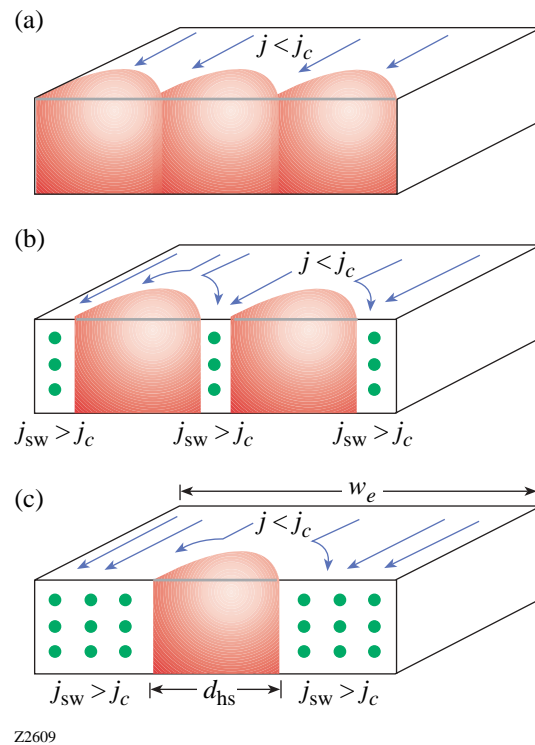

Figure 92.32
Schematic presentation of the dynamics of resistive-barrier formation across a superconducting stripe: (a) high (macroscopic) incident photon flux, (b) the two-photon regime, leading to the generation of two hotspots in the cross section of the superconducting stripe, and (c) the single-photon regime.

hotspot will be formed in our stripe [Fig. 92.32(c)]. As we mentioned above, in the single-photon regime, we postulate that the formation of a macroscopic resistive barrier can be realized only when j_{sw} surpasses j_c, which is associated with macroscopic current redistribution and should lead to a certain time delay in the resistive-state formation.

Even if the two-photon detection mechanism[1,2] does not correspond exactly to the situation presented in Fig. 92.32(b) since the hotspots can either partially overlap or coincide, the scenario illustrated in Fig. 92.32(b) should result in a measurable time delay t_d for the voltage pulse generation, corresponding to the time period between the initial hotspot appearance and the eventual development of a resistive barrier across the entire cross section of the superconducting stripe. In terms of the superconductor dynamics, t_d is the time required for a superconductor energy gap Δ to be reduced to zero by the current in the sidewalks and, for $j_{sw} > j_c$, can be calculated using the Tinkham model[11] as

$$t_d = 2\tau_\Delta \int\limits_0^1 \frac{f^4}{\left[2j_{sw}/\left(3\sqrt{3}\,j_c\right)\right]^2 + f^6 - f^4}\, df, \quad (1)$$

where $\tau_\Delta \cong 2.41\tau_E/\sqrt{1 - T/T_c}$ is the gap relaxation time[9] (τ_E is the inelastic electron–phonon collision time at the Fermi level at T_c) and $f = \Delta/\Delta_0$ ($\Delta_0 = \Delta$ at 0 K).[11]

The devices used in our experiments were $4 \times 4\text{-}\mu m^2$-area, meander-type, NbN stripes with $d = 10$ nm, a nominal width $w = 130$ nm, and the total length of about $30\ \mu m$. The structures were superconducting at $T_c = 10.5$ K and exhibited $j_c = 6 \times 10^6\ A/cm^2$ at 4.2 K. Details of their fabrication and implementation as SSPD's are described in Refs. 2 and 4; here we only wanted to stress that with the constant j_c, I_c of the meander is determined by its narrowest segment, and, according to our supercurrent-enhanced, resistive-state formation model, the narrowest segments of the stripe contribute the most to the SSPD photoresponse.[2] The atomic force microscope images showed that irregularities in our stripes were up to 25 nm, close to the cantilever resolution limit. At the same time, the I_c of the meander structures, measured at 4.2 K, was typically 60% lower than I_c for the control (short) stripe fabricated in the same process. Thus, to account for the width variations, we introduce the effective stripe width w_e, corresponding to the detector segments most active in the resistive-state formation and photon detection, and we estimate w_e to be 80 nm.
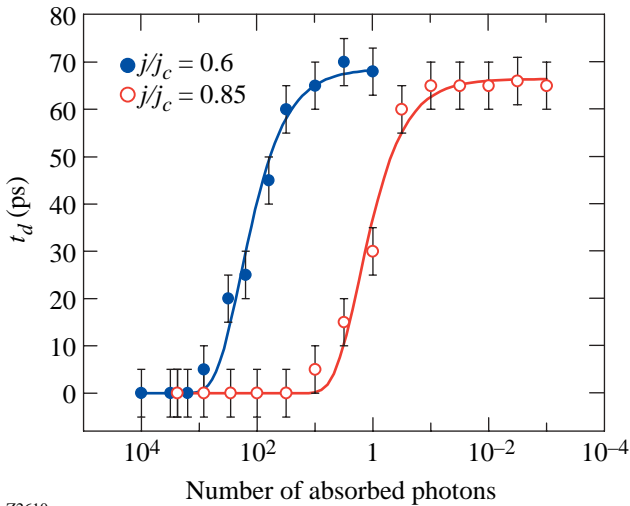
Our devices were mounted inside a cryostat on a cold base plate maintained at 4.2 K, wire-bonded to a 50-Ω microwave stripe line, and connected to the bias and output circuitry through a cryogenic bias-tee.[4] As optical excitation, we used 100-fs-wide pulses from a Ti:Al$_2$O$_3$ laser with a wavelength of 810 nm and a repetition rate of 82 MHz. The laser radiation power was attenuated down to a picowatt range using banks of neutral-density filters. Voltage pulses generated by our SSPD's were amplified directly by a room-temperature amplifier and fed to a synchronously triggered Tektronix 7404 single-shot digital oscilloscope, or they were counted by a fast electronic counter. The photon counter was used to determine the single-photon, two-photon, or multiphoton regimes of operation of our devices, as described in detail in Refs. 1 and 2. The amplifier and the oscilloscope had bandwidths of 0.01 to 12 GHz and 0 to 4 GHz, respectively. Thus, the ~100-ps real-time resolution of our entire readout system was determined mainly by the oscilloscope performance. On the other hand, digital averaging procedures of acquired pulses allowed us to achieve the relative-time resolution (e.g., delays between the photoresponse pulses generated under different photon excitations) of ~5 ps, due to extremely low intrinsic jitter in our measurement system.

Figure 92.33 presents the measured time delays in the photoresponse signal versus the number of absorbed photons, calculated as the photon flux density incident upon the meander multiplied by the device detection efficiency (DE).[2] The data are presented for two experimental bias conditions at $j/j_c = 0.85$ (open circles) and $j/j_c = 0.6$ (closed circles) and correspond to the SSPD single-photon and two-photon regimes of operations, respectively.

We will discuss the single-photon $\left(j/j_c = 0.85\right)$ regime first, remembering that for our $4 \times 4\text{-}\mu m^2$ device, DE for counting single, 810-nm photons at $j/j_c = 0.85$ is ~10^{-3} (Ref. 2). We observe that for large absorbed photon fluxes (macroscopic number of photons per pulse) t_d does not depend on the radiation flux. Clearly, this situation corresponds to the multi-hotspot-generation case presented in Fig. 92.32(a). We will use this condition as a reference and refer to it as $t_d = 0$. When the incident flux is decreased to about 10 absorbed photons/pulse, the arrivals of the photoresponse signals start to be time delayed with respect to the multiphoton response and t_d increases. Subsequently, t_d saturates when the flux density is decreased down to about 10^{-1} absorbed photons/pulse. In this case, we are in the single-photon counting mode [Fig. 92.32(c)]. Thereafter, the arrival of the photoresponse pulse is not further delayed in time scale even if we attenuate

the flux down to 10^{-3} absorbed photons/pulse. We interpret the measured time interval between the multiphoton and the single-photon responses, $\Delta t_d = 65\pm5$ ps, as the time needed for supercurrent redistribution around a single, photon-created hotspot and subsequent formation of the resistive barrier for $j_{sw} > j_c$.
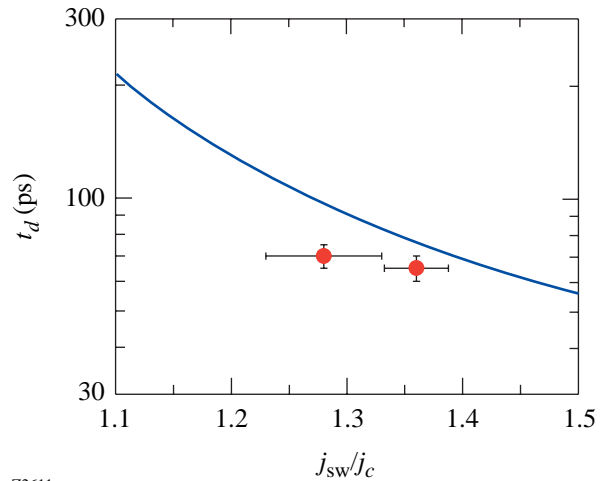
We repeated the same experiment, but with a significantly lower bias current applied to the detector (curve $j/j_c = 0.6$ in Fig. 92.33). In this case, according to Ref. 2, the probability of detecting a single, 810-nm photon by our 4×4-μm^2 device is negligibly small; thus, at least two photons are needed to generate the resistive response. As seen in Fig. 92.33, the observed behavior (closed circles) is very similar to that measured for $j/j_c = 0.85$; we can clearly identify the time-delay phenomenon and find $\Delta t_d = 70\pm5$ ps. The main difference is that the observed photoresponse delay is now shifted into significantly higher levels of the incident photon flux. The value of t_d starts to be nonzero for $\sim 10^3$ absorbed photons/pulse, and it flattens at ~ 10 absorbed photons/pulse. The latter value is very consistent with the two-photon detection mechanism.[1,2]

Finally, we can compare our experimental results with t_d calculated for our experimental conditions, using Eq. (1) and $\tau_E \approx 10$ ps.[10] The current density in the sidewalks in the narrowest (most-active) segments of the meander can be calculated as $j_{sw} = j[w_e/(w_e - d_{hs})]$, where $d_{hs} \approx 30$ nm is the diameter of the hotspot for 810-nm photons.[2] Thus, for the experimental $j/j_c = 0.6$ condition, $j_{sw}/j_c = 0.96$ and is subcritical in a single-hotspot regime. However, doubling the hotspot size[12] gives $j_{sw}/j_c = 1.28$, which is sufficient to generate a resistive barrier across our stripe. In a similar manner, when $j/j_c = 0.85$, j_{sw}/j_c is supercritical and reaches 1.36 when the single hotspot is formed. Figure 92.34 shows the t_d dependence on j_{sw}/j_c; the solid line represents the Tinkham model,[11] while the two closed circles refer to our measured Δt_d values, corresponding to the $j_{sw}/j_c = 1.36$ and $j_{sw}/j_c = 1.28$ conditions, respectively. We note that our experimental values are reasonably close to the theoretical prediction, remembering that the Tinkham theory is applicable for clean superconductors, while our 10-nm-thick NbN films are in the dirty limit. In addition, the discrepancy can be related to the accuracy of our w_e estimation.

Z2610

Figure 92.33
Experimental time delay t_d of the resistive-state formation in a NbN superconducting stripe as a function of the incident absorbed photon flux density. Open circles correspond to t_d measured when the stripe was biased with $j/j_c = 0.85$ (single-photon regime), and closed circles represent $j/j_c = 0.6$ and the two-photon regime. Solid lines are guides to the eye. The measurement error is ±5 ps.

Z2611

Figure 92.34
Time delay t_d as a function of the normalized current in the sidewalks of the superconducting stripe j_{sw}/j_c. The two measured values of Δt_d (solid circles) correspond to the single-hotspot and two-hotspot formation at $j_{sw}/j_c = 1.36$ and $j_{sw}/j_c = 1.28$, respectively. The solid line represents the theoretical prediction, calculated using Eq. (1), and the horizontal error bars are calculated for the hotspot-diameter variations of 30 ± 1 nm.

In conclusion, we observed the time-delay phenomenon in the resistive-state response in ultrathin, submicrometer-width NbN superconducting stripes, excited by single optical photons. The observed phenomenon directly shows that the resistive state across an ultrathin, submicrometer-width superconducting stripe upon absorption of an optical photon is due to photon-induced hotspot formation and subsequent redistribution of the supercurrent into the sidewalks of the stripe. Our measurements agree well with a theoretical prediction based on the Tinkham model of the resistive-state formation in superconducting stripes under the supercurrent perturbation.[11]

ACKNOWLEDGMENT

REFERENCES

1. G. N. Gol'tsman, O. Okunev, G. Chulkova, A. Lipatov, A. Semenov, K. Smirnov, B. Voronov, A. Dzardanov, C. Williams, and R. Sobolewski, Appl. Phys. Lett. **79**, 705 (2001).

2. A. Verevkin, J. Zhang, R. Sobolewski, A. Lipatov, O. Okunev, G. Chulkova, A. Korneev, K. Smirnov, G. N. Gol'tsman, and A. Semenov, Appl. Phys. Lett. **80**, 4687 (2002).

3. S. Somani, S. Kasapi, K. Wilsher, W. Lo, R. Sobolewski, and G. Gol'tsman, J. Vac. Sci. Technol. B, Microelectron. Nanometer Struct. **19**, 2766 (2001).

4. A. Verevkin, J. Zhang, W. Slysz, R. Sobolewski, A. Lipatov, O. Okunev, G. Chulkova, A. Korneev, and G. N. Gol'tsman, "Superconducting Single-Photon Detectors for GHz-Rate Free-Space Quantum Communications," to be published in SPIE's *Free-Space Laser Communication and Laser Imaging II*.

5. A. Verevkin, G. Gol'tsman, and R. Sobolewski, in *OPTO-Canada: SPIE Regional Meeting on Optoelectronic, Photonics, and Imaging* (SPIE, Bellingham, WA, 2002), Vol. TD01, pp. 39–40.

6. A. D. Semenov, G. N. Gol'tsman, and A. A. Korneev, Physica C **351**, 349 (2001).

7. A. M. Kadin and M. W. Johnson, Appl. Phys. Lett. **69**, 3938 (1996).

8. K. S. Il'in, I. I. Milostnaya, A. A. Verevkin, G. N. Gol'tsman, E. M. Gershenzon, and R. Sobolewski, Appl. Phys. Lett. **73**, 3938 (1998).

9. D. J. Frank *et al.*, Phys. Rev. Lett. **50**, 1611 (1983); D. J. Frank and M. Tinkham, Phys. Rev. B **28**, 5345 (1983).

10. K. S. Il'in, M. Lindgren, M. Currie, A. D. Semenov, G. N. Gol'tsman, R. Sobolewski, S. I. Cherednichenko, and E. M. Gershenzon, Appl. Phys. Lett. **76**, 2752 (2000).

11. M. Tinkham, *Introduction to Superconductivity*, 2nd ed., International Series in Pure and Applied Physics (McGraw-Hill, New York, 1996).

12. In a case where two hotspots are present in the film, we have taken the average effective size of the double hotspot across the cross section of the NbN stripe to be $\sqrt{2}d_{hs}$ to take into account a possible overlap between the hotspots.

LLE's Summer High School Research Program

During the summer of 2002, 15 students from Rochester-area high schools participated in the Laboratory for Laser Energetics' Summer High School Research Program. The goal of this program is to excite a group of high school students about careers in the areas of science and technology by exposing them to research in a state-of-the-art environment. Too often, students are exposed to "research" only through classroom laboratories, which have prescribed procedures and predictable results. In LLE's summer program, the students experience many of the trials, tribulations, and rewards of scientific research. By participating in research in a real environment, the students often become more excited about careers in science and technology. In addition, LLE gains from the contributions of the many highly talented students who are attracted to the program.

The students spent most of their time working on their individual research projects with members of LLE's technical staff. The projects were related to current research activities at LLE and covered a broad range of areas of interest including laser optics modeling, analysis of OMEGA implosion experiments, hydrodynamics modeling, cryogenic target physics and characterization, liquid crystal chemistry, thin-film deposition, and the development and control of laser fusion diagnostics (see Table 92.IV).

The students attended weekly seminars on technical topics associated with LLE's research. Topics this year included lasers, fusion, holographic optics, hydrodynamic stability, laboratory astrophysics, computer-controlled optics manufacturing, and microcontrollers and their applications. The students also received safety training, learned how to give scientific presentations, and were introduced to LLE's resources, especially the computational facilities.

The program culminated on 28 August with the "High School Student Summer Research Symposium," at which the students presented the results of their research to an audience including parents, teachers, and LLE staff. The students' written reports will be bound into a permanent record of their work that can be cited in scientific publications. These reports are available by contacting LLE.

One hundred forty-five high school students have now participated in the program since it began in 1989. This year's students were selected from approximately 50 applicants.

At the symposium, LLE presented its sixth annual William D. Ryan Inspirational Teacher Award to Mr. James Keefer, a physics and chemistry teacher at Brockport High School. This award includes a $1000 cash prize. Alumni of the Summer High School Research Program were asked to nominate teachers who played a major role in sparking their interest in science, mathematics, and/or technology. Mr. Keefer was nominated by Priya Rajasethupathy, a participant in the 2000 Summer Program. Priya credits Mr. Keefer with preparing her well for college and writes of her former teacher: "What impresses me most about Mr. Keefer is his teaching style, his ability to communicate with his students and captivate their interest." Mr. Jeff Brown, principal of Brockport High School, also had many words of high praise for Mr. Keefer. He noted that Mr. Keefer "is an exceptional teacher recognized by our students, faculty, administration, and community." He also said that Mr. Keefer "has some unique qualifications" as he is certified in five areas of science (earth science, chemistry, biology, physics, and general science).

Table 92.IV: High School Students and Projects—Summer 2002.

Name	High School	Supervisor	Brief Project Title
Megan Alexander	Honeoye Falls–Lima	J. Zuegel/W. Seka	Picket Pulse Shaping with Phase and Amplitude Modulation in the Frequency Domain
Stefan Astheimer	Honeoye Falls–Lima	P. B. Radha	Estimation of Magnetic Fields in Direct-Drive Implosions
Christine Balonek	Byron–Bergen	K. Marshall	Optical Applications of Lyotropic Liquid Crystalline Polysaccarides
David Dingeldine	Churchville–Chili	J. Knauer	Plasma Energy Measurement with an Open-Cell Metal Foam
Sonya Dumanis	Harley School	V. Smalyuk	Structure of Shell Modulations Near Peak Compression of Spherical Implosions
Sid Ghosh	Pittsford–Mendon	P. Jaanimagi	Secondary Electrons from X-Ray Photocathodes
Kyle Gibney	Livonia	C. Stoeckl	Computer-Controlled Neutron Diagnostics
Sharon Jin	Victor	S. Craxton	A Ray-Tracing Model for Cryogenic Target Uniformity Characterization
Jue Liao	Brighton	R. Epstein	Rayleigh–Taylor Growth Rates for Arbitrary Density Profiles Calculated with a Variational Method
Christopher Moody	Spencerport	D. Harding	Characterization of the Absorption Spectrum of Deuterium for Infrared Wavelengths
Phoebe Rounds	Irondequoit	S. Craxton	Multiple-Tripler Broad-Bandwidth Frequency Conversion
Micah Sanders	Pittsford–Mendon	N. Bassett	Thin Film Characterization of Al_2O_3 Utilizing Reactive Pulsed dc Magnetron Sputtering
Gurshawn Singh	Rush–Henrietta	J. Marozas	2-D Pulsed Laser Beam Modeling Using PROP
Archana Venkataraman	Brighton	F. Marshall	Characterization of Multilayer Diffractors for Framed Monochromatic Imaging
Joy Yuan	Pittsford–Mendon	M. Guardalben	Noncollinear Phase Matching in Optical Parametric Chirped-Pulse Amplification

FY02 Laser Facility Report

Increased user demand was met in FY02 by expanding the available shot time during select weeks. Ten weeks were extended to four shot days by shooting one 8-h day, two 12-h days, and one 16-h day. This adjustment raised the total executed shots by 11%—from 1289 in FY01 to 1428 in FY02 (see Table 92.V). Shaped-pulse cryogenic implosions highlighted the ongoing development of direct-drive cryogenic capability. A total of 21 spherical cryogenic D_2 targets were shot on OMEGA. Some of the cryogenic target shot time was devoted to characterization and system reliability improvements. Planar cryogenic target capability was also activated, and many shots were executed under LLE's Stockpile Stewardship Program (SSP) campaign. Highlights of other achievements and active projects as of the end of FY02 include the following:

- An IR streak camera with pulse-shape analysis software became a key operational tool to optimize pulse-shape performance. Combined with some changes to the control system for pulse-shape setup and upgrades to the regenerative oscillator hardware, the changes have resulted in dramatic improvements to delivered-pulse-shape performance.

- Infrared amplification occurs across a large variety of gain stages. By far, the highest gain stage is the regenerative (regen) amplifier, with 1×10^5 gain. One of the flash-lamp-pumped laser regens for OMEGA was replaced by a diode-pumped version that operates consistently without feedback stabilization. This diode-pumped laser improves pulse-shape performance. The remaining regens on OMEGA will be changed over to the new design in FY03.

- The distributed polarization rotator (DPR)—one of the key optics for beam smoothing on target—was modified for remote removal and reinstallation. The cassette-style removal system retracts the optic from the UV beamline into a protective housing. Having the capability to insert or remove these components improves flexibility for reconfiguring to indirect-drive setups. The full 60-beam complement of actuators will be completed early in FY03.

- The OMEGA laser is designed to provide a high degree of uniformity and flexibility in target illumination. The ability to impose a controlled assymmetric on-target irradiation pattern was developed and used extensively. This capability is used to benchmark multidimensional hydrodynamic simulations by imposing known nonuniform compression conditions on spherical targets. It is also used to modify laser-irradiation conditions for beam-to-beam x-ray yield balance.

- Modifications to the stage-A alignment sensors on OMEGA have streamlined an item of flexibility frequently exploited by LLE principal investigators. The backlighter driver alignment handoff to the OMEGA beamlines was re-engineered to expedite configuration setups that require the use of this source.

- Scientists and engineers from Lawrence Livermore National Laboratory along with LLE collaborators successfully implemented a green (second harmonic, 527 nm) target irradiation capability on one of the 60 OMEGA beams. This capability utilizes the existing OMEGA frequency-conversion crystals with the tripler detuned so that maximum 527-nm conversion is achieved.

- A revised set of direct-drive phase plates was designed and is being fabricated to further optimize irradiation uniformity for spherical implosions. These optics are going to be available in mid-FY03 and are expected to have improved smoothing characteristics in the mid-spatial-frequency range.

Table 92.V: The OMEGA target shot summary for FY02.

Laboratory	Planned Number of Target Shots	Actual Number of Target Shots
LLE	755	720
LLNL*	405	413
LANL	130	132
SNL	20	24
NLUF	120	118
CEA	20	19
Total	1450	1426
LLE ISE		306
LLE SSP		204
LLE RTI		66
LLE LPI		44
LLE Astro		46
LLE Cryo		21
LLE DD		18
LLE PB		15
LLE Total		720
*Includes ten in collaboration with LANL and seven with SNL.		

National Laser Users' Facility and External Users' Programs

During FY02, 698 target shots were taken on OMEGA for external users' experiments. This is the highest number of target shots ever taken by external users on OMEGA in a single year and represents a 16% increase in external user shots over FY01. The external user shots accounted for 49% of the total OMEGA target shots in FY02. External users' experiments were carried out by eight collaborative teams under the National Laser Users' Facility (NLUF) Program as well as collaborations led by scientists from Lawrence Livermore National Laboratory (LLNL), Los Alamos National Laboratory (LANL), Sandia National Laboratory (SNL), the Nuclear Weapons Effects Testing (NWET) Program, and the Commissariat à l'Énergie Atomique (CEA) of France.

NLUF Programs

FY02 was the second of a two-year period of performance for the eight NLUF programs approved for FY01–FY02 experiments. The eight NLUF campaigns received a total of 118 target shots on OMEGA in FY02.

The Department of Energy (DOE) issued solicitations in mid-FY02 for NLUF proposals to be carried out in FY03–FY04. DOE raised the NLUF funding allocation to $800,000 for FY03 and is expected to increase it to $1,000,000 for FY04 to accommodate the high level of interest shown in the use of OMEGA to carry out experiments of relevance to the National Nuclear Security Agency (NNSA) Stockpile Stewardship Program. NLUF participants use these funds to cover their costs for carrying out experiments on OMEGA. The participants do not pay the OMEGA operating costs for carrying out their experiments; the operation of OMEGA is funded by the DOE-LLE Cooperative Agreement.

A total of 13 NLUF proposals were submitted to DOE for consideration for FY03–FY04 support and OMEGA shot allocation. An independent DOE Technical Evaluation Panel comprised of Dr. Tina Back (LLNL), Dr. David Bradley (LLNL), Dr. David Montgomery (LANL), and Dr. Richard Olson (SNL) reviewed the proposals on 10 June 2002 and recommended that up to nine of the proposals be approved for partial funding

and shot allocation during FY03–FY04. Table 92.VI lists the successful proposals.

FY02 NLUF Experiments

The eight NLUF experiments carried out in FY02 included the following:

Atomic Physics of Hot, Ultradense Plasmas.
Principal Investigators: C. F. Hooper, Jr. (University of Florida), D. A. Haynes (Fusion Technology Institute, University of Wisconsin), and collaborators from Los Alamos National Laboratory, the University of Wisconsin, and LLE.

The objective of this study is to produce hot (electron temperature $T_e > 1.5$ keV), dense (electron density ~ 5×10^{24} cm^{-3}) plasmas on OMEGA and to study these plasmas using x-ray spectroscopy. The focus of the work over the last two years has been on studying direct-drive implosions of CH shells filled with deuterium doped with Ar. A total of 11 shots were taken this year, and the results are currently being analyzed.

Determination of Temperatures and Density Gradients in Implosion Cores of OMEGA Targets.
Principal Investigators: R. C. Mancini (University of Nevada, Reno), J. A. Koch (LLNL), and collaborators from Prism Computational Sciences, LLE, LLNL, and Howard University.

The goal of this project is the spectroscopic determination of 1-D temperature and density gradients in implosion cores produced in OMEGA indirect-drive implosion experiments. The method is based on a novel self-consistent analysis of data from simultaneous x-ray line spectra and x-ray monochromatic images. This represents a significant advance on previous efforts of x-ray spectroscopy of implosion cores that relied solely on the analysis of space-integrated spectra to extract spatially averaged temperature and density in the core.

Targets consisted of Ar-doped, D_2-filled plastic shells placed inside Au hohlraums, and the targets were driven by 30 OMEGA UV beams. During FY02, the spectroscopic method

Table 92:VI: List of successful FY03–FY04 NLUF Proposals.

Principal Investigator	Affiliation	Proposal Title
R. P. Drake *et al*.	University of Michigan	Experimental Astrophysics on the OMEGA Laser
B. B. Afeyan	Polymath Research, Inc.	Optical Mixing Controlled Stimulated Scattering Instabilities: Generating Electron Plasma Waves and Ion-Acoustic Waves to Suppress Backscattering Instabilities
R. D. Petrasso and C. K. Li	Massachusetts Institute of Technology	Time Evolution of Capsule ρR and Proton Emission Imaging of Core Structure
C. McKee *et al*.	University of California, Berkeley	OMEGA Laser Studies of the Interaction of Supernova Blast Waves with Interstellar Clouds
R. K. Fisher	General Atomics	High-Spatial-Resolution Neutron Imaging of Inertial Fusion Target Plasmas Using Neutron Bubble Detectors
M. Meyers *et al*.	University of California, San Diego	Dynamic Properties of Shock-Compressed Single Crystals by *in-situ* Dynamic X-Ray Diffraction
H. Baldis *et al.*	University of California, Davis	Studies of Ion-Acoustic Waves (IAW) Under Direct-Drive NIF Conditions
R. Mancini *et al*.	University of Nevada, Reno	Experimental and Modeling Studies of 2-D Core Gradients in OMEGA Implosions
R. Jeanloz	University of California, Berkeley	Recreating Planetary Core Conditions on OMEGA

for core gradient determination was expanded in two ways. First, the original method based on the self-consistent analysis of Ar x-ray line spectra and Ar He$_\beta$ line monochromatic images (i.e., two criteria) was extended to a three-criteria (i.e., more-stringent) method based on the search for plasma gradients that yield the best fits to x-ray line spectra and the Ar He$_\beta$ and Ly$_\beta$ monochromatic emissivities. The spatial distribution of monochromatic emissivities is extracted via an Abel inversion of intensity lineouts from x-ray images. This multi-objective data analysis problem is efficiently solved with a niched Pareto genetic algorithm. The algorithm is general and can be applied to other cases of multi-objective data analysis as well. Second, an alternative technique to analyze the temperature gradient was developed. It is based on the fact that the local ratio (i.e., point-by-point in the plasma source) of Ly$_\beta$ to He$_\beta$ emissivities is a strong function of the temperature with a weak (residual) dependence on the density. As a result, tem-

perature gradients can now be determined by two different techniques and cross-checked for consistency.

The MMI-2 x-ray imager for indirect-drive implosions was successfully fielded and tested. This new instrument uses a target-mounted pinhole array and a flat multilayer-mirror Bragg reflector to record numerous narrowband x-ray images spanning the 3- to 5-keV photon energy range (see Fig. 92.35). The pinhole diameters are 5 μm, and the spatial resolution is 10 μm.

Figure 92.36 shows typical data recorded by MMI-2. Each image spans ≈75 eV along the spectral axis. Groups of images can be combined to produce line-based images. Continuum-based images can also be extracted from the data. As a result, several line- and continuum-based images can now be recorded in the same shot. In particular, the problem of intensity
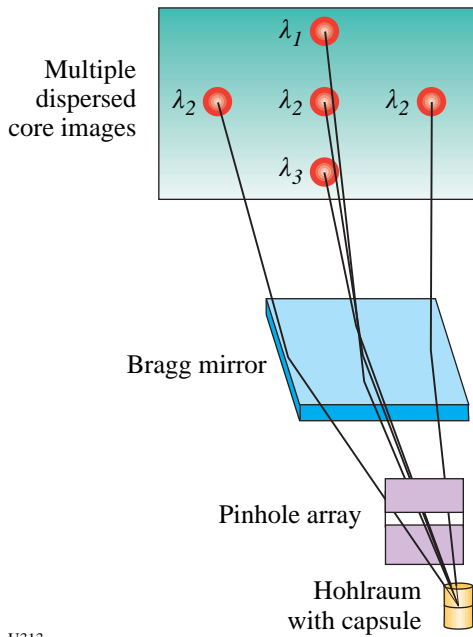
Figure 92.35

Schematic illustrating the concept of the MMI-2 x-ray imager. A target-mounted pinhole array provides numerous high-resolution, high-brightness x-ray images, and in combination with a multilayer Bragg mirror, it produces an array of quasi-monochromatic dispersed core images. This multispectral imaging technique is based on an LLE-developed technique.[1]
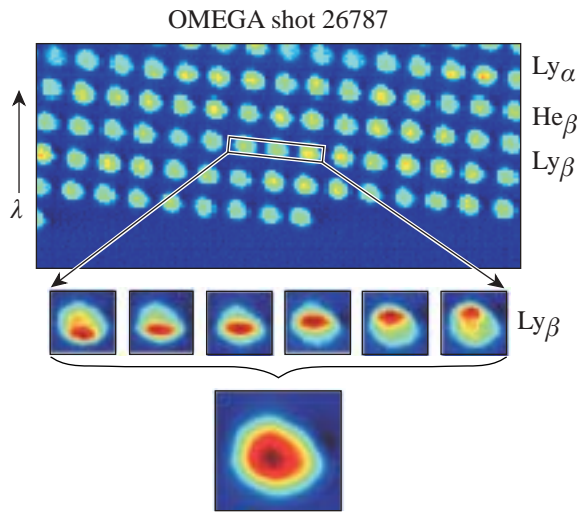
U307

Figure 92.36

An array of implosion-core images recorded with MMI-2 in OMEGA shot 26787. Three Ar line transitions are indicated along the spectral dispersion axis: Ly_α (3.734 Å), He_β (3.369 Å), and Ly_β (3.151 Å). The subgroup of six images shows different portions of each image covered by the Ly_β emission. This subgroup of images is used to produce the Ly_β-based image of the core shown at the bottom of the figure.

and structure of continuum-photon contribution to line-based images can now be addressed with greater accuracy. An interactive data language (IDL)–based code was written to process MMI-2 data, combine subgroups of images, and produce different types of x-ray core images.

Studies of the Fundamental Properties of High-Energy Density Plasmas.
Principal Investigator: R. D. Petrasso (MIT Plasma Science and Fusion Center) and collaborators from MIT, LLE, LLNL, and SUNY Geneseo.

Proper assembly of capsule mass in inertial confinement fusion (ICF) implosions is of fundamental importance for achieving ignition,[2–4] and experimental information about implosion dynamics is crucial both for understanding how assembly occurs and for validating numerical simulations. Without carefully tailored assembly of the fuel, hot-spot ignition planned for the National Ignition Facility (NIF)[2–5] and the Laser Megajoule Facility (LMJ)[6] will fail. Hot-spot ignition relies on shock coalescence to "ignite" the hot spot, followed by burn of the compressed "shell" material (compressive burn). The relationship between these events must be understood to ensure the success of ICF ignition.
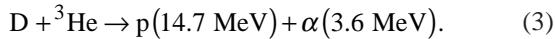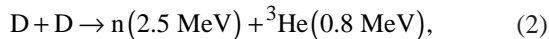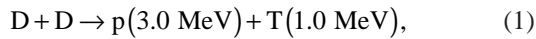
In the last year, the MIT/LLE collaboration, as part of the MIT NLUF program, obtained gated measurements of areal density (ρR) at pivotal moments in the target's evolution: first at shock coalescence and then 400 ps later during compressive burn. These measurements were accomplished through the use of 14.7-MeV protons generated by the fusion of the fuel constituents—deuterium (D) and helium (^{3}He)—in imploding capsules with 24-μm-thick plastic (CH) shells.[7,8] An accurate determination of ρR evolution and asymmetry is made by measuring the proton energy downshift at different times and in many different directions.

Earlier measurements of ρR utilizing primary 14.7-MeV protons[7–9] and secondary protons[10] concentrated on properties and dynamics during compressive burn for implosions of capsules with 20-μm-thick CH shells. These studies included ρR asymmetries,[9–11] fuel–shell mix,[12–15] and the effects of beam smoothing upon fuel ρR.[9,12,16] In addition, x-ray absorption techniques[17] have been used to study aspects of ρR modulations at peak compression and during decompression.

Direct-drive implosions were conducted on OMEGA, with 60 beams of frequency-tripled (351-nm) UV light in a 1-ns square pulse and a total energy of ~21 kJ.[18] Full smoothing of

the laser beams was used,[12] and beam-to-beam energy imbalance was typically ≤5% rms. Two types of hydrodynamically similar capsules were used, all with a nominal diameter of 940 μm and a shell thickness of 24 μm. CH-shell capsules were filled with approximately 6 atm of D_2 and 12 atm of ^{3}He. Capsules with shells of CD (or 1 μm of CD inside of 23 μm of CH) were filled with approximately 20 atm of ^{3}He. The principal diagnostics for this work were high-resolution, charged-particle spectrometers simultaneously viewing each implosion from different directions (the spectrometers and their properties are described in Ref. 8). In addition, the neutron temporal diagnostic (NTD) measured the D fusion burn histories.[19]

The following reactions occur in imploding capsules fueled with D and ^{3}He:

$$D + D \rightarrow p(3.0 \text{ MeV}) + T(1.0 \text{ MeV}), \qquad (1)$$

$$D + D \rightarrow n(2.5 \text{ MeV}) + {}^3\text{He}(0.8 \text{ MeV}), \qquad (2)$$

$$D + {}^3\text{He} \rightarrow p(14.7 \text{ MeV}) + \alpha(3.6 \text{ MeV}). \qquad (3)$$

This analysis uses the high-energy proton of Reaction (3) because it can easily penetrate the larger ρR during compressive burn while, in contrast, the 3.0-MeV protons of Reaction (1) are ranged out. Figure 92.37 shows proton spectra obtained simultaneously at five different viewing angles for shot 24811. In each spectrum, two distinct peaks are clearly evident. The narrow, higher-energy peak is associated with burn of ~40-ps duration at shock coalescence, while the broader, lower-energy peak is associated with the ~150-ps compressive burn that occurs about 400 ps after the shock.[20] For each of the two peaks in each spectrum, the average energy downshift of the 14.7-MeV protons was evaluated and is shown in Fig. 92.38 along with data from several other shots. Through the use of plasma stopping power calculations,[21] these energy downshifts are related to the capsule ρR (Fig. 92.38 and Table 92.VII). The capsule ρR at shock coalescence, which occurs 1.7±0.1 ns after the beginning of the 1-ns laser pulse, is ~13.0±2.5 mg/cm^2. During compressive burn, the average ρR increases to 70±8 mg/cm^2. Since the temperature of the shell is at or below 1 keV at both shock and compression times, and since nearly all energy loss occurs through the shell,[7,10] these ρR determinations are insensitive to exact values of the evolving temperature and density.[21] Table 92.VII summarizes the data of Fig. 92.38, which also show that asymmetries as large as 30 mg/cm^2 in areal density

exist during compressive burn in these implosions. This effect has been reported for capsules with 20-μm-thick shells[9,10] and for cryogenic capsules.[10]

The ion temperature at shock burn can be measured from the spectra. As shown in Fig. 92.39, the shock peak is well fit by a Gaussian. After accounting for the effects of the instrument response,[7,8] a Doppler-derived ion temperature of 6±1 keV is obtained. This temperature is higher than the neutron-derived Doppler-width temperature characterizing the compressive burn, which is about 3 keV. This method of temperature determination from the width of the 14.7-MeV proton spectrum has been previously used for thin-shell, high-temperature implosions.[7] At shock burn (for thick-shell implosions), the shell is relatively "thin," the shock-induced ion temperature is relatively high, and the duration (~40 ps) is sufficiently short that little evolution in ρR occurs. In contrast, the compression
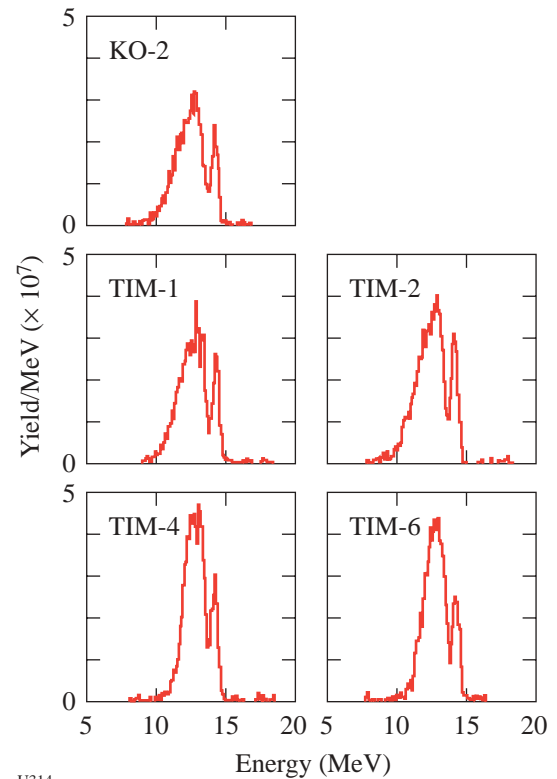

U314

Figure 92.37
Spectra of high-energy protons generated from the fusion of D and ^{3}He in an imploding ICF capsule (shot 24811). The spectrometers viewed the implosion from five different directions; each plot is identified by the OMEGA port used.[8] The narrow high-energy peak is associated with shock-coalescence burn; the broad low-energy peak is associated with compressive burn.
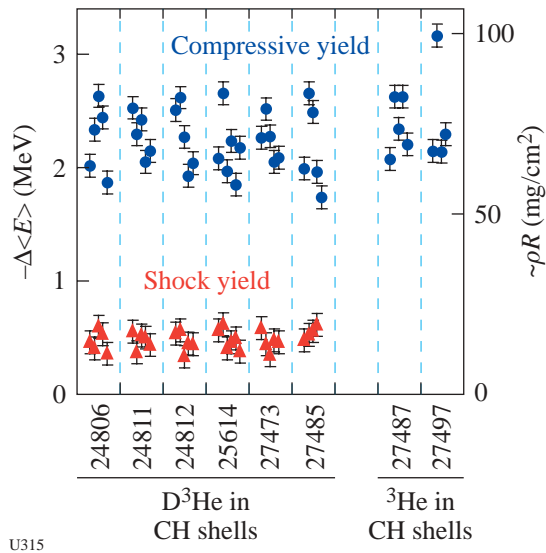
U315
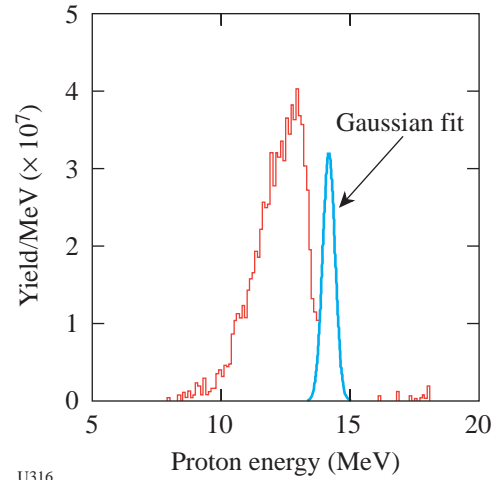
U316

Figure 92.38
The average energy downshifts (from 14.7 MeV) for the shock and compression burn peaks of each spectrum from shot 24811 (as shown in Fig. 92.37) and from several others. From plasma stopping power calculations,[21] values of $\langle\rho R\rangle$ can be associated with the plotted values of ΔE_p, and the right-hand vertical axis scale is meant to show the approximate correspondence (Table 92.VII lists more-exact values for averages over groups of shots).

Figure 92.39
A shock-induced ion temperature can be determined by fitting a Gaussian to the shock peak, correcting for the instrument response, and assuming Doppler broadening. For this spectrum the result is 6.8 keV, and the mean for all spectra from this shot (24811) is 6 keV with a standard deviation of 1 keV.

Table 92.VII: Values of $\langle\rho R\rangle$ inferred from measured D³He proton energy losses (calculated with the slowing-down formalism of Ref. 21, using energies averaged over all available spectra for each shot). For capsules with D³He fuel and CH shells, it was assumed that the slowing was dominated by CH at $T_e \leq 1$ keV and $\rho = 2$ g/cm³ at shock coalescence or 20 g/cm³ at compression burn. For capsules with ³He fuel in CD shells, which produce no shock yield, it was assumed that the slowing was dominated by CD at $T_e \leq 1$ keV and $\rho = 20$ g/cm³. The "±" refers not to measurement uncertainties but to the standard deviation about the mean of individual measurements for each shot.

Shot	Fuel	Shell	$\langle\rho R\rangle_{\text{shock}}$ (mg/cm²)	$\langle\rho R\rangle_{\text{comp}}$ (mg/cm²)
24086	18 atm D³He	24 μm CH	13.2±2.6	70.6±9.7
24811	18 atm D³He	24 μm CH	13.3±2.0	71.6±6.1
24812	18 atm D³He	24 μm CH	13.0±2.5	71.1±9.2
25614	18 atm D³He	24 μm CH	13.7±2.6	67.6±8.7
27473	18 atm D³He	24 μm CH	12.9±2.3	70.1±5.8
27485	18 atm D³He	24 μm CH	15.2±1.6	67.8±12.1
27474	20 atm ³He	24 μm CD	—	79.5±8.3
27479	20 atm ³He	24 μm CD	—	81.5±16.4

burn peak for the protons (as noted previously[7]) is far wider than the Doppler width and, the effects of measured asymmetry[7–9] and geometry[8] notwithstanding, largely reflects ρR evolution over the compressive burn (~150 ps).

To validate the interpretation that the high-energy peak (Fig. 92.37) is due to shock coalescence, and to explore other important aspects of implosion physics, a second series of implosions were performed using a hydrodynamically similar capsule with 20 atm of ^{3}He in a 24-μm-thick CD shell. Spectra from these implosions [see the example in Fig. 92.40(b)] show a single compression peak downshifted in energy by about the same amount as measured in the first series of experiments [see Fig. 92.40(a)]. Notably absent, however, is the shock peak in Fig. 92.40(a) that occurs between 14 and 15 MeV. This means that no D from the shell has mixed into the central, high-temperature region at shock time.[22] Conversely, by the time of compressive burn, mixing of the CD shell with the ^{3}He must have occurred (Fig. 92.40) in order for D^{3}He reactions to be present (see Refs. 12–15 for more discussion of mix).

The spectrum of Fig. 92.40(b) can also be directly interpreted to mean that, at least for these implosions, the shell is not riddled with holes during compressive burn even though low-mode asymmetries exist (Fig. 92.38). If there were holes, there would be a high-energy peak in Fig. 92.40(b). This issue is important since concern exists as to whether shell breakup, as a consequence of Rayleigh–Taylor instability, occurs prior to burn propagation and ignition, thereby quenching ignition.

To improve the understanding of the physical processes and to test the validity of 1-D hydrodynamic simulations in realistic circumstances, we show a comparison of simulated[23] and experimental charged-particle spectra in Fig. 92.41. The basic structure of the experimental data is reproduced reasonably well by the simulation. Of particular relevance is the comparison at shock coalescence since, as experimentally demonstrated, the effects of mix are minimal and 1-D simulations should be at their most accurate because they do not include mix effects. In this context, the ratio of experimental yield to theoretical yield [so called yield-over-clean (YOC)] is about 60%; the predicted ρR is 10 mg/cm^2 while the experimental value is 13 mg/cm^2; the predicted shock temperature is 8 keV, while the measurement is 6±1 keV. It is also noteworthy that the predicted interval between shock and compression burn is 500 ps, while the measured interval is ~400 ps. Since shock timing and coalescence are critical to ignition at the NIF and the LMJ,[2–6] experiments to test the limits of validity of ignition simulation codes should be helpful to this endeavor. In addition, it seems entirely plausible that similar measurements could be made at the NIF at various phases in the development and testing of ignition capsules.
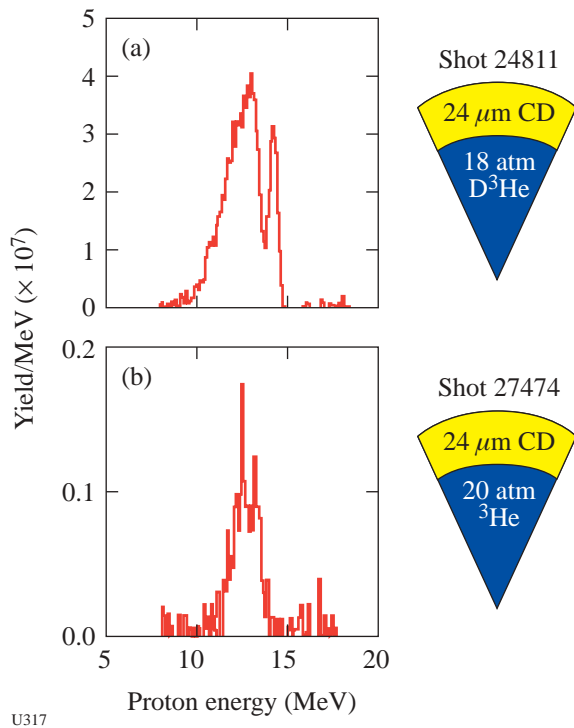

U317

Figure 92.40
The shock-induced burn that is present in plot (a) is absent when the fuel is changed to pure ^{3}He within a CD shell [plot (b)], although the compressive burn is still present because of fuel–shell mix. Besides validating the identification of the shock-induced peak, these data demonstrate the absence of fuel–shell mix in the central regions of the capsule at shock coalescence.
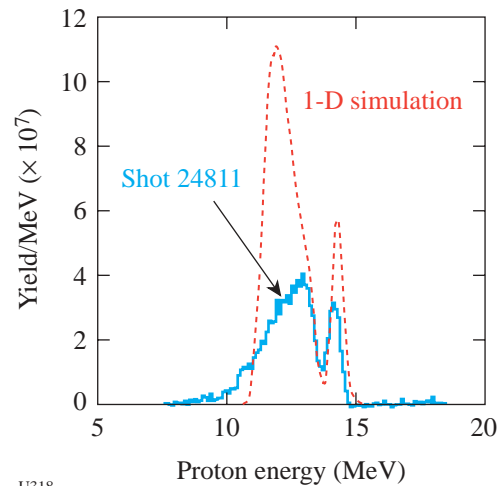

U318

Figure 92.41
A comparison of 1-D simulation to data from shot 24811.

In summary, the first measurements of ρR evolution occurring in ICF implosions were conducted in the course of this past year's work on this program. In the 400-ps interval between shock coalescence and compression burn, the azimuthally averaged ρR changed from 13.0±2.5 to 70±8 mg/cm^2. The experiments demonstrated that fuel–shell mix has not occurred in the central regions of the imploding capsule at shock coalescence, and that the shock-induced temperature is about 6 keV. As mix is inconsequential at this stage of the implosion, these and other measured parameters offer a sensitive test of 1-D shock physics simulations. The experiments further demonstrated that, at least for these types of implosions, gaps and holes do not riddle the shell at compression burn.

Several intriguing avenues exist for advancing these measurements and improving the understanding of implosion dynamics. As ρR is sufficiently small at shock coalescence, 3.0-MeV protons from Reaction (1) will readily penetrate the shell and lead, in principle, to an even more accurate measurement of the shell ρR at that instant. Such experiments, as well as higher-accuracy spectrometers for D^{3}He fusion reactions, are being planned. With more-accurate ρR measurements at shock coalescence, studies will be undertaken to establish whether ρR asymmetries exist at that time, and whether these asymmetries persist and amplify through the compression burn phase,[10,11] thereby accounting for the notable asymmetries that have been measured at that critical stage.

High-Spatial-Resolution Neutron Imaging of Inertial Fusion Target Plasmas Using Bubble Neutron Detectors.
Principal Investigator: R. K. Fisher (General Atomics) and collaborators from LLE, CEA, and LLNL.

Bubble detectors that can detect neutrons with a spatial resolution of 5 to 30 μm are a promising approach to high-resolution imaging of NIF target plasmas. Gel bubble detectors were used in successful proof-of-principle imaging experiments on OMEGA. The results were presented in an invited talk at the October 2001 Meeting of the Division of Plasma Physics of the American Physical Society and published in Physics of Plasmas.[24]

Until recently, bubble detectors appeared to be the only approach capable of achieving neutron images of NIF targets with the desired 5-μm spatial resolution in the target plane. In 2001, however, NIF reduced the required standoff distance from the target, so that diagnostic components can now be placed as close as 10 cm to the target plasma. This will allow neutron imaging with higher magnification and may make it possible to obtain 5-μm-resolution images on the NIF using deuterated scintillators.

Since gel detectors (which consist of ~10-μm-diam drops of bubble detector liquid suspended in an inactive support gel that occupies ~99% of the detector volume) are easy to use, they were chosen for the initial tests on OMEGA. The bubbles could be photographed several hours after the neutron exposure. Imaging NIF target plasmas at neutron yields of 10^{15} will require a higher-detection-efficiency detector. A liquid bubble chamber detector should result in an ~1000-times-higher neutron detection efficiency, which is comparable to that possible using scintillation detectors.

A pressure-cycled liquid bubble detector will require a light-scattering system to record the bubble locations a few microseconds after neutron exposure, when the bubbles have grown to be ~10 μm in diameter. The next major task planned under this grant will be to perform experimental tests to determine how accurately the spatial distribution of the bubble density can be measured under the conditions expected in the NIF. The bubble density will be large enough to produce significant overlap in the two-dimensional images, so we will need to be able to measure bubbles behind bubbles. One of the goals of these tests is to determine if a simple light-transmission approach is feasible. One of the concerns at very high bubble densities is that light scattered out of the path can be rescattered back into the transmitted light path by bubbles in neighboring paths.

Examination of the "Cone-in-Shell" Target Compression Concept for Asymmetric Fast Ignition.[*]
Principal Investigators: R. B. Stephens (General Atomics) and collaborators from LLNL and the Institute of Laser Engineering (ILE), Osaka University, Osaka, Japan.

Investigation of the compression hydrodynamics of fast-ignition targets continued in FY02 with several shots taken on "cone-in-shell" indirect-drive targets. The results from these experiments showed that while the hydrodynamic codes used to design these targets captured the gross dynamics well, there were details of the experiment that were not predicted by the code calculations.

_____

The separation of compression and ignition in the fast-ignition (FI) concept[25] requires a new approach to target design. The strict symmetry and smoothness requirements of a target compressed to generate and enclose an ignition spark by dense, cold fuel are replaced by a much more complex set of considerations. The fusion burn is optimized by creation of a uniformly dense fuel mass. The symmetry of that mass is relatively unimportant, but its surface must be pure DT and accessible to an ignition beam. The ignition energy must be delivered by a short-pulse laser, but the compression drive can be accomplished by any means—laser (direct and indirect drive), heavy ion beam, or *z*-pinch.

S. Hatchett (LLNL) designed an indirect-drive target based on the cone-in-shell FI target concept[26] [Fig. 92.42(a)]: A hollow cone is inserted in the side of the shell to provide a protected line of sight to the assembled fuel mass. Modeling suggests that the presence of the cone substantially changes the target's implosion dynamics [Fig. 92.42(b)]; surprisingly, one should achieve the most-compact target with a deliberately asymmetric drive [Fig. 92.42(c)]. The modeling might not properly capture details of the flow as the shell slides down along the cone surface; there is a concern that high-*Z* material from the cone might mix into the assembled fuel mass, thereby hindering ignition. This model was tested on a scale-1 hohlraum at OMEGA. Each collapse was radiographed with an x-ray framing camera, which took a sequence of 16 x-radiographs (Fig. 92.43). With this information it was possible to determine the implosion velocity and diameter, density, and symmetry at stagnation. X-ray images were taken alternately through different filters to identify any gold contamination in the assembled fuel. The experimental radiographs were very similar to the simulations; apparently the effect of the inserted cone was well described by *LASNEX* modeling, and both the shell and the drive were smooth enough that compression instabilities had minimal effect. As predicted, it was found that an asymmetric drive does seem to result in a more-compact target, but that that configuration also generates a gas flow that blows out the tip of the cone just about at the stagnation point. There were subtle differences between simulation and experiment.
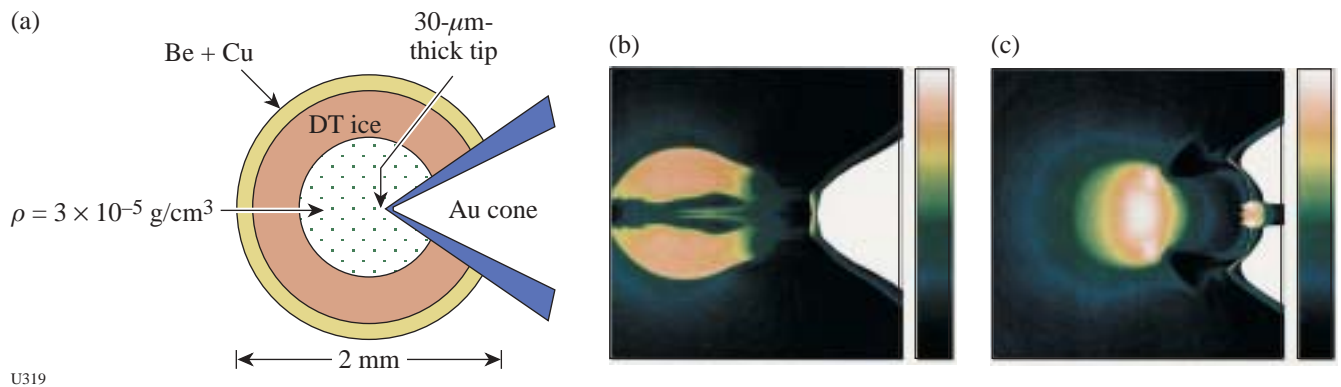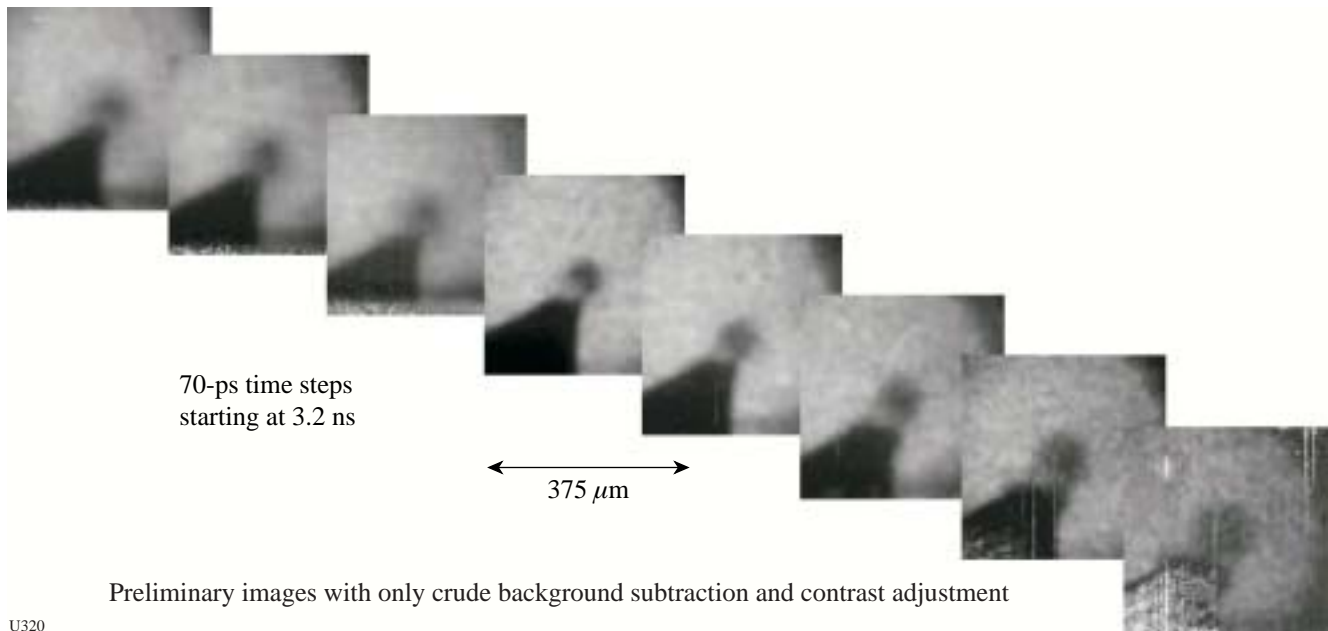

Figure 92.42
(a) Cross section of a FI cryo target designed to implode to $\rho R \sim 2$ g/cm^2 when driven by a 190-eV hohlraum; (b) density cross section of target at stagnation when driven symmetrically; and (c) density cross section when drive is 10% hotter on the side away from the cone.

70-ps time steps
starting at 3.2 ns

← 375 μm →

Preliminary images with only crude background subtraction and contrast adjustment

U320

Figure 92.43
Eight of a series of 16 x-radiographs taken during a test of the cone-in-shell target design on OMEGA. The frames are 70 ps apart.

Supernova Hydrodynamics on the OMEGA Laser.
Principal Investigators: R. Paul Drake (University of Michigan), B. Remington (Center for Laser Astrophysics–ILSA, LLNL), and collaborators from LLNL, CEA Saclary (France), LLE, LANL, University of Arizona, University of Colorado, University of Chicago, SUNY Stony Brook, Naval Research Laboratory, and Eastern Michigan University.

The fundamental motivation for this work is that supernovae are not well understood. Recent observations have clarified the depth of this ignorance by producing observed phenomena that current theory and computer simulations cannot reproduce. Such theories and simulations involve, however, a number of physical mechanisms that have never been studied in isolation. During FY02 experiments were performed under this NLUF Program in compressible hydrodynamics and radiation hydrodynamics, relevant to supernovae and supernova remnants. These experiments produce phenomena in the laboratory that are believed, based on simulations, to be important to astrophysics but that have not been directly observed in either the laboratory or an astrophysical system. The experiments were focused on the scaling of an astrophysically relevant, radiative-precursor shock, preparations for studies of collapsing radiative shocks, and the multimode behavior and onset of turbulence in three-dimensional, deeply nonlinear evolution of the Rayleigh–Taylor (RT) instability at a decelerating, embedded interface. These experiments required strong compression and decompression, strong shocks (Mach ~10 or greater), flexible geometries, and very smooth laser beams, which means that the 60-beam OMEGA laser is the only facility capable of carrying out this program.

The experiments benefited from a strong collaborative effort that coupled a core experimental team to theoretical groups at several institutions. This enabled the development of experimental designs through advance simulations and the comparison of the results of the experiments to simulations by more than one code. A standardized approach to the experiments was also developed, enabling the pursuit of more than one experiment simultaneously, and thus the exploitation of the extensive theoretical capabilities of this collaboration. These experiments are sufficiently complex yet diagnosable, so they are excellent for verification and validation (V&V) of complex computer codes, including those produced by the Advanced Scientific Computing Initiative (ASCI) Alliance Center at the University of Chicago. This program is also a

critical stepping stone toward the use of the National Ignition Facility (NIF) both for fundamental astrophysics and as a critical component of ASCI V&V.

The supernova hydrodynamics experiments conducted in FY02 included the following:

a. Radiative Precursor Shocks: The scaling of radiative precursor shocks was investigated. These experiments involved the initial acceleration of a block of material to high velocity. The block of material then drove a shock wave through low-density foam at approximately 100 km/s, which was fast enough to produce a radiative precursor. The precursor is strongly sensitive to the shock velocity, so it was possible to control it by varying the laser energy. Figure 92.44 shows a photograph of a target used for experiments on OMEGA. Up to ten laser beams struck the front surface of this target, delivering several kJ of energy to an 800-μm-diam spot in a 1-ns pulse. The laser irradiation shocked and accelerated a 60-μm-thick plastic layer that crossed a 160-μm vacuum gap to impact the low-density foam, usually of density 0.01 g/cm^3.
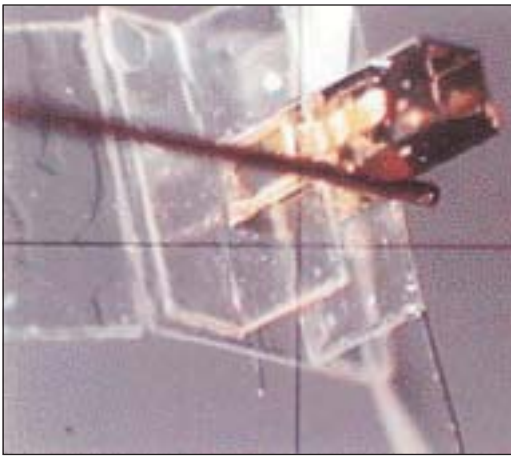

U321

Figure 92.44

An image of the target for the radiative precursor experiments. The laser beams approach from the left, driving a shock wave through the foam contained in the rectangular structure.

The structure of the precursor was investigated using absorption spectroscopy. Additional laser beams irradiated a thulium backlighter plate, permitting an imaging crystal spectrometer to obtain absorption spectra like those shown in Fig. 92.45. Absorption lines were detected from up to six different ionization states. The lines from higher ionization states appear at higher temperatures. From the entire spectrum, one could determine the location of the shock, the temperature of the shocked material, and the temperature profile in the radiative precursor, with the help of the OPAL[27] atomic code. It was observed that the precursor became longer as the laser drive energy increased, and that its behavior was consistent with a simple model of the threshold velocity for the production of a precursor. A paper based on these data was recently published in Physical Review Letters.[28] These experiments are now entering an analysis and writing phase. In addition, it is anticipated that such experiments will provide quality benchmark cases for astrophysical modeling. Participants in such comparisons will include the University of Maryland and the ASCI Flash Center at the University of Chicago.
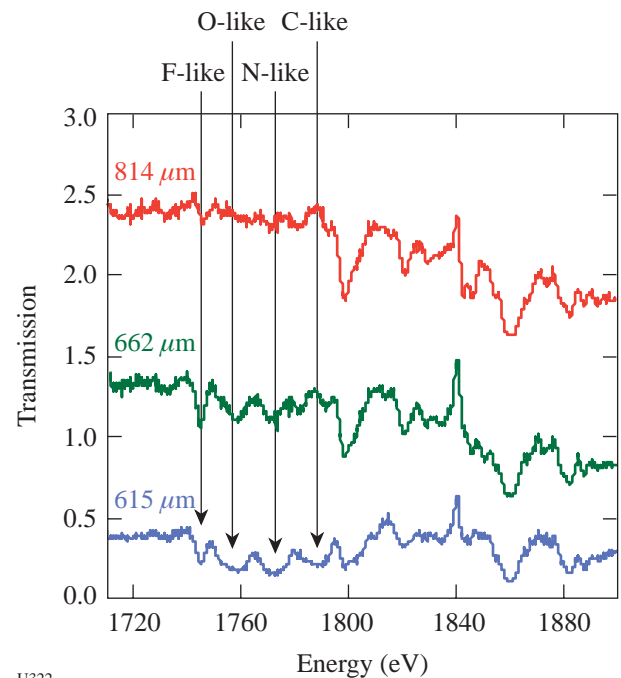
U322

Figure 92.45

Absorption spectra at three locations, showing the spatial development of four of the absorption lines. The spectra are offset vertically for clarity.

b. Radiative Shocks: Astrophysical shocks, when they become cool enough, enter a radiatively collapsing phase in which their density can increase several orders of magnitude. All supernova remnants eventually pass through this phase, and such shocks arise in a number of other contexts. This team's work with radiative-precursor shocks in foams represented a first step into radiative hydrodynamics. With the adoption of gas targets, however, shocks can be produced on OMEGA that

radiatively collapse. Several OMEGA shots were devoted to a preliminary attempt at such an experiment during FY02. They used only radiography as a diagnostic. Figure 92.46 shows the data that were obtained on the first attmpt. The overlaid profile shows the average of a 290-μm-high horizontal strip through the unobstructed portion of the image. One can clearly see the absorption feature due to the shock. Its position confirms that the shock velocity is well above 100 km/s. The laser and diagnostic settings were optimized for other experiments on this day, causing significant motional blurring (and weakening the absorption feature). Much better data can and will be obtained in future experiments. Such experiments will occupy approximately half of the target shots planned for the next year under this NLUF program.

U323

Figure 92.47
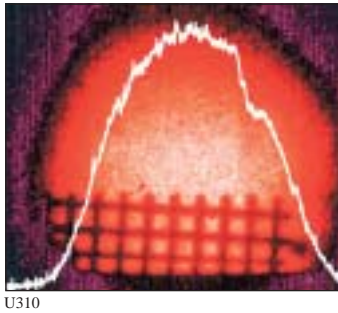Structures developed at 26 ns from a two-mode perturbation.

U310

Figure 92.46
Image and profile from a first attempt to produce a collapsing radiative shock. The notch in the profile toward the right is produced by the shocked gas.

U324

Figure 92.48
Structures developed at 26 ns from an eight-mode perturbation.

c. Multimode Rayleigh–Taylor (RT) Instability at a Decelerating, Embedded Interface: It is fruitful to examine multimode systems because (a) the actual stellar explosions involve many modes and (b) the growth of multimode structures is a more-severe test of simulations. During FY02 data were obtained that showed the time evolution of the structures produced from initial conditions including one mode, two modes, and eight modes. The perturbations were designed to keep the global peak-to-valley amplitude constant at 5 μm as the number of modes changed. Figure 92.47 shows some data that were obtained using a two-mode perturbation, and Fig. 92.48 shows some data for an eight-mode perturbation. At earlier times, the multimode data show articulated spikes. Later, as in these figures, they show the emergence of large-scale features. Additional data are needed and will be obtained soon. The emergence of the large-scale features will be compared with theories of bubble merger. The effect of the number of modes on the width of the "mix region" will also be examined.
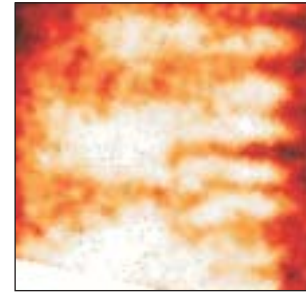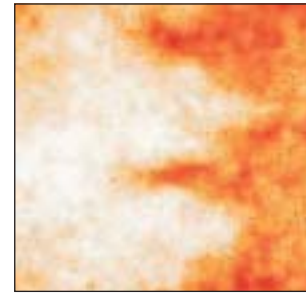
d. Onset of Turbulence in RT Instability at a Decelerating, Embedded Interface: Based on a scaling analysis, it is believed that it will be possible to observe the transition to a turbulent state in the evolution of RT that develops from a 3-D initial condition. Figure 92.49 shows a radiograph of the structures produced from an initial 3-D perturbation that included a single mode with 71-μm wavelength and noise at much shorter wavelengths introduced when the (50-mg/cc) foam was machined. By this time, the unstable fingers have developed significant modal structure and have moved forward and overtaken the shock. Earlier, the fingers have a simpler spectral structure and remain well behind the shock. Later, the ability to distinguish the fingers is lost perhaps due to rapid diffusion caused by turbulence. Continuations of these experiments will determine whether, in fact, the onset of turbulence is being observed, and further analysis will evaluate the implications for astrophysics. Several publications based on this work have appeared in print during the last year.[29–31] One additional manuscript has been submitted for publication.[32]
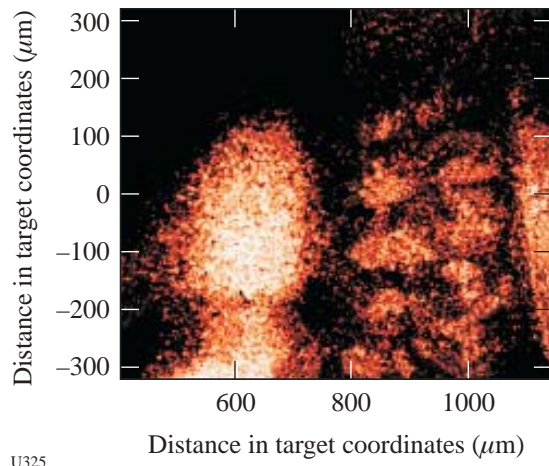
Figure 92.49
An experiment with a 3-D initial single-mode perturbation produced these structures 17 ns into the experiment.

Studies of the Dynamic Properties of Shock-Compressed FCC Crystals by In-Situ *Dynamic X-Ray Diffraction.*
Principal Investigators: H. Baldis (University of California at Davis), D. Kalantar (LLNL), and collaborators from LLNL, LLE, the University of California at San Diego, University of Oxford, and LANL.

This experiment uses time-resolved dynamic x-ray diffraction to investigate the response of a lattice under shock compression. Over the last two years this work included studies of shocked single-crystal Si with peak pressures ranging from <100 kbar to 200 kbar, experiments on single-crystal Cu[32] to study the dislocation density in the post-shocked material (these studies included recovery of shocked samples) at pressures ranging from 100 to 600 kbar, and investigations of deformation substructure in Cu.

Major accomplishments during the reporting period include the following:

- Implementation of multi-target shots. In several series of shots during this year, diffraction targets, VISAR wave profile targets, and shock-recovery targets were simultaneously fielded on shots. This approach greatly increases the effectiveness of target shots providing triple the data per shot than would have been available if the three experiments were individually shot.[33]

- A pressure scan for Si was completed to record multiple lattice planes.
- The wave profile of shocked Si was recorded.
- The shock breakout from 200 mm Cu was used to determine the timing for future diffraction measurements.
- Shocked crystals were recovered and examined.

In recent experiments a multiple film plane (MFP) diagnostic has been implemented that allows the observation of x-ray diffraction from a wide range of lattice planes (Fig. 92.50). The MFP has been used to record diffraction from Si shocked at a range of pressures as seen in Fig. 92.51. Figure 92.52 illustrates the analysis of such images showing a multi-wave structure that depends on intensity. A maximum of 6% compression is observed for the range of pressures attained on Nova and OMEGA in x-ray and direct-drive modes.

A two-phase approach has been adopted to analyze these data. First, the line pattern of known crystal configurations is predicted; then the diffracted lines are fit to the prediction to determine the lattice spacing and unit normal vector. An IDL code is used to calculate the expected diffraction pattern for a given crystal lattice.

Optical Mixing of Controlled Stimulated Scattering Instabilities (OMC SSI) on OMEGA.
Principal Investigator: Bedros Afeyan (Polymath Research Inc.) and collaborators from LLNL, LANL, and LLE

The goal of this experiment is to examine suppression of backscattering instabilities by the externally controlled generation of ion-acoustic-wave or electron-plasma-wave turbulence. The experiments in general consist of using optical mixing techniques to generate resonant ion-acoustic waves (IAW) in flowing plasmas created by the explosion of foils irradiated by the OMEGA laser. During this year the interaction scaling with probe intensity was examined.

The transmission of the probe beam and the Raman reflectivity of the pump beam were measured systematically for a large number of probe beam energies. The scaling of the Raman suppression with probe beam energy was examined, and transmission enhancement at low energies that saturates at high energies was observed (see Fig. 92.53). The energy transfer at high probe energies is significant, and the SRS suppression in the wavelength or plasma density window that corresponds to Mach-1 flow is suppressed significantly, upwards of factors of 8.

U326
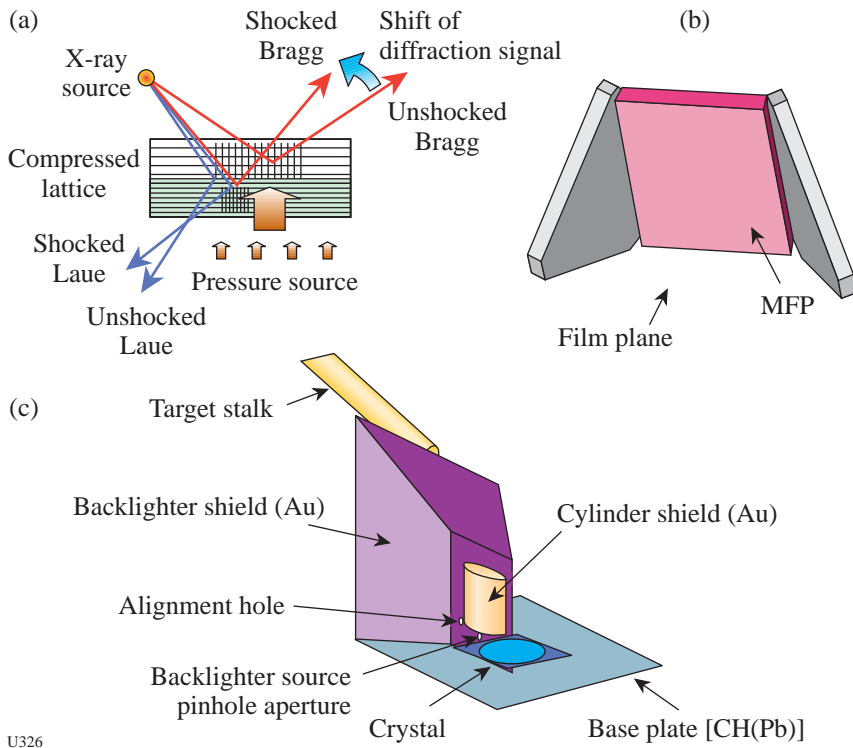
Figure 92.50

(a) Illustration of the concept of dynamic x-ray diffraction in probing response of crystals to laser-driven shocks; (b) schematic showing the MFP diagnostic; and (c) illustration of typical experimental configuration used on the x-ray diffraction experiments.
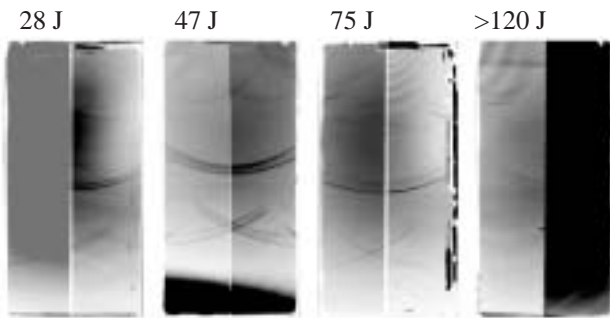
U327

Figure 92.51

Images of a diffracted signal from different lattice planes taken from a shocked-Si experiment on OMEGA at different laser-drive energies.
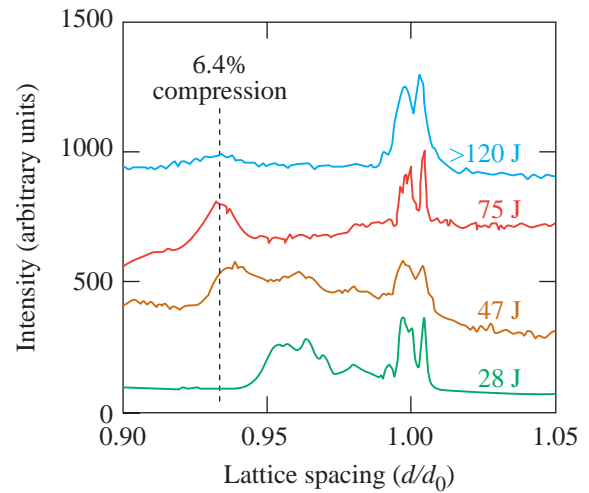
U346

Figure 92.52

Lineout from x-ray diffraction data of Si for various energies showing a maximum lattice compression of ~6.4%.
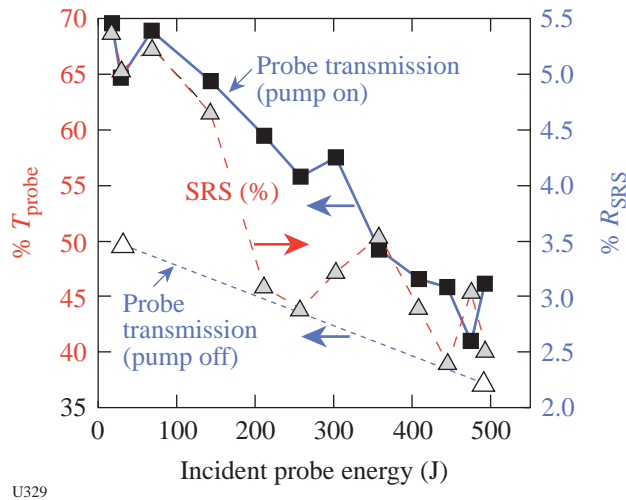
Figure 92.53

Measured transmission of the probe beam and the Raman reflectivity of the pump beam as a function of probe beam energy. Note that with the pump beam off, the transmission of the probe beam is less than 50%, even at moderately low energies, and decreases with energy down to less than 40% at a probe beam energy of ~490 J. The reflectivity of the pump beam falls with increasing probe energy. The energy transfer at high probe energies is significant, and the SRS suppression in the wavelength or plasma density window that corresponds to Mach-1 flow is suppressed significantly, upward of factors of 8.

### FY02 LLNL OMEGA Experimental Program

The LLNL program on OMEGA in FY02 totaled 406 target shots for target ignition physics, high-energy-density science, and NWET (Nuclear Weapons Effects Testing). This represents a 30% increase over the target shots taken by LLNL on OMEGA in FY01. Highlights of these experiments include the following:

Laser–Plasma Interactions: Beam-energy-transfer experiments were continued during FY02 to investigate beam-energy transfer[34] for a variety of NIF target/beam configurations in order to select the optimum configuration to minimize the potential deleterious effects of this process on NIF targets.

To expand the LPI (laser–plasma interaction) database on OMEGA, one of the OMEGA beamlines was modified to allow it to generate second-harmonic radiation for LPI experiments.

Cocktail Hohlraums: Experiments continued to investigate the potential of "cocktail" hohlraum materials to increase the soft x-ray emission and energy coupling to capsule in NIF targets. During FY02, detailed atomic physics model predic-

tions were verified on OMEGA experiments by observing enhanced cocktail re-emission at 450 eV (see Fig. 92.54).
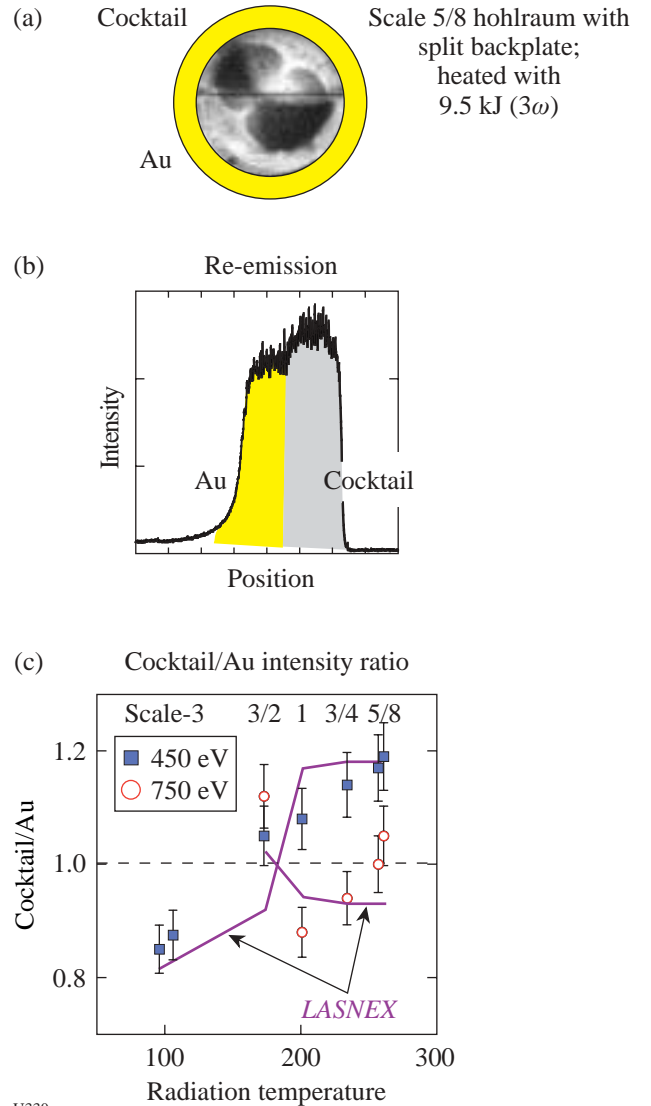
Figure 92.54

During FY02 cocktail hohlraum experiments were conducted on OMEGA that in conjunction with *LASNEX* code simulations indicate that cocktail materials may be advantageous compared to Au for the NIF hohlraums. (a) Cocktail geometry; (b) experimental data from cocktail hohlraum experiment comparing Au and "cocktail" re-emission; (c) cocktail-to-Au intensity ratio at 450 eV (squares) and 750 eV (circles) plotted as a function of radiation temperature from the OMEGA experiments compared to the *LASNEX* predictions.

X-Ray Thomson Scattering: X-ray Thomson scattering can access the density/temperature parameter space that is characteristic of the Fermi degenerate to warm dense matter regime (see Fig. 92.55). OMEGA experiments have demonstrated for the first time spectrally resolved x-ray Thomson scattering

data[35] (Fig. 92.56). These experiments are important because they indicate that x-ray Thomson scattering may work for ICF implosions. Future experiments are planned to investigate superdense matter using this technique.
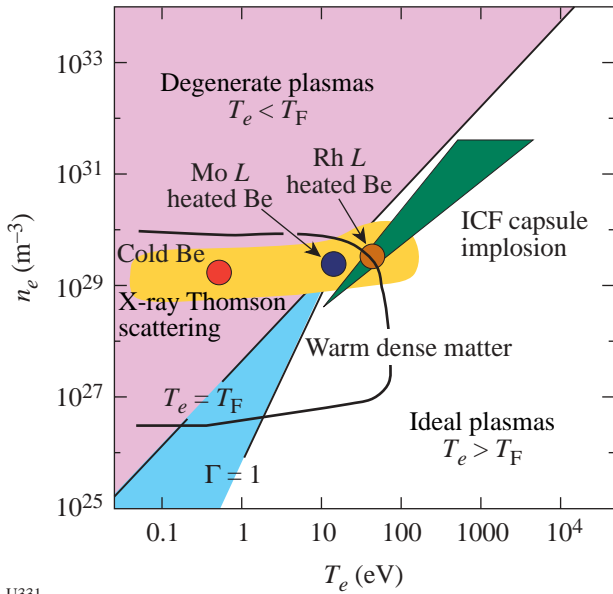
Figure 92.55
The density and temperature space of interest to the study of dense matter showing the relevance of x-ray Thomson scattering as a diagnostic in this regime. The solid points correspond to the measurements made on the OMEGA experiments using Rh and Mo L-shell emission as a source of x-rays to conduct x-ray Thomson scattering measurements on cold and heated Be plasmas.

U331
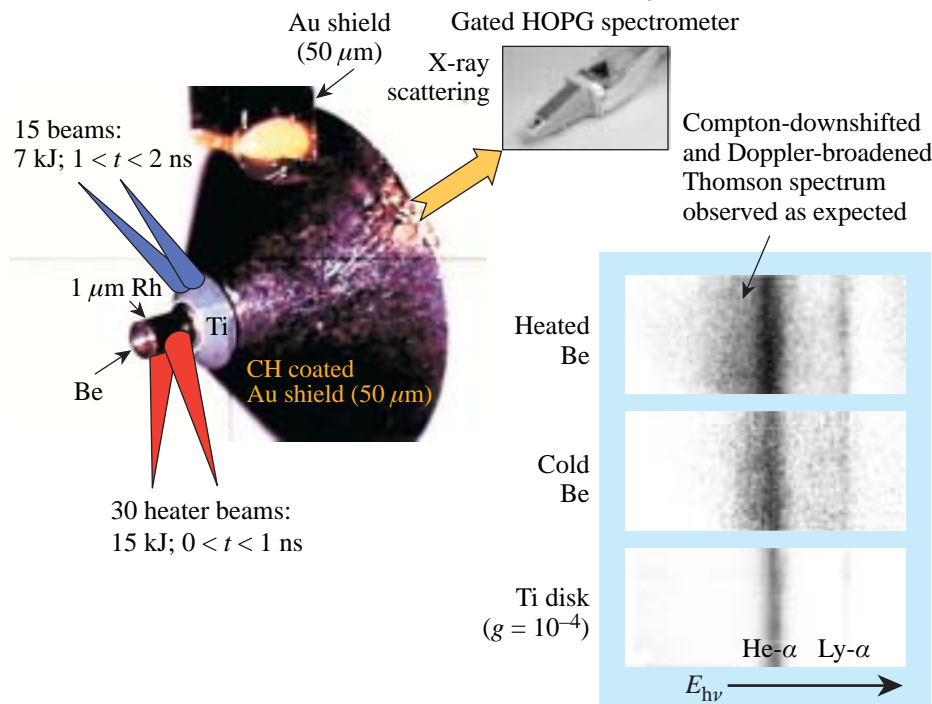
Figure 92.56
Illustration of the x-ray Thomson scattering experiment on OMEGA. Thirty OMEGA beams are used as heater beams to heat a Be plasma. A separate x-ray source is used to probe the hot plasma and produces the scattered Ti-disk spectrum irradiated with up to 15 beams (at the right).

U332

Albedo Experiments: A series of experiments were initiated in FY02 on OMEGA to measure the absolute albedo of a secondary hohlraum as shown in Fig. 92.57. Three detectors are used in this measurement: DANTE, a PCD in H11, and a PCD in P11. DANTE is the primary diagnostic, while the P11 PCD monitors the effect of the secondary hohlraum and the H11 PCD serves as backup for the DANTE measurement. Initial measurements confirmed that the secondary hohlraum has no significant effect on the primary's radiation temperature. In measurements comparing the albedo of Au and U, the Au albedo was observed to be smaller than that of U.

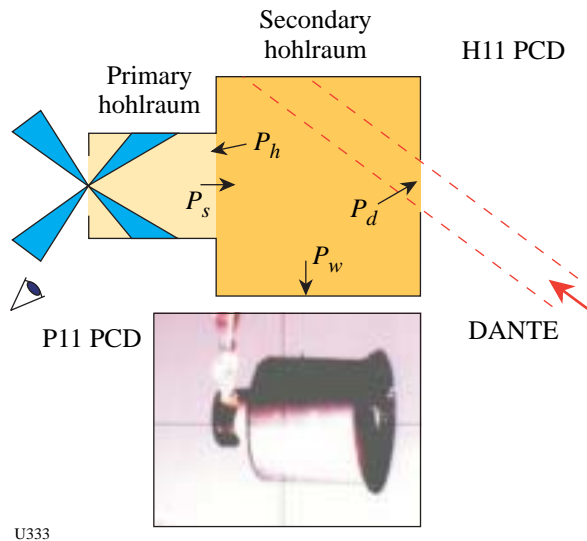and intensity of hot electrons. Scale-1/2 and -1/4 hohlraums were driven in a half-hohlraum configuration, and radiation temperatures of ~350 eV were demonstrated.

Gas-Filled Radiation Sources: Experiments continued under an NWET program to develop high-efficiency x-ray sources for the NIF. During FY02 the experiments were designed to explore x-ray emission in the >10-keV region. Typical targets included Kr-filled CH cans (1.2 mm long, 1.5 mm in diameter). Figure 92.58 shows time-framed x-ray images from two experiments with 0.5-atm- and 1.5-atm-Kr-filled cans. X-ray emission is observed from the full extent of the can (1.2-mm × 1.5-mm diameter) and beyond the duration of the 1-ns laser pulse in both cases.

Figure 92.57
Schematic of the "Albedo" experiment. A half-hohlraum is irradiated by a set of OMEGA beams and provides radiation that heats a secondary hohlraum attached to its back. DANTE is the primary diagnostic viewing the wall of the secondary hohlraum; the H11 PCD is a backup for DANTE. The P11 PCD monitors the primary hohlraum to determine the effect of the secondary on its radiation temperature.

Figure 92.58
X-ray framing camera images from shot 25819 (0.5 atm Kr) and 25818 (1.5 atm Kr) show the pressure dependence in the evolution of >10-keV x-ray emission. The times are referenced to the start of the ~1-ns-long laser pulse.

Hot Hohlraum: A series of experiments are underway on OMEGA to produce high-radiation-temperature hohlraums by reducing the scale size of the hohlraums. Hot hohlraums are needed for NIF opacity experiments, but their physics regime is not well understood. Scaled experiments at OMEGA are used to compare experimental results to theoretical models. The laser coupling to the hohlraum was determined as a function of scale size by measuring x-ray drive, backscatter,

Dynamic Hohlraums: A series of experiments dubbed "dynamic hohlraums" were carried out on OMEGA in direct-drive mode. These experiments were designed to image a radiatively collapsed shock. The configuration is shown schematically in Fig. 92.59. A gas-filled CH shell is irradiated directly by 40 OMEGA beams. To achieve as uniform a drive as possible with only 40 polar beams, the polar-beam energies are lowered in comparison to the rest of the beams. Typical data from these implosions are shown in Fig. 92.60.

Eight beams for framing camera (TIM 5) hit a backlighting target mounted on a stalk.

CH shell
OD 920 μm
ID 880 μm

Ten beams for streak camera (target mounted on TIM 3)

Gas fill

Capsule
(40-beam drive)

Streak camera imaging slit (SSC in TIM 6)

Fill was either
1 atm Xe or
0.75 atm Xe
+ 25 atm D_2.

U335
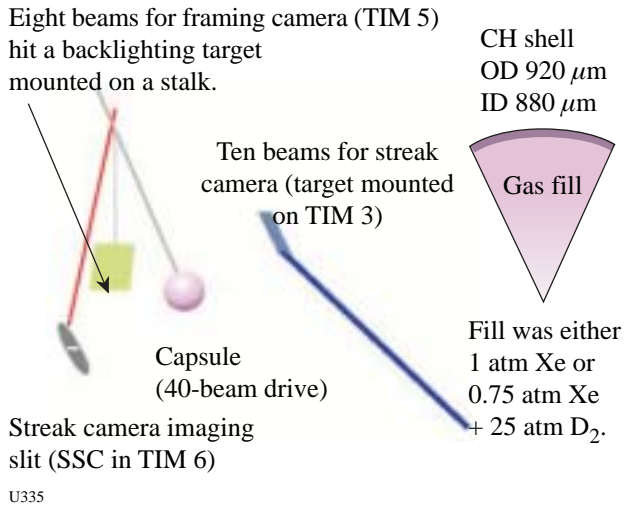
Figure 92.59
Schematic illustration of the "dynamic hohlraum" direct-drive implosion experiment designed to image a radiatively collapsed shock.

27530 (all Xe)   27529 (Xe + D_2)   27527 (all Xe) framing camera

1.64 ns   1.7 ns

2.3

Time

1.0

0.0

2.0 ns

U336
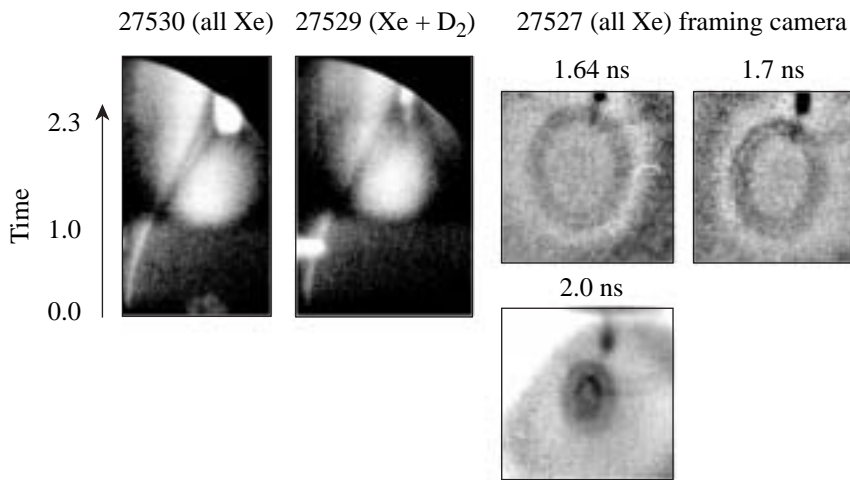
Figure 92.60
Streaked (left) and gated (right) x-ray images of x-ray-backlit implosions of Xe- and Xe/D_2-filled CH shells. The separation between the plastic shell and the collapsed shock is discernable in shots with Xe fill but not on shots with partial D_2 fills

Nonideal Implosions: The nonideal implosion (NIBI) experiment is designed to study highly distorted implosions. This experiment, carried out on OMEGA in FY02, used the direct-drive configuration shown in Fig. 92.61.

Experiments were carried out with symmetrical capsules as well as machined capsules with a 50° radiographic tracer "cap" as shown in Fig. 92.62.

Double-Shell Implosion Experiments: The effect of Au M-band asymmetry on the implosion of double-shell capsules is being investigated on OMEGA. The motivation for this work is that 80% of the radiation reaching the inner shell in a double-shell configuration is 2 to 4 keV Au "M-band" radiation. Simulations indicate that the inner glass shell will suffer an ~25% distortion from an ~10% P2 M-band asymmetry at a convergence of ~60%. To ameliorate this problem, an elongated hohlraum configuration is being explored.
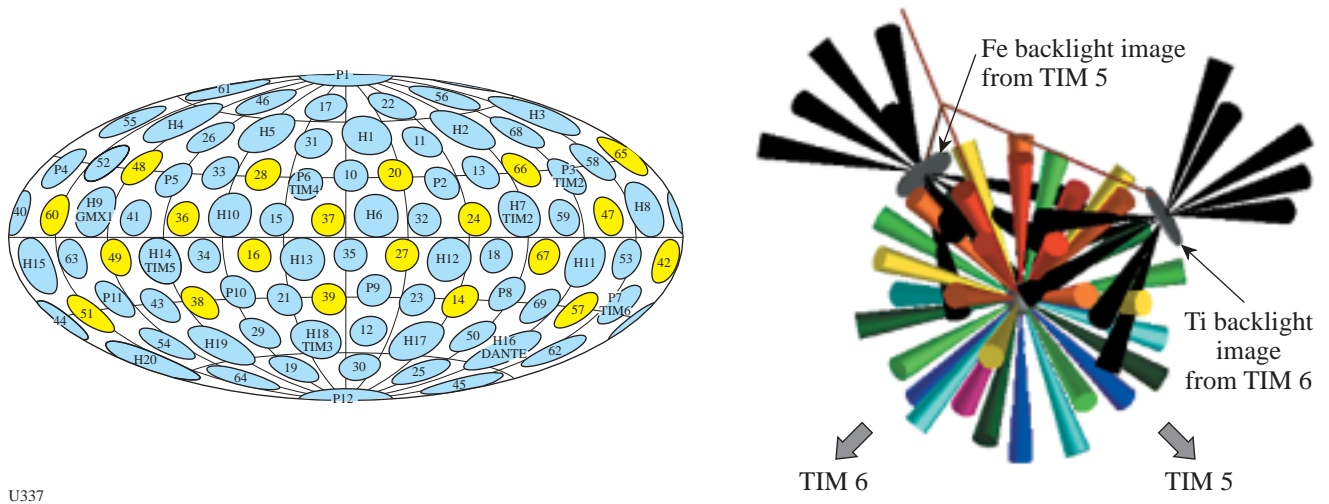
Figure 92.61
System configuration for the OMEGA NIBI experiment. Forty OMEGA beams are used to drive the implosion while twenty beams are used to produce two separate backlighting views. The forty drive beams can be adjusted to produce various asymmetric drive configurations. The beams indicated in yellow on the left are used for the two backlighting views.
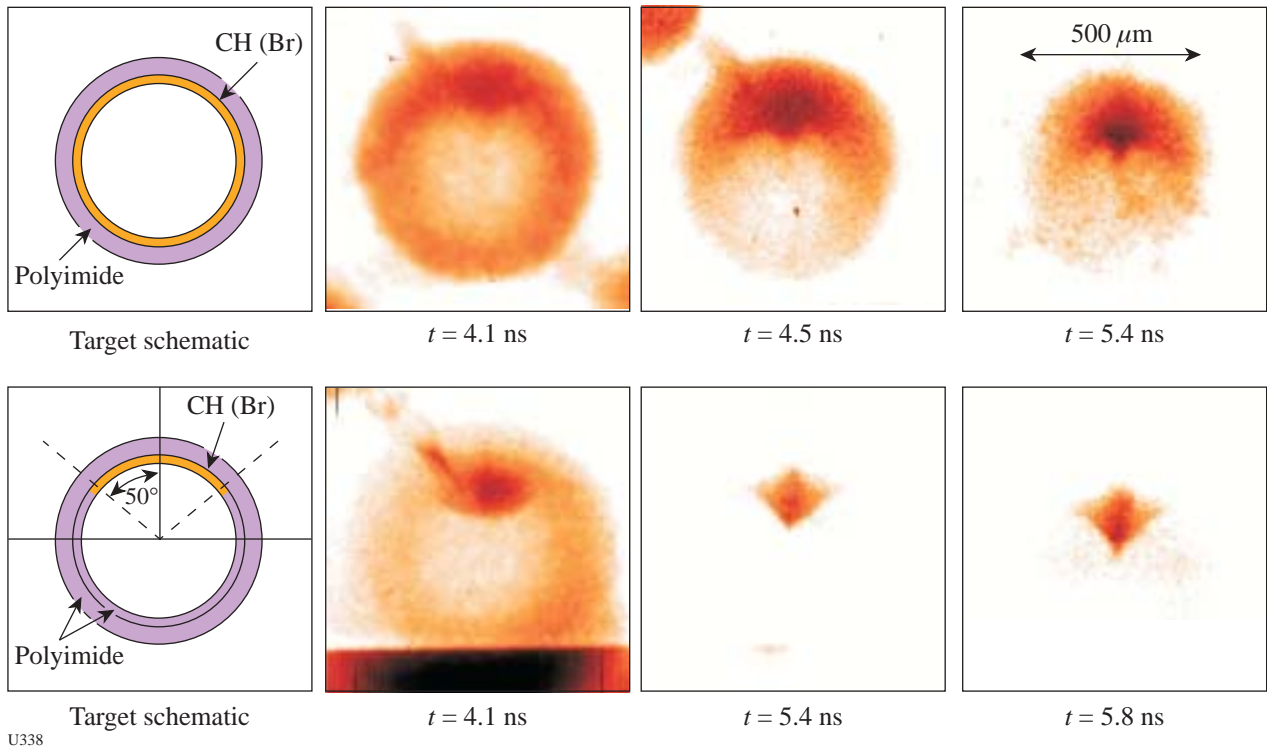
Figure 92.62
Target schematics (left top and bottom) for some of the NIBI implosion targets. The time-gated x-ray-backlit images on the right show the evolution of the core asymmetry when the targets are driven with a strong $\ell = 1$ mode (higher energy on the top pole).

Charged-Particle Spectrometry in Indirect-Drive Implosions: To assess the effectiveness of charged-particle spectrometry on the NIF, a collaborative experiment involving LLNL, MIT PSFC, and LLE was implemented on OMEGA in FY02. During the experiment D^3He-filled shells were imploded in a conventional hohlraum configuration. Wedged-range-filter (WRF) spectrometers were used to measure the yield, spectrum, and spatial distribution of primary D^3He protons. Initial results from these shots indicate that capsule areal density can be measured with this configuration. When viewed through a diagnostic hole in the hohlraum, the proton slowing down indicated a capsule $\rho R \sim 42 \pm 9$ mg/cm^2 compared to a predicted areal density of ~49 mg/cm^2. No large asymmetries in proton emission were observed. It was concluded that charged-particle spectrometry can be an important diagnostic technique for indirect-drive targets. Improvements in the diagnostic were suggested by the results of these experiments to optimize the technique for indirect-drive experiments.

IDrive: Work continued on OMEGA in FY02 to implement the IDrive technique as a high-pressure drive technique for materials studies. One of the goals of this program is to measure the material strength of solid aluminum (6061) at peak pressures of ~300 kbar. The experiments include soft recovery of accelerated foils in order to provide the opportunity for microscopic analysis of the highly strained regions of the materials.

FY02 LANL OMEGA Experimental Program

The LANL program on OMEGA in FY02 continued experiments in support of stockpile stewardship (ACE), cylindrical mix (CYLMIX), and double-shell implosion campaigns and began the asymmetric direct-drive sphere (ADDS) campaign. LANL continued NIF phase-2 diagnostic development and also collaborated with a large national group on the hydrodynamic jet experiment. LANL also provided shock-breakout measurements for the Sandia National Laboratory (SNL) ablator characterization campaign. Each of these experimental campaigns has been documented in pre- and post-shot reports. Highlights of these experiments include the following:

ACE Experiments: The ACE experiments successfully obtained data in support of the Stockpile Stewardship Program. This year a new backlighter configuration was developed that provides views of the experiment at two different times, thus increasing the efficiency of the experiments. In collaboration with AWE, a fluorescence-based spectro-meter was fielded to measure temperatures in radiation-driven experiments.

Asymmetric Direct-Drive Spheres: The goal of the asymmetric direct-drive spheres (ADDS) campaign is to elucidate the effect of mix on imploding capsules. The experiment uses directly driven DT-filled capsules. The energies of each laser beam are adjusted so that the capsule sees a positive or negative drive asymmetry as measured by the second Legendre mode. Theoretical calculations predict a difference in neutron yield and core shape, depending on the sign and magnitude of the asymmetry. The primary diagnostics of mix are neutron yield, imaging of the emitted neutrons, and x-ray imaging (in collaboration with LLE).

Figure 92.63 presents the first simultaneous neutron and x-ray images of asymmetric implosions. The predicted shapes and neutron yields agree with the measurements in direction and magnitude.

CYLMIX: The Richtmyer–Meshkov instability occurs whenever a strong shock passes through an interface between two materials. The CYLMIX experiments study this instability under unique convergent, compressible, miscible plasma conditions in the presence of a strong (Mach number greater than 5) shock. To produce a strong shock, small plastic cylinders (Fig. 92.64) are directly driven by the OMEGA laser.[36] The implosion trajectory has been carefully mapped and simulations tuned to match the measurements, as in Fig. 92.65.

As the cylinders implode, the marker band mixes into the surrounding material and the mix width is measured. This year, extensive measurements spanning several nanoseconds were made of the dependence of the mix width on the initial surface roughness of the marker layer as a function of time. Comparisons with simulations to validate hydrodynamic models have been made.

Hydrodynamic Jet Experiment: LANL also participated in a large collaboration that includes researchers from LLNL, AWE, LLE, U. Michigan, and NRL to simulate jets in supernova explosions.[37] Astrophysical codes will be validated by comparison to OMEGA experimental data. The experiments are presently optimizing the target and diagnostics while design work linking 2-D *LASNEX* calculations to the radiation-hydrodynamic code *RAGE* is underway. Exploratory experiments were conducted this year.

NIF Diagnostics: Development continued on Phase 2 fusion product diagnostics for the NIF. A second Gas–Cerenkov gamma-ray burn-history diagnostic, with increased time reso-
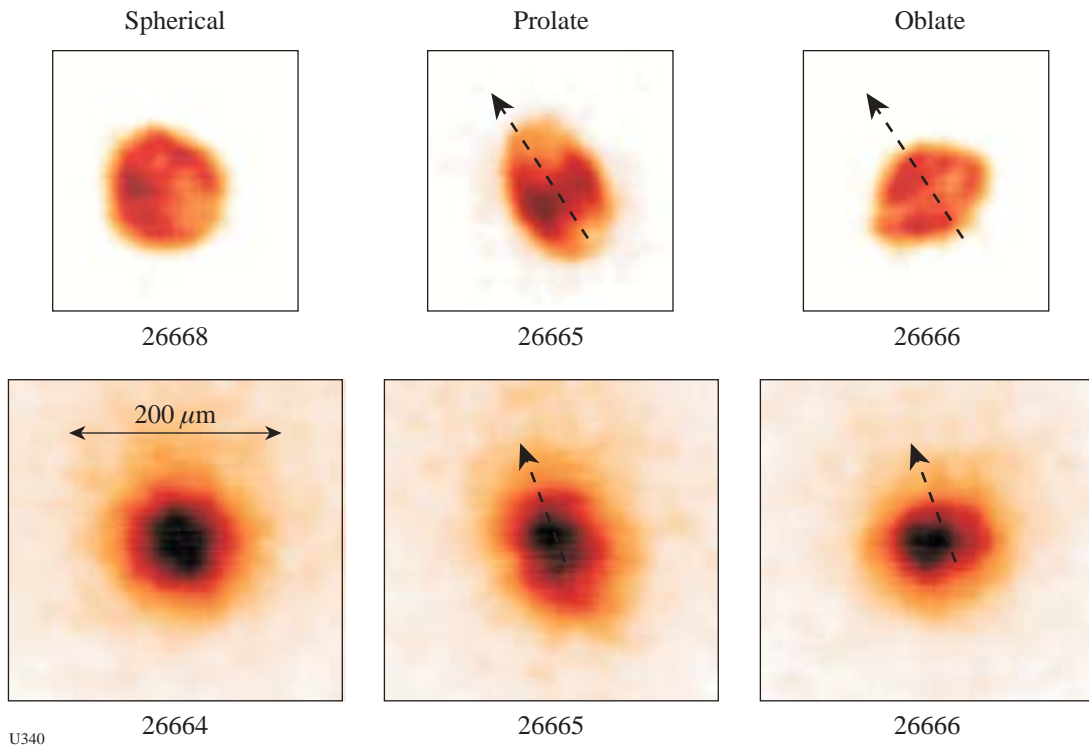
Figure 92.63
X-ray (top) and neutron (bottom) images for three different degrees of asymmetric drive. The x-ray images are from the GMXI diagnostic, and the 14.1-MeV neutron images were obtained in a LANL/CEA/LLE collaboration. All images are as seen by the diagnostic. The arrows indicate the perturbation axis.
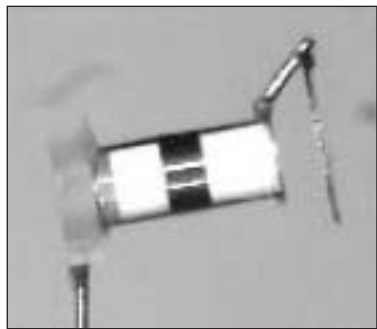
Figure 92.64
A view of a typical CYLMIX target from the side showing the backlighter disk on the right, the Al marker band in the middle, the foam inside the cylinder (white areas), and the viewing aperture on the left. The primary diagnostic is an x-ray framing camera with a line of sight down the axis of the cylinder.
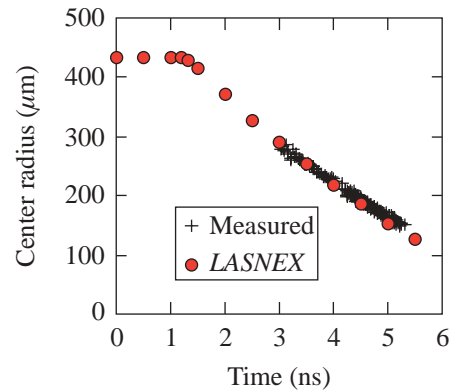
Figure 92.65
Measured radius versus time plot demonstrating good modeling of the experiment.

lution, was built and fielded in conjunction with LLNL. Development continued on the neutron imaging system (NIS), which was a primary diagnostic for the ADDS experiment, as illustrated in Fig. 92.63. The NIS is fielded in collaboration with CEA and LLE.

FY02 SNL OMEGA Programs

SNL carried out a total of 24 target shots on the OMEGA laser in FY02 and also participated in several of the campaigns led by other laboratories. The SNL-led campaigns included the following:

Indirect-Drive Ablator Shock Coalescence: The achievement of indirect-drive ignition of a NIF capsule requires capsule shock timing precision of ~150 ps. The first attempts at time-resolved measurement of the coalescence of two shocks (at pressures of ~10 and 50 Mbar, respectively) in a Be + 0.9% Cu wedge ablator were made in a collaborative effort involving SNL and LANL. The principal diagnostic was the LANL Streaked Optical Pyrometer (SOP).[38] The hohlraum drive for this experiment consisted of a 2-ns square pulse in six beams followed by a 1-ns square pulse in nine beams delayed by 1 ns. As shown in Fig. 92.66, shock coalescence occurred within about 300 ps of the pre-shot calculation.

Indirect-Drive Ablator Shock Velocity at 50 Mbar: The achievement of indirect-drive ignition of a NIF capsule requires capsule ablation pressures in the range of 1 to 100 Mbars. In FY02 SNL/LANL experiments on OMEGA extended the shock velocity data for Be + 0.9% Cu ablator samples to the 50-Mbar level[39] (Fig. 92.67). Shock velocities in the ablator were measured with Be + 0.9% Cu step samples. Al step witness plates were also used to confirm the shock pressure levels generated in the Be + 0.9% Cu ablator samples.

Indirect-Drive Ablator X-Ray Burnthrough Measurements: To achieve indirect-drive ignition of a NIF capsule, ablator burnthrough timing must be predicted to within a few percent. In FY02 SNL/LLNL experiments on OMEGA extended the x-ray burnthrough[39] data for polyimide and Be + 0.9% Cu ablators into the range of 190- to 200-eV hohlraum temperatures. As shown in Fig. 92.68, the experimental technique provides simultaneous measurements of ablator x-ray burnthough and x-ray re-emission (in the interior of the hohlraum). As shown in the figure, experimental arrangements involving multiple sample regions were also tested in the FY02 experiments.
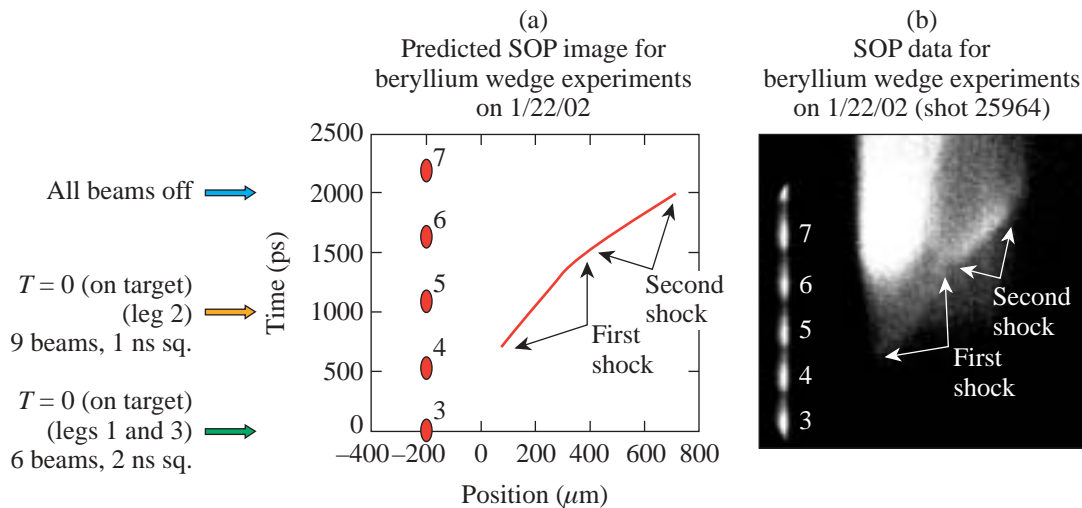
Figure 92.66
Predicted (a) and actual (b) shock coalesence as measured with SOP.
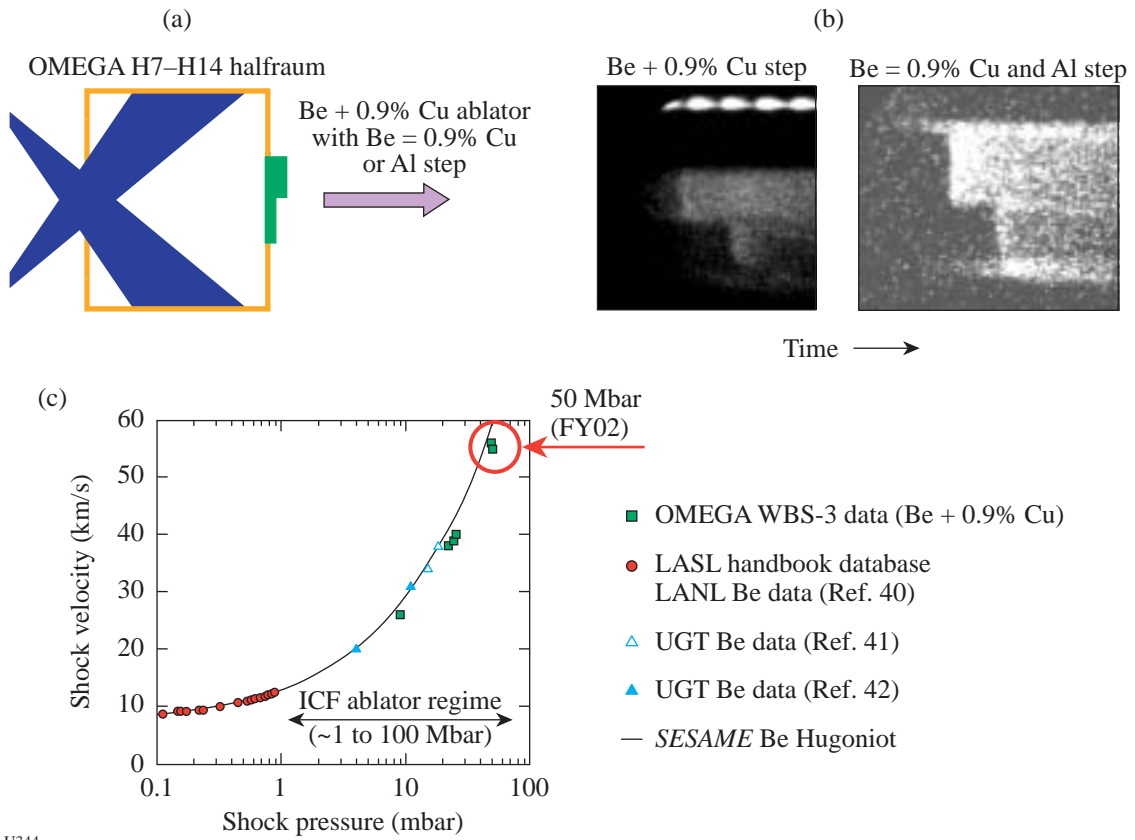
Figure 92.67

(a) Schematic illustrating the setup of a shock velocity measurement experiment. A step target is mounted on the back of a half-hohlraum that is irradiated by a subset of OMEGA beams. (b) Experimental data from two shock velocity measurement experiments. (c) Plot of shock velocity versus shock pressure from the OMEGA experiments compared to data from other sources in the ICF-ablator–relevant regime of interest.
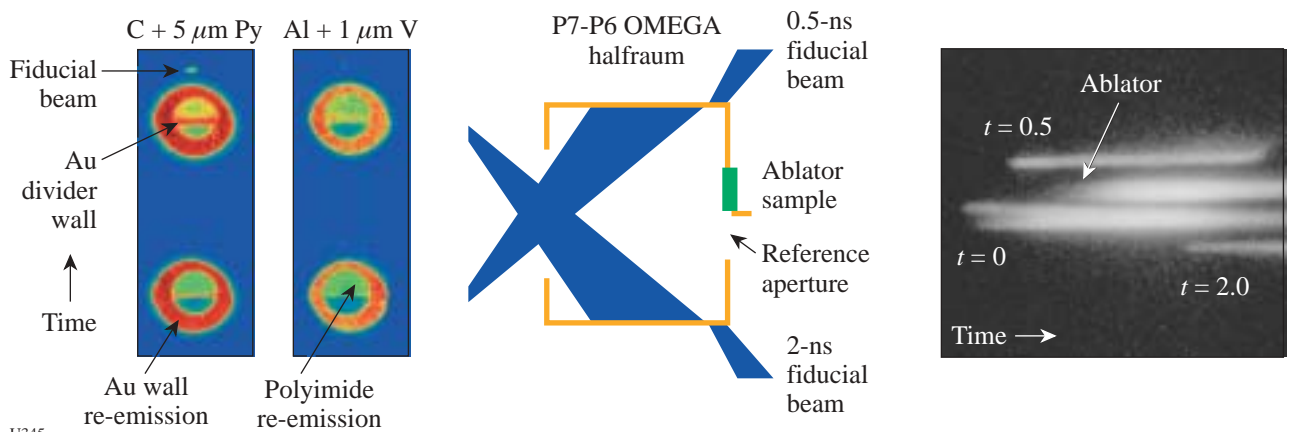
Figure 92.68

Schematic illustrating the ablator burnthrough measurement technique used on the SNL experiments on OMEGA.

Time and Spatially Resolved Measurements of X-Ray Burnthrough and Re-emission in Au and Au:Dy:Nd Foils: A mixture containing two or more high-Z elements can result in a material with a higher Rosseland mean opacity than either of the constituents. Computational simulations of the x-ray re-emission properties of such "cocktail" materials indicate that wall losses in a National Ignition Facility (NIF) ignition-scale hohlraum could be reduced by a significant amount (when compared to walls made of pure Au).[43] In a recent set of experiments on OMEGA a collaborative team including SNL, LLNL, and GA used x-ray framing and streak cameras to simultaneously measure the x-ray burnthrough and re-emission of pure Au and Au:Dy:Nd cocktail samples exposed to a hohlraum radiation temperature of ~160 eV. Although the burnthrough measurements indicate the cocktail has a higher Rosseland mean opacity than pure Au, the measured x-ray re-emission fluxes from the two materials were approximately equivalent.

CEA

CEA had four half-day dedicated shot opportunities on OMEGA during FY02. A total of 19 target shots were provided for experiments including tests of the LMJ three-ring symmetry and other aspects of indirect-drive targets. In addition, CEA participated in collaborative experiments on imaging the neutron core emission using the CEA-provided neutron-imaging system (NIS).[44]

REFERENCES

1. B. Yaakobi, F. J. Marshall, and D. K. Bradley, Appl. Opt. **37**, 8074 (1998).

2. S. W. Haan *et al.*, Phys. Plasmas **2**, 2480 (1995).

3. J. D. Lindl, R. L. McCrory, and E. M. Campbell, Phys. Today **45**, 32 (1992).

4. *Energy and Technology Review*, Lawrence Livermore National Laboratory, Livermore, CA, UCRL-52000-94-12, 1 (1994).

5. M. D. Rosen, Phys. Plasmas **3**, 1803 (1996).

6. M. Andre, M. Novaro, and D. Schirmann, Chocs **13**, 73 (1995); J. Maddox, Nature **372**, 127 (1994).

7. C. K. Li, D. G. Hicks, F. H. Séguin, J. A. Frenje, R. D. Petrasso, J. M. Soures, P. B. Radha, V. Yu. Glebov, C. Stoeckl, D. R. Harding, J. P. Knauer, R. L. Kremens, F. J. Marshall, D. D. Meyerhofer, S. Skupsky, S. Roberts, C. Sorce, T. C. Sangster, T. W. Phillips, M. D. Cable, and R. J. Leeper, Phys. Plasmas **7**, 2578 (2000).

8. F. H. Séguin, J. A. Frenje, C. K. Li, D. G. Hicks, S. Kurebayashi, J. R. Rygg, B.-E. Schwartz, R. D. Petrasso, S. Roberts, J. M. Soures, D. D. Meyerhofer, T. C. Sangster, C. Sorce, V. Yu. Glebov, C. Stoeckl, T. W. Phillips, R. J. Leeper, K. Fletcher, and S. Padalino, "Spectrometry of Charged Particles from Inertial-Confinement-Fusion Plasmas," to be published in the Review of Scientific Instruments.

9. F. H. Séguin, C. K. Li, D. G. Hicks, J. A. Frenje, K. M. Green, R. D. Petrasso, J. M. Soures, D. D. Meyerhofer, V. Yu. Glebov, C. Stoeckl, P. B. Radha, S. Roberts, C. Sorce, T. C. Sangster, M. D. Cable, S. Padalino, and K. Fletcher, Phys. Plasmas **9**, 2725 (2002).

10. F. H. Séguin, C. K. Li, J. A. Frenje, S. Kurebayashi, R. D. Petrasso, F. J. Marshall, D. D. Meyerhofer, J. M. Soures, T. C. Sangster, C. Stoeckl, J. A. Delettrez, P. B. Radha, V. A. Smalyuk, and S. Roberts, Phys. Plasmas **9**, 3558 (2002).

11. R. D. Petrasso, C. K. Li, M. D. Cable, S. M. Pollaine, S. W. Haan, T. P. Bernat, J. D. Kilkenny, S. Cremer, J. P. Knauer, C. P. Verdon, and R. L. Kremens, Phys. Rev. Lett. **77**, 2718 (1996).

12. D. D. Meyerhofer, J. A. Delettrez, R. Epstein, V. Yu. Glebov, V. N. Goncharov, R. L. Keck, R. L. McCrory, P. W. McKenty, F. J. Marshall, P. B. Radha, S. P. Regan, S. Roberts, W. Seka, S. Skupsky, V. A. Smalyuk, C. Sorce, C. Stoeckl, J. M. Soures, R. P. J. Town, B. Yaakobi, J. D. Zuegel, J. Frenje, C. K. Li, R. D. Petrasso, D. G. Hicks, F. H. Séguin, K. Fletcher, S. Padalino, M. R. Freeman, N. Izumi, R. Lerche, T. W. Phillips, and T. C. Sangster, Phys. Plasmas **8**, 2251 (2001).

13. D. D. Meyerhofer, J. A. Delettrez, R. Epstein, V. Yu. Glebov, V. N. Goncharov, R. L. Keck, R. L. McCrory, P. W. McKenty, F. J. Marshall, P. B. Radha, S. P. Regan, S. Roberts, W. Seka, S. Skupsky, V. A. Smalyuk, C. Sorce, C. Stoeckl, J. M. Soures, R. P. J. Town, B. Yaakobi, J. Frenje, C. K. Li, R. D. Petrasso, F. H. Séguin, K. Fletcher, S. Padalino, C. Freeman, N. Izumi, R. A. Lerche, T. W. Phillips, and T. C. Sangster, Plasma Phys. Control. Fusion **43**, A277 (2001).

14. P. B. Radha, J. Delettrez, R. Epstein, V. Yu. Glebov, R. Keck, R. L. McCrory, P. McKenty, D. D. Meyerhofer, F. Marshall, S. P. Regan, S. Roberts, T. C. Sangster, W. Seka, S. Skupsky, V. Smalyuk, C. Sorce, C. Stoeckl, J. Soures, R. P. J. Town, B. Yaakobi, J. Frenje, C. K. Li, R. Petrasso, F. Séguin, K. Fletcher, S. Padalino, C. Freeman, N. Izumi, R. Lerche, and T. W. Phillips, Phys. Plasmas **9**, 2208 (2002).

15. C. K. Li, F. H. Séguin, J. A. Frenje, S. Kurebayashi, R. D. Petrasso, D. D. Meyerhofer, J. M. Soures, J. A. Delettrez, V. Yu. Glebov, P. B. Radha, F. J. Marshall, S. P. Regan, S. Roberts, T. C. Sangster, and C. Stoeckl, Phys. Rev. Lett. **89**, 165002 (2002).

16. C. K. Li, F. H. Séguin, D. G. Hicks, J. A. Frenje, K. M. Green, S. Kurebayashi, R. D. Petrasso, D. D. Meyerhofer, J. M. Soures, V. Yu. Glebov, R. L. Keck, P. B. Radha, S. Roberts, W. Seka, S. Skupsky, C. Stoeckl, and T. C. Sangster, Phys. Plasmas **8**, 4902 (2001).

17. V. A. Smalyuk, V. N. Goncharov, J. A. Delettrez, F. J. Marshall, D. D. Meyerhofer, S. P. Regan, and B. Yaakobi, Phys. Rev. Lett. **87**, 155002 (2001).

18. T. R. Boehly, D. L. Brown, R. S. Craxton, R. L. Keck, J. P. Knauer, J. H. Kelly, T. J. Kessler, S. A. Kumpan, S. J. Loucks, S. A. Letzring, F. J. Marshall, R. L. McCrory, S. F. B. Morse, W. Seka, J. M. Soures, and C. P. Verdon, Opt. Commun. **133**, 495 (1997).

19. R. A. Lerche, D. W. Phillion, and G. L. Tietbohl, Rev. Sci. Instrum. **66**, 933 (1995).

20. R. D. Petrasso, C. K. Li, F. H. Séguin, J. A. Frenje, S. Kurebayashi, P. B. Radha, D. D. Meyerhofer, J. M. Soures, J. A. Delettrez, C. Stoeckl, S. Roberts, V. Yu. Glebov, W. Seka, C. Chiritescu, and T. C. Sangster, Bull. Am. Phys. Soc. **46**, 105 (2001).

21. C. K. Li and R. D. Petrasso, Phys. Rev. Lett. **70**, 3059 (1993).

22. From other D^3He implosion experiments for which the signals are similar in amplitude to those of Fig. 92.38(b), the presence of the shock yield is clearly visible, so the absence of the shock yield in Fig. 92.38(b) is not due to lack of instrument sensitivity.

23. E. Goldman, Laboratory for Laser Energetics Report No. 16, University of Rochester (1973).

24. R. K. Fisher, R. B. Stephens, L. Disdier, J. L. Bourgade, A. Rouyer, P. A. Jaanimagi, T. C. Sangster, R. A. Lerche, and N. Izumi, Phys. Plasmas **9**, 2182 (2002).

25. M. Tabak *et al.*, Phys. Plasmas **1**, 1626 (1994).

26. P. A. Norreys *et al.*, Phys. Plasmas **7**, 3721 (2000).

27. C. A. Iglesias and F. J. Rogers, Astrophys. J. **464**, 943 (1996); F. J. Rogers, F. J. Swenson, and C. A. Iglesias, Astrophys. J. **456**, 902 (1996).

28. P. A. Keiter, R. P. Drake, T. S. Perry, H. F. Robey, B. A. Remington, C. A. Iglesias, R. J. Wallace, and J. Knauer, Phys. Rev. Lett. **89**, 165003 (2002).

29. R. P. Drake and P. A. Keiter, Phys. Plasmas **9**, 382 (2002).

30. R. P. Drake, H. F. Robey, O. A. Hurricane, H. Zhang, B. A. Remington, J. Knauer, J. Glimm, D. Arnett, J. O. Kane, K. S. Budil, and J. Grove, Astrophys. J. **564**, 896 (2002).

31. C. Calder *et al.*, Astrophys. J. Suppl. Ser. **143**, 201 (2002).

32. H. F. Robey *et al.*, "The Onset of Turbulence in High Reynolds Number, Accelerated Flows. Part II. Experiment," submitted to Physics of Fluids.

33. M. A. Meyers *et al.*, in *Shock Compression of Condensed Matter, AIP Conference Proceedings 620* (American Institute of Physics, New York, 2001), pp. 619–622; D. H. Kalantar *et al.*, in *Shock Compression of Condensed Matter, AIP Conference Proceedings 620* (American Institute of Physics, New York, 2001), pp. 615–618.

34. R. K. Kirkwood, J. D. Moody, A. B. Langdon, B. I. Cohen, E. A. Williams, M. R. Dorr, J. A. Hittinger, R. Berger, P. E. Young, L. J. Suter, L. Divol, S. H. Glenzer, O. L. Landen, and W. Seka, Phys. Rev. Lett. **89**, 215003 (2002).

35. S. H. Glenzer *et al.*, Bull. Am. Phys. Soc. **47**, 63 (2002); G. Gregori *et al.*, *ibid.*

36. C. W. Barnes, S. H. Batha, A. M. Dunne, G. R. Magelssen, S. Rothman, R. D. Day, N. E. Elliott, D. A. Haynes, R. L. Holmes, J. M. Scott, D. L. Tubbs, D. L. Youngs, T. R. Boehly, and P. A. Jaanimagi, Phys. Plasmas **9**, 4431 (2002).

37. J. M. Foster *et al.*, Phys. Plasmas **9**, 2251 (2002).

38. J. A. Oertel *et al.*, Rev. Sci. Instrum. **70**, 803 (1999).

39. R. E. Olson *et al.*, Bull. Am. Phys. Soc. **47**, 329 (2002).

40. S. P. Marsh, ed. *LASL Shock Hugoniot Data*, Los Alamos Series on Dynamic Material Properties (University of California Press, Berkeley, CA, 1980).

41. C. E. Ragan III, Phys. Rev. A **25**, 3360 (1982).

42. W. J. Nellis *et al.*, J. Appl. Phys. **82**, 2225 (1997).

43. L. Suter *et al.*, Phys. Plasmas **7**, 2092 (2000).

44. L. Disdier *et al.*, Nucl. Instrum. Methods Phys. Res. A **489**, 496 (2002).

Publications and Conference Presentations

Publications

S. R. Arrasmith, S. D. Jacobs, J. C. Lambropoulos, A. Maltsev, D. Golini, and W. I. Kordonski, "The Use of Magnetorheological Finishing (MRF) to Relieve Residual Stress and Subsurface Damage on Lapped Semiconductor Silicon Wafers," in *Optical Manufacturing and Testing IV*, edited by H. P. Stahl (SPIE, Bellingham, WA, 2001), Vol. 4451, pp. 286–294.

R. Betti, K. Anderson, V. N. Goncharov, R. L. McCrory, D. D. Meyerhofer, S. Skupsky, and R. P. J. Town, "Deceleration Phase of Inertial Confinement Fusion Implosions," Phys. Plasmas **9**, 2277 (2002).

R. Betti, M. Umansky, V. Lobatchev, V. N. Goncharov, and R. L. McCrory, "Hot-Spot Dynamics and Deceleration-Phase Rayleigh–Taylor Instability of Imploding Inertial Confinement Fusion Capsules," Phys. Plasmas **8**, 5257 (2001).

T. R. Boehly, T. J. B. Collins, O. V. Gotchev, T. J. Kessler, J. P. Knauer, T. C. Sangster, and D. D. Meyerhofer, "Observations of Modulated Shock Waves in Solid Targets Driven by Spatially Modulated Laser Beams," J. Appl. Phys. **92**, 1212 (2002).

H. Brunnader, W. T. Shmayda, D. R. Harding, L. D. Lund, and R. Janezic, "Advanced Tritium Recovery System," Fusion Sci. Technol. **41**, 840 (2002).

Y. Cao, H. Li, J. A. Szpunar, and W. T. Shmayda, "Effects of Textures on Hydrogen Diffusion in Nickel," in *Textures of Materials*, Materials Science Forum, Vols. 408–412, edited by D. N. Lee (Trans Tech Publications, Aedermannsdorf, Switzerland, 2002), Part 2, pp. 1139–1144.

H.-M. P. Chen, S. W. Culligan, Y. H. Geng, D. Katsis, and S. H. Chen, "Photoresponsive Glassy Liquid Crystals for Tunable Reflective Coloration," Polymer Preprints **43**, 145 (2002).

T. J. B. Collins and S. Skupsky, "Imprint Reduction Using an Intensity Spike in OMEGA Cryogenic Targets," Phys. Plasmas **9**, 275 (2002).

J. E. DeGroote, S. D. Jacobs, L. L. Gregg, A. E. Marino, and J. C. Hayes, "Quantitative Characterization of Optical Polishing Pitch," in *Optical Manufacturing and Testing IV*, edited by H. P. Stahl (SPIE, Bellingham, WA, 2001), Vol. 4451, pp. 209–221.

W. R. Donaldson, R. Boni, R. L. Keck, and P. A. Jaanimagi, "A Self-Calibrating, Multichannel Streak Camera for Inertial Confinement Fusion Applications," Rev. Sci. Instrum. **73**, 2606 (2002).

W. R. Donaldson, J. H. Kelly, R. L. Keck, and R. Boni, "Predicting and Measuring Optical Pulse Shapes on the OMEGA Laser System," in OSA *Trends in Optics and Photonics (TOPS) Vol. 56, Conference on Lasers and Electro-Optics (CLEO 2001)* (Optical Society of America, Washington, DC, 2001), pp. 158–159.

F. Y. Fan, S. W. Culligan, J. C. Mastrangelo, D. Katsis, S. H. Chen, and T. N. Blanton, "Novel Glass-Forming Liquid Crystals. 6. High-Temperature Glassy Nematics," Chem. Mater. **13**, 458 (2001).

Y. Geng, D. Katsis, S. W. Culligan, J. J. Ou, S. H. Chen, and L. J. Rothberg, "Fully Spiro-Configured Terfluorenes as Novel Amorphous Materials Emitting Blue Light," Chem. Mater. **14**, 463 (2002).

G. Gol'tsman, O. Okunev, G. Chulkova, A. Lipatov, A. Dzardanov, K. Smirnov, A. Semenov, B. Voronov, C. Williams, and R. Sobolewski, "Fabrication and Properties of an Ultrafast NbN Hot-Electron Single-Photon Detector," IEEE Trans. Appl. Supercond. **11**, 574 (2001).

V. N. Goncharov, "Analytical Model of Nonlinear, Single-Mode, Classical Rayleigh–Taylor Instability at Arbitrary Atwood Numbers," Phys. Rev. Lett. **88**, 134502 (2002).

M. J. Guardalben, A. Babushkin, R. S. Craxton, R. L. Keck, W. R. Donaldson, and K. A. Thorp, "Obtaining UV Energy Balance with 1-THz Spectral Bandwidth on the 60-Beam OMEGA Laser," in OSA *Trends in Optics and Photonics (TOPS) Vol. 56, Conference on Lasers and Electro-Optics (CLEO 2001)* (Optical Society of America, Washington, DC, 2001), p. 157.

M. J. Guardalben, L. Ning, N. Jain, D. J. Battaglia, and K. L. Marshall, "Experimental Comparison of a Liquid-Crystal Point-Diffraction Interferometer (LCPDI) and a Commercial Phase-Shifting Interferometer and Methods to Improve LCPDI Accuracy," Appl. Opt. **41**, 1353 (2002).

L. T. Hudson, A. Hennis, R. D. Deslattes, J. F. Seely, G. E. Holland, R. Atkin, L. Marlin, D. D. Meyerhofer, and C. Stoeckl, "A High-Energy X-Ray Spectrometer Diagnostic for the OMEGA Laser," Rev. Sci. Instrum. **73**, 2270 (2002).

I. V. Igumenshchev, "On Angular Momentum Transport in Convection-Dominated Accretion Flows," Astrophys. J. **577**, L31 (2002).

S. D. Jacobs, S. R. Arrasmith, I. A. Kozhinova, S. R. Gorodkin, L. L. Gregg, H. J. Romanofsky, T. D. Bishop II, A. B. Shorey, and W. I. Kordonski, "Effects of Changes in Fluid Composition on Magnetorheological Finishing (MRF) of Glasses and Crystals," in *Initiatives of Precision Engineering at the Beginning of a Millennium*, edited by I. Inasaki (Kluwer Academic Publishers, Boston, 2001), pp. 501–505.

S. D. Jacobs and L. L. Gregg, "Making Waves with the Optics Suitcase," Opt. Photonics News **13**, 12 (2002).

D. Katsis, Y. H. Geng, J. J. Ou, S. W. Culligan, A. Trajkovska, S. H. Chen, and L. J. Rothberg, "Spiro-Linked Ter-, Penta-, and Heptafluorenes as Novel Amorphous Materials for Blue Light Emission," Chem. Mater. **14**, 1332 (2002).

D. Katsis, Y. H. Geng, J. J. Ou, S. W. Culligan, A. Trajkovska, S. H. Chen, and L. J. Rothberg, "Spiro-Linked Ter- and Pentafluorenes for Stable and Efficient Blue Emission," Polymer Preprints **43**, 118 (2002).

R. L. Keck, W. R. Donaldson, V. Yu. Glebov, P. A. Jaanimagi, F. J. Marshall, P. W. McKenty, D. D. Meyerhofer, S. P. Regan, W. Seka, C. Stoeckl, and R. Boni, "Laser and X-Ray Irradiation Diagnostics That Have Paved the Path to Significantly Improved ICF Target Performance," in *Advanced Diagnostics for Magnetic and Inertial Fusion*, edited by P. E. Stott, A. Wootton, G. Gorini, E. Sindoni, and D. Batani (Kluwer Academic/Plenum Publishers, New York, 2002), pp. 181–188.

T. Z. Kosc, K. L. Marshall, S. D. Jacobs, J. C. Lambropoulos, and S. M. Faris, "Electric-Field-Induced Motion of Polymer Cholesteric Liquid-Crystal Flakes in a Moderately Conductive Fluid," Appl. Opt. **41**, 5362 (2002).

I. A. Kozhinova, S. R. Arrasmith, J. C. Lambropoulos, S. D. Jacobs, and H. J. Romanofsky, "Exploring Anisotropy in Removal Rate for Single Crystal Sapphire Using MRF," in *Optical Manufacturing and Testing IV*, edited by H. P. Stahl (SPIE, Bellingham, WA, 2001), Vol. 4451, pp. 277–285.

M. V. Kozlov and C. J. McKinstrie, "Sound Waves in Two-Ion Plasmas," Phys. Plasmas **9**, 3783 (2002).

P. Kús, A. Plecenik, L. Satrapinsky, Y. Xu, and R. Sobolewski, "Superconducting Properties of MgB_2 Thin Films Prepared on Flexible Substrates," Appl. Phys. Lett. **81**, 2199 (2002).

J. M. Larkin, W. R. Donaldson, R. S. Knox, and T. H. Foster, "Reverse Intersystem Crossing in Rose Bengal. II. Fluence Dependence of Fluorescence Following 532-nm Laser Excitation," Photobiochem. Photobiophys. **75**, 221 (2002).

S. V. Lebedev, J. P. Chittenden, F. N. Beg, S. N. Bland, A. Ciardi, D. Ampleford, S. Hughes, M. G. Haines, A. Frank, E. G. Blackman, and T. Gardiner, "Laboratory Astrophysics and Collimated Stellar Outflows: The Production of Radiatively Cooled Hypersonic Plasma Jets," Astrophys. J. **564**, 113 (2002).

C. K. Li, F. H. Séguin, D. G. Hicks, J. A. Frenje, K. M. Green, S. Kurebayashi, R. D. Petrasso, D. D. Meyerhofer, J. M. Soures, V. Yu. Glebov, R. L. Keck, P. B. Radha, S. Roberts, W. Seka, S. Skupsky, C. Stoeckl, and T. C. Sangster, "Study of Direct-Drive, DT-Gas-Filled Plastic Capsule Implosions Using Nuclear Diagnostics at OMEGA," Phys. Plasmas **8**, 4902 (2001).

J. A. Marozas, "Self- and Cross-Phase Modulation of High-Intensity Laser Beams Emerging from a Diamond-Turned KDP Wedge," J. Opt. Soc. Am. B **19**, 75 (2002).

J. A. Marozas, S. P. Regan, J. H. Kelly, D. D. Meyerhofer, W. Seka, and S. Skupsky, "Laser Beam Smoothing Caused by the Small-Spatial-Scale *B*-Integral," J. Opt. Soc. Am. B **19**, 7 (2002).

R. L. McCrory, R. E. Bahr, R. Betti, T. R. Boehly, T. J. B. Collins, R. S. Craxton, J. A. Delettrez, W. R. Donaldson, R. Epstein, J. Frenje, V. Yu. Glebov, V. N. Goncharov, O. V. Gotchev, R. Q. Gram, D. R. Harding, D. G. Hicks, P. A. Jaanimagi, R. L. Keck, J. Kelly, J. P. Knauer, C. K. Li, S. J. Loucks, L. D. Lund, F. J. Marshall, P. W. McKenty, D. D. Meyerhofer, S. F. B. Morse, R. D. Petrasso, P. B. Radha, S. P. Regan, S. Roberts, F. H. Séguin, W. Seka, S. Skupsky, V. A. Smalyuk, C. Sorce, J. M. Soures, C. Stoeckl, R. P. J. Town, M. D. Wittman, B. Yaakobi, and J. D. Zuegel, "OMEGA ICF Experiments and Preparation for Direct-Drive Ignition on NIF," Nucl. Fusion **41**, 1413 (2001).

D. D. Meyerhofer, J. A. Delettrez, R. Epstein, V. Yu. Glebov, V. N. Goncharov, R. L. Keck, R. L. McCrory, P. W. McKenty, F. J. Marshall, P. B. Radha, S. P. Regan, S. Roberts, W. Seka, S. Skupsky, V. A. Smalyuk, C. Sorce, C. Stoeckl, J. M. Soures, R. P. J. Town, B. Yaakobi, J. A. Frenje, C. K. Li, R. D. Petrasso, F. H. Séguin, K. Fletcher, S. Padalino, C. Freeman, N. Izumi, R. A. Lerche, T. W. Phillips, and T. C. Sangster, "Inferences of Mix in Direct-Drive Spherical Implosions with High Uniformity," Plasma Phys. Control. Fusion **43**, A277 (2001).

A. V. Okishev, A. Babushkin, R. E. Bahr, T. R. Boehly, R. Boni, R. S. Craxton, W. R. Donaldson, M. J. Guardalben, P. A. Jaanimagi, S. D. Jacobs, R. L. Keck, J. H. Kelly, T. J. Kessler, S. A. Letzring, S. J. Loucks, F. J. Marshall, R. L. McCrory, S. F. B. Morse, R. G. Roides, T. A. Safford, W. Seka, M. J. Shoup III, M. D. Skeldon, S. Skupsky, J. M. Soures, K. A. Thorp, and J. D. Zuegel, "High-Energy Solid-State Lasers for ICF Applications," in *Proceedings of the International Congress on Optics–XXI Century* (St. Petersburg Institute of Fine Mechanics and Optics, St. Petersburg, Russia, 2000), pp. 10–18.

A. V. Okishev, D. Battaglia, I. Begishev, and J. D. Zuegel, "Highly Stable, Diode-Pumped, Cavity-Dumped Nd:YLF Regenerative Amplifier for the OMEGA Laser Fusion Facility," in *OSA TOPS Vol. 68, Advanced Solid-State Lasers,* edited by M. E. Fermann and L. R. Marshall (Optical Society of America, Washington, DC, 2002), pp. 418–422.

A. V. Okishev, M. D. Skeldon, R. L. Keck, and W. Seka, "A New High-Bandwidth, All-Solid-State Pulse-Shaping System for the OMEGA Laser Facility," in *Laser Optics 2000: Ultrafast Optics and Superstrong Laser Fields*, edited by A. A. Andreev and V. E. Yashin (SPIE, Bellingham, WA, 2001), pp. 69–73.

S. Papernov and A. W. Schmid, "Establishing Links Between Single Gold Nanoparticles Buried Inside SiO_2 Thin Film and 351-nm Pulsed Laser Damage Morphology," in *Laser-Induced Damage in Optical Materials: 2001*, edited by G. J. Exarhos, A. H. Guenther, K. L. Lewis, M. J. Soileau, and C. J. Stolz (SPIE, Bellingham, WA, 2002), Vol. 4679, pp. 282–292.

S. Papernov, A. W. Schmid, R. Krishnan, and L. Tsybeskov, "Using Colloidal Gold Nanoparticles for Studies of Laser Interaction with Defects in Thin Films," in *Laser-Induced Damage in Optical Materials: 2000*, edited by G. J. Exarhos, A. H. Guenther, M. R. Kozlowski, K. L. Lewis, and M. J. Soileau (SPIE, Bellingham, WA, 2001), pp. 146–154.

P. B. Radha, J. A. Delettrez, R. Epstein, V. Yu. Glebov, R. L. Keck, R. L. McCrory, P. W. McKenty, D. D. Meyerhofer, F. J. Marshall, S. P. Regan, S. Roberts, T. C. Sangster, W. Seka, S. Skupsky, V. A. Smalyuk, C. Sorce, C. Stoeckl, J. M. Soures, R. P. J. Town, B. Yaakobi, J. A. Frenje, C. K. Li, R. D. Petrasso, F. H. Séguin, K. Fletcher, S. Padalino, C. Freeman, N. Izumi, R. A. Lerche, and T. W. Phillips, "Inference of Mix in Direct-Drive Implosions on OMEGA," Phys. Plasmas **9**, 2208 (2002) (invited).

S. P. Regan, J. A. Delettrez, R. Epstein, P. A. Jaanimagi, B. Yaakobi, V. A. Smalyuk, F. J. Marshall, D. D. Meyerhofer, W. Seka, D. A. Haynes, Jr., I. E. Golovkin, and C. F. Hooper, Jr., "Characterization of Direct-Drive-Implosion Core Conditions on OMEGA with Time-Resolved Ar *K*-Shell Spectroscopy," Phys. Plasmas **9**, 1357 (2002).

S. P. Regan, J. A. Delettrez, F. J. Marshall, J. M. Soures, V. A. Smalyuk, B. Yaakobi, R. Epstein, V. Yu. Glebov, P. A. Jaanimagi, D. D. Meyerhofer, P. B. Radha, T. C. Sangster, W. Seka, S. Skupsky, C. Stoeckl, R. P. J. Town, D. A. Haynes, Jr., I. E. Golovkin, C. F. Hooper, Jr., J. A. Frenje, C. K. Li, R. D. Petrasso, and F. H. Séguin, "Shell Mix in Compressed Core of Spherical Implosions," Phys. Rev. Lett. **89**, 085003 (2002).

S. P. Regan, J. A. Delettrez, B. Yaakobi, V. A. Smalyuk, F. J. Marshall, R. Epstein, V. Yu. Glebov, P. A. Jaanimagi, D. D. Meyerhofer, P. B. Radha, W. Seka, S. Skupsky, J. M. Soures, C. Stoeckl, R. P. J. Town, D. A. Haynes, Jr., I. Golovkin, C. F. Hooper, Jr., J. A. Frenje, C. K. Li, R. D. Petrasso, and F. H. Séguin, "High-Density, Direct-Drive Implosions on OMEGA," in *Inertial Fusion Sciences and Applications 2001*, edited by K. A. Tanaka, D. D. Meyerhofer, and J. Meyer-ter-Vehn (Elsevier, Paris, 2002), pp. 89–95.

F. H. Séguin, C. K. Li, J. A. Frenje, D. G. Hicks, K. M. Green, S. Kurebayashi, R. D. Petrasso, J. M. Soures, D. D. Meyerhofer, V. Yu. Glebov, P. B. Radha, C. Stoeckl, S. Roberts, C. Sorce, T. C. Sangster, M. D. Cable, K. A. Fletcher, and S. Padalino, "Using Secondary-Proton Spectra to Study the Compression and Symmetry of Deuterium-Filled Targets at OMEGA," Phys. Plasmas **9**, 2725 (2002).

F. H. Séguin, C. K. Li, J. A. Frenje, S. Kurebayashi, R. D. Petrasso, F. J. Marshall, D. D. Meyerhofer, J. M. Soures, T. C. Sangster, C. Stoeckl, J. A. Delettrez, P. B. Radha, V. A. Smalyuk, and S. Roberts, "Measurements of rR Asymmetries at Burn Time in Inertial-Confinement-Fusion Capsules," Phys. Plasmas **9**, 3558 (2002).

W. Seka, R. S. Craxton, R. L. Keck, J. P. Knauer, D. D. Meyerhofer, S. P. Regan, C. Stoeckl, B. Yaakobi, R. E. Bahr, D. Montgomery, H. Baldis, and R. Kirkwood, "Laser–Plasma Interaction Diagnostics for ICF Fusion Research," in *Advanced Diagnostics for Magnetic and Inertial Fusion*, edited by P. E. Stott, A. Wootton, G. Gorini, E. Sindoni, and D. Batani (Kluwer Academic/Plenum Publishers, New York, 2002), pp. 27–30.

A. D. Semenov, G. N. Gol'tsman, and R. Sobolewski, "Hot-Electron Effect in Superconductors and Its Applications for Radiation Sensors," Supercond. Sci. Technol. **15**, R1 (2002).

W. T. Shmayda, A. Bruggeman, J. Braet, and S. Vanderbiesen, "Treatment of Tritiated Solvents," Fusion Sci. Technol. **41**, 721 (2002).

W. T. Shmayda and R. D. Gallagher, "Recovery of Tritium from Pharmaceutical Mixed Waste Liquids," Fusion Sci. Technol. **41**, 726 (2002).

C. R. Shmayda, W. T. Shmayda, and N. P. Kherani, "Monitoring Tritium Activity on Surfaces: Recent Developments," Fusion Sci. Technol. **41**, 500 (2002).

A. B. Shorey, S. D. Jacobs, W. I. Kordonski, and R. F. Gans, "Experiments and Observations Regarding the Mechanisms of Glass Removal in Magnetorheological Finishing," Appl. Opt. **40**, 20 (2001).

A. B. Shorey, K. M. Kwong, K. M. Johnson, and S. D. Jacobs, "Nanoindentation Hardness of Particles Used in Magnetorheological Finishing (MRF)," Appl. Opt. **39**, 5194 (2000).

R. W. Short and A. Simon, "Damping of Perturbations in Weakly Collisional Plasmas," Phys. Plasmas **9**, 3245 (2002).

S. Skupsky, R. Betti, T. J. B. Collins, V. N. Goncharov, D. R. Harding, R. L. McCrory, P. W. McKenty, D. D. Meyerhofer, and R. P. J. Town, "High-Gain Direct-Drive Target Designs for the National Ignition Facility," in *Inertial Fusion Sciences and Applications 2001*, edited by K. A. Tanaka, D. D. Meyerhofer, and J. Meyer-ter-Vehn (Elsevier, Paris, 2002), pp. 243–245.

S. Skupsky, R. L. McCrory, R. E. Bahr, T. R. Boehly, T. J. B. Collins, R. S. Craxton, J. A. Delettrez, W. R. Donaldson, R. Epstein, V. N. Goncharov, R. Q. Gram, D. R. Harding, P. A. Jaanimagi, R. L. Keck, J. P. Knauer, S. J. Loucks, F. J. Marshall, P. W. McKenty, D. D. Meyerhofer, S. F. B. Morse, O. V. Gotchev, P. B. Radha, S. P. Regan, W. Seka, V. A. Smalyuk, J. M. Soures, C. Stoeckl, R. P. J. Town, M. D. Wittman, B. Yaakobi, J. D. Zuegel, R. D. Petrasso, J. A. Frenje, D. G. Hicks, C. K. Li, and F. H. Séguin, "OMEGA Experiments and Preparation for Direct-Drive Ignition on NIF," in *ECLIM 2000: 26th European Conference on Laser Interaction with Matter*, edited by M. Kálal, K. Rohlena, and M. Sinor (SPIE, Bellingham, WA, 2001), Vol. 4424, pp. 27–36.

V. A. Smalyuk, J. A. Delettrez, V. N. Goncharov, F. J. Marshall, D. D. Meyerhofer, S. P. Regan, T. C. Sangster, R. P. J. Town, and B. Yaakobi, "Rayleigh–Taylor Instability in the Deceleration Phase of Spherical Implosion Experiments," Phys. Plasmas **9**, 2738 (2002).

R. Sobolewski, "Ultrafast Optoelectronic Interface for Digital Superconducting Electronics," Supercond. Sci. Technol. **14**, 994 (2001).

R. Sobolewski, Y. Xu, X. Zheng, C. Williams, J. Zhang, A. Verevkin, G. Chulkova, A. Korneev, A. Lipatov, O. Okunev, K. Smirnov, and G. N. Gol'tsman, "Spectral Sensitivity of the NbN Single-Photon Superconducting Detector," IEICE Trans. Electron. **E85-C**, 797 (2002).

C. Stoeckl, C. Chiritescu, J. A. Delettrez, R. Epstein, V. Yu. Glebov, D. R. Harding, R. L. Keck, S. J. Loucks, L. D. Lund, R. L. McCrory, P. W. McKenty, F. J. Marshall, D. D. Meyerhofer, S. F. B. Morse, S. P. Regan, P. B. Radha, S. Roberts, T. C. Sangster, W. Seka, S. Skupsky, V. A. Smalyuk, C. Sorce, J. M. Soures, R. P. J. Town, J. A. Frenje, C. K. Li, R. D. Petrasso, F. H. Séguin, K. Fletcher, S. Padalino, C. Freeman, N. Izumi, R. A. Lerche, and T. W. Phillips, "First Results from Cryogenic-Target Implosions on OMEGA," Phys. Plasmas **9**, 2195 (2002) (invited).

C. Stoeckl, J. A. Delettrez, R. Epstein, V. Yu. Glebov, R. L. Keck, R. L. McCrory, P. W. McKenty, F. J. Marshall, D. D. Meyerhofer, P. B. Radha, S. P. Regan, S. Roberts, W. Seka, S. Skupsky, V. A. Smalyuk, C. Sorce, J. M. Soures, R. P. J. Town, B. Yaakobi, J. A. Frenje, C. K. Li, R. D. Petrasso, F. H. Séguin, K. Fletcher, S. Padalino, C. Freeman, N. Izumi, R. Lerche, T. W. Phillips, and T. C. Sangster, "Core Performance and Mix in Direct-Drive Spherical Implosions on OMEGA," in *Advanced Diagnostics for Magnetic and Inertial Fusion*, edited by P. E. Stott, A. Wootton, G. Gorini, E. Sindoni, and D. Batani (Kluwer Academic/Plenum Publishers, New York, 2002), pp. 19–26.

R. P. J. Town, J. A. Delettrez, R. Epstein, V. N. Goncharov, C. K. Li, R. L. McCrory, P. W. McKenty, P. B. Radha, S. Skupsky, V. Yu. Glebov, D. R. Harding, D. D. Meyerhofer, F. J. Marshall, R. D. Petrasso, S. P. Regan, F. H. Séguin,

W. Seka, V. A. Smalyuk, C. Stoeckl, J. M. Soures, and J. D. Zuegel, "OMEGA Direct-Drive Cryogenic Target Physics," in *Inertial Fusion Sciences and Applications 2001*, edited by K. A. Tanaka, D. D. Meyerhofer and J. Meyer-ter-Vehn (Elsevier, Paris, 2002), pp. 126–131.

F.-Y. Tsai, E. L. Alfonso, S. H. Chen, D. R. Harding, and T. N. Blanton, "Effects of Processing Conditions on the Quality and Properties of Vapor-Deposited Polyimide Shells," Fusion Sci. Technol. **41**, 178 (2002).

F.-Y. Tsai, E. L. Alfonso, D. R. Harding, and S. H. Chen, "Processing Vapor-Deposited Polyimide," J. Phys. D: Appl. Phys. **34**, 3011 (2001).

A. Verevkin, J. Zhang, R. Sobolewski, A. Lipatov, O. Okunev, G. Chulkova, A. Korneev, K. Smirnov, and G. N. Gol'tsman, "Detection Efficiency of Large-Active-Area NbN Single-Photon Superconducting Detectors in the Ultraviolet in Near-Infrared Range," Appl. Phys. Lett. **80**, 4687 (2002).

L. J. Waxer, J. H. Kelly, J. Rothenberg, A. Babushkin, C. Bibeau, A. Bayramian, and S. Payne, "Precision Spectral Sculpting for Narrowband Amplification of Broadband Frequency-Modulated Pulses," Opt. Lett. **27**, 1427 (2002).

C. Williams, G. Sabouret, and R. Sobolewski, "Experiments and Simulations of Electrical Pulse Modulation of Y-Ba-Cu-O Thin Films," IEICE Trans. Electron. **E85-C**, 733 (2002).

C. Williams, Y. Xu, R. Adam, M. Darula, O. Harnack, J. Scherbel, M. Siegel, F. A. Hegmann, and R. Sobolewski, "Ultrafast YBCO Photodetector Based on the Kinetic-Inductive Process," IEEE Trans. Appl. Supercond. **11**, 578 (2001).

B. Yaakobi, C. Stoeckl, T. R. Boehly, R. S. Craxton, D. D. Meyerhofer, and W. Seka, "Measurement of Preheat Due to Fast Electrons in Laser Implosions," in *26th European Conference on Laser Interaction with Matter*, edited by M. Kalal, K. Rohlena, and M. Sinor (SPIE, Bellingham, WA, 2001), Vol. 4424, pp. 392–401.

OMEGA External User Publications

P. A. Amendt, J. D. Colvin, R. E. Tipton, D. E. Hinkel, M. J. Edwards, O. L. Landen, J. D. Ramshaw, L. J. Suter, W. S. Varnum, and R. G. Watt, "Indirect-Drive Noncryogenic Double-Shell Ignition Targets for the National Ignition Facility: Design and Analysis," Phys. Plasmas **9**, 2221 (2002).

C. A. Back, J. Grun, C. Decker, L. J. Suter, J. Davis, O. L. Landen, R. J. Wallace, W. W. Hsing, J. M. Laming, U. Feldman, M. C. Miller, and C. Wuest, "Efficient Multi-keV Underdense Laser-Produced Plasma Radiators," Phys. Rev. Lett. **87**, 275003 (2001).

D. K. Bradley, O. L. Landen, A. B. Bullock, S. G. Glendinning, and R. E. Turner, "Efficient 1–100-keV X-Ray Radiography with Spatial and Temporal Resolution," Opt. Lett. **27**, 134 (2002).

A. C. Calder and E. Y. M. Wang, "Numerical Models of Binary Neutron Star System Mergers. II. Coalescing Models with Post-Newtonian Radiation Reaction Forces," Astrophys. J. **570**, 303 (2002).

L. Disdier, A. Rouyer, D. C. Wilson, A. Fedotoff, C. Stoeckl, J.-L. Bourgade, V. Yu. Glebov, J.-P. Garçonnet, and W. Seka, "High-Resolution Neutron Imaging of Laser-Imploded DT Targets," Nucl. Instrum. Methods Phys. Res. A **489**, 496 (2002).

R. P. Drake and P. A. Keiter, "Rayleigh–Taylor Growth in Decelerating Interfaces," Phys. Plasmas **9**, 382 (2002).

R. P. Drake, H. F. Robey, O. A. Hurricane, Y. Zhang, B. A. Remington, J. P. Knauer, J. Glimm, D. Arnett, J. O. Kane, K. S. Budil, and J. Grove, "Experiments to Produce a Hydrodynamically Unstable Spherically Diverging System of Relevance to Instabilities in Supernovae," Astrophys. J. **564**, 896 (2002).

R. K. Fisher, R. B. Stephens, L. Disdier, J. L. Bourgade, A. Rouyer, P. A. Jaanimagi, T. C. Sangster, R. A. Lerche, and N. Izumi, "High-Resolution Neutron Imaging of Laser Fusion Targets Using Bubble Detectors," Phys. Plasmas **9**, 2182 (2002).

J. M. Foster, B. H. Wilde, P. A. Rosen, T. S. Perry, M. Fell, M. J. Edwards, B. F. Lasinski, R. E. Turner, and M. L. Gittings, "Supersonic Jet and Shock Interactions," Phys. Plasmas **9**, 2251 (2002).

J. A. Frenje, C. K. Li, F. H. Séguin, D. G. Hicks, S. Kurebayashi, R. D. Petrasso, S. Roberts, V. Yu. Glebov, D. D. Meyerhofer, T. C. Sangster, J. M. Soures, C. Stoeckl, C. Chiritescu, G. J. Schmid, and R. A. Lerche, "Absolute Measurements of Neutron Yields from DD and DT Implosions at the OMEGA Laser Facility Using CR-39 Track Detectors," Rev. Sci. Instrum. **73**, 2597 (2002).

D. H. Kalantar, A. M. Allen, F. Gregori, B. Kad, M. Kumar, K. T. Lorenz, A. Loveridge, M. A. Meyers, S. Pollaine, B. A. Remington, and J. S. Wark, "Laser-Driven, High-Pressure, High-Strain-Rate Materials Experiments," in *Shock Compression of Compressed Matter–2001*, AIP Conference Proceedings 620, edited by M. D. Furnish, N. N. Thadhani, and Y. Horie (American Institute of Physics, New York, 2002), pp. 615–618.

O. L. Landen, S. H. Glenzer, M. J. Edwards, R. W. Lee, G. W. Collins, R. C. Cauble, W. W. Hsing, and B. A. Hammel, "Dense Matter Characterization by X-Ray Thomson Scattering," J. Quant. Spectrosc. Radiat. Transf. **7**, 465 (2001).

A. B. Langdon and D. E. Hinkel, "Nonlinear Evolution of Stimulated Scatter in High-Temperature Plasmas," Phys. Rev. Lett. **89**, 015003 (2002).

M. A. Meyers, F. Gregori, B. K. Kad, M. S. Schneider, D. H. Kalantar, B. A. Remington, J. S. Wark, T. Boehly, and G. Ravichandran, "Plastic Deformation in Laser-Induced Shock Compression of Monocrystalline Copper," in *Shock Compression of Compressed Matter–2001*, AIP Conference Proceedings 620, edited by M. D. Furnish, N. N. Thadhani, and Y. Horie (American Institute of Physics, New York, 2002), pp. 619–622.

A. Nickroo, D. G. Czechowicz, E. R. Castillo, and J. M. Pontelandolfo, "Recent Progress in Fabrication of High-Strength Glow Discharge Polymer Shells by Optimization of Coating Parameters," Fusion Sci. Technol. **41**, 214 (2002).

H. F. Robey, T. S. Perry, R. I. Klein, J. O. Kane, J. A. Greenough, and T. R. Boehly, "Experimental Investigation of the Three-Dimensional Interaction of a Strong Shock with a Spherical Density Inhomogeneity," Phys. Rev. Lett. **89**, 085001 (2002).

Conference Presentations

S. Papernov and A. W. Schmid, "Establishing Links Between Single Gold Nanoparticles Buried Inside SiO_2 Thin Film and 351-nm Pulsed Laser Damage Morphology," XXXIII Annual Symposium on Optical Materials for High Power Lasers, Boulder, CO, 1–3 October 2001.

K. L. Marshall, I. A. Lippa, S. Kinsella, M. S. Moore, S. M. Corsello, and A. Ayub, "Chiral Transition Metal Dithiolene Dye Complexes and Their Potential Applications in Liquid Crystal Devices," OSA Annual Meeting and Exhibit 2001, Long Beach, CA, 14–18 October 2001.

B. Yaakobi, F. J. Marshall, T. R. Boehly, R. P. J. Town, D. D. Meyerhofer, and W. Seka, "EXAFS Detection of Laser Shock Heating," Applications of High Field and Short Wavelength Sources IX, Palm Springs, CA, 21–24 October 2001.

The following presentations were made at the 43rd Annual Meeting of the APS Division of Plasma Physics, Long Beach, CA, 29 October–2 November 2001:

K. Anderson, R. Betti, and T. A. Gardiner, "Two-Dimensional Computational Model of Energy Gain in NIF Capsules."

R. Betti, V. N. Goncharov, J. P. Knauer, P. W. McKenty, D. D. Meyerhofer, R. L. McCrory, S. Skupsky, and R. P. J. Town, "Deceleration Phase of Inertial Confinement Fusion Implosions" (invited).

T. R. Boehly, T. J. B. Collins, D. D. Meyerhofer, W. J. Armstrong, D. K. Bradley, R. Cauble, P. M. Celliers, G. W. Collins, and S. G. Glendinning, "Measurements of the Equation of State of Carbon Foams."

T. J. B. Collins, S. Skupsky, R. Betti, V. N. Goncharov, D. R. Harding, R. L. McCrory, P. W. McKenty, R. P. J. Town, and D. D. Meyerhofer, "Wetted-Foam Target Designs for the NIF."

J. A. Delettrez, V. A. Smalyuk, F. J. Marshall, P. B. Radha, and B. Yaakobi, "Simulations of the Effect of Nonuniformity on Shell Conditions in Implosions on the OMEGA Laser."

R. Epstein, J. A. Delettrez, V. N. Goncharov, P. W. McKenty, P. B. Radha, C. Stoeckl, and S. Skupsky, "One-Dimensional Simulation of the Effects of Unstable Mix on Laser-Driven Implosion Experiments."

J. A. Frenje, C. K. Li, F. H. Séguin, S. Kurebayashi, R. D. Petrasso, P. B. Radha, J. M. Soures, D. D. Meyerhofer, V. Yu. Glebov, S. Roberts, C. Stoeckl, and T. C. Sangster, "Studies of Fuel rR on OMEGA from DTH-Gas-Filled Capsules."

T. A. Gardiner, R. Betti, and L. Guazzotto, "Two-Dimensional MHD Simulation of Tokamak Plasmas with Poloidal Flow."

V. Yu. Glebov, D. D. Meyerhofer, P. B. Radha, W. Seka, S. Skupsky, C. Sorce, J. M. Soures, C. Stoeckl, S. Padalino, L. Baumgart, R. Colburn, J. Fuschino, and T. C. Sangster, "Tertiary Neutron Measurements by Carbon Activation."

V. N. Goncharov, R. Betti, J. A. Marozas, P. W. McKenty, S. Skupsky, and R. P. J. Town, "Optimization of Direct-Drive Target Designs for the NIF."

O. V. Gotchev, V. N. Goncharov, P. A. Jaanimagi, J. P. Knauer, and D. D. Meyerhofer, "Streaked X-Ray Imager for Observation of Oscillations of Perturbed Ablation Fronts in Planar ICF Targets During Shock Transit."

D. R. Harding, M. D. Wittman, L. Elasky, L. S. Iwan, and L. D. Lund, "Forming Uniform Deuterium Ice Layers in Cryogenic Targets: Experiences Using the OMEGA Target Handling System."

C. K. Li, F. H. Séguin, J. A. Frenje, S. Kurebayashi, R. D. Petrasso, D. D. Meyerhofer, J. M. Soures, V. Yu. Glebov, P. B. Radha, S. P. Regan, S. Roberts, S. Skupsky, C. Stoeckl, and T. C. Sangster, "Direct-Drive, Spherical Implosions of OMEGA Capsules with 3 to 15 atm of Gas Fill."

J. A. Marozas, "A Reduced-Autocorrelation Phase-Plate Design for OMEGA and NIF."

F. J. Marshall, J. A. Delettrez, R. L. Keck, J. H. Kelly, P. B. Radha, and L. J. Waxer, "Direct-Drive Implosion Experiments with Enhanced Beam Balance on the OMEGA Laser."

D. D. Meyerhofer, B. Yaakobi, F. J. Marshall, T. R. Boehly, and R. P. J. Town, "EXAFS Detection of Laser Shock Heating."

R. D. Petrasso, C. K. Li, F. H. Séguin, J. A. Frenje, S. Kurebayashi, P. B. Radha, D. D. Meyerhofer, J. M. Soures, J. A. Delettrez, C. Stoeckl, S. Roberts, V. Yu. Glebov, W. Seka, C. Chiritescu, and T. C. Sangster, "Experimental Inferences of rR Evolution and the Spatial Extent of Mix from the D^{3}He, 14.7-MeV Proton Line Structure."

P. B. Radha, J. A. Delettrez, R. Epstein, V. Yu. Glebov, V. N. Goncharov, R. L. Keck, R. L. McCrory, P. W. McKenty, F. J. Marshall, D. D. Meyerhofer, S. P. Regan, S. Roberts, W. Seka, S. Skupsky, V. A. Smalyuk, C. Sorce, C. Stoeckl, J. M. Soures, R. P. J. Town, B. Yaakobi, J. A. Frenje, C. K. Li, R. D. Petrasso, F. H. Séguin, K. Fletcher, S. Padalino, C. Freeman, N. Izumi, R. A. Lerche, T. W. Phillips, and T. C. Sangster, "Inferences of Mix in Direct-Drive Spherical Implosion on OMEGA" (invited).

S. P. Regan, J. A. Delettrez, F. J. Marshall, J. M. Soures, V. A. Smalyuk, B. Yaakobi, V. Yu. Glebov, P. A. Jaanimagi, D. D. Meyerhofer, P. B. Radha, W. Seka, S. Skupsky, C. Stoeckl, R. P. J. Town, D. A. Haynes, C. F. Hooper, C. K. Li, R. D. Petrasso, and F. H. Séguin, "Spectroscopic Measurements of Fuel–Pusher Mix in Direct-Drive Implosions on OMEGA."

F. H. Séguin, R. D. Petrasso, C. K. Li, J. A. Frenje, S. Kurebayashi, J. A. Delettrez, J. M. Soures, D. D. Meyerhofer, F. J. Marshall, V. A. Smalyuk, S. Roberts, and T. C. Sangster, "Charged-Particle Measurements of Shell Asymmetries in Imploded Capsules on OMEGA."

W. Seka, S. P. Regan, D. D. Meyerhofer, B. Yaakobi, C. Stoeckl, R. S. Craxton, R. W. Short, H. Baldis, J. Fuchs, and C. Labaune, "Stimulated Brillouin Sidescatter and Backscatter in NIF-Scale Direct-Drive Plasmas."

R. W. Short, R. S. Craxton, W. Seka, and D. D. Meyerhofer, "Interpretation of Single- and Multiple-Beam SBS Observations in OMEGA Long-Scale-Length Plasma Experiments."

V. A. Smalyuk, J. A. Delettrez, V. N. Goncharov, F. J. Marshall, D. D. Meyerhofer, S. P. Regan, and B. Yaakobi, "Measurements of the Growth of Shell Nonuniformities in the Deceleration Phase of Spherical Implosions."

J. M. Soures, D. D. Meyerhofer, J. A. Delettrez, V. Yu. Glebov, J. A. Marozas, F. J. Marshall, P. B. Radha, S. P. Regan, S. Roberts, S. Seka, S. Skupsky, V. A. Smalyuk, C. Stoeckl, R. D. Petrasso, C. K. Li, F. H. Séguin, J. A. Frenje, and T. C. Sangster, "Comparison of the Effect of Different SSD Beam-Smoothing Configurations on Direct-Drive Capsule Implosions."

C. Stoeckl, C. Chiritescu, J. A. Delettrez, R. Epstein, V. Yu. Glebov, D. R. Harding, R. L. Keck, S. J. Loucks, L. D. Lund, R. L. McCrory, P. W. McKenty, F. J. Marshall, D. D. Meyerhofer, S. F. B. Morse, S. P. Regan, P. B. Radha, S. Roberts, W. Seka, S. Skupsky, V. A. Smalyuk, C. Sorce, J. M. Soures, R. P. J. Town, J. A. Frenje, C. K. Li, R. D. Petrasso, F. H. Séguin, K. Fletcher, S. Padalino, C. Freeman, N. Izumi, R. A. Lerche, T. W. Phillips, and T. C. Sangster, "First Results from Cryogenic-Target Implosions on OMEGA" (invited).

S. L. Sublett, J. P. Knauer, D. D. Meyerhofer, S. Skupsky, A. Frank, and A. Y. Poludenenko, "Properties of SiO$_2$ Aerogels Suitable for Astrophysical Experiments."

A. Sunahara, J. A. Delettrez, R. W. Short, and S. Skupsky, "Fokker–Planck Calculation of the ICF Implosion."

R. P. J. Town, J. A. Delettrez, R. Epstein, V. N. Goncharov, R. L. McCrory, P. W. McKenty, P. B. Radha, and S. Skupsky, "OMEGA Direct-Drive Cryogenic-Target Physics."

———————

The following presentations were made at the 6th International Conference on Tritium Science and Technology, Tsukuba, Japan, 6–11 November 2001:

H. Brunnader, W. T. Shmayda, D. R. Harding, L. D. Lund, and R. Janezic, "Advanced Tritium Recovery System."

W. T. Shmayda, A. Bruggeman, J. Braet, and S. Vanderbiesen, "Treatment of Tritiated Solvents."

W. T. Shmayda and R. D. Gallagher, "Recovery of Tritium from Pharmaceutical Mixed Waste Liquids."

C. R. Shmayda, W. T. Shmayda, and N. P. Kherani, "Monitoring Tritium Activity on Surfaces: Recent Developments."

W. T. Shmayda, S. Zukotynski, D. Yeghikyan, and F. Gaspari, "Properties of Amorphous Carbon Films."

———————

R. Epstein, J. A. Delettrez, V. Yu. Glebov, V. N. Goncharov, P. W. McKenty, P. B. Radha, S. Skupsky, V. A. Smalyuk, and C. Stoeckl, "One-Dimensional Simulation of the Effects of Unstable Mix on Neutron and Charged-Particle Yield from Laser-Driven Implosion Experiments," 8th International Workshop on the Physics of Compressible Turbulent Mixing, Pasadena, CA, 9–14 December 2001.

———

A. Sunahara, J. A. Delettrez, R. W. Short, S. Skupsky, and H. Takabe, "Nonlocal Electron Thermal Conduction in Laser Implosions," 15th Computational Fluid Dynamics Symposium, Tokyo, Japan, 19–21 December 2001.

———

D. D. Meyerhofer, B. Yaakobi, T. R. Boehly, F. J. Marshall, and R. P. J. Town, "EXAFS Detection of Heating of Metals by Shocks and Radiation," JOWOG 37, Lawrence Livermore National Laboratory, 28 January–1 February 2002.

———

A. V. Okishev, D. Battaglia, I. Begishev, and J. D. Zuegel, "Highly Stable, Diode-Pumped, Cavity-Dumped Nd:YLF Regenerative Amplifier for the OMEGA Laser Fusion Facility," OSA Advanced Solid-State Lasers, Quebec City, Canada, 3–6 February 2002.

———

W. Seka, "Laser–Plasma Interaction Studies on OMEGA Relevant to Direct-Drive NIF Ignition Targets," LULI Seminar, St. Lary, France, 4 March 2002.

———

W. T. Shmayda and R. D. Gallagher, "Recovery of Tritium from Pharmaceutical Mixed Waste Liquids and Solid Absorbents," 4th International Conference on Isotopes, Cape Town, South Africa, 10–14 March 2002.

———

J. D. Kilkenny, R. L. McCrory, D. D. Meyerhofer, S. F. B. Morse, J. H. Kelly, T. J. Kessler, S. J. Loucks, P. W. McKenty, C. Stoeckl, R. P. J. Town, L. J. Waxer, and J. D. Zuegel, "OMEGA EP: Extended-Performance Capability for the OMEGA Laser System, Including Short-Pulse Capability," Workshop on Ultra-High Field Laser Physics, Chilton, Oxford, 10–12 April 2002.

———

The following presentations were made at the 2002 International Sherwood Fusion Theory Conference, Rochester, NY, 22–24 April 2002:

T. Gardiner and R Betti, "Magnetohydrodynamic Equilibria with Pedestals Induced by Poloidal Flow."

L. Guazzotto and R. Betti, "Stabilization of the Resistive Wall Mode by Differentially Rotating Walls in a High-b Tokamak."

D. D. Meyerhofer, "Direct-Drive Inertial Confinement Fusion Research: Theory and Experiments."

R. W. Short, "Linear Undamped Waves in Near-Maxwellian Plasmas with Applications to Stimulated Raman Scattering in Laser-Produced Plasmas."

———

The following presentations were made at the CLEO/QELS 2002, Long Beach, CA, 19–24 May 2002:

S. G. Lukishova, R. W. Boyd, N. Lepeshkin, R. S. Bennik, and K. L. Marshall, "Feedback-Free Kaleidoscope of Patterns from Nanosecond Laser–Irradiated Nematic Liquid."

A. V. Okishev, D. Battaglia, I. Begishev, and J. Zuegel, "All Solid-State Diode-Pumped Regenerative Amplifier for the OMEGA Laser System."

L. J. Waxer, J. H. Kelly, J. A. Marozas, A. Babushkin, J. Rothenburg, C. Bibeau, A. Bayramian, R. Beach, and S. Payne, "Precision Spectral Shaping Applied to FM Pulses."

———

T. R. Boehly, T. J. B. Collins, D. D. Meyerhofer, D. K. Bradley, R. Cauble, P. M. Celliers, C. W. Collins, S. G. Glendinning, and D. G. Hicks, "Measurements of the Equation of State of Carbon Foams," International Conference on Warm, Dense Matter, Hamburg, Germany, 3–5 June 2002 (invited).

———

J. Li, W. R. Donaldson, and T. Y. Hsiang, "Packaging for a High-Speed Interdigitated GaN UV Photodetector," The 8th International Conference on Electronic Materials, IUMRS-ICEM2002, Xi'an, China, 10–14 June 2002.

———

S. G. Lukishova, R. W. Boyd, N. Lepeshkin, R. S. Bennink, and K. L. Marshall, "Feedback-Free Hexagon Pattern Formation with Nematic Liquid Crystals," IQEC 2002 International Quantum Electronics Conference, Moscow, Russia, 22–28 June 2002.

———

T. Z. Kosc, K. L. Marshall, S. D. Jacobs, and J. C. Lambropoulos, "Electric Field–Induced Rotation of Polymer Cholesteric Liquid Crystal Flakes: Mechanisms and Applications," International Symposium on Optical Science and Technology, Seattle, WA, 7–11 July 2002.

———

The following presentations were made at the 14th Topical Conference on High-Temperature Plasma Diagnostics, Madison, WI, 8–11 July 2002:

V. Yu. Glebov, C. Stoeckl, T. C. Sangster, D. D. Meyerhofer, P. B. Radha, S. Padalino, L. Baumgart, R. Coburn, and J. Fuschino, "Carbon Activation Diagnostic for Tertiary Neutron Measurements."

O. V. Gotchev, P. A. Jaanimagi, J. P. Knauer, F. J. Marshall, D. D. Meyerhofer, N. Bassett, and J. B. Oliver, "High-Throughput, High-Resolution, Kirkpatrick–Baez Microscope for Advanced Streaked Imaging of ICF Experiments on OMEGA."

D. L. McCrorey, R. C. Mancini, V. A. Smalyuk, S. P. Regan, and B. Yaakobi, "Spectroscopic Determination of Compressed-Shell Conditions in OMEGA Implosions Based on Ti K-Shell Line Absorption Analysis."

C. Stoeckl, V. Yu. Glebov, S. Roberts, T. C. Sangster, R. A. Lerche, and C. Sorce, "A TIM-Based Neutron Diagnostic for Cryogenic Experiments on OMEGA."

———

The following presentations were made at the 32nd Anomalous Absorption Conference, Oahu, HI, 21–26 July 2002:

J. A. Delettrez, J. P. Knauer, P. A. Jaanimagi, W. Seka, and C. Stoeckl, "Numerical Investigation of Recent Laser Absorption and Drive Experiments of CH Spherical Shells on the OMEGA Laser."

V. N. Goncharov, J. P. Knauer, P. W. McKenty, S. Skupsky, T. C. Sangster, R. Betti, and D. D. Meyerhofer, "Adiabat Shaping of Direct-Drive Inertial Confinement Fusion (ICF) Implosions Using a High-Intensity Picket."

C. K. Li, F. H. Séguin, J. A. Frenje, S. Kurebayashi, R. D. Petrasso, D. D. Meyerhofer, J. M. Soures, J. A. Delettrez, V. Yu Glebov, F. J. Marshall, P. B. Radha, S. P. Regan, S. Roberts, T. C. Sangster, and C. Stoeckl, "Effects of Fuel–Shell Mix on Direct-Drive, Spherical Implosions on OMEGA."

A. Maximov, J. Myatt, and R. W. Short, "Nonlinear Propagation of Laser Beams in Plasmas Near a Critical-Density Surface."

J. Myatt, A. Maximov, and R. W. Short, "Modeling Laser–Plasma Interaction Physics Under Direct-Drive Inertial Confinement Fusion Conditions."

R. D. Petrasso, R. Rygg, J. A. Frenje, C. K. Li, F. H. Séguin, S. Kurebayashi, B.-E. Schwartz, P. B. Radha, J. M. Soures, J. A. Delettrez, V. Yu. Glebov, D. D. Meyerhofer, S. Roberts, T. C. Sangster, C. Stoeckl, and S. Hatchett, "Capsule Areal-Density Nonuniformities and Evolution Inferred from 14.7-MeV Proton Line Structure in OMEGA D^{3}He Implosions."

S. P. Regan, R. S. Craxton, J. A. Delettrez, D. D. Meyerhofer, T. C. Sangster, W. Seka, and B. Yaakobi, "Experimental Investigation of Expansion Velocity and Gradients in Long-Scale-Length Plasmas on OMEGA."

W. Seka, C. Stoeckl, B. Yaakobi, R. S. Craxton, R. W. Short, and H. Baldis, "Fast-Electron Preheat of Direct-Drive Targets Due to the Two-Plasmon-Decay Instability."

R. W. Short, "A Linear Model of Anomalous Stimulated Raman Scattering and Electron-Acoustic Waves in Laser-Produced Plasmas."

V. A. Smalyuk, J. A. Delettrez, R. Epstein, V. N. Goncharov, F. J. Marshall, D. D. Meyerhofer, S. P. Regan, T. C. Sangster, B. Yaakobi, D. L. McCrorey, and R. C. Mancini, "Measurements of Heat Propagation in Compressed Shells in Direct-Drive Spherical Implosions on OMEGA."

V. A. Smalyuk, P. B. Radha, J. A. Delettrez, V. Yu. Glebov, V. N. Goncharov, J. P. Knauer, D. D. Meyerhofer, S. P. Regan, S. Roberts, T. C. Sangster, S. Skupsky, J. M. Soures, C. Stoeckl, R. P. J. Town, J. A. Frenje, C. K. Li, R. D. Petrasso, and F. H. Séguin, "Areal-Density-Growth Measurements with Proton Spectroscopy in Spherical Implosions on OMEGA."

———————

S. G. Lukishova, A. W. Schmid, and R. W. Boyd, "Near-Field Optical Microscopy of Cholesteric Oligomer Liquid Crystal Layers," 7th International Conference on Near-Field Optics and Related Techniques, Rochester, NY, 11–15 August 2002.

———————

D. W. Griffin and K. L. Marshall, "Phase-Shifting Liquid Crystal Interferometers for Microgravity Fluid Physics," 6th Microgravity Fluid Physics and Transport Phenomena Conference, Cleveland OH, 14–16 August 2002.

———————

S. Papernov and A. W. Schmid, "Damage Behavior of SiO_2 Thin Films Containing Gold Nanoparticles Lodged on a Pre-determined Distance from the Film Surface," XXXIV Annual Symposium on Optical Materials for High-Power Lasers, Boulder, CO, 16–19 September 2002.

———————

S. P. Regan, J. A. Delettrez, F. J. Marshall, J. M. Soures, V. A. Smalyuk, B. Yaakobi, R. Epstein, V. Yu. Glebov, P. A. Jaanimagi, D. D. Meyerhofer, P. B. Radha, T. C. Sangster, W. Seka, S. Skupsky, C. Stoeckl, D. A. Haynes, Jr., I. E. Golovkin, J. A. Frenje, C. K. Li, R. D. Petrasso, and F. H. Séguin, "Experimental Investigation of Shell Mix in the Compressed Core of Spherical Implosions Involving Hot, Dense Spectroscopy," 10th International Workshop on Radiative Properties of Hot Dense Matter, Saint-Malo, Brittany, France, 16–20 September 2002.

———————

S. D. Jacobs, H. M. Pollicove, E. M. Fees, and J. Schoen, "Aspheric Optics Manufacturing for Commercial and Military Systems," First Symposium for Explosive Materials, Weapons, and Military Technology, Ohrid, Republic of Macedonia, 25–28 September 2002.

———————

The following presentations were made at the 2002 OSA Annual Meeting, Orlando, FL, 29 September–3 October 2002:

M. J. Guardalben, J. Keegan, L. J. Waxer, and J. D. Zuegel, "Stability of Optical Parametric Amplification: Spatiotemporal Considerations in the Design of an OPCPA System."

S. G. Lukishova, R. W. Boyd, N. Lepeshkin, A. W. Schmid, and K. L. Marshall, "Feedback-Free Pattern Formation in Dye-Doped Liquid Crystals and Isotropic Liquids."

L. J. Waxer, V. Bagnoud, I. A. Begishev, M. J. Guardalben, J. Puth, and J. D. Zuegel, "Development of a High-Conversion-Efficiency OPCPA System for the OMEGA EP Laser System."